Universitat Jaume I, Departamento de Física
Escuela Superior de Tecnología y Ciencias Experimentales

Interfacial and Bulk Operation of Polymeric Solar Cells by Optoelectronic and Structural Techniques

Teresa Ripollés Sanchis

Tesis Doctoral
Programa de doctorado en Nanociencia y Nanotecnología

Directores
Prof. Germà Garcia Belmonte
Dr. Antonio Guerrero Castillejo

Castellón, Junio 2014

UNIVERSITAT JAUME•I

Universitat Jaume I, Departamento de Física
Escuela Superior de Tecnología y Ciencias Experimentales

Interfacial and Bulk Operation of Polymeric Solar Cells by Optoelectronic and Structural Techniques

Memoria presentada para aspirar al
Grado de Doctor por:

Teresa Ripollés Sanchis

Directores:

Prof. Germà Garcia Belmonte	Dr. Antonio Guerrero Castillejo
Catedrático de Física Aplicada	Doctor investigador

Castellón, 28 August 2014

To my parents

TABLE OF CONTENTS

APPENDIX IV

APPENDIX V

ACKNOWLEDGEMENTS

This Ph.D. Thesis was performed at the Photovoltaic and Optoelectronic Devices Group led by Prof. Juan Bisquert at Universitat Jaume I between January 2011 to December 2013 under financial support from Generalitat Valenciana in the project PROMETEO/2009/058.

I would really like to thank my advisor, Prof. Germà Garcia Belmonte, who introduced me to the organic photovoltaics and physics field. I am grateful to my supervisor Dr. Antonio Guerrero who was involved in directing my work. Without their continuous help and inspiration in my Ph.D. project, I would not have been able to make so many achievements and develop my ideas as a scientist.

I express my thanks to Prof. Juan Bisquert for providing me with his scientific knowledge and strongest support during my Ph.D. career. He has given me the opportunity to take part in many congresses, summer schools as well as work at prestigious universities around the world such as National Chiao Tung University (Taiwan) and Yale University (United States).

Undoubtedly, this work would not have been possible without the contributions of Dr. Mariano Campoy Quiles in ICMAB-CSIC (Barcelona) for his studies based on Variable-angle spectroscopic ellipsometry and Dr. Ramon Tena Zaera in IK4-CIDETEC (San Sebastian) for the synthesis of NiO by electrodeposition from aprotic ionic liquids on glass substrates.

I want to give sincere thanks to all my colleagues from the Photovoltaic and Optoelectronic Devices Group for their kindness and friendship. It was a pleasure for me to have many fruitful discussions with them and for helping me with my research and everyday life.

And finally, I am very thankful for the support of my friends and family, especially my parents. They have been an important part of making me who I am. I would not have come this far without them.

ABBREVIATIONS AND ACRONYMS

Abbreviation	Description	Units
A	Active surface	cm^2
AFM	Atomic Force Microscopy	
AM1.5G	Global reference solar spectrum for photovoltaic performance evaluation	
B	Recombination coefficient	
BHJ	Bulk heterojunction	
c	Speed of light	$3 \cdot 10^8\ m\,s^{-1}$
C	Capacitance	
$C-V$	Capacitance–Voltage measurement	
$C^{-2}-V$	Mott-Schottky measurement	
C_{co}	Contact capacitance	$F\ cm^{-2}$
CE	Counter Electrode	
C_g	Geometric capacitance	$nF\ cm^{-2}$
CNL	Charge Neutrality Level	
C_{ox}	Capacitance of the oxide layer	$F\ cm^{-2}$
CPE	Constant phase elements	
CV	Cyclic Voltammetry	
D_n	Diffusion coefficient	$cm^2\ s^{-1}$
DOS	Density-of-States	
DT	Deep trap state	
E_{HOMO}^{D}	HOMO Energy Level of the donor material	eV
e^-	Electron	
EA	Electron Affinity	
E_c	Energy of the carrier density in a transport level	
E_{CNL}	Charge-Neutrality Level energy	eV
E_F	Fermi Level	
E_{F_0}	Position of the equilibrium Fermi Level	
E_{Fm}	Metal Fermi Level	
E_{Fn}	Electron Fermi Level	
E_{Fp}	Hole Fermi Level	
E_g	Energy bandgap	eV

Abbreviation	**Description**	**Units**
EQE	External Quantum Efficiency	%
ETL	Electron Transporting Layer	
FF	Fill factor	%
FWHM	Full Width Half Maximum	rad
$g(E)$	Carrier occupation of electron DOS	
g_{is}	Interface state distribution IDOS	$\mathrm{cm^{-2}\ eV^{-1}}$
h	Planck constant	$6.626 \cdot 10^{-34}\ \mathrm{J\,s^{-1}}$
h^+	Hole	
HOMO	Highest Occupied Molecular Orbital	eV
HTL	Hole Transporting Layer	
IDOS	Interfacial Density-of-States	
IP	Ionization Potential	
IS	Impedance Spectroscopy	
I_{sc}	Short-circuit current	A
j_{sc}	Short-circuit current density	$\mathrm{mA\ cm^{-2}}$
$j_{\max}$	Maximum obtainable photocurrent density	$\mathrm{mA\ cm^{-2}}$
j_{rec}	Recombination current	
$j-V$	Current density *vs.* voltage applied	$\mathrm{mA\ cm^{-2}}$ *vs.* V
k_{B}	Boltzmann constant	$1.38 \times 10^{-23}\ \mathrm{J\,K^{-1}}$
L	Nanodomain crystalline size	nm
L	Layer thickness	nm
l_{D}	Electron diffusion length	nm
L_{D}	Exciton diffusion length	nm
LUMO	Lowest Unoccupied Molecular Orbital	
MS	Mott-Schottky	
N	Doping density	$\mathrm{cm^{-3}}$
n-doped	Semiconductor *n*-doped	
OPV	Organic Photovoltaic	
p-doped	Semiconductor *p*-doped	
PCE	Power Conversion Efficiency	
PSC	Polymer Solar Cell	
PV	Photovoltaic	

Abbreviation	Description	Units
q	Elementary charge	1.609×10^{-19} C
Q_c	Positive charge at the metal	
Q_is	Interface negative charge	
R	Resistance	Ω cm^{-2}
R2R	Roll-to-roll	
R_co	Contact resistance	Ω cm^{-2}
RE	Reference Electrode	
R_ox	Resistance of the oxide layer	Ω cm^{-2}
R_s	Series resistance	Ω cm^{-2}
R_sh	Shunt resistance	Ω cm^{-2}
RH	Relative humidity	%
SEM	Scanning Electron Microscopy	
T	Temperature	
TCO	Transparent Conductive Oxide	
TPC	Transient Photocurrent	
UV-Vis	Ultraviolet-Visible	
UVO	UV-Ozone cleaning system	
V_app	Applied voltage	
VASE	Variable-angle spectroscopic ellipsometry	
V_F	Fermi Level Splitting	V
V_fb	Flat-band potential	V
V_if	Electronic coupling matrix element	eV
V_oc	Open-circuit voltage	V
WE	Working Electrode	
W_f	Work function	
XRD	X-Ray Diffraction	
α	Occupancy of the bandgap states	
β	β-recombination parameter	
δ	Charge separation at the dipole layer	
Δ	Interface dipole layer, dipole potential drop	V
ΔE_Fp	Difference between E_Fp and E_F0	

Abbreviation	**Description**	**Units**
ΔV_{oc}	Lower lying levels are occupied in the case of low defect density which produces the open-circuit voltage difference	
$\Delta V_{\mathrm{oc}}^{\mathrm{ener}}$	V_{oc} losses owed exclusively to the difference in the recombination energetics	
$\Delta V_{\mathrm{oc}}^{\mathrm{kin}}$	V_{oc} losses owed exclusively to the difference in the recombination kinetics	
ε	Relative dielectric constant	
ε_0	Permittivity of the vacuum, permittivity of the free space	8.85×10^{-12} F m^{-1}
ε_i	Dielectric constant, relative permittivity	
ϕ_{c}	Metal Fermi Level, metal work function	
ϕ_{s}	Organic semiconductor work function	
λ	Wavelength	nm
λ	Reorganization energy	eV
μ	Carrier mobility of electrons and holes	cm^2 V^{-1} s^{-1}
μ_n	Electron mobility	cm^2 V^{-1} s^{-1}
μ_h	Hole mobility	cm^2 V^{-1} s^{-1}
τ_{diff}	Time characteristic of electron diffusion	
τ_{rec}	Effective lifetime	

MATERIALS

Abbreviation	Description
BCP	2,9-Dimethyl-4,7-diphenyl-1,10-phenanthroline ($C_{26}H_{20}N_2$) Bathocuproine
BDT	Benzodithiophene group
BT	Benzothiadiazole group
CB	Chlorobenzene
CIGS	Copper indium gallium diselenide
CPDT	Cyclopentadithiophene
DIO	1,8-diiodooctane
DMF	Dimethyl formamide
DMSO	Dimethyl sulfoxide
DPP	Diketopyrrolopyrrole group
DPP860	Diketopyrrolopyrrole-quinquethiophene alternating copolymer
FTO	Fluorine-doped Tin Oxide
HDT	Hexanedithiol
HT	Hexanethiol
ICBA	1´,1´´,4´,4´´-tetrahydro-di[1,4]methanonaphthaleno[5,6]fullerene-C_{60} ICBA
*i*I	*Iso*indigo
ITO	Indium Tin Oxide
Ni(TFSI)$_2$	Nickel bis (trifluoromethane- sulfonyl) imide
MDMO-PPV	Poly[2-methoxy-5-(3,7-dimethyloctyloxy)-1,4-phenylene-vinylene]
MEH-PPV	Poly[2-methoxy-5-(2-ethylhexyloxy)-1,4-phenylene-vinylene]
NDI	Naphthalene diimide
ODT	Octanedithiol
o-DCB	*o*-dichlorobenzene
OT	Octanethiol
P3HT	Poly(3-hexylthiophene)
P3TMAHT	Poly[3-(6-trimethylammoniumhexyl)thiophene]
PC$_{60}$BM	[6,6]-Phenyl-C_{61}-butyric acid methyl ester
PC$_{70}$BM	[6,6]-Phenyl-C_{71}-butyric acid methyl ester
PCDTBT	Poly[N-9´-heptadecanyl-2,7-carbazole-alt-5,5-(4´,7´-di-2-thienyl-2´,1´,3´-benzothiadiazole)]

Abbreviation	**Description**
PCPDTBT	Poly[2,6-(4,4-bis-(2-ethylhexyl)-4H-cyclopenta[2,1-B;3,4-B´]dithiophene)-alt-4,7-(2,1,3-benzothiadiazole)]
PDI	Perylene diimide
PEDOT:PSS	Poly(3,4-ethylenedioxythiophene)-poly(styrenesulfonate)
PEN	Polyethylene naphthalate
PET	Polyethylene terephthalate
PFN	Poly[(9,9-bis(3′-(N,N-dimethylamino)propyl)-2,7-fluorene)-alt-2,7-(9,9–dioctylfluorene)]
PNDIS-HD	Naphthalene diimide-selenophene 2-hexyl-decyl copolymer
PPV	*p*-phenylene vinylene group
PSEHTT	Thiazolothiazole copolymer
PSS	Poly(styrenesulfonate)
PTB	Benzodithiophene group
PTB7	Poly[[4,8-bis[(2-ethylhexyl)oxy]benzo[1,2-b:4,5-b']dithiophene-2,6-diyl][3-fluoro-2-[(2-ethylhexyl)carbonyl]thieno[3,4-b]thiophenediyl]]
$PYR_{14}TFSI$	1-butyl-1-methyl pyrrolidinium bis (trifluoro methane sulfonyl) imide
SPPO13	2,7-bis(diphenylphosphoryl)-9,9´-spirobi[fluorene]
TBAHFP	Tetra-*n*-butylammonium hexafluorophosphate
TBAP	Tetra butylammonium perchlorate
TCO	Transparent Conductive Oxide
TQ1	Poly[2,3-bis-(3-octyloxyphenyl)quinoxaline-5,8-diyl-alt-thiophene-2,5-diyl]

CHAPTER 1

MAIN CHALLENGES ADDRESSED

The worldwide high energy demand coupled with the global warming concern and fossil fuels availability has recently triggered the search for environmentally friendly alternatives to provide unlimited energy. For this reason in 2004 the European Commission expressed its recommendation for all EU countries to be able to produce 20 % of renewable energy from all their energy demand by 2020. This declaration of intentions was made public in the European Conference for Renewable Energy 'Intelligent Policy Options' and the EU countries agreed to adopt measures to fulfill this recommendation.[1] To complete this goal, the renewable energy sources including biomass, hydro, wind and solar power have experienced major growth in recent years. As the sunlight is an inexhaustible energy source, a great enthusiasm has focused on solar energy. In this field, the silicon-based photovoltaic devices are already on the market. However, this technology is still economically unsustainable due to high manufacturing and processing costs. As a consequence, interest is growing to search for alternative low-cost, efficient and long lifetime photovoltaic technologies. In this regard, Organic Photovoltaic (OPV) technology is a promising candidate to fulfill all this requirements. Materials used in this technology are distinguished by a series of advantages such as their abundance, benefit from high absorption coefficients, can be solution processed, are mechanical flexible, and their electrical properties can be tuned by synthetic methods. However, in order to reach the market further improvement in efficiencies and stability are required and this can only be obtained by the generation of more efficient organic materials, design of new architectures and better understanding of the physical and chemical processes. These topics have not yet been totally developed in the field of OPV. As a consequence, this Ph.D. Thesis focuses on the investigation of OPV technology, especially in aspects of experimental device processing, and optoelectronic and electrical characterization on OPV devices to be readily marketable. More specifically, the topics addressed are the following:

- *Origin of recombination current*. The rate limiting mechanism governing the kinetics of charge carrier recombination in organic solar cells is still under debate. Some models regard recombination as a transport-controlled process similar to that occurring in single phase organic compounds.[2] In addition, such models establish a strong correlation between transport properties, *e.g.*, charge mobility, and recombination kinetics. On the contrary, recent papers have explicitly suggested an alternative approach in which an intimate correlation between the charge recombination and the molecular interfacial properties is proposed.[3] Particularly interesting are the theoretical findings disclosed in the present work, which suggest a high dependence of the charge transfer kinetics on the relative molecular orientations and intermolecular distances.[4] Upon the realization of this work, a clear correlation between the charge recombination kinetics and the charge transfer molecular properties at the donor/acceptor interface (V_{if}) is identified, contrarily to those previous hypotheses found in the literature that consider the transport characteristics as the limiting factor for minimizing the charge recombination. Additionally, significant differences of the charge recombination kinetics (B) depending on the donor/acceptor combination have been identified, which are related to variations in the electronic coupling matrix (V_{if}). Our findings reveal that the blend properties, rather than energetic characteristics of individual constituents, determine those losses that arise from charge recombination.

- *Open-circuit voltage and crystallinity*. It has been demonstrated that the V_{oc} of plastic solar cells is affected by the morphology of the active layer.[5,6] However, the effect of the intrinsic properties of the donor polymer has not been fully investigated. For this purpose, the study of the correlation between the polymer nanodomain size and the V_{OC} values of the operating organic solar cell has been carried out.[7] Our studies confirm that a highly crystalline polymer exhibits low density of *p*-defects within the bandgap. Consequently, and despite the upward offset of the polymer HOMO level caused by the crystallization, the hole Fermi Level is downshifted for more crystalline blends, compared to low crystallinity layers. This is noticed on the higher V_{OC} values acquired for highly crystalline active layers.

- *Transport driving force*. There is some controversy respect to the charge carrier transport in organic solar cells. How to know if the free electrons are transported by drift in the electrical field or diffusion into the bulk active layer? We propose here a model based on hole and electron free charge carriers occupying Gaussian or exponential distributions. Near open-circuit conditions, depletion zones are eliminated, leaving large electroneutral regions where the transport of minority carrier (electrons) should be controlled by diffusion,[8] while the high conductivity of majority carriers (holes) assures rapid shielding. So far, however, the diffusive transport observations that are clearly predicted by this device model have been elusive due to other experimental aspects that interfere with the diffusion signatures. This work shows evidences of the existence of diffusion currents governing the electronic transport at forward bias voltages between maximum power point and V_{OC} in the case of P3HT:PC$_{60}$BM devices.

- *Contact selectivity and interface states*. The properties of the blend active layer attaching the metal cathode should be fully understood because affect the charge carrier extraction. So, what is the effect of the nanoscale-size blend structure in direct contact with the cathode on operating parameters? A combination of ellipsometry and purely electrical (capacitance–voltage) techniques provide information on the relative donor/acceptor surface coverage at the active layer/cathode interface in operating devices. It is demonstrated that surface coverage and contact selectivity are closely related parameters. Besides, a complete view of device integrating the organic/metal contact in connection with the organic bulk active layer is established here. Our unified approach integrates both organic bulk and metal cathode sides, along with interface states forming a contact dipole.[9] This new model is an essential advance in understanding the device formation and operation.

- *Alternative hole transporting layers*. The most common hole transporting layer used until now is the PEDOT:PSS. Its acid character and hygroscopic nature cause corrosion of the ITO and, consequently, device degradation over time. As a result, many materials have been investigated to replace this buffer layer, but most of them are deposited under high vacuum methods, increasing the production costs. Therefore, an alternative is the NiO to replace the well-known PEDOT:PSS as is chemically stable and inert in relation to ITO and P3HT:PC$_{60}$BM.[10] However, NiO contact is highly sensitive to the surface chemistry, crystal orientation and thin film processing.[11,12] We found here the appropriate NiO-deposition and experimental surface conditions to achieve high power conversion efficiency in standard cells.

- *Oxygen and degradation routes*. Finally, it is known that degradation processes can proceed *via* three different physical mechanisms: (*i*) loss of conjugation and irreversible deterioration of the active organic layers, (*ii*) degradation of the interface conductive properties, and (*iii*) mechanical disintegration of device (phase segregation and crystallization). All of them manifest themselves as a change in the electrical properties of the device.[13] In the present work, the degradation mechanism is studied, including effects taking place in the bulk and those at the cathode contact. By exposing the cells to a controlled oxygen environment, it is experimentally observed that the intensity of the P3HT-absorption peak decreases due to the formation of a new chemical species, reducing photocurrent. Besides, the *p*-doping defects are measured which correlate with oxygen or other oxidant exposure. In addition, the diffusion of the oxygen from the blend to the contacts is able to oxidize the cathode, being reflected in a decrease of flat-band voltage value as well as photocurrent. As a result, a direct connection is then established between an oxygen-related degradation route and cell performance parameters.

References

1. A. Jäger-Waldau, *Renew. Sust. Energy Rev.*, 2007, 11, 1414-1437.
2. M. Kuik, L. J. A. Koster, G. A. H. Wetzelaer and P. W. M. Blom, *Phys. Rev. Lett.*, 2011, 107, 256805.
3. S. Yamamoto, A. Orimo, H. Ohkita, H. Benten and S. Ito, *Adv. Energy Mater.*, 2012, 2, 229-237.
4. S. W. Ko, E. T. Hoke, L. Pandey, S. H. Hong, R. Mondal, C. Risko, Y. P. Yi, R. Noriega, M. D. McGehee, J. L. Bredas, A. Salleo and Z. A. Bao, *J. Am. Chem. Soc.*, 2012, 134, 5222-5232.
5. C. J. Brabec, A. Cravino, D. Meissner, N. S. Sariciftci, T. Fromherz, M. T. Rispens, L. Sanchez and J. C. Hummelen, *Adv. Funct. Mater.*, 2001, 11, 374-380.
6. A. Gadisa, M. Svensson, M. R. Andersson and O. Inganas, *Appl. Phys. Lett.*, 2004, 84, 1609-1611.
7. Z. M. Beiley, E. T. Hoke, R. Noriega, J. Dacuña, G. F. Burkhard, J. A. Bartelt, A. Salleo, M. F. Toney and M. D. McGehee, *Adv. Energy Mater.*, 2011, 1, 954-962.
8. M. Burgelman and C. Grasso, *J. Appl. Phys.*, 2004, 95, 2020-2024.
9. F. Zhang, M. Ceder and O. Inganäs, *Adv. Mater.*, 2007, 19, 1835-1838.
10. K. X. Steirer, J. P. Chesin, N. E. Widjonarko, J. J. Berry, A. Miedaner, D. S. Ginley and D. C. Olson, *Org. Electron.*, 2010, 11, 1414-1418.
11. M. D. Irwin, J. D. Servaites, D. B. Buchholz, B. J. Leever, J. Liu, J. D. Emery, M. Zhang, J.-H. Song, M. F. Durstock, A. J. Freeman, M. J. Bedzyk, M. C. Hersam, R. P. H. Chang, M. A. Ratner and T. J. Marks, *Chem. Mater.*, 2011, 23, 2218-2226.
12. H. Yang, C. Gong, G. Hong Guai and C. Ming Li, *Sol. Energy Mater. Sol. Cells*, 2012, 101, 256-261.
13. A. Turak, *RSC Adv.*, 2013, 3, 6188-6225.

CHAPTER 2

INTRODUCTION TO PHOTOVOLTAIC TECHNOLOGIES

2.1. Renewable energy sources

Nowadays, about 65–70 % of electricity consumed in the world is derived from the combustion of fossil fuels such as oil, coal and natural gas,[1] making them essential power generators. However, the combustion of these exhaustive sources has negative influence on both human health and environment. Thus, an extensive search into alternative, clean and long-term sustainable energy sources have triggered the so-called renewable energies.[2] Over the past decade, renewable energy production has experienced a rapid growth as a result of world energy demands, global warming awareness, fossil fuel depletion, have a negative impact on the environment, as well as the high price volatility of oil.[1] The most promising low-carbon inexhaustible sources include wind, geothermal, hydropower, biomass, tidal, and solar.

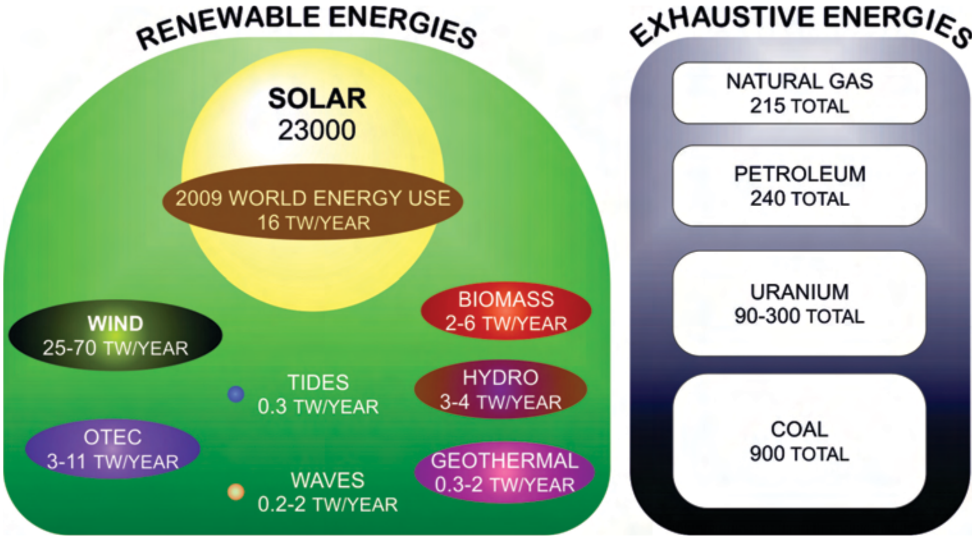

Scheme 2.1. Finite renewable and exhaustive energy reserves in the world (Terawatt/year). Scheme adapted from reference 3.

The full range of energy sources currently available is represented in Scheme 2.1. Two main energy reserves can be found; mainly from renewable and others from fossil-based energy resources. It is highlighted that the solar energy overcomes all other combined renewable sources. The yearly sustainable renewable supply of solar energy received by the emerged continents alone is more than about 25 times larger than the total planetary reserves of coal, and 1500 times larger than the current planetary energy consumption.[4] Therefore, solar photovoltaic technology is a promising example with steadily growing attention from both academic and industrial fields.[3]

2.2. Solar radiation

The sun is the major energy supplier for all nature processes on the earth. From the ultraviolet to the infrared region of the electromagnetic spectrum (200–3000 nm), the sun can emit a huge amount of energy due to the nuclear fusion reaction of its components. The temperature within the photosphere is 5800 K and the energy of the sun corresponds to the radiation emitted by a black body at this temperature. This radiation approaches to a solar spectrum emitted outside the atmosphere and is defined as AM0 spectrum (Figure 2.1). Only 70 % of the sun radiation can penetrate through the atmosphere due to the gases such as CO_2, H_2O and O_3 or other components absorb this radiation.

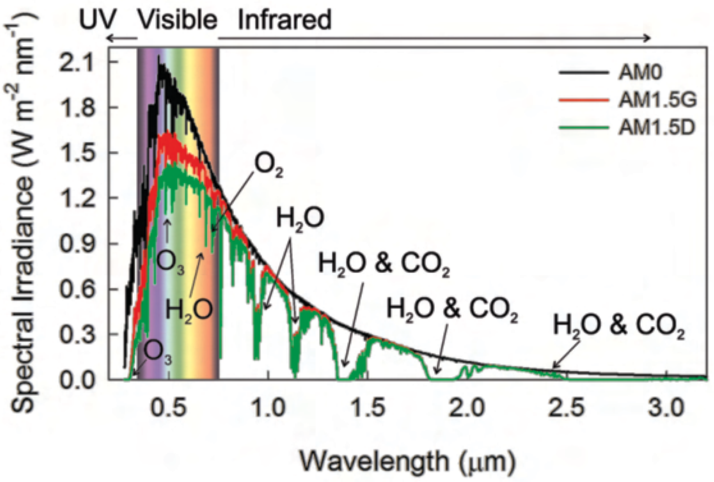

Figure 2.1. Solar irradiance spectrum of the extraterrestrial (AM0) as well as the global (AM1.5G) and the direct (AM1.5D) at the earth's surface. The radiation has been absorbed by molecules at the atmosphere is also represented.

Generally, the solar spectrum is standardized to the AM(x), where x is the inverse of the cosine of the zenith angle of the sun. AM is a measure of how much atmosphere sunlight must travel through to reach the earth's surface. The AM1.5 spectrum was standardized by both the international Organization of Standardization (ISO 9845-1:1992) and, most widely used, by the American Society for Testing and Materials (ASTM E892-87:1992). In AM1.5, the sun is at angle θ of about 48° (Scheme 2.2). For convenience, the flux of the standardized AM1.5 spectrum has been corrected to a fix value of 1000 W m^{-2}.

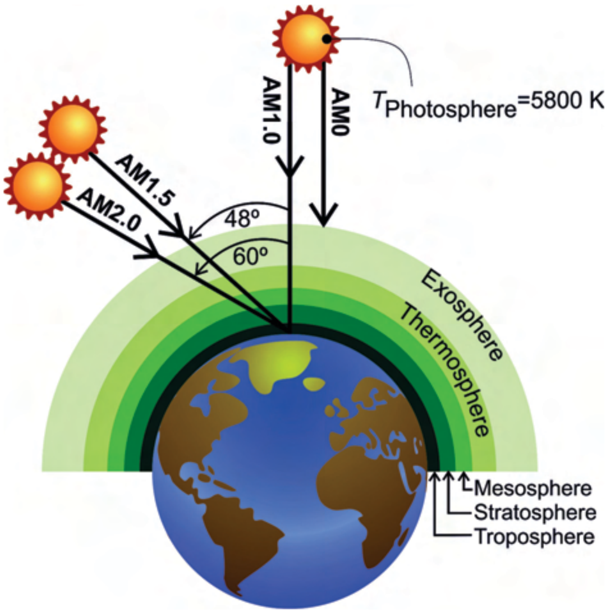

Scheme 2.2. Different angles to measure the sunlight. The standard solar spectrum AM1.5, commonly used in the literature for solar cell efficiency, corresponds to the solar incident radiation angle of 48°. The temperature of the sun in the photosphere is also indicated.

The global AM1.5 solar spectrum (AM1.5G) includes the direct solar spectrum (AM1.5D), being AM1.5 at the earth's surface plus the diffuse components (Figure 2.1). Depending on the device application, different range of the solar spectrum could be interesting. In the case of solar energy conversion, the range between the visible and near infrared light (400–800 nm) is the relevant part, since it contains most of the solar power. Therefore, the organic compounds should absorb in the high wavelength visible range in order to have a good photogeneration of free charge carriers.

2.3. Photovoltaic technologies

The term ‘‘photovoltaic’’ has been coined from the Greek ‘photo’, which means light, and ‘voltaic’ indicates electric from the name of the Italian physicist A. Volta (who gave his name to the electro-motive unit Volt).[1] In 1839, the photovoltaic effect was described for the first time by the French physicist Becquerel, who won the Nobel Prize of Physics together with P. Curie and M. Curie for their discovery of radioactivity. Becquerel observed that when specific materials, namely Pt electrodes covered with AgCl or AgBr in H_2O, were exposed to electro-magnetic radiation led to the production of a small electric current, effect denoted as photoelectrochemistry.[3] Only 50 years later, the first reports based on photoconductivity of a solid-state system were made; and earlier 20th century, studies focused on organic compounds such as anthracene material were started.[1]

The photovoltaic technologies are generally divided into four categories: single-junction devices, multijunction devices, thin-film technologies, and emerging photovoltaic devices. Details of each category are explained below. The market has attracted considerable attention and interest on the power conversion efficiency (PCE) and stability of each photovoltaic technology. Regularly, National Renewable Energy Laboratory (NREL) reports best research-cell efficiencies for the photovoltaic technologies (Figure 2.2).

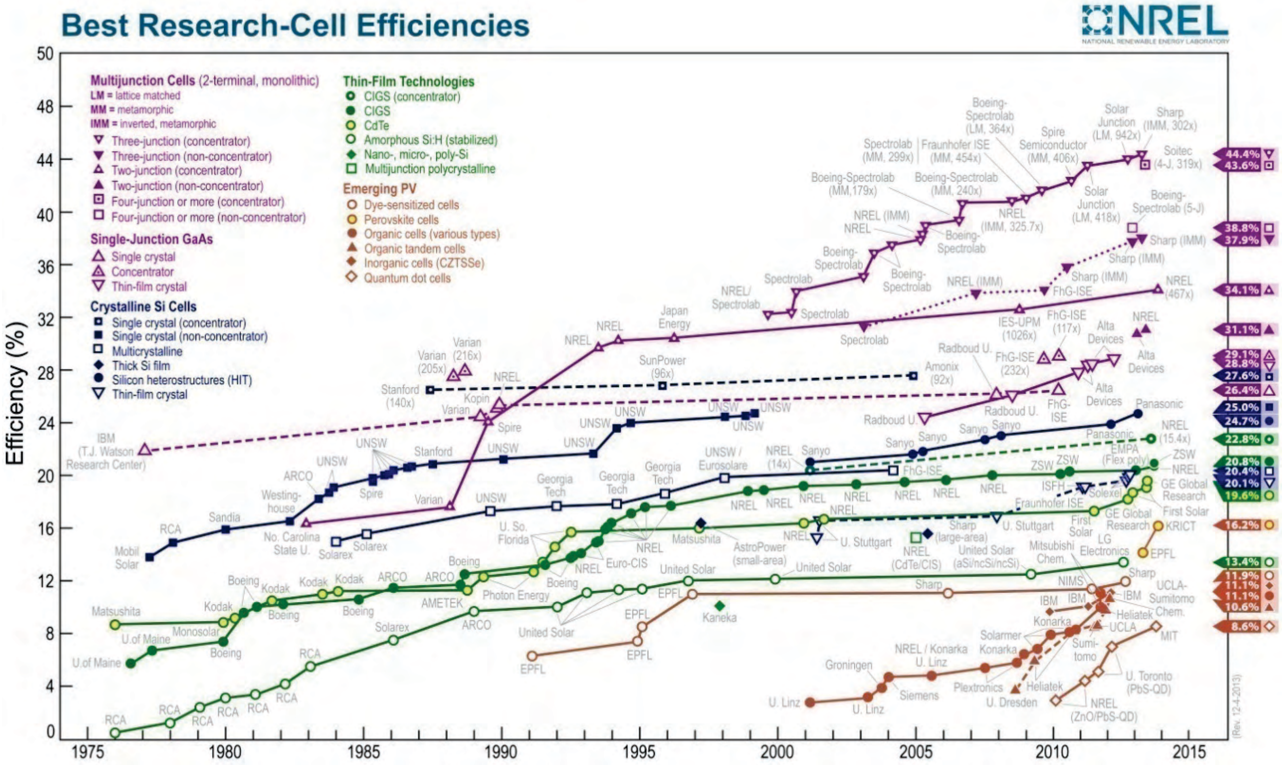

Figure 2.2. The best cell efficiency researched from 1976 to the present is summarized. These data are provided by NREL.

The junction technology (single and multi) is generally composed of III-V semiconductor materials for achieving reliable high performance optoelectronic devices (see Table 2.1).

Traditional crystalline inorganic semiconductors can absorb a continuous spectrum of light. This type of materials provides great carrier mobility because of their high crystallinity three-dimensional rigid lattice. In particular, a Si solar cell with a bandgap of 1.12 eV (a bandgap wavelength of 1109 nm) can reach a maximum short-circuit current (j_{sc}) about 43 mA cm^{-2}. As a result, high PCEs up to 25 % have been reached (see Figure 2.2).[5] Additionally, high purity of Si is environmentally stable and has proved to be a robust photovoltaic technology.[6] In 2008, about 90 % of the whole photovoltaic market was coped by this inorganic material technology. The average annual growth of crystalline Si photovoltaic production capacity was 30–50 % over the last 10 years.[1] Although these numbers seem large, the global share of photovoltaic technology in electricity generation is still marginal. Besides, purification techniques used to produce high quality Si, coupled with the high temperature required and low throughput manufacturing techniques lead to high energy costs. Furthermore, the traditional electrical generation methods like coal and gas centrals, as well as hydroelectric and nuclear power plants need less overall cost of electricity production compared with Si solar cells.[7] Due to all these reasons, intensive research has been conducted towards the development of low-cost photovoltaic technologies.

Table 2.1. Best research efficiencies as well as research institution for photovoltaic devices of 2012/15 complied by Green *et al*.[5]

Category	**Type**	**Area** (cm^2)	**PCE** (%)	j_{sc} (mA cm^{-2})	V_{oc} (V)	***FF*** (%)	**Research organization**
Single-junction	c-Si	4.0c)	25.0±0.5	42.7	0.706	82.8	Sandia
	mc-Si	1.002a)	20.4±0.4	38.0	0.664	80.9	NREL
	Thin-film Si	242.6a)	20.1±0.4	38.14	0.682	77.4	NREL
	a-Si	1.036a)	10.1±0.3	16.75	0.886	67.8	NREL
	Thin-film GaAs	0.9927a)	28.8±0.9	29.68	1.122	86.5	NREL
	mc-GaAs	4.011b)	18.4±0.5	23.2	0.994	79.7	NREL
	c-InP	4.02b)	22.1±0.7	29.5	0.878	85.4	NREL
Multijunction devices	5J GaAs/InP bonded	1.021a)	38.8±1.9	9.56	4.767	85.2	NREL
	InGaP/GaAs/InGaAs	1.047a)	37.9±1.2	14.27	3.065	86.7	AIST
	a-Si/nc-Si/nc-Si	1.006a)	13.4±0.4	9.52	1.963	71.9	NREL
Thin-film technologies	CIGS	0.9974a)	19.8±0.6	34.91	0.716	79.2	NREL
	CdTe	1.0055a)	19.6±0.4	28.59	0.8573	80.0	Newport
Emerging photovoltaic	Dye sensitized	1.005c)	11.9±0.4	22.47	0.744	71.2	AIST
	Single-Organic	1.013c)	10.7±0.3	17.75	0.872	68.9	AIST
	Tandem-Organic	0.1	10.6	10.1	1.53	68.5	Y.Yang *et al.*[8]
	Perovskite	0.2	14.14±0.3	21.3	1.00	66	M. Grätzel *et al.*[9]

Illumination area: aperture area,a) total area,b) and designated illumination.c) Nomenclature: c corresponds to crystalline, mc is multicrystalline and a is noted to amorphous structures.

Among this type of semiconductors, GaAs provides high mobility carrier devices. The single-junction solar cells incorporated quantum dots into the intrinsic region of a single junction *p–i–n*. This addition increases the absorption in the infrared region of the solar spectrum which causes an enhancement in the j_{sc}.[10] In addition, the single-junction is developed to multijunction II-V solar cells whose have also received a lot of attention in recent years, because their conversion efficiency is reported to be as high as 38 % (see Table 2.1).

Furthermore, significant inorganic thin-film technology is also being developed, such as CIGS and CdTe. CIGS is characterized by a direct-gap polycrystalline semiconductor with large optical absorption coefficients,[11] and the CdTe absorbs nearly 100 % of the incident solar radiation with 2 μm of thicknesses.[12]

Finally, the emerging photovoltaic technology is summarized in four divisions, including dye-sensitized solar cells (DSCs), single and tandem organic solar cells (OSCs) and perovskite solar cells. The performance of the well-known DSC is mainly determined by the type of sensitizer, the electrolyte and the properties of the porous semiconducting electrodes that are used in their fabrication. The single layer OSCs are an emerging photovoltaic technology with promising properties such as low cost, flexibility, light weight, transparency and large-area manufacturing compatibility.[13] The tandem or multijunction organic photovoltaic devices tackle simultaneously absorption and thermalization losses. These types of devices are based on the joint of two different cells. On the one hand, a cell with wide bandgap which absorbs photons with high energy, performing higher photovoltage and lower photocurrent, and on the other hand, other cell with small bandgap which absorbs photons with low energy, resulting lower photovoltage and higher photocurrent.[3] Recently, additional research has focused on Perovskite Solar Cells due to fact that a high PCE has been experienced in few months (Figure 2.2). These devices are mainly formed by an organic-inorganic light absorbing semiconductor material with a perovskite polycrystalline structure, $CH_3NH_3PbX_3$, where X is a halide atom (Cl, Br or I) or a combination of some of them.

2.4. References

1. N. Grossiord, J. M. Kroon, R. Andriessen and P. W. M. Blom, *Org. Electron.*, 2012, 13, 432-456.
2. J. A. Carr and S. Chaudhary, *Energy Environ. Sci.*, 2013, 6, 3414-3438.
3. T. Ameri, N. Li and C. J. Brabec, *Energy Environ. Sci.*, 2013, 6, 2390-2413.
4. M. Z. Jacobson and G. M. Masters, *Science*, 2001, 293, 1438-1438.
5. M. A. Green, K. Emery, Y. Hishikawa, W. Warta and E. D. Dunlop, *Prog. Photovolt. Res. Appl.*, 2014, 22, 1-9.
6. M. Wright and A. Uddin, *Sol. Energy Mater. Sol. Cells*, 2012, 107, 87-111.
7. N. S. Lewis, *MRS Bull.*, 2007, 32, 808-820.
8. J. You, L. Dou, K. Yoshimura, T. Kato, K. Ohya, T. Moriarty, K. Emery, C.-C. Chen, J. Gao, G. Li and Y. Yang, *Nat. Commun.*, 2013, 4, 1446.
9. J. Burschka, N. Pellet, S.-J. Moon, R. Humphry-Baker, P. Gao, M. K. Nazeeruddin and M. Gratzel, *Nature*, 2013, 499, 316-319.
10. M. F. Bennett, Z. S. Bittner, D. V. Forbes, S. Rao Tatavarti, S. Phillip Ahrenkiel, A. Wibowo, N. Pan, K. Chern and S. M. Hubbard, *Appl. Phys. Lett.*, 2013, 103, 213902.
11. N. E. Gorji, U. Reggiani and L. Sandrolini, *Thin Solid Films*, 2013, 537, 285-290.
12. J. Gao, X. Di, W. Li, L. Feng, J. Zhang, L. Wu, B. Li, W. Wang, G. Zeng and J. Yang, *Thin Solid Films*, 2014, 550, 638-642.
13. N. Yeh and P. Yeh, *Renew. Sust. Energy Rev.*, 2013, 21, 421-431.

CHAPTER 3

POLYMERIC SOLAR CELLS

3.1. Characteristics of Polymeric Solar Cells

Research community efforts have been devoted to the development of alternative low-cost photovoltaic (PV) manufacturing technologies.[1,2] In 2012, photovoltaic technology provides 2.6 % of the electricity demand at EU level and 5.2 % of the peak demand.[3] In particular, the organic photovoltaic (OPV) technology deserves to gain more attention because the organic semiconductor materials are mainly primary source. The discovery of these materials has led to new and exciting possibilities in other optoelectronic fields, such as organic light-emitting diodes (OLEDs),[4] organic thin-film transistors (OTFTs),[5] and organic memory devices.[6] Compared with their inorganic counterparts, organic materials are very promising due to their numerous properties, including thin-film architecture, high transparency, low-temperature for solution processes, soluble in many organic solvents, low specific weight and mechanical flexibility. Additionally, their absorption coefficients are high, so a layer of a few hundred nanometers can absorb high portion of the solar spectrum.[7] Besides, the electronic bandgap of organic semiconductors can be engineered by chemical design.[8] Regarding efficient solution processes, the printing or coating processes *e.g.*, inkjet printing and roll-to-roll deposition allow a large scale production easily. These deposition routes are attractive for the market because they are suitable for high production speed of up to several meters per second. For example, if 100000 m^2 of film per day could be produced in a single production line with an efficiency of 5 %, this would correspond to a daily capacity of 5 MW.[9] Therefore, a single printing or coating deposition of the layers could produce modules with the production energy volume of over 1 GW per year,[9] being more productive than the currently large production facilities for Si-based PVs. As a consequence, this technology reduces greatly the commercial manufacturing costs in mid-long term, becoming potential and competitive technology.[9] Then, a wide scale of affordability and distribution with less environmental impact is enabled. This last assumption is observed in low energy payback time and low levels of anthropogenic emissions during their lifetime.[10] Finally, this technology offers large modules with freedom of design able to apply to portable charging of small devices which could, for instance, be integrated in clothing and bags. Other possible applications include the integration of OPV products to retractable shades, tents, carport covers, windows,[11] *etc.*

In contrast, there are still some improvements that are necessary before marketing. Efficiency, costs and lifetime/degradation mechanisms of the devices need to fulfill more demanding requirements than those achievable today.[12,13] Regarding efficiency, a single bulk heterojunction (BHJ) cell can achieve ~15 % of PCEs and higher efficiencies with stacking multiple cells.[14] Experimentally, the record certified efficiency reported until now is about 10 %.[15] Therefore, there is still significant room for improvement with respect to research and development, which are necessary to develop OPV cells with high performance. However, these efficiencies remain lower than those exhibited for Si solar cells characterized to achieve 25–30 % (see Table 2.1 in the section 2.3). As regards assessment economics of this technology, low costs can be achieved theoretically, in fact, the cost limiting material is the substrate coated with the conductive oxide, *e.g.*, indium tin oxide (ITO). Current work is ongoing to replace this material by other conductive substrates. Concerning stability issue, the lifetime of OPV technology is around 10 years, being still poor compared to inorganic Si-based solar cells which can operate until 25 years.[13,16]

3.2. Brief history of OPV devices and evolution of device structures

The major events for OPV devices from the beginning of the 19th century to the most recent developments are listed in Table 3.1. As described in Chapter 2, the photovoltaic effect is commonly ascribed to Becquerel, who discovered the photoelectrochemical process. In 1873, Smith investigated the photoconductivity effect in Se, and later this effect was first observed in an organic compound, anthracene, by Pochettino. In the late 1950s and 1960s, the potential use of some organic materials as photoreceptors in imaging systems was recognized.

Table 3.1. Some important milestones in the development of organic solar cells.[17]

Year	Event
1839	Becquerel observed the photoelectrochemical process.
1873	Smith reported the photoconductivity in Se.
1906	Pochettino discovered the photoconductivity in solid anthracene.
1958	Kearns and Calvin worked with MgPc, a photovoltage of 200 mV were measured.
1964	Delacote observed a rectifying effect when CuPc was placed between two different metal electrodes.
1986	Tang published the first donor:acceptor photovoltaic device.
1992	Yokoyama made the first dye:dye photovoltaic cell by co-sublimation.
1993	Sariciftci made the first polymer:C_{60} photovoltaic device.
1994	Yu made the first polymer:C_{60} BHJ of PV.
1995	Independently, Yu and Friend made the first polymer:fullerene and polymer:polymer BHJ photovoltaic cell, respectively.
2000	Peters and van Hal used oligomer-C_{60} dyads:triads as active material in photovoltaic cells.
2001	Schmidt-Mende made a self-organized liquid crystalline solar cell of hexabenzocoronene and perylene.
2001	Ramos used double-cable polymer in photovoltaic cells.

The first OPV device was considered of a single thermally evaporated molecular organic layer sandwiched between two metallic conductors, typically a high work function (W_f) layer (*e.g.*, ITO) and low W_f of a metal layer such as Al, Mg, or Ca to carry out the electron extraction. In Scheme 3.1.a is represented this single-layer organic semiconductor cell, so-called Schottky diode. The organic semiconductor is able to absorb photons incident from sunlight. The semiconductor generates a bound electron/hole pair due to the low dielectric constant and small Bohr radius of carriers. Within the bulk, the exciton dissociation does not occur efficiently because the electric field is insufficient, thus the PCE is severely limited as most of the photogenerated charges are lost by recombination processes.[18] In response, in 1986 Tang *et al.* introduced the thin film donor/acceptor (D/A) bilayer stacked together with a planar interface to create a new OPV cell with an efficiency around 1 %.[19,20] The basic structure of such cell is illustrated in Scheme 3.1.b. The cell was fabricated from CuPc as *p*-type semiconductor and a perylene tetracarboxylic derivative as *n*-type semiconductor sandwiched between a transparent conductive oxide (TCO) and a semitransparent metal electrode. Typically, the materials with relatively high Highest Occupied Molecular Orbital (HOMO) level can be easily *p*-doped, and therefore, these materials can transport holes. These kinds of materials are called electron donor or *p*-type. Conversely, the materials with relatively low Lowest Unoccupied Molecular Orbital (LUMO) level can be easily *n*-doped, and thus, the electrons are transported through these materials. These materials are called electron acceptor or *n*-type. This *p*–*n* device produced a large dissociation field at the material junction. However, the main limitation was that many excitons were unable to reach the interface and were still lost. The parameter defined to take into account if the exciton can diffuse from the donor material to the D/A interface is the exciton diffusion length (L_D). The typical L_D is ~10 nm, one order of magnitude smaller than the optimum thickness required for high optical absorption (≥100 nm).[18] An improvement of the bilayer device is the double which stacks two single heterojunction layers (Scheme 3.1.c).[16]

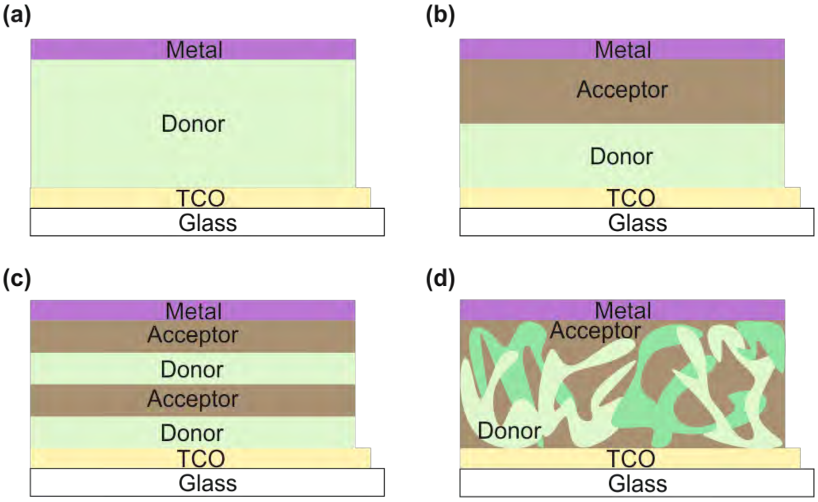

Scheme 3.1. Schematic OPV devices with (a) single-layer, (b) bilayer, (c) double bilayer and (d) bulk heterojunction layer.

The previous structures show certain limitations, including a small surface area between the D/A interfaces and the requirement of long carrier lifetime to ensure that the electrons and holes reach their respective electrodes. However, this problem can be addressed by introducing a bulk (or dispersed) BHJ concept, which reduces the average distance between D–A molecules, keeping the overall thickness of the active layers. BHJ layer consists of donor and acceptor mixture to form an interpenetrated network blend with the distance scale between D–A similar to the exciton diffusion length (Scheme 3.1.d). This layer should have the suitable thickness to absorb more range of the solar spectrum and it is able to diffuse excitons from donor material to the D/A interface, achieving higher quantum efficiencies compared to the bilayer architecture.[16,21] This concept was first demonstrated in 1992 by Yokoyama *et al*. through the co-evaporation of donor and acceptor molecules under high-vacuum conditions.[22] Since the introduction of BHJ concept, a number of D:A cells has been widely exploited, including dye:dye, polymer:dye, polymer:polymer, polymer:fullerene and polymer:nanocrystals blends. The first efficient BHJ polymer solar cells (PSCs) were independently realized in 1995 by Yu *et al*. and Friend *et al*. in polymer:fullerene and polymer:polymer blends, respectively.[23,24] Nonetheless, the polymer:fullerene device shows the highest efficiency among all BHJ OPVs. In 2012, Wu *et al*. investigated an inverted structure OPV device which achieved high efficiency approaching 10 % with the architecture as ITO/PFN/PTB7:$PC_{70}BM/MoO_3$/Al.[25]

The main disadvantage of polymer:fullerene devices is that the fullerene absorption is poor in the solar spectrum range.[26] Regarding the polymer:polymer combination offers potential advantages over the polymer:fullerene blends because the bandgap of the polymer is easily tuned, and hence it is possible to design a device to cover a wider solar spectrum.[27] However, the lack of suitable acceptor polymers (*n*-type) has limited the poor of both photocurrent and efficiency in polymer:polymer BHJ solar cells. For instance, PSCs based on an PNDIS-HD acceptor and a PSEHTT donor exhibit recently a record 3.3 % of PCE.[28] Additionally, other type of photovoltaic cells that have further advantages is based on polymer and nanocrystals (NCs) materials. The large dielectric constants and tunability of the NC shape becomes an alternative method to use for solar energy harvesting. Besides, the higher dielectric constant of inorganic NCs (for instance, ~10.4 for CdSe compared with ~3.9 for PCBM)[29] decreases the coulombic attraction between electrons and holes, facilitating the charge separation.[27] Lately, a number of research groups have been demonstrated 5 % of PCE in the previous devices.[30]

3.3. Mechanism for photocurrent generation in OPV devices

The elementary mechanisms involved from light absorption to collection of carriers at the contacts in OPV devices are commonly accepted in five fundamental steps.[16] The photocurrent generation processes are illustrated in Scheme 3.2. These fundamental steps are summarized in Scheme 3.3 in terms of energy levels diagram.

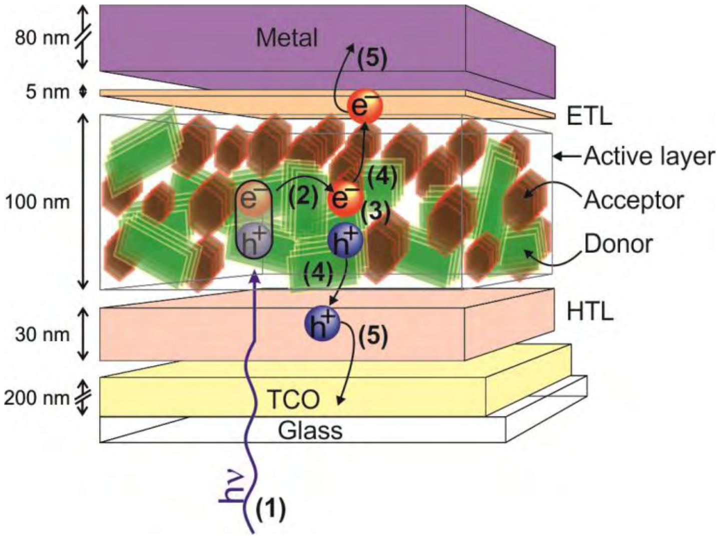

Scheme 3.2. Representative OPV device with the mechanistic steps to carry out the electron extraction under light illumination: 1) light absorption, 2) exciton diffusion, 3) charge dissociation, 4) charge transport, and 5) charge collection. ETL and HTL are named to Electron and Hole Transport Layer, respectively.

Initially, when the sunlight illuminates the surface of the OPV cell, the light must go through several transparent layers (usually ITO and PEDOT:PSS) in order to reach the BHJ photoactive layer composed by acceptor and donor materials. The electron donor polymer absorbs a fraction of these photons from the light, which induces electron excitation from its HOMO to its LUMO, creating a strong electrostatically bound of an electron–hole (e–h) pair called exciton. This process is represented in the step 1 in Scheme 3.3. The fraction of the photons absorbed by the donor material depends on several factors such as the thickness of the active layer, the optical properties of the layers (ITO, hole transport layer, active layer and electron transport layer) and the energy range of photons. Most of the photons are absorbed within the first 100–500 nm of the photoactive layer when this is thick.[13] Other decisive parameter to absorb photons efficiently is how closely the spectral response of the polymer matches with the solar spectrum. Polymers with low bandgap allows absorbing more photons, and consequently, higher currents and PCEs are obtained.[31] Thus, low bandgap materials are needed in order to optimize photon harvesting. For instance, the bandgap of P3HT is 2 eV (this bandgap corresponds to an onset wavelength of ~620 nm) and, as a result, this polymer is only able to harvest up 22.4 % of available photons. Such poor matching of P3HT's photon absorbance with the solar radiation spectrum is an important limitation that has led to the research of new low bandgap materials.[16] There are several possibilities to increase the photon absorption of the polymer:fullerene blend. For example, a significant fraction of energy in the solar spectrum is increased by narrowing the donor polymer bandgap and lower HOMO level values.[32] Besides, the acceptor fullerene material (*e.g.*, PCBM) also plays a crucial role because can absorb a significant part of the (visible) solar spectrum, preferentially a part that is complementary to the absorption of the donor material.[33] To avoid the overlap in the absorption spectra of both materials, tandem or double junction cells are investigated.

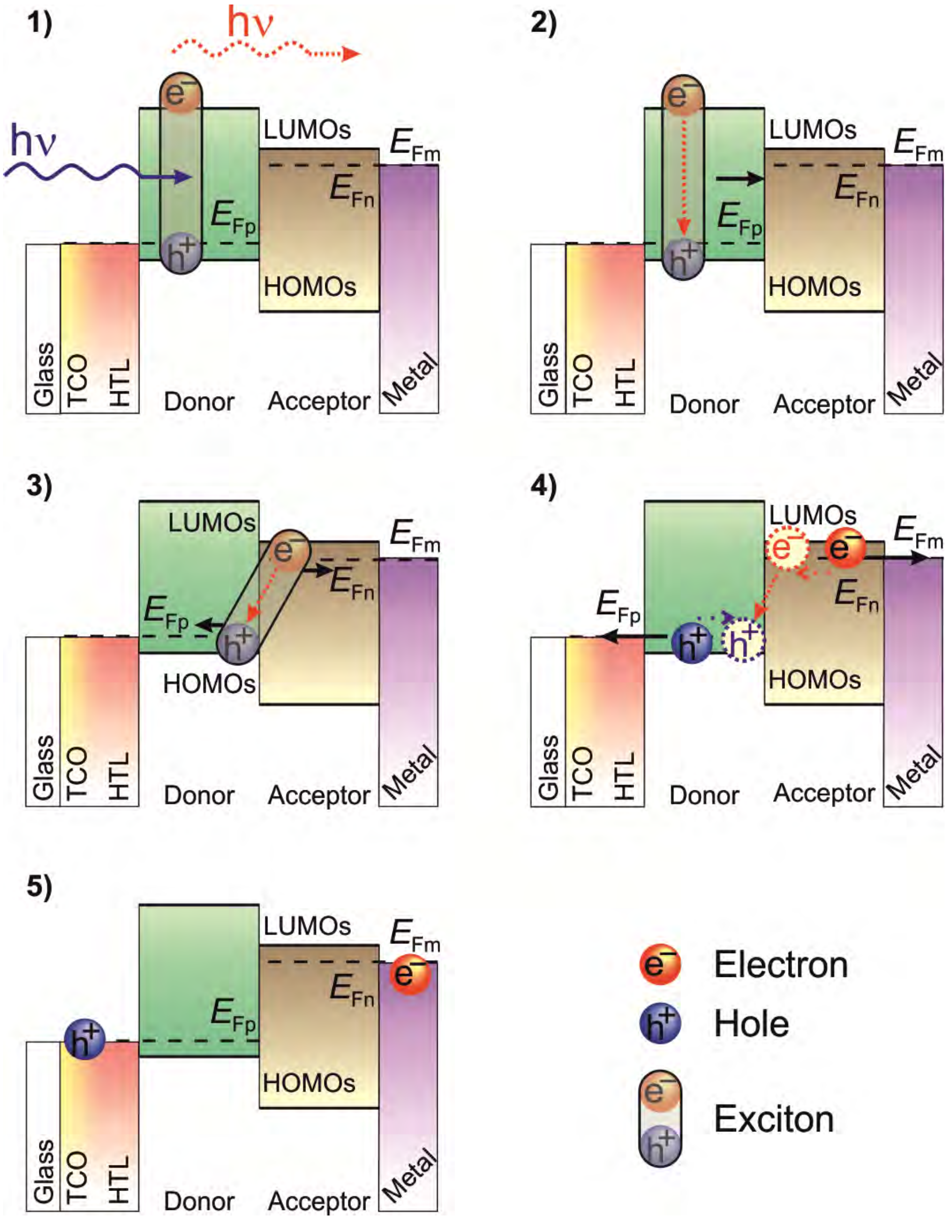

Scheme 3.3. Energy level diagram for photocurrent generation in organic solar cells which involved five fundamental steps: 1) light absorption, 2) exciton diffusion, 3) charge dissociation, 4) charge transport, and 5) charge collection. It is also represented the loss energy mechanisms in red arrows.

Once the exciton is created, the bound e–h diffuses from polymer to D/A interface as shown in the step 2 in Scheme 3.3. The excitons with longer L_D have better opportunities to reach the D/A interface, and thus, the bound e–h breaks up into free carriers. As mentioned above, the L_D in organic semiconductors is limited to 10–50 nm, which is smaller than their optical absorption lengths ($1/\alpha \approx 100\,\text{nm}$).[34] Only the photons absorbed within this range of distances from the interface can contribute to the overall device current. Therefore, the layer thickness should be within the range of their L_D. Unfortunately, to absorb enough light, the polymer layer needs a thickness of at least 10 nm and at that thickness only a fraction of excitons can reach the D/A interface. This is the reason of the poor photoconversion efficiencies in the simple bilayer structures (Scheme 3.1.b) due to their D/A interfaces are beyond of the excitons L_D.[16]

The strong bound e–h pair is dissociated efficiently to free charge carriers almost exclusively at the D/A interface blend before to decay, as illustrated in step 3 of Scheme 3.3. The dissociation process could depend on the local morphology[13] and/or the electric field, however there is a controversy that is currently under discussion.[35] Therefore, an efficient free charge carrier is managed according to the proper active layer materials as well as the device architecture. A large electrostatic force bound excitons exist in these organic materials as a consequence of the low dielectric constants $(\varepsilon_r \approx 3)$ which is insufficient to a direct e–h dissociation.[21,36,37] The exciton binding energy (E_{binding}) of the organic materials is about one order of magnitude (0.4–1.4 eV)[38] higher than the thermal energy $k_B T$ (k_B is the Boltzmann constant and T is the temperature) at room temperature (T_{room}) upon light absorption. As a result, the creation of free carriers is unlikely at T_{room} and the charge recombination occurs. Such as it is explained earlier, the first OPV devices based on a single layer of an organic *p*-conductor (Scheme 3.1.a) exhibited very poor performances.[18] Consequently, two materials with different electron affinities and ionization potentials are required to involve the D/A interface in order to trigger the exciton dissociation. In contrast, Si solar cells are characterized by creating free charges easily at T_{room} when the material is excited[13] because these charge carriers experience only a small force of interaction due to $E_{\text{binding}} < k_B T$ at T_{room}.[39]

After charge dissociation into free carrier, the electrons and holes are transferred separately to the appropriate material in function of the differences in the HOMO and LUMO energy levels of the donor and acceptor materials. The electrons are accepted and transported by the material with higher LUMO level and the holes are transferred to the material that possesses lower HOMO level, as showed in the step 4 of Scheme 3.3. Unfortunately, efficiency drop when the charge travels throughout from the bulk of the active layer to the electrode can recombine or become trapped in disordered interpenetrating networks of organic material (Scheme 3.1.d).[16] Here, the electron and hole mobilities of donor and acceptor materials become important. The charge mobilities depend on several parameters such as the amount of defects and impurities, and the organization/crystallinity of each material.[40]

Once the electrons and holes have reached the respective electrodes, the free charges are collected and passed into the outer circuit to generate the device photocurrent. On the one hand, the electron is collected in the cathode electrode, and on the other hand, the hole is collected in the anode electrode. This process is displayed as step 5 in Scheme 3.3. The charge collection efficiency mainly depends on the energy level matching at the metal/polymer interface and the interfacial defects.[41]

Unfortunately, each of these processes are not totally efficient and give rise to losses (Scheme 3.3), namely non-absorbed photons in step 1), exciton decay in step 2), geminate recombination of the bound pair in step 3), and bimolecular recombination in step 4). These five phases are interrelated. However, improving a single step could but not necessarily lead to improvement of the overall performance.[16]

3.4. Device structure

Different layers composed this thin film technology that must fulfill particular properties to produce maximum efficiency devices. The photoactive layer was sandwiched between TCO and a semitransparent metal electrode and was responsible for absorbing photons and create free charge carrier. As the TCO and the metal contact are generally not selective to only one carrier, additional selective layers to either holes or electrons were deposited between TCO/active layer and metal/active layer, respectively. These layers are denoted as hole transporting layer (HTL) and electron transporting layer (ETL) and are characterized by showing adequate W_f respect to the donor and acceptor materials and decreasing contact resistance. This type of geometry where the electron is extracted in the metal layer is the so-called regular or conventional architecture (glass/ITO/HTL/active layer/ETL/metal) and is depicted in Scheme 3.4.a.

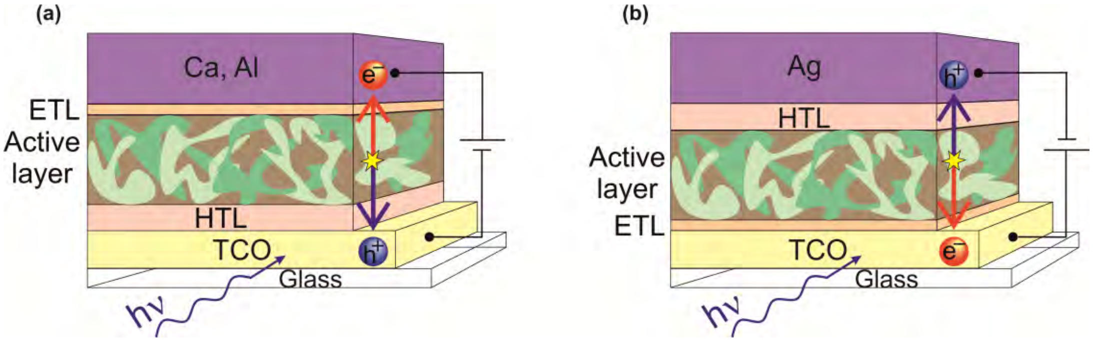

Scheme 3.4. The regular (a) and inverted (b) device geometries with light illumination from the bottom of the cells. The abbreviations are: TCO (transparent conductive oxide), HTL (hole transporting layer), ETL (electron transporting layer). It is also represented the electrons (e^-) and holes (h^+) direction.

However, the regular geometry usually showed important stability issues because low W_f metals such as Al and/or Ca were used (Scheme 3.3). As a consequence, an inverted geometry has been developed because displayed higher stability due to an improvement of the stabilization of the metals *e.g.*, Ag (Scheme 3.4.b). The order of the layers in this type of architecture are reversed with the top metal electrode now being the hole collecting anode, for instance glass/ITO/ETL/active layer/HTL/metal. Here, the electron and hole flow follows the opposite sense respect to the regular structure. Recently, Wu *et al*. has described the highest efficiency OPV solar cell in inverted geometry. The same authors were compared those OPV cells with a conventional geometry achieving lower PCE.[25]

3.5. Materials

The choice of materials to thin film PSCs plays a crucial role to achieve high efficiency and consequently, success of this technology. These materials must be low-cost, stable to different environments and easy to manufacture. In this section, these materials have been briefly considered.

3.5.1. Photoactive layer

The photoactive layer is composed by a blend of materials such as polymer:polymer, polymer:fullerene derivatives or small-molecule:fullerene derivatives as well as polymer:fullerene with carbon nanotubes or nanoparticules such as QDs, ZnO, *etc*. The processable method of the previous combinations of materials is crucial to be a competitive technology. Here, we focus our studies in the polymer:fullerene derivates blended as a BHJ film to implement in PSCs.

Regarding electron donor materials, currently numerous new polymers have been synthesized and studied to acquire specific properties. These new semiconductor polymers should cover a wide range of the solar spectrum (Figure 3.1) in order to maximize the achievable PCE.

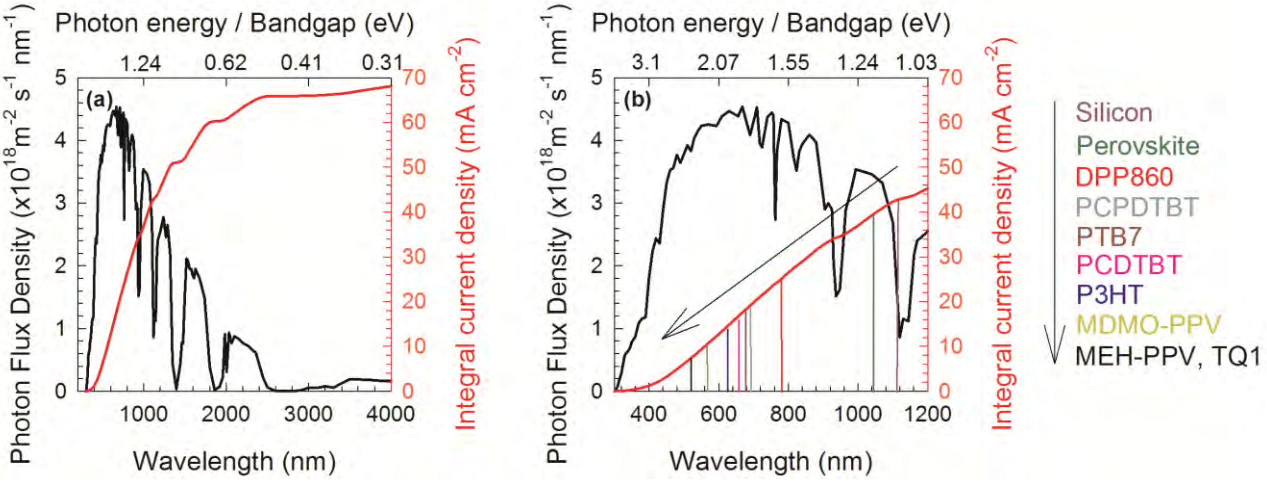

Figure 3.1. (a) Photon flux density at AM1.5G illumination as a function of wavelength or photon energy. The integral of the photon flux (AM1.5G) curve reflects the obtainable maximum current density $j_{\max}$ on the right-axis. In (b) is represented the $j_{\max}$ of several materials listed in Table 3.2.

Figure 3.1 shows the AM1.5G photon flux in the primary axis and the maximum photocurrent density $j_{\max}$ obtainable derived from the AM1.5G photon flux density in the secondary axis versus wavelength and bandgap energy. For the secondary axis plot, it should be noted that the initial value is the bandgap energy and the integration runs over all shorter wavelengths. If we plot the value of the integral for different starting points, we obtain the $j_{\max}$ for a given bandgap.

Table 3.2. Bandgap (E_g), maximum wavelength ($\lambda_{\max}$), and maximum obtainable photocurrent density ($j_{\max}$) for some polymers, perovskite and silicon materials.

Material	E_g (eV)	$\lambda_{\max}$ (nm)	$j_{\max}$ (mA cm^{-2})
MEH-PPV	2.4	516.6	7.18
MDMO-PPV	2.2	563.6	10.29
P3HT	2	619.9	14.16
TQ1	2.4	516.6	7.18
PCDTBT	1.9	652.5	16.51
PTB7	1.84	673.8	18.01
PCPDTBT	1.8	688.8	19.05
DPP860	1.6	774.9	24.75
Perovskite	1.19	1041.9	39.37
Silicon	1.12	1109	42.65

The j_{max} is calculated using the assumption that *EQE* is 100 % for all wavelengths under short-circuit conditions. Lower bandgaps yield higher currents because they absorb larger parts of the spectrum. The j_{max} for multiple polymers, as well as perovskite and silicon are summarized in Table 3.2.

Several researches have been focused on finding the optimal features of polymers to achieve high photoconversion efficiencies. For instance, Scharber *et al.* suggested that efficiencies exceeding 10 % may be obtainable for all polymer:$PC_{60}BM$ blend organic devices if the donor material has its bandgap lower than 1.74 eV and the LUMO level lower than -3.92 eV, with respect to the vacuum level (see energy levels in Scheme 3.5).[42] This fact allows a relatively small bandgap, which can utilize a large portion of the solar spectrum, whilst still the LUMO level offset remains large enough to facilitate excitonic dissociation.[39] Other approach in order to perform high PCEs had been predicted by Marks *et al.* These authors argued that the optimal polymer bandgaps are near of 1.7 eV, achieving efficiencies about 8 % due to an enhancement of charge delocalization near the D/A interface.[43] They described a model taking into account the geminate e–h dissociation *via* charge transfer state.

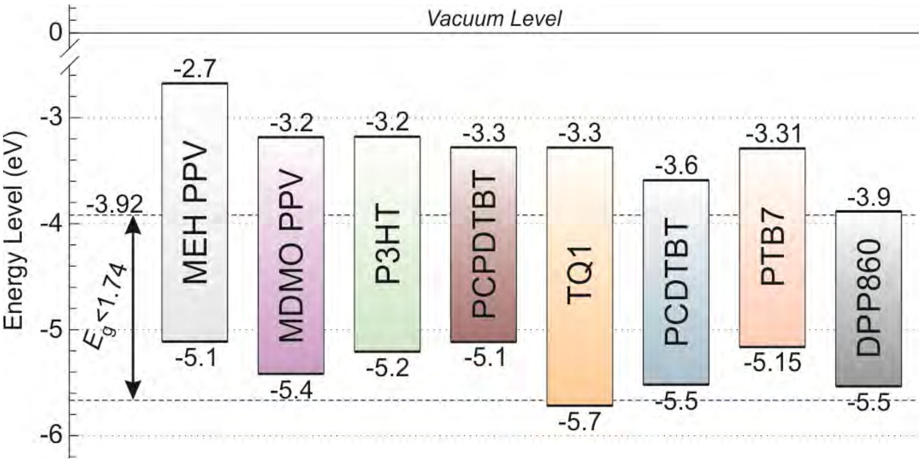

Scheme 3.5. Energy level diagram displaying HOMO and LUMO levels of some donor polymers studied until now which values are taken from the references.[21,36,44-49] Additionally, the bandgaps of some polymers are estimated in the Appendix I. Additionally, it is indicated that to reach efficiencies exceeding 10 % in polymer:PCBM solar cells, the polymer bandgap should be lower than 1.74 eV and the LUMO energy level lower than -3.92 eV, respect to the vacuum level.[32]

Additionally, apart from the optical polymer properties, both electronic and hole mobilities are also important. These materials have in common that the π–conjugate conductive polymer exhibits an alternating single-double bond structure. This property is responsible for the formation of a highly delocalized π–electron system with large electronic polarizability. Consequently, numerous electrical processes may occur, such as absorption of the photons within the visible light region, formation of charge carriers photogenerated, and transport of these charge through them. The charge transport occurs along the short and undisrupted fragments of the polymeric chain by thermally-induced hopping.[50] Moreover, extrinsic charge carriers can be introduced into the organic semiconductors from chemical, photochemical, or electrochemical doping.[51] Besides, the charge transport can be promoted by polymer crystallization since it usually decreases the amount of (energetically) disorder, contributing in this way to improve the performance of OPV solar cells.[40]

On the one hand, one of the earliest donor polymer material based on PPV backbones family is MEH-PPV developed by Wudl *et al.*[52] The MEH-PPV molecular structure is represented in Chart 3.1. In 1995, Yu *et al.* studied the MEH-PPV:C_{60} blend and its fullerene derivatives to give the first OPV solar cell with a high efficiency.[23] After significant optimization, other researchers achieved more than 3.0 % of PCE with PPV-based solar cells, for instance MDMO-PPV polymer (Chart 3.1).[33,53] However, despite these improvements, this kind of polymers were limited by the relatively low hole mobility[54] and narrow light absorption range (see the bandgap in Scheme 3.5), leaving researchers search other donor materials which could produce an improvement in the performance.[45]

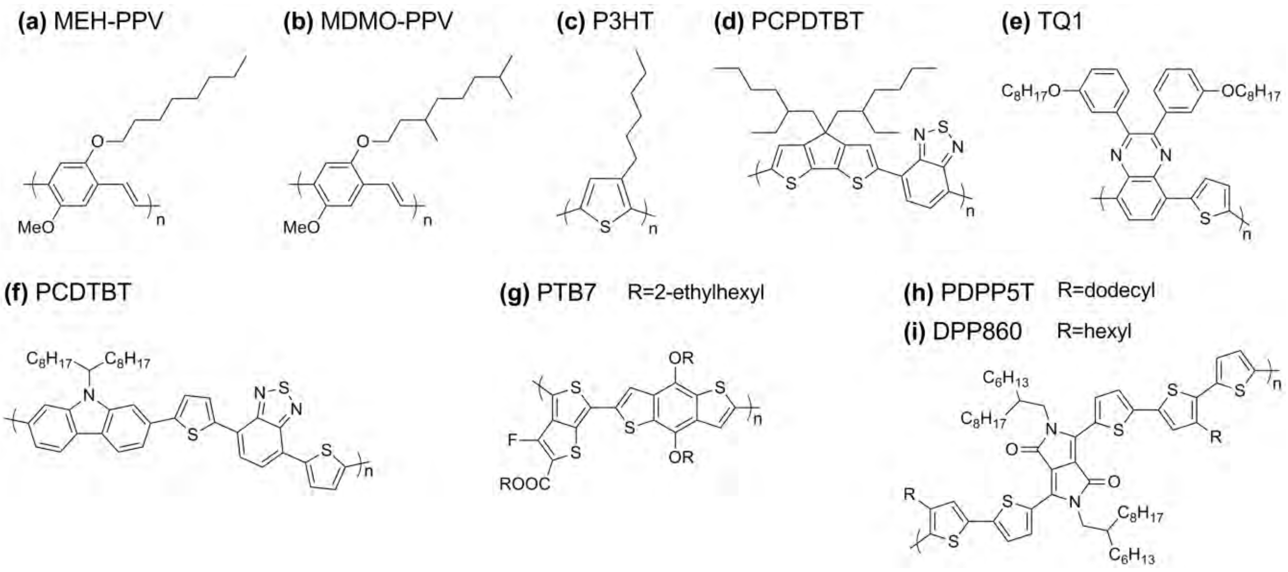

Chart 3.1. Molecular structure of donor polymers such as MEH-PPV (a), MDMO-PPV (b), P3HT (c), PCPDTBT (d), TQ1 (e), PCDTBT (f), PTB7 (g), PDPP5T (h) and DPP860 (i).

From about 2002 onwards, soluble polythiophenes have become the favoured polymer donor materials, especially P3HT (Chart 3.1). Regioregular P3HT possesses many advantages compared to PPV-based polymer, such as a broader spectrum coverage, improvement in environmental stability and higher hole mobility.[55] An intensive research of P3HT:$PC_{60}BM$ system has been carried out, in which optimization has occurred for numerous parameters, mainly in solvent additives,[56] weight % ratio of P3HT and $PC_{60}BM$,[57] light trapping schemes[58] and annealing to improve the nanomorphology.[59] These modifications have provided PCEs of 4–5 %,[55,60] thus attracting worldwide interests in PSCs. However, the efficiency is limited due to the saturation of this polymer system, primarily due to the large bandgap of P3HT, being restrict in the absorption of the solar spectrum portion (see the P3HT bandgap in Scheme 3.5).[39]

Recently, research attention has been focused on CPDT-based polymers, as they are a potential route to low bandgap. One type of these polymers is PCPDTBT which extends its absorption up to 900 nm. The material structure consists of alternating CPDT donor units with BT acceptor units (Chart 3.1), resulting a low optical bandgap (1.8 eV) and high performance in organic field-effect transistor (OFETs) ($\mu_h = 3.3\,\mathrm{cm}^2\ \mathrm{V}^{-1}\ \mathrm{s}^{-1}$ for the polymer with linear alkyl side groups instead of branched 2-ethylhexyl groups) and OPVs (PCE=5.5 %), when blended with fullerene derivatives.[61] An initial efficiency of PCPDTBT-based solar cell have showed of ~3 %.[62] However, several researchers were able to achieve 5.5 % efficiency by incorporating alkanedithiol as additives.[63]

A novel D−A type polymer of low bandgap, based on thiophene and quinoxaline, called TQ1, was easily synthesized by Andersson *et al.* (Chart 3.1).[46] This polymer exhibits good spectral properties with an absorption at higher wavelengths than many of its predecessors, such as P3HT.[64] As a result, it has been successfully applied in solar cells with high performance, up to 7 %.[65]

In 2007, Leclerc *et al.* developed PCDTBT (Chart 3.1) which gave a PCE of 3.6 %.[47] In 2009, Heeger *et al.* increased this efficiency up to 6.1 % by incorporating a TiO_x layer as an optical spacer.[66] In 2011, Tao *et al.* has improved the device performance to 7.1 % of a conventional PCDTBT:$PC_{70}BM$ solar cell by using two polar solvents, DMSO and DMF, as additives in *o*-dichlorobenzene.[67] Additionally, Heeger *et al.* reported an improve of efficiency from 6.3 % to 7.3 % in the PCDTBT:$PC_{70}BM$ embedded with Ag nanoparticle clusters.[68]

In recent years, Yu *et al.* designed PTB7 polymer which belongs to the PTB family (Chart 3.1). PTB7 polymer becomes a great candidate to achieve high efficiencies due to its numerous properties such as low bandgap, good hole mobility, good solubility in organic solvents and polymer alignment which favors charge transport.[69] This polymer has displayed excellent photovoltaic performance of 8.37 % in conventional architecture[70] and a record PCE of 9.2 % in inverted structure.[48] Therefore, it seems that this low bandgap polymer is considered lo lead the way for future improvements in PCE for OPV devices.

Furthermore, other type of polymers based on DPP family with D−A copolymers has gained much attention for their promising application in tandem PSCs and OTFTs.[49,71] The strong electron deficiency of DPP unit endows both the D−A copolymer with ambipolar (hole and electron) transport properties and a strong intermolecular interaction.[72] For instance, the PDPP5T polymer is a DPP-based π−unsubstituted quintethiophene (5T) in repeating units. The hole mobility reaches $1.08\,cm^2\,V^{-1}\,s^{-1}$ without thermal annealing, and a much higher hole mobility of $3.46\,cm^2\,V^{-1}\,s^{-1}$ is obtained annealed at 200 °C, even in an air atmosphere.[72] Janssen *et al.* showed that the use of PDPP5T in a conventional single-junction cell afforded PCE of 5.2 %,[73] whereas for inverted tandem configuration cell a PCE of 5.8 % were obtained.[74,75] Other polymer with similar molecular structure to the PDPP5T is the DPP860 (Chart 3.1) which differs in the alkyl chain: dodecyl and hexyl of the thiophene chain, respectively. This polymer is characterized by a small bandgap (Scheme 3.5), achieving a wide absorbance range from 350 nm to almost 900 nm.

On the other hand, the preferred electron acceptor materials are formed by the buckminsterfullerene C_{60} and its derivatives as illustrated in Chart 3.2. These organic materials are currently considered to be the ideal acceptors in PSCs for several reasons. The LUMO level is energetically deep-lying (see Scheme 3.6),[76] endowing the molecule with a very high electron affinity. Besides, the LUMO of C_{60} molecule is triply degenerate, allowing the fullerene to be reversibly and electrochemically reduced with up to six electrons,[76] thus illustrating its ability to stabilize negative charge. In the early 1990s, Heeger *et al.* and Yoshino *et al.* independently demonstrated electron transfer between a conjugated polymer and fullerene derivatives.[77,78] They observed an ultrafast photoinduced electron transfer process of around 50−100 fs, which dominates over all other photophysical processes present.[51]

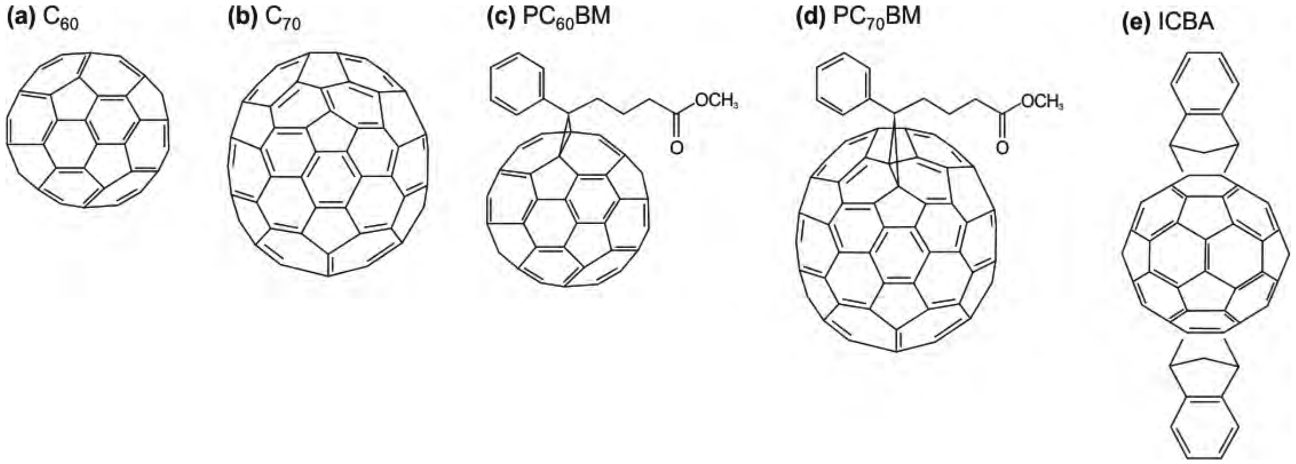

Chart 3.2. Molecular structure of acceptor C_{60} (a) and C_{70} (b) molecules and their fullerene derivatives: $PC_{60}BM$ (c), $PC_{70}BM$ (d) and ICBA (e).

Moreover, C_{60} molecule is characterized by its very high electron mobility of up to $1\,\mathrm{cm}^2\,\mathrm{V}^{-1}\,\mathrm{s}^{-1}$ in field-effect transistors (FETs).[79] These discoveries provided a solid foundation for OPV technology. In 1993, researchers made the first demonstrations of planar heterojunction PSCs, utilizing thin films of a mix between a donor polymer and C_{60} semiconductors to form a BHJ interface.[80] Due to the limited solubility of simple C_{60}, Wudl *et al.* synthesized one of the most important derivative of C_{60} called $PC_{60}BM$.[81] This fullerene derivative represents a milestone in the development of OPV acceptors and is still widely used today due to its solubility,[82] strong electronegativity, high electron mobility and crystal packing to transport charge efficiently.[83]

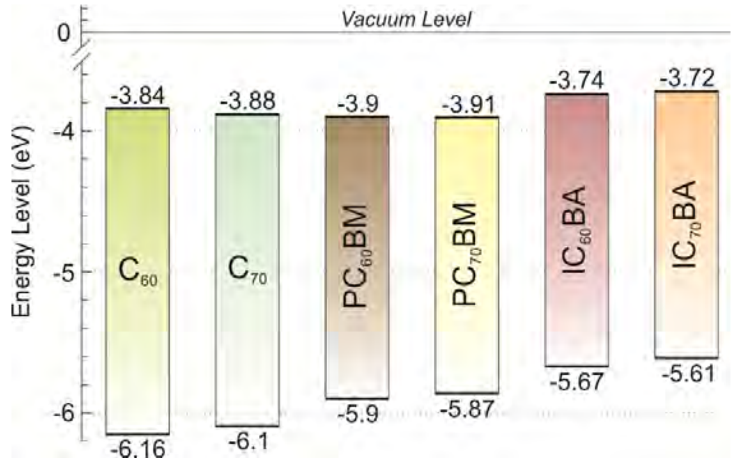

Scheme 3.6. Energy level diagram displaying HOMO and LUMO levels of acceptor fullerene derivatives.[84,85]

Development of novel acceptors is also an interesting field in OPV research due to the possibility to achieve higher efficiencies in OPV cells. For instance, C_{70} derivatives exhibit better absorption than those of C_{60} (see Scheme 3.6). Replacing C_{60} derivatives with C_{70} derivatives often enhances j_{SC} by around 10 %.[20] Besides, using other acceptor materials with up shifted LUMO level leads to a larger value of V_{OC}. One of the most impressive examples of these new novel materials is C_{60} molecule with an indene bisadduct ICBA (Chart 3.2).[86,87] Adding symmetrically such electron-rich indene units to C_{60} molecule, the LUMO energy level of the ICBA (-3.74 eV) is up shifted 0.16 eV compared with $PC_{60}BM$. As a consequence, the P3HT:ICBA devices presented an 40 % improvement on the V_{OC} (0.84 V) respect to the P3HT:$PC_{60}BM$ cells. Although ICBA exhibits superior performance over P3HT, an improvement of the compatibility of fullerene derivatives with other polymer donors remains a challenge.[20]

Furthermore, other types of electron-rich organic materials based on non-fullerene acceptor materials are promising alternatives due to their excellent stability. The amide/imide-based materials such as PDI,[88] NDI,[89] and DPP[90] have been studied (Chart 3.3). Moreover, amide-based acceptor, for instance the *i*I which is an isomer of the well-known dye indigo has been explored.[91]

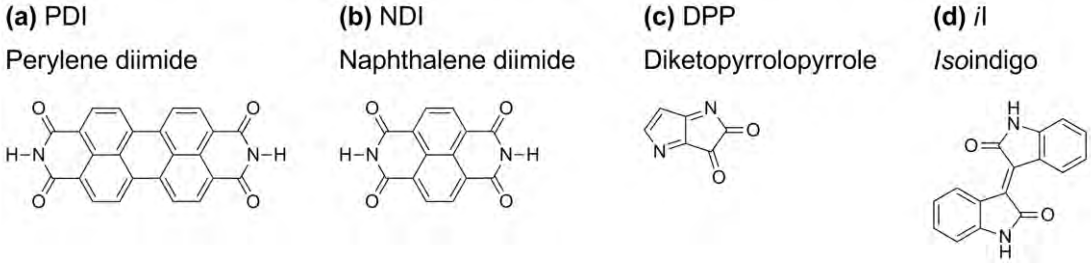

Chart 3.3. Chemical structure of non-fullerene acceptor materials such as PDI (a), NDI (b), DPP (c) and *i*I (d).

3.5.2. Hole transport layer

The most commonly anode interfacial material for OPV and OLED employed is the copolymer PEDOT:PSS (Chart 3.4) up to now. This buffer layer is located between TCO and active layer for the regular OPV devices to reduce the ohmic contact created with the photoactive layer and, consequently an effective hole collection is observed. The advantages of PEDOT:PSS include high conductivity (>200 S cm^{-1}), excellent electrochemical and thermal stability, relatively high transparency to visible light as a thin film, insoluble in organic solvents, large area processing, low cost and flexibility.[92-94] It also smoothes the roughness of the TCO surface reducing the risk of pinholes. This ionic polymer is mostly sold as a water solution/suspension that is applied as a layer in solar cell devices by either spin coating or slot die coating in a Roll-to-Roll (R2R) process.[95] This layer is also helpful to improve the wettability of the metal oxide to the non polar organic active layer, therefore decreasing the risk of delamination that increases the series resistance.[96]

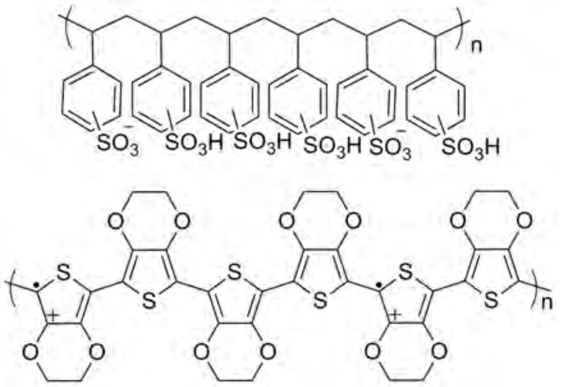

Chart 3.4. Molecular structure of a standard HTL PEDOT:PSS used in PSCs. It is observed two main polymer chains from PEDOT (below) and PSS (above) separately.

The conduction band (CB) of the PEDOT:PSS is higher than the W_f of the ITO, as shown in Scheme 3.7, so its incorporation between ITO and photoactive layer lead to increase V_{oc} values and as a consequence improvements in the PCE. Experimentally, taking into account PEDOT:PSS layer in a OPV device against other cell without this layer, the last device showed lower efficiencies.[97] In addition, an interesting feature of this material is that the CB can be tuned between -4.8 and -5.2 eV relatively easy by different ways such as adding oxidizing or reducing agents,[98] adding NaOH or CsOH,[99] or applying an electrochemical treatment to the dispersion.[100,101]

However, there are some drawback inherent in the use of PEDOT:PSS. The efficiency of this material is limited by its low carrier mobility.[101] Additionally, the PEDOT:PSS can absorb water, probably due to the acidic PSS species (pH of 1–3). As a result, insulating patches are formed at the PEDOT:PSS/active layer interface, and thus, the cell performance is decreased proportionally.[102,103] Besides, this acidic nature triggers the degradation of the ITO, causing the liberation of indium ions which may diffuse through the PEDOT:PSS to the photoactive layer.[104-106] The instability of ITO/PEDOT:PSS interface has been reported by time-of-flight secondary ion mass spectroscopy (TOF-SIMs) and Rutherford backscattering spectrometry (RBS) measurements.[13] Other possible source of corrosion include the reaction with low W_f metals (Al or Ca) used in regular type of geometry devices for the same acidic reason of PSS group. Voroshazi *et al.* investigated the role of PEDOT:PSS in cathode oxidation for PSCs with normal geometry, and they demonstrated that the cathode oxidation was faster due to its hygroscopic nature.[107] Other studies have been shown that even in a dry inert atmosphere, PEDOT:PSS accelerated the degradation presumably due to the residual humidity that can diffuse through the device to the cathode interface where it reacted.[108] These types of degradation pathways can significantly affect the overall performance of the cell over time.

Generally, the appropriate characteristics for an anode interfacial layer in OPV devices are:[109]

- Smoothing the roughness of ITO surface.
- A carrier selective ohmic contacts which requires appropriate energy level alignment.
- High hole mobility to maintain low series resistance.
- High LUMO level to block both electron leakage to the anode and excitons from the donor layer to prevent quenching or dissociation at the anode.
- High bandgap for optical transparency.
- Morphology control over successive organic layer depositions.

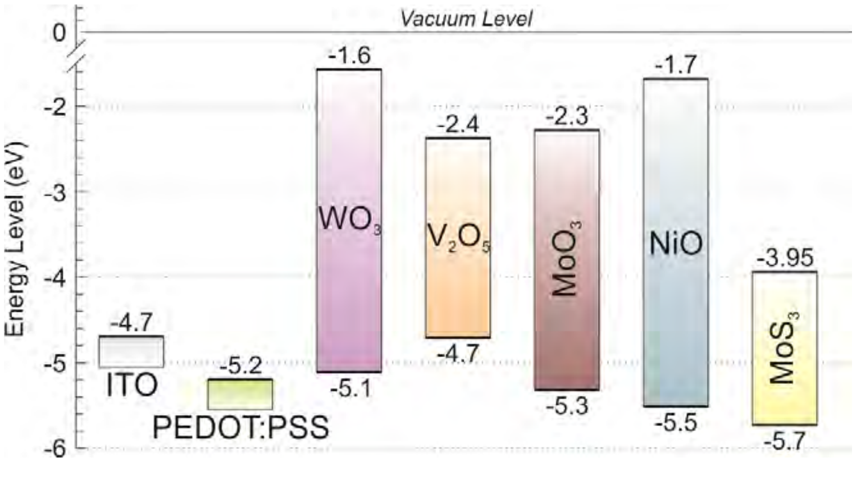

Scheme 3.7. Energy level diagram represents the HOMO level of the PEDOT:PSS and HOMO-LUMO levels of transition metal oxides employed as HTLs. The W_f of the ITO is also added.

Recently, attractive alternative of anode buffer interlayer to conventional OPV devices were studied successfully due to their excellent stability and improvement in the degradation mechanisms.[110-113] New transition metals oxides have been studied, using MoO_x,[110] MoS_x,[105] WO_3,[114] NiO,[21,115] and V_2O_5.[116,117] The inserted layer of metal oxides can modify the W_f of the ITO to enhance the hole injection, improving the cell performance. Scheme 3.7 represents the CBs and valence bands (VBs) of these new metal oxide materials as well as the W_f of the ITO and the CB of the PEDOT:PSS. However, some transition metal oxides are usually incorporated using less convenient vacuum deposition techniques.

3.5.3. Electron transport layer

Metals with low W_f (Ca, Ba and Mg) have been used in the active layer/cathode interface to reduce ohmic contact, extract efficiently electrons, and block hole extraction. However, these metals are highly reactive; as a result, researchers introduced *n*-type inorganic compounds to replace them improving the stability of the device.[20,112]

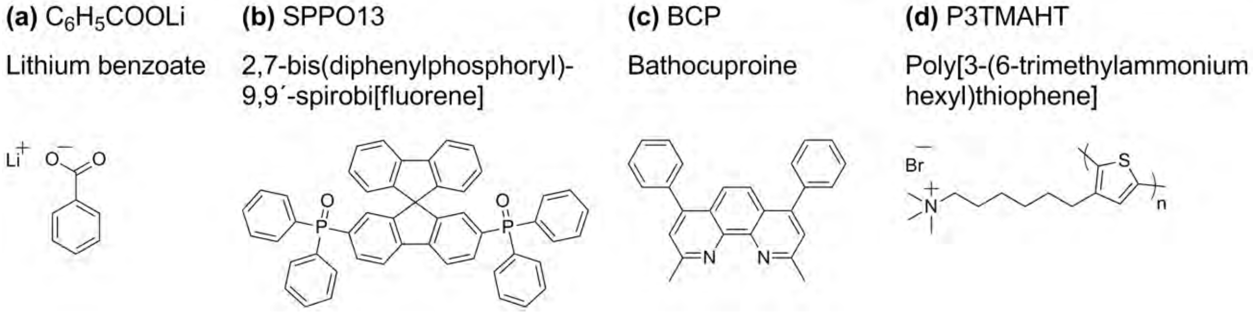

Chart 3.5. Molecular structures of C_6H_5COOLi (a), SPPO13 (b), BCP (c) and P3TMAHT (d).

LiF was the earliest inorganic material used for electron transport due to its appropriate energy alignment with the W_f of the cathode and stability.[23] A mixture of LiF and C_{60} has been explored for this purpose in BHJ solar cells.[118] Xu *et al.* showed a cell lifetime improvement when CuO_x or CuO_x/LiF is added between the P3HT:PC_{60}BM active layer and the Al metal cathode respect to those devices without these ETLs.[119] However, the same authors observed an enhancement of efficiency and stability compared with LiF as an ETL cells when the CrO_x is thermally evaporated between the active layer and the Al cathode.[120] Similarly results were reached for the SPPO13 (Chart 3.5) because this material improved the temperature stability in contrast of LiF-based cells.[121] Other type of buffer layer rely on TiO_x which can be prepared by spin coater of a precursor solution at T_{room}.[122] Additionally, an improvement in both performance and stability is found when a thin layer (~1 nm) of C_6H_5COOLi (Chart 3.5) or Cs_2CO_3 is added.[123,124] Besides, Jin *et al.* reported that using CdSe QD in a thick (~5 nm) interface layer retards the film degradation.[125] Conversely, other study said that CdSe QD interlayer reduces charge recombination by blocking the holes from the active layer to the cathode. Thus, the electrons are efficiently collected.[126] In this scenario, ZnO has become the most common used ETL in inverted devices due to its high electron mobility.[127,128] The addition of organic interfacial modifiers (OIMs) between P3HT:PC_{60}BM and ZnO in inverted geometry achieve 4.69 % of PCE. The OIM layers help to reduce both charge recombination and leakage current by minimizing the number of defect sites and traps. Besides, the compatibility of hydrophilic ZnO with the organic layers is increased by the these layers.[129] Recently, a promising study reported by Jang *et al.* was performed 6.20 % of efficiency, using ZnO as ETL in inverted

PSC incorporating graphene oxide as HTL and PCDTBT:$PC_{70}BM$ as active layer.[130] The energy level diagram of each inorganic material mentioned previously is listed in Scheme 3.8.

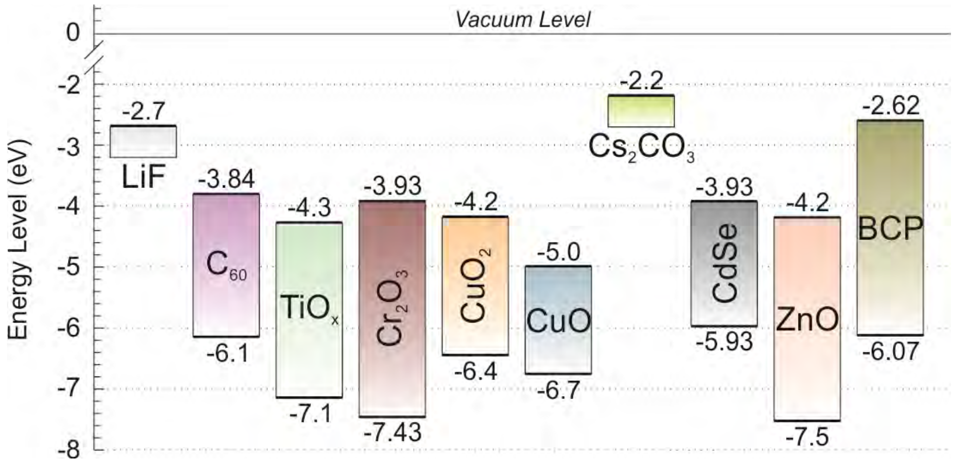

Scheme 3.8. Energy level diagram for several *n*-type materials used in PSCs as electron buffer layers.[131-138]

The previous inorganic *n*-type materials can be easily degraded by moisture and/or oxygen atmosphere on the surface.[139] As a result, new organic molecules have been developed. These materials isolate the oxygen, passivate surface charge traps as well as tune the energy level offset between the organic active layer and the *n*-type semiconducting ETL.[140] These functional molecules are usually joined to the anode or cathode interfaces of the PSCs and form a self-assembled monolayer (SAM) by anchoring groups forming a dipole moment. An effective buffer interlayer, BCP (Chart 3.5), has been deposited between Al cathode and C_{60} acceptor, improving drastically the overall device operation with SubPc as a donor material.[141] However, the BCP deposition often requires high vacuum and high temperature, being undesirable in a low-cost and large-area fabrication process. Other interfacial layer to tune electrode W_f and to act as charge transporting (or blocking) materials is the inclusion of conjugated polyelectrolyte which is functionalized with conjugated polymers in ionic side-chain.[142] They have received considerable interest in past decades because of their main chain can controlled electronic/optical properties, surfactochromicity, and environment-friendly solvent processability with water or polar organic solvents.[143] A considerable improvement in the overall cell performance were reported by Bazan *et al.* when the P3TMAHT (Chart 3.5) is added as a conjugated polyelectrolyte in the active layer/metal cathode interface in a conventional PCDTBT:$PC_{70}BM$-based PSC.[144]

3.5.4. Metal electrode

Metals (Ca, Ba and Mg) are widely used as collector electrodes for OPV due to the possibility to deposit them as electrically conductive films with thicknesses in order of 100 nm. Although metal films thinner than 100 nm generally display a higher resistivity than the corresponding bulk materials, the levels achieved are still sufficient for OPV applications.[13] This decreased conductivity of thin films is caused by surface scattering, grain boundary or impurities scattering, as well as morphological defects.[145,146]

The choice of the metal electrode materials is determined by their W_f (Scheme 3.9),[147] the cell layout (Scheme 3.4) and the energy band diagrams of the bulk active layer materials. In order to reach maximum V_{OC}, the W_f of the metal electrode needs to have an equal or a lower W_f than the LUMO energy level of the electron acceptor compound in the active layer for regular cells.

Inversely, to have an equal or higher W_f value than the HOMO energy level of the electron donor in the case of inverted cells.[13] Blom *et al*. demonstrated that a variation of the metal electrode leads to a universal behavior of the photocurrent when scaled against the effective voltage across the device.[41]

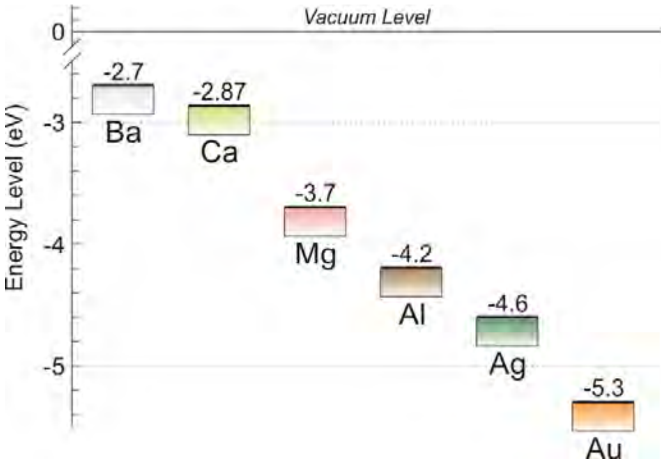

Scheme 3.9. Work function of typical metals used as cathode electrode in regular OPV cells.[131,147]

The typical electron collecting electrodes used for OPV devices are the metals Ca and Al characterized by their low W_f acting as potent reducing agents (see energy diagram in Scheme 3.9).[148] These films are highly reactive; therefore the OPV devices should be stored in oxygen and water free atmosphere either in a glovebox environment or under encapsulation to solve this problem. However, in a real world application, oxygen and water are always present and eventually lead to degradation. In contrast, the dominant reaction seems apparently to be diffusion of water molecules through pores in the metal and reaction to form metal oxides at the interface between the metal and the rest of the device. This metal oxide layer is electrically insulating and creates an electron block barrier. In fact, this effect affects drastically in the performance of the device.[128,149]

Regarding high W_f metal electrode choice (Scheme 3.9), Ag is often selected due to its high stability towards oxidation; as a result, Ag is not prone to OPV degradation by oxygen or water. It is also attractive because it does not need to be evaporated onto the device in vacuum. Instead, it is possible to print/coat emulsions with a high content of Ag particles, using industrially relevant techniques such as printing or spraying, which are compatible with R2R production.[13,56,128] Other high W_f metal electrode is the Au, but is a highly expensive material and is replaced by other more economical and equally electron extraction efficiency.

3.5.5. Transparent anode

TCO films are typically semiconductors that can display metal-like characteristics upon doping. The most widely used are Sn doped In_2O_3 (ITO) and F doped SnO_2 (FTO). Their properties can be tuned by adjustment from both film deposition procedure and component proportions in binary and/or ternary compound alloys.[150] ITO shows high transparency over the visible region, high electrical conductivity, and high W_f of around -4.7 eV.[20] Depending on the TCO surface modifications, such as plasma treatment, covalent attachment of polar groups[151] or adding buffer layers, the wetting and stability of the TCO/active layer interface can be improved. If these precautions are not taken into account, poor adhesion is observed between two layers, favoring the delamination and high series resistance.[13] Additionally, an efficient hole transport occurs when there is low barrier between the W_f of the TCO and the HOMO energy level of the HTL; therefore, the TCO should change the W_f properly by some surface modifications in function of the HTL used.[151,152]

3.5.6. Substrate

Typically the PSCs are built on upon a substrate of transparent glass. This material is cheap, readily available and optically clear. Ultimately, the goal is to move towards flexible plastic substrates which are cheaper and easier to work than brittle glass. This flexible material make possible to use R2R fabrication of OPV cells, becoming an attractive technology for its lower production cost. In view of the recent developments in the field of roll-able and flexible glass, this might change in the future.

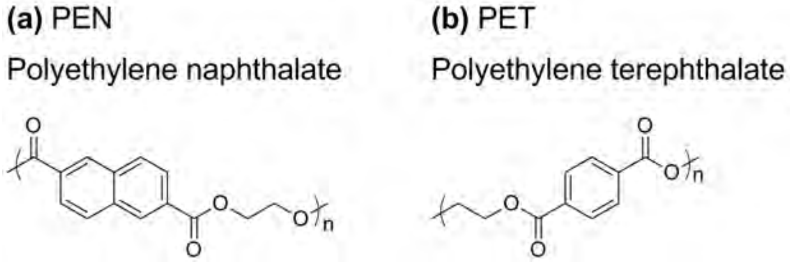

Chart 3.6. A monomer of PEN (a) and PET (b).

Flexible OPV devices are prepared on flexible polymer substrates like PEN or PET films. The structure of each polymer is illustrated in Chart 3.6. Special care should be taken with the encapsulation and some residual moisture and oxygen to remove them once the cell has been encapsulated. It should be noted that these polymers can be adsorbed on the surface of the cell, or even be present in the bulk of the materials, and therefore trigger fast initial decay of the cell.[13] A larger number of flexible devices were studied by Hauch *et al*. These authors demonstrated the low influence against environmental effects of oxygen and water in flexible OPV cells. At 65 ºC and 85 % relative humidity (RH) found lifetimes exceeding 1250 h.[153] Furthermore, Lungenschmied *et al*. reported shelf life of up to 6000 h (to 80 % of its initial performance) based on ITO/PEDOT:PSS/P3HT:$PC_{60}BM$/Al device fabricated on flexible ultrabarriers from NOVA-PLASMA, Inc.[154]

Although most of the flexible OPVs have been fabricated on high cost ITO films grown by a vacuum-based sputtering process, there is a demand for cost effective indium free, vacuum-free and high performance transparent electrodes. To meet those requirements, various types of transparent electrodes were studied such as conducting polymers,[155] carbon nanotubes,[156] graphene,[157] Ag nanomesh,[158] Ag nanowires,[159] Cu nanomesh, Cu nanowire,[160] and oxide-metal-oxide multilayers.[161]

In our laboratory, different substrates electrodes fabricated mainly with glass and PET are analyzed. The suppliers of glass/ITO substrates were XIN YAN, KINTEC, and Thin Film Devices (T.F.D.) with surface resistivities of 7, 10, and 20 $\Omega\ sq^{-1}$, respectively. The PET/ITO substrates were supplied from XIN YAN and Zhuhai Kaivo with surface resistivities of 15 and 45 $\Omega\ sq^{-1}$, respectively. Other transparent conductive layer on PET is the Cu nanowire mesh electrode supplied by Applied Nanotech Holdings, Inc. which replaced the ITO with a low resistivity <0.1 $\Omega\ sq^{-1}$.

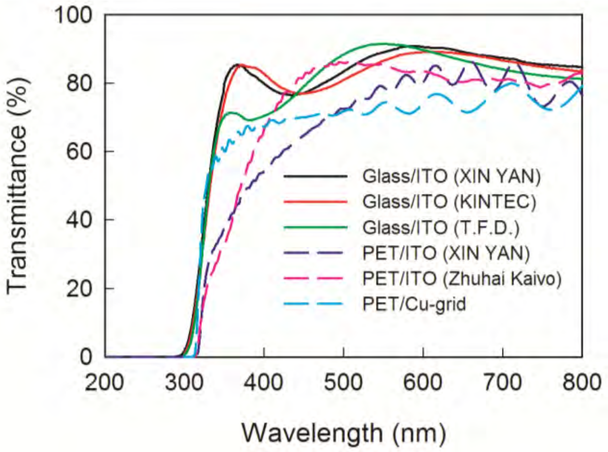

Figure 3.2. UV-Vis spectra for different suppliers of ITO substrate coated glass or PET. It is also added Cu-grid on PET substrate.

As illustrated in Figure 3.2, transmittance spectra for different ITO resistivities on rigid glass and flexible ITO and Cu nanowire mesh on flexible PET is shown. High transparent films are observed for all glass/ITO substrates. However, more differences are shown for the PET/ITO substrates. A decrease of transparency is observed from Zhuhai Kaivo to XIN YAN substrates. It is highlighted that the PET/Cu nanowire mesh substrate show higher transparency at 300–450 nm than the PET/ITO (XIN YAN) substrate.

3.6. Experimental method for device preparation

Over this Ph.D. Thesis development, the conventional structure of PSCs is the main architecture that takes place for almost all experimental procedures. This section details the chemical reagents, materials and BHJ OPV methods.

Several polymer:fullerene blend materials have been studied during this thesis. The donor polymer materials included P3HT (Aldrich or Luminescence Technology Corp.), PCDTBT (1-st Material), PCPDTBT (1-st Material), PTB7 (1-st Material), DPP860 (BASF), and TQ1 (Chalmers University under the project Sunflower). The acceptor fullerene materials were $PC_{60}BM$ (Nano-C, 99.5 %), $PC_{70}BM$ (Solenne or Nano-C, 99 %), and ICBA (Luminescence Technology Corp.). Several additives were used such as hexanethiol (Alfa Aesar, 98 %), octanethiol (Alfa Aesar, 98 %), octanedithiol (Alfa Aesar, 98 %), and 1,8-diiodooctane (Alfa Aesar, 98 %, Cu stabilized). The HTL was the standard PEDOT:PSS pursed by CLEVIOS P AI 4083. Some solvents were employed mainly, chlorobenzene (Aldrich, $\geq$99.5 %), *o*-dichlorobenzene (Aldrich, 99.9 %) and chloroform (Aldrich, 99.9 %). Besides, the metal cathodes for conventional geometry were Ca (Aldrich, 99.995 %) and Ag (Aldrich, 99.99 %) and for inverted geometry were MoO_3 (Aldrich, 99.5 %) and Ag. All these materials were used as received without further purification.

The OPV cell studied follow the device configuration showed in Scheme 3.4.a. Initially, the glass were dipped in a mixture of solvents acetone:ethanol and then, oxygen air is crossed over the surface for total dryness. The surface of the substrate was completely clean after UVO treatment for 5 min under atmosphere ambient. The standard PEDOT:PSS HTL was deposited on the top of the ITO by spin coating at 5500 rpm for 30 s, then at 3000 rpm for 30 s in air. The thickness of the PEDOT:PSS layer was about 35 nm, as determined by a VEECO DEKTACK 6M Stylus Profiler. Drying of PEDOT:PSS film was realized at 130 ºC for 10 min in the atmosphere and the same treatment was repeated into the glovebox to completely remove traces of water. After that, the devices were manipulated all the time into the glovebox until the encapsulation process, unless otherwise stated. The active layers were deposited on the top of PEDOT:PSS layer by spin coater. For instance, if we consider the standard P3HT:$PC_{60}BM$ photoactive layer, the films were spin coated at 900 rpm for 10 s and then were dried slowly into a petri dish covered for about 2 h. The spin coater conditions of the others blends were changed to achieve the optimum active layer thickness, about 100 nm. Before metal evaporation, the samples were heated directly on a hotplate at 130 ºC for 10 min when the active layer was P3HT:$PC_{60}BM$. Finally, the cathode electrode was deposited (5 nm Ca/100 nm Ag) by thermal evaporation at a base pressure of 10^{-6} mbar. The top Ca/Ag electrodes were then encapsulated before testing either epoxy or a photoresin with a glass microscopy slide followed by exposure under UV light for the photoresin samples. Finally, the OPV devices were taken out of the glovebox for device characterization. The active areas of a substrate were 0.09, 0.16 and 0.25 cm^2 as shown in Scheme 3.10.

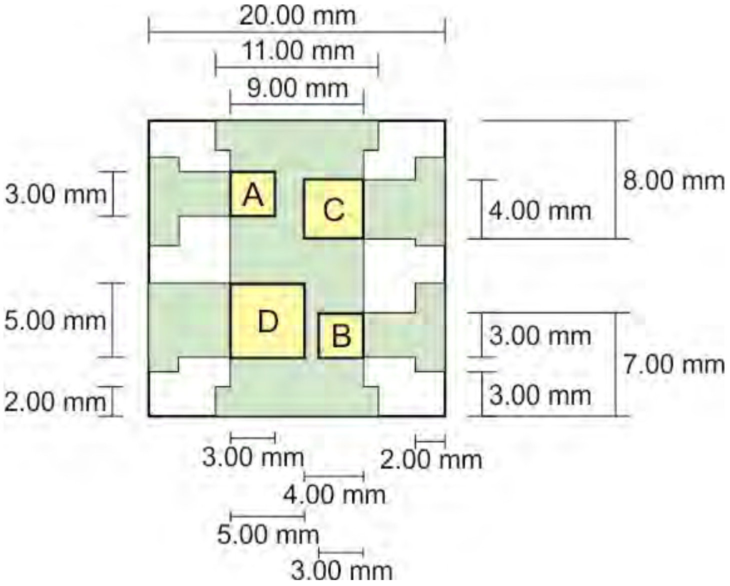

Scheme 3.10. ITO pattern on a glass substrate. Four different cells are checked with active surface 0.09 (Cells A and B), 0.16 (Cell C) and 0.25 (Cell D) cm^2.

Some experimental details to carry out the fabrication of efficient OPV cells are highlighted below for different blend compositions. All this information is recapitulated briefly in Table 3.3. In addition, Table 3.4 summarized the photovoltaic characteristics of different OPV devices obtained in our laboratories under simulated 1 sun illumination.

Photoactive layer based on P3HT and $PC_{60}BM$ blended by 1:1 weight of polymer:fullerene ratio and *o*-dichlorobenzene as solvent were used as a benchmark throughout this thesis. The P3HT:$PC_{60}BM$ solution was stirred at 90 ºC for 2 h until complete dissolution. The active layer thickness was about ~300 nm when the concentration of the solution was 34 mg mL^{-1} using the spin coating conditions stated above. Alternatively, films of ~100 nm were casted with the same conditions explained before and a concentration of 17 mg mL^{-1}. After blend deposition, the BHJ films should be completely dried by introducing them in a petri dish. In addition, this blend was heated at 130 ºC for 10 min before cathode evaporation.

The PCDTBT:$PC_{70}BM$ blend by weight 1:4 of polymer:fullerene ratio used a mixture of solvents chlorobenzene:*o*-dichlorobenzene (1:1, volume ratio) in a concentration of 4 mg mL^{-1}. The solution was stirred until complete dissolution at T_{room}. The BHJ layer was deposited by spin coater, obtaining an optimum thickness about 100 nm. After film deposition and before cathode evaporation, the films were dried and heated directly on a surface of the hotplate at 70 ºC for 30 min in an oxygen free environment glovebox.

Table 3.3. Experimental conditions to manufacture efficient OPV cells: polymer:fullerene ratios (by weight), concentrations, solvents, temperature of the solution (T), annealing treatments (A.T.) before cathode deposition and additives (by weight). Nomenclature: *o*-dichlorobenzene is *o*-DCB, chlorobenzene is CB, chloroform is $CHCl_3$, octanedithiol is ODT and 1,8-diiodooctane is DIO.

Polymer	**Fullerene**	**Ratio**	**Conc.** (mg mL^{-1})	**Solvent**	***T*** (ºC/h)	**A.T.** (ºC/min) or **Additives**
P3HT	$PC_{60}BM$ or $PC_{70}BM$	1:1	17	*o*-DCB	90/2	130/10
PCDTBT	$PC_{70}BM$	1:4	4	CB:*o*-DCB$^{a)}$	Room$^{c)}$	70/30
PCPDTBT	$PC_{70}BM$	1:2	17	*o*-DCB	60/12	5 % ODT
PTB7	$PC_{70}BM$	1:1.5	12	CB	100$^{c)}$	3 % DIO
DPP860	$PC_{70}BM$	1:2	7.5	$CHCl_3$:*o*-DCB$^{b)}$	55/5	-
TQ1	$PC_{70}BM$	1:2.5	30	*o*-DCB	Room$^{c)}$	-

$^{a)}$ 1:1 (by volume); $^{b)}$ 9:1 (by volume); $^{c)}$ until complete dissolution.

The solution of a mixture of PCPDTBT:$PC_{70}BM$, 1:2 by weight of polymer:fullerene ratio, were prepared in *o*-dichlorobenzene and concentration of 17 mg mL^{-1}. This solution was stirred at 60 ºC overnight before deposited by spin coater. This blend required additives to improve the blend morphology. The stock solution of the additive was prepared previously. The mixture of PCPDTBT:$PC_{70}BM$ and the additive solutions was stirred 30 min before to device fabrication at T_{room}. Several additives were studied (hexanethiol, octanethiol, and octanedithiol), but the best PCE results were obtained for the additive octanedithiol in a concentration of 5 % by weight. These films were dried after their deposition by spin coater and annealing treatments were not necessary.

The PTB7:$PC_{70}BM$ solution, polymer:fullerene ratio of 1:1.5 by weight, was prepared with chlorobenzene as solvent in a concentration of 12 mg mL^{-1}. This blend required 3 % (by weight) of 1,8-diiodooctane as an additive The mixture was stirred at 100 ºC until complete dissolution. This BHJ film does not need annealing treatment.

The DPP860:$PC_{70}BM$ blend was prepared at 1:2 polymer:fullerene ratio (by weight) and was dissolved in a mixture of solvents chloroform:*o*-dichlorobenzene (9:1, by volume ratio). The optimum concentration was 7.5 mg mL^{-1}. The solution were stirred at 55 ºC for 5 h and 5 min before using it, this solution was cooled down to T_{room}. The optimum film thickness was about 100 nm. Any thermal annealing was needed after film deposition by spin coater.

The experimental conditions for TQ1:$PC_{70}BM$ BHJ film were required a concentration of 30 mg mL^{-1} with 1:2.5 polymer:fullerene ratio (by weight) and *o*-dichlorobenzene as solvent. The solution was stirred until complete dissolution at T_{room}. After blend deposition by spin coater, the film must be completely dried and any annealing treatment was required. The optimum active layer thickness is around 100 nm.

Table 3.4. The best photovoltaic parameters obtained in our laboratory for different blend compositions on PSCs in regular architecture under simulated AM1.5G irradiation intensity.

Blend	j_{sc} (mA cm^{-2})	V_{oc} (V)	***FF*** (%)	**PCE** (%)
P3HT:PC$_{60}$BM	8.10	0.62	66	3.31
P3HT:PC$_{60}$BM[a)]	10.76	0.59	56	3.5
P3HT:ICBA	8.0	0.87	60	4.2
PCDTBT:PC$_{70}$BM	10.03	0.84	60	5.09
PCPDTBT:PC$_{70}$BM	7.69	0.66	47	2.38
PTB7:PC$_{70}$BM	15.31	0.71	48	5.2
DPP860:PC$_{70}$BM	12.80	0.55	66	4.7
TQ1:PC$_{70}$BM	6.64	0.86	68	3.88

[a)] *Flexible substrate and inverted geometry.*

3.7. Stability & degradation

According to the international consensus of stability testing protocols for OPV materials and devices, basic procedures require minimum instrumentation and protocol requirements likely to be fulfilled in most places. In total, there are three levels: basic (Level 1), intermediate (Level 2) and advanced (Level 3) in function of the capabilities of a wider range of laboratories. Level 3 includes the accredited certifying laboratories.[128] For conditioning and testing in tropical countries, the ambient conditions are defined as 25 ºC and 65 % for the testing temperature and RH, respectively.[162]

The ideal photovoltaic device should present constant performance over time when is illuminated and also show little dependence on being subject to cyclic changes in the environment light/dark, hot/cold, dry/humid.[128] The commercialization of the OPV devices required considerable improvement of stability under operational conditions. Device durability that involves chemical stability and degradation of polymers has always been an important issue for OPV cells. Some studies of non-encapsulated OPV cells lifetime have demonstrated efficiency half life of greater than 1500 h. Kippelen *et al.* have noted that the shelf lifetime of a pentacene/C$_{60}$ cell encapsulated with an Al$_2$O$_3$ film deposited by atomic layer deposition has degraded by 6 % over a 6100 h period, compared to a lifetime of <10 h for an non-encapsulated cell.[163] Brabec has estimated that a cell lifetime of at least 5 years (about 45000 h) is necessary for the commercialization of PSCs.[164]

Physical and/or chemical degradation modes of OPV devices can be divided in two main categories:[13]

- Intrinsic degradation due to changes in the characteristics of the interface between layers of the stacking owing to internal modification of the materials used.
- Extrinsic degradation caused by changes in the cell behavior induced by external triggers, such as water, oxygen, electromagnetic radiations (UV, visible light, IR...), *etc*. The latter is strongly linked to the quality and stability in properties of the encapsulation system, namely the barrier, the substrate and the type of edge sealing used.

Therefore, an increase of the stability of OPV devices requires careful selection of new donor and acceptor materials, alternative barrier layers which are more resistant to oxygen and water, electrode, and encapsulation materials.

3.8. Market & applications

The major suppliers of OPV materials and technology include Heliatek, Solarmer, Mitsubishi, Plextronics, EPFL, Peccell, Sono-tek, and others. Eight19 Limited raised $7 million from the Carbon Trust and Rhodia to develop PSCs. Besides, Konarka made PSC modules commercially available in 2009.[165] Intel has begun some research into PSCs, as well. Additionally, Belectric and Dyesol suggested integrate photovoltaic cells on buildings. The vehicle integrated photovoltaic technology has been a promising area for thin film solar cells. Furthermore, other application could be suitable for off-grid locations due to their independence from large infrastructure. A relative small scale can be incorporated into many products such as portable chargers for consumer electronics.[166] Other interesting application is the integration of PSCs with clothing for powering personal electronic devices is forthcoming. Hany *et al.* have demonstrated a flexible and transparent electrode mesh based on a fabric with metal wires and polymer fibers woven together.[167]

3.9. References

1. J. Schmidtke, *Opt. Express*, 2010, 18, A477-A486.
2. J. Kalowekamo and E. Baker, *Sol. Energy*, 2009, 83, 1224-1231.
3. M. L. Gaëtan Masson, M. Rekinger, I.-T. Theologitis, M. Papoutsi, *Global Market Outlook for Photovoltaics 2013-2017*, European Photovoltaic Industry Association (EPIA), 2013.
4. S. Reineke, M. Thomschke, B. Lussem and K. Leo, *Rev. Mod. Phys.*, 2013, 85, 1245-1293.
5. B. Kumar, B. K. Kaushik and Y. S. Negi, *J. Mater. Sci. Mater.*, 2014, 25, 1-30.
6. P. Heremans, G. H. Gelinck, R. Müller, K.-J. Baeg, D.-Y. Kim and Y.-Y. Noh, *Chem. Mater.*, 2010, 23, 341-358.
7. U. Zhokhavets, T. Erb, G. Gobsch, M. Al-Ibrahim and O. Ambacher, *Chem. Phys. Lett.*, 2006, 418, 347-350.
8. Y. J. Cheng, S. H. Yang and C. S. Hsu, *Chem. Rev.*, 2009, 109, 5868-5923.
9. T. Ameri, N. Li and C. J. Brabec, *Energy Environ. Sci.*, 2013, 6, 2390-2413.
10. D. Yue, P. Khatav, F. You and S. B. Darling, *Energy Environ. Sci.*, 2012, 5, 9163-9172.
11. C. J. Brabec, J. A. Hauch, P. Schilinsky and C. Waldauf, *MRS Bull.*, 2005, 30, 50-52.
12. C. J. Brabec, *Sol. Energy Mater. Sol. Cells*, 2004, 83, 273-292.
13. N. Grossiord, J. M. Kroon, R. Andriessen and P. W. M. Blom, *Org. Electron.*, 2012, 13, 432-456.
14. M. Riede, T. Mueller, W. Tress, R. Schueppel and K. Leo, *Nanotechnology*, 2008, 19, 424001.
15. M. A. Green, K. Emery, Y. Hishikawa, W. Warta and E. D. Dunlop, *Prog. Photovolt: Res. Appl.*, 2014, 22, 1-9.
16. N. Yeh and P. Yeh, *Renew. Sust. Energ. Rev.*, 2013, 21, 421-431.
17. H. Spanggaard and F. C. Krebs, *Sol. Energy Mater. Sol. Cells*, 2004, 83, 125-146.
18. J. A. Carr and S. Chaudhary, *Energy Environ. Sci.*, 2013, 6, 3414-3438.
19. C. W. Tang, *Appl. Phys. Lett.*, 1986, 48, 183-185.
20. G. Li, R. Zhu and Y. Yang, *Nat. Photon.*, 2012, 6, 153-161.
21. L. Dou, J. You, J. Yang, C.-C. Chen, Y. He, S. Murase, T. Moriarty, K. Emery, G. Li and Y. Yang, *Nat. Photon.*, 2012, 6, 180-185.
22. M. Hiramoto, H. Fujiwara and M. Yokoyama, *J. Appl. Phys.*, 1992, 72, 3781-3787.
23. G. Yu, J. Gao, J. C. Hummelen, F. Wudl and A. J. Heeger, *Science*, 1995, 270, 1789-1791.
24. J. J. M. Halls, C. A. Walsh, N. C. Greenham, E. A. Marseglia, R. H. Friend, S. C. Moratti and A. B. Holmes, *Nature*, 1995, 376, 498-500.
25. Z. C. He, C. M. Zhong, S. J. Su, M. Xu, H. B. Wu and Y. Cao, *Nat. Photon.*, 2012, 6, 591-595.
26. Y. Yao, C. J. Shi, G. Li, V. Shrotriya, Q. B. Pei and Y. Yang, *Appl. Phys. Lett.*, 2006, 89, 153507.
27. F. Gao, S. Q. Ren and J. P. Wang, *Energy Environ. Sci.*, 2013, 6, 2020-2040.
28. T. Earmme, Y.-J. Hwang, N. M. Murari, S. Subramaniyan and S. A. Jenekhe, *J. Am. Chem. Soc.*, 2013, 135, 14960-14963.
29. P. Guyot-Sionnest and M. A. Hines, *Appl. Phys. Lett.*, 1998, 72, 686-688.

30. R. Zhou and J. Xue, *Chem. Phys. Chem.*, 2012, 13, 2471-2480.
31. A. Dhanabalan, J. K. J. van Duren, P. A. van Hal, J. L. J. van Dongen and R. A. J. Janssen, *Adv. Funct. Mater.*, 2001, 11, 255-262.
32. M. C. Scharber, D. Wuhlbacher, M. Koppe, P. Denk, C. Waldauf, A. J. Heeger and C. L. Brabec, *Adv. Mater.*, 2006, 18, 789-794.
33. M. M. Wienk, J. M. Kroon, W. J. H. Verhees, J. Knol, J. C. Hummelen, P. A. van Hal and R. A. J. Janssen, *Angew. Chem.-Int. Edit.*, 2003, 42, 3371-3375.
34. B. Verreet, P. Heremans, A. Stesmans and B. P. Rand, *Adv. Mater.*, 2013, 25, 5504-5507.
35. T. M. Burke and M. D. McGehee, *Adv. Mater.*, 2014, 26, 1923-1928.
36. B. C. Thompson and J. M. J. Frechet, *Angew. Chem.-Int. Edit.*, 2008, 47, 58-77.
37. G. Garcia-Belmonte, A. Munar, E. M. Barea, J. Bisquert, I. Ugarte and R. Pacios, *Org. Electron.*, 2008, 9, 847-851.
38. I. G. Hill, A. Kahn, Z. G. Soos and J. R. A. Pascal, *Chem. Phys. Lett.*, 2000, 327, 181-188.
39. M. Wright and A. Uddin, *Sol. Energy Mater. Sol. Cells*, 2012, 107, 87-111.
40. V. Coropceanu, J. Cornil, D. A. da Silva, Y. Olivier, R. Silbey and J. L. Bredas, *Chem. Rev.*, 2007, 107, 926-952.
41. V. D. Mihailetchi, L. J. A. Koster and P. W. M. Blom, *Appl. Phys. Lett.*, 2004, 85, 970-972.
42. M. C. Scharber, D. Mühlbacher, M. Koppe, P. Denk, C. Waldauf, A. J. Heeger and C. J. Brabec, *Adv. Mater.*, 2006, 18, 789-794.
43. J. D. Servaites, B. M. Savoie, J. B. Brink, T. J. Marks and M. A. Ratner, *Energy Environ. Sci.*, 2012, 5, 8343-8350.
44. A. L. Holt, J. M. Leger and S. A. Carter, *J. Chem. Phys.*, 2005, 123, 044704.
45. G. Dennler, M. C. Scharber and C. J. Brabec, *Adv. Mater.*, 2009, 21, 1323-1338.
46. E. Wang, L. Hou, Z. Wang, S. Hellström, F. Zhang, O. Inganäs and M. R. Andersson, *Adv. Mater.*, 2010, 22, 5240-5244.
47. N. Blouin, A. Michaud and M. Leclerc, *Adv. Mater.*, 2007, 19, 2295-2300.
48. Z. He, C. Zhong, S. Su, M. Xu, H. Wu and Y. Cao, *Nat. Photon.*, 2012, 6, 591-595.
49. T. Ripolles-Sanchis, S. R. Raga, A. Guerrero, M. Welker, M. Turbiez, J. Bisquert and G. Garcia-Belmonte, *J. Phys. Chem. C*, 2013, 117, 8719-8726.
50. J. Stephan, S. Schrader and L. Brehmer, *Synth. Met.*, 2000, 111, 353-357.
51. S. Gunes, H. Neugebauer and N. S. Sariciftci, *Chem. Rev.*, 2007, 107, 1324-1338.
52. F. Wudl and G. Srdanov, in *Conducting polymer formed of poly(2-methoxy-5-(2’-ethylhexyloxy)-p-phenylene vinylene). Patent US 5189136 A*, 1993, vol. 5, p. 136.
53. C. J. Brabec, S. E. Shaheen, C. Winder, N. S. Sariciftci and P. Denk, *Appl. Phys. Lett.*, 2002, 80, 1288-1290.
54. V. D. Mihailetchi, H. X. Xie, B. de Boer, L. J. A. Koster and P. W. M. Blom, *Adv. Funct. Mater.*, 2006, 16, 699-708.
55. W. L. Ma, C. Y. Yang, X. Gong, K. Lee and A. J. Heeger, *Adv. Funct. Mater.*, 2005, 15, 1617-1622.

56. L. L. Chang, I. E. Jacobs, M. P. Augustine and A. J. Moule, *Org. Electron.*, 2013, 14, 2431-2443.
57. D. Chirvase, J. Parisi, J. C. Hummelen and V. Dyakonov, *Nanotechnology*, 2004, 15, 1317-1323.
58. X. Yang, A. Uddin and M. Wright, *Phys. Status Solidi-Rapid Res. Lett.*, 2012, 6, 199-201.
59. H. P. Chen, S. Hu, H. D. Zang, B. Hu and M. Dadmun, *Adv. Funct. Mater.*, 2013, 23, 1701-1710.
60. G. Li, V. Shrotriya, J. S. Huang, Y. Yao, T. Moriarty, K. Emery and Y. Yang, *Nat. Mater.*, 2005, 4, 864-868.
61. H. Waters, J. Kettle, S.-W. Chang, C.-J. Su, W.-R. Wu, U. S. Jeng, Y.-C. Tsai and M. Horie, *J. Mater. Chem. A*, 2013, 1, 7370-7378.
62. D. Muhlbacher, M. Scharber, M. Morana, Z. G. Zhu, D. Waller, R. Gaudiana and C. Brabec, *Adv. Mater.*, 2006, 18, 2884-2889.
63. J. Peet, J. Y. Kim, N. E. Coates, W. L. Ma, D. Moses, A. J. Heeger and G. C. Bazan, *Nat. Mater.*, 2007, 6, 497-500.
64. S. Hedström and P. Persson, *J. Phys. Chem. C*, 2012, 116, 26700-26706.
65. Y. Kim, H. R. Yeom, J. Y. Kim and C. Yang, *Energy Environ. Sci.*, 2013, 6, 1909-1916.
66. S. H. Park, A. Roy, S. Beaupre, S. Cho, N. Coates, J. S. Moon, D. Moses, M. Leclerc, K. Lee and A. J. Heeger, *Nat. Photon.*, 2009, 3, 297-303.
67. T.-Y. Chu, S. Alem, S.-W. Tsang, S.-C. Tse, S. Wakim, J. Lu, G. Dennler, D. Waller, R. Gaudiana and Y. Tao, *Appl. Phys. Lett.*, 2011, 98, 253301.
68. D. H. Wang, K. H. Park, J. H. Seo, J. Seifter, J. H. Jeon, J. K. Kim, J. H. Park, O. O. Park and A. J. Heeger, *Adv. Energy Mater.*, 2011, 1, 766-770.
69. Y. Y. Liang, Z. Xu, J. B. Xia, S. T. Tsai, Y. Wu, G. Li, C. Ray and L. P. Yu, *Adv. Mater.*, 2010, 22, E135-E138.
70. Z. C. He, C. M. Zhong, X. Huang, W. Y. Wong, H. B. Wu, L. W. Chen, S. J. Su and Y. Cao, *Adv. Mater.*, 2011, 23, 4636-4643.
71. Z. Chen, M. J. Lee, R. Shahid Ashraf, Y. Gu, S. Albert-Seifried, M. Meedom Nielsen, B. Schroeder, T. D. Anthopoulos, M. Heeney, I. McCulloch and H. Sirringhaus, *Adv. Mater.*, 2012, 24, 647-652.
72. Z. Yi, X. Sun, Y. Zhao, Y. Guo, X. Chen, J. Qin, G. Yu and Y. Liu, *Chem. Mater.*, 2012, 24, 4350-4356.
73. S. Kouijzer, J. J. Michels, M. van den Berg, V. S. Gevaerts, M. Turbiez, M. M. Wienk and R. A. J. Janssen, *J. Am. Chem. Soc.*, 2013, 135, 12057-12067.
74. V. S. Gevaerts, A. Furlan, M. M. Wienk, M. Turbiez and R. A. J. Janssen, *Adv. Mater.*, 2012, 24, 2130-2134.
75. S. Kouijzer, S. Esiner, C. H. Frijters, M. Turbiez, M. M. Wienk and R. A. J. Janssen, *Adv. Energy Mater.*, 2012, 2, 945-949.
76. P. M. Allemand, A. Koch, F. Wudl, Y. Rubin, F. Diederich, M. M. Alvarez, S. J. Anz and R. L. Whetten, *J. Am. Chem. Soc.*, 1991, 113, 1050-1051.

77. N. S. Sariciftci, L. Smilowitz, A. J. Heeger and F. Wudl, *Science*, 1992, 258, 1474-1476.
78. S. Morita, A. A. Zakhidov and K. Yoshino, *Solid State Commun.*, 1992, 82, 249-252.
79. T. B. Singh, N. Marjanović, G. J. Matt, S. Günes, N. S. Sariciftci, A. Montaigne Ramil, A. Andreev, H. Sitter, R. Schwödiauer and S. Bauer, *Org. Electron.*, 2005, 6, 105-110.
80. N. S. Sariciftci, L. Smilowitz, A. J. Heeger and F. Wudl, *Synth. Met.*, 1993, 59, 333-352.
81. F. Wudl, *Acc. Chem. Res.*, 1992, 25, 157-161.
82. J. C. Hummelen, B. W. Knight, F. Lepeq, F. Wudl, J. Yao and C. L. Wilkins, *J. Org. Chem.*, 1995, 60, 532-538.
83. M. T. Rispens, A. Meetsma, R. Rittberger, C. J. Brabec, N. S. Sariciftci and J. C. Hummelen, *Chem. Commun.*, 2003, 2116-2118.
84. Y. F. Yang, F. Arias, L. Echegoyen, L. P. F. Chibante, S. Flanagan, A. Robertson and L. J. Wilson, *J. Am. Chem. Soc.*, 1995, 117, 7801-7804.
85. G. Chen, D. Yokoyama, H. Sasabe, Z. Hong, Y. Yang and J. Kido, *Appl. Phys. Lett.*, 2012, 101, 083904.
86. Y. J. He, H. Y. Chen, J. H. Hou and Y. F. Li, *J. Am. Chem. Soc.*, 2010, 132, 1377-1382.
87. G. J. Zhao, Y. J. He and Y. F. Li, *Adv. Mater.*, 2010, 22, 4355-4358.
88. X. Zhang, Z. H. Lu, L. Ye, C. L. Zhan, J. H. Hou, S. Q. Zhang, B. Jiang, Y. Zhao, J. H. Huang, S. L. Zhang, Y. Liu, Q. Shi, Y. Q. Liu and J. N. Yao, *Adv. Mater.*, 2013, 25, 5791-5797.
89. T. Earmme, Y. J. Hwang, N. M. Murari, S. Subramaniyan and S. A. Jenekhe, *J. Am. Chem. Soc.*, 2013, 135, 14960-14963.
90. P. Sonar, G.-M. Ng, T. T. Lin, A. Dodabalapur and Z.-K. Chen, *J. Mater. Chem.*, 2010, 20, 3626-3636.
91. R. Stalder, J. Mei, K. R. Graham, L. A. Estrada and J. R. Reynolds, *Chem. Mater.*, 2013, 26, 664-678.
92. H. Kim, J. Lee, S. Ok and Y. Choe, *Nanoscale Res. Lett.*, 2012, 7, 5.
93. S. Z. Xiao, S. A. Fernandes, C. Esen and A. Ostendorf, *J. Laser Micro Nanoen.*, 2011, 6, 249-254.
94. S. A. Mauger, L. L. Chang, C. W. Rochester and A. J. Moule, *Org. Electron.*, 2012, 13, 2747-2756.
95. F. C. Krebs, S. A. Gevorgyan and J. Alstrup, *J. Mater. Chem.*, 2009, 19, 5442-5451.
96. J. S. Kim, R. H. Friend and F. Cacialli, *J. Appl. Phys.*, 1999, 86, 2774-2778.
97. F. Nüesch, G. Tornare, L. Zuppiroli, F. Meng, K. Chen and H. Tian, *Sol. Energy Mater. Sol. Cells*, 2005, 87, 817-824.
98. M. P. de Jong, A. W. D. van der Gon, X. Crispin, W. Osikowicz, W. R. Salaneck and L. Groenendaal, *J. Chem. Phys.*, 2003, 118, 6495-6502.
99. C. H. L. Weijtens, V. van Elsbergen, M. M. de Kok and S. de Winter, *Org. Electron.*, 2005, 6, 97-104.
100. A. Petr, F. Zhang, H. Peisert, M. Knupfer and L. Dunsch, *Chem. Phys. Lett.*, 2004, 385, 140-143.

101. K. S. Kang, Y. Chen, H. K. Lim, K. Y. Cho, K. J. Han and J. Kim, *Thin Solid Films*, 2009, 517, 6096-6099.
102. K. Kawano, R. Pacios, D. Poplavskyy, J. Nelson, D. D. C. Bradley and J. R. Durrant, *Sol. Energy Mater. Sol. Cells*, 2006, 90, 3520-3530.
103. J. R. Manders, S. W. Tsang, M. J. Hartel, T. H. Lai, S. Chen, C. M. Amb, J. R. Reynolds and F. So, *Adv. Funct. Mater.*, 2013, 23, 2993-3001.
104. M. P. de Jong, L. J. van Ijzendoorn and M. J. A. de Voigt, *Appl. Phys. Lett.*, 2000, 77, 2255-2257.
105. X. Li, W. Zhang, Y. Wu, C. Min and J. Fang, *ACS Appl. Mater. Interfaces*, 2013, 5, 8823-8827.
106. X. W. Yan, B. Chu, W. L. Li, Z. S. Su, T. Y. Zhang, F. M. Jin, B. Zhao, F. Zhang, D. Fan, Y. Gao, T. Tsuboi, J. B. Wang, H. J. Pi and J. Z. Zhu, *Org. Electron.*, 2013, 14, 1805-1810.
107. E. Voroshazi, B. Verreet, A. Buri, R. Muller, D. Di Nuzzo and P. Heremans, *Org. Electron.*, 2011, 12, 736-744.
108. E. Voroshazi, B. Verreet, T. Aernouts and P. Heremans, *Sol. Energy Mater. Sol. Cells*, 2011, 95, 1303-1307.
109. T. Fleetham, B. O'Brien, J. P. Mudrick, J. G. Xue and J. Li, *Appl. Phys. Lett.*, 2013, 103, 083303.
110. Z. a. Tan, D. Qian, W. Zhang, L. Li, Y. Ding, Q. Xu, F. Wang and Y. Li, *J. Mater. Chem. A*, 2013, 1, 657-664.
111. A. M. Nardes, M. Kemerink, M. M. de Kok, E. Vinken, K. Maturova and R. A. J. Janssen, *Org. Electron.*, 2008, 9, 727-734.
112. A. Turak, *RSC Adv.*, 2013, 3, 6188-6225.
113. E. L. Ratcliff, B. Zacher and N. R. Armstrong, *J. Phys. Chem. Lett.*, 2011, 2, 1337-1350.
114. R. Lampande, G. W. Kim, J. Boizot, Y. J. Kim, R. Pode and J. H. Kwon, *J. Mater. Chem. A*, 2013, 1, 6895-6900.
115. M. D. Irwin, J. D. Servaites, D. B. Buchholz, B. J. Leever, J. Liu, J. D. Emery, M. Zhang, J.-H. Song, M. F. Durstock, A. J. Freeman, M. J. Bedzyk, M. C. Hersam, R. P. H. Chang, M. A. Ratner and T. J. Marks, *Chem. Mater.*, 2011, 23, 2218-2226.
116. A. B. Yusoff, H. P. Kim and J. Jang, *Org. Electron.*, 2013, 14, 858-861.
117. Z. A. Tan, W. Q. Zhang, C. H. Cui, Y. Q. Ding, D. P. Qian, Q. Xu, L. J. Li, S. S. Li and Y. F. Li, *Phys. Chem. Chem. Phys.*, 2012, 14, 14589-14595.
118. D. Gao, M. G. Helander, Z. B. Wang, D. P. Puzzo, M. T. Greiner and Z. H. Lu, *Adv. Mater.*, 2010, 22, 5404-5408.
119. M. D. Wang, F. Y. Xie, W. G. Xie, S. Z. Zheng, N. Ke, J. Chen, N. Zhao and J. B. Xu, *Appl. Phys. Lett.*, 2011, 98, 183304.
120. M. D. Wang, Q. Tang, J. An, F. Y. Xie, J. A. Chen, S. Z. Zheng, K. Y. Wong, Q. A. Miao and J. B. Xu, *ACS Appl. Mater. Interfaces*, 2010, 2, 2699-2702.
121. S. O. Jeon and J. Y. Lee, *Sol. Energy Mater. Sol. Cells*, 2011, 95, 1102-1106.
122. A. Hadipour, R. Muller and P. Heremans, *Org. Electron.*, 2013, 14, 2379-2386.

123. Y. L. Wang, L. Y. Yang, C. Yao, W. J. Qin, S. G. Yin and F. L. Zhang, *Sol. Energy Mater. Sol. Cells*, 2011, 95, 1243-1247.

124. L. Y. Yang, H. Xu, H. Tian, S. G. Yin and F. L. Zhang, *Sol. Energy Mater. Sol. Cells*, 2010, 94, 1831-1834.

125. H. Jin, M. Tuomikoski, J. Hiltunen, P. l. Kopola, A. Maaninen and F. Pino, *J. Phys. Chem. C*, 2009, 113, 16807-16810.

126. J. H. Jeon, D. H. Wang, H. Park, J. H. Park and O. O. Park, *Langmuir*, 2012, 28, 9893-9898.

127. M. S. White, D. C. Olson, S. E. Shaheen, N. Kopidakis and D. S. Ginley, *Appl. Phys. Lett.*, 2006, 89, 143517.

128. M. Jorgensen, K. Norrman, S. A. Gevorgyan, T. Tromholt, B. Andreasen and F. C. Krebs, *Adv. Mater.*, 2012, 24, 580-612.

129. S. H. Eom, M.-J. Baek, H. Park, L. Yan, S. Liu, W. You and S.-H. Lee, *ACS Appl. Mater. Interfaces*, 2013, 6, 803-810.

130. A. R. B. Yusoff, H. P. Kim and J. Jang, *Nanoscale*, 2014, 6, 1537-1544.

131. X. Gong, M. Tong, F. G. Brunetti, J. Seo, Y. Sun, D. Moses, F. Wudl and A. J. Heeger, *Adv. Mater.*, 2011, 23, 2272-2277.

132. M. J. Greaney, S. Das, D. H. Webber, S. E. Bradforth and R. L. Brutchey, *ACS Nano*, 2012, 6, 4222-4230.

133. M. T. Greiner, M. G. Helander, W.-M. Tang, Z.-B. Wang, J. Qiu and Z.-H. Lu, *Nat. Mater.*, 2012, 11, 76-81.

134. A. K. K. Kyaw, X. W. Sun, C. Y. Jiang, G. Q. Lo, D. W. Zhao and D. L. Kwong, *Appl. Phys. Lett.*, 2008, 93, 221107.

135. F.-C. Chen, J.-L. Wu, S. S. Yang, K.-H. Hsieh and W.-C. Chen, *J. Appl. Phys.*, 2008, 103, 103721.

136. M. Wang, F. Xie, W. Xie, S. Zheng, N. Ke, J. Chen, N. Zhao and J. B. Xu, *Appl. Phys. Lett.*, 2011, 98, 183304.

137. Z. Liu, S. Seo and E.-C. Lee, *Appl. Phys. Lett.*, 2013, 103, 133306.

138. J. Li, X. D. Huang, J. Y. Yuan, K. Y. Lu, W. Yue and W. L. Ma, *Org. Electron.*, 2013, 14, 2164-2171.

139. C. E. Small, S. Chen, J. Subbiah, C. M. Amb, S. W. Tsang, T. H. Lai, J. R. Reynolds and F. So, *Nat. Photon.*, 2012, 6, 115-120.

140. T. Sakurai, S. Toyoshima, H. Kitazume, S. Masuda, H. Kato and K. Akimoto, *J. Appl. Phys.*, 2010, 107, 043707.

141. H. Gommans, B. Verreet, B. P. Rand, R. Muller, J. Poortmans, P. Heremans and J. Genoe, *Adv. Funct. Mater.*, 2008, 18, 3686-3691.

142. J. G. Mei and Z. N. Bao, *Chem. Mater.*, 2014, 26, 604-615.

143. H. Shen, C. Kou, M. He, H. Yang and K. Liu, *J. Polym. Sci., Part A: Polym. Chem.*, 2014, 52, 739-751.

144. J. H. Seo, A. Gutacker, Y. M. Sun, H. B. Wu, F. Huang, Y. Cao, U. Scherf, A. J. Heeger and G. C. Bazan, *J. Am. Chem. Soc.*, 2011, 133, 8416-8419.

145. H. Klauk, J. R. Huang, J. A. Nichols and T. N. Jackson, *Thin Solid Films*, 2000, 366, 272-278.
146. K. Norrman and F. C. Krebs, *Sol. Energy Mater. Sol. Cells*, 2006, 90, 213-227.
147. İ. Taşçıoğlu, Ş. Altındal, İ. Polat and E. Bacaksız, *Curr. Appl. Phys.*, 2013, 13, 1306-1310.
148. M. T. Lloyd, D. C. Olson, P. Lu, E. Fang, D. L. Moore, M. S. White, M. O. Reese, D. S. Ginley and J. W. P. Hsu, *J. Mater. Chem.*, 2009, 19, 7638-7642.
149. T. Ripolles-Sanchis, A. Guerrero, J. Bisquert and G. Garcia-Belmonte, *J. Phys. Chem. C*, 2012, 116, 16925-16933.
150. T. Minami, *Semicond. Sci. Technol.*, 2005, 20, S35-S44.
151. Y. H. Tak, K. B. Kim, H. G. Park, K. H. Lee and J. R. Lee, *Thin Solid Films*, 2002, 411, 12-16.
152. H. Kim, A. Pique, J. S. Horwitz, H. Mattoussi, H. Murata, Z. H. Kafafi and D. B. Chrisey, *Appl. Phys. Lett.*, 1999, 74, 3444-3446.
153. J. A. Hauch, P. Schilinsky, S. A. Choulis, S. Rajoelson and C. J. Brabec, *Appl. Phys. Lett.*, 2008, 93, 103306.
154. C. Lungenschmied, G. Dennler, H. Neugebauer, S. N. Sariciftci, M. Glatthaar, T. Meyer and A. Meyer, *Sol. Energy Mater. Sol. Cells*, 2007, 91, 379-384.
155. C.-H. Wu, H.-P. Shen, T.-M. Don and W.-Y. Chiu, *Mater. Chem. Phys.*, 2013, 143, 143-148.
156. D.-Y. Cho, K. Eun, S.-H. Choa and H.-K. Kim, *Carbon*, 2014, 66, 530-538.
157. Z. Liu, J. Li and F. Yan, *Adv. Mater.*, 2013, 25, 4296-4301.
158. J.-S. Yu, G. H. Jung, J. Jo, J. S. Kim, J. W. Kim, S.-W. Kwak, J.-L. Lee, I. Kim and D. Kim, *Sol. Energy Mater. Sol. Cells*, 2013, 109, 142-147.
159. D. Langley, G. Giusti, C. Mayousse, C. Celle, D. Bellet and J. P. Simonato, *Nanotechnology*, 2013, 24, 452001.
160. M.-G. Kang, H. Joon Park, S. Hyun Ahn and L. Jay Guo, *Sol. Energy Mater. Sol. Cells*, 2010, 94, 1179-1184.
161. T. Abachi, L. Cattin, G. Louarn, Y. Lare, A. Bou, M. Makha, P. Torchio, M. Fleury, M. Morsli, M. Addou and J. C. Bernède, *Thin Solid Films*, 2013, 545, 438-444.
162. M. Agbomahena, O. Douheret, B. Kounouhewa, A. Vianou, N. Awanou and R. Lazzaroni, *Sol. Energy Mater. Sol. Cells*, 2013, 117, 93-97.
163. W. J. Potscavage, S. Yoo, B. Domercq and B. Kippelen, *Appl. Phys. Lett.*, 2007, 90, 253511.
164. C. J. Brabec, *Sol. Energy Mater. Sol. Cells*, 2004, 83, 273-292.
165. T. D. Nielsen, C. Cruickshank, S. Foged, J. Thorsen and F. C. Krebs, *Sol. Energy Mater. Sol. Cells*, 2010, 94, 1553-1571.
166. S. Lizin, S. Van Passel, E. De Schepper and L. Vranken, *Sol. Energy Mater. Sol. Cells*, 2012, 103, 1-10.
167. W. Kylberg, F. A. de Castro, P. Chabrecek, U. Sonderegger, B. T.-T. Chu, F. Nüesch and R. Hany, *Adv. Mater.*, 2011, 23, 1015-1019.

CHAPTER 4

CHARACTERIZATION TECHNIQUES FOR PHOTOVOLTAIC DEVICES

4.1. Introduction

Several experimental techniques are required to characterize Polymer Solar Cells (PSCs). Techniques that are going to be used in this Ph.D. Thesis are widely established for the scientific community. In complete devices, the current density–voltage ($j-V$) under illumination or dark conditions and the external quantum efficiency (*EQE*) measurements are the most common and available methods to obtain the device efficiency and the efficiency of collection of carriers as a function of the wavelength. To analyze the absorption properties of the films or solutions ultraviolet-visible (UV-Vis) spectroscopy is used. From that data, the optical bandgap can be calculated for our materials. Besides, the active layer films are also characterized by variable angle spectroscopy ellipsometer (VASE) which provides information on the depth and surface of each polymer and fullerene into a bulk. Purely electrical techniques provide advanced electrical information such as capacitance–voltage ($C-V$) (at constant frequency) and the impedance spectroscopy (IS) (in a range of frequencies). The later techniques are recently attracting more attention due to the large variety of information that can be extracted. The morphology is characterized by x-ray diffraction (XRD) as well as atomic force microscopy (AFM) and scanning electron microscopy (SEM). HOMO and LUMO energy levels are measured from cyclic voltammetry (*CV*) measurements. Finally, from transient photocurrent (TPC) we are able to measure the relaxation time.

4.2. Current density–Voltage measurement

The $j-V$ characteristic of an illuminated solar cell that behaves as an ideal diode *p–n* junction is described by the equation

$$j = j_{\mathrm{dk}} - j_{\mathrm{ph}} = j_0\left[\exp\left(\frac{qV}{k_{\mathrm{B}}T}\right)-1\right]- j_{\mathrm{ph}} \tag{4.1}$$

The first term in equation 4.1 describes the dark diode current density following the Shockley relation j_{dk} and the second term describes a constant photogenerated current density j_{ph} under illumination. The current depends on the area, so the current is usually normalized as a current density, j (units mA cm^{-2}), being current density–voltage $j-V$ curve. j_0 is the saturation current density, q is the electron charge, V is the applied voltage, k_{B} is the Boltzmann constant and T is the temperature. The j_{ph} is closely related to the photon flux incident on the cell, and its dependence on the wavelength of the light reflected in the *EQE* or spectral response as the ratio between the number of free charge carriers created in the outer circuit and the number of incident photons. This behavior can be described by a simple equivalent circuit, in which a diode and current source are connected in parallel. An electrical circuit representing an ideal solar cell is shown in Scheme 4.1.

In real solar cells, there is an ohmic loss occurred due to the influence of parasitic resistances into a solar cell: series resistance, R_{s} , and shunt resistance (in parallel), R_{sh} . The R_{s} is the resistance offered by the solar cell in the path of the current flow. On the contrary, the R_{sh} is referred as the leakage path of the current in a solar cell and, therefore, it is represented in parallel with the current source. The influence of these parameters on the $j-V$ characteristic of the solar cell can be studied using the simplified equivalent circuit model presented in Scheme 4.1.

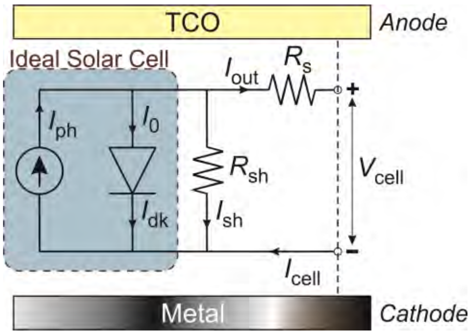

Scheme 4.1. Simplified equivalent circuit of *p*–*n* junction solar cell by one diode. The ideal solar cell is only represented by a diode and a current source connected in parallel. Shunt resistance, R_{sh} and, series resistance, R_s, are also represented as a loss current.

The $j-V$ (Scheme 4.2) characteristic of the one-diode equivalent circuit with R_s and R_{sh} is described by the following equation

$$j = \frac{1}{1+R_s/R_{sh}}\left\{ j_0\left[\exp\left(\frac{q(V_{app}-jAR_s)}{k_BT}\right)-1\right]-\left[j_{ph}-\frac{V_{app}}{AR_{sh}}\right]\right\} \qquad (4.2)$$

where A is the area of the solar cell and R_s is typically much lower than the R_{sh}. For an ideal solar cell having a pronounced diode dependence of the current with voltage, R_s would be zero, and R_{sh} would be infinite. In real cases, the increased R_s and a low R_{sh} determine a modification on the shape of the $j-V$ curve. PSCs are more sensitive to the influence of these resistances and distortions of the $j-V$ curve when R_s and R_{sh} are comparable values.

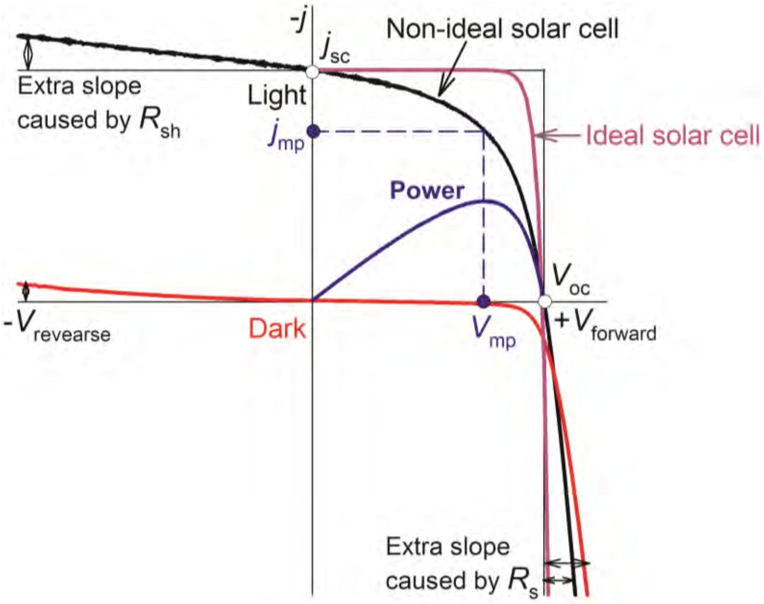

Scheme 4.2. Typical $j-V$ curve under dark (red line) and light (black line) conditions for solar cells. The $j-V$ curve for ideal solar cell is represented in pick line which looks almost like a square. The conditions to simulate the ideal case for equation 4.2 are: $R_s = 0\,\Omega$, $R_{sh} = 10^{30}\,\Omega$, $T = 300\,\mathrm{K}$, $k_B = 1.38\times10^{-23}\,\mathrm{J\,K^{-1}}$, $q = 1.602\times10^{-19}\,\mathrm{Q}$, $A = 0.09\,\mathrm{cm}^2$, $j_0 = 10^{-12}\,\mathrm{A\,cm^{-2}}$, and $j_{ph} = 0.94\,\mathrm{mA\,cm^{-2}}$. The voltage at current zero is the open-circuit voltage, V_{oc}. Inversely, the current at voltage zero is the short-circuit current density, j_{sc}. The maximum power P_{max} ($P_{max} = jV$) is also represented with its voltage and current at maximum power point V_{mp} and j_{mp}, respectively. The effect of shunt (at reverse bias) and series (at forward bias) resistances are also indicated.

Typical $j-V$ characteristic of a non-ideal diode under illumination and dark conditions is shown in Scheme 4.2. An ideal diode look similar to a square as illustrated in Scheme 4.2. Forward bias is referred to positive voltage applied V_{app} with + on the anode (TCO) and – on the cathode (metal), while a negative one (– on TCO and + on metal) is referred to as reverse bias. The curve shows the turn-on and the build-up of the forward bias current in the diode. Without illumination, no currents flows through the diode unless there is external potential applied. However, the $j-V$ curve shift up with incident sunlight and indicates that there is external current flow from the solar cell to a passive load. The following sections widely explain some important photovoltaic parameters extracted from $j-V$ curve.

4.2.1. Short-circuit current

The j_{SC} is the maximum photocurrent density that flows through the external circuit at any illumination level when the electrodes of the solar cell are short circuited ($V_{\text{app}}=0$) (see Scheme 4.2). The j_{SC} depends on the photogeneration of charge free carriers and is proportional to the incident photon flux density on the solar cell, which is determined by the spectrum of the incident light. This parameter is affected by the decrease of the number of charges collected at the electrodes caused by various degradation mechanisms, which impact on the photon absorption, charge dissociation, transport to the electrodes as well as photoactive layer/electrode transfer.[1] To achieve high j_{SC} can be by different ways such as narrowing the bandgap for a broader coverage of the solar spectrum, improve the carrier mobility, intermolecular interaction and molecular chain packing,[2] *etc*. As regards the narrowing the bandgap, some methologies are reported such as designing an alternating donor–acceptor (D–A) structure, stabilizing the quinoid structure, controlling the polymer chain planarity, and tuning the effective conjugation length. Designing an alternating D–A structure is the most common approach. The push-pull driving forces between the donor and acceptor units, together with the photoinduced intramolecular charge transfer, facilitates electron delocalization and the formation of low-bandgap quinoid mesomeric structures over the polymer backbone.[3]

4.2.2. Open-circuit voltage

The V_{OC} is the maximum voltage that a solar cell can deliver when no current flows through the external circuit (see Scheme 4.2). V_{OC} is directly linked to the difference between Fermi Level of electrons and holes as follows[4]

$$qV_{\text{OC}}=E_{\text{Fn}}-E_{\text{Fp}} \tag{4.3}$$

where q is the elementary charge, E_{Fn} is the electrons Fermi Level and E_{Fp} is the holes Fermi Level. The ideal blend conditions to achieve high V_{OC} values correspond to the lower HOMO level of the donor polymer material and the higher LUMO level of the acceptor fullerene material. Taking into the P3HT as a reference for polymer design, the V_{OC} values can vary significantly depending on the fullerene material. For instance, the P3HT solar cell devices based on $PC_{60}BM$ displayed V_{OC} of 0.6 V,[5] 0.87 V for ICBA,[6] 0.89 V for $Lu_3N@C_{80}$-PCBH,[7] and 1.1 V for a dimer of 9,9′-bifluorenylidene backbone as an acceptor material.[8] The P3HT belongs to the thiophene family which is characterized by an electron-rich group. However, the polymer becomes wide-bandgap material by changing this group to others with less electron-rich such as fluorene and carbazole groups. The V_{OC} can be considerably increased by incorporating these units. Cao *et al.*

demonstrated a $V_{oc} \approx 1.0\,\mathrm{V}$ with a polymer that contain a fluorene unit and, the same result was reported by Inganäs *et al.* with a polymer composed of fluorene and quinoxaline alternating units.[9,10] One of the successful examples at the early stage is the PCDTBT polymer based on carbazole and BT groups reported high V_{oc} value of 0.89 V by Leclerc *et al.*[11] Regarding fluorinated BT units, the polymer PBDT-DTffBT showed an enhancement from 0.87 to 0.91 V in V_{oc} compared with that polymer without these units.[12] Later on, several more polymers with the same units were reported with enhanced V_{oc} and efficiencies.[13] Respecting BDT group, a V_{oc} value of 0.92 V was reported.[14] Finally, other markedly increment on V_{oc} results was demonstrated by Chen *et al.* using a quinquethiophene derivative polymer, achieving 1.08 V value.[15]

4.2.3. Fill factor

The *FF* is essentially a measure of quality of the solar cell and describes the 'squareness' of the $j-V$ curve. The solar cells act as a diode but due to the recombination processes at the junction D/A interface, there is a deviation from the ideal diode, archiving *FF* values less than 1. Deviations from the ideal case, and thus the shape of the $j-V$ curve, can be quantitatively characterized by the parasitic loss mechanisms of series R_S and shunt R_{sh} (parallel) resistances. Since the effect of R_{sh} is negligible near open-circuit conditions, the slope of the $j-V$ curve in that vicinity is an indicator of the R_S value. Conversely, since the effect of R_S is negligible near short-circuit conditions, the slope of the curve in that vicinity is an indicator of the R_{sh} value. Figure 4.1 shows the effect of the R_S and R_{sh} on the $j-V$ curve.

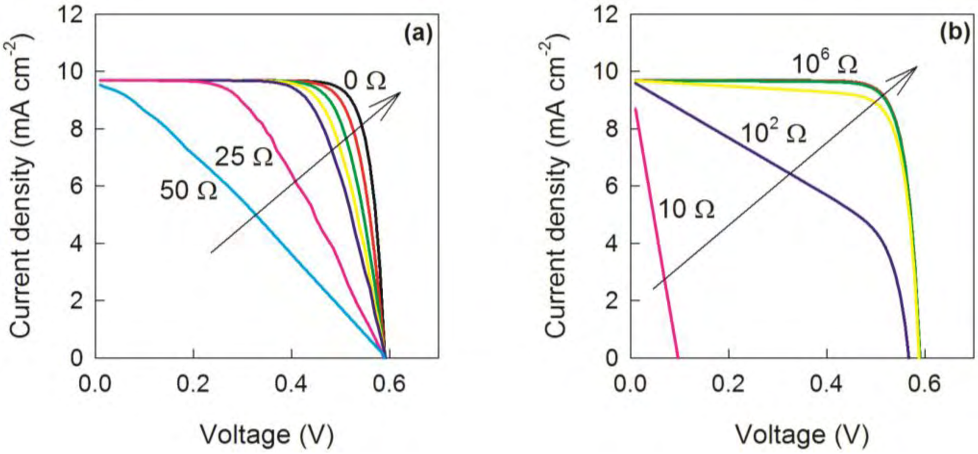

Figure 4.1. Effect of parasitic resistances on the $j-V$ characteristic of a solar cell: (a) varying the R_S (0, 2.5, 5, 7.5, 10, 25, and 50 Ω) and keeping constant the $R_{sh} = 10^6\,\Omega$ and (b) varying the R_{sh} (10, 10^2, 10^3, 10^4, 10^5, and 10^6 Ω) and keeping the $R_S = 0\,\Omega$. Taking into account the equation 4.2 and the constants $T = 298\,\mathrm{K}$, $k_B = 1.38 \times 10^{-23}\,\mathrm{J\,K^{-1}}$, $q = 1.602 \times 10^{-19}\,\mathrm{Q}$, $A = 1\,\mathrm{cm}^2$, $j_0 = 10^{-12}\,\mathrm{A\,cm^{-2}}$, and $j_{ph} = 10\,\mathrm{mA\,cm^{-2}}$.

On the one hand, the R_S is the sum of resistance due to all the components that come in the path of current. This includes the degradation of the bulk, the organic material/metallic electrode interface resistance, and resistance of the metal contact. It is desirable to have the value of R_S as low as possible being $R_S = 0$ the ideal case. However, poor conductivity of the charge carriers is influenced by the thickness of the organic layer and by the density of traps reduced charge carrier injection to the electrodes which is reflected in an increment of the R_S. At high voltages, the conduction is determined mostly by the R_S

$$R_{\mathrm{s}} = \left.\frac{V_{\mathrm{out}}}{I}\right|_{I\to\infty} \tag{4.4}$$

On the one hand, the R_{sh} is due to the leakage across the *p–n* junction. It could be as a consequence of shunt around the periphery of the cell or due to the crystal defect or precipitates of impurities in the junction region. It is desirable to have the value of R_{sh} as high as possible, being $R_{\mathrm{sh}} = \infty$ the ideal case. However, a reduction in R_{sh} is caused by imperfections during the production process within the photoactive film or leakage current at the interface between layers in the device.[16] Such a diversion reduces the amount of current flowing through the solar cell junction and reduces the overall cell performance. At small voltages the ideal diode does not conduct, according to the Kirchoff's laws, the outer current is controlled by the sum of series and parallel resistances, as

$$R_{\mathrm{s}} + R_{\mathrm{sh}} = \left.\frac{V_{\mathrm{out}}}{I}\right|_{I\to I_{\mathrm{sc}}} \tag{4.5}$$

From Scheme 4.2, the *FF* is calculated by the ratio between the maximum obtainable power ($P_{\max} = V_{\mathrm{mp}} I_{\mathrm{mp}}$) to the maximum theoretical power output (P_{T}).

$$FF = \frac{P_{\max}}{P_T} = \frac{V_{\mathrm{mp}}\, j_{\mathrm{mp}}}{V_{\mathrm{oc}}\, j_{\mathrm{sc}}} \tag{4.6}$$

where V_{mp} and j_{mp} are the maximum power point voltage and the current density, respectively. *FF* is often represented as a percentage or one unit.

4.2.4. Power conversion efficiency

From the photovoltaic parameters, can be extracted the power conversion efficiency (PCE or η) of solar cells as the ratio between the $P_{\max}$ generated by a solar cell and the incident input power P_{in} . To allow for valid comparison of device performance, an international standard for input power is used. This standard incident power is equal to the irradiance of AM1.5G spectrum, normalized to an intensity 1000 W m^{-2}, whilst the cell is at a temperature of 25 ºC. The η is determined from the $I - V$ measurement using

$$\eta = \frac{P_{\max}}{P_{\mathrm{in}}} = \frac{V_{\mathrm{mp}} I_{\mathrm{mp}}}{P_{\mathrm{in}}} = \frac{V_{\mathrm{oc}} I_{\mathrm{sc}} FF}{P_{\mathrm{in}}} \tag{4.7}$$

where I_{sc} is the short-circuit current. The irradiance of AM1.5 spectrum can be calculated from the spectral power density $P(\lambda)$, using the following expression

$$P_{\mathrm{in}} = \int_0^{\infty} P(\lambda)\,\mathrm{d}\lambda \tag{4.8}$$

As earlier pointed out, the AM1.5G spectrum is designed for flat plate modules and has a power integrated of 1000 W m^{-2}. In our laboratory, the $j - V$ curves were made using Abet Sun 2000 Solar Simulator where the light intensity was adjusted with an NREL-calibrated Si solar cell.

4.3. External Quantum Efficiency

The *EQE* is defined as the number of photogenerated electrons collected by organic photovoltaic (OPV) cells for each photon absorbed at specific wavelength, often expressed as a percentage. This measurement is also referred to as incident photon-to-current conversion efficiency (*IPCE*). If the absorption spectrum of the solar cell is known, the fraction of absorbed photons can be used to calculate the internal quantum efficiency (*IQE*). This value gives the percentage of photons absorbed by the cell that are converted into electrons as a function of wavelength. Therefore *EQE* or *IPCE* is ultimately limited by the number of photons that can be absorbed within an exciton diffusion length (L_D) from the D/A interface. The *EQE* cannot exceed 100 %, and is generally measured under short-circuit conditions ($V_{app} = 0$) where the electric field within the device is large. The bandgap structure in a semiconductor device introduces wavelength dependent absorbance. A photon with energy larger than the bandgap of the semiconductor is typically absorbed by the material, while a photon with energy smaller than the bandgap is not absorbed. The absorbed photon creates an electron–hole pair charge, which leads to creation of electricity. To determine *EQE*, the power reaching (*P*) of the cell must be known and a current is produced at each wavelength in short-circuit conditions. During a test, the computer records the currents (I_{sc}) produced by the test cell and by a calibrated photo-detector. The *EQE* is then measured by using the following equation

$$EQE(\%)\Big|_{\lambda} = \frac{n_{\text{electrons}}}{n_{\text{photons}}}\times 100\Bigg|_{\lambda} = \left(\frac{I_{sc}/q}{P/hf}\right)\Bigg|_{\lambda} = \left(\frac{I_{sc}/q}{P\lambda/hc}\right)\Bigg|_{\lambda} = \frac{hc}{q}\left(\frac{I_{sc}}{P\lambda}\right)\Bigg|_{\lambda} \qquad (4.9)$$

where h is Planck's constant (6.626×10^{-34} m^2 kg s^{-1}), c is the speed of light (3×10^{8} m s^{-1}), q is the electron charge (1.602×10^{-19} C), λ is the wavelength in meters, I_{sc} is the short-circuit current in amperes and P is the power incident on the cell as measured by a power meter in watts.

Typical *EQE* shapes for the P3HT:PC$_{60}$BM or PCDTBT:PC$_{70}$BM active layer solar cells are represented in Figure 4.2. If all the photons of a certain wavelength are absorbed and the resulting carriers are collected, then the *EQE* at that particular wavelength has a value of 100 %. The *EQE* for photons with energy below the bandgap is zero. Hence the quantum ideal efficiency has a square shape (Figure 4.2). However, the *EQE* for most solar cells is reduced because of the effects of geminate recombination, where charge carriers are not able to move into an external circuit. The same mechanisms that affect the collection probability also affect the *EQE* spectra.

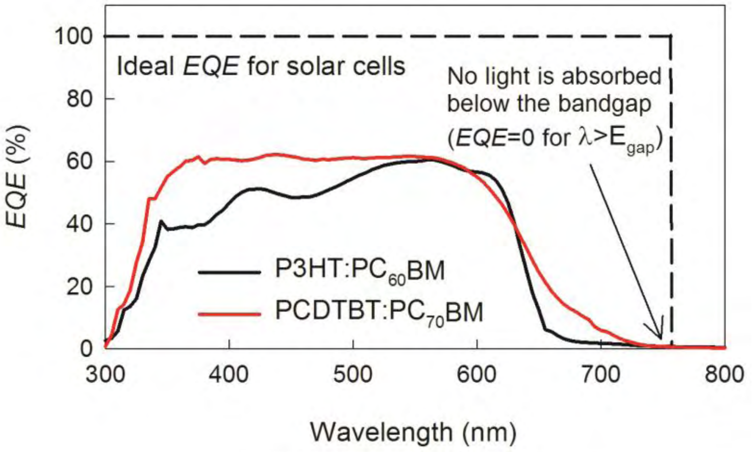

Figure 4.2. *EQE* of P3HT:PC$_{60}$BM- and PCDTBT:PC$_{70}$BM-based OPV solar cells.

This measurement provides information on how efficiently a cell converts photons of a particular wavelength into free electrons. Unlike the $j-V$ measurement under AM1.5G conditions, the *EQE* measurement does not indicate the total power efficiency of the cell. This is because the total output power of the solar cell depends on the operating voltage of the cell and *EQE* values are measured at short-circuit conditions. However, a simple calculation can be done to check for consistency between data obtained from *EQE* and AM1.5G measurements. The j_{SC} of a cell measured under AM1.5 conditions can be compared to a value calculated from the *EQE* data, using the expression

$$j_{\mathrm{SC}} = q \int_{\lambda_{\min}}^{\lambda_{\max}} EQE\, P_{\mathrm{in}}(\lambda)\,\mathrm{d}\lambda \tag{4.10}$$

where $\lambda_{\max}$ and $\lambda_{\min}$ are the wavelengths where the *EQE* vanishes. For the operation of OPV device, *EQE* quantity depends on five parameters, each one has associated a specific efficiency, giving

$$EQE(\lambda) = \eta_{\mathrm{Abs}}(\lambda)\times\eta_{\mathrm{Diff}}(\lambda)\times\eta_{\mathrm{Diss}}(\lambda)\times\eta_{\mathrm{t}}(\lambda)\times\eta_{\mathrm{cc}}(\lambda) \tag{4.11}$$

The energy diagram of a complete OPV cell represented in Scheme 4.3 shows the different efficiencies to extract free charge carrier from photogenerated excitons.

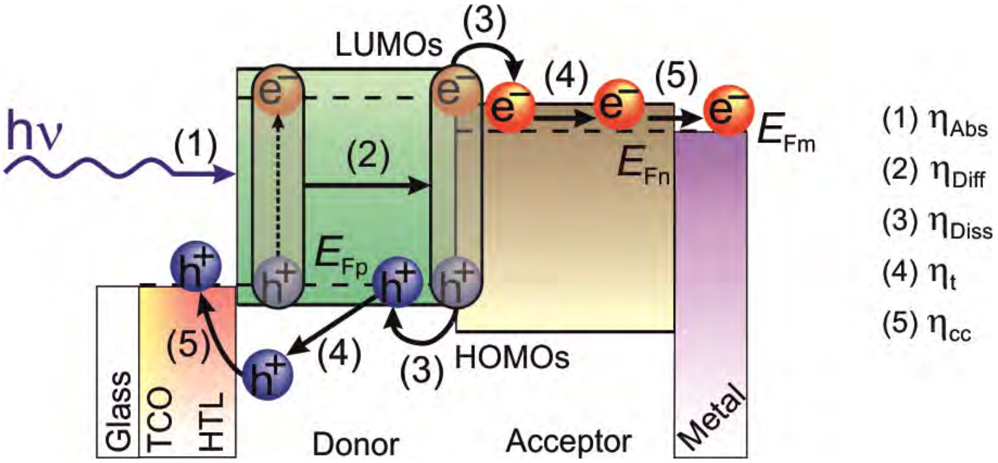

Scheme 4.3. Energy band diagram of a standard PSC. Charge transfer process is illustrated as five key steps. The efficiency of these steps determines the *EQE* of the OPV device.

The absorbance efficiency parameter, η_{Abs}, describes the fraction of incident photons absorbed in the active layer of the OPV device (process exhibits in step 1 in Scheme 4.3) which is determined by both the bandgap and absorption coefficient of the material, whilst the thickness of the active layer also affect the absorption yield.[16] The absorption efficiency can be calculated as

$$\eta_{\mathrm{Abs}} = \frac{\int_{\lambda_1}^{\lambda_2} \lambda A(\lambda, L) I(\lambda)\,\mathrm{d}\lambda}{\int_{\lambda_1}^{\lambda_2} \lambda I(\lambda)\,\mathrm{d}\lambda} \tag{4.12}$$

where $I(\lambda)$ is the spectral irradiance of the AM 1.5G illumination integrated over the wavelength range of the blend absorption, $A(\lambda, L)$ is the fraction of the light absorbed in the active layer at a given wavelength λ and thickness L. This parameter is the most effective way of increasing the j_{SC}.

Additionally, thin film affects the absorbance of the bulk heterojunction (BHJ) photoactive layer depending on the architecture of the device. Some investigations using low bandgap PCPDTBT polymer, in inverting device structure improves light absorption for several thicknesses (75–275 nm). They compared the light-generated current at the most negative bias of -1 V to the η_{Abs}. In accordance with the prediction by optical modeling, the photocurrent of the inverted device at -1 V exceeds the current of the corresponding regular structure for all layer thicknesses. Also, the reverse-bias currents are largest at a layer thickness of 270 nm, which complies with the predicted behavior.[17]

The exciton diffusion efficiency parameter, η_{Diff} , describes the ability of excitons photogenerated which diffused from the donor material to reach a D/A interface (process exhibits in step 2 in Scheme 4.3). The efficiency of exciton diffusion to a D/A interface where dissociation into charge occurs can be expressed as the ratio[18]

$$\eta_{\mathrm{Diff}} = \frac{k_0}{k_0 + k_{\mathrm{XT}} N_{\mathrm{T}} + k_{\mathrm{F}}} \tag{4.13}$$

where k_0 is the exciton decay rate, $k_{\mathrm{XT}} N_{\mathrm{T}}$ is the rate of the exciton quenching at traps (k_{XT} is the bimolecular reaction rate and N_{T} is the trap density) and the exciton loss due to defect creation is expressed by k_{F}, the trap formation rate. When a mixed D/A active layer is used, the excitons dissociate almost immediately following generation, corresponding to a large k_0. The η_{Diff} parameter is dependent on both the excitonic L_{D}, which is a material property, and the distance between excitation and the nearest interface, which is related to the nanoscale design of the photoactive layer. As the excitonic L_{D} in conjugated polymers is very low, control over the D/A arrangement is crucial for successful exciton diffusion. This factor is inversely related to the rate of recombination within the photoactive material.[16]

The dissociation efficiency parameter, η_{Diss}, is related to the separation of bound electron–hole pair in free charge carrier, process exhibits in step 3 in Scheme 4.3. As the electron is still bound within the exciton, the energy offset formed at the D/A interfaces is required to provide a driving force, which releases the electron and the conduction is allowed. This energy offset, typically in the range of 0.1–0.5 eV,[19] must be larger than the excitonic binding energy in the material to facilitate charge transfer. This occurs only at the boundaries between two materials and, therefore, the distribution of the interface throughout the active layer is vitally important for the efficiency of the solar cell.[16]

The transport efficiency parameter, η_{t} , describes the efficiency of charge carrier transport throughout the device (step 4 represented in Scheme 4.3). The charge transport occurs via a process of hopping between energy states and is affected by traps and recombination sites in the photoactive film. The success of this transport depends greatly on the mobility of the associated semiconductors.[16]

The charge collection efficiency parameter, η_{cc}, describes the ability of the charge carriers to be injected into the electrodes from the photoactive layer which parameter depends directly on the electronic composition of the device (step 5 showed in Scheme 4.3). For a successful injection of electrons into the cathode, the LUMO-acceptor material must be lower than the work function (W_{f}) of the metal (respect to the vacuum level). At the same time, for a successful injection of holes into the anode, the HOMO-donor material must be higher than the W_{f} of the transparent anode. The material used for the electrodes should be carefully selected because in function of the W_f of the anode and cathode material is required to provide a direction for the photocurrent. Intermediate layers are commonly used between the photoactive layer and electrodes to make the injection of charge carriers more energetically favorable.[16]

A typical experiment setup for measuring the *EQE* of a solar cell is pictured in Scheme 4.4. From the white-light source, in our case 150 Watt xenon lamp, is coupled with a monochromator. The produced light generates high energy electrons through Xe gas forming a small cloud of plasma. The light emitted from this plasma has a very similar irradiance spectrum to sunlight, with the exception that there are spectral emission lines associated with the gas, especially in the region from 850–900 nm. The *EQE* monochromator uses a grating and a slit to reduce the Xe lamp's spectral output to nearly monochromatic light. The output is therefore light of a given wavelength at a measurable intensity.

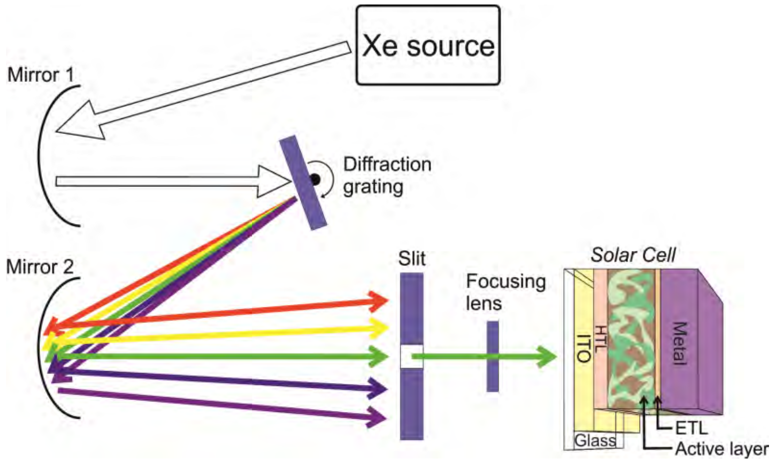

Scheme 4.4. Simplified schematic diagram of the *EQE* layout.

Over this Ph.D. Thesis, the *EQE* measurements were performed by employing a 150 W Xe lamp coupled with a computer controlled monochromator. The photocurrent was measured by using an optical amperimeter 70310 from Oriel Instruments using a Si photodiode to calibrate the system.

4.4. Ultraviolet-Visible Spectroscopy

The UV-Vis spectroscopy refers to absorption spectroscopy in the ultraviolet-visible spectral region. Ultraviolet and visible light are energetic enough to promote electrons from ground state to the excited state. This technique is able to detect the color of a sample in solution or film conditions. For instance, a red color appears visually red because the light at the blue end of the spectrum is absorbed, leaving the red light to be transmitted. The visible spectra lies in the wavelength range of 400–700 nm (Scheme 4.5).

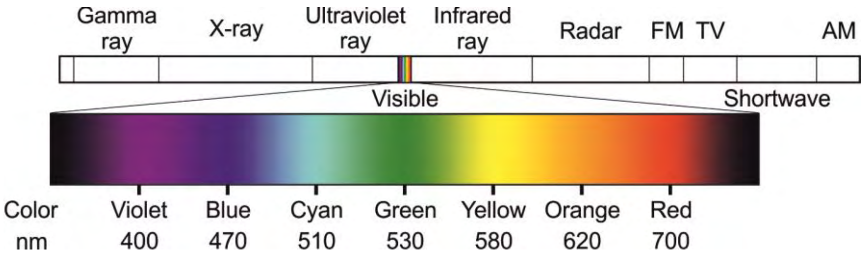

Scheme 4.5. Electromagnetic spectrum with visible light highlighted.

A typical UV-Vis spectrometer setup is illustrated in Scheme 4.6. A beam of light from visible to UV light range source is separated into its component wavelengths by a prism or diffraction grating. Each monochromatic (single wavelength) beam in turn is split into two equal intensity beams by a half-mirrored device. One beam, the sample beam, passes through the unknown absorbance sample (solution or film). The other beam, the reference beam, passes through an identical substrate containing only the reference solution (solvent) or film (glass). The intensities of these light beams are then measured by electronic detectors and are compared. The scheme as described below automatically scans all the component wavelengths in the spectrometer. The UV region scanned is normally from 200 to 400 nm, and the visible range is from 400 to 800 nm. Over this Ph.D. Thesis, the UV-Vis data were recorded from Cary 500 UV-VIS Varian photospectrometer.

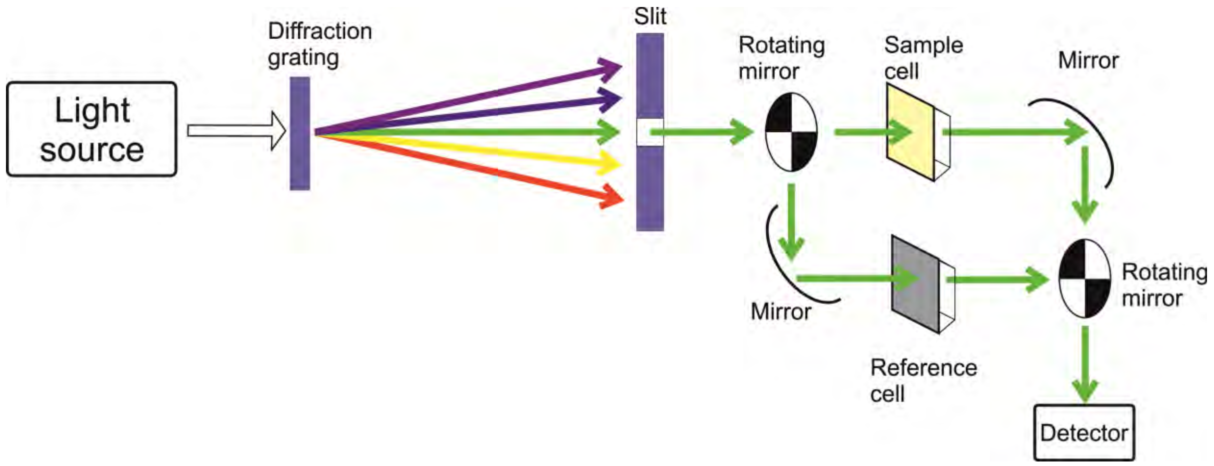

Scheme 4.6. Simplified schematic diagram of the UV-Vis spectrometer works.

4.5. Capacitance–Voltage measurement

Recently, the $C-V$ measurement is a widely accepted technique by the scientific community due to significant parameters can be extracted in systems with metal/semiconductor interface such as PSCs.[20] This purely electrical method is based on a single-frequency measurement when the frequency selected excludes the contributions of confounding phenomena. These measurements are carried out under dark conditions and the AC oscillating amplitude was as low as 20 mV (rms) to maintain the linearity of the response. Usually the $C-V$ measurement is represented as the one over the square of the capacitance as a function of applied potential, $C^{-2}-V$, called Mott-Schottky (Figure 4.3).

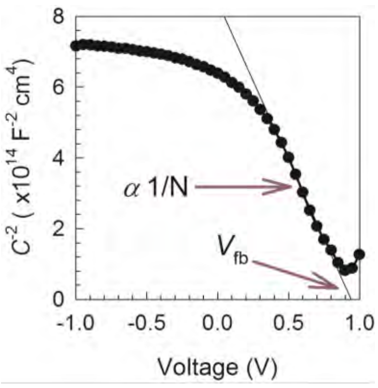

Figure 4.3. Mott-Schottky plot being inverse capacitance squared (C^{-2}) against applied bias under dark conditions of an OPV cell with an architecture of ITO/PEDOT:PSS/PCDTBT:PC$_{70}$BM/Ca/Ag.

A full depletion at reverse bias (-1 V) is exhibited. This constant capacitance is called geometric or dielectric capacitance C_g of the blend. So, the relative dielectric constant, ε , of a specific material is calculated by the equation

$$C_g = \varepsilon\varepsilon_0 \frac{A}{L} \tag{4.14}$$

where ε_0 is the permittivity of the vacuum ($8.85\times10^{-12}\ \mathrm{F\,m^{-1}}$), ε is the relative dielectric constant of the blend, A corresponds to the device active surface, and L is the thickness. Moreover, a linear relationship at low forward bias (0.5–0.8 V) is predicted between C^{-2} and applied potential (V_{app}) by the following expression

$$C^{-2} = \frac{2}{A^2 q\varepsilon\varepsilon_0 N}\left(V_{fb} - V\right) \tag{4.15}$$

where V_{fb} is the flat-band potential and N is the total concentration of defects of the majority carrier in the semiconductor. So, from equation 4.15, the concentration of electrically active acceptor impurities N and V_{fb} can be extracted at reverse and low forward bias from the slope and the extrapolated intersection with the voltage axis, respectively. The density of fully ionized defect states (p-doping level) is the result of defect states within the polymer bandgap caused intrinsic by morphological changes[21] or externally by water, oxygen or other oxidant agent.[22] Besides, it is assumed that the defect density explored from capacitance corresponds to those defects able to follow measuring frequency. The following is an explanation of the N and V_{fb} contributions on the energy diagram of complete PSCs.

4.5.1. Energy level diagrams in semiconductors

One of the main layers due to their electrical functions into the OPV devices is the BHJ film made up of an electron donor material blended with an acceptor electron material. Both materials are organic semiconductors which are able to absorb a photon from sunlight and create free charge carrier. This charge is dissociated and transported through these materials to electrodes. This section describes the basic concepts of the diagram energy levels of the D:A blend semiconductors.

A semiconductor is formed by a valence band (VB) and conduction band (CB) or similarly highest occupied molecular orbital (HOMO) and lowest unoccupied molecular orbital (LUMO) levels, respectively. The electrons are located in the VB and the CB is empty of electrons. When the light strikes the semiconductor, an electron can absorb a photon and is excited from the HOMO level to the LUMO level if the photon energy is equal or higher of difference energy between these two energy levels. This energy region is called bandgap. A hypothetical energy level can be considered in the bandgap called Fermi Level (E_F). Due to thermodynamic equilibrium, the electron has the 50 % probability of being occupied at E_F level at any given time (Scheme 4.7.a). However, a semiconductor could be doped with the external addition of impurities or morphological changes by the processing conditions. Two types of doping (N) are found. On the one hand, the n-doped semiconductor consist in a semiconductor with an excess of electrons and for that reason the E_F level is moved up respect to the un-doped semiconductor close to the LUMO level like is shown in Scheme 4.7.b. On the other hand, p-doped semiconductor corresponds to a semiconductor with an excess of holes and then the E_F level is shifted down closer to the HOMO level compared to that observed for un-doped semiconductor which is represented in Scheme 4.7.c.

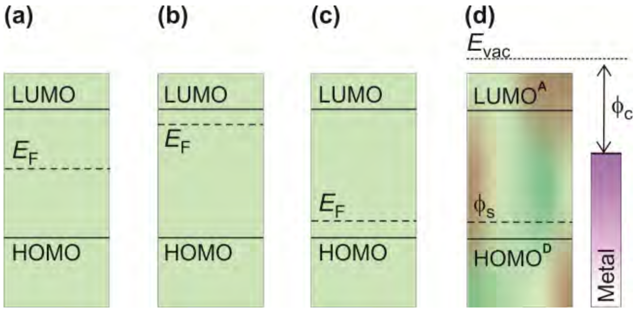

Scheme 4.7. Energy diagrams for un-doped (a), *n*-doped (b) and *p*-doped (c) semiconductors. The Fermi Level E_F is represented in each situation. (d) An active layer formed with a bulk heterojunction *p*-type semiconductors before contact is made. A mismatch between metal cathode ϕ_C and organic semiconductor ϕ_S work functions is observed, $\phi_C - \phi_S$.

The active layer materials employed for OPV are based on *p*-doped semiconductors. Scheme 4.7.d. represents schematically the situation before contact between the organic semiconductors active layer and metal cathode is made. There exists an energy offset between the metal contact and the organic semiconductor work functions, ϕ_C and ϕ_S, respectively. On the active layer side, it is well-known that unintended oxidation of the donor polymer occurs during processing by the presence of oxygen or moisture[22] and/or morphological changes intrinsically during blend processing.[21,23] This confers *p*-doped character to the polymer, yielding as a result a background concentration of mobile holes.

A basic device model is illustrated in Scheme 4.8 for complete and conventional OPV devices under dark conditions.

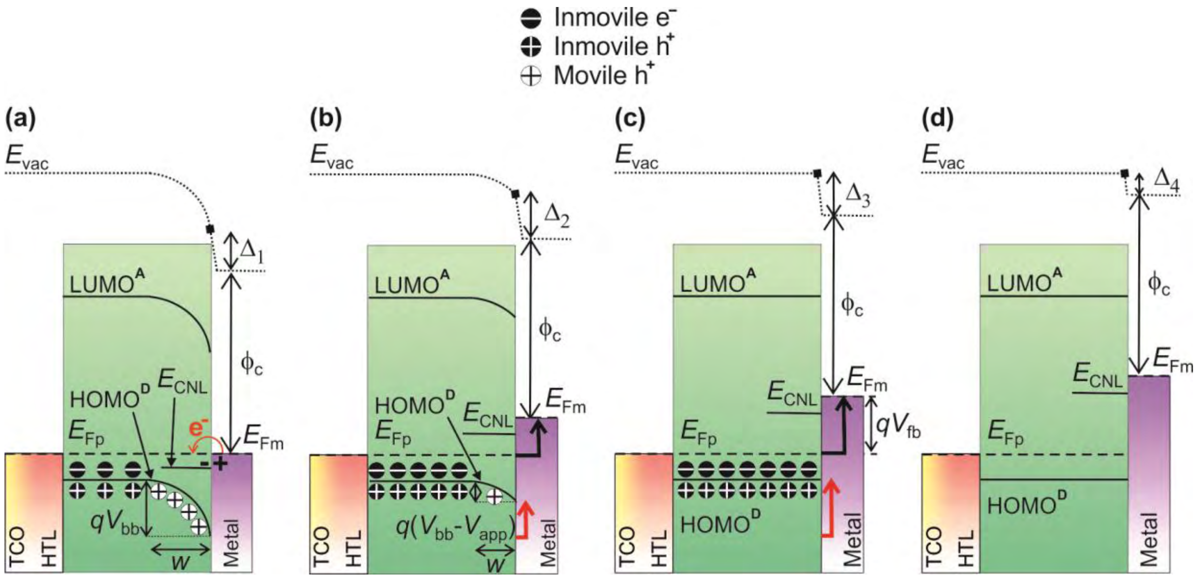

Scheme 4.8. Energy level diagrams of an organic photovoltaic device under dark conditions. (a) At $V_{app} = 0$ V in equilibrium. The vacuum level offset is splitted into two contributions: one arising from the bulk band bending V_{bb}, and then the interface dipole layer Δ. A net charge transfer approaches the metal cathode Fermi Level ϕ_C to charge-neutrality level (E_{CNL}). (b) $V_{app} < V_{bb}$ bias conditions. (c) Flat-band conditions. The potential required to remove the depletion donor HOMO is the flat-band potential, V_{fb} . (d) $V_{app} > V_{bb}$ bias conditions.

Once the active layer is in contact with the metal cathode and anode (Scheme 4.8.a), some contributions should be highlighted. The anode forms a good ohmic contact with the organic layer due to the proper energy alignment between the hole transporting layer and donor polymer HOMO levels. Regarding cathode side, the energy equilibration entails the Fermi Level alignment with a concomitant vacuum level offset that is divided into two contributions (zero bias voltage under dark conditions). Firstly, band bending V_{bb} inside the active layer as a consequence of the hole (mobile charge) depletion zone built up near the cathode contact; and secondly, an interface dipole layer Δ which accommodates part of the vacuum level offset. The dipole layer appears due to a negative charge that is injected on the organic side reducing adjacent fullerene molecules. This negative charge is compensated by a positive charge layer at the metal contact. Accordingly, a simple model that integrates both voltage drops into a unified description of the contact equilibration is described here. An expression for the cathode equilibration is then written as follows[24]

$$qV_{\mathrm{fb}} = E_{\mathrm{Fp}} - \phi_{\mathrm{c}} - \Delta \tag{4.16}$$

where qV_{fb} is the voltage required to overcome the active layer band bending that leads to flat-band conditions, E_{Fp} corresponds to the hole Fermi Level at forward applied voltage of the active layer, ϕ_{c} is the metal work function in equilibrium, and Δ is an interfacial dipole generated between active layer and cathode contact. Here, we assume that E_{Fp} practically corresponds to the Fermi Level at equilibrium.

As illustrated in Scheme 4.8.a, this model implies that in equilibrium the depletion zone occupies a large portion of the active layer due to contact effect. The width of the depletion zone obviously depends on the layer thickness and the p-doping level (N). At a low forward bias the depletion zone decreases as shown in Scheme 4.8.b. In flat-band conditions, $V_{\mathrm{app}} = V_{\mathrm{fb}}$, the depletion layer adjacent between the D:A layer and metal contact disappears and the neutral doped region extends along the whole diode bulk (Scheme 4.8.c). Finally, when the applied potential is higher than the V_{fb}, the dipole potential drop is narrow (Scheme 4.8.d).

4.6. Impedance Spectroscopy

IS is a powerful and non-destructive technique that provides access to the electrical properties of the materials and their interfaces. The mobile charge carrier can be investigated in the bulk or interfacial regions of any kind of solid or liquid material such as ionic, semiconductors, mixed electronic-ionic, and even insulators. This characterization tool involves information about many complex variables such as mass transport, rates of chemical reactions, corrosion, dielectric properties, defects, microstructure, and compositional influences on the conductance of solids. This technique is useful as an empirical quality control procedure, yet it can contribute to the interpretation of fundamental electrochemical and electronic processes.

IS predict aspects of the performance behavior of electrical devices such as chemical sensors, fuel and photovoltaic cells, and it has been used extensively to investigate membrane behavior in living cells. This technique is advantageous respect to other dynamic solar cells characterization techniques because it gives readily information on the internal cell resistances that are directly related to the steady state $j - V$ curve of the cell. For dye-sensitized solar cells (DSSCs), it has become an established method for determining charge carrier lifetimes under a range of operating biases and illumination intensities.[25-27] DSSCs have been successfully modeled by equivalent circuit elements which refer to recombination resistance, chemical capacitance, diffusion of the ionic species in the electrolyte, *etc*. Recently, impedance analysis has begun to be applied to BHJ OPV devices.[28,29] So, the extended knowledge acquired from DSSCs can be applied to PSCs to calculate average charge carrier lifetime, electronic density-of-state, and charge carrier concentrations.

One of the disadvantages of IS technique are mainly associated with possible ambiguities in the interpretation of the impedance spectra to assign an appropriate equivalent circuit model to fit the impedance data. It is necessary to know the system to assign correctly and separately different equivalent circuit elements that are possible to find in an electrical device. Inevitably, all cells are distributed in space, and their microscopic properties may be also independently distributed. Under these conditions, ideal circuit elements may be inadequate to describe the electrical response. Thus, it is often found that the impedance spectra cannot be well approximated by the impedance of an equivalent circuit involving only a finite number of ordinary lumped-constant elements. For instance, it is often used distributed impedance elements such as constant-phase elements (*CPE*s) instead of capacitance (C) in the equivalent circuit greatly aids the process of fitting observed impedance data for a cell with distributed properties.

Other serious problem is that one impedance spectra can be fitted by more than one equivalent circuit model giving exactly the same impedance response. For instance, one ambiguity is presented in this chapter: two equivalent circuit models presented in Figure 4.5.k and Figure 4.5.m can fit two semicircles impedance spectra correctly. An approach to its solution can only be made by employing physical intuition and by carrying out several impedance sets of measurements with different conditions, as discussed in the next section.

4.6.1. Fundamentals of Impedance Spectroscopy

The general approach to IS measurement is applied to a system with electrical contacts. In an IS measurement the solar cell is set to steady state operating conditions defined by the light intensity and cell temperature and the operating point (V and I) along its $I-V$ curve. Basically the IS technique is based on a cell perturbation with an alternating signal AC of small harmonic amplitude and observed the way in which the system follows the perturbation at steady state (Scheme 4.9). Namely, on the DC voltage of the cell is superimposed a small amplitude harmonic AC voltage modulation $\hat{V}(\omega)$, at a certain angular frequency, ω; and the resulting AC current $\hat{I}(\omega)$ response is measured. Or viceversa, a measurement of $\hat{V}(\omega)$ at $\hat{I}(\omega)$ applied. This gives the impedance spectrum $Z(\omega)$ of the cell as follows

$$Z(\omega)=\frac{\hat{V}(\omega)}{\hat{I}(\omega)} \tag{4.17}$$

The symbol $\hat{x}$ over a quantity x indicates that $\hat{x}$ is the complex small amplitude of a sinusoidal AC perturbation of x.

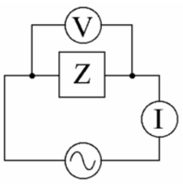

Scheme 4.9. Simplified equivalent circuit model by an alternating voltage source perturbation applied to a device which has a linear response to a voltage perturbation.

An excitation sinusoidal signal $\hat{V}(\omega)$ is superimposed onto the steady-state potential of an electrode, expressed as a function of time (t)

$$V(t) = V_{\mathrm{DC}} + V_{\mathrm{AC}} \cos(\omega t) \tag{4.18}$$

where V_{DC} is the DC voltage that is applied the AC perturbation, V_{AC} is the amplitude (in V) and ω is the angular frequency (in rad s^{-1}). In order to maintain a linear response of the electrode, the modulation amplitude must not exceed of 10–20 mV. Figure 4.4 represents the no-linear and linearity modes when the amplitude is large and small, respectively.

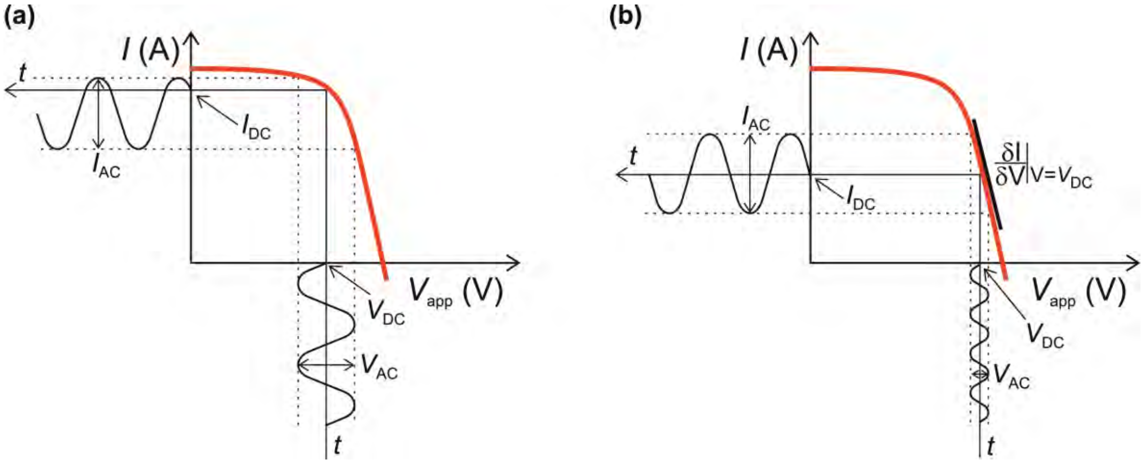

Figure 4.4. Response of the sinusoidal perturbation on $I-V$ curve at large (a) and small (b) amplitude of the AC voltage modulation giving non-linear and linear response, respectively. It is represented the DC voltage that is applied the AC perturbation, V_{DC}, the voltage amplitude, V_{AC}, and the angular frequency, ω. The current response is represented as steady-state DC current I_{DC}, and the current amplitude response as I_{AC}.

In a lineal system, the response of the AC voltage in the $I-V$ curve is a sinusoidal current as a function of time (t)

$$I(t) = I_{\mathrm{DC}} + I_{\mathrm{AC}} \cos(\omega t - \varphi) \tag{4.19}$$

where I_{DC} corresponds to the steady state DC (in amperes) and φ is the phase (in degrees). So, tacking into the sinusoidal part of the applied potential (equation 4.18) and the resulting current intensity (equation 4.19) to the impedance (Z) definition (equation 4.17) gives the equation 4.20

$$Z = \frac{V(t)}{I(t)} = \frac{V_{\mathrm{AC}} \cos(\omega t)}{I_{\mathrm{AC}} \cos(\omega t - \varphi)} = |Z| \frac{\cos(\omega t)}{\cos(\omega t - \varphi)} \tag{4.20}$$

where the impedance expression is function of the magnitude $|Z|$ and the phase shift of the voltage and current signals (φ). The equation 4.20 can be converted in complex version taking into consideration the Euler's relationship ($\exp(i\theta) = \cos(\theta) + i\sin(\theta)$), where $i = \sqrt{-1}$ is the imaginary number and θ is the angle

$$Z = \frac{V_{\mathrm{AC}} \exp(i\omega t)}{I_{\mathrm{AC}} \exp(i\omega t - i\varphi)} = |Z| \exp(i\varphi) = |Z| (\cos(\varphi) + i\sin(\varphi))$$

$$Z = Z' + iZ'' \tag{4.21}$$

Thus, the impedance Z is represented by a vector sum of the real Z' and the imaginary Z'' part (equation 4.21) characterized by the modulus $|Z|$ and the phase shift φ. Scheme 4.10 represents the impedance plot called Argand diagram.

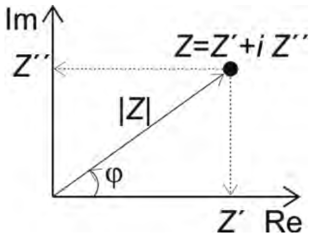

Scheme 4.10. Argand diagram shows relationships among complex impedance, magnitude and phase angle.

From Argand diagram is extracted some arithmetic relationships: Z', Z'', module impedance $|Z|$ and the phase angle φ as

$$Z' = |Z|\cos(\varphi)$$

$$Z'' = |Z|\sin(\varphi)$$

$$|Z| = \sqrt{(Z')^2 + (Z'')^2}$$

$$\varphi = \arctan\left(\frac{Z''}{Z'}\right)$$

Table 4.1 summarizes some simple electrical circuits that are analyzed independently. The first circuit represented in Figure 4.5.a is composed by a pure resistance, R. A sinusoidal voltage is applied as mentioned in equation 4.18. Since Ohm's law always holds

$$Z_R = \frac{V}{I} = R \tag{4.22}$$

The resistance is represented in the real axis in the Nyquist plot as shown in Figure 4.5.b.

Table 4.1. Basic AC electrical elements represented their symbol, scheme and impedance equation.

Denomination	Symbol	Scheme	Impedance
Resistance	R		R
Capacitance	C	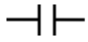	$\frac{1}{i\omega C}$
Inductor	L		$i\omega L$
Constance phase element (*CPE*)	Q_n	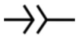	$\frac{(i\omega)^{-n}}{Q_n}$

The second circuit to analyze is composed by a pure capacitance, C, as shown in Figure 4.5.c. A sinusoidal voltage is applied through the C circuit (equation 4.18). The fundamental relation of interest is then

$$I = \frac{\mathrm{d}Q}{\mathrm{d}t} = \frac{\mathrm{d}(CV)}{\mathrm{d}t} = C\frac{\mathrm{d}}{\mathrm{d}t}\left(V_{\mathrm{AC}}\cos(\omega t)\right) = -C\omega V_{\mathrm{AC}}\sin(\omega t) \tag{4.23}$$

Under steady-state condition $\mathrm{d}V(t)/\mathrm{d}t = 0$, and, according to equation 4.19, $I(t) = 0$. The capacitor is equivalent to an open-circuit under steady-state conditions. Now, it is convenient to change the phase terms of the equation 4.23 in complex notation to facilitate the calculations. The impedance (Z) is calculated as follows

$$Z_C = \frac{V}{I} = \frac{1}{i\omega C} \tag{4.24}$$

This circuit depends on the angular frequency ω. In Figure 4.5.d is represented the Nyquist plot for a pure capacitor indicating that depends on the imaginary part of the impedance.

The third circuit to analyze is composed by a pure inductor, L. The relationship between current and potential difference for the inductor is

$$V(t) = L\frac{\mathrm{d}I(t)}{\mathrm{d}t} \tag{4.25}$$

Under steady-state conditions, $\mathrm{d}I(t)/\mathrm{d}t = 0$, and, according to equation 4.18, $V(t) = 0$. Thus, the inductor is equivalent to a short-circuit under steady-state conditions.

Once explained the above, a number of equivalent circuits are able to fit the IS data from the combination in series and/or parallel of the simplest electric elements. Assuming a resistance, R, and capacitance, C, in series as shown in Figure 4.5.e, the same current must flow through the two elements, and the overall potential difference is the sum of the individual voltage drops across the resistor and the capacitor. Thus, according to the definition of impedance given as equation 4.22 and 4.24, the impedance for the series arrangement shown in Figure 4.5.e is given by

$$Z = Z_{\mathrm{R}} + Z_{\mathrm{C}} = R + \frac{1}{i\omega C} \tag{4.26}$$

Here, we are able to distinguish two parts in the impedance equation, Z. The real part of the impedance is equal to R and is independent of frequency ω. The imaginary part tends toward $-\infty$ and the frequency tends toward zero. The DC (zero-frequency) current is equal to zero at any applied potential, and the current at infinite frequency is equal to V/R.

Another important example of an equivalent circuit is the RC parallel combination as shown in Figure 4.5.g. The overall current is the sum of the current flowing in each element, and the potential difference is the same for each dipole. Then, according to the impedance definition (equation 4.21), the impedance for the parallel arrangement shown in Figure 4.5.h is given by

$$Z = \left(\frac{1}{Z_{\mathrm{R}}} + \frac{1}{Z_{\mathrm{C}}}\right)^{-1} \tag{4.27}$$

$$Z = \frac{R}{i\omega RC + 1} \tag{4.28}$$

Impedance contributions are additive for elements in series, whereas the inverse of the impedance, or the admittance $Y(\omega) = 1/Z(\omega)$, is additive for elements in parallel.

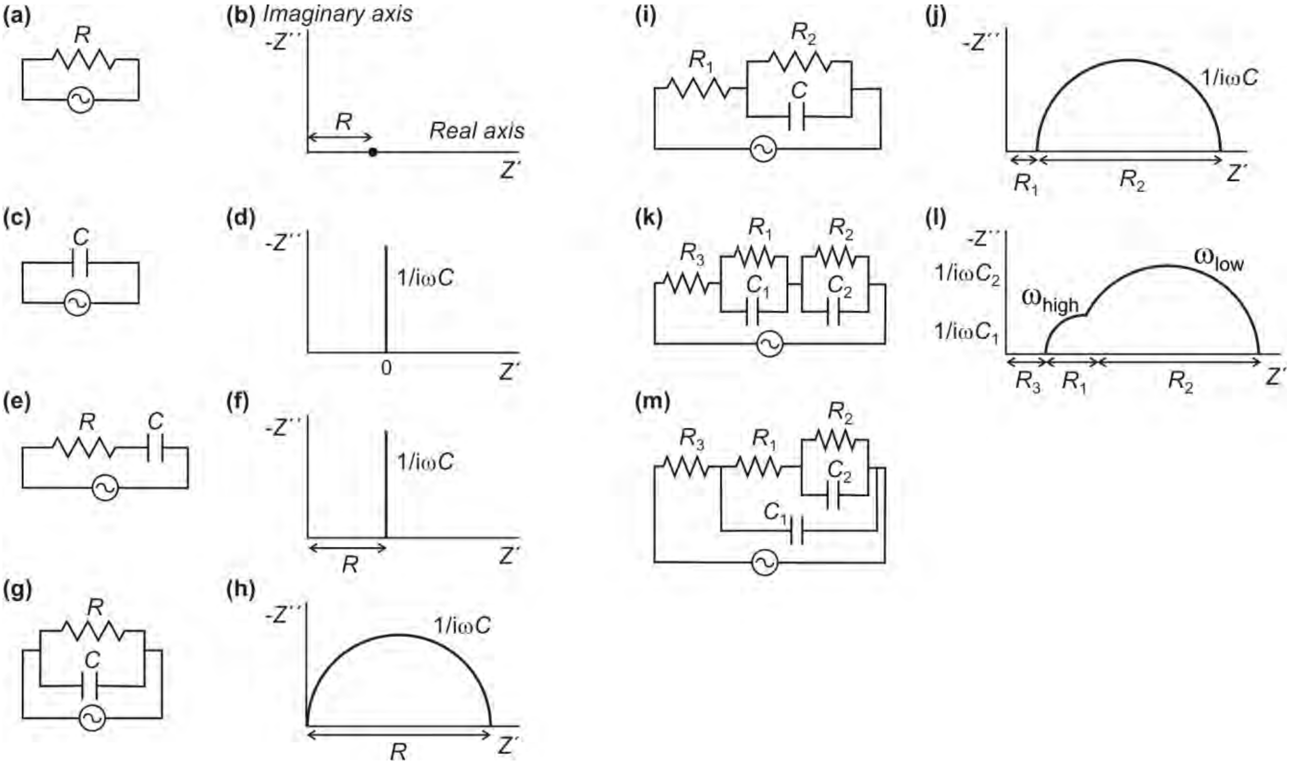

Figure 4.5. Schematic simple equivalent circuit models. It includes some series and parallel combinations between *R* and *C*. The Nyquist plot is also represented for each situation.

Finally, if we consider equivalent circuit showed in Figure 4.5.i, the contribution of the resistance terms to the impedance are R_1 and R_2. The impedance of the capacitor is given by equation 4.24. Then, following the equations 4.26 and 4.27, the impedance of the circuit is therefore given by

$$Z = R_1 + \frac{R_2}{i\omega RC + 1} \tag{4.29}$$

Thus, following this trend we are able to deduce others impedance electrical circuits as shown in Figure 4.5.

A more sophisticated IS spectra can be observed. For instance, the typical 45º line detected at high frequency spectra is represented in Figure 4.6. Two types of spectra can be distinguished in function of the R_1 and R_2 values. The Warburg spectrum (Figure 4.6.a) is found when R_1 is higher than R_2 values and the Gerisher spectrum (Figure 4.6.b) when R_1 is lower than R_2 values. The IS data followed by Warburg spectrum should be fitted by the transmission line model illustrated in Figure 4.6.c. This model consists of a R_1C_1 subcircuit in series with a resistance R_2 in finite sequence. An extra capacitance C_g involved this subcircuit which is observed in the impedance spectra as a small arc at the end of the 45º-line at high frequency. This extra arc is not always distinguished. Finally, a series resistance R_S is located in the model. This model is used in standard geometry PSCs to extract all electrical processes that occurs under illumination conditions.

Two capacitances can be distinguished, geometric C_g and chemical C_μ (C_1) and regarding the resistances, recombination R_{rec} (R_1) and transport R_t (R_2).

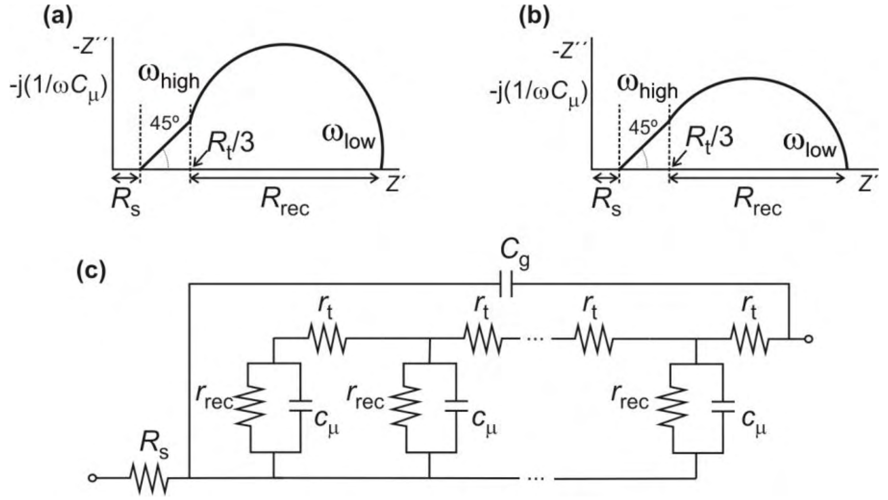

Figure 4.6. (a) Warburg ($R_1 > R_2$) and (b) Gerisher ($R_1 < R_2$) in the impedance spectra. (c) Transmission Line Model for the (a) case. This model represents a finite subcircuit R_1C_1 parallel in R_2 in series with a geometric capacitance C_g that involves this subcircuit. A series resistance R_s is also indicated.

4.6.2. Experimental impedance diagrams

The typical IS results are represented as Nyquist plot and Bode plot showed in Figure 4.7.a and Figure 4.7.b, respectively.

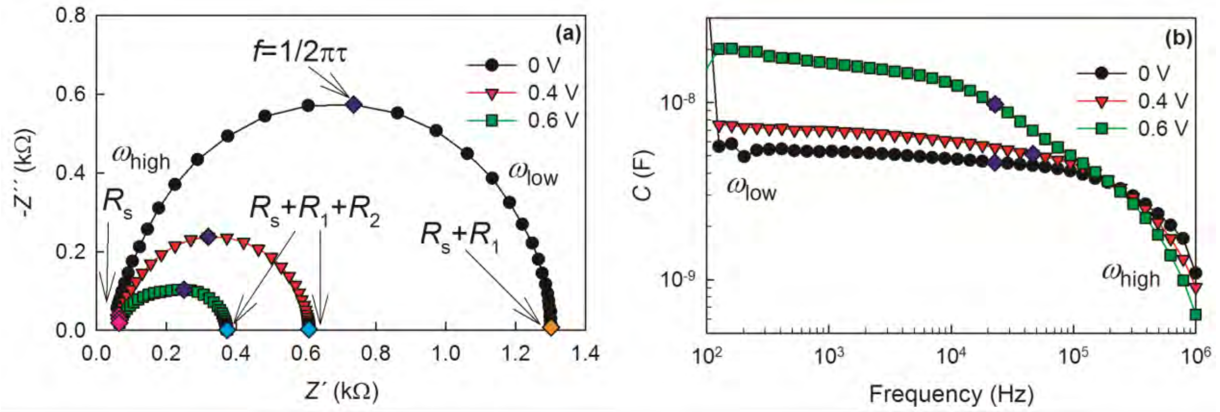

Figure 4.7. Impedance spectra or Nyquist plot (a) and capacitance *vs*. frequency (b) at 0, 0.4 and 0.6 V for a regular T1:PC$_{70}$BM-based solar cell. There are some diamond-shape points to highlight: dark blue points correspond to the high impedance response with a frequency of $f = 1/2\pi\tau$ represented in (a) and (b); pink point is the series resistance R_s; orange point corresponds to the sum of resistances R_s and R_1; and, cyan point is the sum of resistances R_s, R_1 and R_2.

In particular, these plots were performed under 1 sun illumination to T1:PC$_{70}$BM active layer in a regular architecture of PSC. It is shown only the 0, 0.4 and 0.6 biases. Nyquist plot or impedance spectrum represents the $-Z''$ (imaginary impedance part) as a function of Z' (real impedance part). Several parts can be distinguished. The series resistance R_s is observed for all potentials as pink diamond-shape points. At 0 V is observed only one semicircle where two parameters are important such as the sum of resistances R_s and R_1 in the Z'-axis (orange diamond-shape point) and the maximum point in the $-Z''$-axis (dark blue diamond-shape point). At higher voltages, a new arc appears (R_2) in the impedance spectra. So, the sum of three resistances at Z'-axis is calculated R_s, R_1 and R_2. Figure 4.7.b shows the capacitance as a function of the frequency. In this plot, one highlight point is the dark blue diamond-shape because corresponds to the maximum point in the Nyquist plot. Therefore, a semicircle is represented as a subcircuit *RC* with resistance obtained from Nyquist plot and the capacitance from the Bode plot.

IS measurements were performed with Autolab PGSTAT-30 equipped with a frequency analyzer module, and was recorded by applying a small voltage perturbation (20 mV rms). Measurements can be carried out at different light intensity or dark illumination conditions. The range of bias is from zero to close V_{oc} and bias voltage sweeping frequencies from 1 MHz down to 100 Hz.

4.7. Cyclic Voltammetry for determination of HOMO and LUMO levels of organic materials

In electrochemistry field, *CV* is widely used to acquire quantitative information about electrochemical reactions. This technique offers a rapid location of redox potentials of the electroactive species. The measure consists of three electrodes, mainly, working electrode (WE), reference electrode (RE) and counter electrode (CE) (Scheme 4.11). The WE controls the flow of current in the electrochemical measurement and is usually made of an inert metal, such as platinum, gold, silver, glassy carbon, nickel, or palladium. The redox process occurs at the surface of this electrode. The RE provides calibration for the applied potential. The common REs are normal hydrogen electrode and Ag/AgCl electrode. The third electrode is the CE which is often a platinum wire that simply serves to conduct electricity from the signal source through the solution to the other electrodes. These electrodes are immersed into a solution containing the analyte and an excess of a non-reactive electrolyte. The solution is usually high dielectric constant (*e.g.*, water or acetonitrile) to enable the electrolyte to dissolve and help aid the passage of current. The reactant can be either a solution dissolved in low concentration (10^{-3} M) or film substrate. The electrochemically inert salt is added to the solution (for instance NaCl, TBAP or TBAHFP) with high concentration (0.1 M) to allow the current to pass. An example of a voltammetric setup is shown in Scheme 4.11.

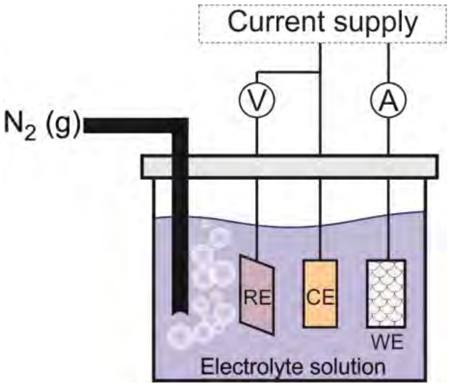

Scheme 4.11. Schematic diagram of electrochemical cell with three electrodes, reference, RE, counter, CE, and working, WE, electrodes. The RE and the CE are connected (labeled 'V') which impose a voltage on the CE. Since the RE is defined as 'zero', the WE must assume an equal but opposite voltage from the CE. The current which flows through the WE can be measured by a separate system labeled 'A'.

Figure 4.8.a shows the nature of the triangular voltage waveform that is applied to the WE. After applying a linear voltage ramp between t_0 and t_1, the ramp is reversed to bring the potential back to its initial value at time t_2. Figure 4.8.b illustrates a typical cyclic voltammogram recorded for a reversible single electrode transfer reaction. The voltage is swept between two values (V_A and V_C) at a fixed rate. When the voltage reaches V_C the scan is reversed and the voltage is swept back to V_A. In this range of voltages, several parts can be distinguished. An increasing amount of current is observed in the parts of the wave labeled A and B when the potential is applied. This is the anodic part of the wave, where oxidation of the molecules is occurring. The point B reaches the maximum flow of electrons. After point B, potential is still applied, but the current associated with the oxidation decreases to the C point due to a depletion of molecules at the electrode. From A to C points a capacitive and Faradaic current is observed. The sequence C–D–A describe the reverse process called cathodic part. When the voltage is decreased, the reverse reduction process occurs, and the molecules are returned to their initial state.

This measurement is widely used because the HOMO and LUMO levels can be calculated from the electrochemical redox peaks as

$$E = \frac{V_B - V_D}{2} \tag{4.30}$$

where V_B and V_D corresponds to the potential in B and D points illustrated in Figure 4.8.b, respectively. The reduction reaction corresponds to the LUMO energy level and the oxidation reaction corresponds to the HOMO energy level.

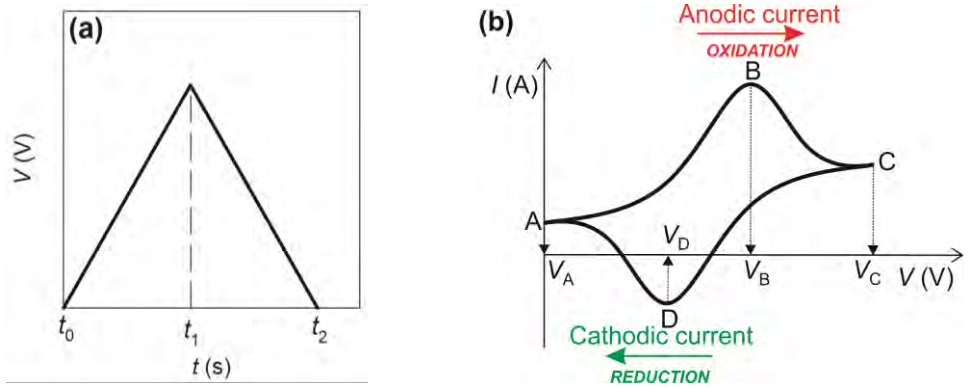

Figure 4.8. (a) A triangular waveform is applied to the WE and (b) cyclic voltammogram measured between V_A and V_C of a single electron transfer reaction.

4.8. Transient Photocurrent

TPC measurements provide additional information about the dynamics of charge separation and charge transport in photovoltaic devices. The TPC experiments consist of exciting a semiconductor with a short pulse of light, and the photocurrent response is measured (Scheme 4.12). In this Ph.D. Thesis, a direct determination of the relaxation time was performed by TPC experiment by connecting the devices to a low input (50 Ω) impedance oscilloscope (Agilent 500 MHz bandwidth) which allows to measure near short-circuit conditions. A nitrogen pumped-dye (Rhodamine) pulsed laser of 596 nm wavelength and 5 ns pulse duration was used to generate a small light perturbation.

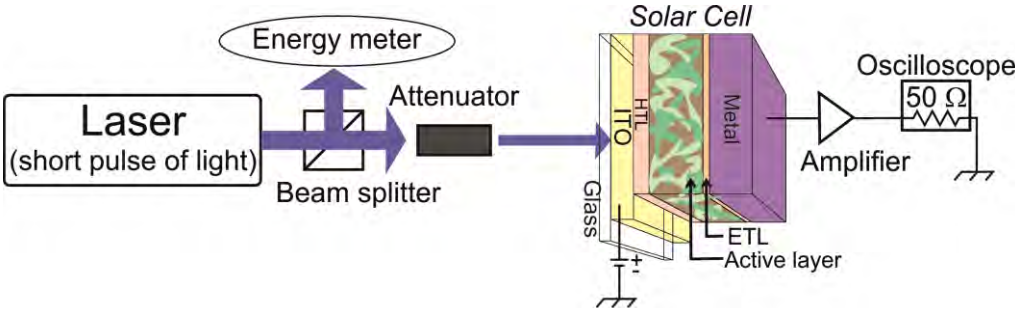

Scheme 4.12. Schematic diagram of the experiment setup for TPC.

4.9. Variable Angle Spectroscopy Ellipsometry

VASE is a powerful simple and non-destructive characterization technique which is able to determine the thickness of several monolayers into a bulk, optical constants, refractive index, surface roughness, and other physical properties of the sample. This technique measures the change in polarization of light reflected from the surface of the material. Two orthogonal polarization components are incident on the material; one is in parallel (E_p) and the other in perpendicular (E_s) to the plane of incidence. Both wave components are different when are reflected from the sample (Scheme 4.13).

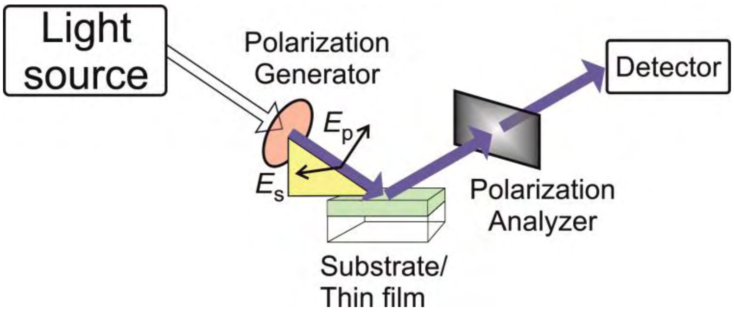

Scheme 4.13. Basic elements of an ellipsometric technique. The incident light beam contains electric field both parallel (E_p) and perpendicular (E_s) to the plane of incidence (yellow rectangle).

From each VASE measurement is obtained two main parameters: the amplitude ratio (ψ) and the phase difference (Δ) for a range of photon energies and incidence angles. These parameters defined the polarization state change. Then, a model is built to predict the material response. If the thickness of the each layer together with their material components (optical constants) is known, the model is a layered structure. On the contrary, if the thickness or the optical constants of a certain layer is unknown, an estimation is given to generate preliminary data from the model. This estimated value is varied until the generated data is approximated to the experimental data. Finally, the fitting step finds the best match between the model and the experiment.

4.10. X-Ray Diffraction

The materials can be structured disorderly or orderly. When the atoms are arranged in a random way similar to the disorder, these materials are called amorphous. One example of amorphous system is the glass. On the contrary, those crystalline materials are characterized by a structure highly organized with the atoms arranged in a regular pattern. There is a smallest volume element called unit cell that is repeated in the three dimensions where the crystal is described. The dimensions of the unit cell is by three axes (a, b and c) and angles (α, β and γ).

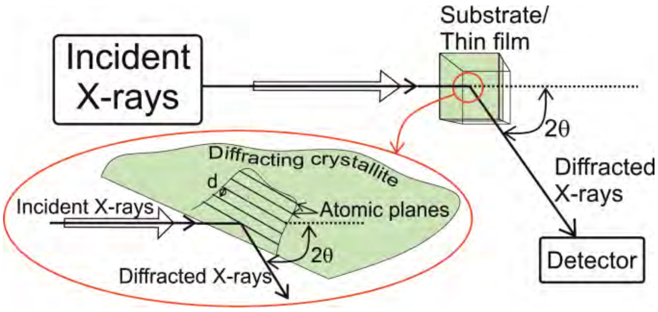

Scheme 4.14. Typical XRD experiment.

The XRD is one of the most important non-destructive tools to analyze crystals. We use this technique to characterize structurally polymer materials when the morphology is changed. XRD uses X-ray (or neutron) diffraction on powder or microcrystalline samples, where ideally every possible crystalline orientation is represented equally. As a result, the orientation average represented in three dimensional reciprocal space is projected onto a single dimension being the single crystal diffraction. Through Bragg's law (Equation 4.31) is possible to explain the interface pattern of X-rays scattered by crystals. The cleavage faces of crystals appear to reflect X-ray beams at certain angles of incidence (theta, θ). The variable d is the distance between atomic layers in a crystal, and the variable lambda λ (λ(Cu k_α) is 1.54 Å) is the wavelength of the incident X-ray beam, and n is an integer.

$$n\lambda = 2d\sin\theta \tag{4.31}$$

The XRD instrumentation is illustrated in Scheme 4.14. The diffractometer used in this Ph.D. Thesis is Bruker D4-Endeavor which is formed by a Cu-tube, diffracted beam monochromator, scintillation detector and charger up to 66 samples automatic. An incident x-rays are centered on the substrate with a thin film of the material. The X-rays diffracted are detected on a detector with 2θ angle.

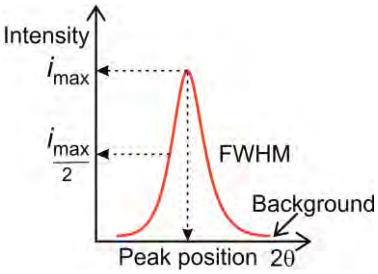

Figure 4.9. Common XRD peak. Some important parameters are highlighted.

The XRD result is shown in Figure 4.9 where highlighted parameters can be extracted such as peak position 2θ of the crystallite and Full Width Half Maximum (FWHM).

4.11. Atomic Force Microscopy

An AFM is a mechanical imaging instrument that provides information about three topography dimensional image of a surface as well as physical properties of a surface. The amplified image is generated by monitoring the motion of an atomically sharp probe as it is scanned across a surface (Scheme 4.15). Single atoms and molecules with nanometer sized deposited on a surface are possible to detect in the AFM images.

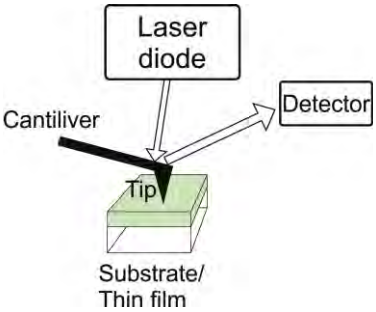

Scheme 4.15. AFM setup.

Figure 4.10 represents typical AFM images for a standard P3HT:PC$_{60}$BM blend unannealed and at 130 ºC for 10 min. It is clearly observed a uniform blend surface when the sample is not heated and the formation of fullerene nano-islands on the surface when the blend is heated. The AFM images showed over this Ph.D. Thesis is from the JSPM-5200 JEOL Scanning Probe Microscope.

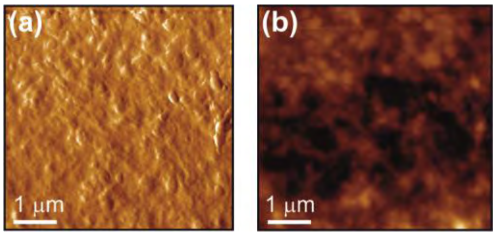

Figure 4.10. AFM images for a P3HT:PC$_{60}$BM (1:0.8 by weight) blend and as a solvent *o*-dichlorobenzene with the experimental conditions as solvent annealing. The roughness (a) and topography (b) are represented.

4.12. Scanning Electron Microscopy

SEM is a type of electron microscope that uses a focused beam of high-energy electrons across a surface of solid specimens to generate a variety of signals giving images. The electrons interact with atoms in the sample, producing signals from the electrons scattered by the object and the secondary electrons produced are detected. The signals that derived from the interaction between electron and sample reveal information in one SEM experiment about the sample including surface topography detail, homogeneity, elemental composition, crystalline structure and orientation of materials. In particular, the SEM images showed in this Ph.D. Thesis performed from the microscope called JEOL 7001F EDX-WDX Oxford, INCA 350/ Wave 200.

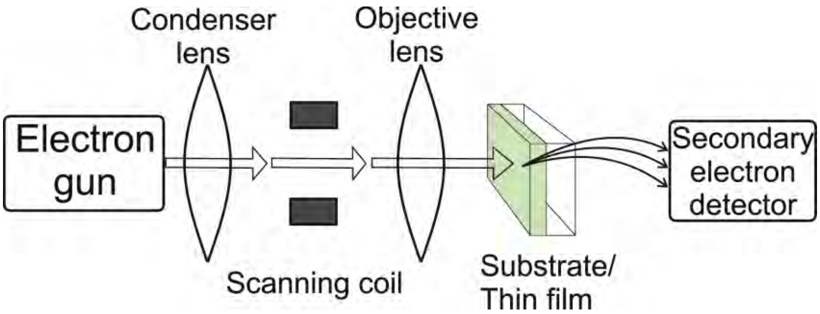

Scheme 4.16. Schematic diagram of a basic construction of SEM.

4.13. References

1. N. Grossiord, J. M. Kroon, R. Andriessen and P. W. M. Blom, *Org. Electron.*, 2012, 13, 432-456.
2. Y. H. Zhou, C. Fuentes-Hernandez, J. Shim, J. Meyer, A. J. Giordano, H. Li, P. Winget, T. Papadopoulos, H. Cheun, J. Kim, M. Fenoll, A. Dindar, W. Haske, E. Najafabadi, T. M. Khan, H. Sojoudi, S. Barlow, S. Graham, J. L. Bredas, S. R. Marder, A. Kahn and B. Kippelen, *Science*, 2012, 336, 327-332.
3. Y. J. Cheng, S. H. Yang and C. S. Hsu, *Chem. Rev.*, 2009, 109, 5868-5923.
4. G. Garcia-Belmonte and J. Bisquert, *Appl. Phys. Lett.*, 2010, 96, 113301.
5. I. Lange, J. Kniepert, P. Pingel, I. Dumsch, S. Allard, S. Janietz, U. Scherf and D. Neher, *J. Phys. Chem. Lett.*, 2013, 4, 3865-3871.
6. G. J. Zhao, Y. J. He and Y. F. Li, *Adv. Mater.*, 2010, 22, 4355-4358.
7. R. B. Ross, C. M. Cardona, D. M. Guldi, S. G. Sankaranarayanan, M. O. Reese, N. Kopidakis, J. Peet, B. Walker, G. C. Bazan, E. Van Keuren, B. C. Holloway and M. Drees, *Nat. Mater.*, 2009, 8, 208-212.
8. F. G. Brunetti, X. Gong, M. Tong, A. J. Heeger and F. Wudl, *Angew. Chem.-Int. Edit.*, 2010, 49, 532-536.
9. Q. Zhou, Q. Hou, L. Zheng, X. Deng, G. Yu and Y. Cao, *Appl. Phys. Lett.*, 2004, 84, 1653-1655.
10. A. Gadisa, W. Mammo, L. M. Andersson, S. Admassie, F. Zhang, M. R. Andersson and O. Inganäs, *Adv. Funct. Mater.*, 2007, 17, 3836-3842.
11. N. Blouin, A. Michaud and M. Leclerc, *Adv. Mater.*, 2007, 19, 2295-2300.
12. L. Dou, J. You, Z. Hong, Z. Xu, G. Li, R. A. Street and Y. Yang, *Adv. Mater.*, 2013, 25, 6642-6671.
13. H. Bronstein, J. M. Frost, A. Hadipour, Y. Kim, C. B. Nielsen, R. S. Ashraf, B. P. Rand, S. Watkins and I. McCulloch, *Chem. Mater.*, 2013, 25, 277-285.
14. S. Wen, X. Bao, W. Shen, C. Gu, Z. Du, L. Han, D. Zhu and R. Yang, *J. Polym. Sci., Part A: Polym. Chem.*, 2014, 52, 208-215.
15. G. Long, X. Wan, B. Kan, Y. Liu, G. He, Z. Li, Y. Zhang, Y. Zhang, Q. Zhang, M. Zhang and Y. Chen, *Adv. Energy Mater.*, 2013, 3, 639-646.
16. M. Wright and A. Uddin, *Sol. Energy Mater. Sol. Cells*, 2012, 107, 87-111.
17. S. Albrecht, S. Schäfer, I. Lange, S. Yilmaz, I. Dumsch, S. Allard, U. Scherf, A. Hertwig and D. Neher, *Org. Electron.*, 2012, 13, 615-622.
18. X. Tong, N. Wang, M. Slootsky, J. Yu and S. R. Forrest, *Sol. Energy Mater. Sol. Cells*, 2013, 118, 116-123.
19. C. J. Brabec, S. Gowrisanker, J. J. M. Halls, D. Laird, S. Jia and S. P. Williams, *Adv. Mater.*, 2010, 22, 3839-3856.
20. F. Fabregat-Santiago, G. Garcia-Belmonte, I. Mora-Sero and J. Bisquert, *Phys. Chem. Chem. Phys.*, 2011, 13, 9083-9118.

21. T. S. Ripolles, A. Guerrero and G. Garcia-Belmonte, *Appl. Phys. Lett.*, 2013, 103, 243306.
22. A. Guerrero, P. P. Boix, L. F. Marchesi, T. Ripolles-Sanchis, E. C. Pereira and G. Garcia-Belmonte, *Sol. Energy Mater. Sol. Cells*, 2012, 100, 185-191.
23. Z. Liang, A. Nardes, D. Wang, J. J. Berry and B. A. Gregg, *Chem. Mater.*, 2009, 21, 4914-4919.
24. A. Guerrero, L. F. Marchesi, P. P. Boix, S. Ruiz-Raga, T. Ripolles-Sanchis, G. Garcia-Belmonte and J. Bisquert, *ACS Nano*, 2012, 6, 3453-3460.
25. J. Bisquert, F. Fabregat-Santiago, I. n. Mora-Seró, G. Garcia-Belmonte and S. Giménez, *J. Phys. Chem. C*, 2009, 113, 17278-17290.
26. J. Bisquert, *Phys. Chem. Chem. Phys.*, 2003, 5, 5360-5364.
27. F. Fabregat-Santiago, J. Bisquert, E. Palomares, L. Otero, D. Kuang, S. M. Zakeeruddin and M. Grätzel, *J. Phys. Chem. C*, 2007, 111, 6550-6560.
28. G. Garcia-Belmonte, A. Munar, E. M. Barea, J. Bisquert, I. Ugarte and R. Pacios, *Org. Electron.*, 2008, 9, 847-851.
29. G. Garcia-Belmonte, P. P. Boix, J. Bisquert, M. Sessolo and H. J. Bolink, *Sol. Energy Mater. Sol. Cells*, 2010, 94, 366-375.

CHAPTER 5

MECHANISMS INFLUENCING THE OPEN-CIRCUIT VOLTAGE

Most of the results showed in this chapter have been published in:

- T. Ripolles-Sanchis, S. R. Raga, A. Guerrero, M. Welker, M. Turbiez, J. Bisquert and G. Garcia-Belmonte, Molecular Electronic Coupling Controls Charge Recombination Kinetics in Organic Solar Cells of Low Bandgap Diketopyrrolopyrrole, Carbazole, and Thiophene Polymers, *J. Phys. Chem. C*, 2013, 117, 8719-8726.

- T. S. Ripolles, A. Guerrero and G. Garcia-Belmonte, Polymer defect states modulate open-circuit voltage in bulk-heterojunction solar cells, *Appl. Phys. Lett.*, 2013, 103, 243306.

5.1. Introduction

Currently, the improvement of photovoltaic parameters and, consequently, the enlargement of the PCEs is one of the major challenges in the PSC field. Therefore, several factors such as light absorption, hole and electron mobilities, charge transport and recombination processes, charge collection as well as blend morphology and stability of the materials must be taken into account. Among the cell parameters playing a role on the overall performance of the devices, V_{oc} is considered one of the crucial variables to be improved. In particular, one of the most common strategies that enable to achieve a higher V_{oc} consists on reducing the charge carrier recombination rate,[1] which is understood as the charge transfer process occurring between occupied acceptor (A) levels and unoccupied donor (D) states. The inhibition of recombination current increases the amount of free charge carriers and, therefore, it increases the likelihood of extracting charge carriers, thus contributing to the photoconversion efficiency. This produces an enlarged offset in the separate Fermi Levels for electrons and holes, E_{Fn} and E_{Fp}, that is measured as an output voltage as[2]

$$qV_{\text{oc}} = E_{\text{Fn}} - E_{\text{Fp}} \tag{5.1}$$

This last condition depends on the ability of the blend to maintain high concentration of separate electron and hole carriers, which is governed by recombination kinetics.[3] Therefore, the main objective of the first section in this chapter is to understand the role of the recombination rates on the obtained V_{oc} by using different donor polymer materials and exploiting the same acceptor fullerene. The recombination kinetics have been studied previously via a variety of experimental methods, including time-of-flight (ToF),[4] photoinduced charge extraction by linearly increasing voltage (photo-CELIV),[4] steady-state current-voltage,[5] double injection currents (DoI),[6] transient absorption spectroscopy (TAS),[7] transient photovoltage (TPV),[8] transient photocurrent (TPC),[9] and impedance spectroscopy (IS).[10,11] In particular, to evaluate the role of the charge carrier recombination kinetics, we have analyzed the device performance by using a purely electrical technique based on impedance measurements of complete cells under 1 sun illumination. Additionally, this last study allowed us to calculate the V_{oc} losses caused by the recombination kinetics.

Another factor influencing photovoltage has a purely energetic origin, as it is illustrated in equation 5.1. The Fermi Level positions, E_{Fn} and E_{Fp}, are highly dependent on the actual energy distribution of electronic states within the effective bandgap $E_{\text{g}} \approx E^{\text{A}}_{\text{LUMO}} - E^{\text{D}}_{\text{HOMO}}$, being the LUMO-acceptor energy level, $E^{\text{A}}_{\text{LUMO}}$, and the HOMO-donor energy level, $E^{\text{D}}_{\text{HOMO}}$. Energy disorder of both acceptor fullerene and donor polymer induces bandgap density-of-states (DOS) (exponential or Gaussian tails and traps) that modulate the light-induced Fermi Level shift.[12] This last mechanism explains how the processing conditions of the sample can alter the output V_{oc}. The formation of the aggregates in the blend active layer is known to be highly influenced by the fabrication methods which could change the final DOS of both donor and acceptor molecular constituents.[13,14] Recent studies have found that variations within the fullerene DOS related to their dissimilar aggregation ability affect the ultimate V_{oc}.[15,16] It was observed that large fullerene DOS limits the Fermi Level upward shift yielding as a result lower V_{oc} values. However, the influence on photovoltage of the polymer energetic disorder/crystallinity has been much less explored.[17] The morphology-related to electronic defects in the donor polymer, which is induced by the experimental methodology, and its repercussion on the achieved V_{OC} is the specific aim of the second section in this chapter.

The morphology of a bulk heterojunction (BHJ) blend affects the extraction paths of electrons and/or holes, and therefore it is critical to improve the photovoltaic parameters and photoconversion efficiency.[18,19] The morphology can be considerably altered by employing a wide variety of methodologies such as the selection of appropriate solvents,[19,20] drying processes,[21] D:A ratio,[19] concentration of materials,[22] thermal treatments,[23,24] or use of additives.[25] In particular, the second section focuses on the study of P3HT polymer intimately blended with a soluble derivative of C_{60} ($PC_{60}BM$). This semicrystalline layer extensively studied in the last decade has reported efficiencies around 3–5 %.[26] The P3HT:$PC_{60}BM$ blend is formed by the P3HT crystalline phase (fibril shape) embedded in an amorphous mixture of P3HT and $PC_{60}BM$. The miscibility of $PC_{60}BM$ in amorphous P3HT hinders the $PC_{60}BM$ crystallization, however, fullerenes can crystallize under certain preparation conditions, for instance, by thermal annealing.[27] Consequently, the $PC_{60}BM$-rich crystalline phases leave space for converting P3HT-amorphous to fibrillar-like P3HT crystals domains. Additionally, an enhancement of the regioregularity of P3HT assists the polymer crystallization, thus promoting the formation of $PC_{60}BM$ crystallites.[28] In 2005, Heeger *et al.* demonstrated by means of structural studies, the orthorhombic crystalline domains with *c*-axis aligned principally along the rubbing direction, as it is shown in Scheme 5.1.[29] The backbones of the macromolecules are stacked along the *b*-axis, which form a plane of parallel backbones with π–electron overlap and with side chains between the planes (along the *a*-axis). There is no π–overlap between these planes due to the long side chains along the *a*-axis.

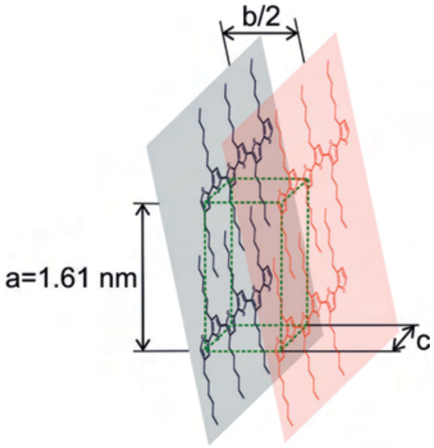

Scheme 5.1. P3HT crystalline structure. The *a*-axis orientation is related to the packing of the alkyl chains of the P3HT crystallites, *b*-axis represents the degree of interchain order, and the *c*-axis shows the degree of conjugation of the P3HT chains. The dashed lines represent the unit cell of the crystalline domains along the *b*-direction.

The efficiencies of P3HT:$PC_{60}BM$ solar cells are drastically improved by controlling the blend processing conditions, and consequently, its morphology. One aspect to consider is the high dependence of the molecular weight of the polymer with the thermal annealing in order to diffuse the $PC_{60}BM$ molecules through the P3HT matrix.[30] Besides, different P3HT:$PC_{60}BM$ ratios also affect the morphology of the blend. For instance, a large $PC_{60}BM$ concentration provided large area of D/A interface and better charge transfer to the respective electrodes, thus achieving a higher j_{SC}.[31] The use of additives such as 1,8-diiodooctane or 1-chloronaphthalene demonstrated to induce a control of the morphology of the blend, thus leaving a room for an improvement of the device performance.[32] The effect of these additives consisted on increasing the crystalline $PC_{60}BM$ domains size in relation to the crystalline P3HT domains, or vice versa when the films are cast by using pure chlorobenzene and nitrobenzene as an additive. Another key aspect to be considered is the thickness of the active layer. A relatively thick film is desirable to maximize the light absorption, but the charge transport restriction and extraction at large film contributes to low *FF* and performance of the OPV device.[33] Guo *et al.* demonstrated that thicker active layers had relatively low electron mobilities compared to hole mobilities. As a result, high contact resistance at the bulk/metal cathode interface prevented efficiently the transport of the photogenerated electrons.[33] The authors controlled the thickness by changing the concentration of the blend solution and the applied pressure. Other way to adjust the film thickness consists on changing the cooling rate of the film. Some studies claimed that slower cooling rates of P3HT:$PC_{60}BM$ film enhanced the polymer crystallinity, and consequently, the efficiencies are improved significantly.[21] In what regards to the solvents, a red-shift of the UV-Vis absorption and *EQE* spectra was observed for a mixture of solvents chlorobenzene:chloroform (3:1, by volume) in P3HT:$PC_{60}BM$ blend. The analysis by AFM showed finely structured phase segregation between P3HT and $PC_{60}BM$.[34] Additionally, it has been demonstrated that the connection between the solvent properties and the later heat treatments is another key factor to be considered. The P3HT crystallinity and the optical absorption was increased when a post-annealing was carried out independently of the solvent used, which created a vertical and interfacial reorganization process.[20] However, the films that were spin-coated from a chloroform solution showed a higher optical absorption and crystallinity than those spin-coated from chlorobenzene solution. Besides, Müller-Buschbaum *et al.* reported that the P3HT:$PC_{60}BM$ blend processed with *o*-dichlorobenzene and annealed after cathode deposition achieved better performance, while the absence of annealing or annealing before contact deposition resulted, in both cases, a significantly worse performance.[35]

5.2. The effect of energetic levels on recombination

This section focuses on the recombination rate of three polymer materials, namely, P3HT, PCDTBT, and DPP860 (Chart 3.1 in the section 3.5.1.), which have different HOMO energy levels, as it is illustrated in Scheme 5.2. In particular, the study aims to analyze the effect of the nature of the polymer on the recombination kinetic mechanisms and its correlation with the V_{oc} behavior.

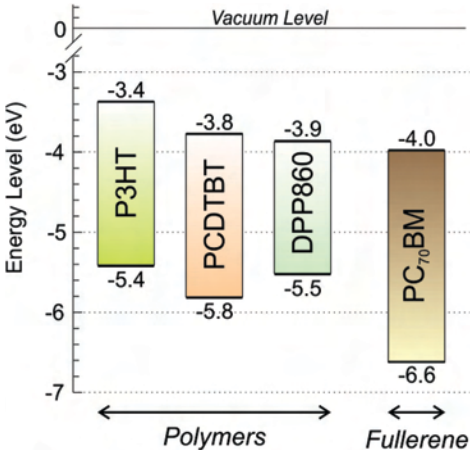

Scheme 5.2. Energy Levels diagram of P3HT-, PCDTBT- and DPP860-polymer materials and $PC_{70}BM$ fullerene material.

The OPV architecture is based on glass/ITO/PEDOT:PSS/blend/Ca/Ag, the blend films were constituted by a polymer (P3HT, PCDTBT, or DPP860) blended with a common fullerene acceptor material ($PC_{70}BM$). The device fabrication is explained in detail in the experimental section described in the Chapter 3 and more specific details are included in Appendix II.[11] The BHJ films were analyzed by UV-Vis spectroscopy and, the photovoltaic devices were characterized by $j-V$ and IS measurements under AM1.5G illumination (1000 W m^{-2}) and *EQE*.

5.2.1. Characterization of the OPV devices

The characteristic $j-V$ curves under simulated 1 sun illumination of polymer:$PC_{70}BM$ solar cells are plotted in Figure 5.1.a and the photovoltaic parameters are summarized in Table 5.1. The P3HT-based solar cell is taken as a reference cell for the sake of comparison to the other two polymers devices.

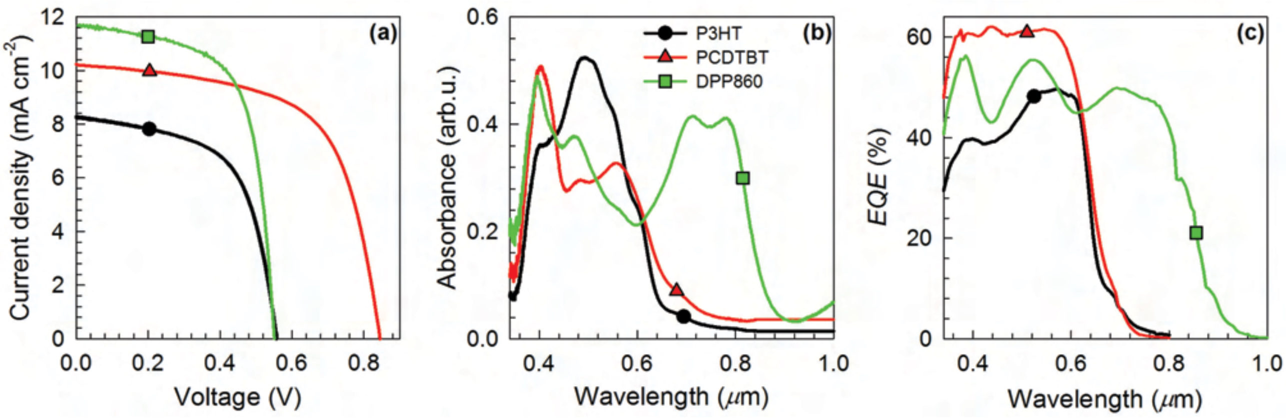

Figure 5.1. $j-V$ plots under simulated 1 sun illumination (a), absorption spectra of the blend on films (b), and *EQE* (c) for standard PSCs with acceptor fullerene material $PC_{70}BM$ and different donor polymers, such as P3HT, PCDTBT and DPP860.

In Figure 5.1.a is observed that the PCDTBT-based solar cell presents higher V_{oc} in comparison to the others devices due to the large E^{D}_{HOMO} respect to the E^{A}_{LUMO} (Scheme 5.2). The photovoltage values of the P3HT- and DPP860-based devices were comparable one each other due to the similar HOMO-level values, -5.4 and -5.5 eV, respectively. Additionally, the highest j_{SC} corresponds to the DPP860-based solar cell because this polymer presents lower bandgap, which improves the light harvesting efficiency in the visible range, as it is observed in the absorption spectrum onset situated near 860 nm (see Figure 5.1.b).

Table 5.1. Photovoltaic and impedance parameters for OPV cells under 1 sun illumination conditions.

Polymer	j_{sc} (mA cm^{-2})	V_{oc} (mV)	***FF*** (%)	**PCE** (%)	**α**	**β**	**γ**
P3HT	8.36	560	59	2.7	0.35	0.71	2.01
PCDTBT	10.21	845	62	5.4	0.32	0.68	2.00
DPP860	12.80	554	66	4.7	0.44	0.78	1.77

The *EQE* spectra (Figure 5.1.b) resembled to the absorbance response and the main absorption peak ascribed to the $PC_{70}BM$ is observed at ~380 nm, while the characteristic peaks of polymers appear at higher wavelengths. It is worth to highlight the absorption and *EQE* onset of the DPP860-based solar cell which is extended up to 900 nm, approximately, as a consequence of the smaller bandgap. In addition, the *EQE* spectrum of the PCDTBT-based OPV device shows a high plateau of about 60 %, which induces a relatively high photon to electron conversion efficiency (5.4 %).

5.2.2. Impedance Spectroscopy of the OPV devices

IS technique allows to discern processes with different characteristics time and consequently analyze the different phenomena occurring in a solar cell. As it is mentioned in the previous chapters, a series of useful electrical parameters such as the chemical capacitance, C_{μ}, and the recombination resistance, R_{rec}, are extracted at the low frequency region of the IS spectra under simulated 1 sun irradiation conditions.[36] These two parameters are represented as a function of the Fermi Level voltage (V_{F}) in Figure 5.2.a and Figure 5.2.b, respectively. V_{F} represents part of the total voltage removed the series resistances.

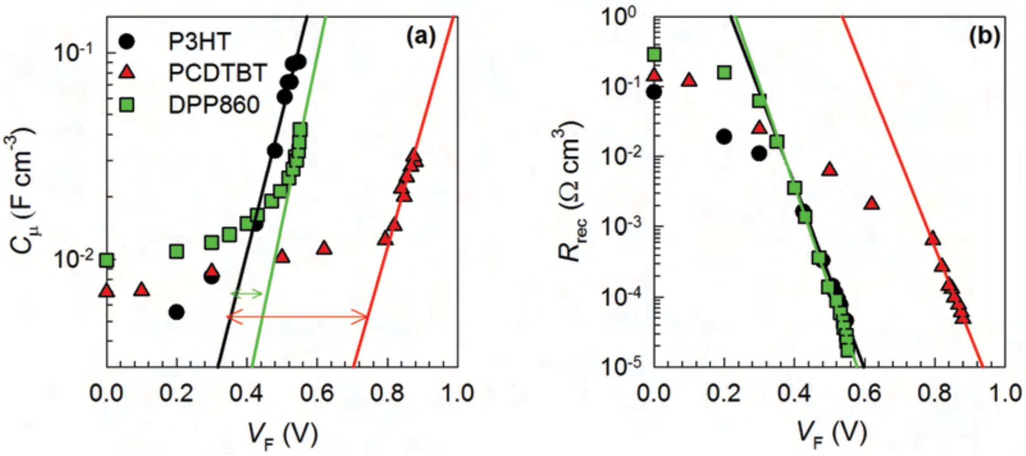

Figure 5.2. Chemical capacitance C_{μ} (a) and recombination resistance R_{rec} (b) results extracted from the impedance spectra using an equivalent circuit model composed by two *RC* in series for P3HT-, PCDTBT-, and DPP860-based solar cells under simulated 1 sun illumination. The arrows represent the voltage shift respect to the P3HT polymer.

The capacitance measured at low voltages in Figure 5.2.a corresponds to a dielectric mechanism, which is originated by the voltage-modulation of the depletion zone built up at the cathode contact. This capacitance collapses near zero voltage to the geometrical capacitance, C_{g}, as it has been shown in our previous work.[10] However, for larger voltages the chemical capacitance C_{μ} exhibits the expected variation originated by the carrier occupation of the electron DOS, *g*(*E*), as $C_{\mu} = q^2 Lg(V_{\text{F}})$, being *L* the active layer thickness. Typically, the measured capacitance is sensitive to the rise of the occupancy of electron states *g*(*E*) in the molecular acceptor due to in many cases the electrons form minority carriers because the semiconductors are *p*-doped

$$g(E) = \frac{N_{\text{L}}}{k_{\text{B}}T_0} \exp\left[\frac{E - E_{\text{LUMO}}}{k_{\text{B}}T_0}\right] \tag{5.2}$$

where N_{L} corresponds to the total level density of the LUMO-acceptor manifold. In zero-temperature approximation, the total electron carrier density, *n*, is given by the integration of DOS up to the Fermi Level as follows

$$n = \int_0^{E_{\text{Fn}}} g(E)\,\mathrm{d}E = N_{\text{L}} \exp\left[\frac{E_{\text{Fn}} - E_{\text{LUMO}}}{k_{\text{B}}T_0}\right] = n_0 \exp\left(\frac{E_{\text{Fn}} - E_{\text{F0}}}{k_{\text{B}}T_0}\right) \tag{5.3}$$

where n_0 accounts the carrier density in the equilibrium and E_{F0} corresponds to the position of the equilibrium Fermi Level.

In Figure 5.2.a is observed that C_μ exhibits an exponential dependence at high voltages like is shown in equation 5.4. The occupancy of the bandgap states $g(E)$ is modulated by a parameter α, which accounts for the characteristic energy of the DOS as $\alpha = T/T_0$, being T_0 the characteristic temperature of the exponential distribution. Using equation 5.4, α parameter can be calculated from the slope of the plots showed in Figure 5.2.a and it is found in the range of $\alpha \approx 0.3-0.4$ (see Table 5.1).

$$C_\mu = C_0 \exp\left(\frac{\alpha q V_F}{k_B T}\right) \tag{5.4}$$

This C_μ extracted from the impedance analysis is then a replica of the bandgap electronic states distribution as the occupation progresses associated with the Fermi Level displacement. Therefore, the exponential rise in the C_μ (Figure 5.2.a) belongs to the DOS occupancy. This energy shift depends on the HOMO polymer position with respect to the LUMO-acceptor level. Since a common acceptor fullerene material is used in this study, it is reasonable that the voltage shift in the capacitance plot is principally attributed to the polymer HOMO level offset, as drawn in Scheme 5.3.a for P3HT and PCDTBT-based cells. As a consequence, we are able to measure the HOMO level of each polymer, taking into account the HOMO P3HT value (-5.4 eV) as a reference (see Appendix I). In Figure 5.2.a is represented the voltage shift as an arrow for each polymer, and the calculated HOMO levels were -5.8 and -5.5 eV for PCDTBT and DPP860, respectively.[37] As it was previously explained, these values indicate the DOS center rather than the onset of state occupancy. In addition, the LUMO levels can be extracted from the absorption spectra in Figure 5.1.b. Finally, the energy diagram is completed as drawn in Scheme 5.3.b. It worth to point out that the capacitive method reported here allows establishing the polymer HOMO position in complete cells when a reference value is given by using alternative techniques.

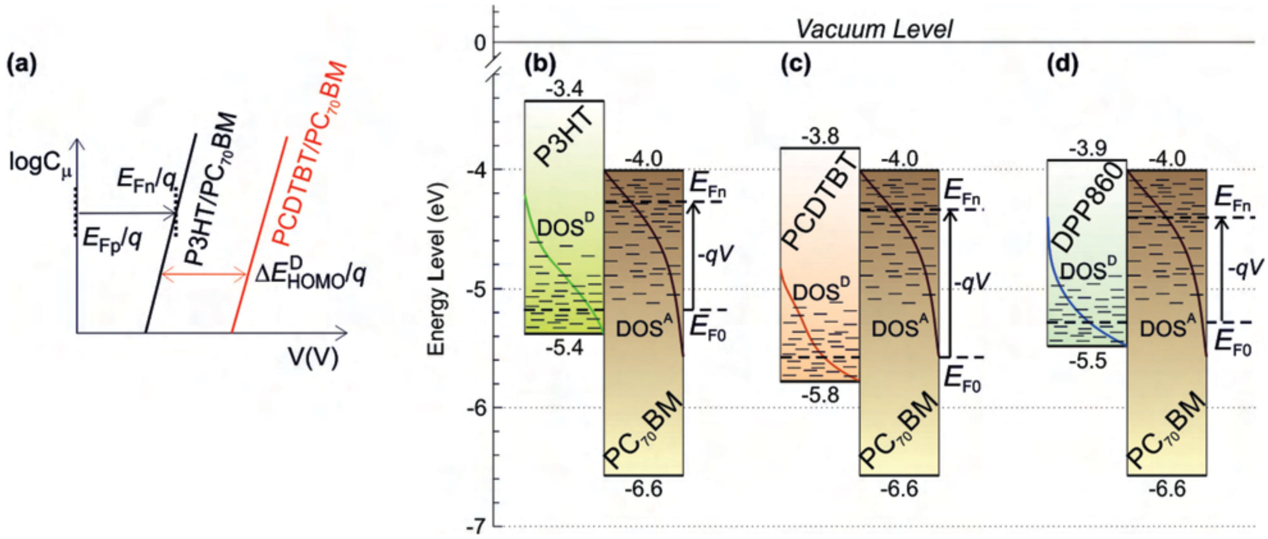

Scheme 5.3. The HOMO levels of PCDTBT and DPP860 were calculated from the shift of the *C–V* plot. The procedure of the PCDTBT polymer is illustrated in (a). Energy diagram of the blends: P3HT:$PC_{70}BM$ (b), PCDTBT:$PC_{70}BM$ (c), and DPP860:$PC_{70}BM$ (d). The DOS has been represented in each diagram being DOS center to the HOMO-donor level. The LUMO levels are estimated from the tail of the absorption spectra (Figure 5.1.b). The HOMO P3HT level was measured by *CV* (Appendix I).

Regarding R_{rec} extracted from impedance conveys information about the recombination flux. Recombination current (j_{rec}) of excess carriers is phenomenologically modeled as

$$j_{\mathrm{rec}} = j_0\left[\left(\frac{n_{\mathrm{c}}}{n_{\mathrm{c}}^0}\right)^{\beta} - 1\right] = j_0\left[\exp\left(\beta\frac{qV_{\mathrm{F}}}{k_{\mathrm{B}}T}\right) - 1\right] \tag{5.5}$$

The previous expression is usually called β-recombination model which includes the β parameter ($\beta \le 1$) accounting for the deviation from the ideal diode equation (inverse of the diode ideality factor of the $j-V$ characteristics) and j_0 corresponds to the saturation of the j_{rec} in dark conditions. The measured R_{rec} is in fact the derivative of the recombination flux, where

$$R_{\mathrm{rec}} = L\left(\frac{\mathrm{d}j_{\mathrm{rec}}}{\mathrm{d}V_{\mathrm{F}}}\right)^{-1} \tag{5.6}$$

being L is the active layer thickness.[38] From Figure 5.2.b, the R_{rec} can be approximated to an exponential dependence at forward voltages approaching V_{oc},

$$R_{\mathrm{rec}} = R_0 \exp\left(\frac{-\beta qV_{\mathrm{F}}}{k_{\mathrm{B}}T}\right) \tag{5.7}$$

as it is expected from the equation 5.5 derivative in the case of high injection, and the R_0 corresponds to the R_{rec} prefactor. Table 5.1 summarizes the β-parameter results ($\beta \approx 0.7-0.8$) from the slope of the plots showed in Figure 5.2.b using the equation 5.7. At lower voltages R_{rec} tends to saturate to a value presumably because the differential resistance measured is not only determined by the j_{rec}, but also by a shunt resistance (R_{sh}) dominating as a consequence of unavoidable parallel leakage currents. We notice that the saturation current, j_0, correlates directly to the R_0 as

$$j_0 = \frac{k_{\mathrm{B}}T}{\beta L R_0} \tag{5.8}$$

Equation 5.8 is a useful tool to determine j_0 avoiding the disturbing effect of leakage currents on the $j-V$ curves. R_0 is extracted from equation 5.7 and then, the j_0 can be calculated from equation 5.8, whose values are summarized in Table 5.2. These results are discussed later on.

The excess electron density, *n*, appears in addition to background equilibrium electron density, n_0 . In dark conditions, the equilibrium densities produce the saturation of the j_{rec} that compensates the thermal generation as follow

$$j_0 = qLBn_0^{\gamma} \tag{5.9}$$

However, actual measurement of the reverse current in dark may not provide j_0 due to the leakage currents.

From equation $n/n_0 = \left(n_c/n_c^0\right)^{\alpha}$, we obviously have the relationship $\gamma = \beta/\alpha$. Looking α and β results extracted from the fitting (Table 5.1), it is observed that $\beta \approx 2\alpha$. This equality satisfies within the experimental error. Therefore, the γ exponent results should be around 2. In the case of DPP860 polymer, a slightly lower exponent is found, $\gamma = 1.77$. This experimental fact lets us simplify the equation 5.5 as $j_{\mathrm{rec}} \propto n^{\gamma}$, with $\gamma \approx 2$, signaling an approximate bimolecular-like behavior for the recombination process, in good accordance with the electroneutrality condition $\mathrm{n} = \mathrm{p}$. Some studies based on IS technique have identified $\gamma \approx 2$,[3,38] while transient analyses usually give $\gamma \geq 2$.[1,39]

From equations 5.5 and 5.6, we derived that the j_{rec} can be written in terms of the R_{rec} as $j_{\mathrm{rec}} = k_{\mathrm{B}}T / \beta q R_{\mathrm{rec}}$,[40] that allows for a straightforward calculation of the recombination coefficient B based on differential resistive and capacitive parameters extracted from IS. By combining equations 5.3 and 5.5 in the case of high injection, B can be expressed as

$$B = \frac{k_{\mathrm{B}}T}{q^2 L n^2 \beta R_{\mathrm{rec}}} \tag{5.10}$$

The derivation of equation 5.10 assumes a rather constant value for *B*, nearly energetic independent of the states taking part on the recombination event. Results of applying equation 5.10 are shown in Figure 5.3.

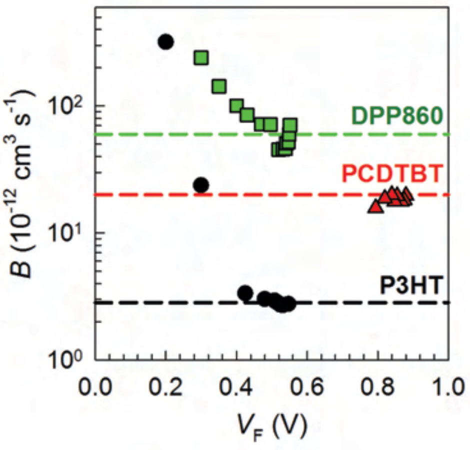

Figure 5.3. Recombination coefficient *B* calculated by equation 5.10 using the parameters extracted from the IS. The horizontal dashed lines mark average values of data points following the exponential behavior in Figure 5.2.b.

At $V_{\mathrm{F}} > 0.4\ \mathrm{V}$, the *B* value for each blend exhibits an almost constant behavior always within the range of $B \approx 10^{-12} - 10^{-11}\ \mathrm{cm}^3\ \mathrm{s}^{-1}$. In the case of P3HT:PC$_{70}$BM devices, a lower *B* is encountered ($B \approx 3 \times 10^{-12}\ \mathrm{cm}^3\ \mathrm{s}^{-1}$) in comparison with PCDTBT:PC$_{70}$BM ($B \approx 2 \times 10^{-11}\ \mathrm{cm}^3\ \mathrm{s}^{-1}$), and DPP860:PC$_{70}$BM ($B \approx 6 \times 10^{-11}\ \mathrm{cm}^3\ \mathrm{s}^{-1}$) solar cells. For lower voltages, *B* departs from the approximate constant value because both R_{rec} and C_{μ} largely deviate from the exponential behavior. It is worth noting that *B* values found for P3HT and PCDTBT are in good agreement with recent results reported using alternative techniques.[41,42] In addition, the results showed in Figure 5.3 point to the fact that the energy location of recombining carriers within the DOS has a minor influence on the *B* value.

5.2.3. Connection to molecular charge transfer parameters

A key parameter to understand the kinetics of charge carrier recombination in solar cells is the j_0 in equation 5.5.[43,44] It is known that j_0 establishes the time scale of recombination through the combined effect of the charge transfer energetic and kinetic. As suggested for inorganic semiconductors,[45] a separation of both effects is proposed in the form

$$j_0 = j_{0\mathrm{k}} \exp\left(-\frac{\beta E_\mathrm{g}}{k_\mathrm{B} T}\right) \tag{5.11}$$

The equation 5.11 describes separately kinetic terms represented by the prefactor $j_{0\mathrm{k}}$ and the energetic contributions stated through bandgap energy E_g. It is highlighted that the lower j_0 values (Table 5.2) correspond to the blends with larger effective E_g as derived from the capacitance voltage shift. In organic semiconductor D:A blend, the E_g value is calculated by an effective gap as $E_\mathrm{g} \approx E_\mathrm{LUMO}^\mathrm{A} - E_\mathrm{HOMO}^\mathrm{D}$. The prefactor $j_{0\mathrm{k}}$ can be estimated as previously explained in equation 5.9 such as

$$j_{0\mathrm{k}} = qLBN_{00}^{\gamma} \tag{5.12}$$

Here, it is proposed that in accordance to the capacitance dependence on voltage, the equilibrium carrier density, N_0, could be expressed as $N_0 = N_{00} \exp\left(-\alpha E_\mathrm{g} / k_\mathrm{B} T\right)$, being N_{00} a parameter accounting for the total density level. This last expression is consistent with equation 5.11 and the form adopted in equation 5.9 by j_0.

It is feasible to determine $j_{0\mathrm{k}}$ taking into account the effective gap, E_g, as derived from the capacitance voltage shift in the equation 5.11. In Table 5.2 is observed that $j_{0\mathrm{k}}$ presents similar trend than the coefficient *B*. Large variations in *B* (or equivalently $j_{0\mathrm{k}}$) depend on the polymer nature, without any correlation with the polymer ionization energy. Therefore, the higher recombining character of DPP860-based cells is confirmed. These results are a strong indication that the recombination kinetics does not depend on the absolute energetics of the HOMO-donor levels. Indeed, the *B* parameter of the PCDTBT-based device, which has deep HOMO positions (-5.8 eV), is located between those observed for much lower ionization energy polymers, as P3HT (-5.4 eV) and DPP860 (-5.5 eV).

Finally, the N_{00} is then measured from the equation 5.12. By examining Table 5.2, it can be observed that N_{00} is in the range of $10^{19} - 10^{20}$ cm^{-3}, in good agreement with the total density of active molecules in the active layer.

Table 5.2. Recombination coefficient, *B*, extracted from IS (equation 5.10). Saturation current, j_0, extracted from equation 5.8, applying the R_rec prefactor, R_0 (equation 5.7). From the effective gap, E_g, is measured the prefactor $j_{0\mathrm{k}}$ in equation 5.11. Total level density N_{00} is extracted from equation 5.12. The electronic coupling matrix V_if is calculated from equation 5.14. Using the P3HT as a reference, the $\Delta V_\mathrm{oc}^\mathrm{kin}$ is measured by equation 5.19 and V'_oc is calculated using the difference: $V'_\mathrm{oc} = V_\mathrm{oc} - \Delta V_\mathrm{oc}$.

Polymer	***B*** (cm^3 s^{-1})	$\boldsymbol{j_0}$ (A cm^{-2})	$\boldsymbol{j_{0k}}$ (A cm^{-2})	$\boldsymbol{N_{00}}$ (cm^{-3})	$\boldsymbol{V_\mathrm{if}}$ (meV)	$\boldsymbol{\Delta V_\mathrm{oc}^\mathrm{kin}}$ (mV)	$\boldsymbol{V'_\mathrm{oc}}$ (mV)
P3HT	3×10^{-12}	4.7×10^{-10}	1.7×10^{4}	7.8×10^{19}	0.09	-	-
PCDTBT	2×10^{-11}	7.8×10^{-14}	3.9×10^{4}	3.5×10^{19}	0.19	85	875
DPP860	$\sim 6\times10^{-11}$	1.5×10^{-10}	2.7×10^{6}	1.7×10^{20}	0.70	110	550

An alternative view regards the charge transfer event itself as the limiting factor in the recombination mechanism. It is then the specific molecular environment at D/A interfaces that states the time scale for recombination. In a previous work, we have reported that there is a low dependence of the recombination kinetics on the fullerene electron affinity and voltage,[3] and, it was concluded, within the framework of the Marcus theory, that the reorganization energy, λ, rather than the polymer HOMO/fullerene LUMO energy offset or the DOS occupancy level, takes control over the charge transfer event. The charge transfer rate k_0 in the semiclassical Marcus expression is written as

$$k_0 = \frac{2\pi}{\hbar} |V_{\text{if}}|^2 \sqrt{\frac{1}{4\pi\lambda k_{\text{B}}T}} \exp\left(-\frac{(\Delta G_0 + \lambda)^2}{4\lambda k_{\text{B}}T} \right) \tag{5.13}$$

where ΔG_0 is the variation of the Gibbs free energy during the reaction and V_{if} corresponds to the electronic coupling matrix element (charge transfer integral) between initial and final states. The ΔG_0 is the difference between acceptor and donor energy level offset, $\Delta G_0 \approx E_{\text{n}} - E_{\text{p}}$.

Recalling again the Marcus model in equation 5.13, if the recombination kinetic goes down slowly, small values of V_{if} and large λ are necessary. We note from Figure 5.3 that the recombination kinetics results slightly dependent on the voltage for a given polymer:fullerene combination. This behavior is in good agreement with a large value for $\lambda \approx 0.7\,\text{eV}$, as stated in recent works.[3] This last observation implies that the observed variation in B might be connected to changes in V_{if}, a parameter that mainly reflects the environment in which polymer/fullerene interfaces are located. It is known that V_{if} highly depends on both relative molecular orientations and intermolecular distances.[46] By comparing equations 5.12 and 5.13, it can be readily considered that $k_0 \approx BN_{00}$ because as noted previously γ coefficient is 2. This last equation allows to calculate V_{if}, assuming that the charge transfer event occurs closely to the maximum rate, in accordance with large λ.[3] Under this assumption, the exponential term in equation 5.13 is close to 1, and it can be obtained that

$$|V_{\text{if}}|^2 = \frac{\hbar\sqrt{4\pi\lambda k_{\text{B}}T}}{2\pi} BN_{00} \tag{5.14}$$

The calculated V_{if} values are listed in Table 5.2. It is observed that low values of V_{if} (<1 meV) mean high inhibiting character of the recombination charge transfer between reduced fullerene molecules and oxidized polymer units.[47] Nevertheless, the relatively more recombining blend containing DPP860 exhibits larger V_{if} value in comparison with the other blend combinations studied.

5.2.4. Determination of energy losses

At V_{oc} conditions, the j_0 is largely exceeded by the j_{rec} (exponential term) in equation 5.5, assuming a voltage-independent photocurrent $j_{\text{ph}} = j_{\text{sc}}$, and equation 5.8, the photovoltage can be expressed as follows

$$V_{\text{oc}} = \frac{k_{\text{B}}T}{q\beta} \ln\left(\frac{j_{\text{sc}}}{j_0} \right) = \frac{k_{\text{B}}T}{q\beta} \ln\left(\frac{R_0 L\beta j_{\text{sc}}}{k_{\text{B}}T} \right) \tag{5.15}$$

This correlation has been recently suggested for the case of dye-sensitized solar cells.[48] Equation 5.15 entails that variations in V_{oc} are linked with two different contributions. V_{oc} is increased at higher photocurrent because photogenerated carrier density achieves larger values. On the contrary, lower dark current j_0 reduces the j_{rec} and allows an increment in the photogenerated carriers. This effect arises from the fact that solar cells operate under the principle of the kinetic balance between light-induced carrier generation and recombination. The unfavorable effect of increased recombination on V_{oc} can be quantified. Taking into account that the term related to differences in j_{sc} as $k_BT/q\beta\ln(j'_{sc}/j_{sc})$ only amounts about 15 meV when DPP860- and P3HT-based cells are compared, this term can be omitted in the next calculations. From equation 5.15, it is derived the differences in V_{oc} between two OPV cells with different recombination rate as

$$\Delta V_{oc} = \frac{k_BT}{q\beta}\ln\left(\frac{j'_0}{j_0}\right) \tag{5.16}$$

In equation 5.16, ΔV_{oc} stands for the V_{oc} enhancement of the cell with lower recombination rate owed to the reduction in dark, j_0, with respect to the value exhibited by the more recombining cell, j'_0. Hence, taking into account equation 5.16, ΔV_{oc} is separated into two contributions using the equation 5.9 as

$$\Delta V_{oc} = \frac{k_BT}{q\beta}\left[\ln\left(\frac{B'}{B}\right) + \ln\left(\frac{n_0'^{\gamma}}{n_0^{\gamma}}\right)\right] \tag{5.17}$$

The last equation can be interpreted by the first summand ($k_BT/q\beta\ln(B'/B)$) as a V_{oc} loss owed exclusively to the difference in the recombination kinetics, ΔV_{oc}^{kin}. The second summand is the ratio between equilibrium carrier densities ($k_BT/q\beta\ln(n_0'^{\gamma}/n_0^{\gamma})$) which can be expressed in terms of the effective bandgap, ΔV_{oc}^{ener}. This term represents the essential influence of the energetics on the recombination kinetics. As indicated in equation 5.2, the equilibrium carrier density, n_0, which determines the j_0, scales with the equilibrium Fermi Level, E_{F0}. Recalling equation 5.2 and taking into account that the energy shift in E_{F0} is caused by the polymer HOMO level offset, a separation of kinetic and energetic terms in equation 5.17 is derived

$$\Delta V_{oc} = \Delta V_{oc}^{kin} + \Delta V_{oc}^{ener} \tag{5.18}$$

where first summand is represented as

$$\Delta V_{oc}^{kin} = \frac{k_BT}{q\beta}\ln\left(\frac{B'}{B}\right) \tag{5.19}$$

and the second summand corresponds to the differences of HOMO levels between two donor materials which have different recombination rate (E'^{D}_{HOMO} represents the more recombination cell) by

$$\Delta V_{oc}^{ener} = \frac{E^{D}_{HOMO} - E'^{D}_{HOMO}}{q} \tag{5.20}$$

Equation 5.18 states that V_{oc} variations among solar cells with different active layers can be simply split into two separated contributions. One related to differences in recombination kinetic time scale and the other exclusively linked with energy HOMO offset of the donors, as far as N_{00} exhibits similar values between the compared cells. The case of comparing acceptors with different LUMO level has been recently treated.[3] If only the recombination kinetics term, $\Delta V_{\mathrm{oc}}^{\mathrm{kin}}$, of equation 5.19 is considered, a significant loss in V_{oc} is observed, about 100 meV (Table 5.2). This voltage drop is exclusively produced by the increment in the recombination kinetics exhibited by PCDTBT- and DPP860-based solar cells in comparison to that occurring for the less recombining P3HT-based devices. Such a shift in V_{oc} caused by recombination losses, entails PCE reduction approximately equal to 20 % in the case of DPP860. Moreover, the application of equation 5.18 allows us to determine $V_{\mathrm{oc}}' = V_{\mathrm{oc}} - \Delta V_{\mathrm{oc}}$, taking the values exhibited by P3HT-based as a reference cell. Estimation of V_{oc} lies within the experimental error as observed in Table 5.1 and Table 5.2.

5.3. The effect of morphology on open-circuit voltage

This section investigates the influence of the processing conditions on the polymer defect states distribution and structural order. Moreover, it is explained how polymer structural order and defect density modulate the achievable output voltage V_{oc}. A standard architecture of sandwich PSC, glass/ITO/PEDOT:PSS/P3HT:$\mathrm{PC_{60}BM}$/Ca/Ag is used in this research. The OPV devices were fabricated as indicated in the experimental section in Chapter 3 (more specific details in Appendix II).[49] Five blend processing conditions that provide different crystallinity and morphology of the blend are analyzed. The experimental variables are: control of the drying rate of the active layer film (long drying times for device 1 and short drying times for devices 3–5), a thermal treatment of the deposited films (devices 3–5) or both conditions (device 2). The fast dry sample represents furthest from equilibrium and the slow cooled device represents closest to the final reorganized state. The annealing differences between these cells are detailed in Table 5.3. The active layer thicknesses of the films were approximately 300 nm (see Appendix II). These layers were characterized by optical techniques such as UV-Vis absorption and XRD. The complete OPV devices were analyzed by $j-V$ under simulated 1 sun illumination (1000 W $\mathrm{m^{-2}}$) and a capacitance method under dark conditions.

5.3.1. Characterization of the active layers

The absorption spectra of P3HT:$\mathrm{PC_{60}BM}$ films (samples 1–5) and a reference of pure P3HT are shown in Figure 5.4.a. These films were prepared in the configuration of glass/ITO/blend or polymer by using different processing conditions. These UV-Vis results present similar behaviour to data previously reported,[20,50] where the $\mathrm{PC_{60}BM}$ absorption is dominant below 400 nm (this characteristic peak of the $\mathrm{PC_{60}BM}$ is not shown in Figure 5.4) and the P3HT band is visible between 450 and 600 nm.[51] A characteristic peak of the P3HT polymer is observed at about 500 nm which provides information on the degree of conjugation of the P3HT chains, and a peak at around 600 nm informs on the degree of interchain order.[21,52] There are evidences to affirm that the introduction of fullerene as $\mathrm{PC_{60}BM}$ into the blend film disturbs the polymer local ordering because the P3HT-polymer pure film absorbance spectrum exhibits a red-shift at 500 nm and a larger absorbance at 600 nm respect to the others blends films. In contrast, comparing with slow and fast drying processing conditions for P3HT:$\mathrm{PC_{60}BM}$ blends, the bands at around 500 nm illustrates a red-shift absorbance for the slow drying blends (devices 1 and 2), indicating longer polymer conjugation lengths than the fast drying samples (devices 3–5). This effect altered the *c*-axis in a network crystalline of the P3HT film as is shown in Scheme 5.1. Similar results are observed in the band at 600 nm where the slow drying produces higher crystallinity (high absorbance intensity) respect to the fast drying films, independently of the heat treatments.

In addition, the optical bandgap can be calculated from the absorption onset at higher wavelengths in the absorbance spectra.[53] Therefore, different processing conditions causes bandgap differences as it is observed in Figure 5.4.a. Comparing the lowest crystalline sample (device 3) with the more crystalline film (device 2), showing bandgap values 1.91 eV and 1.84 eV, respectively, we concluded that the slow drying film has a narrower bandgap.

Finally, regarding the heat treatment samples, the height of the vibronic shoulder at 600 nm increases systematically from un-annealed to 130 ºC annealed films. This effect is observed for fast (devices 3–5) and slow (devices 1–2) drying films, whereas it is more pronounced in the latter samples. These results indicate a poor degree of interchain order for un-annealed P3HT:$PC_{60}BM$ films (see *b*-axis in Scheme 5.1). Therefore, the absorption measurements are very sensitive to differences in crystallinity as it is shown in these experiments.

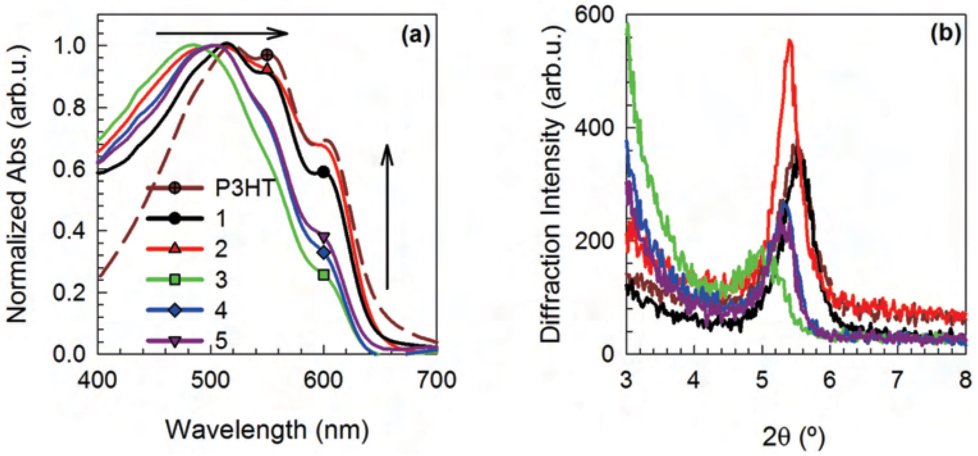

Figure 5.4. UV-Vis spectra (a) and XRD (b) for the P3HT pure and P3HT:$PC_{60}BM$ blends with different processing conditions in film. The UV-Vis spectra have been normalized to the maximum of the P3HT peak at around 500 nm.

The XRD spectra of the films prepared in the configuration glass/ITO/blend or P3HT and using different processing conditions are shown in Figure 5.4.b. All P3HT:$PC_{60}BM$ samples exhibits a single crystalline peak at about 5.4º. That diffraction peak corresponds to the *a*-axis orientation related to the packing of the alkyl chains of the P3HT crystallites (see Scheme 5.1). The corresponding lattice constant $a = 1.61\,\text{nm}$ was calculated using Bragg's law.[50] Unfortunately, XRD data do not provide any information about the *b*- or *c*-axis orientations and, consequently, valuable information on the packing of the thiophene rings is missing. The XRD of a P3HT pure sample presents a peak at about 23º,[21] which is not observed in our P3HT:$PC_{60}BM$ films. So, for this reason the range of angles showed in the Figure 5.4.b is limited to $3^\circ < 2\theta < 8^\circ$. It is remarkable that the relative diffraction intensity depends on the processing conditions of the blends. The films prepared under controlled drying conditions present higher intensity peak at 5.4º. As a result, higher crystalline volume density is formed in the *a*-axis. The others fast dried films present a temperature-dependence. It is noteworthy an increment of the 2θ angle shifts from films not thermally treated to those annealed samples.

As an approximation, the nanodomain size L can be estimated from XRD data by the width and position of the diffraction peak using Scherrer's relation[20]

$$L \cong \frac{0.9\lambda}{\Delta_{2\theta}\cos(\theta)} \tag{5.21}$$

where λ is the wavelength, $\Delta_{2\theta}$ is the full width at half maximum of the peak, and θ is the Bragg angle. The λ characteristic monochromatic of Cu K_α beam is 0.154 nm. The crystalline sizes L for the P3HT:PC$_{60}$BM active layer films with different drying and heating treatments are summarized in Table 5.3. The low P3HT-size domain corresponds to the fast dried film thermally untreated with a value of 14 nm. According to the XRD data upon fast drying annealed, the domain size increases slightly up to about 18 nm. However, L is even higher for an annealed sample that has been slowly dried (sample 2), being lower L value for the un-annealed counterpart (sample 1). These results indicate that after thermal annealing, the PC$_{60}$BM molecules diffused into larger PC$_{60}$BM aggregates and the rearrangement of P3HT improves the packing.[20] Note that the crystallinity monitored by using the XRD diffraction pattern is limited to the *a*-axis, packing of the alkyl chains of the P3HT crystallites. However, the XRD diffraction patterns corroborate that P3HT:PC$_{60}$BM blends provide semicrystalline films.

5.3.2. Characterization of the OPV devices

The $j-V$ curves were measured under simulated AM1.5G irradiation (1000 W m^{-2}). These results are shown in Figure 5.5.a and the photovoltaic parameters are summarized in Table 5.3.

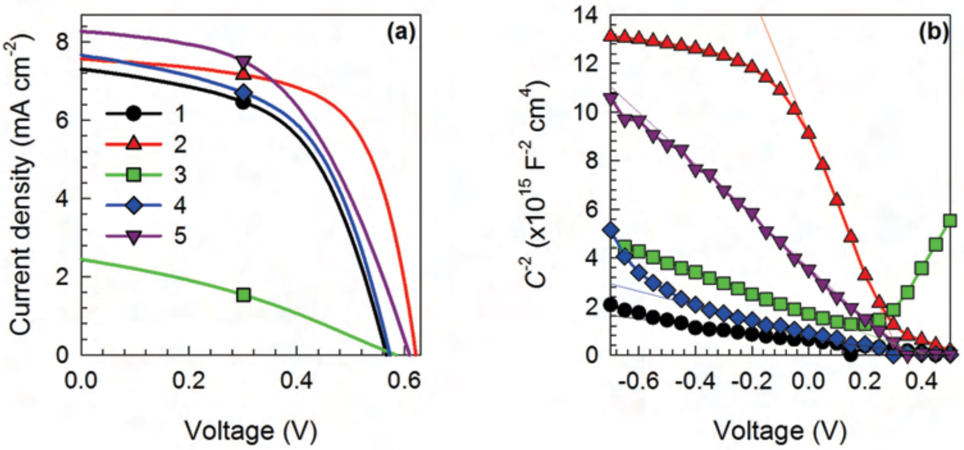

Figure 5.5. (a) $j-V$ curves under simulated 1 sun illumination and (b) Mott-Schottky plot for standard P3HT:PC$_{60}$BM devices using the experimental conditions listed in Table 5.3. It is also shown in (b) the straight line for each Mott-Schottky curve.

Similar $j-V$ results are obtained for films prepared with different methodologies and crystallinity properties.[54,55] For films processed with slow drying, the un-annealed device (device 1) presents low photovoltaic parameters respect to the annealed film (device 2) which provides high V_{OC}. Regarding the fast drying processed films, only the film least crystalline that was not thermally treated (device 3) shows remarkably low j_{SC} and *FF*. Besides, the film annealed at 130 ºC (device 5) present higher in j_{SC} and V_{OC} results, but lower *FF* values respect to the 90 ºC fast drying P3HT:PC$_{60}$BM cell (device 4). As explained below, these photovoltaic responses correlate with data extracted from absorbance and diffraction experiments.

UV-Vis spectra as well as XRD data variations are related to the polymer structural order, but both do not allow direct quantification of electrically active morphological features. For this reason, a purely electrical method is carried out. Generally, larger polymer ordering means smaller amounts of structural defects originated at less crystalline zones where the periodic spacing is broken. Polymer defect states acting as acceptor impurities might originate free holes, as is evidenced by monitoring the polymer conductivity or photoluminescence quenching.[56] The density of defect states is accessible by means of capacitive methods that measure the width of the depletion zone built-up in the vicinity of the cathode contact. Here, we use Capacitance–Voltage ($C-V$) measurements carried out under dark conditions from -1 to 0.5 V at constant frequency of 100 Hz, employing methods described previously.[10]

Table 5.3. The P3HT:PC$_{60}$BM active layer with different processing conditions of the blend. From the XRD experiments is extracted the domain size, *L*, of the P3HT using the equation 5.21. The formula to calculate *L* takes into account the full width at half maximum of the peak $\Delta_{2\theta}$ and the Bragg angle *2θ*. Photovoltaic parameters measured under simulated 1 sun illumination. From the capacitance measurements is calculated the charge carrier concentration *N* using the equation 5.22.

ID	**Conditions**	$\Delta_{2\theta}$ (rad)	2θ (rad)	L (nm)	j_{SC} (mA cm^{-2})	V_{oc} (mV)	FF (%)	**PCE** (%)	N (10^{16} cm^{-3})
1	Slow dry	0.048	5.5	17	7.31	566	54	2.2	4.0
2	Slow dry, 130 ºC[a]	0.047	5.4	21	7.57	621	64	3.0	0.2
3	Fast dry	0.068	4.8	14	2.45	587	32	0.5	1.2
4	Fast dry, 90 ºC	0.043	4.9	18	7.67	572	54	2.4	2.0
5	Fast dry, 130 ºC	0.044	5.1	18	8.28	608	50	2.6	0.4

[a] *Post-cathode annealing.*

The Mott-Schottky plots $C^{-2}-V$ of the devices are shown in Figure 5.5.b, exhibiting a linear relation given by the following expression

$$C^{-2} = \frac{2}{A^{2} q \varepsilon \varepsilon_{0} N}\left(V_{\mathrm{fb}} - V\right) \tag{5.22}$$

where *A* corresponds to active surface of the device, ε is the relative dielectric constant of the blend (for P3HT:PC$_{60}$BM corresponds a $\varepsilon \approx 3$), ε_0 is the permittivity of the vacuum (8.85×10^{-12} F m^{-1}), V_{fb} is the flat-band potential, and *N* is the total concentration of defects (*p*-doping level). From equation 5.22, the concentration of electrically active acceptor impurities *N* and V_{fb} is extracted at reverse and low forward bias from the slope and the extrapolated intersection with the voltage axis, respectively. The charge carrier densities *N* are summarized in Table 5.3. Interestingly, the Mott-Schottky plot does not show full depletion at -1 V for most of the devices, except for the most crystalline film (device 2) in which the C_{g} can be derived from the saturation at reverse bias. It is important to note that these OPV devices have not been exposed to air at any time. Therefore, the defect densities, *N*, measured should mainly correspond to intrinsic defects caused by crystallinity changes (structural impurities/defects of the active layer) rather than originated by air-related polymer oxidation.

5.3.3. Correlation between open-circuit voltage, crystallinity and *p*-doping level

Recalling now absorption and $C-V$ measurements, it is observed that increasing the crystallinity of the polymer leads to decrease doping densities. Indeed, for the OPV device with higher crystallinity (device 2) presents doping densities N about one order of magnitude lower than those OPV devices with poorly crystalline blends (Devices 3 and 4). However, the N of the device 5 decreases at higher temperatures as the P3HT molecules aggregates enable less disperse energetic landscape. Then, the defects are related to the actual surface area of the polymer crystallites. It is plausible to assume that the polymer molecules present at the boundary between regular domains show a different energetic landscape than those molecules found in the middle of a crystallite.

For further analysis, the XRD spectrum in a range of 3º < 2θ < 30º and the Mott-Schottky plot of OPV devices based on the highly amorphous system PCDTBT:PC$_{70}$BM have been measured. In this system, the highly amorphous nature of PCDTBT is manifested in Figure 5.6.a. The active layer film shows only the base line, indicating poor crystallinity of the blend composed of PCDTBT:PC$_{70}$BM. Additionally, the number of impurities, calculated from the equation 5.22, is 1.4×10^{17} cm^{-3} (Figure 5.6.b), taking into account $\varepsilon \approx 3.5$ for PCDTBT:PC$_{70}$BM blend. The N is two orders of magnitude higher than those observed for high crystalline P3HT:PC$_{60}$BM blend in device 2. These results further suggest that the doping density is highly related to the polymer and its degree of structural order.

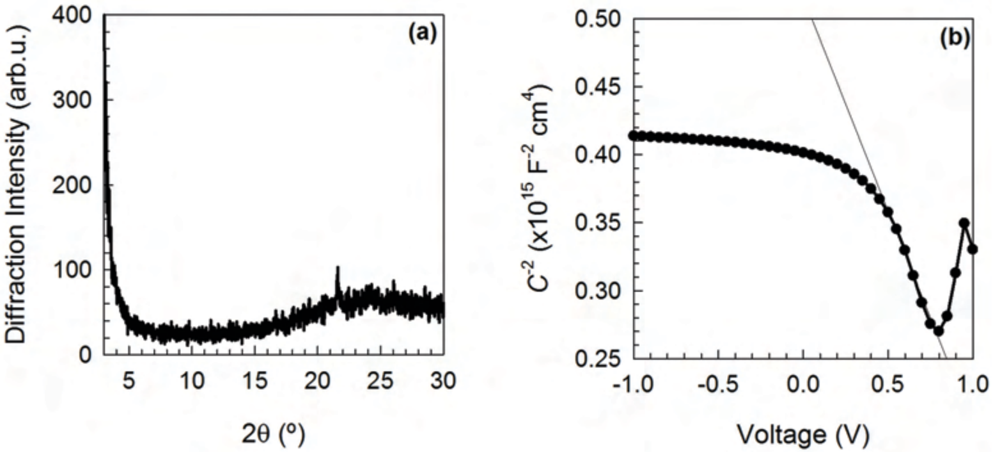

Figure 5.6. XRD (a) and Mott-Schottky (b) plots for a standard 1:1 PCDTBT:PC$_{70}$BM organic solar cell. The configuration of the substrate for the XRD measurement was glass/ITO/PCDTBT:PC$_{70}$BM. The capacitance measurement was performed under dark conditions and a constant frequency at 1000 Hz.

As reported previously, V_{oc} is related to the HOMO-donor level and the LUMO-acceptor level,[57] and, more precisely, to the difference in Fermi Levels of electrons (E_{Fn}) and holes (E_{Fp}) of equation 5.1. It is known that thermal treatment produces an upward shift of the polymer HOMO manifold.[58] This is indeed confirmed by the red-shifted absorption spectra in Figure 5.4.a. The bandgap calculated previously for the post-cathode annealing and un-annealing blend films of device 2 (high crystallinity) and device 3 (poor crystallinity) are 1.84 and 1.91 eV, respectively. For this reason, the V_{oc} of device 2 should be decreased about 40 meV (70 meV is the difference in bandgap) in comparison with device 3 caused by differences in the polymer bandgap. However, the observed trend in our experiments is the opposite. Device 2 shows a V_{oc} result about 35 mV higher than for device 3 (see Table 5.3). Then, it is clear that apart from the effective bandgap of the materials, other factors affect the photovoltage. Here we study a correlation between the polymer disorder degree (lack of crystallinity) and the defect density by means of capacitive tools.

Figure 5.7 connects three different techniques, capacitance (Mott-Schottky), absorbance (UV-Vis spectra) and diffraction (XRD spectra), to study the V_{oc} values extracted from the photovoltaic curves under simulated 1 sun illumination to P3HT:PC$_{60}$BM OPV cells. In Figure 5.7 is observed an exponential trend between the calculated N from capacitance analysis and V_{oc}, in which V_{oc} increases with a reduction of the number of impurities. It is worth noting that P3HT crystallite size corresponds to a concentration of impurities of the order 10^{17} cm^{-3}, in good accordance with the defect density encountered ($10^{15}-10^{16}$ cm^{-3}). The right axes of Figure 5.7 correspond to a measurement of the polymer structural order, extracted from either the inverse of the relative P3HT absorption intensity peak of the vibronic shoulder at 600 nm (Figure 5.4.a) or the inverse of the nanodomain size L value (Table 5.3). Inverse values are used here in order to directly compare with density measurements. It is observed that crystallinity degree (abs^{-1} and L^{-1}) and defect density (N) correlate with the V_{oc} obtained for the studied devices, with the exception of device 1. This is a special case, slow drying without thermal treatment, the residual solvent might be present as a source of external chemical impurities, contributing to the concentration of defects. This fact explains the low V_{oc} exhibited by device 1, in spite of the higher crystallinity of the film. This exception would imply that defect density rather than the actual structural order lies behind the V_{oc} achieved.

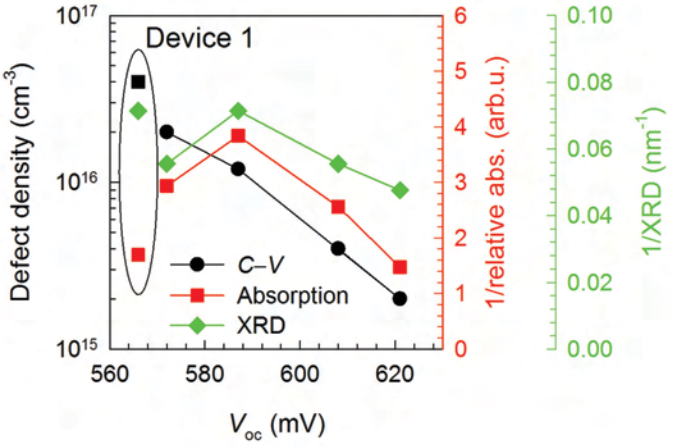

Figure 5.7. Defect density, N, extracted from $C-V$ analysis, inverse of the relative P3HT absorption intensity peak at 600 nm and inverse of the crystallite nanodomain size of L from XRD data *vs*. V_{oc}. The parameters of the device 1 do not follow the general trend.

Only by considering differences in j_{sc} and the diode equation is not possible to explain the observed variations in V_{oc}. The electronic effect of gap defects is associated with their ability to modulate the position of the hole Fermi Level, E_{Fp}, which in fact establishes the V_{oc} as is illustrated in Scheme 5.4. As it is expected from absorbance measurement (Figure 5.4.a), the bandgap energy decreases when the crystallinity blend increased, and consequently the V_{oc} should be lower. However, our observations are opposed; other energy contributions affect the V_{oc} behavior. Under illumination conditions, E_{Fp} undergoes a downward shift with respect to the equilibrium Fermi Level, E_{F0}, which is situated at an upper lying level for more crystalline polymers (see Scheme 5.4). Energy shift results larger for lower defect densities because there are less available electronic states within the bandgap to be occupied by photogenerated charges. Then, more crystalline samples exhibit lower defect density and larger E_{Fp} downshift. Therefore, the defects effect is dominant over variations in the bandgap and it determines the final V_{oc}. For simplicity, we consider that the number of defects created from different processing conditions and/or other annealing treatments, affects mainly the polymer. Scheme 5.4.a and Scheme 5.4.b represent high and low density of defects of the polymer for a standard photovoltaic device under illumination, respectively. Without the decrease in the bandgap, the maximum V_{oc} for device 2 should be about 40 mV higher reaching values of about 660 mV. Electronic states corresponding to fullerene molecules might also vary under different device processing[59] or even more with different fullerenes derivatives.[60] This alters the position of the E_{Fn} and the final output V_{oc}, as is discussed in the previous work where the influence of the LUMO-acceptor level bandgap tails was compared.[15,16] Here, the effect of polymer structural order and how it influences the light-induced shift of E_{Fp} were highlighted.

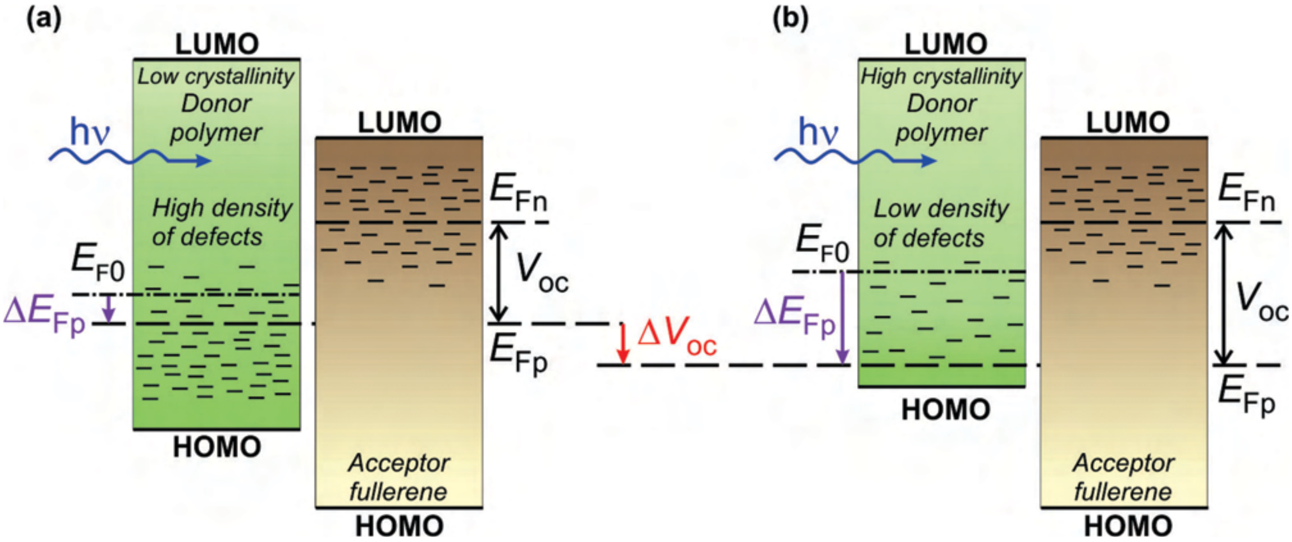

Scheme 5.4. Energy diagram levels of the polymer:fullerene blend under illumination for high (a) and low (b) density of defects into the polymer, keeping the same crystallinity to the fullerene material. E_{F0} represents the position of the equilibrium Fermi Level of the polymer in dark; E_{Fp} and E_{Fn} are the hole and electron Fermi Level, respectively. ΔE_{Fp} represents the difference between E_{Fp} and E_{F0}. The V_{oc} is calculated as the difference between E_{Fp} and E_{Fn}. Lower lying levels are occupied in the case of low N, producing a voltage offset ΔV_{oc}.

5.4. Conclusions

In summary, this chapter is focused on two factors that influence the V_{oc} of the OPV devices: recombination processes and BHJ morphology.

Firstly, the influences on the kinetics of charge carrier recombination were analyzed in three OPV cells with different donor polymers and singular bandgaps (P3HT, PCDTBT and DPP860), keeping an identical acceptor fullerene material ($PC_{70}BM$). Depending on the charge carrier recombination, the electronic coupling V_{if} at polymer/fullerene interface exhibited an increment for DPP860-based solar cell due to its high recombination. Additionally, the V_{oc} losses caused by the recombination kinetics $\Delta V_{\mathrm{oc}}^{\mathrm{kin}}$ were measured. PCDTBT- and DPP860-based cells lost approximately 100 mV in their V_{oc} results, being 20 % losses in the total PCE.

Secondly, the influence of processing conditions, including drying rates and heat treatments, on the morphology of the blend and the photovoltage values has been investigated, using a standard P3HT:$PC_{60}BM$ OPV cells. A favorable V_{oc} result were reflected in an increment of polymer crystallization observed in both the absorption peak at 600 nm (abs^{-1}) and the nanodomain size extracted from the XRD (L^{-1}) spectra, and a decrease of the *p*-doping density. Under illumination, the E_{Fp} achieved more pronounced down-shift to low *p*-doping level polymer respect to the E_{F0} due to less available electronic states within the bandgap to be occupied by photogenerated charges, reaching large V_{oc} values. However, device 1 (un-annealing slow drying film) is an exception because the blend admits a residual solvent molecules, causing an increment in the number of impurities and reaching false values of V_{oc}.

5.5. References

1. A. Maurano, R. Hamilton, C. G. Shuttle, A. M. Ballantyne, J. Nelson, B. O'Regan, W. M. Zhang, I. McCulloch, H. Azimi, M. Morana, C. J. Brabec and J. R. Durrant, *Adv. Mater.*, 2010, 22, 4987–4992.
2. G. Garcia-Belmonte and J. Bisquert, *Appl. Phys. Lett.*, 2010, 96, 113301.
3. A. Guerrero, L. F. Marchesi, P. P. Boix, J. Bisquert and G. Garcia-Belmonte, *J. Phys. Chem. Lett.*, 2012, 3, 1386-1392.
4. T. M. Clarke, J. Peet, A. Nattestad, N. Drolet, G. Dennler, C. Lungenschmied, M. Leclerc and A. J. Mozer, *Org. Electron.*, 2012, 13, 2639-2646.
5. S. R. Cowan, N. Banerji, W. L. Leong and A. J. Heeger, *Adv. Funct. Mater.*, 2012, 22, 1116-1128.
6. A. Armin, G. Juska, B. W. Philippa, P. L. Burn, P. Meredith, R. D. White and A. Pivrikas, *Adv. Energy Mater.*, 2013, 3, 321-327.
7. H. Löslein, T. Ameri, G. J. Matt, M. Koppe, H. J. Egelhaaf, A. Troeger, V. Sgobba, D. M. Guldi and C. J. Brabec, *Macromol. Rapid Commun.*, 2013, 34, 1090-1097.
8. L. Chen, Q. Zhang, Y. Lei, F. Zhu, B. Wu, T. Zhang, G. Niu, Z. Xiong and Q. Song, *Phys. Chem. Chem. Phys.*, 2013, 15, 16891-16897.
9. R. C. I. MacKenzie, C. G. Shuttle, G. F. Dibb, N. Treat, E. von Hauff, M. J. Robb, C. J. Hawker, M. L. Chabinyc and J. Nelson, *J. Phys. Chem. C*, 2013, 117, 12407-12414.
10. F. Fabregat-Santiago, G. Garcia-Belmonte, I. Mora-Sero and J. Bisquert, *Phys. Chem. Chem. Phys.*, 2011, 13, 9083-9118.
11. T. Ripolles-Sanchis, S. R. Raga, A. Guerrero, M. Welker, M. Turbiez, J. Bisquert and G. Garcia-Belmonte, *J. Phys. Chem. C*, 2013, 117, 8719-8726.
12. J. A. Carr and S. Chaudhary, *Energy Environ. Sci.*, 2013, 6, 3414-3438.
13. L. G. Kaake, P. F. Barbara and X. Y. Zhu, *J. Phys. Chem. Lett.*, 2010, 1, 628-635.
14. P. P. Boix, J. Ajuria, R. Pacios and G. Garcia-Belmonte, *J. Appl. Phys.*, 2011, 109, 074514.
15. G. Garcia-Belmonte, P. P. Boix, J. Bisquert, M. Lenes, H. J. Bolink, A. La Rosa, S. Filippone and N. Martín, *J. Phys. Chem. Lett.*, 2010, 1, 2566-2571.
16. A. Sánchez-Díaz, M. Izquierdo, S. Filippone, N. Martin and E. Palomares, *Adv. Funct. Mater.*, 2010, 20, 2695-2700.
17. Z. M. Beiley, E. T. Hoke, R. Noriega, J. Dacuña, G. F. Burkhard, J. A. Bartelt, A. Salleo, M. F. Toney and M. D. McGehee, *Adv. Energy Mater.*, 2011, 1, 954-962.
18. M. A. Brady, G. M. Su and M. L. Chabinyc, *Soft Matter*, 2011, 7, 11065-11077.
19. G. Dennler, M. C. Scharber and C. J. Brabec, *Adv. Mater.*, 2009, 21, 1323-1338.
20. U. Zhokhavets, T. Erb, G. Gobsch, M. Al-Ibrahim and O. Ambacher, *Chem. Phys. Lett.*, 2006, 418, 347-350.
21. B. Xue, B. Vaughan, C.-H. Poh, K. B. Burke, L. Thomsen, A. Stapleton, X. Zhou, G. W. Bryant, W. Belcher and P. C. Dastoor, *J. Phys. Chem. C*, 2010, 114, 15797-15805.

22. S. Wakim, S. Beaupre, N. Blouin, B.-R. Aich, S. Rodman, R. Gaudiana, Y. Tao and M. Leclerc, *J. Mater. Chem.*, 2009, 19, 5351-5358.
23. X. Yang, J. Loos, S. C. Veenstra, W. J. H. Verhees, M. M. Wienk, J. M. Kroon, M. A. J. Michels and R. A. J. Janssen, *Nano Lett.*, 2005, 5, 579-583.
24. F. Padinger, R. S. Rittberger and N. S. Sariciftci, *Adv. Funct. Mater.*, 2003, 13, 85-88.
25. T.-Y. Chu, S. Alem, S.-W. Tsang, S.-C. Tse, S. Wakim, J. Lu, G. Dennler, D. Waller, R. Gaudiana and Y. Tao, *Appl. Phys. Lett.*, 2011, 98, 253301.
26. E. J. Luber and J. M. Buriak, *ACS Nano*, 2013, 7, 4708-4714.
27. W.-R. Wu, U. S. Jeng, C.-J. Su, K.-H. Wei, M.-S. Su, M.-Y. Chiu, C.-Y. Chen, W.-B. Su, C.-H. Su and A.-C. Su, *ACS Nano*, 2011, 5, 6233-6243.
28. S. Vajjala Kesava, R. Dhanker, D. R. Kozub, K. Vakhshouri, U. H. Choi, R. H. Colby, C. Wang, A. Hexemer, N. C. Giebink and E. D. Gomez, *Chem. Mater.*, 2013, 25, 2812-2818.
29. C. Y. Yang, C. Soci, D. Moses and A. J. Heeger, *Synth. Met.*, 2005, 155, 639-642.
30. N. P. Holmes, K. B. Burke, P. Sista, M. Barr, H. D. Magurudeniya, M. C. Stefan, A. L. D. Kilcoyne, X. Zhou, P. C. Dastoor and W. J. Belcher, *Sol. Energy Mater. Sol. Cells*, 2013, 117, 437-445.
31. O. Oklobia and T. S. Shafai, *Solid-State Electron.*, 2013, 87, 64-68.
32. L. Chang, I. E. Jacobs, M. P. Augustine and A. J. Moulé, *Org. Electron.*, 2013, 14, 2431-2443.
33. H. J. Park, H. Kim, J. Y. Lee, T. Lee and L. J. Guo, *Energy Environ. Sci.*, 2013, 6, 2203-2210.
34. S. P. Yang, N. Li, G. Li, J. B. Shi, X. W. Li and G. S. Fu, *Acta Phys. Sin.*, 2013, 62, 014702.
35. S. Guo, M. A. Ruderer, M. Rawolle, V. Körstgens, C. Birkenstock, J. Perlich and P. Müller-Buschbaum, *ACS Appl. Mater. Interfaces*, 2013, 5, 8581-8590.
36. G. Garcia-Belmonte, A. Guerrero and J. Bisquert, *J. Phys. Chem. Lett.*, 2013, 4, 877-886.
37. J. Liu, S. Shao, G. Fang, J. Wang, B. Meng, Z. Xie and L. Wang, *Sol. Energy Mater. Sol. Cells*, 2014, 120, Part B, 744-750.
38. G. Garcia-Belmonte, P. P. Boix, J. Bisquert, M. Sessolo and H. J. Bolink, *Sol. Energy Mater. Sol. Cells*, 2010, 94, 366-375.
39. C. G. Shuttle, B. O'Regan, A. M. Ballantyne, J. Nelson, D. D. C. Bradley, J. de Mello and J. R. Durrant, *Appl. Phys. Lett.*, 2008, 92, 093311.
40. P. P. Boix, A. Guerrero, L. F. Marchesi, G. Garcia-Belmonte and J. Bisquert, *Adv. Energy Mater.*, 2011, 1, 1073-1078.
41. A. J. Ferguson, N. Kopidakis, S. E. Shaheen and G. Rumbles, *J. Phys. Chem. C*, 2011, 115, 23134-23148.
42. F. Etzold, I. A. Howard, N. Forler, D. M. Cho, M. Meister, H. Mangold, J. Shu, M. R. Hansen, K. Müllen and F. Laquai, *J. Am. Chem. Soc.*, 2012, 134, 10569-10583.
43. S. Yamamoto, A. Orimo, H. Ohkita, H. Benten and S. Ito, *Adv. Energy Mater.*, 2012, 2, 229-237.
44. P. Erwin and M. E. Thompson, *Appl. Phys. Lett.*, 2011, 98, 223305.
45. S. M. Sze, *Physics of Semiconductor Devices*, John Wiley & Sons: New York, 1981.
46. Y. Yi, V. Coropceanu and J.-L. Brédas, *J. Am. Chem. Soc.*, 2009, 131, 15777-15783.

47. Y. Yi, V. Coropceanu and J.-L. Bredas, *J. Mater. Chem.*, 2011, 21, 1479-1486.
48. S. R. Raga, E. M. Barea and F. Fabregat-Santiago, *J. Phys. Chem. Lett.*, 2012, 3, 1629-1634.
49. T. S. Ripolles, A. Guerrero and G. Garcia-Belmonte, *Appl. Phys. Lett.*, 2013, 103, 243306.
50. P. Vanlaeke, A. Swinnen, I. Haeldermans, G. Vanhoyland, T. Aernouts, D. Cheyns, C. Deibel, J. D'Haen, P. Heremans, J. Poortmans and J. V. Manca, *Sol. Energy Mater. Sol. Cells*, 2006, 90, 2150-2158.
51. R. Badrou Aïch, Y. Zou, M. Leclerc and Y. Tao, *Org. Electron.*, 2010, 11, 1053-1058.
52. P. J. Brown, D. S. Thomas, A. Köhler, J. S. Wilson, J.-S. Kim, C. M. Ramsdale, H. Sirringhaus and R. H. Friend, *Phys. Rev. B*, 2003, 67, 064203.
53. T. Geiger, S. Kuster, J.-H. Yum, S.-J. Moon, M. K. Nazeeruddin, M. Graetzel and F. Nueesch, *Adv. Funct. Mater.*, 2009, 19, 2720-2727.
54. G. Li, V. Shrotriya, J. Huang, Y. Yao, T. Moriarty, K. Emery and Y. Yang, *Nat. Mater.*, 2005, 4, 864-868.
55. W. Ma, C. Yang, X. Gong, K. Lee and A. J. Heeger, *Adv. Funct. Mater.*, 2005, 15, 1617-1622.
56. Z. Liang and B. A. Gregg, *Adv. Mater.*, 2012, 24, 3258-3262.
57. M. C. Scharber, D. Mühlbacher, M. Koppe, P. Denk, C. Waldauf, A. J. Heeger and C. J. Brabec, *Adv. Mater.*, 2006, 18, 789-794.
58. H. Aarnio, P. Sehati, S. Braun, M. Nyman, M. P. de Jong, M. Fahlman and R. Österbacka, *Adv. Energy Mater.*, 2011, 1, 792-797.
59. E. Verploegen, R. Mondal, C. J. Bettinger, S. Sok, M. F. Toney and Z. Bao, *Adv. Funct. Mater.*, 2010, 20, 3519-3529.
60. K. Akaike, K. Kanai, Y. Ouchi and K. Seki, *Chem. Phys.*, 2013, 415, 31-35.

CHAPTER 6

TRANSPORT MECHANISMS IN POLYMERIC SOLAR CELLS

Most of the results showed in this chapter are already published in:

- T. Ripolles-Sanchis, A. Guerrero, J. Bisquert and G. Garcia-Belmonte, Diffusion-Recombination Determines Collected Current and Voltage in Polymer:Fullerene Solar Cells, *J. Phys. Chem. C*, 2012, 116, 16925-16933.
- A. Guerrero, T. Ripolles-Sanchis, P. P. Boix and G. Garcia-Belmonte, Series resistance in organic bulk-heterojunction solar devices: Modulating carrier transport with fullerene electron traps, *Org. Electron.*, 2012, 13, 2326-2332.

6.1. Introduction

The processes governing charge carrier motion, recombination, and outer interface charge selection and extraction are crucial electronic mechanisms which might affect the conversion efficiencies in OPV solar cells.[1] Particularly important is the overall impact of the electronic transport mechanisms to have effective charge carrier motion into the nanoscale three-dimensional interpenetrated domains of donor (D) polymer and acceptor (A) fullerene as well as in the interface between materials. This chapter is focused on the transport features for carrier transport/extraction to electrodes in OPV solar cells.

There has been several efforts in the last few years to understand the carrier transport properties in nanocrystalline semiconductors and organic materials because they play a key role for current organic/inorganic devices such as dye-sensitized (DSC) and organic photovoltaic (OPV) solar cells,[2] organic and hybrid light-emitting diodes (OLEDs),[3] organic field-effect transistors (OFET),[4] and electrochemical sensors.[5] For all of them, it is important to use high-mobility polymers as the active material. In particular, the polymer most analyzed until now for the OPV technology is the P3HT due to its relatively high charge carrier mobility ($\sim 10^{-4}$ cm^2 V^{-1} s^{-1}) and bandgap (1.9–2.0 eV) which matches well with the maximum intensity of sunlight spectrum.[6]

In organic bulk heterojunction (BHJ) solar cells, two phases in the blend form small aggregates in the order of several nanometers to facilitate an effective charge separation of electrons and holes. Furthermore, each phase should be continuously connected for the transport of the respective charge carrier to reach the electrodes (see Scheme 6.1.a).

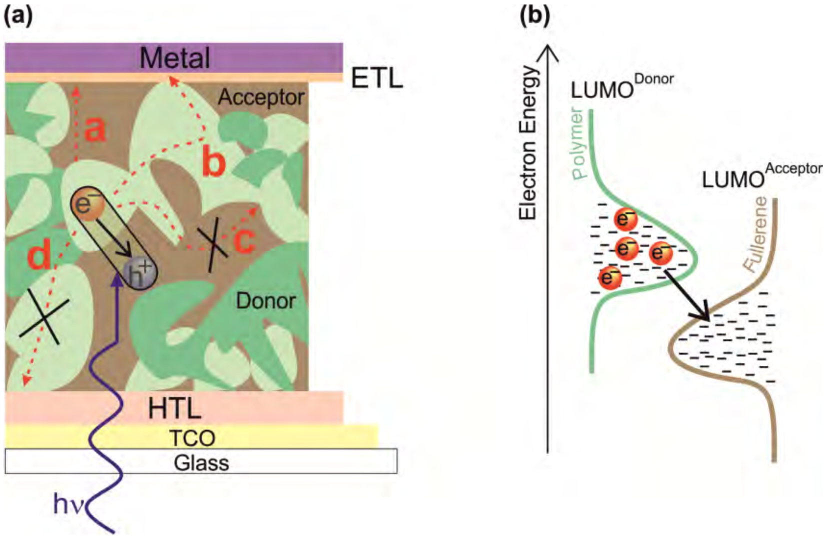

Scheme 6.1. Schematic pathways for electrons to reach the contact in the active layer under illumination conditions (a). The most natural way to extract the photoexcited electron is through the fullerene phase (path a) and polymer phase (path b). The electron could be blocked by the presence of dead end pathway at the fullerene phase (path c) or at the polymer phase (path d). An energy level scheme that highlights the broad density-of-states (DOS) in both the polymer and the fullerene materials (b). Under light intensity, the photoexcited electron is transferred from the LUMO of the polymer to the LUMO of the fullerene which contributes to the charge separation process; the black arrow represents this transition.

The electronic transport mechanism has dramatic effects when relatively thick active layer films are used to enhance light harvesting. This device suffers an incomplete collection of photogenerated charges as the recombination processes take more importance than the transport processes. This last statement is however not general as demonstrated with some polymer:fullerene combinations.[7] Conversely, some thinner films are able to exhibit almost 100 % conversion of absorbed photons into collected carriers,[8] thus indicating that transport mechanisms do not limit the achievable photocurrent.[9] Therefore, quantifying the influence of competing carrier transport and recombination mechanisms on cell performance has become a major topic for organic BHJ photovoltaics.[10,11] In addition, the re-crystallization as well as the inter-diffusion of D–A components (Scheme 6.1.b) depend on the processing conditions of the polymer:fullerene bulk, giving some flexibility in tuning/optimizing nanoscale phase separation and interpenetration of donors and acceptors that is essential and critical to obtain high efficiency in BHJ OPVs.[12]

The subject of this chapter is the interpretation of the transport carrier properties in standard configuration of PSCs by using IS technique. Two systems of PSCs are analyzed electronically. Firstly, an OPV device with an electron blocking layer between BHJ layer and efficient extraction cathode electrode. Here, the electron extraction is blocked by an insulator interlayer (CaO). The transport of electrons is clearly observed by IS measurement due to the posed impediment towards the extraction of carriers. Secondly, a small variable quantity is added in the active layer solution of other material in which holds lower LUMO energy level than those LUMO levels of polymer and fullerene materials of the active layer. This additional material acts like traps located at energies below the transporting electron levels into the active layer, showing a difficulty in the electron extraction. In both studies, a resistance from the electron (minority carrier due to the blend composition is *p*-doped semiconductor material) transport is observed in the IS technique. It has been proposed that the effect of mechanisms in series is observable at high frequencies in the impedance spectra, which were interpreted in connection with electronic transport processes.[13] Very recently impedance analysis has been employed identifying an additional *RC* parallel subcircuit which governs at high frequency response as a combination of bulk transport resistance and geometric capacitance.[14]

6.2. Characterization of OPV devices with working and blocking electron extraction cathode electrodes

Charge transport in efficient OPV solar cell is usually not observed by IS. The reason for this is simple, if the electron transport through polymer:fullerene BHJ layer is efficient the associated resistance to transport is low and other resistive processes are dominant. Then, the transport-related resistance is only detected at high-frequency part of the impedance spectra and in the range of high applied voltages. On the contrary, by blocking one extracting electrode the characteristic transport response resistance can be observed in all range of voltages at high-frequency part of the Nyquist plot. The configuration of the OPV devices was glass/ITO/PEDOT:PSS/P3HT:$PC_{60}BM$/ETL/Ag where ETL is composed by either Ca for working devices or CaO/Ca for blocking devices. In Scheme 6.2 is shown the architecture for blocking OPV devices. The experimental method was detailed in the experimental section of the Chapter 3 and more specific details are listed in Appendix II.[13]

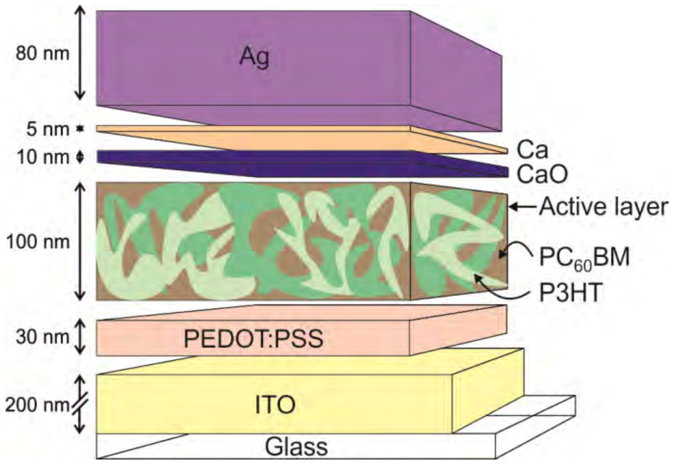

Scheme 6.2. A standard architecture of BHJ solar cells: glass/ITO/PEDOT:PSS/P3HT:$PC_{60}BM$/CaO/Ca/Ag. An oxide insulator layer (CaO) is inserted between the bulk and cathode electrode of different thicknesses (0.5, 5 and 10 nm) to block the electron collection. The efficient CaO blocking layer thickness is 10 nm.

The $j-V$ curves under AM1.5G (1000 W m^{-2}) illumination of cells comprising the same polymer:fullerene (P3HT:$PC_{60}BM$) BHJ film but different ETL structure (Ca and CaO/Ca) are represented in Figure 6.1 and the photovoltaic parameters are summarized in Table 6.1.

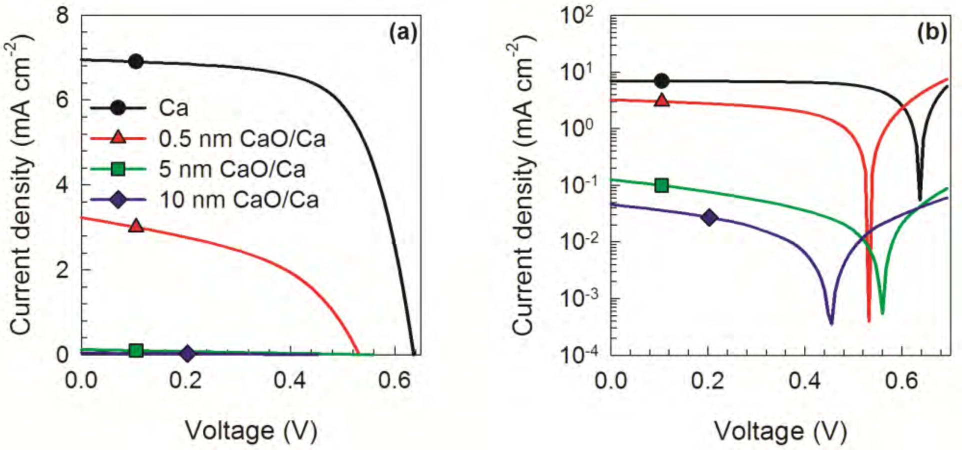

Figure 6.1. $j-V$ curves under simulated 1 sun radiation source for the OPV devices with identical P3HT:$PC_{60}BM$ blend and changing the ETL: an efficient extraction layer (Ca) and block electron collection layer with different thicknesses (0.5, 5 and 10 nm) of an insulator oxide (CaO). These plots represent linear (a) and logarithmical (b) current density-axis.

Figure 6.1 shows the efficient charge extraction for a standard OPV device with a Ca/Ag cathode contact reaching relatively high j_{SC} in agreement with previously reported results, 7.0 mA cm^{-2} (see Table 6.1).[15] However, the CaO insulator behavior is clearly observed in the photocurrent evidenced in Figure 6.1.b. When the oxide layer thickness increases, j_{SC} is severely limited by blocking the extraction of photogenerated electrons at the cathode contact. Noticeably, the blocking effect accounts for a reduction of more than 2 orders of magnitude in j_{SC} for a 10 nm CaO of thickness, while the V_{OC} is only reduced by ~200 mV respect to the efficient extraction cell. This last observation suggests that blocked devices under steady state illumination do not loss completely their ability to accumulate photogenerated carriers despite the oxide layer located at the cathode contact. This occurs because V_{OC} monitors the Fermi Level splitting of separated charge carriers in the blend material $qV_{OC} = E_{Fn} - E_{Fp}$, which are ultimately governed by the electron and hole occupancy of their respective electronic states. The E_{Fn} equilibrates with the cathode metal then producing the measured output voltage despite the presence of the oxide layer.

Table 6.1. Photovoltaic parameters under AM1.5G illumination source (1000 W m^{-2}) for the OPV devices with P3HT:PC$_{60}$BM active layer using different cathode contact, such as Ca/Ag and *x* nm CaO/Ca/Ag, being *x* 0.5, 5 and 10 nm.

Thickness CaO (nm)	j_{sc} (mA cm^{-2})	V_{oc} (mV)	*FF* (%)	**PCE** (%)
0	7.0	636	67	2.94
0.5	3.2	531	46	0.79
5	0.1	550	24	0.02
10	4×10^{-2}	449	28	0.01

The impedance and capacitance spectra showed in Figure 6.2.a and Figure 6.2.c (black dots) represent the typical response in standard OPV solar cells at different applied voltages and frequencies under AM1.5G solar illumination (1000 W m^{-2}).[16] Identical active layer (P3HT:PC$_{60}$BM) but different electron extraction layer (either Ca or 10 nm CaO/Ca) devices are then analyzed. As expected, bulk mechanisms of both devices are comparable due to their similar active layers composition. Two visually distinguishable parts are observed in the Nyquist plot depending on the frequency region: low (Figure 6.2.a) or high (Figure 6.2.b). First of all, the working devices show a large magnitude arc at low frequencies which represents a parallel *RC* subcircuit in the total equivalent circuit model. This part is related to the recombination resistance R_{rec} (caused by carrier recombination flux) and chemical capacitance C_μ (related to the charge accumulation) response.[17-20] At high frequencies, two effects are observed depending on the voltage range: at low bias a purely capacitive and at high forward bias a diffusive contribution. Furthermore, the capacitive response C_μ of the working devices observed in Figure 6.2.c indicates an increase of the capacitance at low frequencies with the bias voltage, which does not reach the value corresponding to the contact capacitance (C_{co}) observed for blocking contacts (C_{ox}). Since Ca is a good electron extraction contact, C_{co} contribution to the impedance spectra is usually hidden. In fact, two different capacitances can be distinguished in the blocking devices as C_μ attains similar values for working cells and C_{co} extracting cathodes; and consequently the C_{co} is extracted for the working devices.

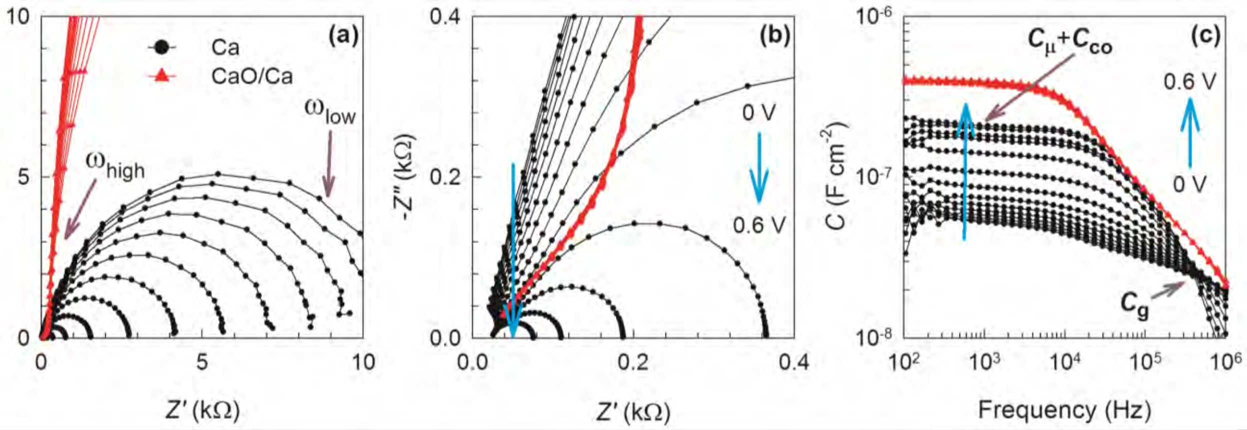

Figure 6.2. Impedance (a) (Expanded impedance spectra at high frequency in (b)) and capacitance (c) spectra for P3HT:PC$_{60}$BM BHJ with working (Ca) and blocking (10 nm CaO/Ca) electrodes solar cells under 1 sun.

As regards $Z''-Z'$ plot of the blocking electron extraction OPV solar cell with 10 nm CaO layer, at low frequency part of the IS spectra is clearly observed a huge resistance response in Figure 6.2.a (red dots) which is in concordance with the current limiting effect represented in Figure 6.1.b. This huge semicircle is attributed to the contact effect in series of resistance and capacitance which the oxide layer is denoted as $R_{ox}C_{ox}$. On the contrary, at high frequency part instead of purely capacitive spectra, a clearly distinguishable diffusion pattern is observed in Figure 6.2.b (red dots) for illuminated samples in all range of voltages. Impedance spectra is selected now to make evident the diffusive mechanism fingerprint as a slope 45° caused by the coupling of diffusive transport R_t and C_μ (Warburg response). Such coupling of transport and charge accumulation mechanisms is described by standard impedance model functions and it is often useful to represent the model in terms of distributed element circuits (transmission line) as discussed later.[21]

Studying more deeply the non-efficient cathode electrode CaO/Ca in a OPV device, Figure 6.3.a shows the evolution of the capacitance spectra $C-f$ measured in open-circuit upon variation of the light intensity from dark conditions until nearly 1 sun illumination. Under dark conditions, the capacitance exhibits the expected flat value originated from the dielectric response of the active layer, this capacitance corresponds to the geometrical capacitance, C_g . As the illumination intensity is increased, capacitance develops a plateau within the frequency range between 1–10 kHz, being originated by the accumulation of excess photogenerated charge carriers (see Figure 6.3.a).[22,23] This capacitance is the C_μ which increases with the irradiation intensity.

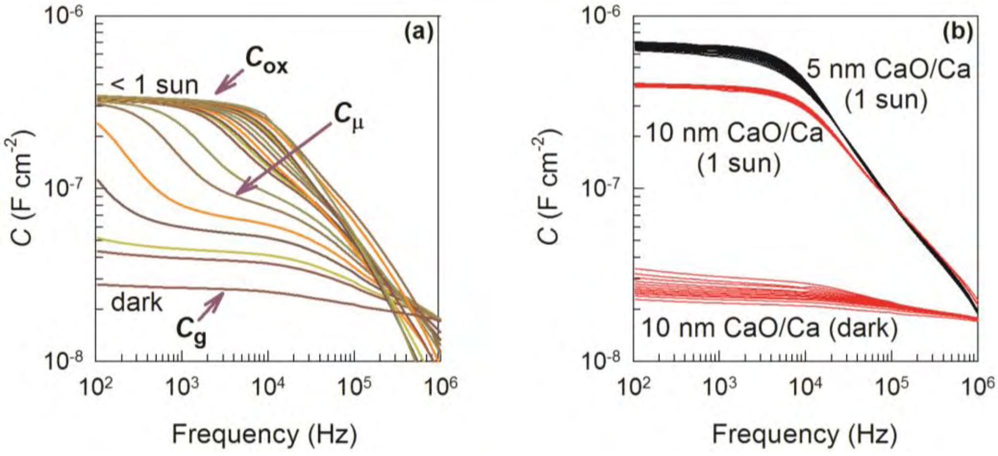

Figure 6.3. (a) Capacitance spectra plots at zero bias applied of a BHJ P3HT:PC$_{60}$BM-based solar cell with the electron extraction blocked with CaO film (10 nm) measured at different light intensities from dark to nearly 1 sun radiation. (b) Capacitance spectra plots of devices blocked with two different CaO layer thicknesses measured under 1 sun illumination (5 nm and 10 nm CaO) and in dark conditions (10 nm CaO). At each condition, the applied voltage is varied within the range of -1 to 1 V. Note here the small variation introduced by the bias voltage.

The total capacitance of the OPV device with 10 nm CaO layer under 1 sun illumination is 1 order of magnitude higher than the measurement carried out under dark conditions in all range of applied voltages (Figure 6.3.b). Interestingly, the low frequency capacitance reached appears not to be very sensitive to the bias voltage in both illumination conditions. This occurs because the external voltage is unable to modify the internal photogenerated V_F and mainly drops at the huge series resistance introduced by the oxide layer. The low frequency capacitance plateau is determined by the CaO layer thickness giving large values of C_{ox} for thin oxide layers (5 nm) under 1 sun illumination, as shown in Figure 6.3.b. This last finding helps us to identify C_{g} and C_{ox} as the limiting capacitances at low (dark) and high illumination conditions.

6.3. Transmission Line Model

A general model accounting for the different impedance responses valid for both blocked and working OPV devices is desired as this can provide quantitative information on the different physical processes taking place in an operating cell. In order to obtain that model, a series of separated mechanisms need to be considered: (i) C_{g} is observed under some experimental conditions (at low voltage for the working OPV solar cell in Figure 6.2.b). (ii) Blocking effect is clearly visible for blocking contacts (CaO) in Figure 6.2.a. This implies an *RC* parallel subcircuit connected in series $R_{\mathrm{co}}C_{\mathrm{co}}$ that must comprises large resistances in the case of oxide layers $R_{\mathrm{co}} = R_{\mathrm{ox}}$, but much smaller for extracting contacts (R_{co}). (iii) For Ca contacts (working devices), the recombination subcircuit is clearly distinguishable $R_{\mathrm{rec}}C_{\mu}$ (see Figure 6.2.a). And finally (iv) diffusion patterns are dominant at high frequency part of the spectra, more evident in the case of blocked devices as a Warburg response and only at high applied biases for the working OPV devices (see Figure 6.2.b) under 1 sun illumination. Integration of points (iii) and (iv) electrical mechanisms relies on regarding equivalent circuits comprising distributed elements, which are usually drawn in terms of transmission line models. This type of impedance pattern belongs to response usually encountered in systems in which carrier transport is determined by coupled diffusion-recombination.[21] Minority carriers (electrons) are able to diffuse within extended bulk neutral regions eventually reaching the electrodes which act as selective contacts. The well-known transmission line model is able to represent such diffusion and recombination impedance response.[21,24] This model has been integrated in standard software to fit the impedance spectra and obtain straightforward the model parameters. The impedance model showed in Scheme 6.3 consists of an equivalent circuit which comprises:

- Distributed transport resistance $r_{\mathrm{t}} = R_{\mathrm{t}}/L$ (being L the active layer thickness), standing for the electron transport. r_{t} is the reciprocal of the electron conductivity σ_{n},
- Distributed chemical capacitance $c_{\mu} = C_{\mu}L$,
- Distributed recombination resistance $r_{\mathrm{rec}} = R_{\mathrm{rec}}/L$ accounting for the electron recombination resistance,
- Series resistance R_{s} in series to the transmission line in order to model contact and wire effects,
- The electrical effect of the cathode contact is modeled by means of $R_{\mathrm{co}}C_{\mathrm{co}}$ parallel subcircuit connected in series with the electron channel, and
- Finally, a capacitor $C_{\mathrm{g}} = \varepsilon\varepsilon_0 A/L$ represents dielectric, geometrical capacitance of the bulk active layer of thickness L and area A.

The equivalent circuit in Scheme 6.3 incorporates the basic phenomenology reported on the impedance response of blocked and working devices as explained previously. Additional assumptions incorporated in the model should be also mentioned: the ohmic character of the anode contact, and the absence of frequency-dispersion in modeling transport properties.

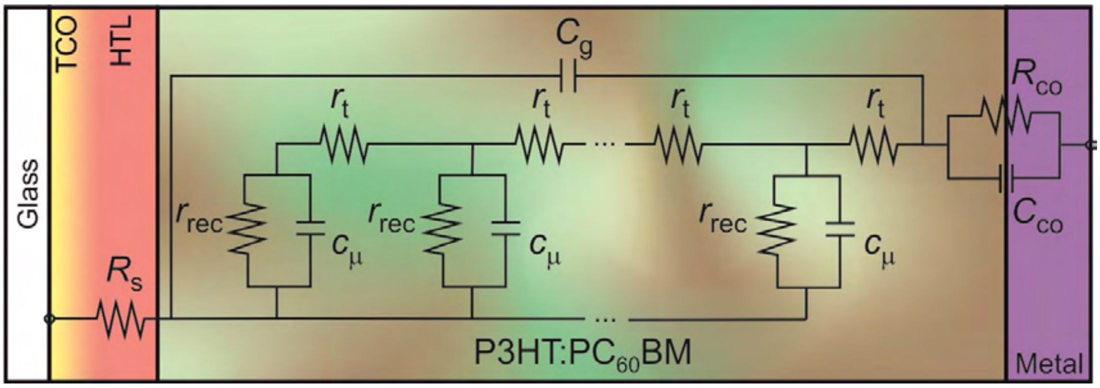

Scheme 6.3. This equivalent circuit model includes a transmission line which is compromising by a circuit distributed elements related to electron transport r_t, recombination r_{rec}, and chemical capacitance c_μ. In parallel to the transmission line a geometrical capacitance C_g is included. In addition, series resistance R_s and contact electrical response $R_{co}R_{co}$ is also added.

The impedance model described contains two characteristic times related to the electron diffusion (transit time),

$$\tau_{diff} = R_t C_\mu \tag{6.1}$$

and the effective lifetime,

$$\tau_{rec} = R_{rec} C_\mu \tag{6.2}$$

respectively.[13] It is assumed that distributed (differential) circuit elements are position-independent as expected for cells in which recombination is not severe, *e.g.*, $\tau_{diff} \le \tau_{rec}$ (or $R_t \le R_{rec}$). For highly recombining devices ($\tau_{diff} > \tau_{rec}$ or $R_t > R_{rec}$) deviations from the Warburg response at high frequencies are usually observed.[24]

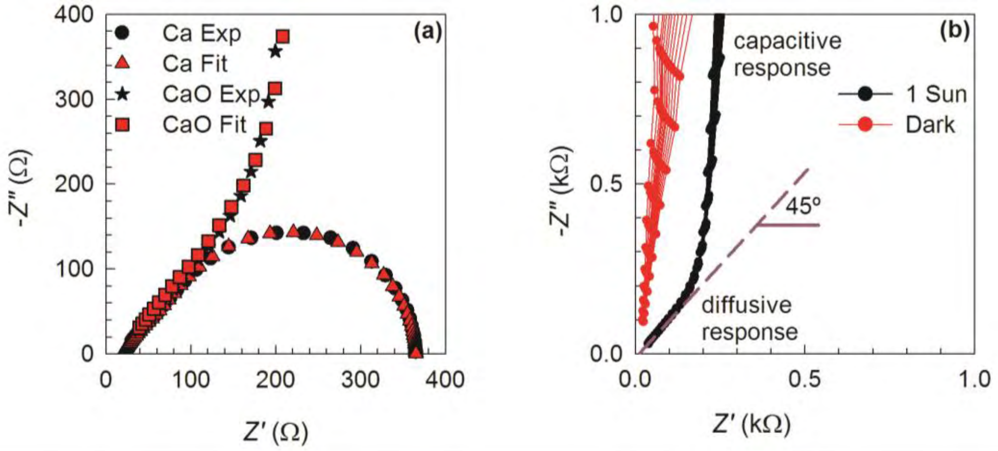

Figure 6.4. (a) Comparison between experimental data and fitting of the impedance response measured under 1 sun illumination at high frequencies part of the spectra for blocked (10 nm CaO/Ca) and operating devices (Ca) at 0.5 V applied voltage. The fit data were obtained from the equivalent circuit model showed in Scheme 6.3. Parameter errors are always below 5 %. (b) Impedance response at high frequency part of the spectra for the block solar cells under 1 sun illumination and dark conditions in all range of voltages.

The comparison between experimental data and fitting results using the previous equivalent circuit model (Scheme 6.3) shows a good agreement as observed in Figure 6.4.a. For instance, the solar cells blocked under illumination shows two visible features that are well supported by the equivalent circuit: the diffusion pattern (Warburg response) at high frequencies appears as a consequence of the transport R_t and the charge storage C_μ coupling. It is important to note that this diffusion fingerprint observed under 1 sun illumination disappears under dark conditions, being more important the capacitance contributions at high frequency part (see Figure 6.4.b). The low frequency part is dominated by the contact subcircuit $R_{co}C_{co}$, which in this case draws a large arc due to the large blocking resistor $R_{co} = R_{ox}$. In the case of working devices, the electron blocking effect is not viewed because R_{co} is very small, so the low frequency response becomes governed through recombination mechanisms modeled by coupling of the parameters R_{rec} and C_μ. It is worth noting that only close to V_{oc} biases (0.5 V as illustrated in Figure 6.4.a), the diffusion pattern is clearly recovered. However, at low voltages (see Figure 6.2.b), the high frequency response turns to be dominated by the C_g.

6.4. Analysis of fitting parameters

From the equivalent circuit model showed in Scheme 6.3, the IS parameters can be extracted for the working (Figure 6.5.a and Figure 6.5.c) and blocking (Figure 6.5.b and Figure 6.5.d) OPV solar cells under simulated 1 sun illumination in a range of frequencies (from 1 MHz to 100 Hz) and voltages (from 0 to close V_{oc} voltages).

Four types of resistances are distinguished at different range of frequencies for working and blocked OPV devices in Figure 6.5.a and Figure 6.5.b, respectively. In particular, two different kind of series resistance have been identified. One related to the transport processes in conductive materials being the R_s which varies poorly between 1–3 Ω cm^2 for both devices. This electrical response is related to conductive ITO and the ohmic contact from the PEDOT:PSS layer. A second resistance associated with the charge transfer events at the outer interfaces between the active layer and the contacts R_{co}. This parameter drastically changes depending on the electron extractive contact with differences of some orders of magnitude. For working devices, R_{co} exceeds R_s by more than 1 order of magnitude at low voltages, but at forward bias near V_{oc} both resistors contribute similarly to the total series resistance. The overall series resistance $R_s + R_{co}$ is referred to the conduction processes connected in series with the internal photovoltaic effect. On the contrary, the total series resistance is very pronounced for the CaO-based device. The voltage drop at short-circuit conditions calculated as $j_{sc}R_{co}$ amounts ~500 mV, being a value that approaches to the V_{oc}. This effect can be interpreted by considering that upon light, the exposure blocked cells are able to store similar photogenerated charge carrier densities regardless of the applied voltage, as this is mainly absorbed within the oxide layer. In open-circuit conditions, the voltage drop in series vanishes in such a way that a measurable photovoltage appears as $V_{oc} = V_F$, being V_F Fermi Level splitting . The opposite device operation is encountered for extracting contacts: since the total series resistance is low, the applied voltage establishes the internal V_F. It has recently observed that P3HT-based solar cells operate under the electronic reciprocity relationship.[25] Under this principle, the voltage V_F fixes the local charge density, and the solar cell operation is viewed as a balance between voltage-independent photocurrent and illumination-independent recombination current (Figure 6.5.b).[9]

R_{rec} follows the expected behavior for the standard OPV device (Figure 6.5.a) decreasing toward forward voltage due to the enhancement of the recombination current as is shown in the equation 5.6. A detailed analysis of the recombination process from R_{rec} has recently been reported.[26] Regarding transport (diffusive) resistance, R_{t} also describes a reduction at forward bias because of the increment in carrier density, as explained later. These resistive circuit elements for working OPV devices are observed the unequal $R_{\mathrm{t}} \leq R_{\mathrm{rec}}$ from 0 V to close V_{OC} (Figure 6.5.a). This entails that the performance of these cells is not limited by the transport of photogenerated carriers, at least for the active layer thickness used here (~100 nm). However, at voltages approaching to V_{OC}, the resistances act similarly $R_{\mathrm{t}} \approx R_{\mathrm{rec}}$, which suggests that thicker active layer films would suffer from deficient charge collection as expected for highly recombining cells ($R_{\mathrm{t}} > R_{\mathrm{rec}}$). Conversely, R_{rec} and R_{t} parameters exhibit rather voltage-independent response for blocked cells. Such values correspond to those encountered with working cells at $V_{\mathrm{app}} \approx 500\,\mathrm{mV}$, again indicating the state of charge reached under illumination using blocking oxide layers.

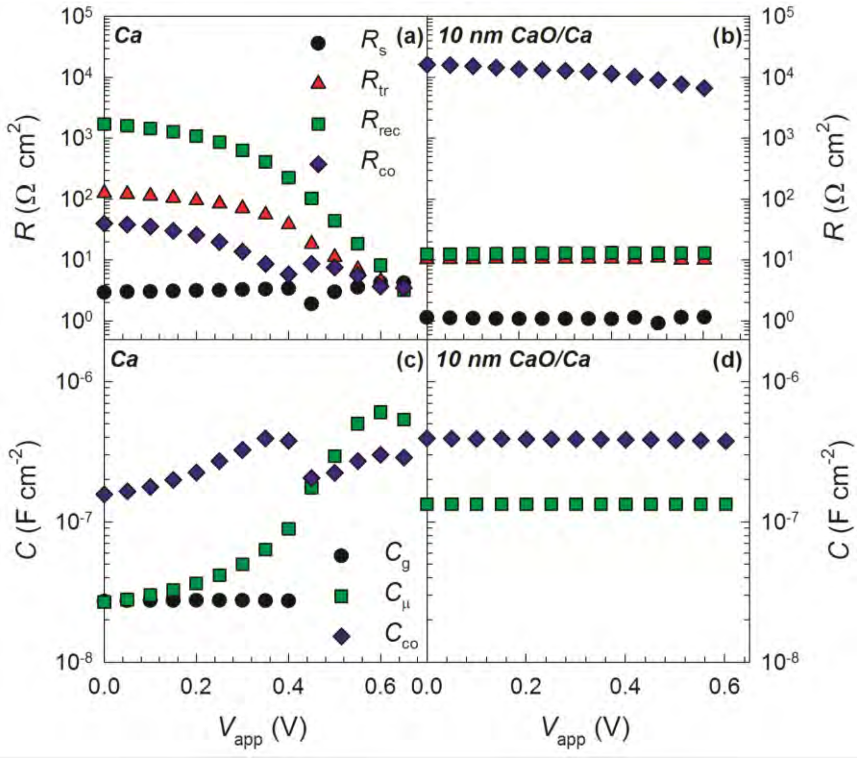

Figure 6.5. IS results extracted from fitting the equivalent circuit model in Scheme 6.3 to impedance spectra (Figure 6.2.a) of a P3HT:PC$_{60}$BM-based device using extracting contacts with Ca: resistance (a) and capacitance (c), and a device blocked with 10 nm of CaO: resistance (b) and capacitance (d). Error bars (<5 %) are omitted because smaller than the dot size.

The capacitances behavior were extracted from the equivalent circuit model showed in Scheme 6.3 under simulated 1 sun illumination for P3HT:PC$_{60}$BM-based with working and blocking cathodes OPV devices. These capacitances are summarized in Figure 6.5.c and Figure 6.5.d for Ca and 10 nm CaO/Ca ETL solar cells, respectively. A quick glance, three different capacitances can be distinguished to the excellent electron extraction cells such as C_{g}, C_{μ} and surprisingly C_{co}. The constant C_{g} ($2.7\times10^{-8}\ \mathrm{F\,cm^{-2}}$) is observed at high frequency part of the IS spectra at low forward bias region as commented upon before in Figure 6.2.c. The C_{μ} exhibits the expected increase as fullerene states are occupied toward forward bias. Interpretation of C_{μ} in terms of the electron density-of-states DOS has been discussed extensively in previous papers.[16] The C_{co} is observed within the same order of magnitude than C_{μ} for working OPV devices at low frequency regime in Figure 6.2.c as is illustrated in Figure 6.5.c. Such capacitance might be originated by dielectric mechanisms occurring at the bulk/metal interface as those proposed in Chapter 7 analyzing the cathode equilibration.[27] The polymer molecules attached to the metal surface cathode show a shift and a broadening of their molecular energy levels as long as the chemical interactions between them are not negligible. These attached molecules are characterized by an energy distribution which has a specific interfacial density-of-states IDOS. That IDOS is different from that encountered in the bulk of the organic layer (DOS). The fullerene molecules close to the metal contact are reduced and formed a dipole layer with an accumulated charge that follows the IDOS, g_{is}. Here, it is assumed that the IDOS directly equilibrates with the Fermi Level of the contacting metal, and therefore, the equation $C_{\mathrm{co}} = q g_{\mathrm{is}}$ is derived straightforwardly. Using the extracted value of $C_{\mathrm{co}} \approx 3.3\times10^{-7}\ \mathrm{F\,cm^{-2}}$, a surface state density $g_{\mathrm{is}} \approx 3\times10^{12}\ \mathrm{cm^{-2}\ eV^{-1}}$ is encountered. Comparing this result with others g_{is} calculated by more authors using alternative methods, the IDOS values are in the range of $10^{12} - 10^{14}\ \mathrm{cm^{-2}\ eV^{-1}}$.[28]

Regarding the capacitances observed for the blocking devices are summarized in C_{μ} and C_{co}. It is interesting to note here that C_{μ} shows a voltage-independent value for blocked cells which approximately corresponds to the chemical capacitance found for working cells at $V_{\mathrm{app}} \approx 500\,\mathrm{mV}$. As indicated above in the resistances explanation for blocked cells, a certain degree of photogenerated charge storage is observed which is responsible for the measured output voltage V_{oc} in these kinds of devices. Besides, it is considered that $C_{\mathrm{co}} = C_{\mathrm{ox}}$ as the response scale with the oxide layer thickness. A value for the dielectric contact of CaO is calculated to be $\varepsilon = 4.2 \pm 0.2$ from the equation $C_{\mathrm{ox}} = \varepsilon\varepsilon_0 A/L$, in good agreement with reported values for this oxide.[29,30]

Additionally, the electron diffusivity D_{n} can be calculated by recalling equation 6.1 through the relationship

$$D_{\mathrm{n}} = \frac{L^2}{\tau_{\mathrm{diff}}} \tag{6.3}$$

where $L \approx 100\,\mathrm{nm}$ corresponds to the total thickness of the active layer (diffusion zone). Figure 6.6 shows the diffusion coefficient D_{n} calculated from the equation 6.3 for the working and 10 nm thick CaO blocking OPV devices.

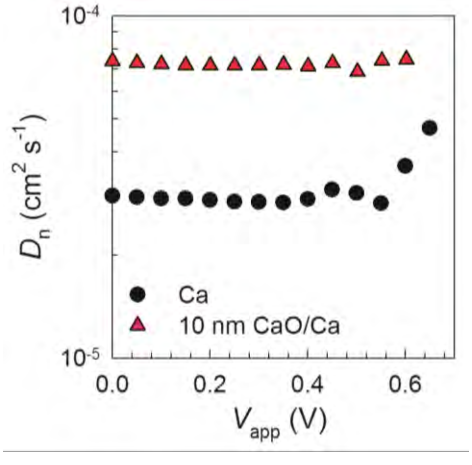

Figure 6.6. Diffusion coefficient D_{n} extracted from the equation 6.3 for OPV devices worked (Ca) and blocked (10 nm CaO/Ca) electron collection. 10 % variation of layer thickness allows explaining differences in values extracted from different cells.

The constant D_n result ($\sim 2.9\times10^{-5}$ cm^2 s^{-1}) for the good electron extraction cells has a slightly increase for voltages approaching V_oc . An identical behavior had been found for other polythiophene derivatives in an electrochemical transistor setup.[31] The small differences in the D_n results for both devices showed in Figure 6.6 can be readily assigned to experimental errors related to the active layer thickness L.

Although the electron statistics depart from dilute concentration conditions (Boltzmann approximation), an estimation of electron mobility might be calculated by using the Nerst–Einstein relationship as

$$\mu_\mathrm{n} = \frac{qD_\mathrm{n}}{k_\mathrm{B}T} \qquad (6.4)$$

being $k_\mathrm{B}T$ the thermal energy.[31] Then, the electron mobility extracted from the IS fitting analysis is approximately 2×10^{-3} cm^2 V^{-1} s^{-1}. This value is in good agreement with that derived using PCBM electron-only devices from $j-V$ measurements, for which current is considered space-charge limited, and hence electrical field-driven rather than diffusion determined.[32]

6.5. Quasi-neutral region within active layer bulk

From the analysis of the impedance spectra, these OPV devices clearly show extended quasi-neutral regions that dominate the device operation for a significant range of applied voltages. This voltage range appears in excess of flat-band voltage established by the collapse of the depletion region formed in the vicinity of the cathode contact.[22] A general band diagram of a standard OPV solar cell is represented in Scheme 6.4.a and Scheme 6.4.b under dark conditions at large forward applied biases and short-circuit conditions, respectively. The band diagram that corresponds to an OPV device with an insulator CaO interlayer to block the electron extraction solar cells is represented in Scheme 6.4.c and Scheme 6.4.d under illumination at open-circuit and short-circuit conditions, respectively.

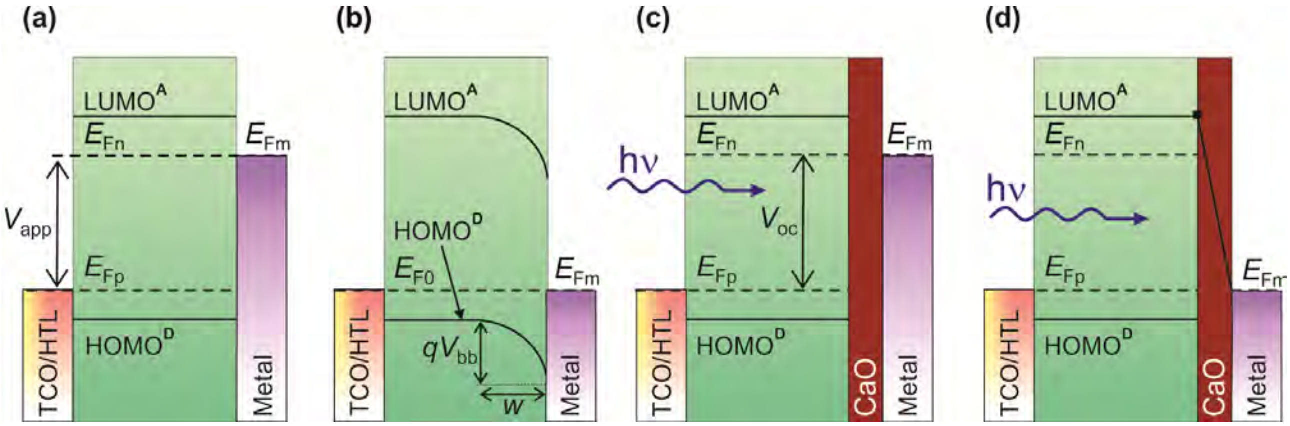

Scheme 6.4. Band diagram for working device with collecting Ca cathode contact under dark (a) at large forward applied voltage and (b) short-circuit conditions. The applied voltage generates the splitting of the Fermi Levels, which align with the contacts producing flat-band conditions (a). In (b), band bending is formed due to the cathode Schottky contact. Band diagram for the OPV solar cells with CaO blocking contacts under illumination at (c) open-circuit and (d) short-circuit conditions. The photogeneration creates a photovoltage (V_oc) by alignment of the respective Fermi Levels (c). A large voltage drops is confined within the oxide layer (CaO) that compensates the photovoltage (d).

In open-circuit conditions, the internal voltage V_F arising from the splitting of the Fermi Levels is fully determined by either the applied voltage or the irradiation intensity (as stated by electronic reciprocity principle) only in the case of good extracting contacts. For blocked devices, light and applied voltages are completely decoupled so that only illumination is able to promote electrons into the fullerene acceptor states yielding measureable values for V_F. This last fact occurs because the Ca cathode metal work function is in intimate contact with the electron Fermi Level within the active layer bulk. The enormous resistance associated to the oxide layer absorbs the applied voltage impeding the Fermi Level rise. When the devices are forced to operate in short-circuit conditions, the impedance of blocked cells does not change significantly since the internal photogenerated charge density keeps the values reached in open-circuit (voltage-independent response) as illustrated in Scheme 6.4.d. It is highlighted that blocking devices can be viewed as operating in flat-band conditions. On the contrary, working cells under short-circuit conditions exhibits some kind of band bending because of the presence of cathode depletion zones as illustrated in Scheme 6.4.b.

The clarification of the presence or absence of extended quasi-neutral regions within the active layer bulk is a central point prior to establish the basics of device physics for organic BHJ solar cells. If quasi-electroneutrality is invoked, then even in the case of current flow space charge regions related to excess carriers cannot be built up, and the analytical treatment of the mathematical system describing the solar device is considerably simplified. The quasi-neutral region depends mainly on two different times processes: carrier lifetime (recombination time), τ_{rec}, and dielectric relaxation time, τ_{die}. The recombination time τ_{rec} is calculated from the equation 6.2 where the R_{rec} and C_{μ} data are extracted in the Figure 6.5.a and Figure 6.5.c, respectively. The dielectric relaxation time is related to the material permittivity $\varepsilon\varepsilon_0$ (ε being the dielectric constant, and ε_0 the vacuum permittivity), and its conductivity, σ, is as follows

$$\tau_{\mathrm{die}} = \frac{\varepsilon\varepsilon_0}{\sigma} \tag{6.5}$$

Therefore, depending on the physics governing of the device operation, two different regimes are possible whether *lifetime* semiconductor regime ($\tau_{\mathrm{rec}} > \tau_{\mathrm{die}}$) or *relaxation* semiconductor regime ($\tau_{\mathrm{rec}} < \tau_{\mathrm{die}}$). The mobile carriers can exist long enough to neutralize charge in $\tau_{\mathrm{rec}} > \tau_{\mathrm{die}}$ operation and, the electroneutrality is not a justifiable assumption in $\tau_{\mathrm{rec}} < \tau_{\mathrm{die}}$ operation. It is assumed that the occurrence of quasi-neutral regions relies on the property that carrier lifetime is much larger than the dielectric relaxation time, $\tau_{\mathrm{rec}} >> \tau_{\mathrm{die}}$. Hence regions of near-zero net local, the recombination processes may occur, implying spatially separated excess of electron and hole concentrations. This enhanced the space charge of dielectric relaxation-dependent decay.[33] For instance, low conductivity amorphous *p-i-n* silicon solar cells were modeled as developing photogenerated hole space charge regions near the *p* contact that concentrate the voltage drop.[34] In the extreme case, currents should be space charge limited as occurring in OLEDs based on low mobility polymers or molecules.[35]

In order to clarify the solar cell operation within the *relaxation* ($\tau_{\mathrm{rec}} < \tau_{\mathrm{die}}$) or *lifetime* ($\tau_{\mathrm{rec}} > \tau_{\mathrm{die}}$) regime, the polymer conductivity σ plays a crucial role, as derived from equation 6.5. The conductivity for a polymer can be calculated by the equation $\sigma = q\mu_{\mathrm{h}}N$ where q is the electron carrier, μ_{h} is the hole mobility, and N is the hole density carrier. For instance, these parameters are published for the archetypical P3HT polymer. The μ_{h} in P3HT depends on different factors and it had been reported as ~10^{-4} cm^2 V^{-1} s^{-1} and the charge carrier concentration N were the order of ~10^{16} cm^{-3}.[6,36] This polymer and many other polymers contain native carriers due to doping, normally of *p*-type. Using the conductivity relationship and a typical permittivity values for this compound (~$3\varepsilon_0$), a value of relaxation time $\tau_{\mathrm{die}} \le 1\,\mu\mathrm{s}$ is obtained. In addition, using different methods to measure experimentally the recombination time approaching V_{oc} at simulated 1 sun irradiation intensity is the order of $\tau_{\mathrm{rec}} \approx 10\,\mu\mathrm{s}$.[37-39] Therefore, a device will be operating in *lifetime* or *relaxation* regime depending on the materials properties. It has suggested that the depletion region built up in the vicinity of the cathode contact collapses at forward bias, giving rise to extended quasi-neutral regions in OPV device.[22,40] Depletion region modulation (spatially confined band bending) by the applied voltage has been identified using alternative methods.[41,42] Since the depletion zone is reduced or even eliminated at operation voltages close to the maximum power point (flat-band voltage lies in the range of 0.4 V in most cases), there remains the neutral region in which transport of minority carrier should be controlled by diffusion[43] while the high conductivity of majority carriers (holes) assures a rapid shielding. So far, however, observation of the diffusive transport that is clearly predicted by this device model has been elusive due to other experimental aspects that interfere with the diffusion signatures.

Here, the relaxation time τ_{die} is measured by looking the first decay characteristic time of light-induced current transient (Figure 6.7)[39] to corroborate the *lifetime* semiconductor regime as observed previously for the P3HT polymer which implies $\tau_{\mathrm{rec}} > \tau_{\mathrm{die}}$.

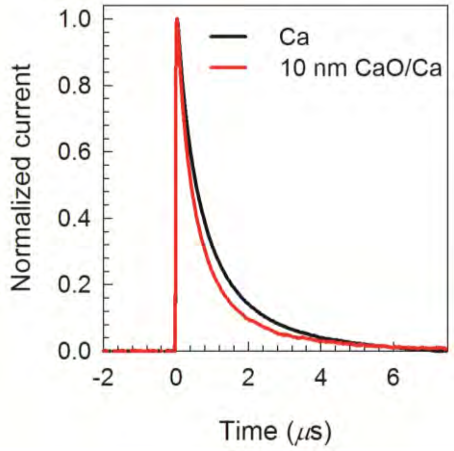

Figure 6.7. Normalized transient photocurrent of P3HT:PC$_{60}$BM photoactive layer with working or blocking electron extraction cathode electrode. The first rapid decay is related to the dielectric relaxation time, which is observed to be within the range of 0.6–0.7 μs.

The observation of diffusion of minority carrier (electrons) through extended neutral regions within the active layer bulk relies on the occurrence of the *lifetime* semiconductor regime. The τ_{rec} is calculated by equation 6.2 giving a result $\tau_{\mathrm{rec}} > 3\,\mu\mathrm{s}$ from the R_{rec} and C_{μ} data extracted in the Figure 6.5.a and Figure 6.5.c, respectively. This is the maximum value that is reached at $V_{\mathrm{app}} \approx V_{\mathrm{oc}}$. A direct determination of the relaxation time results from the exponential response time of current transient presented in Figure 6.7 for both solar cells with either Ca or CaO ETLs. The τ_{die} is systematically measured ($\tau_{\mathrm{die}} \approx 0.65\,\mu\mathrm{s}$) and this result agrees with the estimation proposed previously, the P3HT:PC$_{60}$BM blends operate within the *lifetime* semiconductor regime.

Similar to the distinction between *lifetime* and *relaxation* regimes in terms of the time response can be found using characteristic length scales points to the same underlying physics. The electron length, l_{D}, is defined as an average distance in which mobile carriers can diffuse before recombination, and is related to the D_{n} in equation 6.3 as follows

$$l_{\mathrm{D}} = \sqrt{D_{\mathrm{n}}\tau_{\mathrm{rec}}} \tag{6.6}$$

Semiconductor materials that are heavily doped have high recombination rates and consequently, have short l_{D}. On the contrary, large l_{D} are indicative of longer lifetimes, and therefore, this parameter is an important quality to consider in semiconductor materials.

In the time scale of dielectric relaxation, the characteristic length scale corresponds to the Debye screening length, λ_{D}, that represents the distance in which local electrical fields are confined. From the expression 6.7 can be demonstrated the relation between λ_{D} and τ_{die} as

$$\lambda_{\mathrm{D}} = \sqrt{D_{\mathrm{n}}\tau_{\mathrm{die}}} \tag{6.7}$$

Thus, the occurrence of the lifetime regime as $l_{\mathrm{D}} > \lambda_{\mathrm{D}}$ in terms of a length scale comparison can be formulated. In the case of the analyzed cells values of $\lambda_{\mathrm{D}} \approx 50\,\mathrm{nm}$ are obtained, whereas l_{D} ranges from ~250 nm for low forward voltages down to ~100 nm at $V_{\mathrm{app}} \approx V_{\mathrm{oc}}$. It is then deduced that at high voltages, l_{D} is comparable to the active layer thickness. The working OPV devices analyzed are then in the limit to be considered as these cells have high charge recombination rate due to $L >> l_{\mathrm{D}}$. This last observation explains why thicker films usually exhibit poor performance as bulk transport losses occur before charge collection take place at the contacts. Our analysis offers a straightforward method for complete device performance evaluation.

6.6. Characterization of OPV devices with traps localized in polymer:fullerene blend photoactive layer

Other way to observe bulk transport in a photoactive layer relies on the use of the bis-indene adduct ICBA as an acceptor molecule characterized by having lower LUMO level than that of PCBM and using this second acceptor as a trap, keeping the same donor material, P3HT.

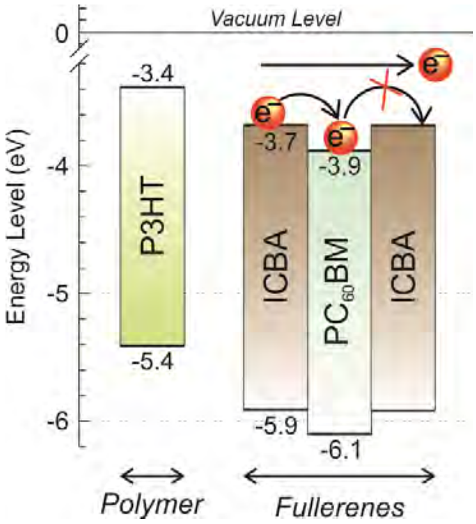

Scheme 6.5. Energy Level diagram of the active layer composed by a donor polymer material (P3HT) and an acceptor fullerene material (ICBA) incorporating small amounts of $PC_{60}BM$ material acting such as trapping sites where electrons are recollected and no-extracted as is shown in the red cross. The electron extraction is effective when the blend is composed only by P3HT:ICBA as is shown in the horizontal arrow.

A representative energy level diagram that shows HOMO and LUMO levels of donor and acceptor is illustrated in Scheme 6.5. From this energy diagram it is derived that $PC_{60}BM$ molecules could act as traps located when a small amount is incorporated into the P3HT:ICBA blend, presumably altering the transport properties of electron carriers. It cannot be discarded that $PC_{60}BM$ incorporation modifies the fullerene energetic landscape.

The architecture of these OPV devices was glass/ITO/PEDOT:PSS/active layer/Ca/Ag. In order to test the $PC_{60}BM$ traps concentration into the P3HT:ICBA photoactive layer, a control concentration of $PC_{60}BM$ (0.1 and 1 %) is added to the active layer, and those cells are compared with 0 % $PC_{60}BM$ in the P3HT:ICBA active layer device. Solar cells were prepared as described in the experimental section in Chapter 3 and more specific details are explained in Appendix II.[14] These OPV devices with different blend compositions have been tested by $j-V$ under simulated 1 sun irradiation (1000 W m^{-2}), absorption spectroscopy and *EQE* (Figure 6.8). The photovoltaic parameters are summarized in Table 6.2. Additionally, the IS technique is also employed under simulated AM1.5G illumination intensity.

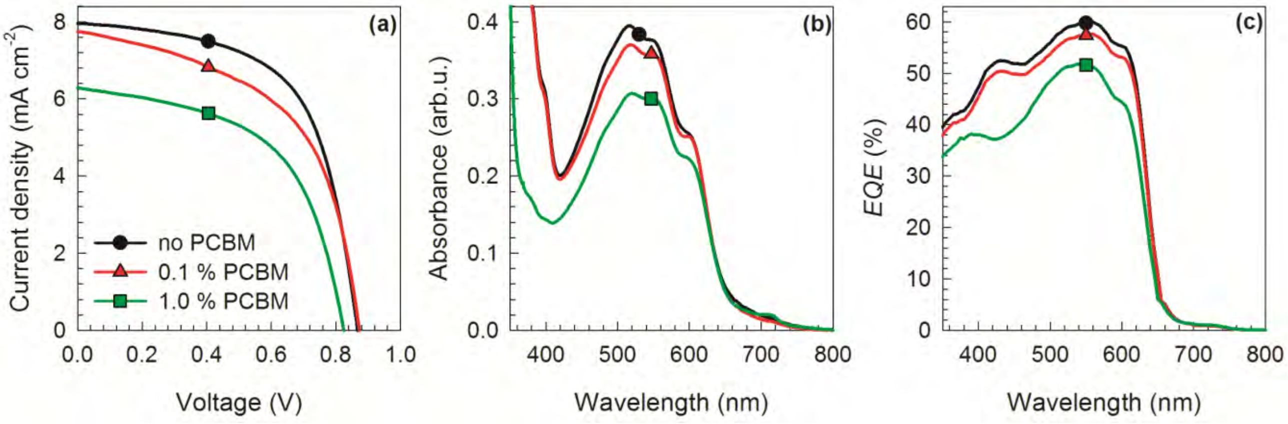

Figure 6.8. $j-V$ curves under simulated 1 sun irradiation (1000 W m^{-2}) (a), UV-Vis spectra (b), and *EQE* spectra (c) for the standard P3HT:ICBA-based device and other standard photovoltaic devices with P3HT:$PC_{60}BM$ blend adding traps with $PC_{60}BM$ (0.1 % and 1 %). The metal cathode contact used was Ca/Ag.

Figure 6.8.a shows typical $j-V$ curves where the increment of the $PC_{60}BM$ percentage into the blend P3HT:ICBA clearly shows a decrease in the j_{SC}. For small amount of $PC_{60}BM$ (0.1 %) in the active layer, the reduction in j_{SC} is only of 5 %, while $PC_{60}BM$ large amounts (1 %) induce 28 % photocurrent losses. This large reduction in j_{SC} might be related to lower light absorption caused by the use of less optimized blend morphology when $PC_{60}BM$ molecules are included, as it is observed in the UV-Vis spectra of the films in Figure 6.8.b. The absorption of the P3HT shoulder at ~600 nm drops around 10 % for $PC_{60}BM$ content from 0 to 1 %.[44] However, *EQE* spectra showed in Figure 6.8.c do not follow the absorption spectra profile, which peaks are encountered around 520 nm. Instead it shows a rather flat shape between 450 and 600 nm. For 1 % of $PC_{60}BM$ content, the decrease in *EQE* is about 20 % with respect to P3HT:ICBA-based cells. The charge collection probability represented by *EQE* exhibits larger reduction in comparison to that expected from absorption spectra. This entails that the sole decrease in absorption is not able to explain the large j_{SC} losses reported in Figure 6.8.a which should be then related with mechanisms occurring after light illumination.

Table 6.2. Photovoltaic parameters to P3HT:ICBA devices with two different cathodes (Ca/Ag and LiF/Al) and changing the concentration of the traps doping level into the photoactive layer with the addition of $PC_{60}BM$.

Cathode	**% PCBM**	j_{sc} (mA cm^{-2})	V_{oc} (mV)	***FF*** (%)	**PCE** (%)
Ca/Ag	0	8.0	872	60	4.2
Ca/Ag	0.1	7.7	877	54	3.7
Ca/Ag	1	5.7	805	54	2.9
LiF/Al	0	6.2	735	59	2.7
LiF/Al	0.1	5.9	681	47	1.9
LiF/Al	1	3.4	662	55	1.2

As regards IS measurement, the Nyquist plot $(Z'-Z'')$ observed in Figure 6.9.a for the OPV devices with different photoactive layer compositions comprise two visually distinguishable parts. At low frequencies, a large semicircle is observed and this arc represents a *RC* subcircuit. As explained in previous works this part is related to the C_μ (connected to carrier storage) and R_{rec} (derivative of the carrier recombination flux) response.[18,45,46] At high frequencies, an additional semicircle *RC* is clearly distinguishable in Figure 6.9.a at larger forward voltages $(0.7-0.8$ V$)$ for these OPV devices with different bulk composition. These IS parameters are attributed to the R_t and the C_g exclusive of the photoactive layer.

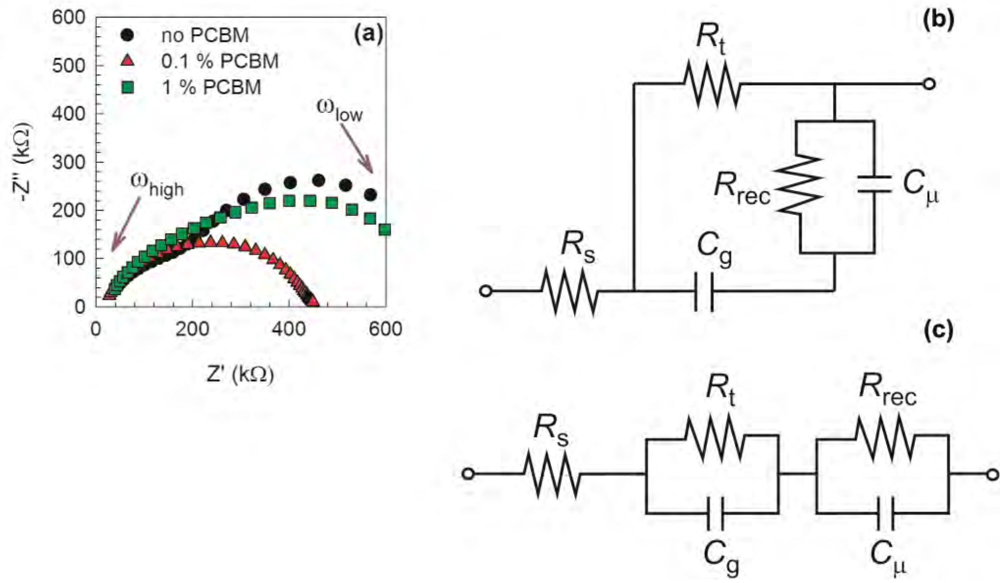

Figure 6.9. (a) Nyquist plot at 700 mV for the OPV devices with structure glass/ITO/PEDOT:PSS/active layer/Ca/Ag under simulated 1 sun illumination intensity (1000 W m^{-2}). The active layers studied here are P3HT:ICBA, P3HT:ICBA+0.1 % $PC_{60}BM$, and P3HT:ICBA+1 % $PC_{60}BM$. (b) Simple equivalent circuit model used to the fit of the impedance data. This model consists in a resistance r_t in series with a *RC* in parallel. (c) Other possible equivalent circuit model which consists in two *RC* subcircuits in series.

It is important to highlight that the Nyquist plot observed in Figure 6.9.a is not observed a clear transmission line at high frequency part as in the cases of P3HT:$PC_{60}BM$ working (cathode was Ca/Ag) and blocking (cathode was CaO/Ca/Ag) OPV devices showed in Figure 6.4. There are several reasons to explain these two different shapes in the $Z'-Z''$ plot. Several theoretical studies are focused in the electron diffusion length (l_D) where at higher recombination rate (low l_D) a distorted semicircle appears at high frequencies.[24] Some previous reports explained that depending on the processing experimental conditions, the morphology along the active layer might be change[47,48] forming different concentration domain of polymer or fullerene along the blend film. These modifications through the active layer cause changes in the conductivity in different sites in the film. Other important point is the possible carrier trapping into the polymer which could affect to the shape of the impedance spectra. However, it is considered that the active layer is homogenous along the total thickness after processing and electrical measurements. Therefore, the IS parameters (R_t, R_{rec} and C_μ) are fitted correctly using the transmission line model. This model assumes invariable IS parameters forward the total active layer thickness. However, as it has been shown in Chapter 7 for several polymer:fullerene systems, the fullerene phase can be located close to the cathode contact. Particularly, the P3HT:ICBA blend could be analyzed deeper to calculate fullerene concentration near the cathode and finally justify the formation of an additional arc at high frequencies showed in the Nyquist plot (Figure 6.9.a). Despite these reasons, this matter should be study deeper in the future to clarify either a second semicircle or transmission line at higher frequencies depending on the bulk active layer.

The IS parameters are extracted from the equivalent circuit model drawn in Figure 6.9.b and are summarized in Figure 6.10 as a function of applied voltage. This equivalent circuit model is similarly structured as the transmission line model (Scheme 6.3) but without finite diffusive R_t, R_{rec} and C_μ (Warburg response). An alternative equivalent circuit model is comprised by two *RC* subcircuits in series (Figure 6.9.c) which is also possible to fit two semicircles in the impedance spectra, but the fitting goodness is low.[14] The resistance extracted at low frequency part of the $Z'-Z''$ plot is represented in Figure 6.10.a. The R_{rec} behaves practically in the same way with small differences related to variation in layer thicknesses. This observation entails that the PC$_{60}$BM incorporation does not alter significantly recombination mechanisms. The C_μ of the 1 % PC$_{60}$BM-based device (Figure 6.10.b) is observed a negative voltage shift related to lower lying energy levels introduced by PC$_{60}$BM molecules after interaction with ICBA (Scheme 6.5).

Other important electronic processes are extracted at high frequency part of the impedance spectra (Figure 6.9.a). For instance, the overall impedance response includes a resistance connected in series $R_S \sim 2\ \Omega\ \mathrm{cm}^2$, being practically independent of the voltage. R_S can be attributed to ITO sheet and wires contributions. This general trend is always reproduced despite modifications introduced either blend composition or cathode contact. The cramped arc observed at high frequency part of the Nyquist plot (Figure 6.9.a) is attributed to $R_t - C_g$ contributions. To differentiate between contact contributions and bulk photoactive layer effects, two different cathodes (Ca/Ag and LiF/Al) in OPV solar cells are studied with the same blend composition in Figure 6.10.c and Figure 6.10.d which represent the R_t and C_g, respectively. The metal contact studies are highly interesting to corroborate that this *RC* semicircle is referred to transport-related resistance and singular capacitance from the bulk.

It is clearly observed that when PC$_{60}$BM trap molecules are not incorporated into the photoactive layer, the R_t exhibits low values (10–30 Ω cm^2) irrespective of the cathode contact used (Figure 6.10.c). If lower amounts of PC$_{60}$BM molecules are inserted (0.1 %), the R_t slightly decreases with the applied voltage because trapping effects are very limited. And, for larger PC$_{60}$BM concentration (1 %), the R_t response changes drastically for both cathode contacts. In this last case, the R_t decreases from ~100 Ω cm^2 at low voltages to 10 Ω cm^2 for voltages in excess of V_{oc}. This kind of behavior observed for the transport resistance R_t can be understood in terms of a trap-modulated conductivity mechanism. The LUMO of ICBA levels form a sort of transporting band, while $PC_{60}BM$ molecules behave as trapping sites for negative polarons (electrons) as schematically drown in Scheme 6.5.

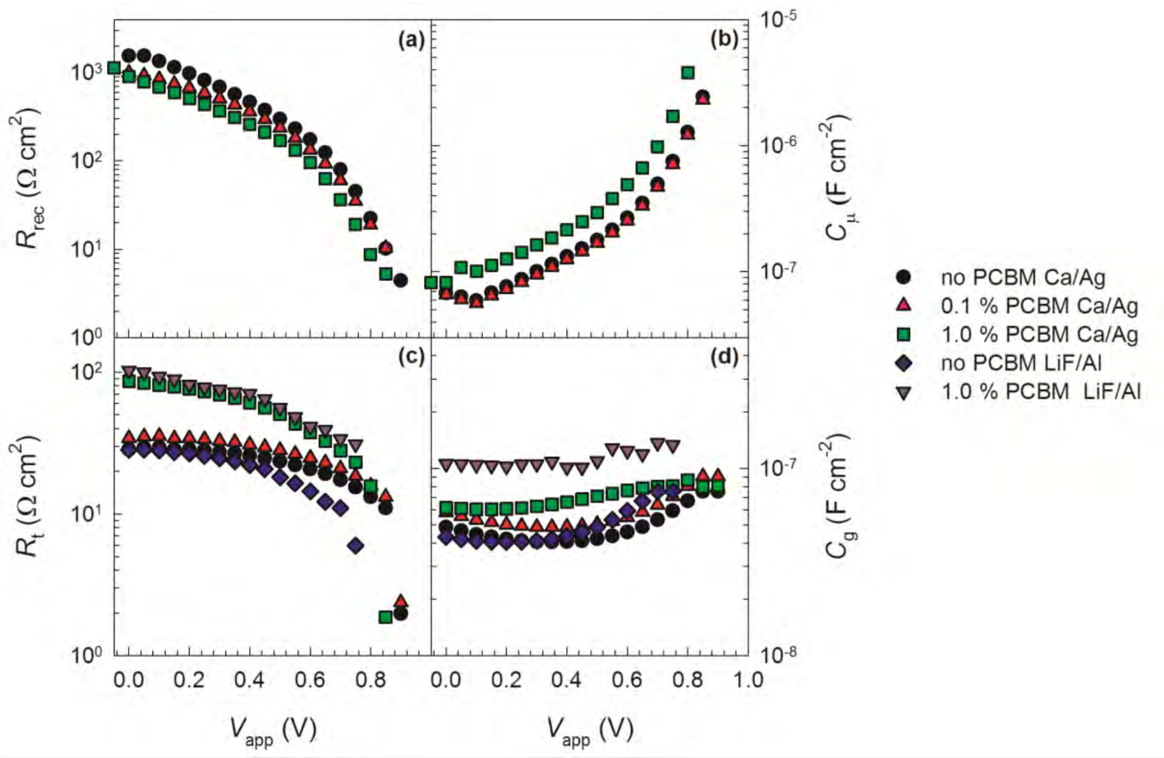

Figure 6.10. Impedance parameters (a) recombination resistance, R_{rec}, (b) chemical capacitance, C_{μ}, (c) bulk transport resistance, R_t, and (d) geometrical capacitance, C_g, extracted from the equivalent circuit model showed in Figure 6.9.b. These two last parameters are compared with two different cathode contacts: Ca/Ag and LiF/Al. Error bars calculated from fitting smaller than the dot size.

The applied voltage is also influenced on R_t by modifying the LUMO-acceptor level occupancy. At low applied bias, the $PC_{60}BM$ trap sites are not populated because of a deeper position of the E_{Fn}. Mobile electrons can then easily undergo trapping producing a decrease in the carrier conductivity. As the E_{Fn} rises following the increment in forward voltage, the $PC_{60}BM$ trap sites are eventually occupied losing their influence on R_t. Interestingly, the R_t exhibits values that are fullerene content-independent at large forward voltage as expected when trapping sites are no longer active. The above mentioned conduction mechanism is highly sensitive to the kinetics of trapping/release of trapped electrons at $PC_{60}BM$ molecules. While the inclusion of fast traps does not modify the carrier conductivity,[2] slow trapping would have large influence on the transport mechanisms producing conductivity changes. It is worth noting that similarity of R_t values at forward bias allows discarding morphology effects as originating R_t differences.

To discern between contact from bulk origins two different cathode contacts have been deposited, namely Ca/Ag and LiF/Al. It is observed in Figure 6.10.c that R_t behaves in a way that appears independent of the cathode contact used. For 1 % $PC_{60}BM$ fullerene content the same increment in R_t is experimentally found. It is worth noticing the poor performance of cells contacted with LiF/Al (see Table 6.2). This is presumably caused by interactions at the cathode interface that impede a proper charge extraction. Despite this evident limitation at the cathode interface, bulk transport properties exhibit similar behavior than that obtained for devices contacted with Ca/Ag. These experimental trends reinforce our previous idea pointing to transport rather than interface origin for the high frequency impedance response (Figure 6.9.a). However it cannot be completely excluded the possibility that anode interface or PEDOT:PSS layer contribute to R_t in the case of lower $PC_{60}BM$ content.

There are some distinctions in the R_t results when two OPV solar cells with identical polymer (P3HT) and different acceptor material ($PC_{60}BM$ and ICBA) with Ca/Ag as cathode contact are compared. The R_t of both devices has the same behavior with the applied voltage but the P3HT:$PC_{60}BM$ device is dramatically higher than the ICBA-based solar cell (Figure 6.10.c). The different acceptor material causes changes on the morphology of the blend which is directly reflected to the electron transport. In addition, the capacitive element C_g exhibits a rather constant value which is related to geometrical and dielectric mechanisms (Figure 6.10.d). This value depends only on the active layer composition. The C_g extracted is $2.7 \times 10^{-8}\ \mathrm{F\,cm^{-2}}$ and $4.9 \times 10^{-8}\ \mathrm{F\,cm^{-2}}$ for the P3HT:$PC_{60}BM$ and P3HT:ICBA OPV solar cells, respectively.

6.7. Conclusions

This chapter has provided a general impedance model in standard and other OPV devices with some modifications in the architecture or blend composition. The analytical impedance method presented is a tool that allows us to determine and separate different resistive contributions affecting the solar cell operation such as transport, recombination and contact. This work mainly focused on the transport properties observed in a complete and operation PSCs. In all cases, the transport effects are observed at high frequency part in the impedance spectra like transmission line or cramped semicircle. The Nyquist plot of the P3HT:PC$_{60}$BM-based solar cells show not only the transport properties of the electron extraction but also the contact effect even when the cathode is collected efficiently (Ca). Besides, the charge transport properties are clearly observed in the P3HT:PC$_{60}$BM OPV devices with the addition of oxide interlayer between active layer and metal cathode and a huge contact resistance from the insulator CaO film. The transmission line circuit accounting for these bulk processes is found to be valid regardless of the selected structure for the cathode contact (Ca or CaO/Ca). Additionally, other way to analyze the charge transport into the active layer could be by the insertion of small amounts of other material into the polymer:fullerene bulk which is characterized to have lower LUMO energy level than the polymer and fullerene LUMO’s. This located trap affect to modulate the electron conductivity showed in the impedance spectra like a small semicircle at low frequency part. IS appears as a powerful tool applicable to evaluate losing mechanisms in complete PSCs. It would be interesting to extend this analysis to other blend constituents in OPV cells, particularly different donor polymers, to fully evaluate its applicability.

6.8. References

1. N. S. Sariciftci, L. Smilowitz, A. J. Heeger and F. Wudl, *Science*, 1992, 258, 1474-1476.
2. J. Bisquert, *Phys. Chem. Chem. Phys.*, 2008, 10, 3175-3194.
3. B. Minaev, G. Baryshnikov and H. Agren, *Phys. Chem. Chem. Phys.*, 2014, 16, 1719-1758.
4. C. Liu, Y. Xu, G. Ghibaudo, X. B. Lu, T. Minari and Y. Y. Noh, *Appl. Phys. Lett.*, 2014, 104, 013301.
5. K. K. Liu, H. Y. Pang, J. R. Zhang, H. P. Huang, Q. Liu and Y. H. Chu, *RSC Adv.*, 2014, 4, 8415-8420.
6. K. K. H. Chan, S. W. Tsang, H. K. H. Lee, F. So and S. K. So, *J. Polym. Sci., Part B: Polym. Phys.*, 2013, 51, 649-658.
7. J. Peet, L. Wen, P. Byrne, S. Rodman, K. Forberich, Y. Shao, N. Drolet, R. Gaudiana, G. Dennler and D. Waller, *Appl. Phys. Lett.*, 2011, 98, 043301.
8. S. H. Park, A. Roy, S. Beaupre, S. Cho, N. Coates, J. S. Moon, D. Moses, M. Leclerc, K. Lee and A. J. Heeger, *Nat. Photon.*, 2009, 3, 297-303.
9. P. P. Boix, A. Guerrero, L. F. Marchesi, G. Garcia-Belmonte and J. Bisquert, *Adv. Energy Mater.*, 2011, 1, 1073-1078.
10. S. R. Cowan, N. Banerji, W. L. Leong and A. J. Heeger, *Adv. Funct. Mater.*, 2012, 22, 1116-1128.
11. D. Credgington and J. R. Durrant, *J. Phys. Chem. Lett.*, 2012, 3, 1465-1478.
12. G. Li, V. Shrotriya, J. S. Huang, Y. Yao, T. Moriarty, K. Emery and Y. Yang, *Nat. Mater.*, 2005, 4, 864-868.
13. T. Ripolles-Sanchis, A. Guerrero, J. Bisquert and G. Garcia-Belmonte, *J. Phys. Chem. C*, 2012, 116, 16925-16933.
14. A. Guerrero, T. Ripolles-Sanchis, P. P. Boix and G. Garcia-Belmonte, *Org. Electron.*, 2012, 13, 2326-2332.
15. M. Reyes-Reyes, K. Kim and D. L. Carroll, *Appl. Phys. Lett.*, 2005, 87, 083506.
16. F. Fabregat-Santiago, G. Garcia-Belmonte, I. Mora-Sero and J. Bisquert, *Phys. Chem. Chem. Phys.*, 2011, 13, 9083-9118.
17. G. Perrier, R. de Bettignies, S. Berson, N. Lemaitre and S. Guillerez, *Sol. Energy Mater. Sol. Cells*, 2012, 101, 210-216.
18. W. L. Leong, S. R. Cowan and A. J. Heeger, *Adv. Energy Mater.*, 2011, 1, 517-522.
19. B. J. Leever, C. A. Bailey, T. J. Marks, M. C. Hersam and M. F. Durstock, *Adv. Energy Mater.*, 2012, 2, 120-128.
20. Y. Zhang, X. D. Dang, C. Kim and T. Q. Nguyen, *Adv. Energy Mater.*, 2011, 1, 610-617.
21. J. Bisquert, *J. Phys. Chem. B*, 2002, 106, 325-333.
22. J. Bisquert and G. Garcia-Belmonte, *J. Phys. Chem. Lett.*, 2011, 2, 1950-1964.
23. J. Bisquert, *Phys. Chem. Chem. Phys.*, 2003, 5, 5360-5364.
24. A. Pitarch, G. Garcia-Belmonte, I. Mora-Sero and J. Bisquert, *Phys. Chem. Chem. Phys.*, 2004, 6, 2983-2988.

25. C. Donolato, *Appl. Phys. Lett.*, 1985, 46, 270-272.
26. A. Guerrero, L. F. Marchesi, P. P. Boix, J. Bisquert and G. Garcia-Belmonte, *J. Phys. Chem. Lett.*, 2012, 3, 1386-1392.
27. A. Guerrero, L. F. Marchesi, P. P. Boix, S. Ruiz-Raga, T. Ripolles-Sanchis, G. Garcia-Belmonte and J. Bisquert, *ACS Nano*, 2012, 6, 3453-3460.
28. M. A. Baldo and S. R. Forrest, *Phys. Rev. B*, 2001, 64, 085201.
29. R. C. Whited, C. J. Flaten and W. C. Walker, *Solid State Commun.*, 1973, 13, 1903-1905.
30. S. M. Rekhson and O. V. Mazurin, *J. Am. Ceram. Soc.*, 1974, 57, 327-328.
31. G. Garcia-Belmonte, J. Bisquert and G. S. Popkirov, *Appl. Phys. Lett.*, 2003, 83, 2178-2180.
32. V. D. Mihailetchi, J. K. J. van Duren, P. W. M. Blom, J. C. Hummelen, R. A. J. Janssen, J. M. Kroon, M. T. Rispens, W. J. H. Verhees and M. M. Wienk, *Adv. Funct. Mater.*, 2003, 13, 43-46.
33. W. van Roosbroeck and H. C. Casey, *Phys. Rev. B*, 1972, 5, 2154-2174.
34. E. A. Schiff, *Sol. Energy Mater. Sol. Cells*, 2003, 78, 567-595.
35. L. Bozano, S. A. Carter, J. C. Scott, G. G. Malliaras and P. J. Brock, *Appl. Phys. Lett.*, 1999, 74, 1132-1134.
36. C. R. Singh, G. Gupta, R. Lohwasser, S. Engmann, J. Balko, M. Thelakkat, T. Thurn-Albrecht and H. Hoppe, *J. Polym. Sci., Part B: Polym. Phys.*, 2013, 51, 943-951.
37. A. Maurano, R. Hamilton, C. G. Shuttle, A. M. Ballantyne, J. Nelson, B. O'Regan, W. M. Zhang, I. McCulloch, H. Azimi, M. Morana, C. J. Brabec and J. R. Durrant, *Adv. Mater.*, 2010, 22, 4987–4992.
38. G. Garcia-Belmonte, P. P. Boix, J. Bisquert, M. Sessolo and H. J. Bolink, *Sol. Energy Mater. Sol. Cells*, 2010, 94, 366-375.
39. A. J. Morfa, A. M. Nardes, S. E. Shaheen, N. Kopidakis and J. van de Lagemaat, *Adv. Funct. Mater.*, 2011, 21, 2580-2586.
40. G. Garcia-Belmonte, A. Munar, E. M. Barea, J. Bisquert, I. Ugarte and R. Pacios, *Org. Electron.*, 2008, 9, 847-851.
41. J. Lee, J. Kong, H. Kim, S. O. Kang and K. Lee, *Appl. Phys. Lett.*, 2011, 99, 243301.
42. J. V. Li, A. M. Nardes, Z. Q. Liang, S. E. Shaheen, B. A. Gregg and D. H. Levi, *Org. Electron.*, 2011, 12, 1879-1885.
43. M. Burgelman and C. Grasso, *J. Appl. Phys.*, 2004, 95, 2020-2024.
44. V. Shrotriya, J. Ouyang, R. J. Tseng, G. Li and Y. Yang, *Chem. Phys. Lett.*, 2005, 411, 138-143.
45. G. Garcia-Belmonte, P. P. Boix, J. Bisquert, M. Sessolo and H. J. Bolink, *Sol. Energy Mater. Sol. Cells*, 2010, 94, 366-375.
46. Y. Zhang, X.-D. Dang, C. Kim and T.-Q. Nguyen, *Adv. Energy Mater.*, 2011, 1, 610–617.
47. Y. H. Lin, Y. T. Tsai, C. C. Wu, C. H. Tsai, C. H. Chiang, H. F. Hsu, J. J. Lee and C. Y. Cheng, *Org. Electron.*, 2012, 13, 2333-2341.
48. T. Tromholt, M. V. Madsen, J. E. Carle, M. Helgesen and F. C. Krebs, *J. Mater. Chem.*, 2012, 22, 7592-7601.

CHAPTER 7

CONTACT EFFECTS ON POLYMERIC SOLAR CELLS

Most of the results showed in this chapter are already published in:

- A. Guerrero, L. F. Marchesi, P. P. Boix, S. Ruiz-Raga, T. Ripolles-Sanchis, G. Garcia-Belmonte and J. Bisquert, How the Charge-Neutrality Level of Interface States Controls Energy Level Alignment in Cathode Contacts of Organic Bulk-Heterojunction Solar Cells, *ACS Nano*, 2012, 6, 3453-3460.

- A. Guerrero, B. Dörling, T. Ripolles-Sanchis, M. Aghamohammadi, E. Barrena, M. Campoy-Quiles and G. Garcia-Belmonte, Interplay between Fullerene Surface Coverage and Contact Selectivity of Cathode Interfaces in Organic Solar Cells, *ACS Nano*, 2013, 7, 4637-4646.

- T. Ripolles-Sanchis, A. Guerrero, E. Azaceta, R. Tena-Zaera and G. Garcia-Belmonte, Electrodeposited NiO anode interlayers: Enhancement of the charge carrier selectivity in organic solar cells, *Sol. Energy Mater. Sol. Cells*, 2013, 117, 564-568.

7.1. Introduction

Bulk heterojunction (BHJ) solar cells are typically formed by a donor polymer blended with an acceptor fullerene. This active layer is deposited between efficient electrodes as commonly ITO anode and a low work function metal cathode. An additional layer is deposited between the donor:acceptor (D:A) BHJ layer and the electrodes to enhance electron and hole extraction by reducing contact resistance. These buffer layers are usually denoted as electron transport layer (ETL) and hole transport layer (HTL), acting simultaneously as a hole-blocking layer and an electron-blocking layer, respectively. The outer interface structures play a significant role in establishing optimal contact conditions for efficient extraction (or blocking) of charge carriers. In particular, the HTL layer provide a better energy level alignment with the HOMO of the donor material than ITO in conventional structure.[1] Buffer layers of different nature are currently employed to enhance both efficiency and cell stability by improving contact performance. For these reasons, the main objective of this chapter provides deep understanding of the energetic aspects in operation mechanism of cathode and anode electrode on working OPV devices. A particular importance of this chapter is to study of a complete model which describes the anode and cathode energy levels behavior on the bulk layer. To date, we have considered that the BHJ consists of a blend of electron donor and acceptor materials, uniformly distributed. However, the specific relative surface coverage of polymer or fullerene at the electrode interfaces is likely to also have an impact on the carrier selectivity. It is recognized that the nanoscale-size blend structure attaching the contact is much less studied and, therefore, constitutes other important part of this work.

Currently, a wide range of physical techniques is available to provide information on the energy levels and morphological or structural properties of the blends and interfaces.[2,3] Concretely, it is necessary to know the energy levels of each material to understand how energy level alignment between layers takes place. For this purpose, several techniques can be used such as kelvin probe, ultraviolet photoelectron spectroscopy (UPS) and x-ray photoelectron spectroscopy (XPS). To characterize the structure and length scales of the D/A domains have been generally used other structural techniques can be used such as grazing incidence x-ray diffraction (GIXRD), atomic force microscopy (AFM), or transmission electron microscopy (TEM). Additionally, information related to the depth profile concentration of organic blends has been obtained by means of GIXRD, cross-section scanning electron microscope (SEM), neutron reflectivity, near-edge x-ray absorption fine structure spectroscopy (NEXAFS), dynamic secondary ion mass spectroscopy (SIMS), variable angle spectroscopic ellipsometry (VASE), *etc.*

The previous techniques can be extremely useful to characterize the film energetically and morphologically. However, these techniques have some crucial limitations on relation between morphology structure and device performance properties. For instance, some techniques are limited by their accuracy under device operation conditions, *e.g.*, the metallic contact affects the resolution of results obtained by VASE. Attempts to obtain a direct relationship between the vertical phase segregation and contact selectivity in operating cells have provided unexpected contradictory results. Particularly, a morphology comprised by three different phases has been suggested for the P3HT:PC_{60}BM device using NEXAFS, namely, polymer/blend/polymer at both anode and cathode interfaces. However, a P3HT upper layer adjacent to the cathode is expected to be detrimental in the device performance due to the *p*-character of the polymer. But, the good performance observed has been justified by the diffusion of Al during deposition or the annealing step. Therefore, it would be interesting to find a technique that could provide structural information at the active layer/contact interface on working cells, establishing a direct relationship between vertical segregation (*e.g.*, D/A coverage at the interface) and device performance (*e.g.*, contact selectivity). Thus, it could potentially help to disentangle the respective contributions to the cell operation from surface coverage by organic compounds and extracting/blocking interlayers.

The first part of this chapter is addressed to the issue of electronic equilibration of the cathode contact in BHJ solar cells by using the information extracted from an exclusively electrical $C-V$ technique such as flat-band potential V_{fb}.[4] A simple model is proposed here that integrates both contributions, namely, qV_{fb} and dipole height Δ, into a unified description of the contact equilibration. The model is formulated in terms of charge neutrality level (CNL) and interfacial density-of-states (IDOS) as parameters. It is then explained how the band bending and the dipole layer strength can be readily derived from the experiment.

Secondly, several experiments are carried out to corroborate the operation of the mentioned model. Initially, the CNL position is determined varying the metal cathode (Ca, Al, Ag and Au) in standard P3HT:$PC_{60}BM$ active layer cells. This level governs the dipole layer Δ contribution through the partial IDOS occupancy. Once the cathode electrode behavior is known, the composition of the blend should be considered. Towards that end, a variation of the ratio P3HT: x fullerene ($PC_{60}BM$, $PC_{70}BM$ and ICBA) blend composition let us understand the origin and function of interface states withstanding the dipole layer voltage drop. Regarding the active layer/cathode interface, the ellipsometry and the capacitance techniques are combined to provide information about the relative D/A surface coverage at that interface in operating devices. For this purpose, low bandgap polymer PCPDTBT and the soluble fullerene $PC_{70}BM$ have chosen. To investigate the vertical phase segregation, several additives were added to the blend, namely, HDT, OT, and ODT. Additionally, to generalize this research, another three D/A systems are investigated. The donors under this study were: P3HT, PCDTBT, and PTB7. These polymers were blended with either $PC_{60}BM$ or $PC_{70}BM$ to provide the following systems: P3HT:$PC_{60}BM$, PCDTBT:$PC_{70}BM$, and PTB7:$PC_{70}BM$. A correlation was found between leakage current, j_{sc}, and FF with the degree of fullerene surface coverage at the cathode interface, which can be controlled by using proper experimental conditions.

And finally, a new anode electrode is undertaken. The main objective is to find the appropriate experimental surface conditions for NiO buffer interlayer to be employed in a common OPV device, comparing mainly with a standard PEDOT:PSS as HTL. The NiO was prepared on top of ITO by a versatile cathodic electrochemical deposition method from aprotic ionic liquids.[5] This deposition appears to be viable vacuum-free approach to integrate HTL in BHJ solar cells in a single-step process. Besides, this method avoids the thermal treatments after deposition which are needed in the aqueous-based electrodeposition[6] and, consequently, traces of $Ni(OH)_2$ are presented even after annealing treatments.[7] Varying the thickness (30 nm and 50 nm) and the sequence of the treatments annealing and ultraviolet-ozone (UVO) of NiO films, the work function of this metal oxide is able to change dramatically. Here, it is considered that the UVO treatment followed in these experiments produces similar effects to those occurring after O_2-plasma treatment.[8,9] The main characteristics of the O_2-plasma are: removing organic contaminants by chemical reaction with highly reactive oxygen radicals and ablation by energetic oxygen ions, promoting surface oxidation and hydroxylation (OH groups), and increasing the surface wettability that affects to the surface properties.[10]

7.2. Model of Contact Operation

In this section, the measure of V_{fb} and dipole layer are explained in detail by considering simple electrostatic arguments.[11,12] Scheme 7.1 represents the flat-band conditions under dark for different active layer compositions in a standard OPV device either only polymer or blend with polymer and fullerene rich in the active layer/cathode interface. As shown in Scheme 7.1.a, the lack of dipole in the polymer-based cell gives a V_{fb} relation to $qV_{\mathrm{fb}} = E_{\mathrm{Fp}} - \phi_{\mathrm{c}}$. However, following the energetic relations in Scheme 7.1.b and Scheme 7.1.c for blend OPV devices, the V_{fb} is expressed as a function of the dipole potential drop Δ as previously mentioned in Chapter 4 in the equation 4.16 ($qV_{\mathrm{fb}} = E_{\mathrm{Fp}} - \phi_{\mathrm{c}} - \Delta$). Additionally, to rationalize these singular interfaces, a key parameter that takes into account the interface equilibration is the CNL, which is defined as the energy level that results in a surface without net charge.

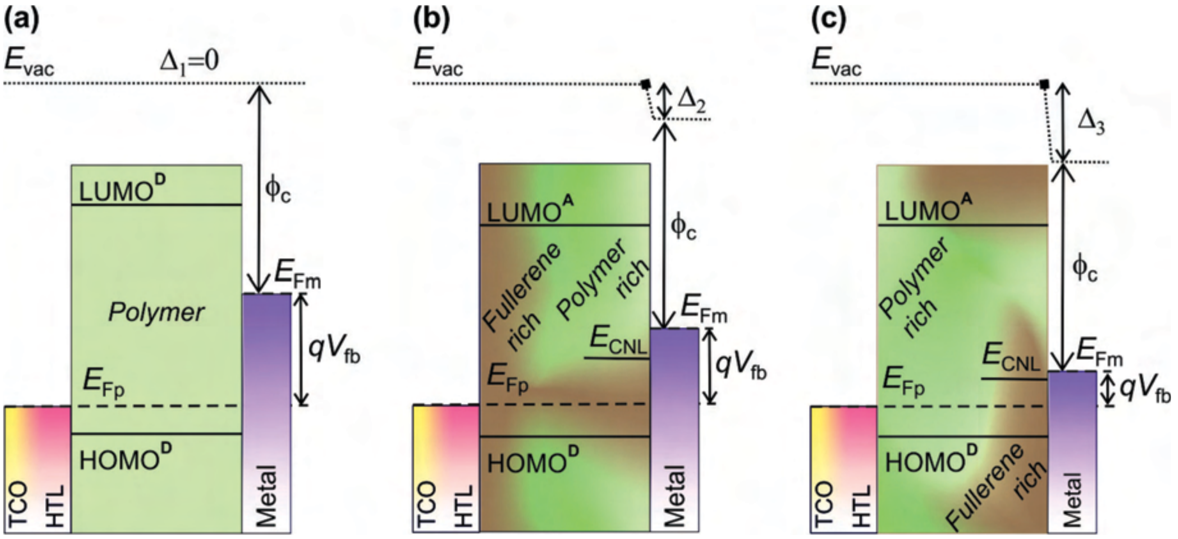

Scheme 7.1. Energy diagram of flat-band conditions under dark illumination for complete OPV devices with different active layer compositions, namely, polymer (a) and blend with polymer (b) and fullerene (c) rich in the active layer/cathode interface.

The interface dipole contribution is related to the interface charge as

$$\Delta = \frac{\delta Q_{\mathrm{is}}}{\varepsilon_{\mathrm{i}}\varepsilon_0} \tag{7.1}$$

where ε_{i} is the dielectric constant of the interlayer (*e.g.*, for the blend P3HT:PC$_{60}$BM layer corresponds to $\varepsilon_{\mathrm{i}} = 3$), ε_0 is the permittivity of the free space (8.85×10^{-12} F m^{-1}), and δ stands for the charge separation at the dipole layer ($\delta \approx 5$ Å), assuming that a molecular monolayer accommodates the interface charge. Q_{is} is the interface negative charge which is fully compensated by a positive charge at the metal Q_{c}, that is $-Q_{\mathrm{is}} = Q_{\mathrm{c}}$ at flat-band conditions.

The interface charge is obtained by assuming that the occupation of the interface state distribution IDOS, g_{is}, is governed by the position of the metal Fermi Level, E_{Fm},

$$Q_{\mathrm{is}} = -q\int_{E_{\mathrm{CNL}}}^{E_{\mathrm{Fm}}} g_{\mathrm{is}}\,\mathrm{d}E \tag{7.2}$$

Here, the integral extends from E_{CNL} to E_{Fm}, as shown in Scheme 7.1.b and Scheme 7.1.c. Since the E_{Fm} position depends on the applied voltage to achieve flat-band conditions (Scheme 7.1), in which $E_{\mathrm{Fm}} = E_{\mathrm{Fp}} - qV_{\mathrm{fb}}$, it is clear from equations 7.1 and 7.2 that Δ is dependent on qV_{fb}. In general, equation 7.2 should be solved numerically after considering an adequate IDOS. By assuming that g_{is} varies weakly between E_{CNL} and E_{Fm}, equation 7.2 can be approximated as

$$Q_{\mathrm{is}} = qg_{\mathrm{is}}\left(E_{\mathrm{CNL}} - E_{\mathrm{Fm}}\right) \qquad (7.3)$$

From equation 4.16 can be then rewritten as follows

$$qV_{\mathrm{fb}} = E_{\mathrm{Fp}} - \phi_{\mathrm{c}} - \frac{q\delta g_{\mathrm{is}}}{\varepsilon_{\mathrm{i}}\varepsilon_{0}}\left(E_{\mathrm{CNL}} - E_{\mathrm{Fp}} + qV_{\mathrm{fb}}\right) \qquad (7.4)$$

After some calculations, a linear relationship between qV_{fb} and ϕ_{c} is obtained, with a negative slope equaling the parameter S

$$qV_{\mathrm{fb}} = E_{\mathrm{Fp}} - E_{\mathrm{CNL}} - S\left(\phi_{\mathrm{c}} - E_{\mathrm{CNL}}\right) \qquad (7.5)$$

where, the parameter S accounts for the effect of g_{is} on the contact energetic and it is expressed as follows when a constant IDOS g_{is} is assumed

$$S = \frac{1}{1 + q\delta g_{\mathrm{is}}/\varepsilon_{\mathrm{i}}\varepsilon_{0}} \qquad (7.6)$$

From the equation 7.6, large interface intensity values, $g_{\mathrm{is}} >>$, entail $S \approx 0$ in such a way that the barrier becomes independent of the metal work function, ϕ_{c}. On the contrary, $g_{\mathrm{is}} <<$ would imply $S \approx 1$, recovering the so-called Schottky limit.

In this model, specific gap states are assumed at the surface in the metal contact. The character of the surface states changes from mostly acceptor materials, approaching the bottom of the CB to mostly donor materials close to the top of the VB. In this scenario, E_{CNL} represents the energy that marks the separation between two classes of states within the IDOS. It is also assumed that the interface states readily achieve equilibrium with the metal electronic states. If the E_{Fm} is initially above of the E_{CNL}, then electrons are transferred to IDOS, while the opposite is true if the E_{Fm} lies below of the E_{CNL}. The net consequence of the transference to this type of surface states distribution is that a dipole is built in such a way that the E_{Fm} tends to align with the E_{CNL}. In fact, several metals are compared in the next section to corroborate the relatively weak sensitivity of the organic CNL to the metal/organic interaction. If the IDOS is very high, all E_{Fm} are pulled to the same energy level (E_{CNL}). Therefore, it is said that the interface undergoes to Fermi Level pinning. In this case, the interfacial states are able to accommodate all of the charge required to equilibrate a large portion of offset in metal and organic semiconductor work functions as $\phi_{\mathrm{c}} - \phi_{\mathrm{s}}$. In general, the equilibration takes place in both dipole layer and band bending contributions.

7.3. Dependence of flat-band values and dipole layers on cathode metals

Several electron extraction metals (Ca, Al, Ag and Au) with different ϕ_{c} were investigated in this section to correlate V_{fb}, E_{Fm} as well as Δ. To carry out this research, regular sandwich PSCs were used with an architecture of glass/ITO/PEDOT:PSS/P3HT:PC$_{60}$BM/metal. The ϕ_{c} of selected metal contacts are shown in Scheme 7.2. All of these OPV devices were prepared as described in the experimental section in the Chapter 3 (more specific details are listed in Appendix II).[13]

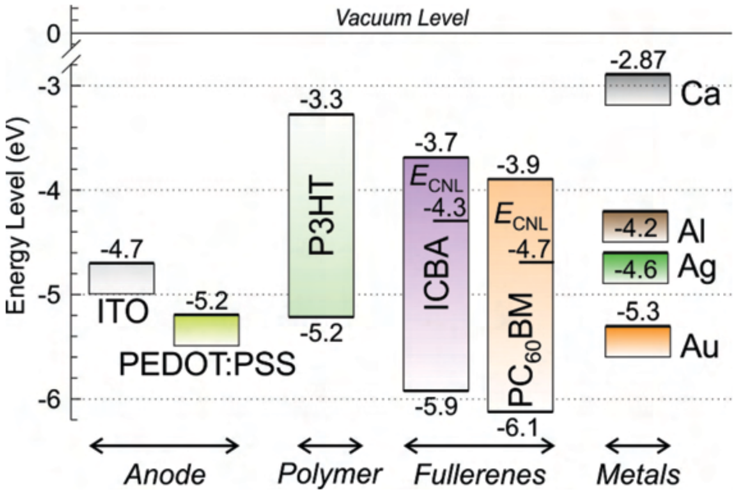

Scheme 7.2. Energy Levels diagram of P3HT-polymer, ICBA- and PCBM-fullerene materials and cathode metals such as Ca, Al, Ag and Au. The charge neutrality level energy, E_{CNL}, of each fullerene material is also represented which were calculated previously by equation 7.5.

The P3HT:PC$_{60}$BM PSCs using different cathode metals were characterized by $j-V$ characteristics under simulated AM1.5G illumination (1000 W m^{-2}). These results are plotted in Figure 7.1 and summarized in Table 7.1. The efficiency obtained is relatively low because the P3HT:PC$_{60}$BM active layer thickness is higher respect to the optimum (~350 nm) that is about ~100 nm using this blend.[14]

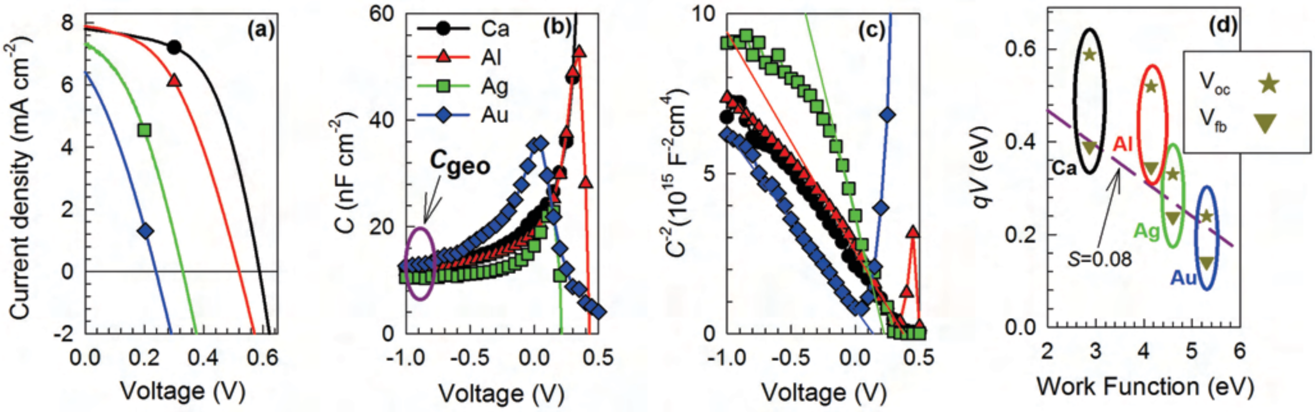

Figure 7.1. Several cathode metals (Ca, Al, Ag and Au) were characterized by OPV with structure of glass/ITO/PEDOT:PSS/P3HT:PC$_{60}$BM/metal (a) $j-V$ under 1 sun illumination and (b) $C-V$ measurement under dark conditions. The geometrical capacitance C_{g} can be extracted in (b). The MS plot is represented in (c). Experimental values of V_{fb} and V_{oc} as a function of the metal work function ϕ_{c} used in the cathode contact is plotted in (d).

The E_{CNL} value was calculated from equation 7.5 and is represented in Scheme 7.2. The CNL location is given for a P3HT:PC$_{60}$BM blend and take into account the ϕ_{c} of the metals: Ca, Al, and Ag, which would transfer negative charge to the interfacial states. However, Au gives rise to a positive charge sheet on the organic side and, therefore, this metal has not been considered to the calculation of the E_{CNL}.

The photovoltaic characteristics showed in Figure 7.1.a indicates the highest V_{oc} values for the cell with a low ϕ_c metal such as Ca. However, metals with ϕ_c higher than the $PC_{60}BM$ LUMO level (~3.9 eV), a voltage loss appears as a consequence of the electron energy mismatch between the active layer and the extracting contact. Besides, Ca and Al metal cathode electrodes were optimum option to extract electrons in P3HT:$PC_{60}BM$ blend observed in the j_{sc} results (see Table 7.1). But, there are loss mechanisms that cause a decrease in the *FF* value to the Al respect to the Ca cells. As a consequence, the PCE leads to achieve an improvement to the Ca device.

Table 7.1. Different cathode metals in thick P3HT:$PC_{60}BM$ solar cells were characterized by photovoltaic measurements under simulated 1 sun irradiation and Mott-Schottky analysis: doping density (*N*) and flat-band potential (V_{fb}). Metal Fermi Level (E_{Fm}) and dipole potential drop (Δ) is calculated by Scheme 4.8 ($E_{Fm} = E_{Fp} + qV_{fb}$) and equation 7.1, respectively.

Cathode	j_{sc} (mA cm^{-2})	V_{oc} (V)	*FF* (%)	PCE (%)	*N* (10^{15} cm^{-3})	V_{fb} (V)	E_{Fm} (eV)	Δ (eV)
Ca	7.81	0.59	56	2.6	6.6	0.39	4.56	1.69
Al	7.91	0.52	45	1.8	4.7	0.35	4.60	0.45
Ag	7.36	0.33	30	1.0	2.5	0.24	4.71	0.11
Au	6.50	0.24	30	0.5	7.1	0.14	4.80	-0.49

The C_g can be estimated (~10 nF cm^{-2}) from Figure 7.1.b at reverse bias (-1 V) which caused the modulation of depletion zone when the voltage is changed. By examining the MS plot $C^{-2} - V$ represented in Figure 7.1.c, two parameters are extracted: doping density level *N* and the V_{fb} from the slope and the intercept of voltage axis, respectively. It is observed that the V_{fb} values change with the cathode metal, keeping the same active layer. Additionally, the V_{fb} followed the same trend as V_{oc} for higher ϕ_c metals, as observed in Figure 7.1.d. However, V_{fb} is found to be about 0.4 V in the case of Ca as the cathode contact, being far below to the V_{oc} achieved. It is worth noting that, despite a large variation (>0.2 eV) among the metal cathode ϕ_c, only a small change is observed for V_{fb} (~0.2–0.1 eV) as listed in Table 7.1. Accordingly the slope between qV_{fb} and the metal ϕ_c (see Figure 7.1.d) is experimentally observed to be very small, $S = 0.08$. For the calculation of *S* had not considered the case of Au as previously stated. In previous papers, Bisquert *et al.* have already related these low V_{fb} values found for low ϕ_c metals to the presence of a dipole layer made up at the organic layer/metal interface.[15]

7.4. Dependence of flat-band values and dipole layers on the composition of the blend

Experiments varying the blend composition and ratio of P3HT: *x* fullerene have been carried out with the aim of checking the effect of the LUMO-acceptor level position on the cathode energetic. Three different fullerene acceptor materials were studied such as indene-C_{60} bisadduct (ICBA), $PC_{60}BM$ and $PC_{70}BM$ whose molecular structures were illustrated in Chart 3.2 in the section 3.5.1. The architecture of these OPV cells was glass/ITO/PEDOT:PSS/active layer/Ca/Ag. All experimental details were explained in the experimental section in the Chapter 3 and more specific details are found in Appendix II.[13] HOMO and LUMO energy levels of these fullerenes along with P3HT polymer are shown in Scheme 7.2, including the E_{CNL} of each fullerene calculated previously from equation 7.5. Here, it would not expect significant changes in the position of CNL by using different content of the same fullerene, although this mainly depends on the actual IDOS distribution. However, it is supposed that the IDOS (g_{is}) varies by changing the type of fullerene. The V_{fb} results extracted from the MS curves are plotted versus P3HT: *x* fullerene ratio in Figure 7.2.

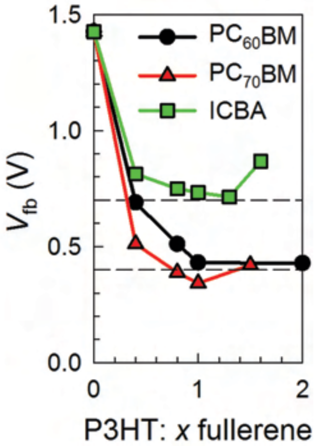

Figure 7.2. Variation of the flat-band voltage V_{fb} with the blend ratio for different acceptor fullerene materials (PC$_{60}$BM, PC$_{70}$BM and ICBA). The donor polymer material is P3HT. Lines are used to guide the eyes. The horizontal dash lines refer to the V_{fb} constant values at 0.4 and 0.7 V to PCBM and ICBA, respectively.

A large value of $V_{fb} = 1.5\,\mathrm{V}$ is obtained for the devices with P3HT-only active layer (Figure 7.2), which is in rather good agreement with the expected large offset between the metal and organic semiconductor work functions, $\phi_C - \phi_S \approx 1.9\,\mathrm{eV}$, as drawn in Scheme 7.1.a. Here, the cathode contact ability to form a dipole layer is very limited because no acceptor molecules are present at the interface. The band bending is then the principal mechanism to equilibrate the contact in accordance to the Schottky limit explained in the previous section. When the amount of fullerene molecules are increased in the photoactive layer, independently of the fullerene material, V_{fb} decreased markedly. This fact is expected because the amount of acceptor states attached to the cathode metal increased, and then, the dipole voltage offset Δ enlarged. This case is illustrated in Scheme 7.1.c. On the contrary, an important effect on the contact equilibration is observed when low coverage of fullerene molecules was attached at the contact interface (small IDOS) (see Scheme 7.1.b). A reduction of the g_{is} (larger *S*) might envisage an increment in band bending as inferred from equation 4.16.

It is interesting to note that V_{fb} value reached a plateau ($V_{fb} \approx 0.4\,\mathrm{V}$) at blend ratio close to 1:1 for PC$_{60}$BM- and PC$_{70}$BM-based OPV devices (Figure 7.2). As explained previously for PC$_{60}$BM-based cells, the E_{Fm} approximately coincides with that calculated for $E_{CNL} \approx 4.7\,\mathrm{eV}$. Since the same trend is illustrated when ICBA is used as a fullerene acceptor (with a different value for the flat-band plateau $V_{fb} \approx 0.7\,\mathrm{V}$), being CNL shifted to lower energy positions. In this case, a value of $E_{CNL} \approx 4.3\,\mathrm{eV}$ were obtained. Such downward displacement is in qualitative agreement with the general IDOS energy shift caused by the fullerene LUMO level offset (Scheme 7.2). Although ICBA acquired different properties as compared with PCBM molecules, it might also be possible for the same blend ratio (~1:1) that a reduced amount of ICBA molecules covers the cathode interface. This would imply that the increase in V_{fb} is explained by differences in concentration rather than molecular energetics.

Notwithstanding previous results, these two blends (P3HT:PCBM and P3HT:ICBA) with 1:1 ratio exhibited very similar morphology as illustrated in the AFM (Figure 7.3) and cross-section SEM (Figure 7.4) images.

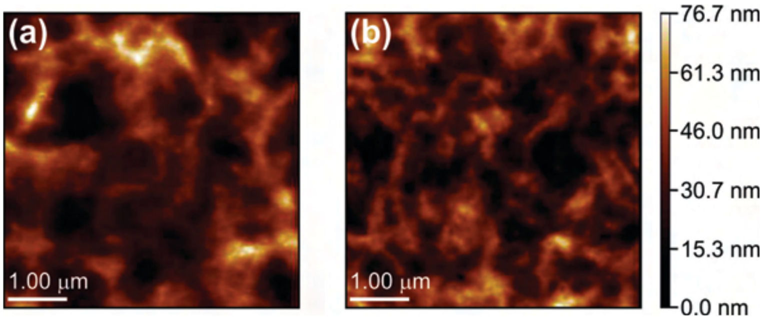

Figure 7.3. AFM images of P3HT:$PC_{60}BM$ (1:1) (a) and P3HT:ICBA (1:1) (b) surfaces.

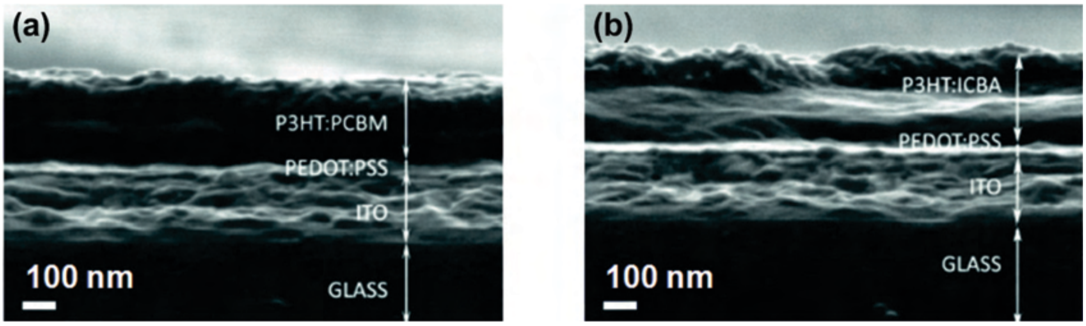

Figure 7.4. Cross section SEM images of thick (~350 nm) P3HT:$PC_{60}BM$ and P3HT:ICBA blend films.

In brief, $C-V$ measurements were used to understand the underlying mechanisms involved in the formation of dipoles at the active layer/cathode contact interface.[13] Several models have been proposed to account for the energy level alignment at interfaces, depending on the degree of interaction between the metal contact and the deposited organic layer. When that chemical interaction is not negligible, it is expected that molecules attached to the metal surface undergo both a shift and a broadening of their molecular energy levels. Energy distribution of the attached molecules should be modeled by a specific IDOS which differs from that encountered in the bulk of the organic layer (DOS). The situation is even more featured for interfaces formed by metals deposited onto organic layers because the metal can diffused to active layer and created bonds in a rough surface. To rationalize these kinds of interfaces, a simple, albeit robust model was proposed based on the energy equilibration in the interface in which the CNL is located at a given position within the IDOS.[16-18] In the work described above, the $C-V$ measurements were very sensitive to all interfacial materials such as donor, acceptor, metallic contact, and their relative concentration. Regarding the donor and acceptor molecules, the position of the HOMO and LUMO levels as well as the ratio of each component at the interface were decisive. It was observed that the only way to ensure efficient electric contact between the cathode metal and the active layer is by the presence of chemically reduced fullerene molecules attached to the interface.[13] It is then inferred from the previous discussion that band bending and dipole layer strength are extremely dependent on the amount and nature of fullerene molecules (PCBM and ICBA) attached to the metal cathode. Particularly, the V_{fb} value is a high sensitive parameter to the amount of the polymer or fullerene in the boundary of the metal contact. Therefore, to corroborate these MS analyses, an ellipsometry technique called VASE is used to describe the vertical phase segregation in a blend in the following section.

7.5. Concordance between Variable Angle Spectroscopy Ellipsometry and Mott-Schottky techniques

VASE technique has been successfully employed due to its highly sensitive and non-destructive characteristics.[19,20] This technique explores the vertical and lateral phase segregation in an organic bulk film. However, the effect of the metallic evaporated contact on the top of the BHJ film is ignored. Some films formed with low bandgap polymer PCPDTBT blended with soluble fullerene $PC_{70}BM$ were studied by VASE technique. The blend morphology was changed by adding several additives such as HDT, OT and ODT. To this purpose, a range of models have used to fit the ellipsometric experimental data for the blend films on glass/ITO/PEDOT:PSS substrates. VASE experiments were entirely carried out at ICMAB-CSIC thanks to the expertise of Dr. Campoy-Quiles. Additionally, these films were also used in complete and regular structure OPV devices to analyze them by $C-V$ technique under dark conditions (Figure 7.5.a). The experimental procedure were explained in detail in the experimental section of the Chapter 3 and more specific details are showed in Appendix II.[21] Both techniques, VASE and $C-V$, are compared in Figure 7.5.b.

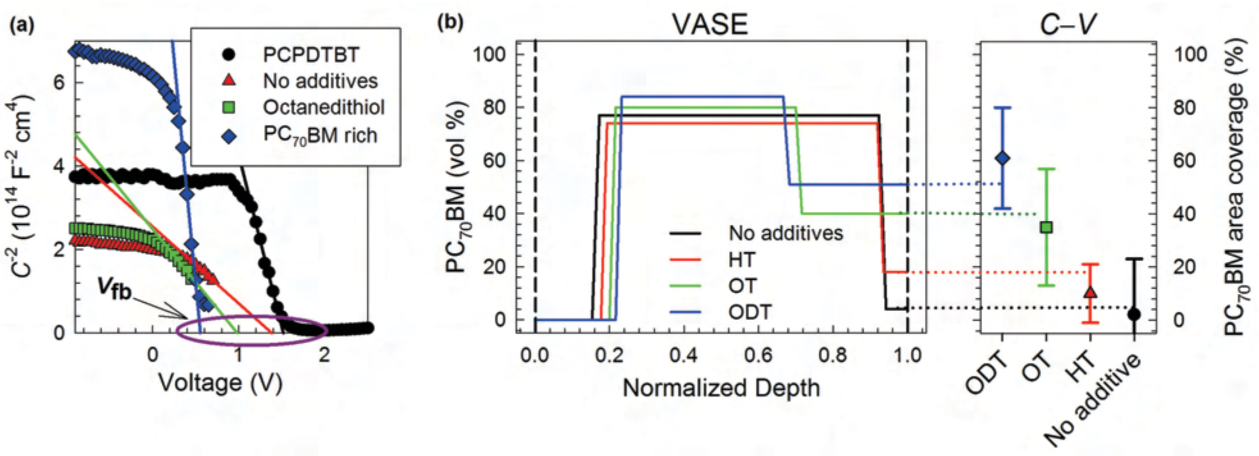

Figure 7.5. (a) MS plot for a number of OPV devices varying the active layer composition such as PCPDTBT-rich, PCPDTBT:$PC_{70}BM$ (1:2) without additives and with ODT, and $PC_{70}BM$-rich. (b) Comparison between phase segregation profile from VASE and fullerene surface concentration obtained by $C-V$ technique.

As regards $C-V$ measurements, the V_{fb} value of pure polymer and fullerene-rich devices represented the extreme cases of full active layer/cathode coverage by polymer and fullerene, respectively. If it is assumed a linear relationship between V_{fb} values and surface coverage at the bulk/metal interface, the V_{fb} results of devices fabricated with additives can be employed to estimate the relative surface coverage percentage. Thus, the MS technique is adopted as a measurement of the fullerene coverage at the contact surface. For instance, Figure 7.5.a represents the MS plot for the two extremes of polymer and fullerene-rich (PCPDTBT:$PC_{70}BM$ ratio of 1:6 by weight) devices and a standard ratio (1:2 by weight) of PCPDTBT:$PC_{70}BM$ without additives and with ODT. On the one hand, the high V_{fb} values are obtained for the device fabricated with PCPDTBT polymer only. This is due to the fact that the dipole contribution plays a secondary role, with the work function mismatch between the polymer and metal mainly accommodated by the bulk band bending (Scheme 7.1.a). On the other hand, the blend rich of fullerene close to the metal interface yielded much lower values of V_{fb}. The high concentrations of fullerene in the blend lead to stronger dipoles because of the larger charge associated to reduced fullerene (charge transfer from the metal). The overall net effect is the practical alignment of the E_{Fm} and CNL position (Scheme 7.1.c). As a consequence, the V_{fb} values of others two devices (without additives and ODT cells) are found in the range of the two extremes of V_{fb} values (polymer and fullerene-rich cells).

VASE results showed that in the middle of the film depth there is a fullerene-rich interlayer, sandwiched between two polymer-rich layers at the substrate and air interfaces, as schematically illustrated in Figure 7.5.b for all samples. Incorporating additives in the blend solution quantitatively modifies the profile, while keeping the same general trend. Interestingly, the deduced $PC_{70}BM$ coverage at the surface and the depth of the surface interlayer increased from the sample processed without additives to those with additives. The volume concentration of $PC_{70}BM$ at the surface is the highest for ODT and then gradually decreases for OT, HT, and finally for the samples processed without additives (Figure 7.5.b). The percentage of fullerene material coverage on the cathode surface is listed in Table 7.2. Therefore, VASE technique strongly indicates a dependence of D/A relative surface coverage on the specific additives used in the processing of the films. These results are in agreement with the MS data showed in Figure 7.5.b because this tool detects the degree of fullerene or polymer located at the active layer/cathode interface in complete devices.

In particular, AFM analysis of PCPDTBT:$PC_{70}BM$ with and without ODT as a blend additive shows a lack of surface morphology differences between samples processed with additive from those that do not use additive (Figure 7.6).

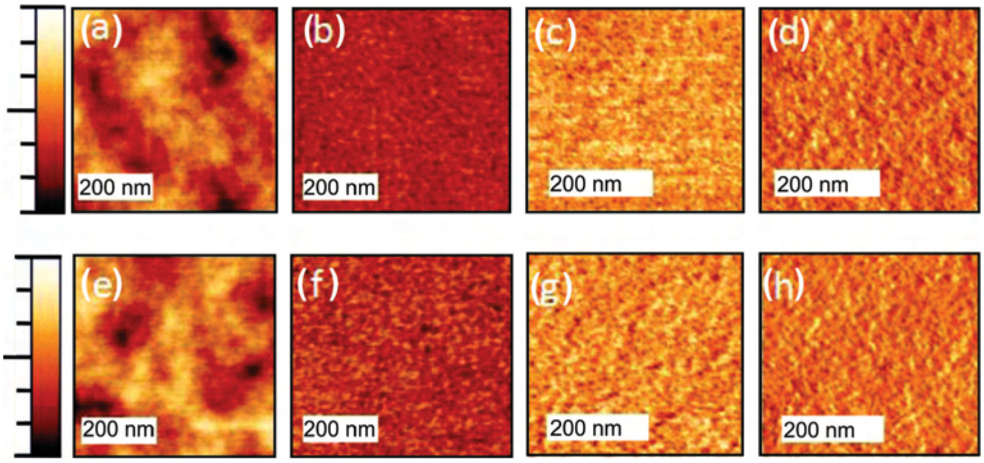

Figure 7.6. AFM images: surface topography (a, e), phase (b, f), adhesion (c, g) and stiffness (d, h) images for PCPDTBT:$PC_{70}BM$ films without (top row) and with (bottom row) ODT as an additive. The Z scale in the topographic images goes from 0 to 4.47 nm in (a) and from 0 to 3.39 nm in (e).

Whereas topography images are dominated by surface roughness, the frequency shift is more sensitive to the nanostructure of the organic films. Interestingly, the images showed a remarkable resemblance between the morphology and the contact potential maps in the two types of samples with rms roughness values being 0.55 and 0.46 nm to samples processed without and with ODT in the blend, respectively. This poor differences in the surface morphology and contact potential maps is also apparent when looking at other superficial traits, such as adhesion, and evidences a fine nanoscale intermixing of the two components constituting this system.[22] On the contrary, the P3HT:$PC_{60}BM$ system, for which micrometer-scale $PC_{60}BM$ aggregates appear protruding from the surface upon annealing.[23]

7.6. Correlation between surface coverage and device performance

In order to design BHJ solar cells with optimum efficiencies, apart from a perfect control of film morphology, engineering of interfacial layers is of vital importance. This is because such strongly selective electrodes minimize leakage current, which is an indication of undesired hole flux crossing the cathode contact. Although detailed discussion on the relation of phase segregation with the overall cell performance is complex, general conclusions are partially extrapolated from the PCPDTBT:PC$_{70}$BM system to other blend combinations including, P3HT:PC$_{60}$BM, PCDTBT:PC$_{70}$BM, and PTB7:PC$_{70}$BM. The performance results under simulated 1 sun irradiation and other important parameters of these BHJ cells are summarized in Table 7.2. In particular, the characteristic $j-V$ curves under 1 sun illumination and dark conditions are plotted in Figure 7.7 to the PCPDTBT:PC$_{70}$BM system. The experimental procedure of each blend was listed in the experimental section of Chapter 3 and more specific details are explained in Appendix II.

Table 7.2. Device performance parameters of polymer:fullerene solar cells fabricated under different processing conditions. The percentage of fullerene material coverage on the cathode surface and the shunt resistance, R_{sh}, are calculated for each system. The current density, j_{dark}, under dark conditions is also listed.

Polymer: fullerene	**Cond.**	j_{sc} (mA cm^{-2})	V_{oc} (V)	*FF* (%)	**PCE** (%)	**Fullerene**[a] (%)	R_{sh} (Ω cm^2)	j_{dark} [b] (10^{-5} A cm^{-2})
PCPDTBT: PC$_{70}$BM	No additives	4.87	0.48	29	0.67	2	324	367.0
	HT	6.68	0.61	34	1.37	9	541	248.3
	OT	6.84	0.64	39	1.69	35	621	222.3
	ODT	7.69	0.66	47	2.38	60	1802	57.7
P3HT: PC$_{60}$BM	As cast	2.46	0.58	33	0.48	60	89	11.4
	Annealed	8.10	0.62	66	3.31	90	8800	3.4
PCDTBT: PC$_{70}$BM	As cast	4.72	0.86	33	1.36	28	13900	15.0
	Annealed	5.90	0.90	35	1.89	65	146200	0.1
PTB7: PC$_{70}$BM	No additives	10.2	0.72	42	3.09	35	23000	6.3
	Diiodoctane	10.8	0.78	64	5.40	81	644000	0.3

[a] Fullerene coverage on the cathode; [b] at -1 V in dark conditions.

The device performance is strongly dependent of the additives (HT, OT and ODT) with different boiling points into the PCPDTBT:PC$_{70}$BM devices. As illustrated in Figure 7.7.a, under simulated 1 sun illumination all device performance parameters are found to be maximum when ODT is used and, consequently, the best PCE (Table 7.2). These photovoltaic parameters gradually decrease for devices with additives OT, HT and without additives, respectively. Furthermore, the $j-V$ curves under dark conditions (Figure 7.7.b) exhibited a diode response because a trend in the leakage current at -1 V (j_{dark}) is clearly observed. Particularly, the best performing device (see Table 7.2) presented high j_{sc}, high proportion of fullerene at the cathode (as deduced from $C-V$ analysis) and low j_{dark} at -1 V. The same results are illustrated for the shunt resistance, R_{sh}, that are about one order of magnitude higher for the device that contain a high proportion of fullerene at the surface of contact. Injection of holes from the cathode contact at reverse bias originates low R_{sh}. Both facts, j_{dark} and R_{sh}, are a clear manifestation of enhanced selectivity of the contact when a high proportion of fullerene is present at the cathode.

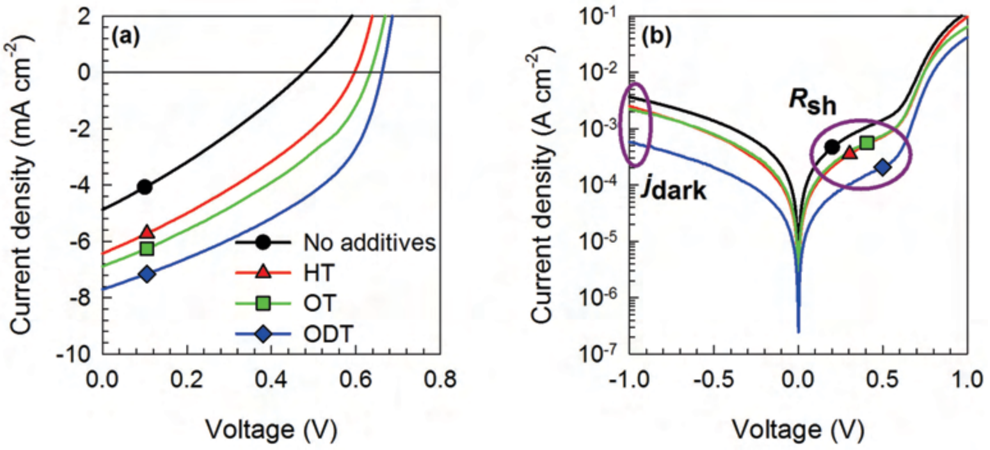

Figure 7.7. (a) $j-V$ under simulated AM1.5G illumination (1000 W m^{-2}) for PCPDTBT:PC$_{70}$BM PSCs without and including several additives such as HT, OT and ODT; (b) $j-V$ under dark conditions for the same devices. The shunt resistance, R_{sh}, and leakage current, j_{dark}, are remarked in Figure (b).

It is highlighted here that such correlations are also observed for P3HT, PCDTBT and PTB7-based cells blended either with PC$_{60}$BM or PC$_{70}$BM (see Table 7.2). For these cells, the annealing process increased the fullerene concentration close to the cathode contact (as deduced from $C-V$ analysis), in good agreement with the enhancement in j_{sc}, markedly large R_{sh} values, and much low j_{dark} at -1 V. In the case of PTB7, it is noteworthy that increased notably *FF* through larger R_{sh}.

7.7. Resistance effects on the anode contact

In this section, the primary focus is on the hole extraction layer in a regular OPV device by substituting the standard PEDOT:PSS layer to another material such as NiO. As it has been previously described in the Chapter 4 in the section 4.5.1., the HTL creates an ohmic contact in the HTL/bulk interface. However, the work function of NiO is highly dependent of its thickness and surface treatments, being crucial parameter for proper energy alignment between HTL and active layer. Therefore, in order to evaluate this oxide as HTL, different thicknesses (30 nm and 50 nm) and annealing/UVO sequence treatments were tested to optimize the overall cell performance. Under optimum NiO conditions, the photovoltaic results are comparable respect to those for the standard PEDOT:PSS architecture OPV cell. These PSCs were prepared as described in the experimental section in the Chapter 3 and more specific details are listed in Appendix II.[24] The characterization of these NiO films were carried out by SEM and UV-Vis spectroscopy illustrated in Figure 7.8 and Figure 7.9, respectively. Additionally, these films were analyzed in complete OPV devices and were characterized by $j-V$ curves under simulated AM1.5G illumination (1000 W m^{-2}) and *EQE* (Figure 7.10). In order to know the resistance effect of these films, the OPV cells were tested by IS under simulated 1 sun radiation intensity. The impedance spectra at 300 mV are showed in Figure 7.11 and the impedance results in Figure 7.12.

The morphology of NiO layers was analyzed by SEM images. The ITO surface (Figure 7.8.a) was covered of NiO by electrodeposition passing a charge density of 13 mC cm^{-2} (Figure 7.8.b and the cross section is illustrated in Figure 7.8.d) and 25 mC cm^{-2} (Figure 7.8.c). From SEM images is observed a decrease of roughness for the samples obtained after applying 13 mC cm^{-2} respect to the

25 mC cm^{-2} samples. The decrease of the roughness for thick layers was confirmed by AFM images.[5]

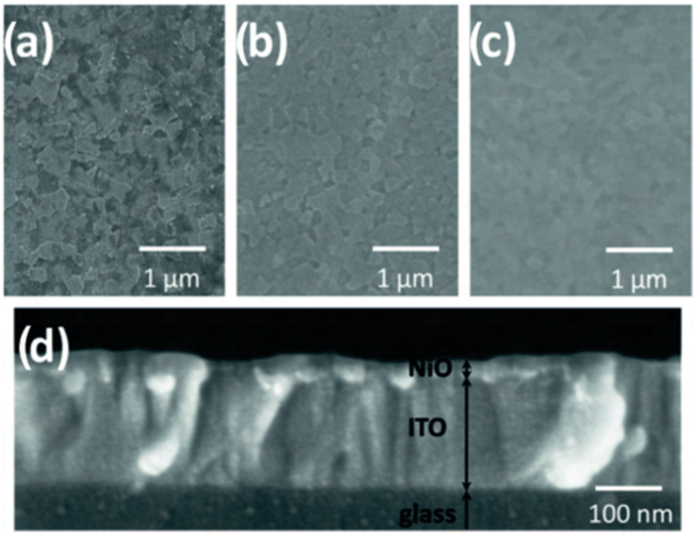

Figure 7.8. Top view SEM micrographs of a naked ITO substrate (a) and NiO layers electrodeposited by passing a charge density of 13 (b) and 25 mC cm^{-2} (c). The Figure (d) shows a cross section SEM micrograph of the sample showed in Figure (b).

The substrates coated with different HTLs were characterized by UV-Vis spectra (Figure 7.9). The samples investigated consist of a glass/ITO/HTL structure.

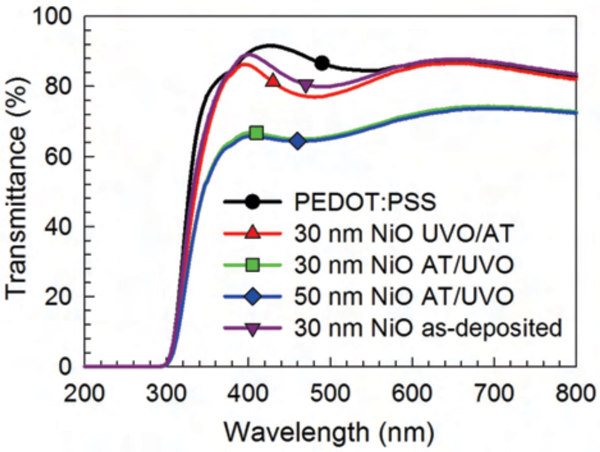

Figure 7.9. UV-Vis spectra for different hole extraction layers. The configuration of these substrates was glass/ITO/HTL, being HTLs mainly PEDOT:PSS, 30 nm NiO (as deposited, UVO/AT and AT/UVO) and 50 nm NiO (AT/UVO).

It is known that the NiO work function and transparency characteristics depend strongly of the NiO preparation. For this reason, thickness and UVO-annealing treatments were analyzed in the surface of NiO films. In particular, the 30 nm NiO were tested by three different surface conditions as as-deposited, UVO treatment and then annealing treatment (AT) (denoted as UVO/AT) and AT/UVO sequence. Additionally, 50 nm NiO AT/UVO was also characterized. It is well-known that the PEDOT:PSS has high transmittance as shown in Figure 7.9 which property is adequate to have high transparent anode electrode. The highest transmittance of the standard PEDOT:PSS was comparable to the 30 nm NiO as-deposited and UVO/AT. Then, the same reduction of the transmittance was observed to the NiO AT/UVO surface treatments at 30 nm and 50 nm which is reflected in the photovoltaic characteristics as discussed later. The last transmittance results indicated an independence of the NiO thickness (30 nm and 50 nm), which is contrary to that found in the literature, high variation in the transmittance spectra when the surface NiO sequence was annealing/UVO treatment.[25]

The electrical properties of the glass/ITO/HTL/P3HT:$PC_{60}BM$/Ca/Ag solar cells with NiO (Scheme 7.3) and PEDOT:PSS as buffer layers are shown as $j-V$ curves (Figure 7.10.a) under simulated AM1.5G illumination (1000 W m^{-2}) and the photovoltaic parameters are summarized in Table 7.3. The *EQE* is plotted in Figure 7.10.b for PEDOT:PSS and 30 nm NiO (AT/UVO) devices.

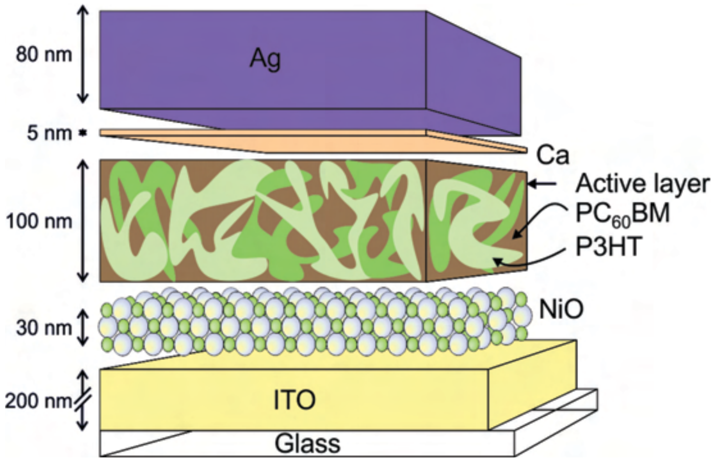

Scheme 7.3. A conventional architecture of OPV solar cells using as a hole extracting interlayer a crystalline NiO film.

A strong influence in the photovoltaic parameters is observed in Figure 7.10.a when the NiO surface treatments were carried out by UVO, AT or untreated (as-deposited) as well as the different thicknesses. The NiO as-deposited device showed the lowest photovoltaic parameters (see Table 7.3), indicating that the surface treatments are necessary to improve contact conditions. However, the order of the surface treatments is also affected in the photovoltaic results.

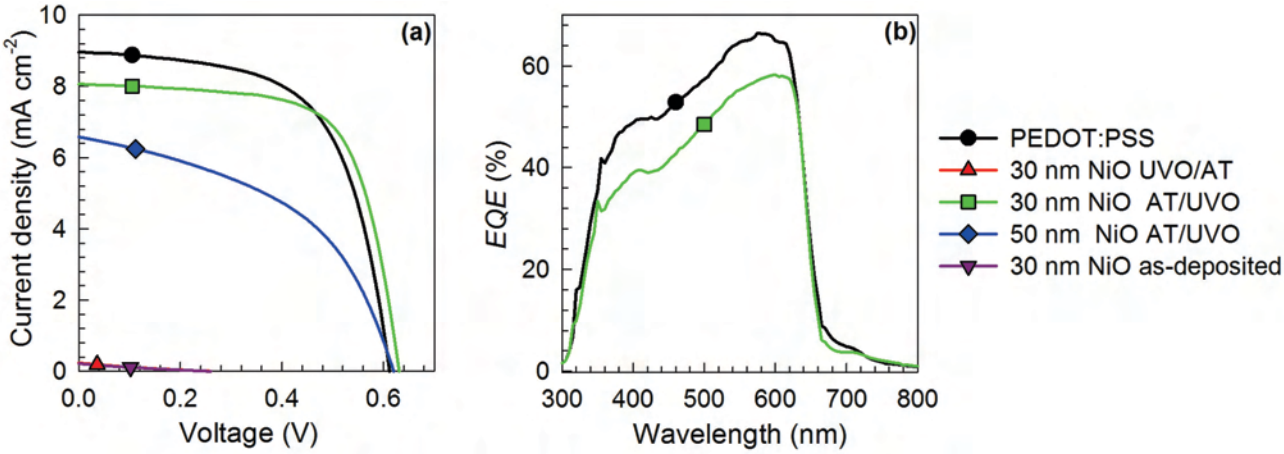

Figure 7.10. (a) $j-V$ curves under simulated 1 sun illumination (1000 W m^{-2}) for a standard (PEDOT:PSS) and four different NiO surface conditions solar cells. (b) *EQE* measurement for a standard device glass/ITO/PEDOT:PSS/P3HT:$PC_{60}BM$/Ca/Ag and the PSC with best conditions to the NiO interlayer such as 30 nm NiO (AT/UVO).

For instance, the photovoltaic parameters of the 30 nm NiO film cell annealed before of UVO treatment (AT/UVO) was more favored than the UVO/AT surface treatment. Specifically, the V_{OC} was directly affected mainly, from 630 mV for the 30 nm NiO (AT/UVO) cell to 260 mV for the 30 nm NiO (UVO/AT) cell. These results suggest that the NiO film with the previous UVO treatment exhibits blocking characteristics as next explained in describing IS results. As reported, the O_2-plasma treatment, similar to UVO treatment, on the surface of NiO films provided a significant increase in the work function (from -4.7 to -5.3 eV) and is largely attributed to an increase in concentration of NiOOH species on the surface, resulting a large surface dipole.[8]

Other important aspect was the NiO thickness (30 and 50 nm) with an identical surface treatment (AT/UVO). Here, lower j_{SC} and *FF* parameters were observed to the 50 nm NiO-based device compared to 30 nm NiO-based device. At same transmittance spectra (see Figure 7.9), the 50 nm NiO acted like a blocking layer because the NiO film hindered the hole extraction at the anode contact, consequently, lower photovoltaic parameters were observed.

Table 7.3. Photovoltaic characteristics of glass/ITO/HTL/P3HT:PC_{60}BM/Ca/Ag solar cells under simulated 1 sun illumination (1000 W m^{-2}) using PEDOT:PSS and NiO like HTL's. The nomenclature *l* is the HTL thickness and AT means annealing treatment. The selectivity *s* % is calculated from the impedance data by the equation 7.7.

HTL	***l*** (nm)	**Process**	j_{sc} (mA cm^{-2})	V_{oc} (mV)	***FF*** (%)	**PCE** (%)	***s*** (%)
PEDOT:PSS	30	Standard	8.97	611	62	3.39	95.0
NiO	30	UVO/AT	0.42	260	19	0.02	-
NiO	30	AT/UVO	8.06	630	67	3.44	99.6
NiO	50	AT/UVO	6.58	620	47	1.92	85.0
NiO	30	as-deposited	0.20	258	23	0.01	-

The optimum photovoltaic result corresponded to the 30 nm-thick NiO treated at the surface with UVO after annealing (AT/UVO). The PCE is 3.44 %, comparable to a common device with PEDOT:PSS acting as HTL (3.39 %). The main differences were observed in the j_{SC} and *FF* results, but both devices achieved similar V_{OC} (see Table 7.3). The lower j_{SC} for the 30 nm thick NiO (AT/UVO)-based solar cell was attributed to the lower transmittance spectra as showed in Figure 7.9. However, the lastly device had an improvement in the *FF* in comparison to PEDOT:PSS-based cell. *FF* is known to be connected to resistive effects, either in series or in parallel, which limits the electrical power delivered by a solar cell. Improvement in contact resistive effects derives from the capacity of the outer anode interface for simultaneous hole extraction and electron blocking, a feature that states the contact selectivity. Such *FF* increment is discussed below.

A typical impedance response ($Z' - Z''$ plot) of PSCs is shown in Figure 7.11. The appropriate equivalent circuit model that provides a high quality to fit two arcs for these IS data is also included in Figure 7.11. This model has a R_S resulting from the electrode contacts. At lower frequencies, the $Z' - Z''$ plot is related to the R_{rec} and C_μ, both are represented as $R_{rec} - C_\mu$ subcircuit and are illustrated in the impedance spectra as a large arc dominant. The R_{rec} is related to the recombination flux and C_μ related to carrier storage.[26] At higher frequencies, an additional arc is clearly observed in the $Z' - Z''$ plot for the 30 nm-thick NiO (UVO/AT)-based solar cell represented in Figure 7.11. This high frequency arc is also visible, although to a minor extend, with the others devices as shown in Figure 7.11 for 30 nm NiO (AT/UVO)-based solar cell. This extra arc at high frequencies is represented by a parallel interlayer resistance (R_i) and capacitance (C_i) as $R_i - C_i$ subcircuit. However, in some devices at low voltages, sometimes the arc at high frequencies disappears and those cases the equivalent circuit used to fit the IS data is only a R_s in series with $R_{rec} - C_\mu$ subcircuit. Thus, this extra arc is directly dependent on the HTL/active layer interface.

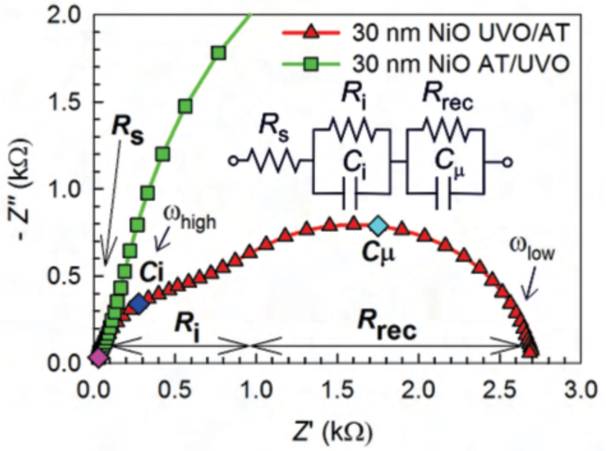

Figure 7.11. Nyquist plots for 30 nm-thick NiO (UVO/AT and AT/UVO)-based solar cells at 300 mV voltage under simulated AM1.5G 1 sun illumination (1000 W m^{-2}). The equivalent circuit model is also represented which comprises a series resistance, R_s, interlayer resistance, R_i, interlayer capacitance, C_i, recombination resistance, R_{rec}, and chemical capacitance, C_μ.

The R_i, C_i, R_{rec}, and C_μ as a function of the applied voltage are showed in Figure 7.12. The R_i contribution illustrated in Figure 7.12.a shows high (70 Ω cm^2) and independent applied voltage value for 30 nm NiO (UVO/AT)-based solar cell. Therefore, this NiO film apparently acted as an insulator film. A similar behavior has been studied in Chapter 6 with an insulator CaO layer located between active layer and cathode electrode.[27] Besides, with the same thickness (30 nm) but different order of the surface NiO treatments seems crucial to the R_i behavior; lower R_i results were achieved for the NiO (AT/UVO)-based respect to the NiO (UVO/AT)-based devices. This is likely due to a better matching in the energy levels at the interface. Furthermore, thick NiO interlayer (50 nm) compared with the thin NiO (30 nm) at the same surface conditions (AT/UVO), the R_i was also affected ~ 30 and <10 Ω cm^2, respectively. Even so, all of those cells at AT/UVO conditions had lower R_i than UVO/AT treatments OPV device. The standard device (PEDOT:PSS as HTL) and 30 nm NiO (AT/UVO)-based solar cell presented similar R_i results to the overall series resistance (<10 Ω cm^2). These results are in concordance with the *FF* data showed in Table 7.3, which were influenced not only for the R_s but also for the recombination current (j_{rec}) and R_{sh} determined by the slope of the $j - V$ curves near short-circuit conditions.

Regarding R_{rec} results follow the expected shape (Figure 7.12.b), the R_{rec} at forward voltage decreases due to the enhancement of the j_{rec}.[28] The working devices within the same active layer but different HTLs, 30 nm NiO (AT/UVO) and PEDOT:PSS, had an identical decreasing R_{rec} behavior at forward voltages. Besides, the 30 nm NiO (UVO/AT)-based solar cell showed voltage invariant for the R_{rec} due to NiO film behaved as an insulator interlayer using these specific treatments on the NiO surface. However, the main differences observed in R_{rec} behavior were focused at low applied voltages. In that voltage region, the R_{rec} tends to saturate because this resistance is not governed by the recombination flux but by a R_{sh} caused by additional leakage currents flowing in parallel.[29] It is clearly observed the high R_{sh} (~3 kΩ cm^2) for the 30 nm NiO (AT/UVO)-based solar cell comparing with the others devices (~200 Ω cm^2) at low voltages in Figure 7.12.b. This effect is shown in the $j-V$ curve which had a nearly flat response at low voltages (Figure 7.10.a) and also in the increment of the *FF*, improving its performance (Table 7.3). The interplay between hole extraction (low R_i values) and leakage current blocking (high R_{sh}) is used to define the carrier selectivity degree exhibited by the anode contact. Here, the contact selectivity, *s*, can be expressed as

$$s = 1 - \frac{R_i}{R_{sh}} \tag{7.7}$$

Selectivity values are summarized in Table 7.3, being fully selective contact $s = 1$. It is noted that *s* correlates with *FF* as expected. The definition of contact selectivity in equation 7.7 tries to capture the balance between the charge (hole) extraction ability of the anode and the detrimental leakage current flowing in parallel to the photocurrent. The ratio between R_i and R_{sh} compares the anode opposition to the hole extraction in the energy-generating quadrant of the $j-V$ curve and the resistance caused by the leakage current.

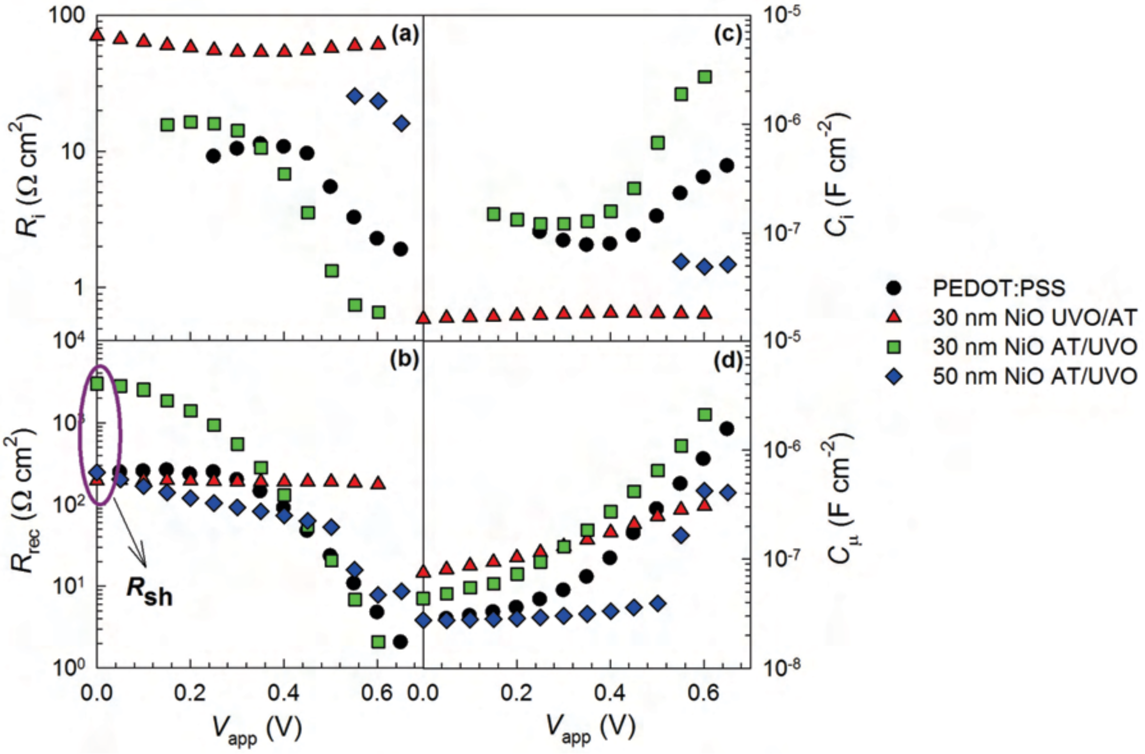

Figure 7.12. (a) Interlayer resistance R_i, (b) interlayer capacitance C_i, (c) recombination resistance R_{rec}, and (d) chemical capacitance C_μ as a function of the applied voltage extracted from the fit of the IS data using an equivalent circuit model showed in Figure 7.11 or only $R_s - (R_{rec} - C_\mu)$ when the interface contribution is not pronounced.

The C_i represented in Figure 7.12.c showed an identical C_i increment toward forward voltages for two working OPV cells with 30 nm NiO (AT/UVO) and PEDOT:PSS HTLs. On the contrary, the other two devices, namely, 30 nm NiO (UVO/AT)- and 50 nm NiO AT/UVO-based cells, displayed relatively lower constant C_i values. These differences seem to be connected to the change between dielectric to charge accumulation mechanisms at the interlayer.

Finally, the C_μ results were represented in Figure 7.12.d. At lower voltages, all OPV devices exhibited the expected capacitance response originated by the modulation of the depletion zone built up at the cathode contact, which collapses to the C_g near zero voltage.[30] At higher voltages, the C_μ values of the working OPV devices, 30 nm NiO (AT/UVO) and PEDOT:PSS HTL-based cells, exhibited the expected increase as fullerene states are occupied toward forward bias.[28] However, the 30 nm NiO (UVO/AT)-based device showed a capacitance voltage-independent under illumination related to the blocking behavior such as some previous studies with an insulating layer described in Chapter 6.[27]

7.8. Conclusions

A detailed analysis of the cathode energy equilibration of BHJ solar cells has provided. The Fermi Level mismatch established between the cathode metal and the organic layer is equilibrated by the vacuum level offset and split into two contributions: spatially extended band bending in the organic bulk and voltage drop at the interface dipole layer. The MS analysis allowed us to extract both the V_{fb} (band bending) and the p-doping density level. It has experimentally been observed that the dipole layer withstands a large part of the total Fermi Level mismatch when the blend ratio approached to ~1:1 (polymer:fullerene ratio). Interface states were related to fullerene reduced molecules covering the metal contact. Due to $C-V$ measurement is highly sensitive to the fullerene interface DOS, the relative D/A coverage at the blend/cathode interface were evaluated. $C-V$ results were in good agreement with coverage values deduced from VASE technique. To validate this technique, a variety of blends acting as BHJ layers (PCPDTBT:PC$_{70}$BM, P3HT:PC$_{60}$BM, PCDTBT:PC$_{70}$BM, and PTB7:PC$_{70}$BM) confirmed those results. System-tailored thermal annealing and the use of proper additives were able to yield favorable vertical segregation profiles, as a result, induced fullerene-rich interfaces at the cathode.

Regarding HTL, it produces an ohmic contact between ITO anode and bulk layer with an additional weak resistance that depends on the material used. An appropriate NiO work function aligned with the HOMO-donor was achieved by changing the surface NiO experimental conditions. Different thicknesses (30 nm and 50 nm) and UVO/heat sequence (either UVO/AT or AT/UVO) were analyzed to NiO films synthesized by electrodeposition from aprotic ionic liquids. A strong effect was observed on the $j-V$ curves and IS when the surface NiO conditions were modified. The 30 nm NiO (UVO/AT) interlayer acted like an insulator film in the solar cell due to the voltage-independent observed in the IS results. The performance parameters of the 30 nm (AT/UVO) HTL-based device were comparable with a standard PEDOT:PSS HTL-based device. NiO interlayers presented a superior electrical response as evidenced by the reduction in the overall R_{s}, and larger R_{sh}. These two parameters allowed us to explain the higher *FF* observed for 30 nm-thick NiO AT/UVO devices. The proposed analytical technique based on IS can be further used when different contact structures are compared, allowing for a quantification of the carrier selectivity. Thus, these results suggested that NiO is a promising candidate for HTL in OPV cells.

7.9. References

1. R. Lampande, G. W. Kim, J. Boizot, Y. J. Kim, R. Pode and J. H. Kwon, *J. Mater. Chem. A*, 2013, 1, 6895-6900.
2. Y. H. Zhou, C. Fuentes-Hernandez, J. Shim, J. Meyer, A. J. Giordano, H. Li, P. Winget, T. Papadopoulos, H. Cheun, J. Kim, M. Fenoll, A. Dindar, W. Haske, E. Najafabadi, T. M. Khan, H. Sojoudi, S. Barlow, S. Graham, J. L. Bredas, S. R. Marder, A. Kahn and B. Kippelen, *Science*, 2012, 336, 327-332.
3. W. Chen, M. P. Nikiforov and S. B. Darling, *Energy Environ. Sci.*, 2012, 5, 8045-8074.
4. F. Fabregat-Santiago, G. Garcia-Belmonte, I. Mora-Sero and J. Bisquert, *Phys. Chem. Chem. Phys.*, 2011, 13, 9083-9118.
5. E. Azaceta, S. Chavhan, P. Rossi, M. Paderi, S. Fantini, M. Ungureanu, O. Miguel, H.-J. Grande and R. Tena-Zaera, *Electrochim. Acta*, 2012, 71, 39-43.
6. H. Yang, C. Gong, G. Hong Guai and C. Ming Li, *Sol. Energy Mater. Sol. Cells*, 2012, 101, 256-261.
7. E. Azaceta, N. T. Tuyen, D. F. Pickup, C. Rogero, J. E. Ortega, O. Miguel, H.-J. Grande and R. Tena-Zaera, *Electrochim. Acta*, 2013, 96, 261-267.
8. E. L. Ratcliff, J. Meyer, K. X. Steirer, A. Garcia, J. J. Berry, D. S. Ginley, D. C. Olson, A. Kahn and N. R. Armstrong, *Chem. Mater.*, 2011, 23, 4988-5000.
9. K. X. Steirer, P. F. Ndione, N. E. Widjonarko, M. T. Lloyd, J. Meyer, E. L. Ratcliff, A. Kahn, N. R. Armstrong, C. J. Curtis, D. S. Ginley, J. J. Berry and D. C. Olson, *Adv. Energy Mater.*, 2011, 1, 813-820.
10. M. Gołda, M. Brzychczy-Włoch, M. Faryna, K. Engvall and A. Kotarba, *Mater. Sci. Eng., C*, 2013, 33, 4221-4227.
11. A. M. Cowley and S. M. Sze, *J. Appl. Phys.*, 1965, 36, 3212-3220.
12. A. M. Cowley, *J. Appl. Phys.*, 1966, 37, 3024.
13. A. Guerrero, L. F. Marchesi, P. P. Boix, S. Ruiz-Raga, T. Ripolles-Sanchis, G. Garcia-Belmonte and J. Bisquert, *ACS Nano*, 2012, 6, 3453-3460.
14. G. Li, V. Shrotriya, Y. Yao and Y. Yang, *J. Appl. Phys.*, 2005, 98, 043704.
15. J. Bisquert and G. Garcia-Belmonte, *J. Phys. Chem. Lett.*, 2011, 2, 1950-1964.
16. J. Bardeen, *Phys. Rev.*, 1947, 71, 717-727.
17. H. Vazquez, F. Flores, R. Oszwaldowski, J. Ortega, R. Perez and A. Kahn, *Appl. Surf. Sci.*, 2004, 234, 107-112.
18. H. Vazquez, W. Gao, F. Flores and A. Kahn, *Phys. Rev. B*, 2005, 71, 041306.
19. S. Engmann, V. Turkovic, P. Denner, H. Hoppe and G. Gobsch, *J. Polym. Sci., Part B: Polym. Phys.*, 2012, 50, 1363-1373.
20. I. Burgués-Ceballos, M. Campoy-Quiles, L. Francesch and P. D. Lacharmoise, *J. Polym. Sci., Part B: Polym. Phys.*, 2012, 50, 1245-1252.
21. A. Guerrero, B. Dorling, T. Ripolles-Sanchis, M. Aghamohammadi, E. Barrena, M. Campoy-Quiles and G. Garcia-Belmonte, *ACS Nano*, 2013, 7, 4637-4646.

22. J. Peet, J. Y. Kim, N. E. Coates, W. L. Ma, D. Moses, A. J. Heeger and G. C. Bazan, *Nat. Mater.*, 2007, 6, 497-500.
23. M. Campoy-Quiles, T. Ferenczi, T. Agostinelli, P. G. Etchegoin, Y. Kim, T. D. Anthopoulos, P. N. Stavrinou, D. D. C. Bradley and J. Nelson, *Nat. Mater.*, 2008, 7, 158-164.
24. T. Ripolles-Sanchis, A. Guerrero, E. Azaceta, R. Tena-Zaera and G. Garcia-Belmonte, *Sol. Energy Mater. Sol. Cells*, 2013, 117, 564-568.
25. S. Pereira, A. Gonçalves, N. Correia, J. Pinto, L. Pereira, R. Martins and E. Fortunato, *Sol. Energy Mater. Sol. Cells*, 2014, 120, Part A, 109-115.
26. G. Garcia-Belmonte, P. P. Boix, J. Bisquert, M. Sessolo and H. J. Bolink, *Sol. Energy Mater. Sol. Cells*, 2010, 94, 366-375.
27. T. Ripolles-Sanchis, A. Guerrero, J. Bisquert and G. Garcia-Belmonte, *J. Phys. Chem. C*, 2012, 116, 16925-16933.
28. G. Garcia-Belmonte, A. Guerrero and J. Bisquert, *J. Phys. Chem. Lett.*, 2013, 4, 877-886.
29. A. Guerrero, L. F. Marchesi, P. P. Boix, J. Bisquert and G. Garcia-Belmonte, *J. Phys. Chem. Lett.*, 2012, 3, 1386-1392.
30. A. Guerrero, P. P. Boix, L. F. Marchesi, T. Ripolles-Sanchis, E. C. Pereira and G. Garcia-Belmonte, *Sol. Energy Mater. Sol. Cells*, 2012, 100, 185-191.

CHAPTER 8

DEGRADATION MECHANISMS IN POLYMERIC SOLAR CELLS

Most of the results showed in this chapter are already published in:

- A. Guerrero, P. P. Boix, L. F. Marchesi, T. Ripolles-Sanchis, E. C. Pereira and G. Garcia-Belmonte, Oxygen doping-induced photogeneration loss in P3HT:PCBM solar cells, *Sol. Energy Mater. Sol. Cells*, 2012, 100, 185-191.

8.1. Introduction

Device durability, which involves stability and degradation mechanisms, is a vital interest topic on the OPV devices, playing an important role on the cell performance losses.[1,2] Up to date, there have been a large number of reports available in the literature on degradation mechanisms, mainly based on interfaces,[3,4] active materials,[4,5] contacts,[6] diffusion of molecular oxygen and water into the device,[7] interlayer and electrode diffusion,[1] electrode reaction with the organic materials,[8,9] *etc*. Probably the severest one is that PSCs usually experience fast degradation processes with exposure to oxygen, water, and long time UV illumination.[10] In regular OPV cell is usually located under ambient conditions which means under oxygen atmosphere and/or moisture experimental conditions. Degradation of OPV cells results from several simultaneous processes of degradation that change the physical, optical, electrical, and mechanical properties of the materials.[11] That information can be analyzed by the techniques listed in Table 8.1.

Table 8.1. Useful and relevant techniques for studying degradation mechanisms in OPVs.[12]

Technique	Bulk analysis	Surface analysis	2D imaging	Depth profiling	Destructive analysis	Non-destructive analysis	Chemical information	Morphological information
I–V curve	●					●		
EQE	●					●		
IS	●					●	●	●
UV-Vis	●				●	●	●	●
IR[a)]	●				●	●	●	
X-ray reflec.[b)]	●				●	●		●
RBS[c)]	●				●	●	●	●
ToF-SIMS[d)]		●	●	●	●		●	●
XPS[e)]		●	●	●	●		●	●
AFM		●	●		●		●	●
SEM		●	●		●			●
IM[f)]		●	●		●			●
2D-Imagy[g)]	●		●			●	●	●
FM[h)]	●		●				●	
Ellipsometry	●			●		●	●	●

[a)] IR: infrared spectroscopy; [b)] X-ray reflectometry; [c)] RBS: rutherford backscattering; [d)] ToF-SIMS: time-of-flight-secondary ion mass spectrometry; [e)] XPS: X-ray photoelectron spectroscopy; [f)] IM: interference microscopy; [g)] efficiency 2D-imagy; [h)] FM: fluorescence microscopy.

This chapter studies the effect on the P3HT:PC$_{60}$BM blend and the metal contact when both materials are exposed to different oxygen doping levels in complete OPV cells by $C-V$ measurements. Therefore, the Table 8.1 is completed by the $C-V$ technique. A reversible reaction between polymer and oxygen has been identified and this phenomenon affects the j_{SC} and the PCE results. Moreover, the metallic contact oxidation may occur simultaneously with the blend degradation. In order to confirm that oxidation of the active layer by oxygen is taking place, an external oxidant agent (NOBF$_4$) was also added in the blend, corroborating that the metal electrode does not degrade at low oxidant conditions. Then, a robust fabrication method in air is carried out and the samples are treated with different oxidant sources prior to cathode deposition.[13] The cell preparation procedure allows us to separate the degradation contributions originated at the device bulk from those occurring at the outer interface.

8.2. Optical properties of materials in the presence of molecular oxidants

UV-Vis spectroscopy was carried out for both *p*-doped and extra degraded P3HT solutions. An increment of oxygen doping level was performed by increasing the oxygen time exposure ($t_1 < t_2 < t_3$). The UV-Vis spectra results are represented in Figure 8.1. It is clearly shown the creation of new species that rapidly reduces the pure P3HT absorption intensity at 450 nm. The new absorption band is generated towards the red region with a maximum peak at 810 nm, which is attributed to polaronic transitions.[14] This new band is then assigned here to the specie P3HT-O_2 formed by the reaction of P3HT and oxygen.

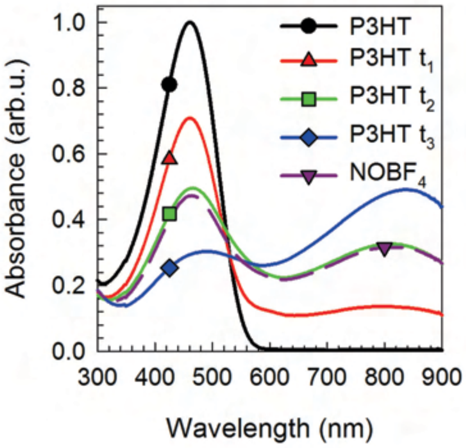

Figure 8.1. UV-Vis spectra in solution of commonly *p*-doped P3HT and extra-doped P3HT with an oxygen exposure time increased $t_1 < t_2 < t_3$ on P3HT solution (solvent *o*-DCB). It is also represented the addition of $NOBF_4$ (1×10^{-2} M) into the P3HT:PC_{60}BM blend solution to act as an oxidant of the P3HT-polymer.

As it is reported in literature, the oxygen produces new specific interaction with the polymer moiety in the P3HT:PC_{60}BM active layer, as shown in the reversible reaction[15]

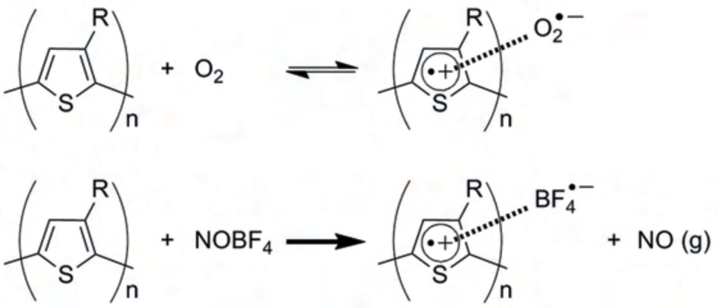

Scheme 8.1. Reversible reaction between P3HT and molecular oxygen producing new specie P3HT-O_2 proposed in literature (top). Reaction suggested for P3HT with the oxidant $NOBF_4$ (bottom).

8.3. Characterization of OPV devices: effect of the O_2 and $NOBF_4$ as oxidizing agents

Four different oxygen doping concentrations (doped cells) were compared with a pristine device (undoped externally cell). The reference cell (device 1) was prepared under the standard procedure with an architecture of glass/ITO/PEDOT:PSS/P3HT:$PC_{60}BM$/Ca/Ag (more details were explained in experimental section in the Chapter 3). Devices 2–5 were treated by increasing the oxygen doping level into the active layer with the same architecture as the reference cell. Device 2 was prepared with an exhaustive drying process to carefully eliminate the traces of water. This sample was placed in a sealed portable chamber with no-return valves to provide a flow of dry synthetic compressed air (ca. N_2 80 % and O_2 20 %) for 2 h. Devices 3 and 4 were treated with dry synthetic compressed air after P3HT:$PC_{60}BM$ annealing without exhaustively removing the traces of water. Finally, device 5 was doped with oxygen by saturation of the P3HT:$PC_{60}BM$ solution with dry oxygen before spin coating. These films (1–5) were analyzed by UV-Vis spectroscopy and the OPV devices were characterized by *EQE* and $j-V$ under AM1.5G light (1000 W m^{-2}). These results are plotted in Figure 8.2 and the photovoltaic (PV) results are summarized in Table 8.2.

Devices 2–5 were extra-doped with oxygen, producing new P3HT-O_2 species in different concentrations; as a result, the oxygen diffuses from the active layer to the Ca electrode producing a new insulator CaO layer in the interface P3HT:$PC_{60}BM$/Ca. The reaction between the Ca electrode and oxygen is as follows[16]

$$2\,\mathrm{Ca} + \mathrm{O_2} \rightarrow 2\,\mathrm{CaO}$$

The thickness of the CaO interlayer increases with the oxygen doping concentration from device 2 to 5. Additionally, the photovoltaic parameters were drastically reflected because the electrons path extraction was blocked.

Table 8.2. Photovoltaic parameters under 1 sun illumination, j_{IPCE} from the integration of *EQE* plot; doping levels (*N*), and flat-band potential (V_{fb}) derived from equation 5.22 in the MS plot for the tested cells.

ID	Dopant	Doping O_2 /Conc. $NOBF_4$	j_{sc} (mA cm^{-2})	V_{oc} (mV)	*FF* (%)	PCE (%)	j_{IPCE} (mA cm^{-2})	*N* (10^{16} cm^{-3})	V_{fb} (mV)
1	None	Reference cell	8.13	599	58	2.8	8.17	1.0	405
2	O_2	2 h[a),b)]	7.98	601	55	2.6	8.09	1.1	543
3	O_2	1 h[b)]	7.77	600	45	2.1	8.28	1.1	455
4	O_2	2 h[b)]	6.94	580	45	1.8	7.27	1.5	438
5	O_2	Dry air bubbled 10 min	6.99	560	50	1.9	7.60	2.3	319
6	$NOBF_4$	5×10^{-7} M[c)]	7.50	585	62	2.7	8.16	1.8	456
7	$NOBF_4$	1×10^{-6} M[c)]	7.17	572	61	2.5	7.97	3.5	471
8	$NOBF_4$	2×10^{-6} M[c)]	6.36	525	57	1.9	7.60	4.4	507
9	$NOBF_4$	1×10^{-2} M[d)]	5.74	525	45	1.4	5.52	10.8	390

[a)] Exhaustive drying step; [b)] flow of dry air passed through film in a chamber in the dark; [c)] stock solution in o-DCB; [d)] stock solution in acetonitrile and LiF/Al was the cathode contact.

The ‘un-doped’ and external oxygen doped blends were characterized by UV-Vis spectra showed in Figure 8.2.a. The reference and the increase exposition to dry synthetic air films (films 1–3) exhibited similar absorption spectra in terms of intensities and absorption onsets. These results are in agreement with the discussions of Egelhaaf *et al.*[17] However, films 4 and 5 showed a reduction in the absorption intensity, more pronounced at 650–700 nm region. Additionally, *EQE* measurements of the corresponding cells were also performed (see Figure 8.2.b). By integrating the

EQE spectrum, the j_{IPCE} was measured at short-circuit conditions, indicating the maximum obtainable photocurrent (Table 8.2). There is a correlation for all cells under study between intensities obtained from absorption and *EQE* spectra: reduced absorption led to reduce charge collection in the same proportion. Interestingly, none of the cells show increase of charge collection at range of 700–800 nm.

Figure 8.2.c shows relatively high efficiency (2.8 %) with high *FF* and V_{oc} for the reference cell (device 1). However, its j_{SC} is considerably low (~8 mA cm^{-2}) with respect to the thin cells (~10 mA cm^{-2})[18] due to the fact that the active layer thickness is about 400 nm. As expected, when the oxygen exposure is increased in the active layer, the device performance is affected (Table 8.2). Nevertheless, device 2 presents similar photovoltaic results respect to the reference cell because it was meticulously dried and treated with dry synthetic air for 2 h. Device 3 (1 h oxygen treatment and no additional drying step) presents similar V_{oc} to that of reference cell and device 2, but the j_{SC} was slightly reduced and the *FF* strongly decreased. An additional hour of exposure to oxygen of device 4, further decreased j_{SC} and V_{oc} was also affected. Modifying the exposure method to oxygen for device 5 provided very similar device parameters to those of device 4 with slightly reduced V_{oc} and increased *FF*.

The previous findings strongly indicate that the decrease in j_{SC} observed in the complete cells is primary caused by decreasing in light absorption, and not by losses produced during carrier transport to the collecting electrodes. The observed simultaneous reduction in intensity of both absorption and *EQE* spectra should be related to a loss in photogeneration of mobile carriers because collection efficiency diminishes as oxidation level is raised. Additionally, the decrease in photovoltage can also be explained by a decrease in photogeneration as V_{oc} depends on the amount of light absorbed that is able to yield separated charge carriers.

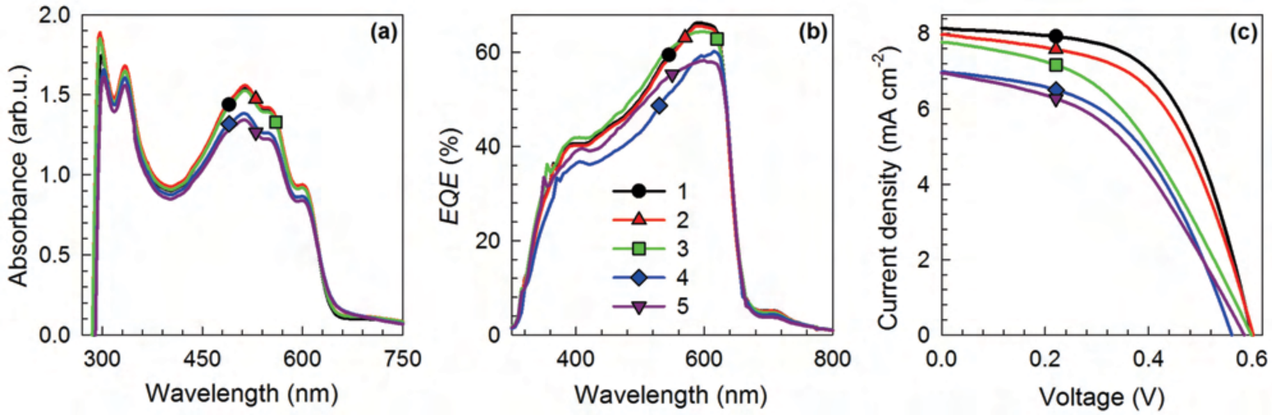

Figure 8.2. The P3HT:PC$_{60}$BM active layer un-doped extra (device 1) and oxygen concentration increment on the blend (devices 2–5) were characterized on films by (a) UV-Vis spectra and the standard OPV devices by (b) *EQE*, and (c) $j-V$ curves under 1 sun illumination.

Furthermore, in order to truly understand the effect of oxidants in the active layer, further experiments with an external addition chemical material such as NOBF$_4$ were carried out. Such oxidant agent allows us to investigate active layer *p*-doping without the effect of Ca oxidation. An irreversible reaction is proposed between P3HT polymer and NOBF$_4$ confirmed by NO gas evolution (Scheme 8.1). It was observed that the P3HT:PC$_{60}$BM solution with the highest NOBF$_4$ concentration (sample 9) is analyzed by UV-Vis spectroscopy (Figure 8.1). P3HT also reacts with this oxidant, generating analogous reaction products. The main consequence is that the P3HT absorption band intensity decreases and a new specie, $P3HT^{+}:BF_4^{-}$, is created, which absorbs at ~810 nm. A further increase in the $P3HT^{+}:BF_4^{-}$ concentration in the film was obtained by spin cast undoped solution of P3HT:PC_{60}BM, followed by a treatment of the film with $NOBF_4$ dissolved in acetonitrile. It is highlighted that the others samples prepared in this work (films 6–8) were considerably lower doped than the sample 9 (see Table 8.2) and their absorption band was only manifested as a small increase in the concentration at ~810 nm.

The second set of OPV devices used $NOBF_4$ as the oxidizing agent in the P3HT:PC_{60}BM blend were fabricated by similar procedure for the device 5 but using $NOBF_4$ in solution instead of dry synthetic air. An increase in $NOBF_4$ concentration is reported from 6 to 9 samples (Table 8.2). These films (6–9) were analyzed by UV-Vis spectroscopy and the OPV devices were characterized by *EQE* and $j-V$ under simulated AM1.5G (1000 W m^{-2}) sunlight (Figure 8.3). The photovoltaic performance is summarized in Table 8.2. Note that the heavily-doped blend with 1×10^{-2} M $NOBF_4$ concentration was rinsed with further acetonitrile to avoid the presence of the oxidant at the interface and reduce Ca oxidation. However, after cathode evaporation the Ca was severely oxidized and provided very low cell efficiency (0.006 %) with very poor photocurrent or photovoltage. Obviously, this cell was not suitable for *EQE* measurements and did not represent a good comparison within the series. In fact, this provided a good evidence for CaO generation. Cathode oxidation was partially avoided by replacing the contact configuration from Ca/Ag to LiF/Al/Ag with an increase of efficiency, 1.4 %. The selection of this cathode is motivated by an increased stability expected of LiF towards oxidant species compared to Ca. This assumption was confirmed from results obtained for device 9, whereby, the photovoltage exhibited larger values, indicating cathode relative stabilization.

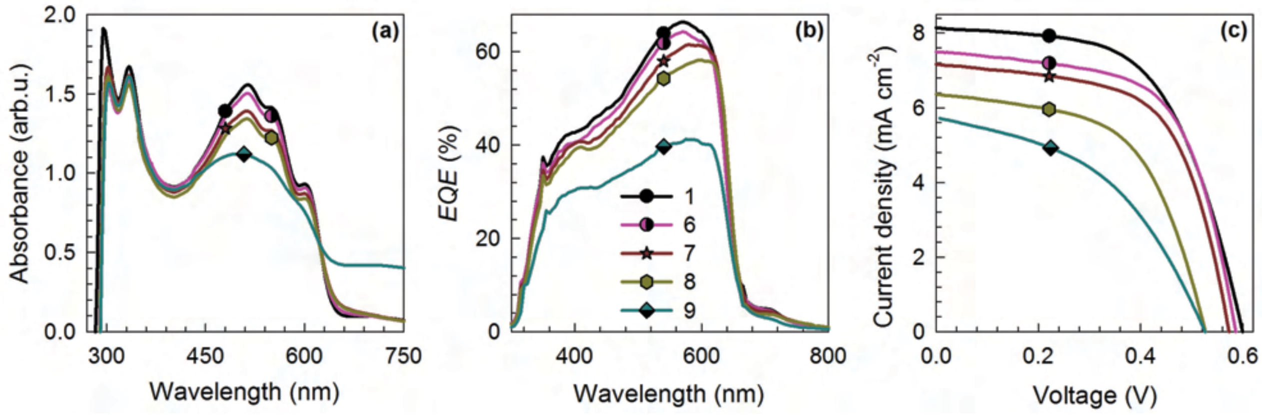

Figure 8.3. The P3HT:PC_{60}BM blend un-doped extra (device 1) and increment of $NOBF_4$ concentration on the blend (devices 6–9) were characterized on films by (a) UV-Vis spectra and the standard OPV devices by (b) *EQE* and (c) $j-V$ curves under 1 sun illumination. Note here that the cathode of devices 1, 6–8 is composed by Ca/Ag and device 9 by LiF/Al/Ag.

Absorbance spectra (Figure 8.3.a) of the blend films without the cathode contact for the $NOBF_4$ doping showed similar effect that those observed for the oxygen doped films. Increasing the concentration of $NOBF_4$ led to decreased intensity of the P3HT absorption and increased absorption towards long wavelengths. Once again, there is a correlation between the reduction in intensity of absorption in film, the *EQE* spectra and photocurrent (Figure 8.3). Very interestingly, this new chemical species observed in the absorption spectra did not contribute to the final extracted current as can be observed from the *EQE* results. It is clearly noticeable for device 9, using high $NOBF_4$

doping, which despite showing a clear band in the red region in the absorbance spectra does not contribute to the extracted charges as inferred from the low *EQE* measurement. In addition, as occurs for oxygen doping cells, j_{sc} and V_{oc} results gradually decreases when the NOBF$_4$ concentration increases. However, in contrast to samples doped with oxygen, the *FF* is slightly reduced for devices 6–8 and significantly decreased for device 9.

8.4. Dependence of *p*-doping level on the concentration of the oxidizing agents

Here, two external impurities were added on the P3HT:PC$_{60}$BM blend such as O$_2$ and NOBF$_4$ with different concentrations. This *p*-doping level resulted from defect states within the polymer bandgap can be measured by $C-V$ analysis.[19] In particular, standard P3HT:PC$_{60}$BM solar cells shows Mott-Schottky (MS) $C^{-2}(V)$ characteristics, exhibiting full depletion at reverse bias (-1 V) and a linear relationship at low forward bias (0.0–0.5 V).[19,20] An estimation of the C_{g} gives rise to a value of 7 nF cm^{-2}. Taking into account that the capacitance values observed are higher than C_{g} and that depletion width is below 100 nm at -1 V, it concludes that full depletion has not been obtained for devices with high *p*-doping levels. Here, device 1 shows a depletion width at -1 V of 350 nm, which is close to the device thickness, indicating that at this voltage the cell begins to be fully depleted, and explains why the $C^{-2}(V)$ curve exhibits saturation as the cells are reversely polarized.

The MS plots for doping caused by oxygen (devices 2–5) and NOBF$_4$ (devices 6–9) agents oxidants into the P3HT:PC$_{60}$BM blend in standard devices are represented in Figure 8.4.a and Figure 8.4.b, respectively. The reference cell, un-doped external cell (device 1), is also added in both plots. These curves clearly show different slopes for different doping concentration controlled externally of each active layer. The density of fully ionized defect states (*p*-doping level) *N* was derived from the slope by using the equation 5.22. It is assumed that the defect density explored from capacitance corresponds to those defects able to follow measuring frequency. The total concentration of acceptor impurities (intrinsic defects with additional immobile charge as O_2^- or BF_4^- counterions) for these two oxidant agents and the reference cells are summarized in Table 8.2. The total charge carrier density *N* confirms the lowest doping level ($\approx 1\times10^{16}$ cm^{-3}) for control device 1. This minimum doping level corresponds to structural defects of the polymer, and to extrinsic impurities that are inherent to the processing and purity degree of chemicals used.[20] For cells treated with molecular oxygen (devices 2–4), it is observed that under most of the conditions, the density of fully ionized acceptor impurities is increased from 1.1×10^{16} to 1.5×10^{16} cm^{-3} with respect to those obtained for reference device 1. It is interesting to note that devices 2 and 4 were exposed to oxygen for 2 h, being meticulously dried in different way. The totally dried cell (device 2) exhibits similar doping levels to that of reference device 1 and device 4 shows slightly higher doping levels. By comparison of the performance characteristics of devices 3 and 4, it is clear that the reduced performance is due to additional exposure to oxygen and not to reaction with traces of water. Slightly higher values are obtained for device 5 doped by oxygen saturation of the blend in solution prior to the annealing step. As regards cells treated with NOBF$_4$ (devices 6–9) is clearly observed that an increment of the oxidant concentration into the active layer directly affect to the *N*, being even two orders of magnitude higher for device 9 respect to the reference cell.

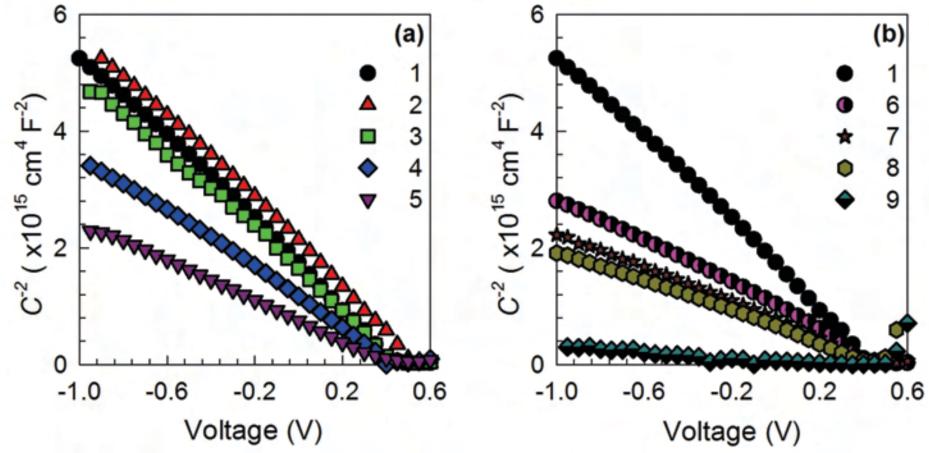

Figure 8.4. Mott-Schottky plots $C^{-2}(V)$ for standard P3HT:PC$_{60}$BM PSCs when the active layer is doped by O_2 (a) or $NOBF_4$ (b).

$C-V$ analysis provides direct information about the density of dopants that are actually ionized, contributing to the conductivity (*p*-doping). Therefore, oxidant doping modifies the concentration of mobile hole carriers as new chemical species are created. The immobile O_2^- or BF_4^- counterions contribute to the formation of a hole depletion zone near the cathode contact (band bending region), which was monitored by the $C-V$ technique (Figure 8.4). As observed, total concentrations of acceptor impurities are qualitatively in agreement with the spectroscopic measurements and the decrease in photocurrent observed for the complete cells. Figure 8.5 illustrates this correlation, including all cells studied. As can be seen an experimental relationship $j_{sc} \propto N^{-0.14}$ is found between photocurrent and doping level extracted from $C-V$ analysis.

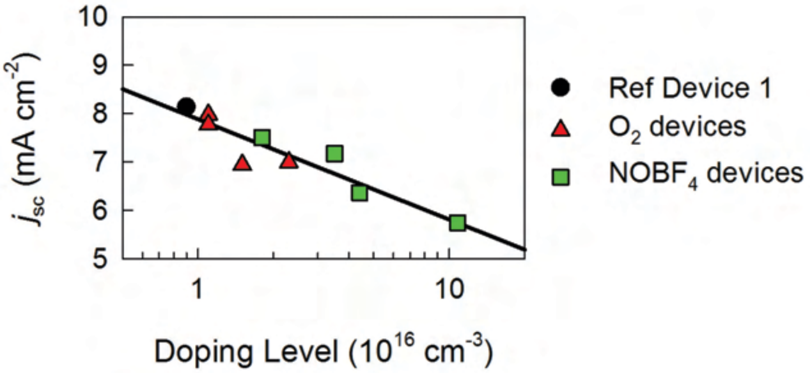

Figure 8.5. Correlation between short-circuit current density j_{sc} and doping level *N*. Data correspond to the reference cell 1, O_2 (cells from 2 to 5) and $NOBF_4$ (cells from 6 to 9) treated cells. The experimental relationship found is $j_{sc} \propto N^{-0.14}$.

However, it is hard to understand how an increment of *p*-doping level within two orders of magnitude (from 1×10^{16} cm^{-3} of device 1 up to $\approx 10^{17}$ cm^{-3} of device 9) is able to induce such a large decrease in light absorption (Figure 8.1), which is reflected in a reduction of photocurrent from 8.13 mA cm^{-2} (reference cell) down to 5.74 mA cm^{-2} (device 9). This apparent discrepancy can be solved by recalling that $C-V$ analysis only monitors the density of fully ionized charge species (those participating in the modulation of the depletion zone). It is then necessary to distinguish between O_2^- or BF_4^- counterions able to yield mobile hole carriers, from those that keep the hole attached forming the neutral complex $P3HT^+ : O_2^-$ (or $P3HT^+ : BF_4^-$) as shown in Scheme

8.2.a. Therefore, it is highlighted that only a portion of the total oxidized polymer units contribute to increase the mobile hole concentration.

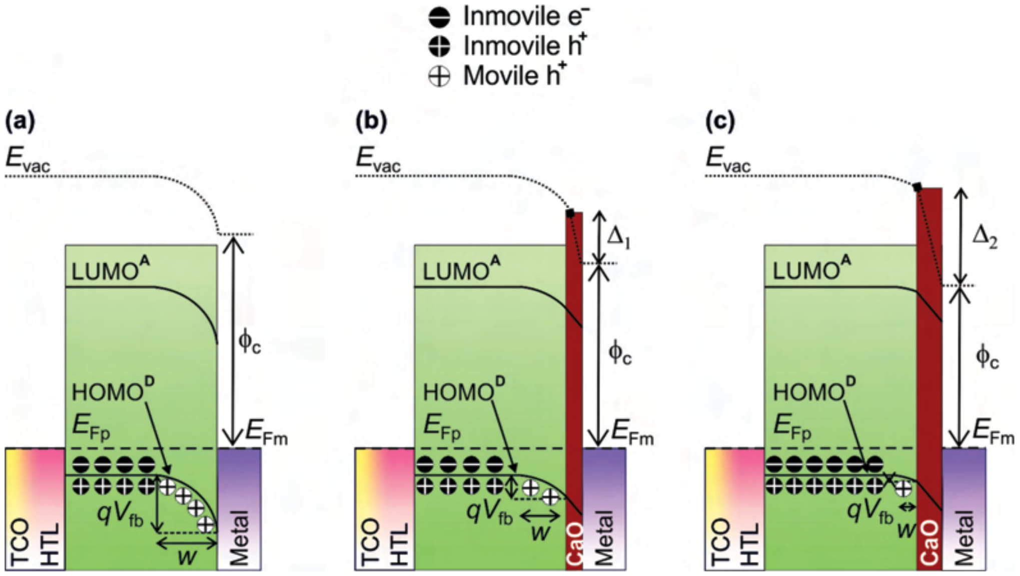

Scheme 8.2. Energy diagrams of *p*-doped blend (D:A) in a photovoltaic device with a sandwich structure, consisting of hole transport layer (HTL)/active layer/electron transport layer (ETL) in a direct metal contact (a). The flat-band voltage V_{fb} behavior when the blend is low (b) or heavily (c) *p*-doped externally with oxygen. The oxygen into the blend is then diffused to the top of the cathode (Ca) creating a new layer of CaO. The V_{fb} value is extracted from the difference between the hole Fermi Level E_{Fp} and the metal work function ϕ_C. When the bulk and the metal are in contact, the E_{Fp} and the metal Fermi Level, E_{Fm}, are aligned.

Other important parameter that can be extracted from the MS plot is the V_{fb} in the intercept of straight line with the voltage axis in Figure 8.4. V_{fb} corresponds to the energy offset between the hole Fermi Level (E_{Fp}) and the cathode metal effective work function (ϕ_c) (see Scheme 8.2.a). A V_{fb} value of 405 mV was obtained for device 1. This value increases for device 2, treated with oxygen, and followed with a gradual decrease for the subsequent samples from values of 455 mV (device 3) to 319 mV (device 5). This indicates that upon exposure to oxygen, part of the molecular oxygen produces $P3HT^{+}:O_2^{-}$ complexes, while other part generates CaO, being responsible for a drop in V_{fb} as schematically depicted in Scheme 8.2.b and Scheme 8.2.c. This oxide accommodates part of the applied voltage during $C-V$ measurement because of the formation of a dipole layer Δ. Thus, an increase in the oxygen exposure provides simultaneously P3HT *p*-doping increment and decrease in V_{fb} like it is shown in Scheme 8.2.c. This situation is clearly observed for samples treated with $NOBF_4$, where no oxidation of the metallic contact has taken place. Consequently, V_{fb} increases with increasing doping concentrations as the E_{Fp} further approaches the HOMO of the P3HT.

8.5. Conclusions

This work showed the origin of performance parameter degradation produced by oxygen external impurities to the standard P3HT:$PC_{60}BM$ active layer OPV device. The P3HT polymer creates a new specie with O_2 oxidizing agent which is characterized by red-shift absorption and reduces the P3HT absorption peak. Therefore, this specie is the responsible of a photocurrent reduction due to the minor amount of P3HT available. Additionally, loss in photovoltage for cells doped with molecular oxygen is in agreement with the reduced light absorption that generates less charge carriers, inhibiting the Fermi Level splitting (photovoltage) to some extent. The oxygen diffuses from the active layer to the Ca cathode surface creating an insulating CaO film, being an irreversible degradation. In this work, generation of this oxide takes place only in a small degree, which is the responsible of a decrease in the *FF*. These conclusions are supported by $C-V$ measurements, which provided values for degree of oxygen doping levels in the films and evidences for CaO generation in the V_{fb} values. To confirm these results, the $NOBF_4$ were also tested as an oxidizing agent characterized to have major number of impurities and without cathode oxidation. It is noteworthy that the number of impurities are attributed to the density of fully ionized charge species ($\mathrm{P3HT}^+$) and not to the hole attached forming the neutral complex $\mathrm{P3HT}^+:\mathrm{O}_2^-$ or $\mathrm{P3HT}^+:\mathrm{BF}_4^-$.

8.6. References

1. N. Grossiord, J. M. Kroon, R. Andriessen and P. W. M. Blom, *Org. Electron.*, 2012, 13, 432-456.
2. M. Jørgensen, K. Norrman, S. A. Gevorgyan, T. Tromholt, B. Andreasen and F. C. Krebs, *Adv. Mater.*, 2012, 24, 580-612.
3. G. Williams, Q. Wang and H. Aziz, *Adv. Funct. Mater.*, 2013, 23, 2239-2247.
4. J. U. Lee, J. W. Jung, J. W. Jo and W. H. Jo, *J. Mater. Chem.*, 2012, 22, 24265-24283.
5. F. Deschler, A. De Sio, E. von Hauff, P. Kutka, T. Sauermann, H. J. Egelhaaf, J. Hauch and E. Da Como, *Adv. Funct. Mater.*, 2012, 22, 1461-1469.
6. R. A. Street, P. P. Khlyabich and B. C. Thompson, *Org. Electron.*, 2013, 14, 2932-2939.
7. A. Gaur and P. Kumar, *Polym. Adv. Technol.*, 2013, 24, 630-637.
8. C. F. Zhang, Y. Hao, S. W. Tong, Z. H. Lin, Q. A. Feng, E. T. Kang and C. X. Zhu, *IEEE Trans. Electron Dev.*, 2011, 58, 835-842.
9. A. Turak, *RSC Adv.*, 2013, 3, 6188-6225.
10. W. C. Yang, Y. Yao and C. Q. Wu, *Org. Electron.*, 2013, 14, 1992-2000.
11. P. Kumar, A. Sharma and D. P. Singh, *Prog. Photovolt: Res. Appl.*, 2013, 21, 950-959.
12. M. Jorgensen, K. Norrman and F. C. Krebs, *Sol. Energy Mater. Sol. Cells*, 2008, 92, 686-714.
13. A. Guerrero, P. P. Boix, L. F. Marchesi, T. Ripolles-Sanchis, E. C. Pereira and G. Garcia-Belmonte, *Sol. Energy Mater. Sol. Cells*, 2012, 100, 185-191.
14. J. Hwang, D. B. Tanner, I. Schwendeman and J. R. Reynolds, *Phys. Rev. B*, 2003, 67, 115205.
15. M. S. A. Abdou, F. P. Orfino, Y. Son and S. Holdcroft, *J. Am. Chem. Soc.*, 1997, 119, 4518-4524.
16. S. Cros, M. Firon, S. Lenfant, P. Trouslard and L. Beck, *Nucl. Instrum. Meth. B*, 2006, 251, 257-260.
17. A. Seemann, T. Sauermann, C. Lungenschmied, O. Armbruster, S. Bauer, H. J. Egelhaaf and J. Hauch, *Sol. Energy*, 2011, 85, 1238-1249.
18. M. Reyes-Reyes, K. Kim and D. L. Carroll, *Appl. Phys. Lett.*, 2005, 87, 083506.
19. F. Fabregat-Santiago, G. Garcia-Belmonte, I. Mora-Sero and J. Bisquert, *Phys. Chem. Chem. Phys.*, 2011, 13, 9083-9118.
20. T. S. Ripolles, A. Guerrero and G. Garcia-Belmonte, *Appl. Phys. Lett.*, 2013, 103, 243306.

CHAPTER 9

CONCLUSIONS AND FUTURE WORK

This Ph.D. Thesis described the interfacial and bulk operation mechanisms in complete PSCs using optoelectronic and structural techniques. Theoretical and experimental models were employed in order to understand the electrical processes that occur in the OPV devices under dark and light illumination conditions. In particular, the charge recombination and/or transport processes are analyzed as a function of the experimentally controlled BHJ morphological variation, as well as the degradation of the active layers and metal cathode of the devices. Additionally, the physical and the chemical processes that occur under the previous conditions are associated with the photoconversion efficiency and the lifetime stability of the OPV cell. The following conclusions are inferred from the studies developed during the realization of this thesis

- A variety of BHJ solar cells containing different polymers with singular ionization energy and absorption properties (P3HT, PCDTBT and DPP860), keeping the same acceptor fullerene material, showed that the kinetics of the charge carrier recombination is influenced by the electronic coupling at polymer/fullerene interface (V_{if}). Besides, a correlation between molecular mixture V_{if} of the donor/acceptor (D/A) system and loss in V_{oc} is observed because the V_{oc} parameter depends on the separation of the hole and electron Fermi Levels, therefore, an improvement of this value is observed when the charge is separated and not recombined. Thus, high V_{oc} results in OPV cells are addressed when the electronic coupling matrix is reduced ($V_{\mathrm{if}} < 1\,\mathrm{meV}$). As a result, the OPV devices are able to evaluate from the intermolecular distances at polymer/fullerene interfaces, being a useful guide for improvement OPV cell performance as a subsequent work.
- As regards morphological properties of the bulk in PSCs, several optical and electronic techniques were used to observe changes in the active layer properties, which impact directly on the V_{oc} and consequently on the overall cell performance. It was observed that an increase of polymer crystallinity in the bulk and a reduction of charge carrier concentration in the polymer leads to the optimum conditions to achieve large V_{oc}.
- There are some experimental evidences near open-circuit conditions that the electrons are diffused by quasi-neutral regions within active layer instead of electrical field by drift. The electron transport properties were considered in complete and working OPV devices mainly in two different systems. On the one hand, by adding located traps into the polymer:fullerene BHJ film. On the other hand, by adding an insulator interlayer between bulk and metal cathode electrode, thus inducing a blocking of the electron collection. The electronic processes that occur under light illumination have been described successfully by a general impedance model, including recombination, transport (diffusion), charge storage and contact effects. The analysis performed needs to be extended to PSCs by comprising other blend constituents, particularly different donor polymers, to fully evaluate its application degree.
- A wide analysis of the cathode energy equilibration with the organic bulk heterojunction layer of OPV devices is showed in detail from the study of the blend composition, the fullerene ratio as well as the metal cathode. Essentially, the Fermi Level mismatch established between organic layer and metal cathode is equilibrated by the vacuum level offset and split into two contributions: band bending in the organic bulk and voltage drop at the interface dipole layer. When the polymer:fullerene ratio is 1:1, a Fermi Level mismatch is showed mainly due to the dipole layer at the interface. In addition, a key parameter that establishes an efficient electron extraction is the amount of polymer or fullerene material that covered the surface of the active

layer/metal cathode interface. Accordingly, the surface coverage is measured from the combination of ellipsometry and capacitance−voltage techniques for the PCPDTBT:PC_{70}BM cell and extended knowledge for other blend composition such as P3HT:PC_{60}BM, PCDTBT:PC_{70}BM and PTB7:PC_{70}BM.

- Regarding our research, the NiO is an ideal candidate to replace the PEDOT:PSS as an anode buffer layer in standard OPV devices. The NiO was synthesized on the top of the ITO by electrodeposition from aprotic ionic liquids. The surface experimental conditions of the NiO film lead to variety of work function changes. Particularly, the OPV device with 30 nm NiO thickness and sequentially annealing and UVO treatments on the NiO surface conditions reached comparable performance parameters to a standard PEDOT:PSS cell.
- One of the critical factors of the OPV technology is the stability issue. In order to investigate the lifetime mechanism on the OPV cells, several experiments have been reached to understand the origin of the performance parameter on the degradation processes produced by external oxidizing factors such as oxygen and $NOBF_4$. These agents affect on the reduction of the electron extraction and, consequently, the photocurrent is decreased, due to the formation of a new compound into the bulk which reduces the polymer concentration. Additionally, the oxygen also degrades irreversibly the Ca metal cathode, forming an insulator CaO layer evidenced in the oxygen doping levels and V_{fb} data by Mott-Schottky measurements. This study is highly interesting because the PV market is concerned in the external degradation factors due to the OPV modules are located outdoor.
- Elementary polymer characterization was performed to measure the highest occupied molecular orbital (HOMO), lowest unoccupied molecular orbital (LUMO) and bandgap. The HOMO and LUMO levels can be calculated from the cyclic voltammetry. However, sometimes the reduction or oxidation peaks are not clearly observed. Besides, the bandgap energy was calculated from the intersection of the absorption and emission curves.

In view to the previous studies, the development of additional studies would be interesting with the aim of clarifying some aspects derived from the results of this thesis.

Firstly, designing the appropriate electron donor and/or acceptor materials with the following features such as low bandgap, high solubility with organic solvents, high crystallinity domain sizes, *etc*. Those materials should induce a favorable electron photoexcitation, diffusion and transport through the donor:acceptor (D:A) blend properly towards the electrode. Once these materials are acquired, high power conversion efficiencies can be obtained taking into account several experimental details such as concentration, D:A ratio, solvents, annealing treatments, *etc*. Furthermore, as has been discussed over this Ph.D. Thesis, in order to achieve higher V_{oc} results some requirements have to consider such as high crystalline polymer, poor charge carrier concentration and low electron coupling at the polymer/fullerene interface (V_{if}). However, these results were focused on the polymer properties, but with regard to the fullerene properties may be affected when the morphology of the bulk is modified. Additionally, is the density of the defects on the fullerene affected? And consequently, is the electron Fermi Level (E_{Fn}) shifted?

Regarding to electron and hole extraction, the charge carrier has to cross an efficient transport layer to electrodes. The buffer layers should be compatible with deposition from solution methods to avoid thermal evaporation deposition and present high transmittance. Here, the most important aim to achieve high cell efficiencies is to ensure the lowest contact resistant between layers and the proper energy level alignment between these layers and the D:A blend materials. Additionally, the contact electrodes should be highly stable, mainly under ambient conditions to achieve efficient charge extraction. For instance, the material must not have low work function due to its easy degradation process. As a result, the new anode and cathode buffer layers and electrodes should improve the OPV cell efficiency.

Not only the previous materials are highlighted important to achieve high efficiencies but also the architecture of the devices also takes decisive role. Throughout this thesis only the regular architecture was studied, but the inverse configuration is well-known to provide better stability and overall cell performance. It could be interesting to prove other geometries which include high stable and low-cost materials, flexible substrates and easy processing. It would be interesting to know the energy contributions on inverted geometry solar cell and/or other architectures because directly affects on the cell performance.

Furthermore, the scientific community has a strong commitment to improve the cell stability to extend the lifetime of the OPV devices. We analyzed the oxygen atmosphere effect in this thesis. However, other external factors such as different illumination intensities, temperature, encapsulation methods and humidity conditions are also able to degrade the bulk and the metal cathode layers. As a future work, these factors should be investigated.

The impedance spectroscopy as well as capacitance–voltage ($C-V$) measurements are required to complete the characterization of OPV devices. Both techniques defined the overall cell performance. Those new materials should corroborate our findings on the recombination and transport properties by using the complete impedance model deduced from our results. Additionally, the degradation mechanisms can be observed by both impedance spectroscopy and the $C-V$ technique.

In summary, experimental and theoretical studies were carried out in this Ph.D. Thesis to understand correctly the electrical processes that occur under dark and light illumination conditions. Stability, degradation, recombination, transport and contact effect issues were deeply analyzed in complete and operable OPV devices. All these studies could contribute successfully on the optimization of OPV and consequently pave the way for a future commercialization.

APPENDIX I

Determination of HOMO and LUMO levels of organic semiconductor materials

An organic semiconductor is characterized by HOMO and LUMO energy levels and their energy difference is called bandgap. The HOMO level is the highest occupied molecular orbital and the LUMO level is the lowest unoccupied molecular orbital. The HOMO is the orbital responsible to electron donor and the LUMO accepted it. These levels can be measured by cyclic voltammetry (*CV*) measurement. At forward and reverse biases is observed the HOMO and LUMO levels, respectively. Some semiconductor materials have some problems to measure these peaks due to the difficulty to loss or gain of electrons in the molecular structure. And consequently, oxidation or reductions peaks are weak intensity or even do not appear. This appendix is discussed the measurements of the HOMO level from the *CV* technique and the LUMO level from the difference between bandgap and HOMO level of several highlight polymers to OPV technology. The oxidation peak (HOMO level) is represented as the middle voltage between two peaks (direct and reverse) in the *CV* diagram. Additionally, the bandgap will be measured from the wavelength intersection of the absorbance and fluorescence curves of each semiconductor using the follow equation

$$E_g(\mathrm{eV}) = \frac{hc}{q\lambda} = \frac{1239.95}{\lambda(\mathrm{nm})} \qquad \text{(AI.1)}$$

being h Planck constant (6.626×10^{-34} J s^{-1}), c speed of light (3×10^{8} m s^{-1}), q elementary charge (1.602×10^{-19} Q), and wavelength (units nm). The *CV* measurements were carried out using three electrodes. The working electrode was a glass/ITO substrate and on the top was deposited a film of the polymer. The experimental conditions of the polymer were the optimum conditions to each polymer summarized in Chapter 3. The counter electrode was a platinum wire and the Ag/AgCl electrode was considered the reference electrode. These electrodes were immersed into an inert 0.1 M TBAHFP solution. The absorption and light emission measurements were carried out using an Andor iDus DV-420A intensified CCD with thermoelectric cooling coupled with a Newport 77400 MS125TM spectrograph for detection and an infrared laser diode (λ_{exc}=405 nm, 5 mW) as excitation light source. Table AI.1 showed the HOMO and LUMO energy levels as well as the energy bandgap obtained in our laboratory using de previous methologies.

Table AI.1. HOMO and LUMO levels of several polymers. HOMO level is extracted from the CV measurement; energy bandgap (E_g) from the intersection of the absorbance and fluorescence spectra; and LUMO energy is taken by the difference between E_g and HOMO level.

Polymer	**HOMO** (eV)	**LUMO** (eV)	E_g (V)
P3HT	-5.4	-3.33	1.95
TQ1	-5.85	-4.05	1.80
PCDTBT	-	-	1.93
PTB7	-5.45	-	1.63$^{a)}$
PCPDTBT	-5.34	-	1.39$^{a)}$
DPP860	-5.77	-	1.42$^{a)}$

$^{a)}$ *Optical Bandgap.*

To begin with the most common polymer used in OPV solar cells is the P3HT. Figure AI.1 shows the *CV* and the absorbance and fluorescence curves. From Figure AI.1.a can be measured the HOMO level as -5.4 eV. We adopt here the criterion of extracting the position of the P3HT HOMO level from the maximum current at the oxidation peak as indicated. This criterion situates the HOMO level at the DOS maximum, and allows viewing the tail of the distribution entering the effective bandgap at less negative energies. The oxidation peak onset value (about -5.2 eV) is in good agreement with that usually reported for this polymer.[1] The bandgap extracted from Figure AI.1.b is 1.95 eV, being the LUMO level -3.33 eV value. These results are in concordance with the literature data.[1]

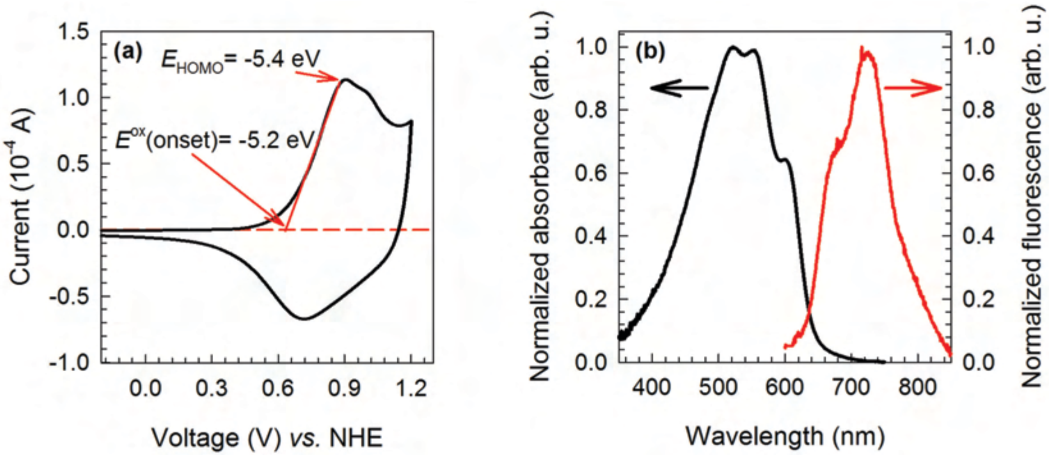

Figure AI.1. *CV* diagram (a) and absorbance and fluorescence spectra (b) of the P3HT polymer in film.

Other polymer analyzed here is the TQ1. The *CV* diagram (Figure AI.2.a) observed for this polymer shows at direct direction a well defined peak and other two peaks with low intensity that not be taken into account for calculating the HOMO energy level. Additionally, at reverse process shows a wide and undefined peak that we cannot consider. So, the HOMO level is therefore -5.85 eV. The bandgap is measured from Figure AI.2.b being 1.80 eV.[2]

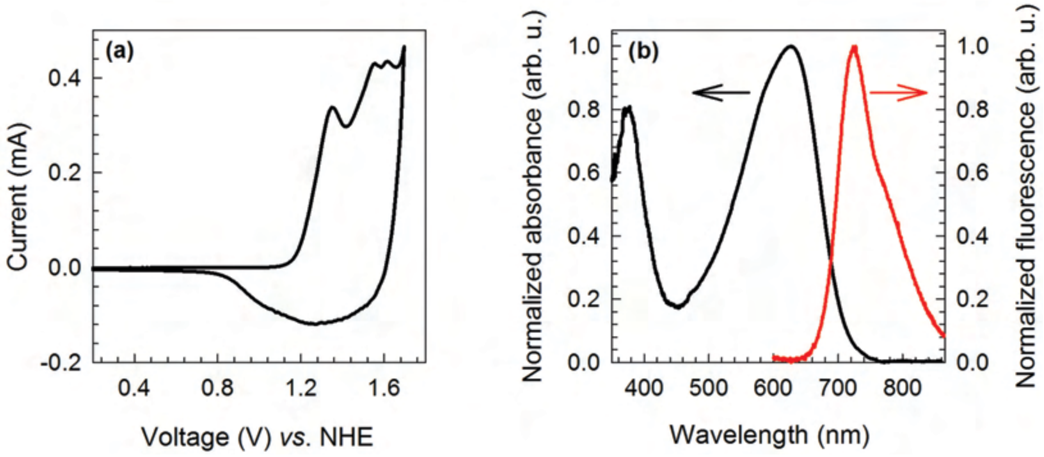

Figure AI.2. *CV* diagram (a) and absorbance and fluorescence spectra (b) of the TQ1 polymer in film.

Taking into account the PCDTBT polymer, the *CV* diagram does not show a defined peak in the standard *CV* experimental conditions which were used for the rest of these polymers. Furthermore, the bandgap measured (1.93 eV) from Figure AI.3 is in concordance with the literature data.[3]

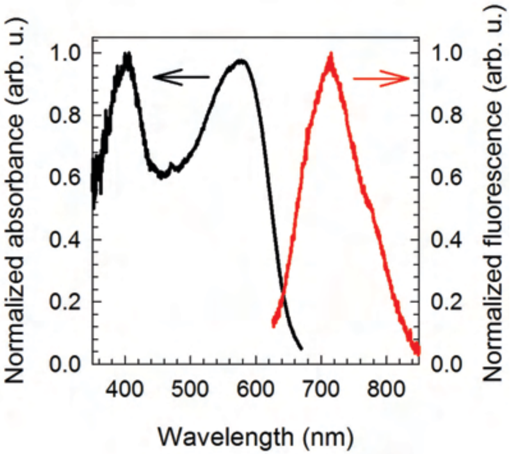

Figure AI.3. Absorbance and fluorescence spectra of PCDTBT polymer in film.

The *CV* diagram illustrated for PTB7 polymer presents a slightly peak at direct direction and no peaks at reverse direction (Figure AI.4.a). So, the HOMO energy level is -5.45 eV by these electrochemical conditions. Additionally, the fluorescence spectra show noisy signal. Therefore, the optical bandgap E_g^{opt} is only deduced from the onset of the polymer absorption spectrum in film observed in Figure AI.4.b (1.63 eV). These results differ slightly from the published data.[4]

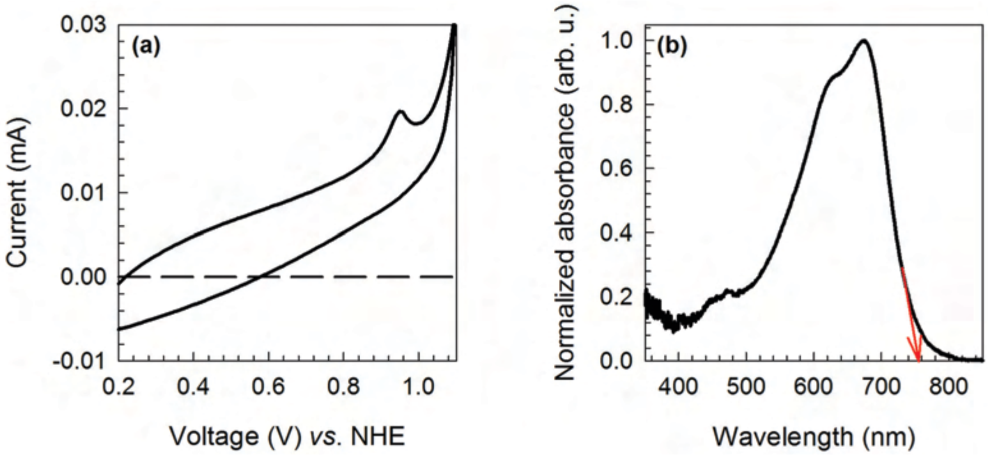

Figure AI.4. *CV* diagram (a) and absorbance spectrum (b) of the PTB7 polymer in film.

The PCPDTBT polymer displayed well defined peaks in the redox process as is shown in Figure AI.5.a, achieving a HOMO energy level of -5.34 eV. As occurred for the last polymer, the fluorescence spectrum exhibits a noisy signal and therefore, the optical bandgap E_g^{opt} (1.39 eV) is obtained from the absorbance spectra in the Figure AI.5.b, being similar result already published.[5]

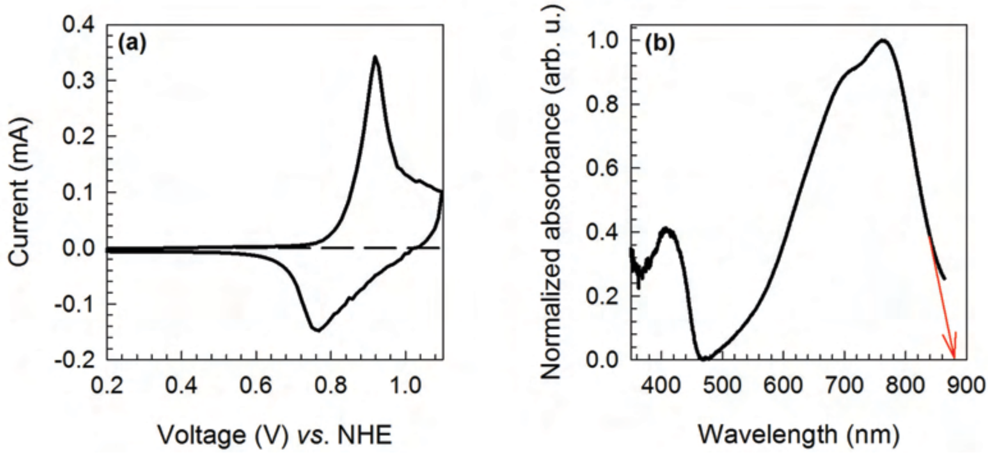

Figure AI.5. *CV* diagram (a) and absorbance spectrum (b) of the PCPDTBT polymer in film.

Finally, the DPP860 polymer exhibits the HOMO energy level at 5.77 eV value extracted from the *CV* measurement (Figure AI.6.a). The E_g^{opt} value is obtained from the absorbance spectrum in Figure AI.6.b being 1.42 eV. This polymer shows similar molecular structure to the PDPP5T polymer. Both polymers exhibit similar optical bandgap.[6]

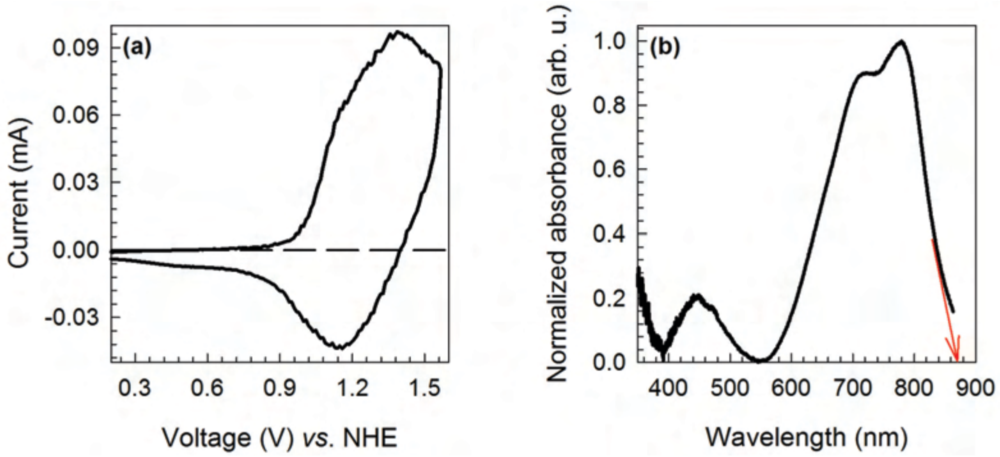

Figure AI.6. *CV* diagram (a) and absorbance spectrum (b) of the DPP860 polymer in film.

References

1. M. Al-Ibrahim, H. K. Roth, U. Zhokhavets, G. Gobsch and S. Sensfuss, *Sol. Energy Mater. Sol. Cells*, 2005, 85, 13-20.
2. E. Wang, L. Hou, Z. Wang, S. Hellström, F. Zhang, O. Inganäs and M. R. Andersson, *Adv. Mater.*, 2010, 22, 5240-5244.
3. L. Zhao, S. Zhao, Z. Xu, W. Gong, Q. Yang, X. Fan and X. Xu, *Appl. Phys. A*, 2013, 114, 1361-1368.
4. Z. He, C. Zhong, S. Su, M. Xu, H. Wu and Y. Cao, *Nat. Photon.*, 2012, 6, 591-595.
5. H. Waters, J. Kettle, S.-W. Chang, C.-J. Su, W.-R. Wu, U. S. Jeng, Y.-C. Tsai and M. Horie, *J. Mater. Chem. A*, 2013, 1, 7370-7378.
6. S. Kouijzer, S. Esiner, C. H. Frijters, M. Turbiez, M. M. Wienk and R. A. J. Janssen, *Adv. Energy Mater.*, 2012, 2, 945-949.

APPENDIX II

Experimental methods for device preparation

Some specific details about experimental methods are explained schematically in this appendix to perform PSCs for the chapters from 5 to 8. The nomenclature that is used over this appendix is listed such as *T* corresponds to the temperature of the blend in solution, S.C. is the spin coater conditions of the blend, A.T. is assigned to the annealing treatment before metal cathode deposition, and finally, *L* denoted to the active layer thickness.

A. Chapter 5

A.1. Experimental details for the section 5.2.1.

Table AII.1. Additional experimental details used in the section 5.2.1.

Polymer	**Fullerene**	**Ratio**[a)]	**Solvent**	**Conc.** mg mL^{-1}	***T*** (°C)[d)]	**S.C.** (rpm/s)	***L*** (nm)	**A.T.** (°C/min)
P3HT	$PC_{70}BM$	1:1	*o*-DCB	17	Room	1200/30	~110	130/20
PCDTBT	$PC_{70}BM$	1:4	CB:*o*-DCB[b)]	4	70	1000/60	~100	70/30
DPP860	$PC_{70}BM$	1:2	$CHCl_3$:*o*-DCB[c)]	7.5	55	7500/15	~50	Room

[a)] Polymer:fullerene (by weight); [b)] 1:2.5 (by volume); [c)] 9:1 (by volume); [d)] all solutions were stirred at the mentioned temperature for at least 16 h prior to device fabrication and were cooled down to room temperature 5 min before use it.

A.2. Experimental details for the section 5.3.2.

The blend conditions for all OPV devices were P3HT:$PC_{60}BM$ (1:1 by weight) and the concentration was 34 mg mL^{-1}.

Table AII.2. Additional experimental details used in the section 5.3.2.

ID	**Conditions**	**S.C.** (rpm/s)	**A.T.** (°C/min)	***L*** (nm)
1	Slow dry[a)]	900/10	Room	345
2	Slow dry[a)]	900/10	130/10[b)]	360
3	Fast dry	3500/120	Room	288
4	Fast dry	3500/120	90/10	271
5	Fast dry	3500/120	130/10	310

[a)] After active layer deposition by spin coater, the substrates were introduced into a petri dish and covered for 2 h; [b)] post-cathode annealing.

B. Chapter 6

B.1. Experimental details for the section 6.2.

The P3HT:$PC_{60}BM$ (1:0.8 ratio by weight) blend were prepared from dry *o*-DCB and the solution was stirred at room temperature for 24 h prior to device fabrication. The concentration used was 17 mg mL^{-1} to obtain active layer thickness of ~110 nm. The P3HT:$PC_{60}BM$ layer was deposited at speeds of 1200 rpm for 20 s followed by a slow drying process into a petri dish to provide a dry film. For cells requiring the blocking layer of CaO, a layer of Ca was thermally evaporated with a particular thickness (0.5, 5 and 10 nm). Then, the Ca evaporated was oxidized using ambient conditions overnight. At this point, all samples were thermally annealed at 130 °C for 10 min to provide adequate blend morphology and to promote oxygen desorption.

B.2. Experimental details for the section 6.6.

The P3HT:ICBA (1:0.8 ratio by weight, *o*-DCB as a solvent and concentration of 17 mg mL^{-1}) blends were stirred at room temperature for 2 h before device preparation. Besides, a known amount of PC$_{60}$BM was added (0.1 and 1 % by weight) into the P3HT:ICBA solution to perform located traps into the blend. The spin coater condition of the active layers was at 1200 rpm for 1 min to obtain a thickness of each film about 110 nm. Before cathode deposition, an annealing treatment into the glovebox was carried out at 150 °C for 10 min. Finally, the thermal cathode deposition was performed as 5 nm Ca/100 nm Ag or 1 nm LiF/100 nm Al.

C. Chapter 7

C.1. Experimental details for the section 7.3.

The P3HT:PC$_{60}$BM blend were characterized by 1:1 ratio (polymer:fullerene) by weight, *o*-DCB as a solvent, concentration of 34 mg mL^{-1} and the solution was stirred at room temperature 24 h before use the solution. The final active layer thickness was ~350 nm. Four different metal cathodes (Ca, Al, Ag and Au) were thermally evaporated (5 nm) and then 100 nm Ag was added to encapsulate the devices.

C.2. Experimental details for the section 7.4.

The different P3HT:fullerene ratios were studied (Table AII.3), being PC$_{60}$BM, PC$_{70}$BM, and ICBA the acceptor materials. The active layer thicknesses were ~ 100 nm reached by the spin coater at speeds of 1200 rpm for 30 s followed by a slow drying of the film into a petri dish. At this point, samples were thermally annealed at 130 °C for 20 min into the glovebox. The P3HT:PC$_{60}$BM and P3HT:PC$_{70}$BM solutions were prepared 24 h before use them and 2 h to the P3HT:ICBA solution.

Table AII.3. Different ratios (by weight) of P3HT: *x* fullerene.

P3HT: *x* PC$_{60}$BM	P3HT: *x* PC$_{70}$BM	P3HT: *x* ICBA
0	0	0
0.4	0.4	0.4
0.8	0.8	0.8
1.0	1.0	1.0
2.0	1.5	1.3
3.0	2.0	1.6
-	3.0	2.0
-	-	4.0

C.3. Experimental details for the section 7.5.

Four different devices are distinguished to the Mott-Schottky study. The active layer composition is performed by a pure PCPDTBT polymer, PCPDTBT:PC$_{70}$BM (1:2 ratio by weight) blend, ODT as an additive (5 % by weight) into the blend, and a rich fullerene blend (PCPDTBT:PC$_{70}$BM, 1:6 ratio by weight). The active layer thicknesses were ~40 nm.

The Variable Angle Spectroscopy Ellipsometry is compared with the capacitance–voltage measurement using different cells. To carry out this study, the active layer includes PCPDTBT:PC$_{70}$BM (1:2 ratio by weight) blend and ODT, OT and HT as additives (5 % by weight) into the blend. The solutions of additives were prepared and stirred 30 min before addition to the solution containing PCPDTBT:PC$_{70}$BM. The solution that did not contain additives was diluted with additional *o*-DCB to obtain the same final concentration. Once the additives and PCPDTBT:PC$_{70}$BM solutions were mixed, the mixtures were further stirred for 30 min at room temperature prior to device fabrication.

C.4. Experimental details for the section 7.6.

Table AII. 4. Some additional experimental details used in section 7.6.

Polymer	**Fullerene**	**Ratio**[a)]	**Additives**[b)]	***L*** (nm)	**A.T.** (°C/min)
PCPDTBT	PC$_{70}$BM	1:2	-	~100	-
			5 % HT		-
			5 % OT		-
			5 % ODT		-
P3HT	PC$_{60}$BM	1:1	-	~100	-
			-		130/10
PCDTBT	PC$_{70}$BM	1:1	-	~100	-
			-		130/10
PTB7	PC$_{70}$BM	1:1	-	~100	-
			3 % DIO		-

[a)] Polymer:fullerene (by weight); [b)] by weight.

C.5. Experimental details for the section 7.7.

Thin films of NiO were synthesized by electrochemical reduction of oxygen in an aprotic ionic liquid. This route allows the single-step deposition of metal oxides. The PYR$_{14}$TFSI used is as an aprotic ionic liquid which contain Ni(TFSI)$_2$ in concentration of 5×10^{-2} M. The importance of PYR$_{14}$TFSI lies in its aprotic nature. This material provides a labile proton free media in which an oxygenated precursor such as oxygen can be reduced avoiding the generation of hydroxide species. In this way, metal oxides (*via* 1 in Scheme AII.1) can be formed from metal cations that in the presence of OH$^-$ would precipitate as metal hydroxides (*via* 2 in Scheme AII.1) as stable compounds.

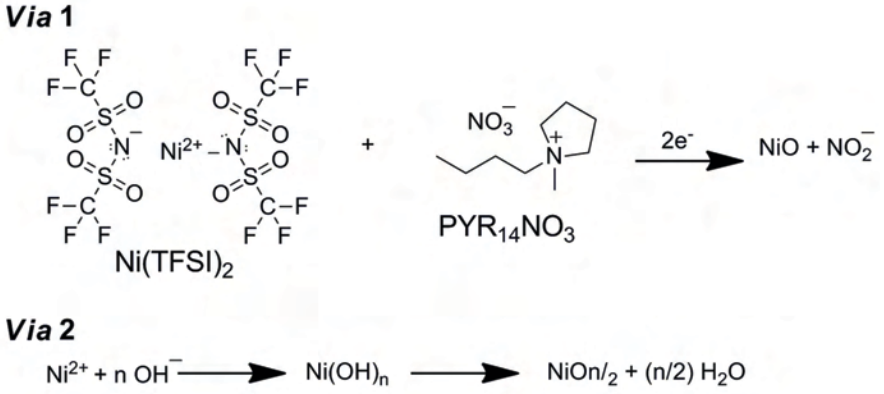

Scheme AII.1. Formation of NiO through *via* 1 and Ni(OH)$_n$ through *via* 2.

APPENDIX III

Resumen

A. Objeto y objetivos de la investigación

La preocupación sobre el calentamiento global y la limitación de combustibles fósiles como el petróleo, el carbón y el gas natural, conduce a aumentar el interés por encontrar una energía alternativa que se caracterice por ser ilimitada y que no perjudique el medio ambiente. Por esta razón, en Enero del 2004 en Berlín se organizó una conferencia llamada European Conference for Renewable Energy 'Intelligent Policy Options' donde recomendaban a las instituciones de la Unión Europea (UE) el poder abastecerse de un 20 % de energía procedente de fuentes renovables para el año 2020.[1] Las energías renovables se clasifican en geotérmica, biomasa, hidroeléctrica, eólica y solar o fotovoltaica. Para llevar a cabo el objetivo de la UE, en los últimos años, han aumentado las investigaciones en el desarrollo de estas energías alternativas, tanto en las instituciones privadas como en las públicas. En concreto, la comunidad científica centra un gran interés por la energía solar o fotovoltaica debido a que la luz solar es una fuente inagotable de energía. En este campo, ya están en comercialización los dispositivos fotovoltaicos basados en el silicio. Sin embargo, esta tecnología sigue siendo económicamente insostenible ya que los procesos de fabricación son muy elevados. Como consecuencia, ha aumentado el interés por buscar una alternativa fotovoltaica capaz de ser más económica, eficiente y estable a lo largo del tiempo. Una de las fuentes emergentes de energía solar son las células solares orgánicas o también llamadas células solares poliméricas. Esta tecnología está basada en materiales orgánicos semiconductores que se caracterizan por ser abundantes, con altos coeficientes de absorción, utilizan disoluciones en su fabricación evitando condiciones de alto vacío abaratando su coste, poseen flexibilidad mecánica, pueden modificar la banda prohibida del semiconductor cambiando la estructura molecular a través de la síntesis, *etc*. En la actualidad, están aumentando las investigaciones basadas en este tipo de células solares ya que todavía hay aspectos que no han sido analizados adecuadamente. Por ejemplo, para poder conseguir mayores eficiencias y una gran estabilidad frente a diferentes condiciones experimentales tanto de iluminación como de humedad en el dispositivo, se tienen que investigar nuevos materiales orgánicos semiconductores capaces de absorber en un mayor rango del espectro solar, además hay que diseñar geometrías para mejorar la extracción de la carga, también se tienen que investigar los procesos físico-químicos que tienen lugar dentro de la capa activa o en la interfaz entre los electrodos y la capa activa… Todos estos aspectos han de ser optimizados. Por todo ello, esta tesis doctoral se centrará especialmente en el análisis de las propiedades opto-electrónicas y estructurales de las células solares orgánicas previamente fabricadas para facilitar así su comercialización.

B. Planteamiento y metodología utilizados

La organización de esta tesis doctoral se detalla a continuación,

- El capítulo 1 resume los principales problemas que tienen en la actualidad las células solares orgánicas y cómo se dará solución en los diferentes capítulos que componen esta tesis doctoral.
- El capítulo 2 introduce los diferentes tipos de energías renovables de los cuales sólo nos centraremos en la tecnología fotovoltaica. Como ya se sabe, las células solares de silicio son las que se encuentran en la actualidad en comercialización por alcanzar una alta eficiencia. Sin

embargo, debido a su alto coste de producción, otros dispositivos emergentes como son las células solares orgánicas provocan un gran interés siendo el principal tema de esta tesis doctoral.

- El capítulo 3 describe de forma detallada todos los aspectos importantes que tiene una célula solar polimérica. Al principio del capítulo, se explica cómo surgieron este tipo de células y cómo han evolucionado hasta la actualidad estos dispositivos. Después se explican las características generales, como son: el mecanismo de fotogeneración de corriente bajo iluminación solar y los tipos de geometrías. A continuación, una amplia sección define todos los materiales necesarios para su fabricación. Posteriormente se explican los diferentes procedimientos experimentales que se utilizan para su fabricación en función de la capa activa que se vaya a utilizar. Para terminar este capítulo, se informa sobre la estabilidad y los procesos de degradación que tienen lugar junto con una amplia visión de las empresas que los comercializan y sus posibles aplicaciones.
- El capítulo 4 se centra en explicar las técnicas experimentales que se utilizan a lo largo de toda la tesis para la caracterización de las capas activas y los dispositivos fotovoltaicos. La principal técnica es la respuesta de densidad de corriente–voltaje ($j-V$) bajo iluminación. Otras técnicas de gran interés son, la eficiencia cuántica externa, la espectroscopia UV-Visible, las medidas de capacidad–voltage ($C-V$), la espectroscopia de impedancia y la medida de fotocorriente transitoria. Por otro lado, para la caracterización de la capa activa se han utilizado las siguientes técnicas: la espectroscopia de difracción de Rayos-X, la espectroscopia elipsométrica de ángulo variable, la microscopia de fuerza atómica y la microscopia electrónica de barrido. Por último, la caracterización de los polímeros se realizará con la técnica de voltametría cíclica.
- El capítulo 5 se centra en la influencia del potencial a circuito abierto (V_{oc}) cuando los procesos de recombinación y las propiedades morfológicas de la capa activa son modificadas.
- El capítulo 6 estudia las propiedades de transporte que posee la capa activa en una célula solar orgánica convencional. Para este estudio, el transporte electrónico será bloqueado de dos formas diferentes. Por un lado, se bloquea la extracción de electrones utilizando una capa aislante entre la capa activa y el cátodo metálico. Por otro lado, de añade de forma controlada en la disolución de la capa activa un material con un nivel de energía LUMO menor al de los componentes de la capa activa. De este modo, el material añadido actúa como trampas localizadas dificultando el paso de los electrones.
- El capítulo 7 desarrolla el efecto de los contactos en dispositivos completos de células solares orgánicas. El cátodo forma una barrera Schottky entre la capa activa y el metal, dicha barrera puede ser modificada en función de los materiales de la capa activa o los metales del electrodo. En el lado del ánodo se forma un contacto óhmico entre la capa transportadora de huecos y la capa activa. La película estándar que se suele utilizar como capa que bloquea el paso de los electrones en una geometría convencional es el PEDOT:PSS. Debido a sus numerosas desventajas, utilizamos el NiO para sustituir al PEDOT:PSS.
- El capítulo 8 analiza los mecanismos de degradación. Se incluye tanto aspectos de la capa activa como del cátodo. La capa del P3HT:PC$_{60}$BM es degradada mediante la exposición de forma contralada de oxígeno formando una nueva especie P3HT-O$_2$ y oxidando el metal de la intercapa de la capa activa/metal. Para separar estas dos contribuciones, otro agente oxidante

como es el $NOBF_4$, es añadido a la disolución dador:aceptor donde sólo afectará a la capa activa en concreto al polímero.

Para llevar a cabo esta tesis doctoral se sigue secuencialmente los siguientes pasos: primero, la preparación de la célula solar; segundo, la caracterización eléctrica y/o óptica; tercero, el análisis de los resultados obtenidos de cada dispositivo fotovoltaico; y por último, según los resultados obtenidos, se detalla un modelo teórico que ilustre los principales procesos electrónicos como son la recombinación, el transporte y el efecto de los contactos.

- Dos tipos de geometrías pueden tener las células solares orgánicas en función de la extracción de la carga. La geometría convencional donde el electrón es extraído a través del metal del cátodo y la geometría invertida donde el electrón se extrae a través de la capa transparente conductora con óxido (TCO). Cada una de estas geometrías se caracteriza por poseer diferentes capas con materiales semiconductores con niveles de energía y metales con funciones de trabajo diferentes. Esta tesis doctoral se centrará en la geometría convencional compuesta por vidrio/ITO/PEDOT:PSS/capa activa/Ca/Ag. La capa activa está compuesta por una mezcla interpenetrada de un polímero y un derivado del fullereno. Principalmente los materiales semiconductores dadores de electrones son: MEH-PPV, MDMO-PPV, P3HT, PCPDTBT, PCDTBT, PTB7, *etc*; los aceptores de electrones son derivados del fullereno: PCBM y ICBA. Esta capa será la encargada de absorber un fotón de la luz solar (material dador) y excitar un electrón para poder extraerlo a través del material aceptor hasta llegar al contacto.
- Entre las medidas de caracterización de las células solares, una de las más importantes es la respuesta eléctrica mediante curvas $j-V$ en la oscuridad y en condiciones de iluminación estándar (AM1.5), para la determinación de los parámetros fotovoltaicos. Por otro lado, una de las técnicas más utilizadas a lo largo de esta tesis doctoral es la espectroscopia de impedancia. Mediante los espectros de impedancia se ha analizado con especial detalle las propiedades de transporte, recombinación y contactos de los diferentes elementos que componen la célula y su influencia sobre las características DC de las mismas.
- Por último, se han desarrollado modelos que describen el comportamiento de las principales propiedades eléctricas de los materiales en estos dispositivos orgánicos. Se presta especial atención a los fenómenos de transporte electrónico, recombinación de carga e inyección de carga eléctrica a través de la interfaz orgánico/metal en las células solares poliméricas.

C. Aportaciones originales

Esta tesis doctoral contiene numerosos progresos para el desarrollo comercial de las células solares poliméricas. A continuación se detallan las principales aportaciones.

En el capítulo 5 es novedoso estudiar el comportamiento del potencial a circuito abierto en función de los procesos de recombinación y los cambios morfológicos de la capa activa. Para empezar, sigue siendo una incógnita el mecanismo que limita la cinética de la recombinación de la carga en las células solares orgánicas. Algunos modelos consideran la recombinación de la carga como un proceso de transporte controlado en similitud a lo que ocurre en una única fase formada por compuestos orgánicos.[2] Sin embargo, dichos modelos establecen una alta correlación entre el transporte, *e.g.* las propiedades de movilidad, y la cinética de recombinación. Por otro lado, otros trabajos recientes han sugerido explícitamente que siguiendo diferentes enfoques, la recombinación de la carga está estrechamente relacionada con las propiedades interfaciales moleculares.[3]

Particularmente interesantes son los resultados teóricos que observan una alta dependencia del proceso cinético de la transferencia de carga sobre las orientaciones moleculares relativas y las distancias intermoleculares.[4] A través de unos estudios, hemos comprobado que las diferencias en la recombinación de la carga entre diferentes combinaciones de dador/aceptor están relacionadas con las variaciones en la matriz de acoplamiento electrónico. Nuestros resultados revelan que las pérdidas causadas por recombinación de la carga son debidas a las propiedades de la mezcla dador:aceptor en lugar de las características energéticas de los constituyentes individuales. Por tanto, se concluye que la escala de tiempo para la recombinación de la carga está vinculada con las propiedades moleculares de la transferencia de carga en la interfaz con el dador/aceptor en lugar de con las características de transporte antes de que las cargas separadas se unan.

Respecto a las propiedades de transporte están analizadas en el Capítulo 6. Algunos investigadores indican que en equilibrio, en oscuridad y condiciones de circuito cerrado, el transporte de electrones en las células solares orgánicas es causado por un campo eléctrico interno constante situado en todo el espesor de la capa activa. Este modelo se llama metal-aislante-metal (metal-insulator-metal, MIM). Sin embargo, este modelo no tiene en cuenta las trampas[5] ni las condiciones de contorno.[6] Es por ello que suponemos otro modelo basado en portadores de cargas libres (huecos y electrones). Estos portadores pueden ser atrapados en una distribución gausiana o exponencial, donde el campo eléctrico se determina por la ecuación de Poisson. En este caso, el transporte de portadores libres vendrá dado por difusión, conducción y condiciones de contorno. Este último modelo incluye un contacto óhmico en el ánodo y una barrera Schottky en el cátodo. Si la zona depletionada es reducida o incluso eliminada en los voltajes de trabajo cercanos al punto de potencia máxima (el potencial de banda plana, flat-band potential V_{fb}), sigue existiendo una región neutra en la que el transporte de portadores minoritarios (electrones) debe ser controlado por difusión, mientras que la alta conductividad de portadores mayoritarios (huecos) asegura un apantallamiento rápido. Sin embargo, hasta ahora, la observación del transporte difusivo que está claramente predicho por este modelo ha sido difícil de alcanzar debido a otros aspectos experimentales que interfieren con los patrones de difusión. El tema principal del capítulo 6 es mostrar la evidencia por primera vez de la existencia de corrientes de difusión que rigen el transporte electrónico en potenciales de polarización directa entre el punto de máxima potencia y V_{oc} en el caso de P3HT: $PC_{60}BM$.

El objetivo principal de la primera sección del capítulo 7, es otro factor que ha sido mucho menos estudiado como es el contacto entre la capa activa nanoestructurada con el cátodo metálico. A pesar de las ideas esenciales que han proporcionado los modelos anteriores, aún no se ha establecido una visión completa del dispositivo que incluya el contacto entre la capa dadora:aceptora con el metal. Este enfoque unificado que integra tanto la capa activa como el cátodo metálico, junto con los estados interfaciales, es un avance fundamental que se aborda en este capítulo. Para corroborar el comportamiento de este modelo, se proporciona información sobre cómo afecta energéticamente el recubrimiento del dador o aceptor en la interfaz de la capa activa/cátodo metálico en dispositivos completos. Esta información se obtiene mediante la combinación de dos técnicas, una es la elipsometría y la otra es puramente eléctrica ($C-V$).

La segunda sección del capítulo 7 se centra en la capa de extracción de huecos y bloqueante de electrones. Hasta el momento, la capa transportadora de huecos más utilizada es el PEDOT:PSS, pero debido a sus numerosas desventajas, se trata de buscar una alternativa más eficiente y estable. El carácter ácido y la naturaleza higroscópica del PEDOT:PSS causa la corrosión del ITO y en consecuencia el indio podría difundirse dentro de la capa activa, degradándola. Hay muchas alternativas para reemplazar esta capa, pero la mayoría de ellas utilizan condiciones de alto vacío para su deposición siendo un gran inconveniente. Por el contrario, las películas del NiO pueden ser preparadas por electrodeposición catódica convirtiéndose en un perfecto candidato.[7] Sin embargo, el contacto de NiO es altamente sensible a las posibles reacciones químicas que tienen lugar en su superficie, la orientación del cristal y el tratamiento superficial.[8] El capítulo 7 se centra en la búsqueda de las condiciones experimentales óptimas para la película de NiO y así lograr una alta eficiencia de conversión de energía. En concreto, se observó que sobre una superficie con 30 nm de espesor de NiO se realiza secuencialmente un tratamiento térmico y después un tratamiento de radiación ultravioleta-ozono (UVO), se alcanzan eficiencias comparables con el dispositivo estándar con PEDOT: PSS.

Por último, en el capítulo 8 trata el problema de la degradación y estabilidad que poseen las células solares poliméricas bajo ciertas condiciones experimentales. Hay una controversia con el papel que hace el oxígeno como fuente de degradación en las células solares orgánicas. Por un lado, se ha publicado que el polímero P3HT forma un complejo con el oxígeno.[9,10] Sin embargo, se ha publicado que una película sólida de polímero P3HT incluso a altas concentraciones permanece inalterada frente al estado singlete del oxígeno.[11] Por lo tanto, la degradación de la película parece tener lugar a través de un mecanismo de radicales que requiere la superación de una energía de activación.[12] Curiosamente, estudios recientes sobre mecanismos de degradación inducidos por el oxígeno en las células solares poliméricas con P3HT han identificado interacciones reversibles e irreversibles con el oxígeno y este polímero.[13,14] En particular en el capítulo 8, observamos experimentalmente que mediante la exposición controlada de oxígeno a la capa activa que está formada por una mezcla de P3HT:PC$_{60}$BM hay una disminución simultánea de fotocorriente (j_{sc}) y del pico de absorción del P3HT debido a la formación de un nuevo componente en la mezcla dador:aceptor que absorbe hacia la región del rojo en el espectro visible. A partir del análisis $C-V$ se calcula el aumento del nivel de dopaje tipo p cuando aumenta la concentración de oxígeno y una disminución del potencial de banda plana V_{fb} debido a una oxidación del contacto metálico causado por la difusión de oxígeno desde la capa activa hasta el cátodo. Es por ello que se establece una conexión directa entre el mecanismo de degradación debido a la acción del oxígeno con los parámetros fotovoltaicos de una célula solar orgánica.

D. Conclusiones obtenidas y Futuras líneas de investigación

Esta tesis doctoral describe los mecanismos de funcionamiento de la capa activa y de la interface entre la capa activa y los electrodos en células solares orgánicas completas utilizando técnicas optoelectrónicas y estructurales. Los modelos teóricos y procedimientos experimentales se han llevando a cabo con el fin de entender todos los procesos eléctricos que tienen lugar en las células solares poliméricas bajo condiciones de iluminación de luz y oscuridad. Esta tesis doctoral se ha centrado en cambios morfológicos de la capa activa, procesos de recombinación y de transporte y en mecanismos de degradación. A continuación, se detallan las principales conclusiones inferidas.

- Hemos demostrado que la cinética de la recombinación de portadores de carga está influenciada por el acoplamiento electrónico (V_{if}) en la interfaz polímero/fullereno en una gran variedad de células solares poliméricas que contienen polímeros con diferentes propiedades de energía de ionización y de absorción. En particular, el acoplamiento electrónico molecular del sistema dador:aceptor (V_{if}) se correlaciona con la pérdida en el voltaje a circuito abierto (V_{oc}).

Llegamos a la conclusión de que para lograr un alto rendimiento en las células solares orgánicas es necesario reducir el acoplamiento electrónico ($V_{\mathrm{if}} < 1\,\mathrm{meV}$). Como resultado, somos capaces de describir nuestro sistema con distancias intermoleculares en la interfaz polímero:fullereno siendo una guía útil para mejorar el rendimiento de células solares poliméricas para un futuro trabajo.

- Mediante la utilización de técnicas ópticas (difracción de rayos-X y espectroscopia de absorbancia) y electrónicas (capacidad–voltage) se observaron cambios morfológicos en las propiedades de la capa activa que impactan directamente en el valor del V_{oc} y en consecuencia en el rendimiento general de la célula solar. Llegamos a la conclusión de observar simultáneamente tres efectos cuando se consiguen altos valores de V_{oc}: aumento en la cristalinidad del polímero, mayor tamaño del dominio de polímero y menor concentración de portadores. Sin embargo, este estudio se centra en las propiedades del polímero, pero las propiedades del fullereno pueden ser perturbadas cuando se modifica la morfología de la capa activa. Además, la densidad de los defectos en el fullereno se ven afectados? Y, en consecuencia, el nivel de fermi de los electrones (E_{Fn}) cambia?
- Llegamos a las propiedades de transporte en dispositivos orgánicos completos y operativos. Por primera vez, los procesos electrónicos que ocurren bajo iluminación se han descrito con éxito utilizando un modelo de impedancia general, incluyendo la recombinación, el transporte (difusión), el almacenamiento de carga y los efectos de contacto tanto para dispositivos que funcionan correctamente como para los que se ha dificultado la transporte electrónico. Para estos últimos dispositivos, ya sea añadiendo una capa intermedia aislante entre la capa activa y el cátodo metálico o trampas localizadas dentro de la capa activa, en ambos casos el transporte electrónico se ve dificultado. Este análisis debería de ampliarse a las células solares orgánicas que comprendan otros componentes de la capa activa, en particular con diferentes polímeros, para evaluar plenamente su grado de aplicación.
- Hemos mostrado un análisis completo del equilibrio energético del cátodo en las células solares orgánicas. El desajuste del nivel de fermi establecido entre la capa orgánica y el cátodo metálico se equilibra por el nivel de vacío offset junto con dos contribuciones: el potencial de la banda depletionada y la caída de potencial debida a la formación de un dipolo en la interfaz entre la capa activa y el cátodo metálico. Cuando la proporción polímero:fullereno es 1:1, el desajuste del Fermi Nivel se debe principalmente a la capa del dipolo en la interfaz. Además, un parámetro clave que establece una eficiente extracción electrónica, y por tanto una alta eficiencia, es la cantidad de polímero o fullereno que se encuentra en la interface de la capa activa/cátodo. Para ello, se ha determinado este valor mediante la combinación de las técnicas de elipsometría (variable-angle spectroscopic ellipsometry, VASE) y capacidad–voltage para la capa activa compuesta por PCPDTBT:$\mathrm{PC_{70}BM}$. Para validar estos resultados, una gran variedad de mezclas de polímero:fullereno, como son: P3HT:$\mathrm{PC_{60}BM}$, PCDTBT:$\mathrm{PC_{70}BM}$ y PTB7:$\mathrm{PC_{70}BM}$, fueron analizadas confirmando los resultados. Este estudio se centra en una geometría convencional, pero sería interesante conocer las contribuciones energéticas en una célula solar orgánica tipo invertida.
- Según los estudios realizados, se concluye que es posible conseguir eficiencias comparables de células solares con PEDOT:PSS, sustituyendo esta capa por otra de NiO si ésta es tratada superficialmente con unas condiciones experimentales concretas. Una capa de NiO sintetizada

por electrodeposición a partir de líquidos iónicos apróticos, tiene las siguientes condiciones experimentales óptimas: un espesor de 30 nm y la superficie se trata de forma secuencial primero con una calcinación y después un tratamiento ultravioleta-ozono (UVO). Estas condiciones hacen tener la posición correcta de la función de trabajo del NiO para una correcta extracción de huecos e inhibición del paso de los electrones. Un trabajo adicional sería investigar otra capa extractora de huecos que pueda mejorar notablemente la eficiencia de una célula convencional reduciendo la resistencia óhmica.

- Uno de los factores críticos de la tecnología fotovoltaica orgánica es la problemática con la estabilidad. Con el fin de saber el origen de la degradación en las células solares orgánicas, dos agentes oxidantes externos se han añadido a la capa activa, como son el oxígeno y el $NOBF_4$. Estos agentes reducen la extracción de electrones debido a la formación de un nuevo compuesto que disminuye la concentración del polímero. Además, el oxígeno también degrada irreversiblemente al cátodo metálico, formando CaO donde se ve evidenciado en los niveles de dopaje de oxígeno N y en el potencial de banda plana V_{fb} calculado a partir de las medidas de Mott-Schottky. Además, el agente $NOBF_4$ no reacciona con el cátodo como se muestra en los resultados de MS. En general, el mercado fotovoltaico tiene un gran interés en los factores de degradación externos debido a que los módulos se ubican a la intemperie. En concreto, este trabajo analiza el efecto de la atmósfera de oxígeno. Sin embargo, otros factores externos, tales como diferentes intensidades de iluminación, temperatura, métodos de encapsulación y condiciones de humedad también son capaces de degradar la capa activa y el cátodo metálico. Como trabajo futuro, estos factores externos deberían ser investigados.
- Por último, los niveles de energía HOMO y LUMO de los polímeros orgánicos semiconductores se determinan a partir de la voltametría cíclica (*CV*). Sin embargo, a veces los picos de oxidación o reducción no se observan con claridad porque hay poca afinidad para extraer o añadir electrones a la estructura molecular, respectivamente. La energía de la banda prohibida se calcula a partir de la intersección de las curvas de absorción y de emisión.

En resumen, esta tesis doctoral ha llevado a cabo estudios experimentales y teóricos para entender perfectamente los procesos eléctricos que se producen bajo condiciones de iluminación y oscuridad en células solares orgánicas. Los problemas en procesos de recombinación y el transporte, el efecto de los contactos y mecanismos de degradación fueron analizados profundamente en dispositivos orgánicos completos. Todos estos estudios ayudarían en la optimización de las células solares poliméricas y por consiguiente facilitarían su comercialización.

E. Referencias

1. A. Jäger-Waldau, *Renew. Sust. Energy Rev.*, 2007, 11, 1414-1437.
2. M. Kuik, L. J. A. Koster, G. A. H. Wetzelaer and P. W. M. Blom, *Phys. Rev. Lett.*, 2011, 107, 256805.
3. S. Yamamoto, A. Orimo, H. Ohkita, H. Benten and S. Ito, *Adv. Energy Mat.*, 2012, 2, 229-237.
4. S. W. Ko, E. T. Hoke, L. Pandey, S. H. Hong, R. Mondal, C. Risko, Y. P. Yi, R. Noriega, M. D. McGehee, J. L. Bredas, A. Salleo and Z. A. Bao, *J. Am. Chem. Soc.*, 2012, 134, 5222-5232.
5. M. T. Neukom, N. A. Reinke and B. Ruhstaller, *Sol. Energy*, 2011, 85, 1250-1256.
6. R. C. I. MacKenzie, T. Kirchartz, G. F. A. Dibb and J. Nelson, *J. Phys. Chem. C*, 2011, 115, 9806-9813.

7. H. Yang, C. Gong, G. Hong Guai and C. Ming Li, *Sol. Energy Mater. Sol. Cells*, 2012, 101, 256-261.
8. M. D. Irwin, J. D. Servaites, D. B. Buchholz, B. J. Leever, J. Liu, J. D. Emery, M. Zhang, J.-H. Song, M. F. Durstock, A. J. Freeman, M. J. Bedzyk, M. C. Hersam, R. P. H. Chang, M. A. Ratner and T. J. Marks, *Chem. Mater.*, 2011, 23, 2218-2226.
9. M. S. A. Abdou, F. P. Orfino, Y. Son and S. Holdcroft, *J. Am. Chem. Soc.*, 1997, 119, 4518-4524.
10. A. Aguirre, S. C. J. Meskers, R. A. J. Janssen and H. J. Egelhaaf, *Org. Electron.*, 2011, 12, 1657-1662.
11. M. Manceau, A. Rivaton and J. L. Gardette, *Macromol. Rapid Commun.*, 2008, 29, 1823-1827.
12. M. V. Madsen, T. Tromholt, A. Bottiger, J. W. Andreasen, K. Norrman and F. C. Krebs, *Polym. Degrad. Stabil.*, 2012, 97, 2412-2417.
13. A. Seemann, T. Sauermann, C. Lungenschmied, O. Armbruster, S. Bauer, H. J. Egelhaaf and J. Hauch, *Sol. Energy*, 2011, 85, 1238-1249.
14. A. Sperlich, H. Kraus, C. Deibel, H. Blok, J. Schmidt and V. Dyakonov, *J. Phys. Chem. B*, 2011, 115, 13513-13518.

APPENDIX IV

Conferences, Workshops, Summer schools and Awards

Conferences

- **3rd Hybrid and Organic Photovoltaics Conference (HOPV11)**, Valencia (Spain), 15th to 18th May 2011.
- **Scientific Meeting on Nanomaterials for Clean Energies (NMCE)**, Valencia (Spain), 25th May 2011.
- **Up-converting materials: from fundamentals to applications**, Castellón (Spain), 4th April 2013.
- **5th International Conference on Hybrid and Organic Photovoltaics (HOPV13)**, Seville (Spain), 5th to 8th May 2013. Poster titled ‘Equivalent circuit model for electronic transport in bulk-heterojunction solar cells’.

Workshops

- **Spain-Japan cooperation Workshop on Quantum Dot Sensitizers**, Aldea Roqueta, (Castellón, Spain), 8th March 2011.
- **Workshop on nano-bio: applications in energy, sensors and medicine**, Castellón (Spain), 27th September 2013.

Summer schools

- **XII Escuela Nacional de materiales Moleculares**, Benicasim (Castellón, Spain), 6th to 11th February 2011. Oral communication titled ‘Nanostructured solar cells with organic dyes’.
- **Nanostructured Hybrid Materials for Energy Conversion and Storage**, Bari (Ostuni, Italy), 5th to 10th June 2011. Poster titled ‘Measurement of oxygen doping levels in P3HT:PCBM blends on organic solar cells’.
- **IV European School on Molecular Nanoscience (ESMolNa)**, Peñíscola (Castellón, Spain), 23rd to 28th October 2011. Oral communication titled ‘Measurement of oxygen doping levels in P3HT:PCBM blends on organic solar cells’.
- **International Conference on Simulation of Organic Electronics and Photovoltaics (SimOEP12)**, Oliva (Valencia, Spain), 10th to 14th June 2012. Poster titled ‘Equivalent circuit model for electronic transport to apply in bulk-heterojunction solar cells’.
- **I-CAMP Summer School on Renewable and Sustainable Energy**, Boulder (Colorado, USA), 16th July to 11th August 2012. Poster titled ‘Equivalent circuit model for electronic transport to apply in bulk-heterojunction solar cells’.

Awards

- Best Poster Award in the Summer School **Nanostructured Hybrid Materials for Energy Conversion and Storage**, Bari (Ostuni, Italy), 5th to 10th June 2011. Poster was titled ‘Measurement of oxygen doping levels in P3HT:PCBM blends on organic solar cells’.

- **I-CAMP Fellowship to attend University of Colorado Boulder**, $1500 fellowship including living expense and registration fee.

APPENDIX V

Publication list

Publications related with this thesis:

- A. Guerrero, P. P. Boix, L. F. Marchesi, T. Ripolles-Sanchis, E. C. Pereira and G. Garcia-Belmonte, Oxygen doping-induced photogeneration loss in P3HT:PCBM solar cells, *Sol. Energy Mater. Sol. Cells*, 2012, 100, 185-191.
- A. Guerrero, L. F. Marchesi, P. P. Boix, S. Ruiz-Raga, T. Ripolles-Sanchis, G. Garcia-Belmonte and J. Bisquert, How the Charge-Neutrality Level of Interface States Controls Energy Level Alignment in Cathode Contacts of Organic Bulk-Heterojunction Solar Cells, *ACS Nano*, 2012, 6, 3453-3460.
- T. Ripolles-Sanchis, A. Guerrero, J. Bisquert and G. Garcia-Belmonte, Diffusion-Recombination Determines Collected Current and Voltage in Polymer:Fullerene Solar Cells, *J. Phys. Chem. C*, 2012, 116, 16925-16933.
- A. Guerrero, T. Ripolles-Sanchis, P. P. Boix and G. Garcia-Belmonte, Series resistance in organic bulk-heterojunction solar devices: Modulating carrier transport with fullerene electron traps, *Org. Electron.*, 2012, 13, 2326-2332.
- T. Ripolles-Sanchis, S. R. Raga, A. Guerrero, M. Welker, M. Turbiez, J. Bisquert and G. Garcia-Belmonte, Molecular Electronic Coupling Controls Charge Recombination Kinetics in Organic Solar Cells of Low Bandgap Diketopyrrolopyrrole, Carbazole, and Thiophene Polymers, *J. Phys. Chem. C*, 2013, 117, 8719-8726.
- A. Guerrero, B. Dörling, T. Ripolles-Sanchis, M. Aghamohammadi, E. Barrena, M. Campoy-Quiles and G. Garcia-Belmonte, Interplay between Fullerene Surface Coverage and Contact Selectivity of Cathode Interfaces in Organic Solar Cells, *ACS Nano*, 2013, 7, 4637-4646.
- T. Ripolles-Sanchis, A. Guerrero, E. Azaceta, R. Tena-Zaera and G. Garcia-Belmonte, Electrodeposited NiO anode interlayers: Enhancement of the charge carrier selectivity in organic solar cells, *Sol. Energy Mater. Sol. Cells*, 2013, 117, 564-568.
- T. S. Ripolles, A. Guerrero and G. Garcia-Belmonte, Polymer defect states modulate open-circuit voltage in bulk-heterojunction solar cells, *Appl. Phys. Lett.*, 2013, 103, 243306.

Other publications:

- Teresa S. Ripolles, C. Koenigsmann, B. J. Brennan, C. F.A. Negre, J. A. Torre, M. Koepf, A. C. Durrell, R. L. Milot, V. S. Batista, G. W. Brudvig, R. H. Crabtree, C. A. Schmuttenmaer, J. Bisquert, Substitution of a Hydroxamic Acid Anchor into the MK-2 Dye for Enhanced Photovoltaic Performance and Water Stability in a DSSC, *Phys. Chem. Chem. Phys.*, 2014, accepted.

- B. Suarez, V. Gonzalez-Pedro, T. S. Ripolles, R. S. Sanchez, L. Otero and I. Mora-Sero, Recombination Study of Combined Halides (Cl, Br, I) Perovskite Solar Cells, *J. Phys. Chem. Lett.*, 2014, 5, 1628-1635.

- T. Ripolles-Sanchis, B.-C. Guo, H.-P. Wu, T.-Y. Pan, H.-W. Lee, S. R. Raga, F. Fabregat-Santiago, J. Bisquert, C.-Y. Yeh and E. W.-G. Diau, Design and characterization of alkoxy-wrapped push-pull porphyrins for dye-sensitized solar cells, *Chem. Commun.*, 2012, 48, 4368-4370.

- E. M. Barea, V. Gónzalez-Pedro, T. Ripollés-Sanchis, H.-P. Wu, L.-L. Li, C.-Y. Yeh, E. W.-G. Diau and J. Bisquert, Porphyrin Dyes with High Injection and Low Recombination for Highly Efficient Mesoscopic Dye-Sensitized Solar Cells, *J. Phys. Chem. C*, 2011, 115, 10898-10902.

- E. Barea, X. Xu, V. Gonzalez-Pedro, T. Ripolles-Sanchis, F. Fabregat-Santiago and J. Bisquert, Origin of efficiency enhancement in Nb_2O_5 coated titanium dioxide nanorod based dye sensitized solar cells, *Energy Environ. Sci.*, 2011, 4, 3414-3419.

Solar Energy Materials & Solar Cells 100 (2012) 185–191

Contents lists available at SciVerse ScienceDirect

Solar Energy Materials & Solar Cells

journal homepage: www.elsevier.com/locate/solmat

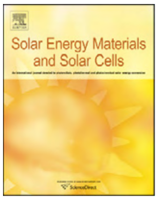

Oxygen doping-induced photogeneration loss in P3HT:PCBM solar cells

Antonio Guerrero [a,*], Pablo P. Boix [a], Luís F. Marchesi [a,b], Teresa Ripolles-Sanchis [a], Ernesto C. Pereira [b], Germà Garcia-Belmonte [a,*]

[a] Photovoltaic and Optoelectronic Devices Group, Departament de Física, Universitat Jaume I, ES-12071 Castelló, Spain
[b] Laboratório Interdisciplinar de Electroquímica e Cerâmica (LIEC), Universidade Federal de São Carlos, São Carlos, Brazil

ARTICLE INFO

Article history:
Received 5 December 2011
Received in revised form
5 January 2012
Accepted 14 January 2012
Available online 7 February 2012

Keywords:
Organic photovoltaics
Oxygen doping
Capacitance
Degradation

ABSTRACT

This work investigates the loss in performance induced by molecular oxygen in bulk heterojunction solar cells. We observe that upon exposure to molecular oxygen both formation of $P3HT^+:O_2^-$ complex and metal oxidation at the interface between the active layer and metallic contact occur. These two different effects were separately investigated using $NOBF_4$ as an oxidant. Our procedure has allowed studying p-doping of the active layer independently from contact degradation. A loss in photocurrent is associated with formation of $P3HT^+:O_2^-$ complex, which reduces the concentration of neutral P3HT present in the film in accordance with absorption and external quantum efficiency spectra. This complex is regarded as a source of a pathway of reversible degradation. Capacitance–voltage measurements allow for an accurate extraction of p-doping levels of the active layer produced by the presence of charged O_2^- species. In addition, one of the irreversible degradation pathways is identified to be oxidation of the metallic contact to form CaO. This oxide forms a thin dipole layer producing a voltage drop across the active layer/Ca interface, which has a direct impact on the open circuit voltage and fill factor.

1. Introduction

Organic solar cells have attracted much attention over the last decade, and currently power conversion efficiencies over 8% have been reported [1]. In order to obtain further improvements in long-term solar cell performance a detailed understanding of the device stability and degradation mechanisms is required [2]. Known degradation mechanisms include diffusion of molecular oxygen and water into the device [3], degradation of interfaces [4], degradation of the active material [5], interlayer and electrode diffusion[6] or electrode reaction with the organic materials [7]. In regular architecture solar cells prepared in ambient conditions oxygen has always been regarded as a source of cell performance losses [8]. In terms of chemical modifications oxygen plays an important role as it is responsible for chemical degradation pathways in the dark and, more rapidly, in combination with light [4]. Indeed, degradation of systems comprising P3HT [9] and C_{60} [10,11] induced by oxygen has been reported to decrease carrier mobilities and enhance trap densities. Additionally, the effect of oxygen has normally been related to degradation of the metallic aluminium or calcium contact to form oxides in a regular configuration [12].

There is some controversy on the role of oxygen as a degradation source. On one hand, P3HT has been reported to form a complex with oxygen [13,14]. However, in the solid state even at high concentrations of singlet oxygen the solid film has been reported to remain unaltered [15]. Thus, degradation of the film appears to take place through a radical mechanism that requires overcoming an activation energy [16]. Interestingly, recent studies on degradation pathways induced by oxygen of semi-permeable bulk heterojunction cells have identified components of both reversible and irreversible degradations [17]. In that work, reversible degradation of the cells in the presence of oxygen resulted mainly in the reduction of short circuit current, while the loss in light absorption was negligible. However, we experimentally observe by submitting the cells to a controlled oxygen exposure that a simultaneous decrease in both photocurrent and absorption exists in agreement with the increase of p-doping level extracted from capacitance–voltage analysis. A direct connection is then established between an oxygen-related degradation route and cell performance parameters.

The specific goal of our work is to understand the effects of oxygen on the active layer blend (P3HT:PCBM) and contact in bulk heterojunction cells of regular configuration. Since the metallic contact oxidation may occur simultaneously with the blend degradation, we follow a robust fabrication method in air

---

* Corresponding authors. Tel.: +34 964 387463; fax: +34 964 729218.
E-mail addresses: aguerrer@uji.es (A. Guerrero), garciag@uji.es (G. Garcia-Belmonte).

0927-0248/$ - see front matter © 2012 Elsevier B.V. All rights reserved.
doi:10.1016/j.solmat.2012.01.012

and treat the samples with different oxidant sources prior to cathode deposition. The cell preparation procedure allows us to separate degradation contributions originated at the device bulk from those occurring at the outer interface. Recently, regular organic solar cells fabricated in air have been reported to provide similar performances to those of devices produced under a nitrogen atmosphere [18]. This fact would suggest that the origin of device degradation is not induced during device fabrication, but because of oxygen or water diffusion. Hence chemical degradation begins to be evident only after the cathode has been deposited and the cell has been completed. The present work demonstrates the formation of a P3HT complex with oxygen (highly reversible), which is related to the photocurrent decrease and monitored through capacitance–voltage measurements. Additionally, generation of metallic oxide layers as CaO at the cathode contact interface (completely irreversible) is observed.

2. Experimental

2.1. Samples preparation and oxygen exposure

In this work we follow photovoltaic cells fabrication process carried out in air [18]. A detailed description of the experimental conditions can be found in Appendix A. We briefly describe here the process for our control cell (cell 1, Table 1). First, we prepared all the mixed P3HT:PCBM solutions in a glovebox filled with a nitrogen atmosphere using dry *o*-dichlorobenzene (ODCB). Films are spin cast in air and the active layer was “solvent annealed” in a Petri dish for 2 h. At this point cells were transferred to the glovebox to undergo a thermal annealing treatment to provide an “oxygen free” active layer. For our photovoltaic cells we found optimum cell efficiencies when heated at 150 °C for 10 min and these conditions were used for all devices described in this work. Cell 1 was kept in the glovebox throughout the time from the thermal treatment to device encapsulation [19]. Note that device encapsulated is required to avoid oxygen contamination from the environment. The polymer solar cells were fabricated with a standard sandwich structure of ITO/PEDOT:PSS/P3HT:PCBM/Ca/Ag.

As reported by Mattis et al. [20] the annealing temperature required to promote oxygen desorption needs to be above 120 °C. Thus, we did not carry out a second thermal treatment after contact evaporation, which usually improves cell performance. For oxygen doped samples a second annealing treatment would induce oxygen desorption and in that case we would not be able to measure the intentionally introduced oxygen doping (see Table 1). Hence only one annealing step is necessary to obtain an adequate morphology and to provide effective oxygen desorption in P3HT prior to cathode deposition. As a result optimum efficiencies were found for devices with an active layer thickness of 400 nm. This is considerably higher than values usually reported in P3HT:PCBM photovoltaic cells (ca. 150–250 nm). All the cells presented in this study followed this processing; introduction of oxygen or a different oxidant into the system was carried out as explained below.

Oxygen treatment is implemented at different stages. For sample 2, traces of water that may be present in the films (i.e. PEDOT:PSS is highly hygroscopic) are carefully eliminated in the glovebox after the “solvent cure” step. The substrate was placed under vacuum and was heated to 50 °C for 1 h. Further traces of water were eliminated by introducing the sample in a high vacuum chamber in the glovebox at a pressure of 1×10^{-6} mbar overnight. After this exhaustive elimination of water the film was annealed to obtain an adequate morphology. The sample was placed in a sealed portable chamber with no-return valves to provide a flow of dry synthetic compressed air (ca. nitrogen 80% and oxygen 20%) for 2 h. Cells 3 and 4 were treated with dry synthetic compressed air after annealing in the same setup without exhaustively removing traces of water. Finally, sample 5 was doped with molecular oxygen by saturation of the P3HT:PCBM solution with dry oxygen before spin coating.

In a second set of experiments $NOBF_4$ was used as the oxidant. For cells 6–8 this oxidant is introduced in the system before spincasting the active layer. P3HT reacts with $NOBF_4$ to provide a very dark solution and a solid. The reaction product was added to the P3HT:PCBM blend to provide the $NOBF_4$ concentration described in Table 1 ($\sim1\times10^{-6}$ M). On the other hand, sample 9 was treated with $NOBF_4$ in acetonitrile directly after spin-coating the active layer at considerably higher concentration (1×10^{-2} M).

3. Results

3.1. Current density–voltage curves

Fig. 1 shows the current density–voltage curves for all analyzed samples and Table 2 summarizes their photovoltaic parameters. Optimum efficiencies were found for devices with an active layer thickness of 400 nm. Considering this large thickness, the reference sample (cell 1) shows a relatively high efficiency (2.8%) with high fill factor (FF) and open circuit voltage (V_{oc}). However, the short circuit current (J_{sc}) is considerably lower than that obtained for thinner cells which are reported to provide 10 mA cm^{-2} [21]. Cells doped with oxygen show decreased performance with increasing oxygen exposure. Cell 2 that was meticulously dried and treated with dry synthetic air for 2 h shows very similar results to those obtained for the reference cell. Cell 3 (1 h oxygen treatment and no additional drying step) shows similar V_{oc} to that of the reference cell and cell 2. However, the J_{sc} was slightly reduced and the FF decreases from 58% for cell 1 to 45% for cell 3. An additional hour of exposure to oxygen of cell 4 further decreased the photocurrent and the photovoltage began to be affected. Modifying the exposure method to oxygen for cell 5 provided very similar device parameters to those of cell 4 with slightly reduced V_{oc} and increased FF.

Table 1
Summary of preparation method and main characteristics.

ID	Dopant	Method	Time/concentration	Notes
1	None	–	–	Reference cell
2	O_2	Flow of dry air passed through film in a chamber in the dark	2 h	Exhaustive drying step
3	O_2	Flow of dry air passed through film in a chamber in the dark	1 h	
4	O_2	Flow of dry air passed through film in a chamber in the dark	2 h	
5	O_2	Dry air bubbled through active layer solution in the dark	10 min	
6	$NOBF_4$	Dopant added to active layer solution	5×10^{-7} M	Stock solution in dichlorobenzene
7	$NOBF_4$	Dopant added to active layer solution	1×10^{-6} M	Stock solution in dichlorobenzene
8	$NOBF_4$	Dopant added to active layer solution	2×10^{-6} M	Stock solution in dichlorobenzene
9	$NOBF_4$	Dopant added to active layer solution	1×10^{-2} M	Stock solution in acetonitrile, and LiF/Al cathode contact

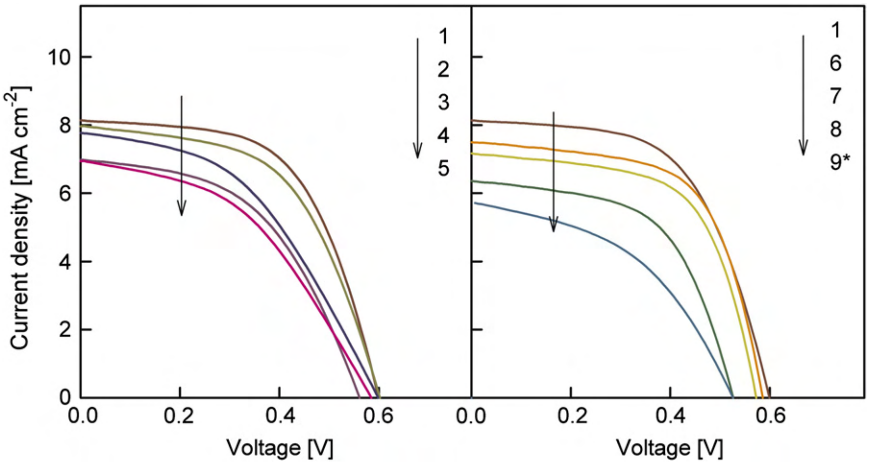

Fig. 1. Representation of the current density–voltage curves of photovoltaic cells doped under different oxidant conditions: molecular oxygen (left) and $NOBF_4$ (right). *A different metallic contact was used (LiF/Al/Ag).

Table 2
Performance summary of solar cells with doping levels and V_{fb} extracted from *C–V* measurements.

ID	J_{sc} (mA cm^{-2})	V_{oc} (mV)	FF (%)	PCE (%)	n ($\times 10^{16}$ cm^{-3})	V_{fb} (mV)
1	8.13	598	58	2.8	0.9	467
2	7.98	601	55	2.6	1.1	543
3	7.77	600	45	2.1	1.1	455
4	6.94	580	45	1.8	1.5	438
5	6.99	560	50	1.9	2.3	419
6	7.50	585	62	2.7	1.8	456
7	7.17	572	61	2.5	3.5	471
8	6.36	525	57	1.9	4.4	507
9	5.74	525	45	1.4	10.8	390

A second set of devices used $NOBF_4$ as the oxidizing agent. We followed a fabrication process analogous to that employed for cell 5 but using $NOBF_4$ in solution instead of dry synthetic air. The current density–voltage curves for cells doped with $NOBF_4$ are shown in Fig. 1 (right). As occurrs for oxygen doping, an increment in solution concentration containing $NOBF_4$ decreases J_{sc} and V_{oc} gradually. However, in contrast to samples doped with oxygen, where the FF is reduced significantly, devices doped with $NOBF_4$ show only a slight decrease for sample 8. Processing conditions for sample 9 involved high concentrations of $NOBF_4$. It should be noticed that in order to obtain a working device with conditions for cell 9, a different metallic contact was used (LiF/Al/Ag). Interestingly, the replacement of the metallic contact for both helps to recover device performance (from 0.006% to 1.4%). A detailed discussion can be found in Appendix A.

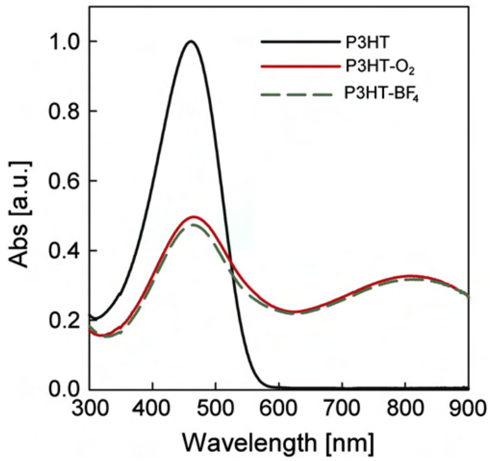

Fig. 2. Comparison of UV–vis spectra of P3HT in *o*-dichlorobenzene solution with the spectra of the P3HT solution after exposure to molecular oxygen ($P3HT^{+}–O_2^{-}$) and $NOBF_4$ ($P3HT–BF_4^{-}$).

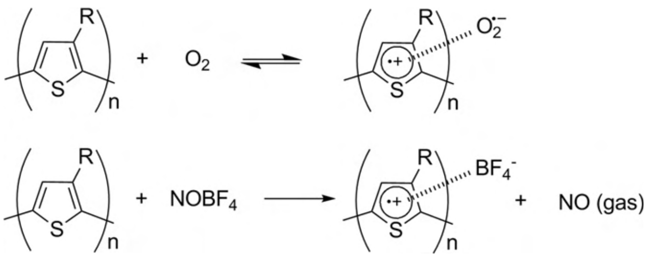

Scheme 1. Transfer complex formation of P3HT in the presence of oxygen as proposed in literature (top) and proposed reaction of P3HT with the oxidant $NOBF_4$ (bottom).

3.2. Optical properties of materials, and films and relation with EQE

In order to understand whether the reaction of P3HT:PCBM blend with molecular oxygen gives rise to similar polymer oxidation as those obtained with $NOBF_4$ we carried out characterization by absorption measurements in solution. First a solution containing PCBM in ODCB was treated with either molecular oxygen or $NOBF_4$ at room temperature and no spectroscopic difference was observed after 24 h. Then, a solution containing P3HT in ODCB was treated with dry oxygen for 30 s at room temperature. The spectrum is shown in Fig. 2 and clearly shows that the creation of new species reduces the intensity of the absorption peak of P3HT as this polymer takes part in complex formation. A new absorption band is generated towards the infrared with a maximum peak at 810 nm, which is attributed to polaronic transitions [22]. This new band is then assigned here to the complex $P3HT^{+}:O_2^{-}$ formed by reaction of P3HT and oxygen (Scheme 1, top) [13]. Additionally, the reaction product between P3HT and $NOBF_4$ was also characterized by absorption measurements. Both reactions of P3HT with either O_2 or $NOBF_4$ produce similar absorption response in solution using ODCB as solvent. Chemically the main difference between both oxidants is that in this last case we expect the reaction to be irreversible as

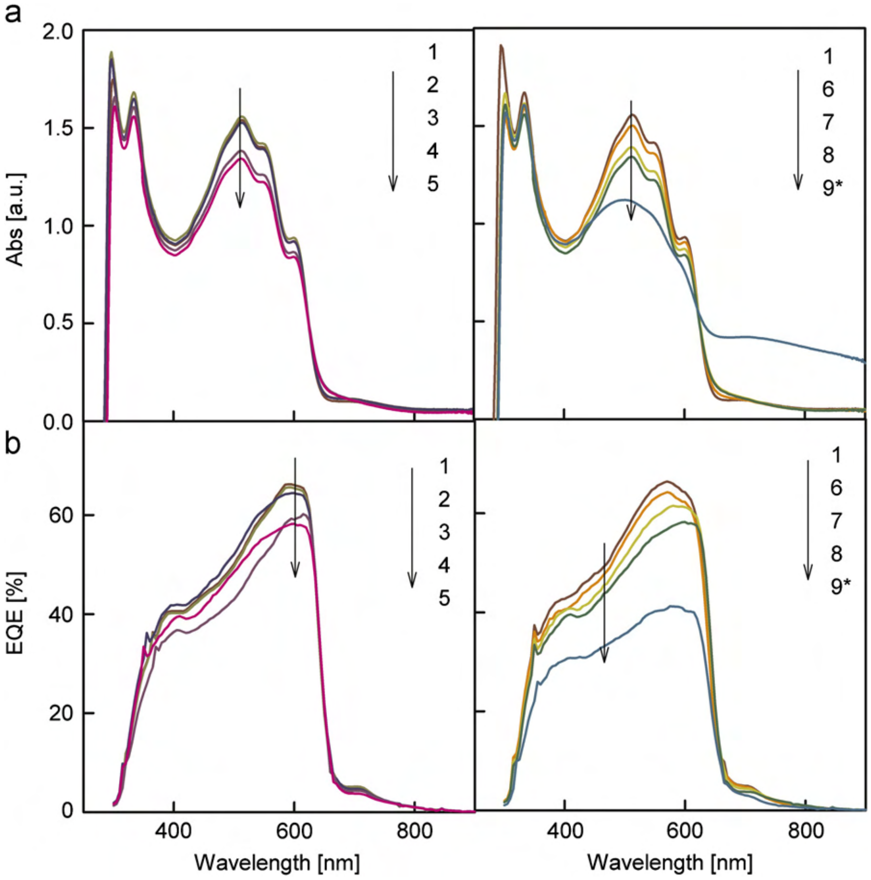

Fig. 3. Correlation between film absorption spectra (a) and EQE spectra of completed cells (b) for different oxidant conditions: molecular oxygen (left) and $NOBF_4$ (right). *A different metallic contact was used (LiF/Al/Ag).

NO gas is evolved (Scheme 1, bottom) the counterion being BF_4^- for the second oxidant.

In order to analyze the effect of oxygen doping on the photocurrent we measure the steady-state absorption of films processed under the same conditions of the referred cells (without the cathode contact). Films 1–3 exhibit similar absorption spectra in terms of intensities and absorption onsets (Fig. 3a, left). These findings are in perfect agreement with those discussed by Seeman et al. [17], in which they did not observe any change in the absorption intensity with exposure to dry synthetic air. However, films 4 and 5 show reduced absorption intensity for P3HT and, interestingly, the intensity in absorption in the 650–700 nm region is slightly altered. Similarly, films doped with $NOBF_4$ confirmed the same trend observed for oxygen doping. Increasing the concentration of $NOBF_4$ led to decreased intensity of the P3HT absorption and increased absorption towards long wavelengths.

EQE measurements of the corresponding cells were also performed. A correlation for all cells under study between intensities obtained from absorption spectra and EQE is clear: reduced absorption led to reduced charge collection in the same proportion. Interestingly, none of the cells show increase of charge collection in the 700–800 nm region. This is especially noticeable for cell 9 using high $NOBF_4$ concentration, which despite showing a clear band in the red region does not contribute to the extracted charges as inferred from EQE measurements.

3.3. Capacitance–voltage analysis.

Analysis of capacitance–voltage (*C*–*V*) measurements has become a standard technique to extract relevant material parameters. In previous work, we showed that for organic photovoltaics information extracted from *C*–*V* measurements are related to the p-doping level resulting from defect states within the polymer band gap [23]. Standard P3HT:PCBM solar cells showed Mott–Schottky characteristics, exhibiting full depletion at reverse bias and a linear relationship at low forward bias (0.0–0.5 V) [23]. The density of fully ionized defect states (p-doping level) *n* was derived from the slope by means of the Mott–Schottky relation

$$C^{-2} = \frac{2(V_{fb} - V)}{A^2 q \varepsilon \varepsilon_0 n} \quad (1)$$

where *A* corresponds to the device active surface, ε is the relative dielectric constant of the blend, ε_0 the permittivity of the vacuum and *n* the total concentration of acceptor impurities (intrinsic

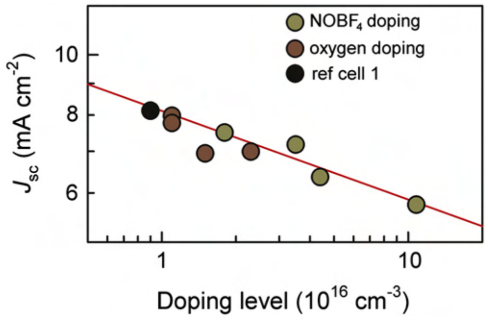

Fig. 4. Correlation between short-circuit current density and doping level. Data correspond to reference cell 1, and oxygen and $NOBF_4$ treated cells. The experimental relationship $J_{sc} \propto n^{-0.14}$ is encountered.

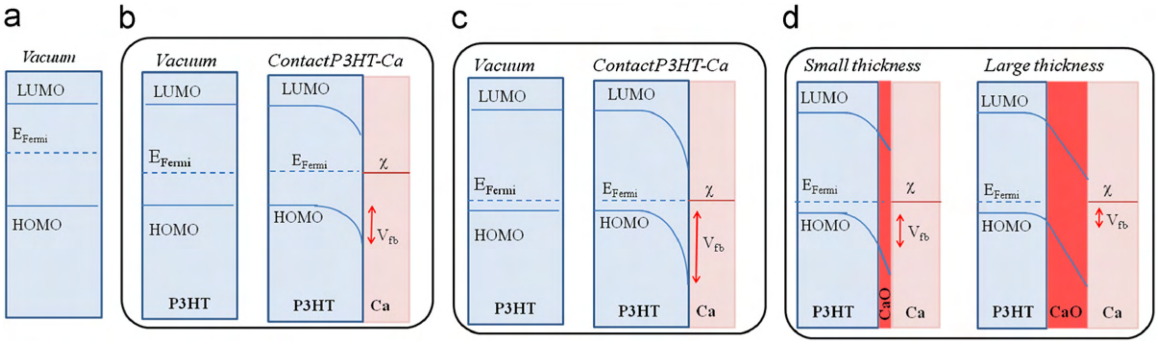

Fig. 5. Energy diagrams of an organic semiconductor showing the effect of a variation of doping levels and presence of a dielectric interlayer (CaO): (a) un-doped semiconductor, (b) semiconductor p-type doped, (c) semiconductor heavily p-doped and (d) effect of CaO thickness.

defects with additional charged immobile O_2^- or BF_4^- counter-ions). It is assumed that the defect density explored from capacitance corresponds to those defects able to follow measuring frequency. Thus, by analyzing the curve $C^{-2}(V)$ one can extract V_{fb} from the intercept and the total concentration of acceptor impurities from the slope (n). The intercept of this straight line with the real axis is related to the flat-band potential, which corresponds to the energy offset between the hole Fermi level and the cathode metal effective work function (see Fig. 5b). Recently, this technique has been used to monitor oxygen doping levels in polymer solar cells [17].

By analysis of the C–V measurements we were able then to obtain accurate values for p-doping of the polymer. It is worth noting that C–V Mott–Schottky analysis is sensitive only to the density of ionized impurity levels. A Mott–Schottky plot for our devices clearly shows different slopes for the samples exposed to oxygen under different experimental conditions (Appendix A). For clarification, it is important to note that the reported Mott–Schottky plots do not show full depletion at -1 V of reverse bias. An estimation of the geometric capacitance gives rise to a value of 7 nF/cm^2. Taking into account that the capacitance values observed are higher than this and that depletion width is below 100 nm at -1 V we can conclude that full depletion has not been obtained for devices with high doping levels. On the other hand, device 1 shows a depletion width at -1 V of 350 nm, which is close to the device thickness, indicating that at this voltage the cell begins to be fully depleted, and explains why the $C^{-2}(V)$ curve exhibits saturation as cells are reversely polarized (see Appendix A).

The results extracted from Mott–Schottky plots are summarized in Table 1. The total concentration of acceptor impurities (n) confirms the lowest doping level (0.9×10^{16} cm^{-3}) for control sample 1. This minimum doping level corresponds to structural defects of the polymer, and to extrinsic impurities that are inherent to the processing and purity degree of chemicals used. Values for cells treated with oxygen range from 1.0 to 1.5×10^{16} molecules cm^{-3}. Slightly higher values are obtained for cell 5 doped by oxygen saturation of the spin coating solution.

Alternatively, the doping densities of samples doped with a stock solution of $P3HT^+$:BF_4^- (cells 6–8) are clearly higher than those obtained with oxygen. This supports that with $NOBF_4$ used as oxidant irreversible processes take place (oxidant desorption is not possible). Finally, cell 9 doped with a highly concentrated solution of $NOBF_4$ gives rise to the highest doping levels (10.8×10^{16} cm^{-3}).

In addition to the doping levels, V_{fb} was calculated by analysis of the Mott–Schottky characteristics. A baseline flat-band voltage value of 467 mV was obtained for sample 1. This increased for cell 2, treated with oxygen, and followed with a gradual decrease for the subsequent samples. On the other hand, for samples treated with $NOBF_4$, where no oxidation of the metallic contact is expected (cells 4–8) increasing doping concentrations of the oxidant increases V_{fb} from values of 456 to 507 mV. Sample 9 provides a low value of 390 mV. The observed trends will be explained in detail in Section 4.

4. Discussion

4.1. Correlation between photocurrent and doping level.

Our experimental methodology enabled us to treat the P3HT:PCBM layer with oxygen before contacting the cathode metal. As supported by absorption measurements in solution it appears that PCBM does not react with oxidants such as molecular oxygen or $NOBF_4$ in ODCB at room temperature. P3HT does react with molecular oxygen to form $P3HT^+$:O_2^- complexes. We consider such complex formation as a primary source of solar cell long-term degradation. A correlation is observed between the measured doping levels, absorption spectra of the films, EQE results and the photocurrent obtained for operating cells. Thus, cells 1–3 show similar film absorption and EQE spectra with a measured maximum current of ~8 mA/cm^2. On the contrary, cells 4 and 5 exhibit reduced collection of charge carriers to provide a maximum current of ~7 mA/cm^2. These results correlate with the obtained J_{sc}, and corroborate the relationship between oxygen doping and loss in photocurrent through reduction in absorption caused by lower concentration of neutral P3HT. The drop in V_{oc} is explained by a reduction in light absorbed, because fewer photogenerated carriers reduce the occupancy of polymer and fullerene electronic states and then inhibit the Fermi level splitting, which is the ultimate origin of the photovoltage [24]. This type of performance loss is expected to be partially reversible through oxygen desorption via further annealing treatments.

For cells treated with molecular oxygen we observe that under most conditions the density of fully ionized acceptor impurities is increased with respect to those obtained for reference cell 1. Attempts to increase the doping levels from oxygen-free sample 1 to slightly doped sample 2 show this slight effect (Table 1). It is interesting to note that cells 2 and 4 both were exposed to oxygen for 2 h, but the former meticulously dried. Whilst the totally dried cell exhibits similar doping levels to that of reference cell 1, cell 4 shows slightly higher doping levels. By comparison of the performance characteristics of cells 3 and 4 it is clear that the reduced performance is due to additional exposure to oxygen and not to reaction with traces of water. Higher doping concentrations were obtained using a molecular oxygen doping process in solution (cell 5) prior to the annealing step.

Oxidation of the metallic contact with oxygen or water present at the interface was nevertheless expected. Thus, in order to totally avoid generation of CaO and truly understand the effect of oxidants in the active layer we carried out further experiments with $NOBF_4$. Such an oxidant agent allows us to investigate active layer p-doping without the effect of calcium oxidation. As previously commented upon, P3HT does indeed react with both oxidants, generating analogous reaction products. The main consequence of this is that the P3HT absorption band intensity decreases. This intensity reduction is also observed when film absorption measurements are carried out on the $NOBF_4$ treated samples (Fig. 3a, right). Additionally, a slight increase in the intensity in the 650–700 nm region is also observed for samples 7 and 8 doped with $NOBF_4$. This increase in intensity is assigned to generation of the complex $P3HT^+:BF_4^-$ as supported by the spectra of cell 9 ,whereby the concentration of $NOBF_4$ was increased by 10^4 factor during film preparation. Interestingly, the EQE and current density results obtained for completed doped cells clearly correlate with the film absorption measurements. Note that the newly generated species do not contribute to the collected charges.

The previous findings strongly indicate that the decrease in photocurrent density observed in the complete cells is primary caused by a decrease in light absorption, and not by losses produced during carrier transport to the collecting electrodes. Because collection efficiency diminishes as oxidation level is raised, the observed simultaneous reduction in intensity of both absorption and EQE spectra should be related to a loss in photogeneration of mobile carriers. Additionally, the decrease in photovoltage can also be explained by a decrease in photogeneration as V_{oc} depends on the amount of light absorbed that is able to yield separated charge carriers.

As aforementioned C–V analysis provides direct information about the density of dopants that are actually ionized, contributing to the conductivity (p-doping). Therefore oxidant doping modifies the concentration of mobile hole carriers as new chemical species are created. The immobile O_2^- or BF_4^- counterions contribute to the formation of a hole depletion zone near the cathode contact (band bending), which was monitored by the C–V technique. As observed, total concentrations of acceptor impurities are qualitatively in agreement with the spectroscopic measurements and the decrease in photocurrent observed for the complete cells. Fig. 4 illustrates this correlation, including all cells studied. As observed an experimental relationship $J_{sc} \propto n^{-0.14}$ is found between photocurrent and doping level extracted from C–V analysis. However it is hard to understand how an increment of p-doping level within one order of magnitude (from $\sim 10^{16}\,\mathrm{cm}^{-3}$ up to $10^{17}\,\mathrm{cm}^{-3}$) is able to induce such a large decrease in light absorption, which gives rise to ~33% reduction in photocurrent (from $8.13\,\mathrm{mA\,cm^{-2}}$ down to $5.74\,\mathrm{mA\,cm^{-2}}$). Oxidation levels as calculated from the C–V analysis are only in the range of 0.1–0.01% of polymer monomers taking part in the reactions drawn in Scheme 1. This apparent discrepancy can be solved by recalling that C–V analysis only monitors the density of fully ionized charge species (those participating in the modulation of the depletion zone). It is then necessary to distinguish between O_2^- (or BF_4^-) counterion able to yield mobile hole carriers, from those that keep the hole attached forming the neutral complex $P3HT^+:O_2^-$ (or $P3HT^+:BF_4^-$). Therefore we remark that only a portion of the total oxidized polymer units contribute to increase the mobile hole concentration.

4.2. Effect of metal cathode oxidation

Regarding the variation in V_{fb} observed for cells doped with oxygen, Fig. 5 shows different energy diagrams that explain the effect of increasing the p-doping concentration. An undoped semiconductor before contacting exhibits an energy diagram as that showed in Fig. 5a. The difference in energy between the Fermi level (E_F) and the HOMO will be the same as the difference in energy between E_F and the LUMO. As the material is doped (p-type), E_F will shift on approaching the HOMO of the polymer. The difference in energy between the HOMO and E_F will become smaller as we increase the concentration of p-dopants (Fig. 5b and c). In addition, when the active layer is placed in contact with a metal, E_F and the effective work function of the metal equilibrate at the interface. This equilibration gives rise to band bending (electrical field confinement) at the interface vicinity [23]. The flat band potential equals the energy offset between the hole Fermi level and the effective cathode work function. As p-doping is increased the position of the Fermi level will shift towards low energies, producing an increment in V_{fb}. This situation is clearly observed for samples treated with $NOBF_4$, where no oxidation of the metallic contact has taken place. Thus, V_{fb} increases with increasing doping concentrations as the hole E_F approaches further the HOMO of the P3HT.

Evidences for CaO generation are found for samples treated with oxygen. For cells 2–5, V_{fb} gradually decreases from values of 543 mV (sample 2) to 419 mV (sample 5). By comparison of cells 5 and 6 with similar doping levels, it is clear from the values obtained from V_{fb} that oxidation of calcium takes place faster for the sample containing molecular oxygen as dopant. This indicates that upon exposure to oxygen, part of the molecular oxygen will produce $P3HT^+:O_2^-$ complexes, while other part will generate calcium oxide. Generation of CaO will then be responsible for a drop in V_{fb} as schematically depicted in Fig. 5c and d [25]. This oxide accommodates part of the applied voltage during C–V measurement because of the formation of a dipole layer. Similar energy level shifts have been reported previously for organic/metal interfaces [26]. Thus, an increase in the oxygen exposure provides simultaneously P3HT p-doping increment and decrease in V_{fb}. It is important to note that generation of CaO has taken place to a very small degree as supported by a slightly increased series resistance observed for the sample doped with molecular oxygen (see Appendix A). Presence of CaO clearly has a negative impact on FF, which reduces from nearly 60 to 45, contrary to the case of using $NOBF_4$ as dopant. It is interesting to note that cells doped with $NOBF_4$ (samples 6–8) benefit from high FF regardless of the doping concentration. This indicates that the presence of the complex $P3HT^+:BF_4^-$ does not have a negative impact on the FF. On the other hand, FF was significantly reduced when contact oxidation had taken place.

5. Conclusions

In conclusion this work shows the origin of performance parameter degradation produced by oxygen treatment of the active layer. The different effects induced by oxygen were separated using $NOBF_4$ as an oxidant. Evidences for generation of the complex $P3HT^+:O_2^-$ have been shown on complete cells. This complex is responsible for photocurrent reduction. Loss in photovoltage for cells doped with molecular oxygen is in agreement with the reduced light absorption that generates less charge carriers, inhibiting the Fermi level splitting (photovoltage) to some extent. On the other hand, irreversible degradation induced by oxygen is attributed to calcium oxide formation. In this work, generation of this oxide takes place only to a small degree, which is responsible for a decrease in FF. These conclusions are supported by capacitance–voltage measurements, which provide values for degree of oxygen doping levels in the films and evidences for CaO generation.

Acknowledgments

We thank financial support from Ministerio de Educacion y Ciencia under Project HOPE CSD2007-00007 (Consolider-Ingenio

2010), Generalitat Valenciana under Project PROMETEO/2009/058 and Conselho Nacional de Desenvolvimento Científico e Tecnológico (CNPq) under Process 201380/2010-2.

Appendix A. Supplementary material

Supplementary data associated with this article can be found in the online version at doi:10.1016/j.solmat.2012.01.012.

References

[1] M.A. Green, K. Emery, Y. Hishikawa, W. Warta, Solar cell efficiency tables (version 35), Progress in Photovoltaics 18 (2010) 144–150.

[2] M. Jørgensen, K. Norrman, F.C. Krebs, Stability/degradation of polymer solar cells, Solar Energy Materials and Solar Cells 92 (2008) 686–714.

[3] K. Norrman, S.A. Gevorgyan, F.C. Krebs, Water-induced degradation of polymer solar cells studied by (H_2O)-O-18 labeling, ACS Applied Materials and Interfaces 1 (2009) 102–112.

[4] M.O. Reese, A.J. Morfa, M.S. White, N. Kopidakis, S.E. Shaheen, G. Rumbles, D.S. Ginley, Pathways for the degradation of organic photovoltaic P3HT:PCBM based devices, Solar Energy Materials and Solar Cells 92 (2008) 746–752.

[5] M. Manceau, A. Rivaton, J.L. Gardette, S. Guillerez, N. Lemaitre, The mechanism of photo- and thermooxidation of poly(3-hexylthiophene) (P3HT) reconsidered, Polymer Degradation and Stability 94 (2009) 898–907.

[6] H.J. Kim, H.H. Lee, J.J. Kim, Real time investigation of the interface between a P3HT:PCBMlayer and an Al electrode during thermal annealing, Macromolecular Rapid Communications 30 (2009) 1269–1273.

[7] C.F. Zhang, Y. Hao, S.W. Tong, Z.H. Lin, Q.A. Feng, E.T. Kang, C.X. Zhu, Effects of cathode confinement on the performance of polymer/fullerene photovoltaic cells in the thermal treatment, IEEE Transactions on Electron Devices 58 (2011) 835–842.

[8] F.C. Krebs, S.A. Gevorgyan, J. Alstrup, A roll-to-roll process to flexible polymer solar cells: model studies, manufacture and operational stability studies, Journal of Materials Chemistry 19 (2009) 5442–5451.

[9] J. Schafferhans, A. Baumann, C. Deibel, V. Dyakonov, Trap distribution and the impact of oxygen-induced traps on the charge transport in poly(3-hexylthiophene), Applied Physics Letters 93 (2008) 093303.

[10] A. Tapponnier, I. Biaggio, P. Gunter, Ultrapure C-60 field-effect transistors and the effects of oxygen exposure, Applied Physics Letters 86 (2005) 112114.

[11] T. Matsushima, M. Yahiro, C. Adachi, Estimation of electron traps in carbon-60 field-effect transistors by a thermally stimulated current technique, Applied Physics Letters 91 (2007) 103505.

[12] M.T. Lloyd, D.C. Olson, P. Lu, E. Fang, D.L. Moore, M.S. White, M.O. Reese, D.S. Ginley, J.W.P. Hsu, Impact of contact evolution on the shelf life of organic solar cells, Journal of Materials Chemistry 19 (2009) 7638–7642.

[13] M.S.A. Abdou, F.P. Orfino, Y. Son, S. Holdcroft, Interaction of oxygen with conjugated polymers: charge transfer complex formation with poly(3-alkylthiophenes), Journal of the American Chemical Society 119 (1997) 4518–4524.

[14] A. Aguirre, S.C.J. Meskers, R.A.J. Janssen, H.-J. Egelhaaf, Formation of metastable charges as a first step in photoinduced degradation in p-conjugated polymer: fullerene blends for photovoltaic applications, Organic Electronics 12 (2011) 1657–1662.

[15] M. Manceau, A. Rivaton, J.L. Gardette, Involvement of singlet oxygen in the solid-state photochemistry of P3HT, Macromolecular Rapid Communications 29 (2008) 1823–1827.

[16] H. Hintz, H.J. Egelhaaf, L. Luer, J. Hauch, H. Peisert, T. Chasse, Photodegradation of P3HT—a systematic study of environmental factors, Chemistry of Materials 23 (2011) 145–154.

[17] A. Seemann, T. Sauermann, C. Lungenschmied, O. Armbruster, S. Bauer, H.J. Egelhaaf, J. Hauch, Reversible and irreversible degradation of organic solar cell performance by oxygen, Solar Energy 85 (2011) 1238–1249.

[18] S.J. Wu, J.H. Li, Q.D. Tai, F. Yan, Investigation of high-performance air-processed poly(3-hexylthiophene)/methanofullerene bulk-heterojunction solar cells, Journal of Physical Chemistry C 114 (2010) 21873–21877.

[19] A. Guerrero, K. Kulbaba, M. Bochmann, Alkyl zinc chlorides as new initiators for the polymerization and copolymerization of isobutene, Macromolecular Chemistry and Physics 209 (2008) 1714–1720.

[20] B.A. Mattis, P.C. Chang, V. Subramanian, Performance recovery and optimization of poly(3-hexylthiophene) transistors by thermal cycling, Synthetic Metals 156 (2006) 1241–1248.

[21] G. Li, V. Shrotriya, J.S. Huang, Y. Yao, T. Moriarty, K. Emery, Y. Yang, High-efficiency solution processable polymer photovoltaic cells by self-organization of polymer blends, Nature Materials 4 (2005) 864–868.

[22] J. Hwang, D.B. Tanner, I. Schwendeman, J.R. Reynolds, Optical properties of nondegenerate ground-state polymers: three dioxythiophene-based conjugated polymers, Physical Review B 67 (2003) 115205.

[23] F. Fabregat-Santiago, G. Garcia-Belmonte, I. Mora-Seró, J. Bisquert, Characterization of nanostructured hybrid and organic solar cells by impedance spectroscopy, Physical Chemistry and Chemical Physics 13 (2011) 9083–9118.

[24] P.P. Boix, A. Guerrero, L.F. Marchesi, G. Garcia-Belmonte, J. Bisquert, Current–voltage characteristics of bulk heterojunction organic solar cells: connection between light and dark curves, Advanced Energy Materials 1 (2011) 1073–1078.

[25] J. Bisquert, G. Garcia-Belmonte, A. Munar, M. Sessolo, A. Soriano, H.J. Bolink, Band unpinning and photovoltaic model for P3HT–PCBM organic bulk heterojunctions under illumination, Chemical Physics Letters 465 (2008) 57–62.

[26] H. Ishii, N. Hayashi, E. Ito, Y. Washizu, K. Sugi, Y. Kimura, M. Niwano, Y. Ouchi, K. Seki, Kelvin probe study of band bending at organic semiconductor/metal interfaces: examination of Fermi level alignment, Physica Status Solidi A: Applied Research 201 (2004) 1075–1094.

How the Charge-Neutrality Level of Interface States Controls Energy Level Alignment in Cathode Contacts of Organic Bulk-Heterojunction Solar Cells

Antonio Guerrero,[†] Luís F. Marchesi,[†,‡] Pablo P. Boix,[†] Sonia Ruiz-Raga,[†] Teresa Ripolles-Sanchis,[†] Germà Garcia-Belmonte,[†,*] and Juan Bisquert[†]

[†]Photovoltaic and Optoelectronic Devices Group, Departament de Física, Universitat Jaume I, ES-12071 Castelló, Spain and
[‡]Laboratório Interdisciplinar de Eletroquímica e Cerâmica (LIEC), Universidade Federal de São Carlos, São Carlos, Brazil

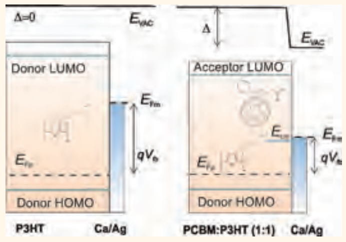

ABSTRACT Electronic equilibration at the metal–organic interface, leading to equalization of the Fermi levels, is a key process in organic optoelectronic devices. How the energy levels are set across the interface determines carrier extraction at the contact and also limits the achievable open-circuit voltage under illumination. Here, we report an extensive investigation of the cathode energy equilibration of organic bulk-heterojunction solar cells. We show that the potential to balance the mismatch between the cathode metal and the organic layer Fermi levels is divided into two contributions: spatially extended band bending in the organic bulk and voltage drop at the interface dipole layer caused by a net charge transfer. We scan the operation of the cathode under a varied set of conditions, using metals of different work functions in the range of ∼2 eV, different fullerene acceptors, and several cathode interlayers. The measurements allow us to locate the charge-neutrality level within the interface density of sates and calculate the corresponding dipole layer strength. The dipole layer withstands a large part of the total Fermi level mismatch when the polymer:fullerene blend ratio approaches ∼1:1, producing the practical alignment between the metal Fermi level and the charge-neutrality level. Origin of the interface states is linked with fullerene reduced molecules covering the metal contact. The dipole contribution, and consequently the band bending, is highly sensitive to the nature and amount of fullerene molecules forming the interface density of states. Our analysis provides a detailed picture of the evolution of the *potentials* in the bulk and the interface of the solar cell when forward *voltage* is applied or when photogeneration takes place.

KEYWORDS: metal–organic interfaces · photovoltaic devices · cathode contact · charge-neutrality level · dipole layer · band bending

In organic photovoltaic devices, outer interface structures play a significant role in establishing optimal contact conditions for efficient extraction (or blocking) of charge carriers. Buffer layers of different nature are currently employed to enhance both power conversion efficiency (PCE) and cell stability by improving contact performance. Several materials have been explored to enhance the electron selectivity of the cathode contact: alkali metal compounds (LiF, *etc.*), metal oxides (TiO_x, ZnO, *etc.*), and low molecular weight organic compounds have been reported to contribute to the overall PCE and solar cell lifetime, as reviewed in recent reports.[1−3] Among those approaches, the effect of the dipole moment associated with self-assembled monolayers (SAM) attached to the interface, which alter the energy level alignment between the cathode metal and the bulk of the blend,[4] is particularly interesting, as well as the inclusion of conjugated polyelectrolyte interlayers.[5] In all of these cases, the energy shift induced by the charge dipole built up at interface layers enables the use of air-stable high work function metals. It is then inferred that electrostatic mechanisms occurring at the nanometer scale, both in the active layer bulk and at interfaces, have a great influence on the overall device operation.[6,7]

Interface dipole layers are regarded as a determining ingredient of the metal/organic contact equilibration.[8−12] Several models have been proposed to account for the energy level alignment at interfaces, depending on the degree of interaction between the metal contact and the deposited organic layer. When the chemical interaction between the metal and contacting conjugated molecules or polymers is not negligible, it is expected that molecules attached to the metal surface undergo both a shift and a broadening of their molecular energy levels. Energy distribution of the attached molecules should be modeled by a specific interfacial density of states (IDOS) which differs from that encountered in the bulk of the organic layer. The situation is

* Address correspondence to garciag@fca.uji.es.

Received for review February 2, 2012 and accepted March 30, 2012.

10.1021/nn300486a

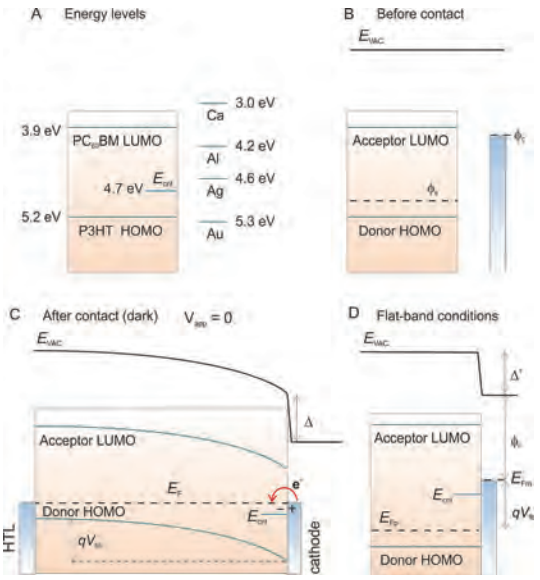

Figure 1. **(A) Energy levels of organic materials and cathode metals. E_{CNL} signals the position of the charge-neutrality level. (B) Diagram describing the situation before the cathode contact is made: there exists a mismatch between organic and metal work functions, $\phi_c - \phi_s$, which should be equilibrated after contact. (C) In equilibrium ($V_{app} = 0$ in the dark), the vacuum level offset is split into two contributions: one arising from the bulk band bending qV_{bb}, the other caused by the interface dipole layer Δ. A net charge transfer approaches the metal Fermi level to CNL. (D) In flat-band conditions, $V_{app} = V_{fb}$, the dipole layer Δ′ persists in such a way that $qV_{fb} = qV_{bb} - \Delta + \Delta'$.**

even more featured for interfaces formed by metals deposited onto organic layers because of metal diffusion and the creation of bonding sites in a rough surface.

To rationalize these kinds of interfaces, a key parameter accounting for the interface equilibration is the charge-neutrality level (CNL) located at a given position within the IDOS.[13−15] The formation of an interface dipole layer Δ whose sign depends on the energy difference, $E_{CNL} - \phi_c$, entails a charge transfer that pulls the metal Fermi level ϕ_c toward CNL (E_{CNL}). As an illustration, given the CNL location in Figure 1A, the metals Ca, Al, and Ag would transfer negative charge to the interfacial states, while Au gives rise to a positive charge sheet on the organic side. The formation of interface dipoles directly produces an offset in the vacuum level.

Despite the essential insights that the previous models have provided, a complete view of device-integrated metal/organic contact, including the connection with the organic bulk forming the active layer in solar cells, has not been established yet. This unified approach that integrates both metal cathode and organic bulk sides, along with interface states, is an essential advance in understanding device formation and operation and constitutes the main subject of this work.

In a real device, overall equilibration of the cathode contact should also consider the interaction with the organic layer bulk.[16,17] Before contact is made, there exists an energy offset between the metal and the organic semiconductor work functions, ϕ_c and ϕ_s, respectively, as schematically illustrated in Figure 1B. Donor polymers as poly-(3-hexylthiophene), P3HT can easily undergo oxidation (p-doping) when exposed to the air or moisture,[18,19] producing a change in the hole conductivity.[20] Accordingly, we have proposed very recently that doping of the organic layer produces native mobile charges in the organic blend, which gives rise to the *separate* equilibration of each contact. Due to the p-doped character of the polymer, ϕ_s is located approaching the donor HOMO level ($E^D_{HOMO} \sim$ 5.2 eV for P3HT). Whereas the cathode equilibrates the mismatch $\phi_c - \phi_s$, which is accommodated between the spatially distributed band bending within the blend layer, and the local voltage drop at the interface Δ, the anode forms a good ohmic contact because of the proper energy alignment. The band bending occurs as a consequence of the hole depletion zone built up near the contact. A detailed explanation on the depletion zone formation and consequences on the device performance has been recently published.[21] Experimental techniques such as Kelvin probe[17,22] and ultraviolet photoelectron spectroscopy[23] have given evidence of the formation of depletion zones at metal/organic contacts with the corresponding band bending. This is schematically drawn in Figure 1C. The voltage V_{bb} accounts solely for the band bending part, with Δ being caused by the presence of an interfacial dipole layer. The dipole layer exhibits a negative charge on the organic side which is compensated by a positive charge at the metal contact. Accordingly, the overall vacuum level offset can be split into two parts: one originated by the spatially extended depletion region, and the other confined at the interface dipole layer. An expression for the cathode equilibration is then written as follows

$$qV_{bb} = E_F - \phi_c - \Delta \tag{1}$$

Here $E_F = \phi_s$ corresponds to the Fermi level in equilibrium.

In this work, we address the issue of electronic equilibration of the cathode contact in bulk-heterojunction solar cells by using the information extracted from an exclusively electrical technique such as the Mott−Schottky analysis of capacitance−voltage ($C-V$) characteristics.[24] In general, capacitance in organic devices is observed to be frequency-dependent because of the presence of defect state distributions,[25] however, in reverse, and low forward voltage capacitance usually exhibits a plateau at intermediate frequencies (100 Hz to 1 kHz), which allows for an estimation of the depletion zone width.[24,26,27] A simple model is proposed here that integrates both voltage drops, namely, qV_{bb} and Δ, into a unified description of the contact equilibration. The model is formulated in terms of CNL and IDOS as parameters. It is then explained how the band bending and the dipole layer strength can be readily derived from the experiment. By varying the metal used in the cathode contact, we are able to determine the CNL position which governs the dipole layer contribution through the partial IDOS occupancy. Moreover, the use of solar cells prepared from three different fullerene acceptors and the variation of the blend composition let us understand the origin and function of interface states withstanding the dipole layer voltage drop.

The model developed here provides important and detailed information of a core aspect of BHJ solar cell device operation,[21] which is the evolution of the *potentials* in the bulk and the interface when either forward *voltage* is applied or photogeneration takes place.

RESULTS AND DISCUSSION

Capacitance–Voltage Characteristics. Solar cells of structure indium tin oxide (ITO)/poly(3,4-ethylenedioxythiophene):poly(styrene sulfonic acid) (PEDOT:PSS)/P3HT:fullerene/metal were prepared as described in the Methods section. In order to test the effect of the acceptor LUMO level shift on the cathode energetics, different fullerene acceptors have been tested, namely, indene-C_{60} bisadduct (ICBA), [6,6]-phenyl-C_{61}-butyric acid methyl ester ($PC_{60}BM$), and similar C_{71} derivative ($PC_{70}BM$). Capacitance measurements for Mott–Schottky analysis were performed as explained in Methods. AC oscillating amplitude was as low as 20 mV (rms) to maintain the linearity of the response, and measuring frequency was fixed in the low-frequency range (100 Hz) as reported in previous papers.[24]

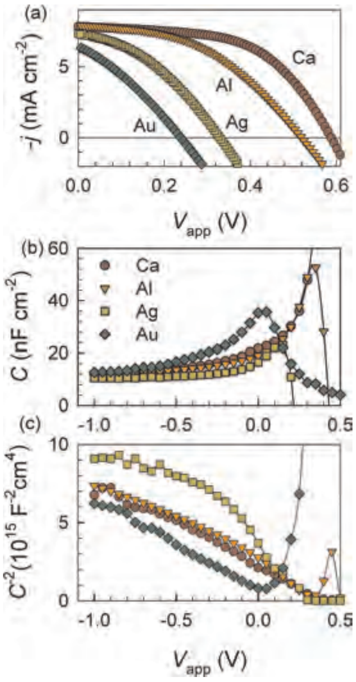

Figure 2. (A) Current–voltage characteristics of devices with structure ITO/PEDOT:PSS/P3HT:PCBM/metal. (B) Capacitance–voltage characteristics showing full depletion in reverse and the rise in capacitance toward forward voltages caused by the reduction in depletion region width. (C) Mott–Schottky plots from which the p-doping level N and flat-band voltage V_{fb} are extracted.

TABLE 1. Photovoltaic Parameters and Parameters Extracted from the Capacitance Mott–Schottky Analysis of Thick P3HT: Fullerene Solar Cells with Different Cathode Metal

P3HT:$PC_{60}BM$ (350 nm)	j_{sc} (mA cm^{-2})	V_{oc} (V)	FF	PCE (%)	N (10^{15} cm^{-3})	V_{fb} (V)	E_{Fm} (eV)	Δ (eV)
Ca	7.81	0.59	0.56	2.6	6.6	0.39	4.56	1.69
Al	7.91	0.52	0.45	1.8	4.7	0.35	4.60	0.45
Ag	7.36	0.33	0.30	1.0	2.5	0.24	4.71	0.11
Au	6.50	0.24	0.30	0.5	7.1	0.14	4.80	−0.49

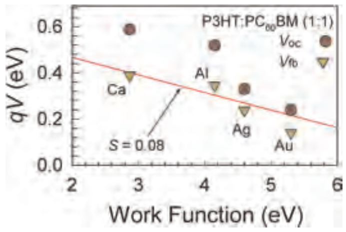

Figure 3. Experimental values of V_{fb} and V_{oc} as a function of the metal used in the cathode contact Ca, Al, Ag, or Au. While V_{oc} is higher the lower the metal work function is, V_{fb} saturates around ~0.4 V. The slope S defined in eq 7 is calculated from the linear fit considering Ca, Al, and Ag.

An example of the measured current–density voltage j–V characteristics under simulated AM1.5G illumination (1000 W m^{-2}) of P3HT:PC_{60}BM solar cells using different cathode metals is plotted in Figure 2a. Relatively low power conversion efficiency (Table 1) is obtained with devices comprising a Ca cathode presumably because of the active layer thickness (~350 nm) used. We will later show the response of thinner films. Capacitance measured in the dark is drawn as a function applied voltage. The expected increase in capacitance in excess of the geometrical value ($C_g \approx 10$ nF cm^{-2}) is observed (Figure 2b) because of the modulation of depletion zone by the change of voltage.[24] Recent studies using different techniques support the interpretation of the capacitance rise at low forward voltages in terms of the formation of a depletion zone near the cathode contact.[22,28] By examining Figure 2c, which corresponds to Mott–Schottky plots, one can realize how the flat-band voltage V_{fb} extracted from the intercept value changes with the cathode metal (see Supporting Information and Table 1). We systematically observed that low work function metals such as Ca yield higher open-circuit voltage V_{oc} values (see Figure 3). For metals with work function higher than the fullerene LUMO level (~3.9 eV), a voltage loss appears as a consequence of the electron energy mismatch between the active layer and the extracting contact. The flat-band voltage resulting from the Mott–Schottky analysis follows the same trend as V_{oc} for higher work function metals, as observed in Figure 3. However, in the case of Ca as the cathode contact, it is found to be $V_{fb} \approx 0.4$ V, far below the V_{oc} achieved. It is worth noting that, despite a large variation (>2 eV) among the metal cathode work functions, only a small change is observed for V_{fb} ($\sim$0.4–0.2 V as listed in Table 1). Accordingly the slope between qV_{fb} and the metal work function ϕ_c is experimentally observed to be very small, $S = 0.08$. Because of the reasons given below, we have left aside the case of Au in this slope calculation. We have already related in previous papers these low V_{fb} found for low work function metal values to the presence of a dipole layer made up at the organic layer/metal interface.[21]

Model for Determination of Flat-Band Voltage and Dipole Layer. We will next show how to calculate the flat-band voltage by considering simple electrostatic arguments.[29,30] At flat-band voltage, the space charge through the depletion layer is negligible, and therefore, the interface negative charge Q_{is} is fully compensated by a positive charge at the metal Q_c, that is, $-Q_{is} = Q_c$. By examining Figure 1D, one can readily express the flat-band voltage as a function of the dipole potential drop Δ' (in flat-band conditions)

$$qV_{fb} = E_{Fp} - \phi_c - \Delta' \qquad (2)$$

Here E_{Fp} corresponds to the hole Fermi level at forward applied voltage. We assume that E_{Fp} practically corresponds to the Fermi level at equilibrium (Figure 1C). The interface dipole contribution is related to the interface charge as

$$\Delta' = \frac{\delta Q_{is}}{\varepsilon_i \varepsilon_0} \qquad (3)$$

where ε_i accounts for the dielectric constant of the interface layer ($\varepsilon_i \sim 3$ for an organic layer), ε_0 is the permittivity of the free space, and δ stands for the charge separation at the dipole layer ($\delta \sim 5$ Å), assuming that a molecular monolayer accommodates the interface charge.

As previously introduced, the CNL plays a determining role in the interface equilibration. In this model, specific gap states are assumed at the surface in contact with the metal. The character of the surface states changes from mostly acceptor type approaching the bottom of the conduction band to mostly donor type close to the top of the valence band. E_{CNL} represents the energy that marks the separation between the two classes of states within the IDOS. It is also assumed that the interface states readily achieve equilibrium with the metal electronic states. If the Fermi level of the metal is initially above E_{CNL}, then electrons are transferred to IDOS, while the opposite is true if the Fermi level of the metal lies below CNL. The net consequence of the transference to this type of surface states distribution is that a dipole is built such that the Fermi level of the metal will tend to align with the charge-neutrality level. The fact that different metals can be compared is due to the relatively weak sensitivity of the organic CNL to the metal/organic interaction.[15] If the IDOS is very high, all metal Fermi levels will be pulled to the same place, E_{CNL}, and the interface is said to undergo Fermi level pinning. In this case, the interfacial states are able to accommodate all of the charge required to equilibrate a large portion of offset in work functions $\phi_c - \phi_s$.[13] In general, the equilibration consists both of the dipole layer contribution and the band bending.[29]

The interface charge is obtained by assuming that the occupation of the interface state distribution IDOS, g_{is}, is governed by the position of the metal Fermi level, E_{Fm}

$$Q_{is} = -q \int_{E_{CNL}}^{E_{Fm}} g_{is} dE \qquad (4)$$

Here, the integral extends from the charge-neutrality level to E_{Fm}, as shown in Figure 1D. As remarked before, it is assumed that the interface states are in intimate connection (equilibrium) with the metal Fermi level through a very thin separating layer (<10 Å). The dipole layer then is transparent to electrons, while it can withstand a potential difference across it. In the specific case of organic devices, the dipole layer formed between interface organic molecules and metal contacts has been taken into account in previous models on charge injection through metal/organic interfaces.[16,31,32]

Since the E_{Fm} position depends on the applied voltage to achieve flat-band conditions, in which $E_{Fm} = E_{Fp} - qV_{fb}$, it is clear from eqs 3 and 4 that Δ' is dependent on qV_{fb}. In general, eq 4 should be solved numerically after considering an adequate IDOS. By assuming that g_{is} varies weakly between E_{CNL} and E_{Fm}, eq 4 can be approximated as $Q_{is} = qg_{is}(E_{CNL} - E_{Fm})$. Equation 2 can be then rewritten as follows

$$qV_{fb} = E_{Fp} - \phi_c - \frac{q\delta g_{is}}{\varepsilon_i \varepsilon_0}(E_{CNL} - E_{Fp} + qV_{fb}) \qquad (5)$$

After some calculations, one arrives at the expression

$$qV_{fb} = E_{Fp} - E_{CNL} - S(\phi_c - E_{CNL}) \qquad (6)$$

The parameter S, which accounts for the effect of g_{is} on the contact energetics, is expressed as follows when a constant IDOS g_{is} is assumed

$$S = \frac{1}{1 + q\delta g_{is}/\varepsilon_i \varepsilon_0} \qquad (7)$$

It is important to note that large interface density values, $g_{is} \gg$, entail $S \approx 0$ in such a way that the barrier becomes independent of the metal work function. On the contrary, $g_{is} \ll$ would imply $S \approx 1$ recovering the so-called Schottky limit. Equation 6 predicts a linear relationship between qV_{fb} and ϕ_c, with a negative slope equaling the parameter S.

Strictly speaking, calculations made in flat-band conditions $V_{app} = V_{fb}$ (which are related to the experimental procedure to extract V_{bb}) might not coincide with those occurring in equilibrium ($V_{app} = 0$). In other words, parameters in eq 1 and eq 2 could differ because of the voltage dependence of the dipole contribution. This issue was discussed by Cowley,[30] who arrived at the conclusion that $qV_{fb} = qV_{bb} - \Delta + \Delta'$. The variation of the dipole strength $\Delta - \Delta'$ is proportional to the factor $S(2q\varepsilon_s\varepsilon_0N)^{1/2}(\delta/\varepsilon_i\varepsilon_0)$, which can be readily evaluated assuming typical values for the doping level extracted from the slope of the Mott–Schottky analysis $N \sim 10^{16}$ cm^{-3} (see Supporting Information) and the dielectric permittivity of the organic bulk $\varepsilon_s \sim 3$. In our case, the correction results in negligible values of <0.1 meV, which allows us to safely identify $V_{fb} = V_{bb}$ and $\Delta = \Delta'$. These last equalities support the procedure of determining the band bending from the intercept of the Mott–Schottky plot. In terms of the device operation, it entails that forward applied voltages $V_{app} < V_{fb}$ reduce the band bending, while they leave unaltered the voltage drop at the dipole layer; that is, there is no significant change in the interface charge Q_{is}.

Experimental Determination of Flat-Band Values and Dipole Layers. Equation 6 predicts the behavior observed in Figure 3. A linear fitting results in $S = 0.08$ with $g_{is} = 4 \times 10^{14}$ cm^{-2} eV^{-1} calculated using eq 7. The low value encountered for the parameter S indicates a significant degree of Fermi level pinning, and this implies a large shift for the metal Fermi level displacement along the polymer band gap in the process of contact equilibration. From eq 6, an estimation of CNL can also be evaluated from the linear fit. This last calculation gives a value E_{CNL} = 4.7 eV. The position of the Fermi level corresponding to the p-doped organic blend is approximated by means of an expression $E_{Fp} \approx E^{D}_{HOMO} - k_BT \ln(N_{HOMO}/p_0)$, which assumes Boltzmann statistics for the hole occupancy of the HOMO levels. The density of states at the HOMO level is taken as $N_{HOMO} \sim 10^{20}$ cm^{-3}, and the background hole density caused by the doping as extracted from the Mott–Schottky analysis results in $p_0 = N \sim 5 \times 10^{15}$ cm^{-3} (see Supporting Information and Table 1). Under these assumptions, one arrives at $E_{Fp} \approx 4.95$ eV, a value that is located at deeper energies with respect to E_{CNL}. The position reached by the metal Fermi level calculated as $E_{Fm} = E_{Fp} - qV_{fb}$ indicates that the interface states exercise a large influence to locate it near CNL (see Table 1). Because the Au work function lies at larger values than E_{CNL} (see Figure 1A), the calculation of the parameter S has not considered this value.

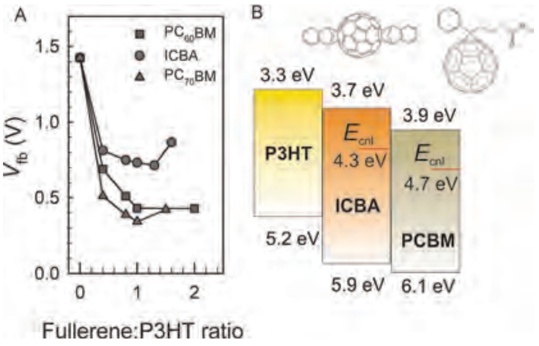

Figure 4. (A) Variation of the flat-band voltage with the blend ratio for different fullerenes. Lines are used to guide the eyes. (B) Energy diagram indicating the position of the CNL and the corresponding fullerene energy levels.

The previous analysis leads us to view the cathode contact energetics as drawn in Figure 1C. The main portion of the work function mismatch, $\phi_c - \phi_s$, is not equilibrated by the space charge region (majority carrier depletion zone) but through the voltage drop at the interface dipole layer. The question that arises at this stage concerns the nature of the interface states responsible for the dipole layer formation. Also noticeable is the deep location of the charge-neutrality level E_{CNL} = 4.7 eV with respect to the vacuum level. We propose here that the negative charge on the organic side of the interface is originated by reduced fullerene molecules attached to the metal contact and energetically located within the effective band gap IDOS. In the vicinity of the metal, the energy spread of fullerene LUMO levels produced by the inherent disorder of the organic blend is expected to be even larger than that encountered in fullerene bulk molecules.

The assumption of a constant g_{is} used in the derivation of eq 6 is an oversimplification of the actual IDOS, in any case, the low value found for the parameter S points to a large interfacial DOS at lower energies which effectively pins the metal Fermi level at ~4.6 eV with respect to the vacuum level (see Table 1). This energy approximately coincides with the position extracted for CNL. We remark here that this value is also in agreement with the observed saturation in the Fermi level of PCBM layers on coated substrates[33] as derived from ultraviolet (UPS) and X-ray (XPS) photoelectron spectroscopy.

Dependence of Flat-Band Values and Dipole Layers on the Composition of the Blend. In order to gain further insight into the origin of the interface states and reinforce our conjecture which links IDOS to reduced fullerene molecules, we have performed a series of experiments varying the blend composition. Three different fullerene acceptors have been tested: namely, ICBA, PC$_{60}$BM, and PC$_{70}$BM, with the aim of checking the effect of the acceptor LUMO level shift on the cathode energetics. In addition, the P3HT:fullerene blend ratio is varied with the aim to experimentally determine the sensitivity of the contact energetics to the organic composition. The j–V characteristics corresponding to these experiments are shown in Supporting Information. In these experiments, the cathode metal is kept unaltered to low work function Ca. Summarized in Figure 4A is the variation in V_{fb} as a function of the

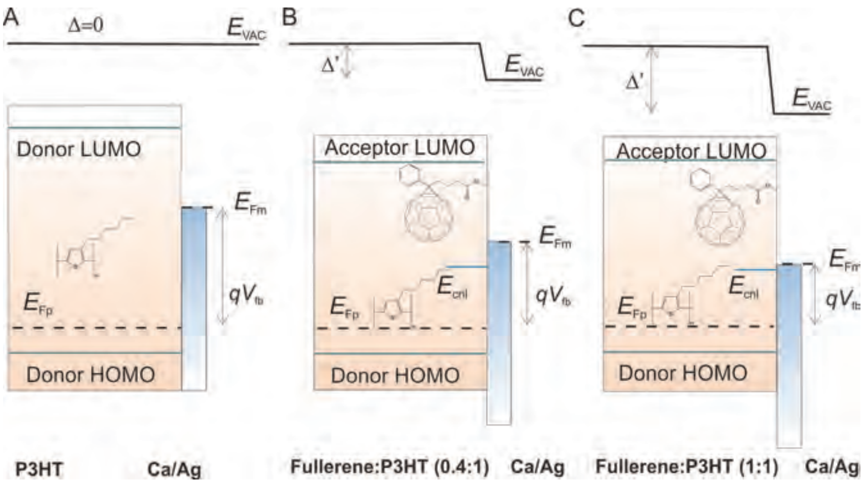

Figure 5. Diagram of the cathode contact in flat-band conditions. (A) Flat vacuum level and large V_{fb} because of the dipole layer absence in the case of the active layer comprising only polymer. (B) Case of low content of fullerene: the dipole layer accommodates a small portion of the work function offset, and the metal Fermi level is situated above the CNL. (C) For larger fullerene content, E_{Fm} is practically pinned at CNL, and a large dipole layer appears.

fullerene:P3HT blend ratio for three different fullerenes used. The first experimental finding to note is the value obtained for devices prepared with only polymer V_{fb} = 1.5 V, which is in rather good agreement with the expected large offset between the metal and organic layer work functions, $\phi_c - \phi_s \approx 1.9$ eV, as drawn in Figure 5A. Here the cathode contact ability to form a dipole layer is very limited because no acceptor molecules are present at the interface. The band bending is then the principal mechanism to equilibrate the contact in accordance to the Schottky limit.

By incrementing the amount of fullerene molecules in the device, V_{fb} steeply decreases (Figure 4A), as expected when the amount of acceptor states attached to the cathode metal increases, then enlarges the dipole voltage drop. The effect of incrementing the fullerene content of the blend is illustrated in Figure 5. These diagrams correspond to flat-band conditions. Lower coverage of the contact interface by fullerene molecules (small IDOS) has an important effect on the contact equilibration. By reducing g_{is} (larger S), one might envisage an increment in band bending as inferred from eq 1. When the fullerene amount is increased, interface coverage reaches a maximum, then reduces V_{fb} and enlarges the dipole voltage offset Δ. Interestingly, V_{fb} reaches a plateau at blend ratio approaching 1:1. As drawn in Figure 5C, the metal Fermi level approaches the charge-neutrality level for a blend ratio of $\sim$1:1. We would not expect significant changes in the position of CNL by using different content of the same fullerene, although this mainly depends on the actual IDOS distribution (Figure 5B,C).

Another key aspect of this investigation is to explore the effect of the fullerene energetics on the cathode equilibration. By changing the type of fullerene, it is expected that the IDOS varies, as well. Reported LUMO energy levels for ICBA and PC$_{60}$BM (3.74 and 3.91 eV, respectively) show a shift of 0.17 eV as calculated from cyclic voltammetry.[34] These energy levels are shown in Figure 4B as well as those corresponding to P3HT. By examining Figure 4A, one can observe that both PC$_{60}$BM- and PC$_{70}$BM-based devices yield a flat-band voltage plateau for blend ratio ($\sim$1:1) of $V_{fb} \sim 0.4$ V. As explained previously, the metal Fermi level approximately coincides with that calculated for the charge-neutrality level $E_{CNL} \approx 4.7$ eV. Since the same trend is observed when ICBA is used as fullerene acceptor (with a different value for the flat-band plateau $V_{fb} \sim 0.7$ V), one can infer that CNL is shifted to lower energy positions. In this case, we obtain a value of $E_{CNL} \approx 4.3$ eV. Such downward displacement is in qualitative agreement with the general IDOS energy shift caused by the fullerene LUMO level offset (Figure 4B). Because ICBA has different properties as compared with PCBM molecules, it might also be possible for the same blend ratio ($\sim$1:1) that a reduced amount of ICBA molecules covers the cathode interface. This would imply that the increase in V_{fb} is explained by differences in concentration rather than molecular energetics. We show in Supporting Information, AFM and cross-section SEM images of P3HT:PCBM and P3HT:ICBA films, which exhibit very similar morphology. These experiments reinforce the idea of an energy-related origin for the differences observed in $C-V$ analysis between PCBM- and ICBA-based devices. It is then inferred from the previous discussion that band bending and dipole layer strength are extremely dependent on the amount and nature of fullerene molecules attached to the metal cathode.

Effect of Cathode Interlayers. Cathode electron-selective interlayers are commonly used to both enhance energy level alignment and to prevent holes from crossing the contact. The inclusion of these interlayers is supposed to largely modify the interface electronic

TABLE 2. Photovoltaic Parameters and Parameters Extracted from the Capacitance Mott−Schottky Analysis of Thin P3HT:Fullerene Solar Cells with Different Cathode Interlayers

$P3HT:PC_{60}BM$ (100 nm)	j_{sc} (mA cm^{-2})	V_{oc} (V)	FF	PCE (%)	N (10^{15} cm^{-3})	V_{fb} (V)	E_{Fm} (eV)	Δ (eV)
Ca	8.72	0.62	0.62	3.4	10	0.42	4.53	1.66
BCP/Ca	8.00	0.63	0.63	3.2	25	0.44	4.51	1.64
LiF/Al	7.73	0.60	0.62	3.0	20	0.44	4.51	0.36
C_{60}/Ca	7.68	0.61	0.60	2.8	47	0.48	4.47	1.60

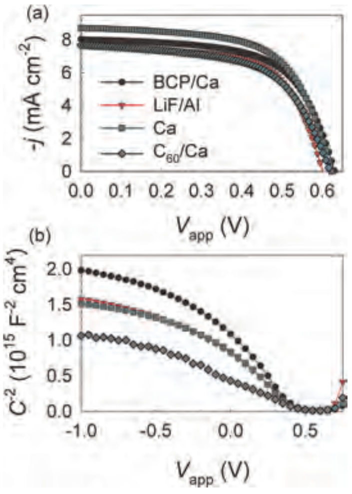

Figure 6. (a) Current−voltage characteristics of devices with structure ITO/PEDOT:PSS/P3HT:PCBM/cathode contact as indicated. (b) Mott−Schottky plots from which the p-doping level N and flat-band voltage V_{fb} are extracted. Note the similar value obtained from the voltage intercept around 0.4 V.

structure which enhances the device performance. We have studied here the effect of LiF,[35] bathocuproine BCP,[36] and evaporated C_{60} thin layers on interfacial properties as displayed in the Mott−Schottky characteristics. Details on the deposition methods of these interlayers can be obtained in Supporting Information. In these experiments, thinner active P3HT:PCBM layers (100 nm) have been used which has allowed increasing the cell performance (PCE > 3%) as observed by comparing Tables 1 and 2 for Ca cathode contact. In Figure 6, $j-V$ curves and Mott−Schottky plots are shown. It is observed that V_{fb} extracted from the intercept (Figure 6b) is located around 0.4 V despite the use of different interlayers. This observation indicates that the CNL underpins the contact at $E_{Fm} \approx 4.5$ eV, in agreement with results presented in the previous sections. Interestingly, V_{fb} is observed to be highly active layer thickness-independent: 0.39 V for 350 nm thick film and 0.42 V for 100 nm thick film in the case of Ca cathode. This finding reinforces the idea of the crucial role played by interface states on the local equilibration of the contact.

We finally remark that the equilibration at the cathode interface is the key mechanism to understand the photovoltaic effect.[21] When the solar device operates in high forward (or large illumination intensities under open-circuit conditions), the rise of the bulk electron Fermi level induces an increment within the occupancy of fullerene DOS states. A good connection between the internal and the cathode metal Fermi level is now assured by the interface states identified here using capacitance methods.

CONCLUSION

We have provided a detailed analysis of the cathode energy equilibration of bulk-heterojunction solar cells. The Fermi level mismatch established between the cathode metal and the organic layer is equilibrated by the vacuum level offset and split into two contributions: spatially extended band bending in the organic bulk and voltage drop at the interface dipole layer. The Mott−Schottky analysis allows us to extract both the flat-band voltage (band bending) and the p-doping density. It has been experimentally observed that the dipole layer withstands a large part of the total Fermi level mismatch when the blend ratio approaches ∼1:1. Interface states are related to fullerene reduced molecules covering the metal contact. We have concluded that the dipole contribution, and consequently the band bending, is highly sensitive to the fullerene interface DOS.

METHODS

Device Fabrication. Polymer solar cells were fabricated with a standard sandwich structure of ITO/PEDOT:PSS/P3HT:fullerene/metal/Ag and 9 mm^2 of active area. PEDOT:PSS was spin-coated in air at 5500 rpm for 30 s onto an ITO-coated glass substrate (10 Ω/sq), film thickness of ∼35 nm. The substrates were heated at 120 °C for 10 min to remove traces of water and were transferred to a glovebox equipped with a thermal evaporator. The P3HT:fullerene layer was deposited at speeds of 1200 rpm for 30 s followed by a slow drying of the film in a Petri dish. At this point, samples were thermally annealed at 130 °C for 20 min. Sequential evaporation of the interfacial layer or metal was carried out at a base pressure of 3×10^{-6} mbar under study and was terminated by evaporation of a protective Ag layer (100 nm). Devices were encapsulated by using a pressure-sensitive glue (polyisobutylene, Oppanol B 12 SFN from BASF) and a glass microscope slide. Samples were then taken out of the glovebox for device characterization. A detailed description of the structures can be found in Supporting Information.

Device Characterization. Current density−voltage and capacitance measurements were carried out by illumination with a 1.5G illumination source (1000 W m^{-2}) using an Abet Sun 2000 solar simulator. The light intensity was adjusted with a calibrated Si solar cell. Capacitance was recorded by applying a small voltage perturbation (20 mV rms) at 100 Hz. Measurements were carried out in the dark at different bias voltage to extract the capacitance−voltage characteristics. These measurements were performed with Autolab PGSTAT-30 equipped with a frequency analyzer module.

Conflict of Interest: The authors declare no competing financial interest.

Acknowledgment. We thank financial support from Ministerio de Educacion y Ciencia under project HOPE CSD2007-00007 (Consolider-Ingenio 2010), and Generalitat Valenciana (Prometeo/2009/058, ACOMP/2009/056 and ACOMP/2009/095). L.F.M. acknowledges Conselho Nacional de Desenvolvimento Científico e Tecnológico (CNPq) for a grant (Processo: 201380/2010-2).

Supporting Information Available: The capacitance−voltage analysis performed to extract the background charge density and the flat-band voltage is explained, along with examples of *j*−*V* curves and fabrication conditions. Analysis of active layer topography and device cross section is also provided. This material is available free of charge *via* the Internet at http://pubs.acs.org.

REFERENCES AND NOTES

1. Steim, R.; Koglera, F. R.; Brabec, C. J. Interface Materials for Organic Solar Cells. *J. Mater. Chem.* **2010**, *20*, 2499–2512.
2. Ratcliff, E. L.; Zacher, B.; Armstrong, N. R. Selective Interlayers and Contacts in Organic Photovoltaic Cells. *J. Phys. Chem. Lett.* **2011**, *2*, 1337–1350.
3. Po, R.; Carbonera, C.; Bernardia, A.; Camaioni, N. The Role of Buffer Layers in Polymer Solar Cells. *Energy Environ. Sci.* **2011**, *4*, 285–310.
4. Yip, H.-L.; Hau, S. K.; Baek, N. S.; Ma, H.; Jen, A. K.-Y. Polymer Solar Cells That Use Self-Assembled-Monolayer-Modified ZnO/Metals as Cathodes. *Adv. Mater.* **2008**, *20*, 2376–2382.
5. Seo, J. H.; Gutacker, A.; Sun, Y.; Wu, H.; Huang, F.; Cao, Y.; Scherf, U.; Heeger, A. J.; Bazan, G. C. Improved High-Efficiency Organic Solar Cells *via* Incorporation of a Conjugated Polyelectrolyte Interlayer. *J. Am. Chem. Soc.* **2011**, *133*, 8416–8419.
6. Wang, D. H.; Moon, J. S.; Seifter, J.; Jo, J.; Park, J. H.; Park, O. O.; Heeger, A. J. Sequential Processing: Control of Nanomorphology in Bulk Heterojunction Solar Cells. *Nano Lett.* **2011**, *11*, 3163–3168.
7. Schmidt-Hansberg, B.; Sanyal, M.; Klein, M. F. G.; Pfaff, M.; Schnabel, N.; Jaiser, S.; Vorobiev, A.; Müller, E.; Colsmann, A.; Scharfer, P.; *et al.* Moving through the Phase Diagram: Morphology Formation in Solution Cast Polymer-Fullerene Blend Films for Organic Solar Cells. *ACS Nano* **2011**, *5*, 8579–8590.
8. Ishii, H.; Sugiyama, K.; Ito, E.; Seki, K. Energy Level Alignment and Interfacial Electronic Structures at Organic/Metal and Organic/Organic Interfaces. *Adv. Mater.* **1999**, *11*, 605–625.
9. Crispin, X.; Geskin, V.; Crispin, A.; Cornil, J.; Lazzaroni, R.; Salaneck, W. R.; Bredas, J.-L. Characterization of the Interface Dipole at Organic/Metal Interfaces. *J. Am. Chem. Soc.* **2002**, *124*, 8131–8141.
10. Hwang, J.; Wan, A.; Kahn, A. Energetics of Metal−Organic Interfaces: New Experiments and Assessment of the Field. *Mater. Sci. Eng. R* **2009**, *64*, 1–31.
11. Braun, S.; Salaneck, W. R.; Fahlman, M. Energy-Level Alignment at Organic/Metal and Organic/Organic Interfaces. *Adv. Mater.* **2009**, *21*, 1450–1472.
12. Salaneck, W. R.; Seki, K.; Kahn, A.; Pireaux, J.-J. *Conjugated Polymer and Molecular Interfaces. Science and Technology for Photonic and Optoelectronic Applications*; Marcel Dekker: New York, 2002.
13. Bardeen, J. Surface States and Rectification at a Metal Semi-conductor Contact. *Phys. Rev.* **1947**, *71*, 717–727.
14. Vázquez, H.; Flores, F.; Oszwaldowski, R.; Ortega, J.; Pérez, R.; Kahn, A. Barrier Formation at Metal−Organic Interfaces: Dipole Formation and the Charge Neutrality Level. *Appl. Surf. Sci.* **2004**, *234*, 107–112.
15. Vázquez, H.; Gao, W.; Flores, F.; Kahn, A. Energy Level Alignment at Organic Heterojunctions: Role of the Charge Neutrality Level. *Phys. Rev. B* **2005**, *71*, 041306(R).
16. Baldo, M. A.; Forrest, S. R. Interface-Limited Injection in Amorphous Organic Semiconductors. *Phys. Rev. B* **2001**, *64*, 085201.
17. Ishii, H.; Hayashi, N.; Ito, E.; Washizu, Y.; Sugi, K.; Kimura, Y.; Niwano, M.; Ouchi, Y.; Seki, K. Kelvin Probe Study of Band Bending at Organic Semiconductor/Metal Interfaces: Examination of Fermi Level Alignment. *Phys. Status Solidi A* **2004**, *201*, 1075–1094.
18. Abdou, M. S. A.; Orfino, F. P.; Son, Y.; Holdcroft, S. Interaction of Oxygen with Conjugated Polymers: Charge Transfer Complex Formation with Poly(3-alkylthiophenes). *J. Am. Chem. Soc.* **1997**, *119*, 4518–4524.
19. Hoshino, S.; Yoshida, M.; Uemura, S.; Kodzasa, T.; Takada, N.; Kamata, T.; Yase, K. Influence of Moisture on Device Characteristics of Polythiophene-Based Field-Effect Transistors. *J. Appl. Phys.* **2004**, *95*, 5088–5093.
20. Liang, Z.; Nardes, A.; Wang, D.; Berry, J. J.; Gregg, B. A. Defect Engineering in π-Conjugated Polymers. *Chem. Mater.* **2009**, *21*, 4914–4919.
21. Bisquert, J.; Garcia-Belmonte, G. On Voltage, Photovoltage and Photocurrent in Bulk Heterojunction Organic Solar Cells. *J. Phys. Chem. Lett.* **2011**, *2*, 1950–1964.
22. Lee, J.; Kong, J.; Kim, H.; Kang, S.-O.; Lee, K. Direct Observation of Internal Potential Distributions in a Bulk Heterojunction Solar Cell. *Appl. Phys. Lett.* **2011**, *99*, 243301.
23. Nishi, T.; Kanai, K.; Ouchi, Y.; Willis, M. R.; Seki, K. Evidence for the Atmospheric p-Type Doping of Titanyl Phthalocyanine Thin Film by Oxygen Observed as the Change of Interfacial Electronic Structure. *Chem. Phys. Lett.* **2005**, *414*, 479–482.
24. Fabregat-Santiago, F.; Garcia-Belmonte, G.; Mora-Seró, I.; Bisquert, J. Characterization of Nanostructured Hybrid and Organic Solar Cells by Impedance Spectroscopy. *Phys. Chem. Chem. Phys.* **2011**, *13*, 9083–9118.
25. Boix, P. P.; Garcia-Belmonte, G.; Muñecas, U.; Neophytou, M.; Waldauf, C.; Pacios, R. Determination of Gap Defect States in Organic Bulk Heterojunction Solar Cells from Capacitance Measurements. *Appl. Phys. Lett.* **2009**, *95*, 233302.
26. Morfa, A. J.; Nardes, A. M.; Shaheen, S. E.; Kopidakis, N.; van de Lagemaat, J. Time-of-Flight Studies of Electron-Collection Kinetics in Polymer:Fullerene Bulk-Heterojunction Solar Cells. *Adv. Funct. Mater.* **2011**, *21*, 2580–2586.
27. Nalwa, K. S.; Mahadevapuram, R. C.; Chaudhary, S. Growth Rate Dependent Trap Density in Polythiophene-Fullerene Solar Cells and Its Implications. *Appl. Phys. Lett.* **2011**, *98*, 093306.
28. Li, J. V.; Nardes, A. M.; Liang, Z.; Shaheen, S. E.; Gregg, B. A.; Levi, D. H. Simultaneous Measurement of Carrier Density and Mobility of Organic Semiconductors Using Capacitance Techniques. *Org. Electron.* **2011**, *12*, 1879–1885.
29. Cowley, A. M.; Sze, S. M. Surface States and Barrier Height of Metal Semiconductor Systems. *J. Appl. Phys.* **1965**, *65*, 3212–3220.
30. Cowley, A. M. Depletion Capacitance and Diffusion Potential of Gallium Phosphide Schottky-Barrier Diode. *J. Appl. Phys.* **1966**, *37*, 3024–3032.
31. Garcia-Belmonte, G.; Bolink, H. J.; Bisquert, J. Capacitcance−Voltage Characteristics of Organic Light-Emitting Diodes Varying the Cathode Metal: Implications for Interfacial States. *Phys. Rev. B* **2007**, *75*, 085316.
32. Bisquert, J.; Garcia-Belmonte, G.; Munar, A.; Sessolo, M.; Soriano, A.; Bolink, H. J. Band Unpinning and Photovoltaic Model for P3HT-PCBM Organic Bulk Heterojunctions under Illumination. *Chem. Phys. Lett.* **2008**, *465*, 57–62.
33. Xu, Z.; Chen, L. M.; Chen, M.-H.; Li, G.; Yang, Y. Energy Level Alignment of Poly(3-hexylthiophene):[6,6]-Phenyl-C61-Butyric Acid Methyl Ester Bulk Heterojunction. *Appl. Phys. Lett.* **2009**, *95*, 013301.
34. He, Y.; Chen, H.-Y.; Hou, J.; Li, Y. Indene-C60 Bisadduct: A New Acceptor for High-Performance Polymer Solar Cells. *J. Am. Chem. Soc.* **2010**, *132*, 1377–1382.
35. Shaheen, S. E.; Brabec, C. J.; Sariciftci, N. S.; Padinger, F.; Fromherz, T.; Hummelen, J. C. 2.5% Efficient Organic Plastic Solar Cells. *Appl. Phys. Lett.* **2001**, *78*, 841–843.
36. Chang, C.-C.; Lin, C.-F.; Chiou, J.-M.; Ho, T.-H.; Tai, Y.; Lee, J.-H.; Chen, Y.-F.; Wang, J.-K.; Chen, L.-C.; Chen, K.-H. Effects of Cathode Buffer Layers on the Efficiency of Bulk-Heterojunction Solar Cells. *Appl. Phys. Lett.* **2010**, *96*, 263506.

THE JOURNAL OF
PHYSICAL CHEMISTRY C

Article

pubs.acs.org/JPCC

Diffusion-Recombination Determines Collected Current and Voltage in Polymer:Fullerene Solar Cells

Teresa Ripolles-Sanchis, Antonio Guerrero, Juan Bisquert, and Germà Garcia-Belmonte*

Photovoltaic and Optoelectronic Devices Group, Departament de Física, Universitat Jaume I, ES-12071 Castelló, Spain

ABSTRACT: The basic operating mechanisms of organic bulk-heterojunction cells comprising poly(3-hexylthiophene (P3HT): [6,6]-phenyl-C_{61}-butyric acid methyl ester (PCBM) blends are examined based on the selection of diverse materials as cathode contact. The use of both highly and poorly efficient cathodes in combination with impedance spectroscopy allows for a clear-cut separation of the physical mechanisms occurring within the active layer bulk from those taking place at the organic blend-contact interface. The system under study uses either Ca or CaO as the efficient and blocking contact, respectively. The impedance analysis demonstrates that charge carriers (electrons) move by diffusion within extended quasi-neutral regions, so that the cell operation is governed by the kinetic competition between charge transport toward the outer contacts and loss by recombination. It is also observed that contacts contribute with an additional, non-negligible, series resistance that accounts for the electron extraction process. The comparison between active layer thickness and the carrier diffusion length allows exclusion of bulk transport losses as a highly detrimental factor for this class of solar cells.

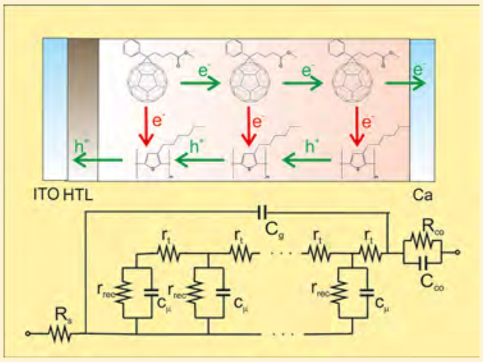

1. INTRODUCTION

In the pursuit for engineering versatile and cheap light-harvesting solar cells, organic solar technologies have demonstrated in the past few years their ability to reach competitive levels of power conversion efficiency (PCE). Innovations in materials design (i.e., low bandgap polymers or use of additives) and cell architectures (i.e., incorporation of carrier selective interlayers or a better blend morphology control) have allowed achieving over 10% in PCE.[1] Further performance improvements might result from a detailed understanding of the loss mechanisms reducing PCE. In addition to phenomena determining charge photogeneration, deeper knowledge about processes governing charge carrier motion, recombination, and outer interface charge selection and extraction might become crucial. Particularly important is the overall impact of the electronic transport mechanisms, which have dramatic effects when relatively thicker active layer films are used to enhance light harvesting. Thinner films are usually able to exhibit almost 100% conversion of absorbed photons into collected carriers,[2] thus indicating that transport mechanisms do not limit the achievable photocurrent.[3] Most thicker active layer devices suffer from an incomplete collection of photogenerated charges as recombination processes have sufficient time to affect charges being transported. This last statement is however not general as demonstrated with some polymer:fullerene combinations.[4] Therefore, quantifying the influence of competing carrier transport and recombination mechanisms[5,6] on cell performance has become a major topic for organic bulk-heterojunction photovoltaics.

The clarification of the presence or absence of extended quasi-neutral regions within the active layer bulk is a central point prior to establishing the basics of device physics for organic bulk-heterojunction solar cells. If quasi-electroneutrality is invoked, then even in the case of current flow space charge regions related to excess carriers cannot be built up, and the analytical treatment of the mathematical system describing the solar device is considerably simplified.[7] The dielectric relaxation time is related to the material permittivity $\varepsilon\varepsilon_0$ (ε being the dielectric constant, and ε_0 the vacuum permittivity), and its conductivity σ is as follows:

$$\tau_{\mathrm{die}} = \frac{\varepsilon\varepsilon_0}{\sigma} \tag{1}$$

The assumption of the occurrence of quasi-neutral regions relies on the property that carrier lifetime (recombination time, τ_{rec}) is much larger than the dielectric relaxation time τ_{die}. If $\tau_{\mathrm{rec}} > \tau_{\mathrm{die}}$ mobile carriers can exist long enough to neutralize charge. Depending on whether $\tau_{\mathrm{rec}} > \tau_{\mathrm{die}}$ (*lifetime* semiconductor regime), or $\tau_{\mathrm{rec}} < \tau_{\mathrm{die}}$ (*relaxation* semiconductor regime), the physics governing the device operation changes drastically. In the relaxation semiconductor regime, electroneutrality is not a justifiable assumption. Hence regions of near-zero net local recombination may occur, implying spatially separated excess electron and hole concentrations. This will enhance the space charge of dielectric relaxation-dependent decay.[8] For instance, low-conductivity amorphous *p-i-n* silicon solar cells were modeled as developing photogenerated hole space charge regions near the *p* contact that concentrate the voltage drop.[9] In the extreme case, currents should be space charge limited as

Received: June 16, 2012
Revised: July 21, 2012
Published: July 23, 2012

dx.doi.org/10.1021/jp305941f | *J. Phys. Chem. C* 2012, 116, 16925−16933

occurring in organic light-emitting diodes based on low-mobility polymers or molecules.[10]

In order to classify the solar cell blend as operating within the relaxation ($\tau_{rec} < \tau_{die}$), or lifetime ($\tau_{rec} > \tau_{die}$) regime, the polymer conductivity plays a crucial role, as derived from eq 1. It has previously been established that many polymers used for photovoltaic applications contain native carriers due to doping, normally of p-type.[11] The archetypical regioregular poly(3-hexylthiophene) (P3HT) is known to have a background hole density of order $p_0 \approx 10^{16}$ cm^{-3},[12,13] which taking into account the reported mobility ($\mu_h \approx 10^{-4}$ cm^2 V^{-1} s^{-1}) in diode configuration,[14,15] the relationship $\sigma = q\mu_h p_0$ and typical permittivity values for this compound ($\sim 3\varepsilon_0$) yields a value for the relaxation time of $\tau_{die} \leq 1$ μs. Typical recombination times experimentally found approaching open-circuit voltage V_{oc} at 1 sun irradiation intensity, by using different methods, are on the order $\tau_{rec} \approx 10$ μs.[16,17] A device will then be operating in lifetime or relaxation regime depending on the materials properties. Indeed, many active layer blends can be viewed as a specific case of lifetime semiconductors. We have suggested that the depletion region built up in the vicinity of the cathode contact, collapses at forward bias giving rise to extended quasi-neutral regions in organic photovoltaic device.[18,19] Depletion region modulation (spatially confined band bending) by the applied voltage has been identified using alternative methods.[13,20,21]

Since the depletion zone is reduced or even eliminated at operation voltages close to the maximum power point (flatband voltage lies in the range of 0.4 V in most cases), there remains the neutral region in which transport of minority carrier should be controlled by diffusion[22] while the high conductivity of majority carriers (holes) assures rapid shielding. So far, however, observation of the diffusive transport that is clearly predicted by this device model has been elusive, due to other experimental aspects that interfere with the diffusion signatures.

This work aims to show evidence for the first time of the existence of diffusion currents governing the electronic transport at forward bias voltages between maximum power point and V_{oc} in the case of P3HT:PCBM-based cells. It is observed by means of impedance spectroscopy methods that typical diffusive impedance patterns (Warburg response) occur either at large bias voltage for working bulk-heterojunction solar cells, or using devices in which a blocking layer has been inserted between the active layer and cathode contact. Moreover, the analysis incorporates all relevant mechanisms which are expected to intervene within the active layer bulk, namely: carrier transport, recombination current, and charge storage. The impedance response is modeled by means of transmission line models previously introduced in analyzing electron diffusion and recombination in thin layers[23] and later for organic solar cells.[18]

Finally, by altering the structure of the cathode contact, we have identified and modeled the effect of the outer interfaces.[24,25] Two different cathodes (electron extracting or blocking layer) have allowed the observation of the additional resistive and capacitive responses occurring at the interface that have a significant effect on the measured current−voltage characteristics (*j*-*V*). A complete small-amplitude electrical model is presented which permits a fine analysis of determining physical processes taking place in operating devices.

2. EXPERIMENTAL SECTION

2.1. Device Fabrication. P3HT (Aldrich), PEDOT:PSS (CLEVIOS P AI 4083), o-dichlorobenzene (Aldrich, 99.9%), Ca (Aldrich, 99.995%) and silver (Aldrich,99.99%) were used as received without further purification. All manipulations were carried out in a glovebox under a nitrogen atmosphere unless otherwise stated. P3HT:PCBM blends (1:0.8) were prepared from dry o-dichlorobenzene and were stirred at R.T. for 24 h prior to device fabrication. Concentrations based on P3HT of 17 mg/mL were used to obtain active layer thickness of ∼110 nm.

Polymer solar cells were fabricated using a standard sandwich structure of ITO/PEDOT:PSS/P3HT:PCBM/Cathode, and 9 mm^2 of active area (cathode = Ca/Ag or CaO/Ca/Ag). Precleaned ITO coated glass substrates (10 Ω/sq) were treated in a UV−O_3 chamber for 5 min followed by the deposition of PEDOT:PSS by spin coating in air at 5500 rpm for 30 s, film thickness of ∼35 nm. The substrates were heated at 120 °C for 10 min to remove traces of water and were transferred to a glovebox equipped with a thermal evaporator. The P3HT:PCBM layer was deposited at speeds of 1200 rpm (thickness was about 110 nm) for 20 s followed by a slow drying process in a petry dish to provide a dry film. For cells requiring the blocking layer a layer of calcium was evaporated to the desired blocking layer thickness. The evaporated Ca was oxidized using ambient conditions overnight. At this point, all samples were thermally annealed at 130 °C for 10 min to provide an adequate morphology and to promote oxygen desorption. Evaporation of the finished contact was carried out at a base pressure of 3×10^{-6} mbar with Ca/Ag (5/100 nm). Devices were encapsulated with a photoresin and a glass microscopy slide followed by exposure under UV light. Samples were then taken out of the glovebox for device characterization.

2.2. Device Characterization. Current density−voltage and impedance spectroscopy measurements were carried out by varying irradiation intensity (1.5G illumination source 1000 W m^{-2}) using an Abet Sun 2000 Solar Simulator. The light intensity was adjusted with a calibrated Si solar cell. Impedance spectroscopy measurements were performed with Autolab PGSTAT-30 equipped with a frequency analyzer module, and was recorded by applying a small voltage perturbation (20 mV rms). Measurements were carried out at different light intensity and bias voltage sweeping frequencies from 1 MHz down to 100 Hz. The light intensity was measured using an optical power meter 70310 from Oriel Instruments, where a Si photodiode was used to calibrate the system. Direct determination of the relaxation time was performed by transient photocurrent experiment TPC by connecting the devices to a low input (50 Ω) impedance oscilloscope (Agilent 500 MHz bandwidth) which allows measuring near short-circuit conditions. A nitrogen pumped-dye pulsed laser of 596 nm wavelength and 5 ns pulse duration was used to generate a small light perturbation.

3. RESULTS

The device structure used in this work is based on a sandwich structure of indium tin oxide (ITO)/poly(3,4-ethylenedioxythiophene): poly(styrene sulfonic acid) (PEDOT:PSS)/poly-(3-hexylthiophene) (P3HT): [6,6]-phenyl-C_{61}-butyric acid methyl ester (PCBM)/Cathode, (cathode = Ca/Ag or CaO/Ca/Ag). Active layer thickness is situated around 100 nm. Structures used are schematically drawn in Figure 1(a). With

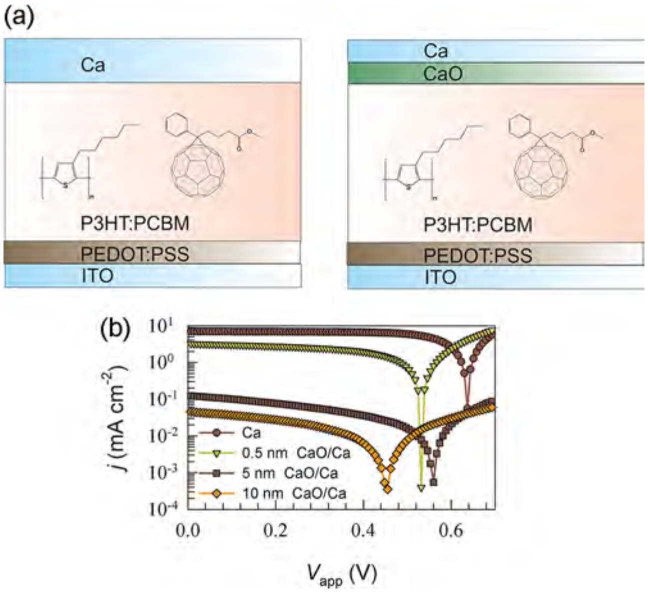

Figure 1. (a) Device configuration of analyzed bulk-heterojunction devices: ITO/PEDOT:PSS/P3HT:PCBM/cathode. Two different cathodes are used: efficient collecting contact based on Ca and insertion of an oxide layer (CaO) of different thickness that blocks the electron collection. (b) $j-V$ curves under 1 sun illumination corresponding to devices using different cathode contact structures. The oxide layer thickness is indicated, ranging from 0.5 to 10 nm.

the aim of studying transport mechanisms under conditions of suppression of dc current flux, a blocking cathode contact has been tested by including CaO layers of different thickness. For thicker oxide layers (10 nm), a complete electron blockage is observed. As we will next explain, blocked cells let us probe the internal electron motion under illumination without the perturbing influence of dc current flowing.

3.1. Effect Blocking Contacts. Figure 1(b) represents $j-V$ characteristics under 1.5G illumination (1000 W m^{-2}) of cells comprising the same organic blend but different cathode contact structure (Table 1). The dramatic effect that the CaO layer produces on the achievable photocurrent is evident in Figure 1(b). As the oxide layer thickness grows, j_{sc} is severely limited by blocking the extraction of photogenerated electrons at the cathode contact. Noticeably, the blocking effect accounts for a reduction of more than 2 orders of magnitude in j_{sc}, while the open-circuit voltage V_{oc} is only reduced by ~200 mV. This last observation suggests that blocked devices under steady-state illumination do not loss completely their ability to accumulate photogenerated carriers despite the oxide layer located at the cathode contact. This occurs because V_{oc} monitors in fact the Fermi level splitting of separated charge carriers in the blend material $qV_F = E_{Fn} - E_{Fp}$, which are ultimately governed by the electron and hole occupancy of their respective electronic states. The electron Fermi level equilibrates with the cathode metal then producing the measured output voltage despite the presence of the oxide layer.

Table 1. Device Operation Parameters under 1.5G Illumination Source (1000 W m^{-2}) for the Devices with P3HT:PCBM Active Layer Using Different Cathodes, Ca/Ag, and Different Blocking Layer (CaO) Thicknesses: 0.5 nm, 5 nm, and 10 nm in CaO/Ca/Ag Cathodes[a]

		j_{sc} (mA cm^{-2})	V_{oc} (mV)	FF	PCE (%)
P3HT:PCBM cathode Ca/Ag		7.0	636	0.67	2.94
P3HT:PCBM cathode CaO/Ca/Ag	CaO (0.5 nm)	3.2	531	0.46	0.79
	CaO (5 nm)	0.1	550	0.24	0.02
	CaO (10 nm)	4×10^{-2}	449	0.28	0.01

[a] Average values shown with variations below 10% for different samples.

A close look at the impedance response of blocked solar devices (with 10 nm-thick CaO layer) let us corroborate that the charge carriers are being stored as suggested previously. Figure 2(a) shows the evolution of the capacitance spectra $C - f$ measured in open-circuit upon variation of the light intensity from dark conditions until nearly 1 sun. Dark capacitance exhibits the expected flat value originated from the dielectric response of the active layer (geometrical capacitance C_g). As the illumination is raised up, capacitance develops a plateau within the frequency range between 100 Hz−1 kHz which signals to the accumulation of excess photogenerated charge

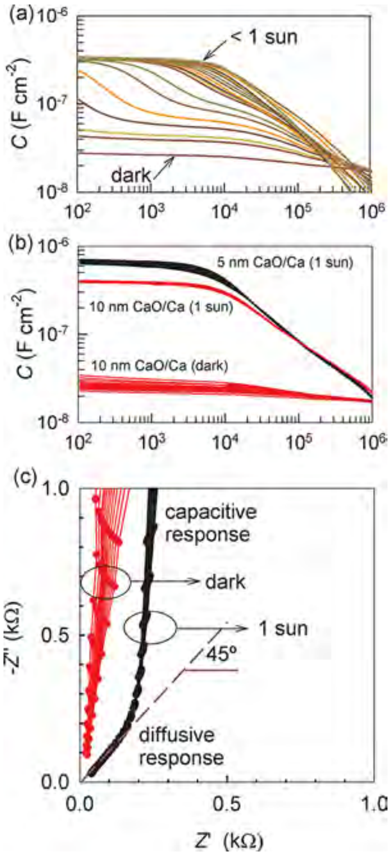

Figure 2. (a) Capacitance spectra plots of a device blocked with CaO (10 nm) measured at different light intensities from the dark to nearly 1 sun illumination, and zero bias. (b) Capacitance spectra plots of devices blocked with two different CaO layer thicknesses measured under 1 sun illuminations and in the dark. At each condition, the applied voltage is varied within the range of −1 to 1 V. Note here the small variation introduced by the bias voltage. (c) Impedance spectra comparison of the impedance plot measured under 1 sun illumination (right spectra) and dark conditions (left spectra) of a device blocked with CaO (10 nm). Applied voltage is varied as in (b).

carriers. The total increase in capacitance over C_g amounts to more than 1 order of magnitude as observed in Figure 2(b) that compares dark and light (1 sun) responses under variation of the applied voltage. Interestingly, the reached low-frequency capacitance appears not to be very sensitive to the bias voltage. This occurs because the external voltage is unable to modify the internal photogenerated V_F and mainly drops at the huge series resistance introduced by the oxide layer. We checked that the low-frequency capacitance plateau is determined by the CaO layer thickness giving larger values of C_{ox} for thinner oxide layers, as shown in Figure 2(b). This last finding helps us to identify C_g and C_{ox} as the limiting capacitances at low (dark) and high illumination conditions. The chemical capacitance C_μ, originated by the storage of photogenerated charges,[19,26] increases with increasing the irradiation intensity and is observed in the middle frequency range. We note here that oxide layers have also been used in MOS structures to investigate the quantum (chemical) capacitance of graphene sheets, in which the graphene capacitance is connected in series with the gate capacitance,[27] similar to the effect found here.

The previous results account for the basic capacitive phenomenology as extracted from the low-frequency part of the spectra. The resistive component at low frequencies exhibits a huge resistor in accordance with the current limiting effect observed in Figure 1(b). By looking at the high-frequency response ($f > 10$ kHz), the behavior changes radically. Instead of purely capacitive spectra, a clearly distinguishable diffusion pattern is observed in Figure 2(c) for illuminated samples. Impedance spectra ($Z''-Z'$) is selected now to make evident the diffusive mechanism fingerprint as a 45°-slope caused by the coupling of diffusive transport and chemical capacitance (Warburg response). Such a coupling of transport and charge accumulation mechanisms is described by standard impedance model functions[23] and it is often useful to represent the model in terms of distributed element circuits (transmission lines) as discussed later. Note that the response is still basically capacitive in the dark, as observed by the nearly vertical responses in Figure 2(c), but this behavior shifts to diffusive only when excess photogenerated charges are created. Interestingly, the effect of illumination is totally decoupled from the bias voltage influence for blocked devices, as deduced form the similar response found by variation of V_{app}.

3.2. Response of Working Devices.

It is interesting to compare the above presented results of devices incorporating CaO layers with those yielded by good extracting contacts as Ca metal. We stress here that the only modification now with respect to the blocked devices is that the blocking layer is not present, leaving the rest of the cell unaltered. In this case, similar bulk mechanisms are then expected. However, contrary to the complete decoupled effect of light and applied voltage observed for blocked devices, it has been demonstrated that sufficiently thin active layers and good extracting contacts ensure electronic reciprocity[28] (i.e., voltage and local charge density are univocally determined).[3] If electronic reciprocity is obeyed, then the same charge density is obtained either as photogenerated charges (producing certain photovoltage) or injected charges (caused by an applied voltage) when V_{app} and the photovoltage attain the same value. One can infer by examining Figure 3(a) that the applied bias voltage has a great influence on low-frequency capacitance because now charge carriers are injected from the contacts. A similar effect producing a rise in capacitance is observed when devices are measured at different illumination intensities in open-circuit conditions (not shown).

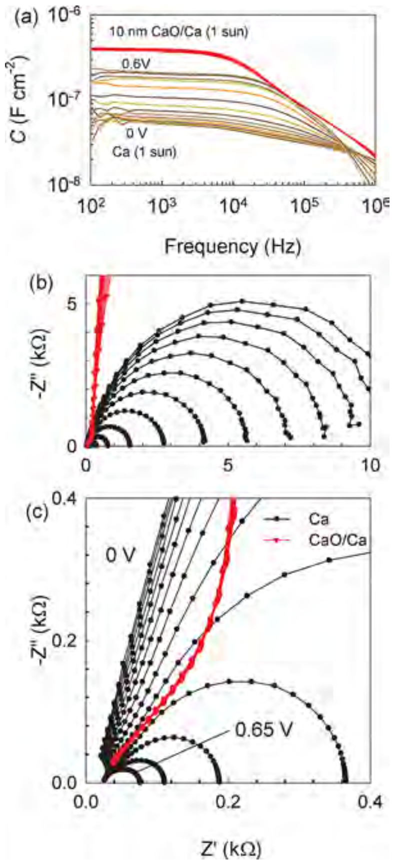

Figure 3. Impedance response from devices using either a good electron collector (Ca) or a blocking layer (CaO). (a) Capacitance spectra measured under 1 sun illumination by varying the applied voltage between 0 and 0.6 V. (b) Impedance spectra plots measured at 1 sun light intensity showing features at low frequencies: recombination *RC* arc for extracting contacts, and capacitive behavior for blocking contacts. (c) Detail of the high frequency region: a transition is observed between spectra dominated by the geometrical capacitance (low bias voltage) and diffusion patterns at high bias near open circuit voltage.

The impedance response of working bulk heterojunction solar cells has been summarized in previous reports.[29] We usually observed that the impedance spectra comprise two visually distinguishable parts. At lower frequencies, a large parallel *RC* subcircuit (represented by a semicircle in $Z'-Z''$ plot) dominates as observed in Figure 3(b). This part is related to the chemical capacitance C_μ (connected to carrier storage) and recombination resistance R_{rec} (derivative of the carrier recombination flux) response,[17,30−33] and kinetic recombination parameters such as the lifetime τ_{rec} can be extracted from this information. At higher frequencies, and bias voltages approaching V_{oc} spectra are usually more featured, exhibiting in some cases an additional arc. Figure 3(c) shows a comparison between electron blocking and extracting solar cells. As we will explain later, the high-frequency part changes from being purely capacitive C_g at low forward bias to diffusive at high forward bias.

4. TRANSMISSION LINE MODEL

A general model accounting for the different impedance responses valid for both blocked and working devices is desired as this can provide quantitative information on the different physical processes taking place in an operating cell. In order to obtain such a model, a series of separated mechanisms need to be considered: (i) Geometrical capacitance C_g is observed under some experimental conditions (low voltage for Ca cathode, and dark for CaO contacs). (ii) Blocking effect is clearly visible for blocking contacts (CaO). This implies an RC parallel subcircuit connected in series $R_{co}C_{co}$ that must comprises large resistances in the case of oxide layers $R_{co} = R_{ox}$, but much smaller for extracting contacts. (iii) For Ca contacts (working devices), the recombination subcircuit is clearly distinguishable $R_{rec}C_{\mu}$. And finally (iv) diffusion patterns are dominant at high frequencies, more evident in the case of blocked devices as a Warburg response. Integration of points (iii), and (iv) electrical mechanisms relies on regarding equivalent circuits comprising distributed elements, which are usually drawn in terms of transmission line models. This type of impedance pattern belongs to responses usually encountered in systems in which carrier transport is determined by coupled diffusion-recombination.[23] Minority carriers (electrons) are able to diffuse within extended bulk neutral regions eventually reaching the electrodes which act as selective contacts. Transmission line models able to represent such diffusion-recombination impedance response are well-known,[23,34] and have been integrated in standard software so that fitting the impedance spectra to obtain the model parameters is straightforward. The impedance model in Figure 4(a) consists of an equivalent circuit which comprises:

- Distributed resistors $r_t = R_t/L$ (being L the active layer thickness), standing for the electron transport. r_t is the reciprocal of the electron conductivity σ_n,
- Distributed chemical capacitance $c_{\mu} = C_{\mu}L$, and
- $r_{rec} = R_{rec}/L$ accounting for the electron recombination resistance.

Since holes are regarded as majority carriers (a hole background density exists in the dark) an equipotential line suffices to represent their contribution because of the sufficiently high conductivity of the materials, provided that the lifetime regime ($\tau_{rec} > \tau_{die}$) is satisfied as previously discussed. The impedance model described contains two characteristic times related to the electron diffusion (transit time),

$$\tau_{diff} = R_t C_{\mu} \tag{2}$$

and the effective lifetime,

$$\tau_{rec} = R_{rec} C_{\mu} \tag{3}$$

respectively.[23] It is assumed that distributed (differential) circuit elements are position-independent as expected for cells in which recombination is not severe, i.e., $\tau_{diff} \leq \tau_{rec}$ (or $R_t \leq R_{rec}$). For highly recombining devices ($\tau_d > \tau_{rec}$ or $R_t > R_{rec}$) deviations from the Warburg response at high-frequencies are usually observed.[34] An additional series resistance is needed to model contact and wire effects, R_s. The electrical effect of the cathode contact is modeled by means of $R_{co}C_{co}$ parallel subcircuit connected in series with the electron channel. Finally, a capacitor $C_g = \varepsilon\varepsilon_0/L$ represents dielectric, geometrical capacitance of the active layer bulk.

The equivalent circuit in Figure 4(a) incorporates the basic phenomenology reported on the impedance response of blocked and working devices as explained in previous sections. Additional assumptions incorporated in the model should be also mentioned: the ohmic character of the anode contact, and the absence of frequency-dispersion in modeling transport properties. As an example of the fitting ability, Figure 4(b) draws the comparison between experimental data and fits corresponding to two particular impedance responses. For blocked solar cells under illumination, two visible features are well supported by the equivalent circuit: the diffusion pattern (Warburg response) at high-frequencies appears as a consequence of the transport R_t and charge storage C_{μ} coupling. The low-frequency part is dominated by the contact subcircuit $R_{co}C_{co}$, which in this case draws a large arc because of the huge blocking resistor $R_{co} = R_{ox}$. In the case of working devices, the electron blocking effect is not viewed because $R_{co} \ll$ in such a way that the low-frequency response becomes governed through recombination mechanisms modeled by coupling of the parameters R_{rec} and C_{μ}. It is worth noting that at forward bias below V_{oc} [0.50 V as illustrated in Figure 4(b)] the diffusion pattern is clearly recovered. For lower voltages [see Figure 3(c)], the high frequency response turns to be dominated by the geometrical capacitance. A fitting procedure was checked by evaluating F statistics. Confidence intervals and correlation between parameters both provide a discriminating tool for stating the best set of fitting parameters. Confidence levels are in all cases high enough (>99%) to consider the parameter values, a very good estimation of the model quantities. In all cases, the regression coefficient of fits $r^2 >$

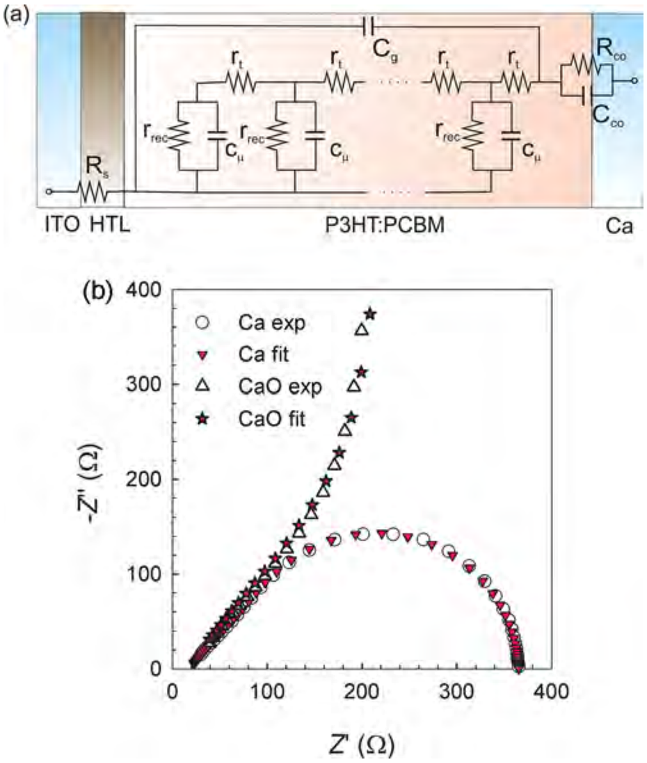

Figure 4. (a) The equivalent circuit (transmission line model) used in this work comprising circuit distributed elements related to electron transport r_t, recombination r_{rec}, chemical capacitance c_{μ}. In addition, geometrical capacitance, C_g, and series resistance, R_s, are connected to the transmission line. Contact electrical response is modeled by means of $R_{co}C_{co}$ parallel subcircuit. (b) Impedance response measured under 1 sun illumination at high frequencies for blocked (10 nm CaO) and operating devices (Ca cathode) at 0.50 V applied voltage. Comparison between experimental data and fitting is shown. Parameter errors are always below 5%.

0.995. The combination of these statistics (namely the dependences between parameters, confidence levels, and regression coefficients) signals the high accuracy that can be reached using the circuit model of Figure 4(a). Resulting errors bars are always below 5% of the parameter value.

5. ANALYSIS OF FITTING PARAMETERS

5.1. Resistive Elements. We discuss the interpretation of parameters extracted from fitting of the equivalent circuit model in Figure 4(a) to impedance data collected under 1 sun irradiation intensity by varying bias voltage. Figure 5 shows the four types of resistive effects that contribute to the cell operation. Low series resistances R_s = 1−3 Ω cm^2 are found that are related to conductive ITO and PEDOT:PSS layer electrical response. Contact resistance R_{co} changes by orders of magnitude between blocking (including CaO), and extracting cathodes. It is worth noting that our method is able to detect contact resistance contributions *even in the case of working devices*, which is a rather significant aspect for practical implementation of the technology. The overall series resistance is $R_s + R_{co}$, these are the conduction processes connected in series with the internal photovoltaic effect. As in the case of including a CaO layer the total series resistance is so pronounced, the voltage drop at short-circuit conditions calculated as $j_{sc}R_{co}$ amounts ∼500 mV, a value that approaches V_{oc}. This can be interpreted by considering that upon light exposure blocked cells are able to store similar photogenerated charge carrier densities regardless of the applied voltage, as this is mainly absorbed within the oxide layer. In open-circuit conditions, the voltage drop in series vanishes in such a way that a measurable photovoltage appears as $V_{oc} = V_F$.

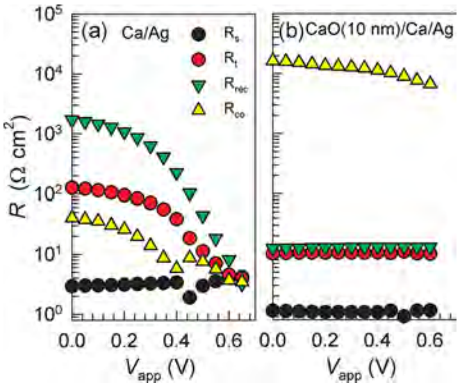

Figure 5. Resistance values extracted from fitting the circuit model in Figure 4(b) to impedance spectra of a device P3HT:PCBM-based device using extracting contacts with Ca (a), and a device blocked with 10 nm of CaO (b). Error bars (<5%) are omitted because smaller than the dot size.

The opposite device operation is encountered for extracting contacts: since the total series resistance is low, the applied voltage establishes the internal V_F. We have recently observed that P3HT-based solar cells operate under the electronic reciprocity relationship.[28] Under this principle, the voltage (Fermi level splitting) V_F fixes the local charge density, and the solar cell operation is viewed as a balance between voltage-independent photocurrent and illumination-independent recombination current.[3]

R_{rec} follows the expected behavior decreasing toward forward voltage due to the enhancement of the recombination current. A detailed analysis of the recombination process from R_{rec} has recently been reported.[35] We note here that the transport (diffusive) resistance, R_t, also describes a reduction at forward bias because of the increment in carrier density as we explain later. It is also interesting to point out that for blocked cells, R_{rec} and R_t exhibit rather voltage-independent values. Such values correspond to those encountered with working cells at V_{app} ≈ 500 mV, again indicating the state of charge reached under illumination using blocking oxide layers.

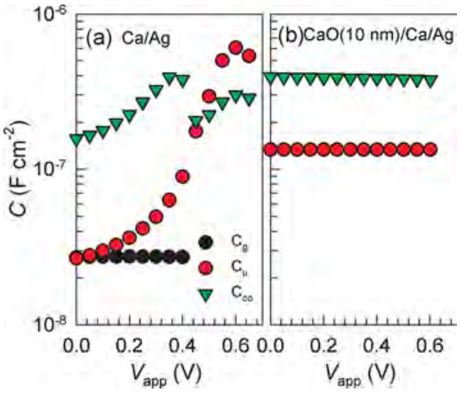

Figure 6. Capacitance values extracted from fitting the circuit model in Figure 4(b) to impedance spectra of a device P3HT:PCBM-based device using extracting contacts with Ca (a), and a device blocked with 10 nm of CaO (b). Error bars (<5%) are omitted because smaller than the dot size.

5.2. Capacitive Elements. A comparison of the capacitive parameters between blocking and working cells extracted from impedance fitting can be viewed in Figure 6. By using Ca cathode metal, it is observed that C_g exerts an influence on the high-frequency part of the spectra in the low forward bias region as commented upon before in Figure 3(c). The chemical capacitance, C_μ, exhibits the expected increase as fullerene states are occupied toward forward bias. Interpretation of C_μ in terms of the electron density-of-states DOS has been discussed extensively in previous papers.[17,29] It is worth noting here that C_μ shows a voltage-independent value for blocked cells which approximately corresponds to the chemical capacitance found for working cells at V_{app} ≈ 500 mV. As discussed in comparing the resistances of blocked cells reach a certain degree of photogenerated charge storage that is responsible for the measured output voltage V_{oc}. The capacitive effect of the cathode contacts C_{co} can be extracted by fitting the response of both types of photovoltaic devices. For blocked cells, this capacitive value coincides with that measured in the low-frequency regime as observed in Figure 2(b). One can directly connect $C_{co} = C_{ox}$ as the values scale with the oxide layer thickness. A value for the dielectric contact of CaO is calculated to be $\varepsilon = 4.2 \pm 0.2$, in good agreement with reported values for this oxide.[36,37] However, in the case of working devices, a contact capacitance is also observed within the same order of magnitude. Such capacitance might be originated by dielectric mechanisms occurring at the interface as those recently proposed in analyzing the cathode equilibration.[25] Reduced fullerene molecules in close contact to the metal contact form a dipole layer with an accumulated charge that follows the interfacial density-of-states IDOS g_{is}. Because it is assumed that the IDOS directly equilibrates with the Fermi level of the contacting metal, one can straightforwardly derive that C_{co} =

qg_{is}. Using the extracted value of $C_{co} \approx 3 \times 10^{-7}$ F cm^{-2}, a surface state density $g_{is} \approx 3 \times 10^{12}$ cm^{-2} eV^{-1} is encountered. We note here that IDOS values within the range of 10^{12}–10^{14} cm^{-2} eV^{-1} have been calculated by other authors using alternative methods.[38]

5.3. Diffusion Coefficient.

The electron diffusivity (chemical diffusion coefficient) can be calculated by recalling eq 2 through the relationship:[39]

$$D_n = \frac{L^2}{\tau_{\text{diff}}} \tag{4}$$

Here, $L \approx 100$ nm corresponds the thickness of the diffusion zone (active layer thickness). It is shown in Figure 7 that the diffusion coefficient derived from eq 4 in the case of blocked devices with 10 nm-thick CaO layer, and working solar cells. In this last type of device, D_n exhibits a rather constant value that starts to slightly increase for voltages approaching V_{oc}. A similar slight increment in D_n was identified using other polythiophene derivatives in an electrochemical transistor setup.[40] Differences in D_n between both types of cells (blocking and working) can be readily assigned to experimental errors related to the active layer thickness determination. Although the electron statistics depart from dilute concentration conditions (Boltzmann approximation), an estimation for the electron mobility might be calculated by using the Nernst–Einstein relationship as $\mu_n = qD_n/k_BT$ (k_BT being the thermal energy).[40,41] The electron mobility extracted from fits exhibits a value approximately equal to 2×10^{-3} cm^2 V^{-1} s^{-1}. This value is in good agreement with that derived using PCBM electron-only devices from J–V measurements, for which current is considered space-charge-limited, and hence electrical field-driven rather than diffusion-determined.[42] Also the time-of-flight current transient response of thick devices has provided similar values.[13]

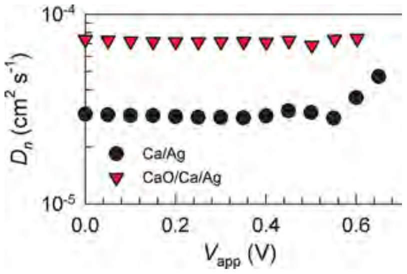

Figure 7. Diffusion coefficient as a function of the applied bias of working and blocked devices with 10 nm of CaO. Variation of layer thickness of 10% allows explaining differences in values extracted from different cells.

6. DISCUSSION

Analysis of the impedance response of working (extracting Ca cathode metal) and blocking (CaO interlayer) solar cells devices clearly shows that extended quasi-neutral regions dominate the device operation for a significant range of applied voltages. This voltage range appears in excess of that (flat-band voltage) established by the collapse of the depletion region formed in the vicinity of the cathode contact.[19] A general picture on the operation of bulk-heterojunction solar cells arises from our experiments: In open-circuit conditions [Figure 8(a), (b)], the internal voltage V_F arising from the splitting of the Fermi levels is fully determined either by the applied voltage or the irradiation intensity (as stated by electronic reciprocity principle) only in the case of good extracting contacts. For blocked devices, light and applied voltages are completely decoupled so that only illumination is able to promote electrons into fullerene acceptor states yielding measurable values for V_F. This last fact occurs because the Ca cathode metal work function is in intimate contact with the electron Fermi level within the active layer bulk. The enormous resistance associated to the oxide layer absorbs the applied voltage impeding the Fermi level rise. When devices are forced to operate in short circuit conditions, the impedance of blocked cells does not change significantly since the internal photogenerated charge density keeps the values reached in open-circuit (voltage-independent response) as illustrated in Figure 8(d). We note that in the previous cases, devices can be viewed as operating in flat-band conditions. On the contrary, working cells under short-circuit conditions exhibits some kind of band bending because of the presence of cathode depletion zones as illustrated in Figure 8(c).

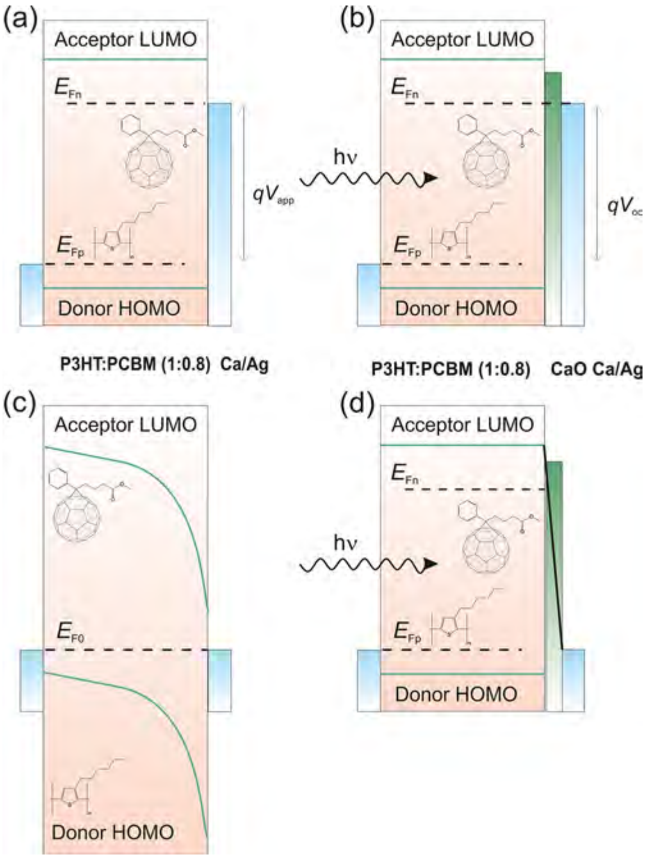

Figure 8. Band diagram of working device with collecting Ca cathode contacts at large forward applied voltage (a) and short-circuit conditions (c). The applied voltage generates the splitting of the Fermi levels, which align with the contacts producing flat-band conditions (a). Band bending resulting from the cathode Schottky contact (c). For blocking contacts (CaO layer) under illumination photogeneration creates a photovoltage (open-circuit conditions) by alignment of the respective Fermi levels (b). In short-circuit (d), a large voltage drop is confined within the oxide layer that compensates the photovoltage.

From the analysis of the resistive circuit elements, it turns out that $R_t \leq R_{rec}$ as plotted in Figure 5. This entails that the performance of these cells is not limited by the transport of photogenerated carriers, at least for the active layer thickness used here ($L \approx 100$ nm). We observe that at voltages approaching V_{oc}, R_t and R_{rec} exhibit similar values, which suggests that thicker active films would suffer from deficient charge collection as expected for highly recombining cells (i.e., $R_t > R_{rec}$). It is also worth noting that two different kinds of series resistance effects have been identified: one related to the transport processes in conductive materials R_s, and another one associated with the charge transfer events at the outer interfaces between the active layer and the contacts R_{co}. While R_{co} exceeds R_s by more than 1 order of magnitude at low voltages, both resistors contributes similarly to the total series resistance at forward bias near V_{oc}.

As stated in the Introduction, the observation of diffusion of minority carriers through extended neutral regions within the active layer bulk relies on the occurrence of the lifetime semiconductor regime. The blends of donor and acceptor molecules is regarded as an effective semiconducting medium in which holes act as majority carriers. The lifetime regime implies that $\tau_{rec} > \tau_{die}$, and this statement can be confirmed by comparing independent measurements of τ_{rec} using eq 3, and τ_{die} by looking at the first decay characteristic time of light-induced current transients.[13] From C_μ and R_{rec} as shown in Figures 5 and 6, it can be inferred that $\tau_{rec} > 3$ μs. This is a minimum value that is reached at $V_{app} \approx V_{oc}$. A direct determination of the relaxation time τ_{die} results from the exponential response time of current transients presented in Figure 9 for both Ca and CaO cathodes. We systematically measured $\tau_{die} \approx 0.65$ μs in good agreement with the estimation proposed in the Introduction. This last finding indicates that P3HT:PCBM blends operate within the relaxation semiconductor regime. Similar to the established distinction between lifetime and relaxation regimes in terms of the response times ($\tau_{rec} > \tau_{die}$), a comparison of characteristic length scales points to the same underlying physics. The diffusion length is defined as an average distance in which mobile carriers can diffuse before recombination, and is related to the diffusion coefficient in eq 4 as follows:

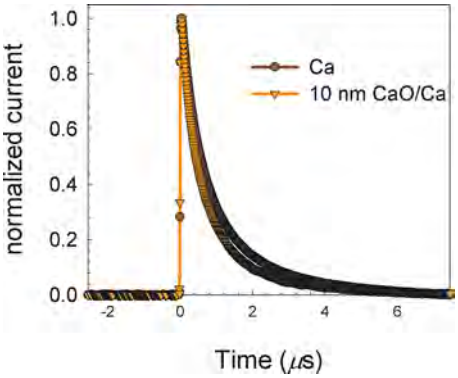

Figure 9. Example of normalized transient photocurrent of P3HT:PCBM devices using blocking and extracting electrodes. The first rapid decay is related to the dielectric relaxation time, which is observed to be within the range of 0.6−0.7 μs.

$$L_n = \sqrt{D_n \tau_{rec}} \qquad (5)$$

In the time scale of dielectric relaxation the characteristic length scale corresponds to the Debye screening length λ_D that represents the distance in which local electrical fields are confined. It can be demonstrated that an expression as eq 5 results relating λ_D and τ_{die} in such a way that,

$$\lambda_D = \sqrt{D_n \tau_{die}} \qquad (6)$$

Thus, the occurrence of the lifetime regime as $L_n > \lambda_D$ in terms of a length scale comparison can be formulated. In the case of the analyzed cells values of $\lambda_D \approx 50$ nm are obtained, whereas L_n ranges from ~250 nm for low forward voltages down to ~100 nm at $V_{app} \approx V_{oc}$. It is then deduced that at high voltages L_n is comparable to the active layer thickness. The photovoltaic devices analyzed operating under these conditions are then in the limit of being considered as highly recombining solar cells for which $L \gg L_n$. This last observation explains why thicker films usually exhibit poor performance as bulk transport losses occur before charge collection take place at the contacts. Our analysis offers a straightforward method for complete device performance evaluation.

7. CONCLUSIONS

This work provides a general impedance model that is tested using two extremely different sets of P3HT:PCBM-based devices: reasonably efficient solar cells and devices where the electron collection has been blocked. The first type relies on an efficient collecting Ca cathode and the second on the addition of oxide interlayers (CaO) between the active layer and the cathode contact. The transmission line circuit accounting for the bulk processes is found to be valid irrespective of the structure selected for the cathode contact. It is observed that coupling of diffusion and recombination currents suffices to model electrical mechanisms occurring at the organic blend. The analytical impedance method presented is a tool that allows us to determine and separate different resistive contributions affecting the solar cell operation. By confronting transport (diffusion) resistance to recombination resistance, rapid quantification of carriers lost during the transit to the outer contacts is found. In addition, the effect of the cathode contact is modeled by means of series resistance and capacitance elements, providing further evidence and determination about the important and detrimental effect of contacts. We finally note that the analysis performed here needs to be extended to organic solar cells comprising other blend constituents, particularly different donor polymers, to fully evaluate its application degree.

■ AUTHOR INFORMATION

Corresponding Author

*Tel.: +34 964 387548; fax: +34 964 729218; e-mail: garciag@fca.uji.es.

Notes

The authors declare no competing financial interest.

■ ACKNOWLEDGMENTS

We thank financial support from Ministerio de Educacion y Ciencia under project HOPE CSD2007-00007 (Consolider-Ingenio 2010), Generalitat Valenciana (Prometeo/2009/058, ACOMP/2009/056, ACOMP/2009/095, and ISIC/2012/008 Institute of Nanotechnologies for Clean Energies), and FP7 European project ORION (Large CP-IP 229036-2).

■ REFERENCES

(1) Green, M. A.; Emery, K.; Hishikawa, Y.; Warta, W.; Dunlop, E. D. *Prog. Photovoltaics* **2012**, *20*, 12−20.

(2) Park, S. H.; Roy, A.; Beaupré, S.; Cho, S.; Coates, N.; Moon, J. S.; Moses, D.; Leclerc, M.; Lee, K.; Heeger, A. J. *Nat. Photonics* **2009**, *3*, 297−302.

(3) Boix, P. P.; Guerrero, A.; Marchesi, L. F.; Garcia-Belmonte, G.; Bisquert, J. *Adv. Energy Mater.* **2011**, *1*, 1073−1078.
(4) Peet, J.; Wen, L.; Byrne, P.; Rodman, S.; Forberich, K.; Shao, Y.; Drolet, N.; Gaudiana, R.; Dennler, G.; Waller, D. *Appl. Phys. Lett.* **2011**, *98*, 043301.
(5) Cowan, S. R.; Banerji, N.; Leong, W. L.; Heeger, A. J. *Adv. Funct. Mater.* **2012**, *22*, 1116−1128.
(6) Credgington, D.; Durrant, J. R. *J. Phys. Chem. Lett.* **2012**, *3*, 1465−1478.
(7) Fonash, S. J. *Solar Cell Device Physics*, 2nd ed.; Elsevier: Burlington, 2010.
(8) van Roosbroek, W.; Casey, H. C. *Phys. Rev. B* **1972**, *5*, 2154−2175.
(9) Schiff, E. A. *Sol. Energy Mater. Sol. Cells* **2003**, *78*, 567−595.
(10) Bozano, L.; Carter, A.; Scott, J. C.; Malliaras, G. G.; Brock, P. J. *Appl. Phys. Lett.* **1999**, *74*, 1132−1134.
(11) Gregg, B. A.; Liang, Z. *Adv. Mater.* **2012**, *24*, 3258−3262.
(12) Liang, Z.; Nardes, A.; Wang, D.; Berry, J. J.; Gregg, B. A. *Chem. Mater.* **2009**, *21*, 4914−4919.
(13) Morfa, A. J.; Nardes, A. M.; Shaheen, S. E.; Kopidakis, N.; Lagemaat, J. v. d. *Adv. Funct. Mater.* **2011**, *21*, 2580−2586.
(14) Mozer, A. J.; Sariciftci, N. S. *Chem. Phys. Lett.* **2004**, *389*, 438−442.
(15) Goh, C.; Kline, R. J.; McGehee, M. D.; Kadnikova, E. N.; Fréchet, J. M. J. *Appl. Phys. Lett.* **2005**, *86*, 122110.
(16) Maurano, A.; Hamilton, R.; Shuttle, C. G.; Ballantyne, A. M.; Nelson, J.; O'Regan, B.; Zhang, W.; McCulloch, I.; Azimi, H.; Morana, M.; Brabec, C. J.; Durrant, J. R. *Adv. Mater.* **2010**, *22*, 4987−4992.
(17) Garcia-Belmonte, G.; Boix, P. P.; Bisquert, J.; Sessolo, M.; Bolink, H. J. *Sol. Energy Mater. Sol. Cells* **2010**, *94*, 366−375.
(18) Garcia-Belmonte, G.; Munar, A.; Barea, E. M.; Bisquert, J.; Ugarte, I.; Pacios, R. *Org. Electron.* **2008**, *9*, 847−851.
(19) Bisquert, J.; Garcia-Belmonte, G. *J. Phys. Chem. Lett.* **2011**, *2*, 1950−1964.
(20) Lee, J.; Kong, J.; Kim, H.; Kang, S.-O.; Lee, K. *Appl. Phys. Lett.* **2011**, *99*, 243301.
(21) Li, J. V.; Nardes, A. M.; Liang, Z.; Shaheen, S. E.; Gregg, B. A.; Levi, D. H. *Org. Electron.* **2011**, *12*, 1879−1885.
(22) Burgelman, M.; Grasso, C. *J. Appl. Phys.* **2004**, *95*, 2020.
(23) Bisquert, J. *J. Phys. Chem. B* **2002**, *106*, 325−333.
(24) Ratcliff, E. L.; Zacher, B.; Armstrong, N. R. *J. Phys. Chem. Lett.* **2011**, *2*, 1337−1350.
(25) Guerrero, A.; Marchesi, L. F.; Boix, P. P.; Ruiz-Raga, S.; Ripolles-Sanchis, T.; Garcia-Belmonte, G.; Bisquert, J. *ACS Nano* **2012**, *6*, 3453−3460.
(26) Bisquert, J. *Phys. Chem. Chem. Phys.* **2003**, *5*, 5360−5364.
(27) Xu, H.; Zhang, Z.; Penga, L.-M. *Appl. Phys. Lett.* **2011**, *98*, 133122.
(28) Donolato, C. A *Appl. Phys. Lett.* **1985**, *46*, 270−272.
(29) Fabregat-Santiago, F.; Garcia-Belmonte, G.; Mora-Seró, I.; Bisquert, J. *Phys. Chem. Chem. Phys.* **2011**, *13*, 9083−9118.
(30) Leong, W. L.; Cowan, S. R.; Heeger, A. J. *Adv. Energy Mater.* **2011**, *1*, 517−522.
(31) Zhang, Y.; Dang, X.-D.; Kim, C.; Nguyen, T.-Q. *Adv. Energy Mater.* **2011**, *1*, 610−617.
(32) Leever, B. J.; Bailey, C. A.; Marks, T. J.; Hersam, M. C.; Durstock, M. F. *Adv. Energy Mater* **2012**, *2*, 120−128.
(33) Perrier, G.; deBettignies, R.; Berson, S.; Lemaître, N.; Guillerez, S. *Sol. Energy Mater. Sol. Cells* **2012**, *101*, 210−216.
(34) Pitarch, A.; Garcia-Belmonte, G.; Mora-Seró, I.; Bisquert, J. *Phys. Chem. Chem. Phys.* **2004**, *6*, 2983−2988.
(35) Guerrero, A.; Marchesi, L. F.; Boix, P. P.; Bisquert, J.; Garcia-Belmonte, G. *J. Phys. Chem. Lett.* **2012**, *3*, 1386−1392.
(36) Whited, R. C.; Flaten, C. J.; Walker, W. C. *Solid State Commun.* **1973**, *13*, 1903−1905.
(37) Rekhson, S. M.; Mazurin, O. V. *J. Am. Ceram. Soc.* **1974**, *57*, 327.
(38) Baldo, M. A.; Forrest, S. R. *Phys. Rev. B* **2001**, *64*, 085201.
(39) Bisquert, J. *J. Phys. Chem. B* **2004**, *108*, 2323−2332.
(40) Garcia-Belmonte, G.; Bisquert, J.; Popkirov, G. *Appl. Phys. Lett.* **2003**, *83*, 2178−2180.
(41) Bisquert, J. *Phys. Chem. Chem. Phys.* **2008**, *10*, 3175−3194.
(42) Mihailetchi, V. D.; van Duren, J. K. J.; Blom, P. W. M.; Hummelen, J. C.; Janssen, R. A. J.; Kroon, J. M.; Rispens, M. T.; Verhees, W. J. H.; Wienk, M. M. *Adv. Funct. Mater.* **2003**, *13*, 43−46.

Organic Electronics 13 (2012) 2326–2332

Contents lists available at SciVerse ScienceDirect

Organic Electronics

journal homepage: www.elsevier.com/locate/orgel

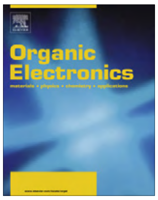

Series resistance in organic bulk-heterojunction solar devices: Modulating carrier transport with fullerene electron traps

Antonio Guerrero, Teresa Ripolles-Sanchis, Pablo P. Boix, Germà Garcia-Belmonte *

Photovoltaic and Optoelectronic Devices Group, Departament de Física, Universitat Jaume I, ES-12071 Castelló, Spain

ARTICLE INFO

Article history:
Received 26 April 2012
Received in revised form 21 June 2012
Accepted 25 June 2012
Available online 17 July 2012

Keywords:
Photovoltaic devices
Current–voltage characteristics
Series resistance
Transport
Trapping

ABSTRACT

Series resistance is one of the key parameters affecting the performance of organic photovoltaic devices. Several electronic mechanisms arising from different structures within the solar cell can contribute to increasing it. We focus on the series resistance origin by altering the acceptor transport properties trough the incorporation of fullerene traps located at energies below the transporting electron levels. Indene-C_{60} bisadduct as acceptor molecule blended with poly(3-hexylthiophene) forms the active layer in which small amounts of [6,6]-phenyl-C_{61}-butyric acid methyl ester have been added as trapping sites. A complete analysis of the impedance response has allowed identifying bulk transport resistive circuit elements in the high-frequency part of the spectra. Series resistance is observed to be dependent on the concentration of fullerene traps, thus indicating a connection between bulk transport processes and resistive elements. By comparing different contacts it has been discarded that outer cathode interfaces influence the series resistance experimentally extracted from impedance spectroscopy.

1. Introduction

Series resistance R_s has been recognized as one of the key parameters affecting the performance of organic photovoltaic devices through reduction of the solar cell fill factor [1]. For larger series resistance values even short-circuit current might decrease. Usually R_s is estimated from the current–voltage J–V curve slope at large forward voltage where the current flow is not longer limited by the internal carrier recombination but by the potential drop at R_s. However it cannot be discarded that processes contributing to R_s are voltage-dependent through physical mechanisms originated at different layers or interfaces within the device. Transparent contact layers as indium tin oxide ITO, and carrier transporting interlayers of different kind could increase R_s significantly. Interfaces between the active layer blend and interlayers or metallic contacts may well add more resistance in series because of partial energy level alignment which affects optimal interface charge transfer. Finally charge carrier transport within the active layer itself could also be a source for incrementing the series resistance. The overall impact of electronic transport mechanisms is recognized to have dramatic effects when relatively thicker active layer films are used to enhance light harvesting [2]. While thinner films are able to exhibit almost 100% conversion of absorbed photons into collected carriers [3], thus indicating that transport mechanisms do not limit the achievable photocurrent [4], thicker active layer devices suffer from an incomplete collection of photogenerated charges. It is also known that in real devices the sole analysis of the J–V characteristics does not help discerning which series mechanism is effectively dominating R_s. Therefore the overall cell performance might be improved by quantifying operating mechanisms involved in series resistance increase.

A standard technique able to separate different resistive and capacitive contributions to the overall solar cells electrical response is impedance spectroscopy. This alternating current probing tool explores electrical mechanisms occurring within the frequency range of interest in organic solar devices, usually from 10 MHz down to 1 Hz. By using this

---

* Corresponding author. Tel.: +34 964 387548; fax: +34 964 729218.
E-mail address: garciag@fca.uji.es (G. Garcia-Belmonte).

1566-1199/$ - see front matter © 2012 Elsevier B.V. All rights reserved.
http://dx.doi.org/10.1016/j.orgel.2012.06.043

analytical method we have identified circuit elements related to recombination current governing the low-frequency part of the impedance spectra [4,5]. Differential resistive (recombination resistance) and capacitive (chemical capacitance) processes were connected to recombination flux derivative and charge storage, respectively [6–8]. It has also been proposed that the effect of mechanisms in series is observable at high frequencies through more featured impedance spectra, which were interpreted in connection with electronic transport processes [9]. Very recently impedance analysis has been employed by others groups identifying a RC parallel subcircuit governing the high frequency response as a combination of bulk transport resistance and geometrical capacitance [10,11].

Although connecting the high-frequency impedance response to electronic transport within the solar cell bulk is a reasonable working hypothesis, no conclusive prove has been given which allows discarding additional mechanisms such as outer interfacial effects contributing to the series resistance. Deeper knowledge about the processes affecting R_s is then essential to improve power conversion efficiency and the overall cell performance. In order to progress on the R_s origin we have altered the acceptor transport properties by introducing fullerene traps located at energies below the transporting electron levels. This experimental procedure has allowed modulating the electron mobility with the consequent modification of the impedance high-frequency response. Therefore we have unambiguously identified RC parallel subcircuit elements acting at high frequencies with bulk transport processes determining R_s.

2. Results and discussion

Indene-C_{60} bisadduct (ICBA) [12,13] has been proposed as acceptor molecule to achieve open-circuit voltage V_{oc} higher than 0.8 V when poly(3-hexylthiophene (P3HT) is used as donor polymer. Compared to [6,6]-phenyl-C_{61}-butyric acid methyl ester (PCBM) a shift in open-circuit voltage $\Delta V_{oc} \approx 0.2$ V is observed, in good agreement with the less negative lower-occupied molecular orbital (LUMO) level position of ICBA molecule. Cyclic voltammetry analysis of PCBM and ICBA molecules reveals a negative shift in the reduction peak of 0.17 V caused by the ICBA molecular LUMO position (−3.74 eV) compared to PCBM (−3.91 eV) [12] as illustrated in Fig. 1a. From this energy diagram it is derived that PCBM molecules could act as trapping sites when a small amount is incorporated into the ICBA:P3HT blend, presumably altering the transport properties of electron carriers. It cannot be discarded that PCBM incorporation modifies the fullerene energetic landscape. Solar cells of structure indium tin oxide (ITO)/poly(3,4-ethylenedioxythiophene):poly(styrene sulfonic acid) (PEDOT:PSS)/P3HT:fullerene/cathode (being cathode contact either Ca/Ag or LiF/Al), were prepared as described in the Section 3.1. In order to test the effect of the PCBM traps on the conducting properties of ICBA different fullerene acceptor composition has been tested: P3HT:ICBA, P3HT:ICBA(PCBM 0.1%), and P3HT:ICBA(PCBM 1%) blends. Typical J–V curves are shown in Fig. 1b for Ca/Ag cathode contact. Photovoltaic parameters are listed in Table 1. By examining Fig. 1b one can realize that the incorporation of PCBM molecules largely reduces the short-circuit current J_{sc}. For small amount of PCBM (0.1%) reduction in J_{sc} is only of 5%, while PCBM larger amounts (1.0%) induce 28% photocurrent losses. This large reduction in J_{sc} might be related to lower light absorption caused by a less optimized blend morphology when PCBM molecules are included. Absorption and device external quantum efficiency (*EQE*) for different blend compositions are presented in Fig. 2. One can observe in Fig. 2a that the absorption at ~600 nm drops around 10% for PCBM content from 0% to 1%. However *EQE* spectra shown in Fig. 2b do not follow the absorption spectral profile which peaks around 520 nm. Instead it shows a rather flat shape between 450 and 600 nm. For

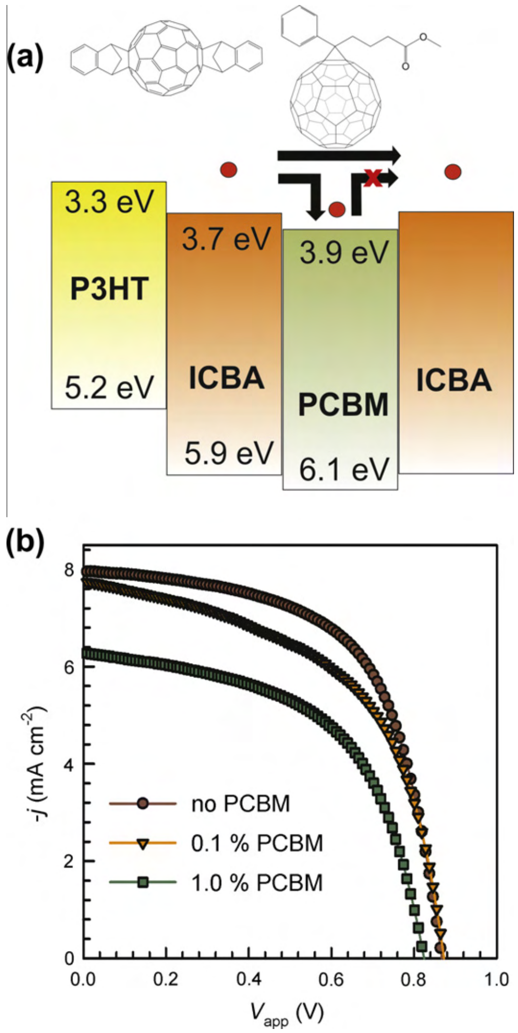

Fig. 1. (a) Energy level diagram of the active polymer and fullerene molecules used. Note that PCBM LUMO level is situated at more negative energies with respect to ICBA LUMO, then acting as trapping sites for electrons moving trough ICBA molecules. (b) J–V curves corresponding to P3HT:ICBA(no PCBM), P3HT:ICBA(PCBM 0.1%), and P3HT:ICBA(PCBM 1.0%) blends for Ca cathode contact.

Table 1
Photovoltaic parameters corresponding to P3HT:fullerene solar cells with different cathode metal.

		J_{sc} (mA cm^{-2})	V_{oc} (mV)	*FF*	*PCE* (%)	*FF*[a]	*PCE*[a] (%)
P3HT:ICBA cathode Ca/Ag	No. PCBM	8.0	872	0.60	4.2	0.80	5.5
	0.1% PCBM	7.7	877	0.54	3.7	0.74	5.0
	1.0% PCBM	5.7	805	0.54	2.9	0.69	3.5
P3HT:ICBA cathode LiF/Al	No. PCBM	6.2	735	0.59	2.7		
	0.1% PCBM	5.9	681	0.47	1.9		
	1.0% PCBM	3.4	662	0.55	1.2		

[a] Corrected fill factor *FF* and power conversion efficiency *PCE* by elimination of the series resistance potential drop in the case of Ca contact.

1.0% of PCBM content the decrease in *EQE* is about 20% with respect to P3HT:ICBA-based cells. It is then observed that charge collection probability represented by *EQE* exhibits larger reduction in comparison to that expected from absorption spectra. A direct comparison between absorption and *EQE* spectra cannot be performed without caution because geometry of the absorption measurement is different to the structure of a device with electrodes. Despite this alerting point experiments suggest in this case that the sole decrease in absorption is not able to explain the large J_{sc} losses reported in Fig. 1 which should be then linked with mechanisms occurring after light interaction.

We move now our attention to possible series resistance influences. It is known that *J–V* characteristics is severely distorted by effect of the series resistance, even producing a reduction in the measured J_{sc} with respect to the photocurrent in the case of significant R_s values [1]. Indeed voltage and current are distorted by elements in the device unrelated to the internal operation of the photoactive layer, so that *J–V* curve is usually modeled by means of a behavior as [14]

$$J = \frac{1}{1 + R_s/R_p}\left\{J_0\left[\exp\left(\beta\frac{V_{app} - JR_s}{k_BT/q}\right) - 1\right] - \left[J_{ph} - \frac{V_{app}}{R_p}\right]\right\} \qquad (1)$$

Here V_{app} stands for the applied voltage, and the photocurrent J_{ph} is reduced by the shunt resistance R_p. In addition k_BT accounts for the thermal energy, q is the elementary charge, and J_0 stands for the dark current. The expression in Eq. (1) includes the parameter β accounting for the deviation from the diode ideal equation (inverse of the diode ideality factor). Interestingly the potential drop at the series resistance evaluated at zero bias $J_{sc}R_s$ modifies the measured J_{sc} with respect to the photocurrent J_{ph}. We will next explore by using impedance spectroscopy the origin and contributing mechanisms of the series resistance.

An example of the impedance spectroscopy response is shown in Fig. 3. AC oscillating amplitude was as low as 20 mV (rms) to maintain the linearity of the response, and the measuring frequency range was located between 1 MHz and 100 Hz. Impedance measurements have been performed at different applied voltages under 1 sun illumination. The comparison between light and dark responses of P3HT:PCBM solar devices was addressed in a previous work [4] concluding that a master *J–V* curve is obtained after correcting the ohmic voltage drop at the series resistance. In the case of relatively low series resistance values this allows studying exclusively light impedance responses to obtain relevant cell parameters. It is observed in Fig. 3 that the impedance spectra comprise two visually distinguishable parts. At lower frequencies a large *RC* subcircuit (represented by a semicircle in Z'–Z'' plot) dominates. As explained in previous works this part is related to the chemical capacitance C_μ (connected to carrier storage) and recombination resistance R_{rec} (derivative of the carrier recombination flux) response [6–8]. R_{rec} and C_μ as a function of the applied voltage are drawn in Fig. 4. As observed exactly the same behavior is found with small differences presumably related to variation of fullerene energetics. By examining Fig. 4b one can observe a negative voltage shift in the capacitance of 1.0% PCBM content devices with respect to that of P3HT:ICBA cells. Such voltage shift is

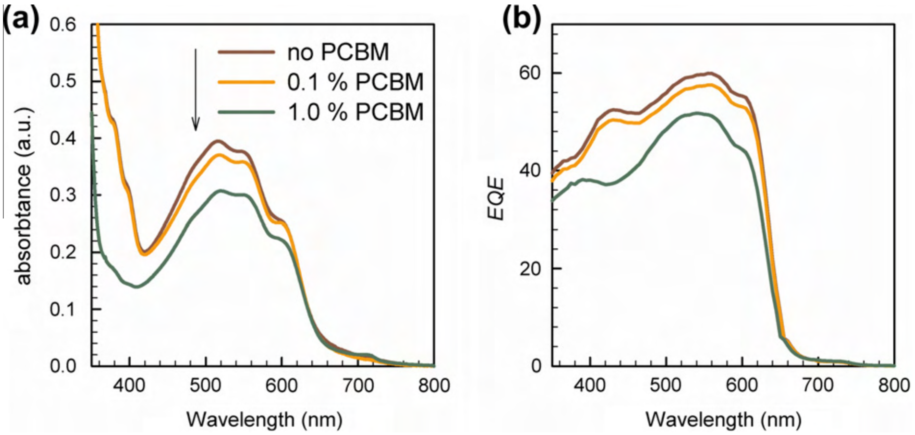

Fig. 2. (a) Absorption spectra of P3HT:ICBA films incorporating different content of PCBM molecules as indicated. (b) External quantum efficiency spectra of P3HT:ICBA devices incorporating different content of PCBM molecules.

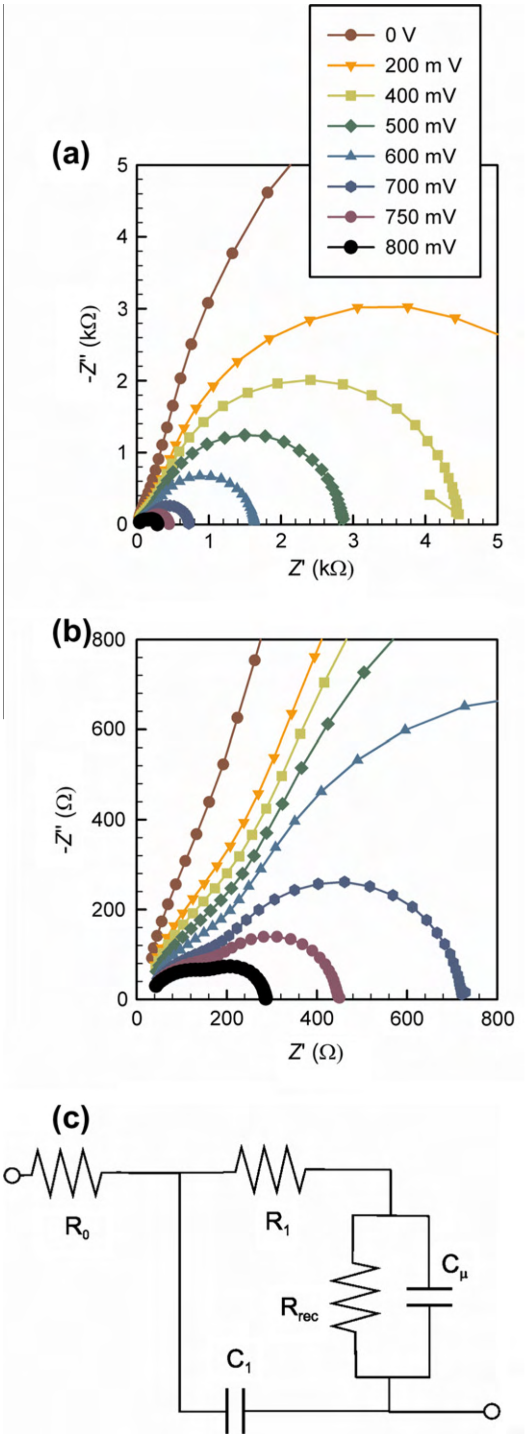

Fig. 3. (a) Impedance spectra for different applied voltage values as indicated obtained for the structure ITO/PEDOT:PSS/P3HT:ICBA/Ca under 1 sun illumination intensity. (b) Detail of the impedance spectra in Fig. 3(a) showing the high-frequency R_1C_1 contribution (left) and the main $R_{rec}C_{\mu}$ arc (right). (c) Simple equivalent circuit using in data fitting.

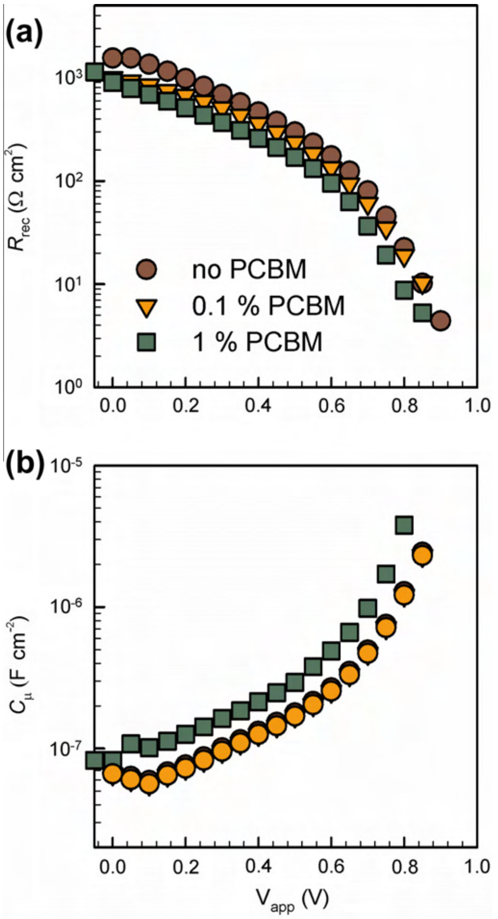

Fig. 4. (a) Recombination resistance and (b) chemical capacitance obtained from fitting of impedance spectra using the equivalent circuit of Fig. 3c. Error bars calculated from fitting smaller than the dot size.

related to lower lying energy levels introduced by PCBM molecules after interaction with ICBA. If this energy shift is corrected a collapse of the R_{rec}–V_{app} plots in Fig. 4a are obtained. Similar R_{rec} behavior entails that the PCBM incorporation does not alter significantly recombination mechanisms [15].

In this work we will focus our attention on electronic processes affecting the high-frequency part of the impedance spectra. In Fig. 3b an additional semicircle R_1C_1 is clearly distinguishable at larger forward voltages 0.7–0.8 V and higher frequencies, which is connected here to transport effects as discussed later. The overall impedance response also includes a resistance connected in series $R_0 \approx 2\ \Omega\,\text{cm}^2$ that is attributed to ITO sheet and wires contributions, and results practically voltage-independent. This general trend is always reproduced despite modifications introduced either in the blend composition, or cathode contact. The circuit model used in fitting is drawn in Fig. 3c. Alternative circuit models as that comprising two *RC* subcircuits in series have been checked producing in this case slightly poor fittings (see Supplementary data file). For the relevant voltage range (<0.7 V) parameter errors are always below 5%, what allows omitting error bars in Figs. 4 and 5 because they are smaller than the dot size.

A close look at the variation of R_1C_1 high-frequency subcircuit elements with the applied voltage is plotted in Fig. 5. When PCBM trap molecules are not incorporated into the active layer R_1 exhibits low values (30–10 Ω cm^2) irrespective of the cathode contact used. If lower amounts of PCBM molecules are inserted (0.1%) slightly higher R_1 values are encountered. The response changes drastically when the PCBM content amounts 1.0% of acceptor molecules. In this last case a large R_1 contribution is found that steeply decreases from $\sim$100 Ω cm^2 at low voltages down to 10 Ω cm^2 for voltages in excess of V_{oc}. This kind of behavior observed for the transport-related resistance R_1 can be understood in terms of a trap-modulated conductivity mechanism as follows: acceptor ICBA LUMO levels form a sort of transporting band, while PCBM molecules behave as trapping sites for negative polarons (electrons) as schematically drown in Fig. 1a. When the amount of PCBM is low R_1 slightly decreases with the applied voltage because trapping effects are very limited. For larger PCBM concentration the probability of electron trapping increases then reducing the carrier mobility, and consequently the measured resistance. The applied voltage also has an influence on R_1 by modifying the acceptor LUMO level occupancy. For low applied bias PCBM trap sites are not populated because of a deeper position of the electron Fermi level. Mobile electrons can then easily undergo trapping producing a decrease in the carrier conductivity. As the electron Fermi level rises following the increment in forward voltage PCBM trap sites are eventually occupied losing their influence on R_1. Interestingly R_1 exhibits values that are fullerene content-independent at larger forward voltage as expected when trapping sites are no longer active. The above mentioned conduction mechanism is highly sensitive to the kinetics of trapping/release of trapped electrons at PCBM molecules. While the inclusion of fast traps does not modify the carrier conductivity [16], slow trapping would have large influence on the transport mechanisms producing conductivity changes. It is worth noting that similarity to R_1 values at forward bias allows discarding morphology effects as originating the R_1 differences observed. On the other hand the capacitive element C_1 exhibits a rather constant value which is related to geometrical and dielectric mechanisms. Variations of C_1 observed among samples might be caused by a combination of several factors: differences in active layer thickness, changes in blend permittivity by PCBM incorporation, or influence of contact capacitive effects could all be behind the actual C_1 value. Nevertheless C_1 differences are limited by a factor of 2.

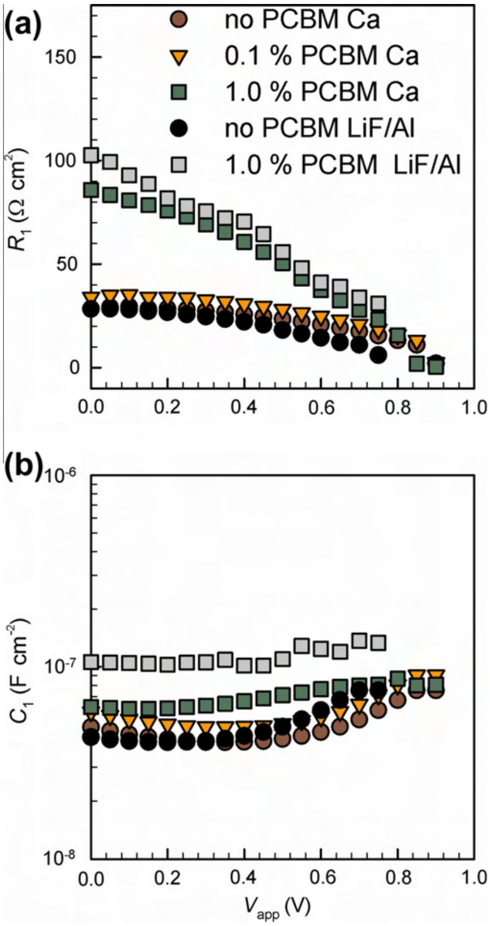

Fig. 5. (a) Bulk transport resistance and (b) geometrical, dielectric capacitance obtained from fitting of impedance spectra using the equivalent circuit of Fig. 3c. Two different cathode contacts are compared: Ca and LiF/Al. Error bars calculated from fitting smaller than the dot size.

We now return to the issue concerning the outer interface contribution on the measured series resistance, in contrast to the transport-originated mechanism discussed previously. To discern between contact from bulk origins two different cathode contacts have been deposited, namely Ca and LiF/Al. It is observed in Fig. 5 that R_1 behaves in a way that appears independent of the cathode contact used. For 1.0% PCBM fullerene content the same increment in R_1 is experimentally found. It is worth noticing the poor performance of cells contacted with LiF/Al (see Table 1). This is presumably caused by interactions at the cathode interface that impede a proper charge extraction. Despite this evident limitation at the cathode interface, bulk transport properties exhibit similar behavior than that obtained for devices contacted with Ca. These experimental trends reinforce our previous idea pointing to transport rather than interface origin for the high-frequency impedance response. However it cannot be completely excluded the possibility that anode interface or PEDOT:PSS layer contribute to R_s in the case of lower PCBM content.

When the combined contribution of R_1 and R_0 is connected in series $R_s = R_1 + R_0$, it is feasible to calculate the voltage responsible for the photovoltaic effect as

$$V_F = V_{app} - JR_s \tag{2}$$

in accordance to Eq. (1). We have explained in previous papers how V_F is in fact originated by the Fermi level splitting corresponding to separate carriers [5]. The actually measured J–V characteristics exhibits then a distortion in the voltage axis with respect to the Fermi level splitting produced by the series resistance potential drop [4]. This voltage axis correction allows for an estimation of the achievable power conversion efficiency in the case of complete elimination of the series resistance effect as listed in Table 1 for Ca cathode contact. After correction of R_s effect *PCE* increases as expected but it does not reach a similar value because differences in J_{sc} caused by absorption losses, and reduction in V_{oc} ($\sim$70 meV) originated by fullerene energetics variation are still present. The approach implied by Eq. (2) should be taken with caution because the series resistance potential drop is only a useful approximation of a rather complex picture concerning the Fermi level distribution across the active layer thickness [17]. In general terms transport mechanisms are coupled with charge storage and recombination (represented by C_μ and R_{rec}) in a transmission line circuit model [9], instead of the circuit comprising lumped elements as in Fig. 3c. Only in those cases in which the transport resistance is significantly lower than R_{rec} the application of the correction in Eq. (2) is fully justified. A detailed analysis including transmission line circuits will be addressed in forthcoming works.

3. Conclusion

We have focused on carrier transport effects by means of a simple equivalent circuit model directly derived from the inspection of impedance spectra corresponding to P3HT:ICBA bulk-heterojunction solar cells. By incorporating PCBM molecules into the blend electron traps have been created which modulate the electron conductivity. Consequently the high-frequency part of the impedance spectra undergoes significant alteration in its resistive component. It has been demonstrated by using different cathode contacts that high-frequency resistances only depend on the active layer blend composition, and not on the outer contact structure. Impedance spectroscopy appears then as a powerful tool applicable to evaluate losing mechanisms in complete and operative organic solar cells.

3.1. Methods

3.1.1. Device fabrication

P3HT (Aldrich), ICBA (Luminescence Technology Corp.), $PC_{60}BM$ (Nano-C, 99.5%), PEDOT:PSS (CLEVIOS P AI 4083), *o*-dichlorobenzene (Aldrich, 99.9%), Ca (Aldrich, 99.995%), silver (Aldrich, 99.99%), LiF (Aldrich, 99.995%) and Al (Kurt J. Lesker, 99.999%) were used as received without further purification. All manipulations were carried out in a glovebox under a nitrogen atmosphere unless otherwise stated. P3HT:fullerenes blends were prepared from dry *o*-dichlorobenzene (1:0.8, 17 mg/ml) and were stirred at R.T. for 2 h before sample preparation. The fullerene acting as an electron trap ($PC_{60}BM$) when added provided a concentration of either 0.1% or 1% by weight. Polymer solar cells were fabricated with a standard sandwich structure of ITO/PEDOT:PSS/P3HT:Fullerenes/Cathode, and 9 mm^2 of active area (Cathode = Ca/Ag or LiF/Al). PEDOT:PSS was spin coated in air at 5500 rpm for 30 s onto an ITO coated glass substrate (10 Ω/sq), film thickness of $\sim$35 nm. The substrates were heated at 120 °C for 10 min to remove traces of water and were transferred to a glovebox equipped with a thermal evaporator. The P3HT:fullerene layer was deposited at speeds of 1200 rpm (thickness was about 110 nm) for 60 s to provide a dry film. At this point, samples were thermally annealed at 150 °C for 10 min. Evaporation was carried out at a base pressure of 3×10^{-6} mbar with the cathode under study either Ca/Ag (5/100 nm) or LiF/Al (1/100 nm). Devices were sealed with a photoresin and a glass microscopy slide followed by exposure under UV light. Samples were then taken out of the glovebox for device characterization.

3.1.2. Device characterization

Current density–voltage and impedance spectroscopy measurements were carried out by illumination with a 1.5 G illumination source (1000 W m^{-2}) using an Abet Sun 2000 Solar Simulator. The light intensity was adjusted with a calibrated Si solar cell. Impedance spectroscopy measurements were performed with Autolab PGSTAT-30 equipped with a frequency analyzer module, and was recorded by applying a small voltage perturbation (20 mV rms). Measurements were carried out at 1 sun light intensity at different DC bias voltage sweeping frequencies from 1 MHz down to 100 Hz. UV/Vis data was obtained from films using a Cary 300 Bio Spectrophotometer. External Quantum Efficiency (*EQE*) measurements were performed using a 150 W Xe lamp coupled with a monochromator controlled by a computer. The light intensity was measured using an optical power meter 70310 from Oriel Instruments where a Si photodiode was used to calibrate the system.

Acknowledgements

We thank financial support from Ministerio de Educacion y Ciencia under Project HOPE CSD2007-00007 (Consolider-Ingenio 2010), Generalitat Valenciana (Prometeo/2009/058, ACOMP/2009/056, ACOMP/2009/095, and ISIC/2012/008 Institute of Nanotechnologies for Clean Energies), and FP7 European Project ORION (Large CP-IP 229036-2).

Appendix A. Supplementary data

Supplementary data associated with this article can be found, in the online version, at http://dx.doi.org/10.1016/j.orgel.2012.06.043.

References

[1] R.A. Street, K.W. Song, S.R. Cowan, Influence of series resistance on the photocurrent analysis of organic solar cells, Org. Electron. 12 (2011) 244–248.
[2] S.R. Cowan, N. Banerji, W.L. Leong, A.J. Heeger, Charge formation, recombination, and sweep-out dynamics in organic solar cells, Adv. Funct. Mater. 22 (2012) 1116–1128.
[3] S.H. Park, A. Roy, S. Beaupré, S. Cho, N. Coates, J.S. Moon, D. Moses, M. Leclerc, K. Lee, A.J. Heeger, Bulk heterojunction solar cells with internal quantum efficiency approaching 100%, Nat. Photonics 3 (2009) 297–302.
[4] P.P. Boix, A. Guerrero, L.F. Marchesi, G. Garcia-Belmonte, J. Bisquert, Current–voltage characteristics of bulk heterojunction organic solar cells: connection between light and dark curves, Adv. Energy Mater. 1 (2011) 1073–1078.

[5] J. Bisquert, G. Garcia-Belmonte, On voltage, photovoltage and photocurrent in bulk heterojunction organic solar cells, J. Phys. Chem. Lett. 2 (2011) 1950–1964.
[6] G. Garcia-Belmonte, P.P. Boix, J. Bisquert, M. Sessolo, H.J. Bolink, Simultaneous determination of carrier lifetime and electron density-of-states in P3HT:PCBM organic solar cells under illumination by impedance spectroscopy, Sol. Energy Mater. Sol. Cells 94 (2010) 366–375.
[7] W.L. Leong, S.R. Cowan, A.J. Heeger, Differential resistance analysis of charge carrier losses in organic bulk heterojunction solar cells: observing the transition from bimolecular to trap-assisted recombination and quantifying the order of recombination, Adv. Energy Mater. 1 (2011) 517–522.
[8] Y. Zhang, X.-D. Dang, C. Kim, T.-Q. Nguyen, Effect of charge recombination on the fill factor of small molecule bulk heterojunction solar cells, Adv. Energy Mater. 1 (2011) 610–617.
[9] G. Garcia-Belmonte, A. Munar, E.M. Barea, J. Bisquert, I. Ugarte, R. Pacios, Charge carrier mobility and lifetime of organic bulk heterojunctions analyzed by impedance spectroscopy, Org. Electron. 9 (2008) 847–851.
[10] B.J. Leever, C.A. Bailey, T.J. Marks, M.C. Hersam, M.F. Durstock, In situ characterization of lifetime and morphology in operating bulk heterojunction organic photovoltaic devices by impedance spectroscopy, Adv. Energy Mater. 2 (2012) 120–128.
[11] G. Perrier, R. deBettignies, S. Berson, N. Lemaître, S. Guillerez, Impedance spectrometry of optimized standard and inverted P3HT-PCBM organic solarcells, Sol. Energy Mater. Sol. Cells 101 (2012) 210–216.
[12] Y. He, H.-Y. Chen, J. Hou, Y. Li, Indene-C60 Bisadduct: a new acceptor for high-performance polymer solar cells, J. Am. Chem. Soc. 132 (2010) 1377–1382.
[13] G. Zhao, Y. Hi, Y. Li, 6.5% Efficiency of polymer solar cells based on poly(3-hexylthiophene) and Indene-C 60 bisadduct by device optimization, Adv. Mater. 22 (2010) 4355–4358.
[14] S.M. Sze, Physics of Semiconductor Devices, second ed., John Wiley and Sons, New York, 1981.
[15] A. Guerrero, L.F. Marchesi, P.P. Boix, J. Bisquert, G. Garcia-Belmonte, Recombination in organic bulk heterojunction solar cells: small dependence of interfacial charge transfer kinetics on fullerene affinity, J. Phys. Chem. Lett. 3 (2012) 1386–1392.
[16] J. Bisquert, Interpretation of electron diffusion coefficient in organic and inorganic semiconductors with broad distribution of states, Phys. Chem. Chem. Phys. 10 (2008) 3175–3194.
[17] A. Pitarch, G. Garcia-Belmonte, I. Mora-Seró, J. Bisquert, Electrochemical impedance spectra for the complete equivalent circuit of diffusion and reaction under steady-state recombination current, Phys. Chem. Chem. Phys. 6 (2004) 2983–2988.

THE JOURNAL OF PHYSICAL CHEMISTRY C
Article
pubs.acs.org/JPCC

Molecular Electronic Coupling Controls Charge Recombination Kinetics in Organic Solar Cells of Low Bandgap Diketopyrrolopyrrole, Carbazole, and Thiophene Polymers

Teresa Ripolles-Sanchis,[†] Sonia R. Raga,[†] Antonio Guerrero,[†] Matthias Welker,[‡] Mathieu Turbiez,[‡] Juan Bisquert,[†] and Germà Garcia-Belmonte*[,†]

[†]Photovoltaic and Optoelectronic Devices Group, Departament de Física, Universitat Jaume I, ES-12071 Castelló, Spain
[‡]BASF Schweiz AG, Schwarzwaldallee 215, CH-4002 Basel, Switzerland

Ⓢ *Supporting Information*

ABSTRACT: Low-bandgap diketopyrrolopyrrole- and carbazole-based polymer bulk-heterojunction solar cells exhibit much faster charge carrier recombination kinetics than that encountered for less-recombining poly(3-hexylthiophene). Solar cells comprising these polymers exhibit energy losses caused by carrier recombination of approximately 100 mV, expressed as reduction in open-circuit voltage, and consequently photovoltaic conversion efficiency lowers in more than 20%. The analysis presented here unravels the origin of that energy loss by connecting the limiting mechanism governing recombination dynamics to the electronic coupling occurring at the donor polymer and acceptor fullerene interfaces. Previous approaches correlate carrier transport properties and recombination kinetics by means of Langevin-like mechanisms. However, neither carrier mobility nor polymer ionization energy helps understanding the variation of the recombination coefficient among the studied polymers. In the framework of the charge transfer Marcus theory, it is proposed that recombination time scale is linked with charge transfer molecular mechanisms at the polymer/fullerene interfaces. As expected for efficient organic solar cells, small electronic coupling existing between donor polymers and acceptor fullerene ($V_{\mathrm{if}} < 1$ meV) and large reorganization energy ($\lambda \approx 0.7$ eV) are encountered. Differences in the electronic coupling among polymer/fullerene blends suffice to explain the slowest recombination exhibited by poly(3-hexylthiophene)-based solar cells. Our approach reveals how to directly connect photovoltaic parameters as open-circuit voltage to molecular properties of blended materials.

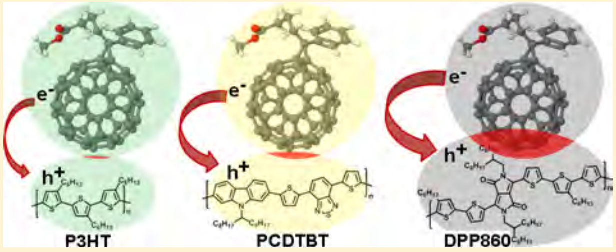

1. INTRODUCTION

Organic photovoltaic technology can potentially reduce production costs of solar energy by adopting cheaper printing technologies. New insights on materials properties and interface engineering have led very recently to achieve power conversion efficiencies near 10% in the case of bulk-heterojunction solar cell structures.[1] Improvement in solar cell efficiency partially relies upon achieving higher open-circuit voltages V_{oc} by limitation of the charge carrier recombination flux,[2] which is understood as the process of charge transfer occurring between occupied acceptor levels and unoccupied donor states. By inhibiting recombination current to some extent the amount of charge carriers involved in the photovoltaic operation is enhanced. This produces an enlarged offset in the separate carrier Fermi levels, E_{Fn} and E_{Fp} for electrons and holes, that finally is measured as an output voltage,[3]

$$qV_{\mathrm{F}} = E_{\mathrm{Fn}} - E_{\mathrm{Fp}} \tag{1}$$

The Fermi level position is highly dependent on the actual energy distribution of electronic states DOS within the effective bandgap $E_{\mathrm{g}} \approx E_{\mathrm{LUMO}}(A) - E_{\mathrm{HOMO}}(D)$. The energetically disordered environment spreads the DOS forming large electronic distributions within the bandgap. But even more important is chemical interactions that tend to aggregate molecular units in extended clusters with altered DOS.[4] The occurrence of aggregates is known to be highly influenced by the processing conditions followed during the cell construction.[5] For instance, the use of different solvents is critical in establishing the final DOS of both acceptor and donor molecular constituents.[6] The interplay between materials energetics and charge recombination kinetics does establish the achievable open-circuit voltage. Hence practical knowledge might be gained if a separation between the repercussion on V_{oc} of energetics from recombination kinetics is accomplished in complete devices after materials processing.[7]

The rate limiting mechanism governing the kinetics of charge carrier recombination in organic solar cells is still uncertain. Some models regard recombination as a transport-controlled process in similarity to that occurring in single phase organic compounds,[8] and express it by means of Langevin-like

Received: March 20, 2013
Revised: April 2, 2013
Published: April 2, 2013

dx.doi.org/10.1021/jp402751v | *J. Phys. Chem. C* 2013, 117, 8719−8726

recombination coefficients B_L directly related to the carrier mobility μ of electrons and holes as $B_L = q\mu/\varepsilon$ (ε being the effective permittivity of the blend).[9] However, such models establish a strong correlation between transport, mobility properties, and recombination kinetics, which is rarely observed from separate determinations of the recombination coefficient B and μ. Instead, we conclude that the time scale for charge recombination is linked with charge transfer molecular properties at the donor/acceptor interface rather than with transport characteristics before separate carriers meet each other. Recent papers have explicitly suggested, following different approaches, that charge recombination is closely related to molecular interfacial properties.[10] Particularly interesting are theoretical findings observing a high dependence of the charge transfer event kinetics on the relative molecular orientations and intermolecular distances.[11] Recalling the Marcus approach for electronic charge transfer, we have ascertained that differences in charge recombination among different acceptor/donor combinations are related to variations in the electronic coupling matrix, while all investigated blends exhibit a relatively high reorganization energy $\lambda \approx 0.7$ eV. Our findings reveal that blend properties rather than energetic characteristics of individual constituents determine losses caused by charge recombination.

To evaluate the role of the charge carrier recombination kinetics on the achievable open-circuit voltage of polymer/fullerene solar cells and separate it from that owed to the donor HOMO position, we have analyzed the device performance by using a purely electrical technique based on impedance measurements of complete cells under illumination. Performance is compared of solar cells comprising [6,6]-phenyl-C$_{71}$-butyric acid methyl ester (PC$_{70}$BM) as acceptor fullerene and different donor polymers: namely, poly(3-hexylthiophene (P3HT), poly[[9-(1-octylnonyl)-9H-carbazole-2,7-diyl]-2,5-thiophenediyl-2,1,3-benzothiadiazole-4,7-diyl-2,5-thiophenediyl] (PCDTBT),[12] and low bandgap diketopyrrolopyrrole-oligothiophene copolymer (DPP860, see Figure 1). We have identified polymer HOMO levels that govern the photovoltaic operation of the active blend by determining the rise of the capacitance at forward voltage. Carrier recombination current is evaluated from the analysis of the resistive response. Energy losses expressed as reduction in V_{oc} amount to approximately 100 mV for increments in recombination coefficient of about 1 order of magnitude in the case of DPP860 or PCDTBT in comparison with P3HT. Such reduction is finally originated by a slightly stronger electronic coupling. Impedance measurements allow determining relevant effects influencing V_{oc}, and connects them to microscopic, molecular parameters. Our approach can be used as an orienting guide for further solar cell improvement in combination with morphological and theoretical data.

2. EXPERIMENTAL SECTION

Materials. P3HT (Luminescence Technology Corp.), PCDTBT (1-Material), PC$_{70}$BM (Nano-C, 99%), PEDOT/PSS (CLEVIOS P AI 4083), *o*-dichlorobenzene (Aldrich, 99.9%), chloroform (Aldrich, 99.9%), Ca (Aldrich, 99.995%), and silver (Aldrich, 99.99%) were used as received without further purification. DPP860 was synthesized following a similar route, as previously reported for PDPP5T[13] with slight variations concerning the alkyl chains attached to the thiophene units, and was supplied by BASF (see Figure 1). All manipulations were carried out in a glovebox under a nitrogen atmosphere unless otherwise stated. P3HT/PC$_{70}$BM solutions (1:1 ratio) were prepared in *o*-dichlorobenzene (17 mg/mL) and were stirred at room temperature. PCDTBT/PC$_{70}$BM solutions (1:4, 4 mg/mL) were prepared in a chlorobenzene/1,2-dichlorobenzene (1:2.5 volume ratio) mixture and were stirred at 70 °C. DPP860/PC$_{70}$BM (1:2, 7.5 mg/mL) were prepared in a 1,2-dichlorobenzene/chloroform mixture (1:9 volume ratio) and were stirred at 55 °C. All solutions were stirred at the mentioned temperature for at least 16 h prior to device fabrication and were cooled down to room temperature 5 min before use.

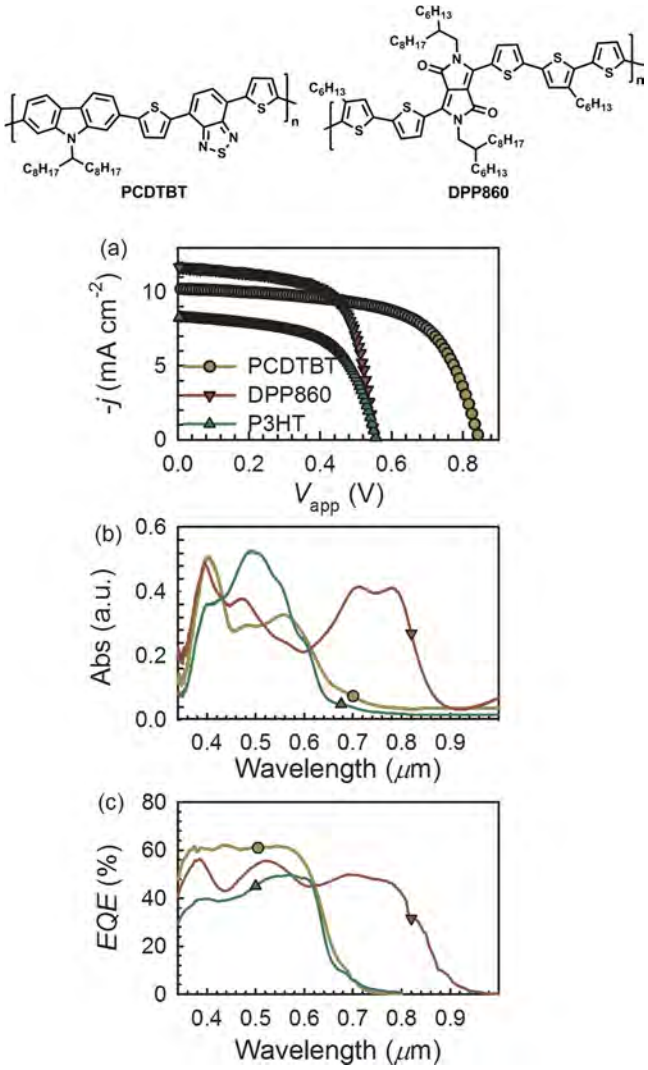

Figure 1. (a) Current density−voltage characteristics of typical devices ITO/PEDOT:PSS/polymer:PC$_{70}$BM/Ca/Ag using P3HT, PCDTBT, and DPP860 as polymer donors. (b) Absorption and (c) external quantum efficiency spectra showing the difference between small (DPP860) and large bandgap (P3HT and PCDTBT) donors.

Device Fabrication. Polymer solar cells were fabricated with a standard sandwich structure of ITO/PEDOT:PSS/donor:PC$_{70}$BM/Ca/Ag and 9 mm^2 of active area. PEDOT/PSS was spin coated in air at 5500 rpm for 30 s onto an ITO-coated glass substrate (10 Ohm/sq), film thickness of ∼35 nm. The substrates were heated at 120 °C for 10 min to remove traces of water and were transferred to a glovebox equipped with a thermal evaporator. The P3HT/PC$_{70}$BM layer was deposited at speeds of 1200 rpm (thickness was about 110 nm) for 30 s,

Table 1. Photovoltaic Parameters and Parameters Extracted from Impedance Spectroscopy Analysis of Polymer/$PC_{70}BM$ Solar Cells[a]

	j_{sc} (mA cm^{-2})	V_{oc} (mV)	FF	PCE (%)	α	β	γ	E_{HOMO} (eV)
P3HT	8.36	560	0.59	2.7	0.35	0.71	2.01	−5.4
PCDTBT	10.21	845	0.62	5.4	0.32	0.68	2.00	−5.8
DPP860	12.80	554	0.66	4.7	0.44	0.78	1.77	−5.5

[a] Polymer E_{HOMO} extracted from capacitance plot in Figure 2b assuming the value for P3HT determined from voltammetry methods (Supporting Information).

followed by a slow drying of the film in a Petri dish. At this point, P3HT/$PC_{70}BM$ devices were thermally annealed at 130 °C for 20 min. Devices based on PCDTBT/$PC_{70}BM$ blends were spin-coated at 1000 rpm for 60 s (∼100 nm) and films were thermally annealed at 70 °C for 30 min. Finally, DPP860/$PC_{70}BM$ blends were spin-coated over prerotating substrates at a speed of 7500 rpm; 25 μL of solution was used for 2 × 2 cm substrates to provide a ∼50 nm active layer thickness, and no additional drying step was required. Evaporation was carried out for all samples at a base pressure of 3×10^{-6} mbar, and Ca (10 nm) and Ag (100 nm) were sequentially evaporated. The top Ca/Ag electrodes were then encapsulated with epoxy and a glass slide before testing.

Device Characterization. Current density−voltage and impedance measurements were carried out by illumination with a 1.5G illumination source (1000 W m^{-2}) using an Abet Sun 2000 Solar Simulator. The light intensity was adjusted with a calibrated Si solar cell. Impedance spectra were recorded by applying a small voltage perturbation (20 mV rms) at frequencies from 1 MHz to 1 Hz. Measurements were carried out under 1 sunlight intensity sweeping the DC voltage in the range 0 to V_{oc}. These measurements were performed with Autolab PGSTAT-30 equipped with a frequency analyzer module. Recombination resistance R_{rec} and chemical capacitance C_μ were directly extracted from the low-frequency region, as previously reported.[14]

3. RESULTS AND DISCUSSION

DOS and Capacitance Response. Solar cells of structure indium tin oxide (ITO)/poly(3,4-ethylenedioxythiophene)/poly(styrene sulfonic acid) (PEDOT/PSS)/polymer/$PC_{70}BM$/Ca/Ag, were prepared as described in the Experimental Section. To test the effect of the donor LUMO level shift on the overall recombination kinetics and open-circuit voltage, three different donor polymers have been analyzed: namely, P3HT, PCDTBT, and DPP860. Impedance spectroscopy measurements were performed with Autolab PGSTAT-30 by applying a small ac perturbation to maintain the linearity of the response, as described in previous work.[7a]

An example of the measured current-density voltage $j-V$ characteristics under simulated AM1.5G illumination (1000 W m^{-2}) of polymer/$PC_{70}BM$ solar cells is plotted in Figure 1a. We systematically observed that V_{oc} at 1 sun illumination results in higher values for cells processed with PCDTBT because of the more negative value of the HOMO respect to the vacuum level.[12a] In good accordance with recent works,[15] low bandgap character of DPP860 is observed in the absorption spectrum onset situated near 860 nm (see Figure 1b). This enlarged absorption produces a higher photocurrent as listed in Table 1.

To separate the influence of the charge carrier recombination process on the achievable V_{oc} from the aforementioned effect of the donor HOMO level position, we have performed a series of impedance measurements in polymer/$PC_{70}BM$ BHJ solar cells by varying the applied voltage at 1 sun irradiation intensity. The method to extract resistive (R_{rec} recombination resistance) and capacitive (C_μ chemical capacitance) parameters from impedance measurements was addressed in previous papers.[7a,16] We show in Figure 2 the variation of R_{rec} and C_μ as a function of the voltage. At low voltages the measured capacitance responds to a dielectric mechanism. It is originated by the voltage-modulation of the depletion zone built up at the cathode contact, which collapses to the geometrical capacitance near zero voltage, as has been shown in our previous work.[16a] The analysis is particularly useful for solar cells in which there is no severe limitation to the charge transport.[14] By examining Figure 2, one can observe that for larger voltages the chemical capacitance exhibits the expected variation on voltage originated by the carrier occupation of electron density-of-states (DOS), $g(E)$ as $C_\mu = q^2Lg(V_F)$,[16a] L being the active layer thickness. It has been shown that in many cases electrons form a sort of minority carrier due to p-doping.[17] This makes the measured capacitance sensitive to the rise of the occupancy of electron states in the molecular acceptor. The occupancy of bandgap states is modulated by a parameter α, which accounts for the

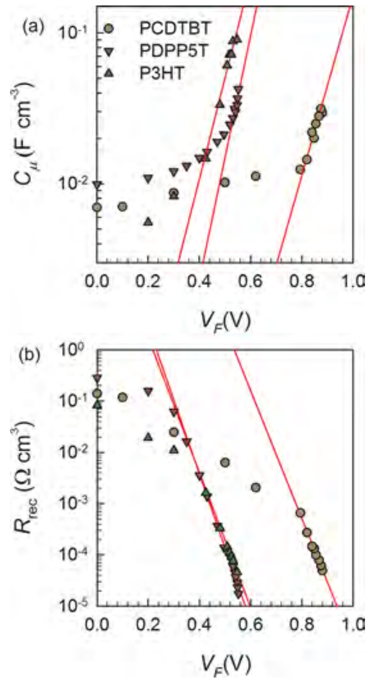

Figure 2. (a) Comparison of specific chemical capacitance−voltage response of polymer/$PC_{70}BM$-processed devices extracted from impedance analysis. Straight lines correspond to exponential fits as $C_\mu = C_0 \exp(\alpha q V_F/k_BT)$. (b) Specific recombination resistance R_{rec} as a function of the voltage. Straight lines correspond to exponential fits as $R_{rec} = R_0 \exp(-q\beta V_F/k_BT)$. In both plots the applied voltage V_{app} is assimilated to V_F.

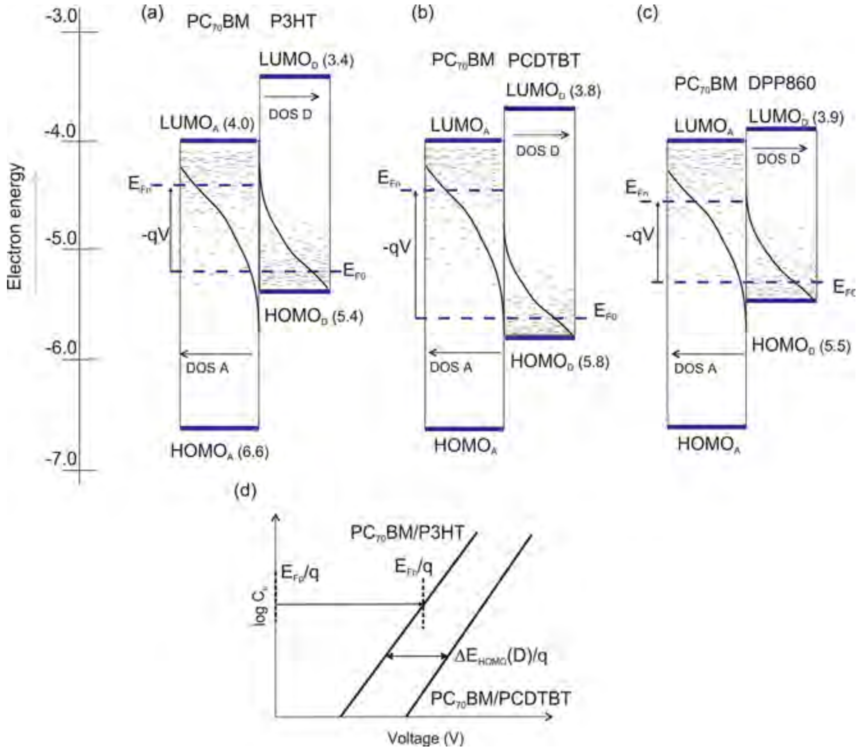

Figure 3. Energy diagram representing the polymer HOMO and fullerene LUMO manifolds (DOS) indicating the central value of the distribution. (a) P3HT HOMO level is estimated from CV analysis (Supporting Information). (b) PCDTBT and (c) DPP860 HOMO levels calculated from the shift of the capacitance−voltage plot. The procedure is illustrated in (d). Polymer LUMO levels are estimated from the tail of the absorption spectra in Figure 1b. The origin of the photovoltage is indicated.

characteristic energy of the DOS $\alpha=T/T_0$, being T_0 the characteristic temperature of the exponential distribution

$$g(E) = \frac{N_L}{k_B T_0} \exp[(E - E_{LUMO})/k_B T_0] \tag{2}$$

N_L stands for the total level density of the acceptor LUMO manifold. The equilibrium value of the carrier density is given by

$$n_0 = N_L \exp\left(\frac{E_{F0} - E_{LUMO}}{k_B T_0}\right) \tag{3}$$

which depends on the position of the equilibrium Fermi level E_{F0}. In zero-temperature approximation, the total electron carrier density is given by the integration of DOS up to the Fermi level

$$\begin{aligned} n &= \int_0^{E_{Fn}} g(E)\mathrm{d}E \\ &= N_L \exp\left(\frac{E_{Fn} - E_{LUMO}}{k_B T_0}\right) \\ &= n_0 \exp\left(\frac{E_{Fn} - E_{F0}}{k_B T_0}\right) \end{aligned} \tag{4}$$

It is observed in Figure 2a that C_μ exhibits an exponential dependence at high voltages, that is, $C_\mu = C_0 \exp(\alpha q V_F/k_B T)$, with $\alpha \approx 0.3$−0.4 (see Table 1). C_μ extracted from the impedance analysis is then a replica of the bandgap electronic state distribution as the occupation progresses following the Fermi level displacement.[17a]

It is also useful to introduce the carrier density in a transport level at the energy E_c

$$n_c = n_c^0 \exp\left(\frac{E_{Fn} - E_{F0}}{k_B T}\right) \tag{5}$$

Equation 5 is most useful in the case of a multiple trapping mechanism in which a sharp distinction can be made between free and trapped electrons. The special feature of the carriers at the transport level is that charge density relates simply to the voltage V_F as

$$n_c = n_c^0 \exp\left(\frac{qV_F}{k_B T}\right) \tag{6}$$

This last equation assumes that the majority carrier concentration is not significantly modified so that $E_{Fp} \approx E_{F0}$. Because actual measurements are often performed as a function of voltage, the free carrier density is a useful index of the voltage V_F, in order to formulate a recombination model. In general, the experimental relevance of a free carrier density must be proved by transport measurements, and one relies on the total carrier density introduced in eq 4. For the case of an exponential distribution of traps, one can convert from free to total carrier density by the expression

$$\frac{n}{n_0} = \left(\frac{n_c}{n_c^0}\right)^\alpha \tag{7}$$

By combining eqs 6 and 7, the total carrier density reproduces the slope of the experimental exponential behavior found in the capacitance as $n = n_0 \exp(\alpha q V_F/k_B T)$ in accordance with eq 4. The DOS occupancy (identified from the exponential rise in the chemical capacitance) is shifted in energy depending on the polymer HOMO position with respect to the acceptor LUMO level. In the devices studied here, the same acceptor fullerene is used so that it is reasonable to relate the voltage shift in the capacitance plot of Figure 2a principally to the polymer HOMO level offset. To take P3HT HOMO as a reference CV analysis has been performed giving a value ∼−5.4 eV (see Supporting Information) within the range found in previous works.[18] We adopt the criterion of extracting the HOMO level from the maximum of the oxidation peak (DOS center). This criterion situates the oxidation peak onset on the tail of the DOS (∼−5.2 eV) and, consequently, within the effective bandgap energies. The energy disorder broadens the HOMO manifold being the DOS center a measurement of the HOMO level mean. This is illustrated in Figure 3.

The voltage shift in Figure 2a is then interpreted in terms of the polymer HOMO offset, as drawn in Figure 3d. By taking this voltage shift and the HOMO reference value for P3HT a value of −5.5 eV for DPP860 HOMO can be calculated, and lower position is derived for PCDTBT HOMO (−5.8 eV).[12a] As explained previously, these values indicate the DOS center rather than the onset of state occupancy. From the absorption spectra in Figure 1b, the energy diagram in Figure 3 is derived. We remark here that the capacitive method reported allows establishing the polymer HOMO position in complete cells when a reference is known and measured using alternative techniques.

Resistive Response and Recombination Kinetics. The differential resistance R_{rec} extracted from impedance conveys information about the recombination flux. Recombination of excess carriers is phenomenologically modeled as

$$j_{\mathrm{rec}} = j_0\left[\left(\frac{n_{\mathrm{c}}}{n_{\mathrm{c}}^0}\right)^{\beta} - 1\right] = j_0\left[\exp\left(\beta\frac{qV_{\mathrm{F}}}{k_{\mathrm{B}}T}\right) - 1\right] \tag{8}$$

The expression in eq 8 for the recombination current is usually labeled as the β-recombination model that includes the parameter β accounting for the deviation from the ideal diode equation (inverse of the diode ideality factor), being j_0 the dark, saturation recombination current.[19] Recombination resistance is defined from the recombination current derivative[7a]

$$R_{\mathrm{rec}} = L\left(\frac{\mathrm{d}j_{\mathrm{rec}}}{\mathrm{d}V_{\mathrm{F}}}\right)^{-1} \tag{9}$$

By examining Figure 2b, one can infer that the recombination resistance corresponds to an approximate exponential behavior $R_{\mathrm{rec}} = R_0 \exp(-\beta qV_{\mathrm{F}}/k_{\mathrm{B}}T)$, as expected from the eq 8 derivative in the case of high injection. A straightforward estimation of the β-parameter is obtained that results in $\beta \approx 0.7{-}0.8$ (see Table 1). At lower voltages R_{rec} tends to saturate presumably because the differential resistance measured is not only determined by the recombination flux but also by a shunt resistance caused by additional parallel leakage currents.

Equation 8 can be alternatively written in terms of a power-law dependence of the total carrier density as

$$j_{\mathrm{rec}} = qLB[n^{\gamma} - n_0^{\gamma}] \tag{10}$$

where B represents a recombination coefficient that establishes the time scale for recombination kinetics.

The excess electron n density appears in addition to background equilibrium electron density n_0. In the dark, the equilibrium densities produce the saturation recombination current that compensates the thermal generation,

$$j_0 = qLBn_0^{\gamma} \tag{11}$$

However, actual measurement of the reverse current in the dark may not provide j_0 due to leakage currents. From eq 7 we obviously have the relationship $\gamma = \beta/\alpha$.

By looking at α and β values extracted from experiments (Table 1), it is observed that $\beta \approx 2\alpha$ is satisfied within the experimental error. The γ exponent results then in values approximately around 2. In the case of DPP860, a slightly lower exponent is found, $\gamma = 1.77$. This experimental fact lets us write eq 8 as $j_{\mathrm{rec}} \propto n^{\gamma}$, with $\gamma \approx 2$, signaling an approximate bimolecular-like behavior for the recombination process in good accordance with the electroneutrality condition $n = p$. It has been identified in some studies based on impedance spectroscopy that $\gamma \approx 2$,[7a,20] while transient analyses usually give $\gamma \geq 2$.[2,21]

From eqs 8 and 9 we derived that the recombination current can be written in terms of the recombination resistance as $j_{\mathrm{rec}} = k_{\mathrm{B}}T/\beta qR_{\mathrm{rec}}$,[14] that allows for a straightforward calculation of the recombination coefficient B based on differential resistive and capacitive parameters extracted from impedance spectroscopy. By combining eqs 8 and 4 in the case of high injection, one arrives at

$$B = \frac{k_{\mathrm{B}}T}{q^2Ln^2\beta R_{\mathrm{rec}}} \tag{12}$$

The derivation of eq 12 assumes a rather constant value for the recombination coefficient, nearly independent of energetics of the states taking part on the recombination event. Results of applying eq 12 are shown in Figure 4. It is observed that for $V_{\mathrm{F}} > 0.4$ V the recombination coefficient for each blend does exhibit an almost constant behavior always within the range of $B \approx 10^{-12}{-}10^{-11}$ cm^3 s^{-1}. In the case of P3HT/PC$_{70}$BM devices, a lower coefficient $B = 2 \times 10^{-12}$ cm^3 s^{-1} is encountered in comparison with PCDTBT/PC$_{70}$BM ($B = 2 \times 10^{-11}$ cm^3 s^{-1}), and DPP860/PC$_{70}$BM ($B \approx 6 \times 10^{-11}$ cm^3 s^{-1}) solar cells. For lower voltages, B departs from the approximate constant value because both R_{rec} and C_{μ} largely deviate from the exponential behavior. It is worth noting that recombination coefficient values found for P3HT and PCDTBT are in good agreement with recent results obtained using alternative techniques.[22] In addition, results in Figure 4

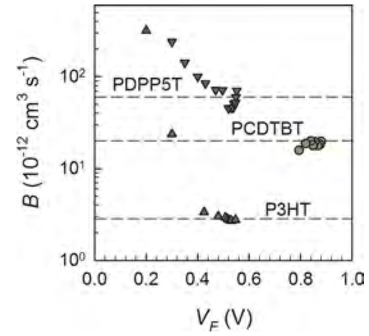

Figure 4. Recombination coefficient B calculated by means of eq 12 using the parameters extracted from the impedance analysis. Horizontal dashed lines mark average values of data points following the exponential behavior in Figure 2.

Table 2. Recombination Coefficient B Extracted from Impedance Analysis[a]

	B (cm^3 s^{-1})	j_0 (A cm^{-2})	j_{0k} (A cm^{-2})	N_{00} (cm^{-3})	V_{if} (meV)	ΔV_{oc}^{kin} (mV)	V_{oc}' (mV)
P3HT	2×10^{-12}	4.7×10^{-10}	1.7×10^{4}	7.8×10^{19}	0.09		
PCDTBT	2×10^{-11}	7.8×10^{-14}	3.9×10^{4}	3.5×10^{19}	0.19	85	875
DPP860	$\sim 6 \times 10^{-11}$	1.5×10^{-10}	2.7×10^{6}	1.7×10^{20}	0.70	110	550

[a] Saturation current, j_0, and exponential prefactor, j_{0k} in eq 13. Total level density N_{00}, calculated from eq 14, and resulting electronic coupling V_{if}. ΔV_{oc}^{kin} corresponding to the kinetic term in eq 20b. V_{oc}' calculated with eq 20, taking V_{oc} of P3HT-based cells as reference.

point to the fact that the energy location of recombining carriers within the DOS has a minor influence on the recombination coefficient value.

Connection to Molecular Charge Transfer Parameters. A key parameter to understand the kinetics of charge carrier recombination in solar cells is the saturation current j_0 in eq 8.[10b,23] It is known that j_0 establishes the time scale of recombination through the combined effect of the charge transfer energetics and kinetics. As suggested for inorganic semiconductors,[23a] one can propose a separation of the form

$$j_0 = j_{0k} \exp\left(-\frac{\beta E_g}{k_B T}\right) \tag{13}$$

An expression that explicitly separates kinetic terms represented by the prefactor j_{0k} from energetic contributions stated through bandgap energy E_g. In inorganic materials, E_g is a single function of the semiconductor. However, in organic blends the effective gap $E_g = E_{LUMO}(A) - E_{HOMO}(D)$ is a function of the relative energetics of the blend components. Therefore, assessing the influence of energetics on j_0 is a matter that requires careful investigation. In accordance to the capacitance dependence on voltage, we propose a background equilibrium carrier density as $N_0 = N_{00} \exp(-\alpha E_g/k_B T)$, being N_{00} a parameterer accounting for the total level density. It is worth noting that the last expression is consistent with eq 13 and the form adopted by j_0 previously introduced in eq 11. Such identification readily allows connecting j_{0k} and B as

$$j_{0k} = qLBN_{00}^{\gamma} \tag{14}$$

Our approach permits evaluating j_{0k} directly from the impedance analysis rather than from the j−V characteristic usually masked by leakage currents at low bias voltages. Equation 13 and fittings of the recombination resistance in Figure 2b provide the value for j_0 (see Table 2). Blends with larger effective gap yields lower j_0 values, as expected. It is feasible to determine j_{0k} taking into account the effective gap, as derived from the capacitance voltage shift. It is observed in Table 2 that j_{0k} qualitatively follows the trend exhibited by B, confirming the higher recombining character of DPP860-based cells. A consistency proof relies upon evaluating N_{00} taking into account the relationship in eq 14. By examining Table 2, one can observe that N_{00} encountered is within the range of 10^{19}–10^{20} cm^{-3}, in good agreement with the total density of active molecules in the active layer.

These findings are a strong indication that the recombination kinetics does not depend on the absolute energetics of the donor HOMO levels. Indeed, deeper HOMO positions, as is the case of PCDTBT (−5.8 eV), result in recombination coefficients in between those observed for much lower ionization energy polymers as P3HT (−5.4 eV) and DPP860 (−5.5 eV). Some approaches, connected to the original Langevin theory on the recombination in single phases, related recombination coefficient B_L directly to the carrier mobility μ exhibited by electrons and holes as $B_L = q\mu/\varepsilon$.[9b] This gives a volumetric recombination flux as $U_L = B_L np$. Understanding the reported recombination coefficient values in Figure 4 in terms of transport features, as derived from Langevin-like recombination approaches is difficult. Similar electron mobilities are expected because of the use of the same fullerene, and it is not evident how DPP380 exhibits more than 1 order of magnitude greater hole mobility than P3HT to explain faster recombination.

An alternative view regards the charge transfer event itself as the limiting rate factor of the recombination mechanism. It is then the specific molecular environment at donor−acceptor interfaces that sates the time scale for recombination. In a previous work[20] we have reported on the small dependence of the recombination kinetics on the fullerene electron affinity and voltage. It was concluded within the framework of the Marcus theory that the reorganization energy, λ, rather than the polymer HOMO/fullerene LUMO energy offset or the DOS occupancy level, takes control over the charge transfer event. The charge transfer rate k_0 in the semiclassical Marcus expression is written as

$$k_0 = \frac{2\pi}{\hbar} |V_{if}|^2 \sqrt{\frac{1}{4\pi\lambda k_B T}} \exp\left(-\frac{(\Delta G_0 + \lambda)^2}{4\lambda k_B T}\right) \tag{15}$$

where ΔG_0 is the variation of the Gibbs free energy during the reaction and V_{if} corresponds to the electronic coupling matrix element (charge transfer integral) between initial and final states. We identify here ΔG_0 with the acceptor and donor energy level offset, $\Delta G_0 \sim E_n - E_p$.

In the experiments presented here, large variations in B (or equivalently j_{0k}) are observed among polymers, without any correlation with the polymer ionization energy. Recalling again the Marcus approach in eq 15, one can infer that, to slow down the recombination kinetics, small values of V_{if} and large λ are necessary. We note from Figure 4 that the recombination kinetics results slightly dependent on the voltage for a given polymer/fullerene combination. This behavior is in good agreement with a large value for $\lambda \approx 0.7$ eV, as stated in recent works.[20] This last observation would imply that the observed variation in B might be connected to changes in V_{if}, a parameter that mainly reflects the environment in which fullerene/polymer interfaces are located. It is known that it highly depends on both relative molecular orientations and intermolecular distances.[11a] By comparing eq 14 and eq 15, one can readily arrive at $k_0 = BN_{00}$ because $\gamma = 2$ as noted previously. This last identification allows us to calculate V_{if}, assuming that the charge transfer event occurs closely to the maximum rate, in accordance with a large reorganization energy. Under this assumption, the exponential term in eq 15 is close to 1, and it can be obtained that $|V_{if}|^2 = Bn_{00}\hbar(4\pi\lambda k_B T/2\pi)$. The calculated electronic coupling matrix V_{if} values are listed in Table 2. One can observe that when very low, <1 meV, values are found, it signals the high inhibiting character of the recombination charge transfer between reduced fullerene molecules and oxidized polymer units.[24] Nevertheless, the relatively more recombining blend containing DPP860 exhibits larger V_{if} value in comparison with the other combinations studied.

Determination of Energy Losses. The previous analysis based on impedance measurements allows for an estimation of the actual donor HOMO level considering the P3HT HOMO as a well-established reference. Taking into account the recombination current in eq 8, a useful representation of the j−V characteristics results by including the photocurrent term j_{ph},

$$j = j_0\left[\exp\left(\beta\frac{qV_F}{k_BT}\right) - 1\right] - j_{ph} \tag{16}$$

At V_{oc}, the saturation current is largely exceeded by the recombination term in eq 8, and assuming a voltage-independent photocurrent $j_{ph} = j_{sc}$, one readily arrives at

$$V_{oc} = \frac{k_BT}{q\beta}\ln\left(\frac{j_{sc}}{j_0}\right) \tag{17}$$

Equation 17 entails that variations in V_{oc} are linked with two different contributions. Higher photocurrent increases V_{oc} because photogenerated carrier density attains larger values. On the contrary, lower dark current j_0 reduces the recombination flux also allowing for an increment in the photogenerated carriers. This is because solar cells function under the principle of the kinetic balance between light-induced carrier generation and recombination. The detrimental effect of increased recombination on V_{oc} can be easily quantified. We notice that the term related to differences in short-circuit current as $k_BT/q\beta\ \ln(j_{SC}'/j_{SC})$ only amounts about 15 meV when DPP860- and P3HT-based cells are compared so that it can be omitted in the following calculations. From eq 17 it is derived that

$$\Delta V_{oc} = \frac{k_BT}{q\beta}\ln\left(\frac{j'_0}{j_0}\right) \tag{18}$$

In eq 18, ΔV_{oc} stands for the V_{oc} enhancement (for the less recombining cell) owed to the reduction in dark current recombination j_0 with respect to the value exhibited by the more recombining cell j'_0. Hence, using eq 11 one can separate two contributions in eq 17 as

$$\Delta V_{oc} = \frac{k_BT}{q\beta}\left[\ln\left(\frac{B'}{B}\right) + \ln\left(\frac{n'^{\gamma}_0}{n_0^{\gamma}}\right)\right] \tag{19}$$

The first summand $k_BT/q\beta\ln(B'/B)$ is easily interpreted as a V_{oc} loss owed exclusively to the difference in the recombination kinetics. The second summand $k_BT/q\beta\ \ln(n_0'^{\gamma}/n_0^{\gamma})$, which derives from a ratio between equilibrium carrier densities, can be expressed in terms of the effective bandgap. This term represents the essential influence of the energetics on the recombination kinetics. As stated in eq 2, the equilibrium carrier density n_0, which determines the saturation current j_0, scales with the equilibrium Fermi level E_{F0}. Recalling eq 2 and taking into account that the energy shift in E_{F0} is caused by the polymer HOMO level offset a separation of kinetics and energetics terms in eq 19 is derived

$$\Delta V_{oc} = \Delta V_{oc}^{kin} + \Delta V_{oc}^{ener} \tag{20a}$$

where

$$\Delta V_{oc}^{kin} = \frac{k_BT}{q\beta}\ln\left(\frac{B'}{B}\right) \tag{20b}$$

$$\Delta V_{oc}^{ener} = \frac{E_{HOMO}(D) - E'_{HOMO}(D)}{q} \tag{20c}$$

Equation 20a explicitly states that V_{oc} variations among solar cells comprising different active materials can be simply split into two separated contributions: one related to differences in recombination kinetic time scale, the other exclusively linked with energy HOMO offset of the donors, as far as N_{00} exhibits similar values between the compared cells. The case of comparing acceptors with different LUMO level has been recently treated.[20] If only the recombination kinetics term of eq 20b is considered one can arrive at quantifying a significant loss in open-circuit voltage of about 100 meV (Table 2) exclusively produced by the increment in the recombination kinetics exhibited by PCDTBT- and DPP860-based solar cells in comparison to that occurring for less recombining P3HT-based devices. Such a shift in V_{oc} caused by recombination losses entails power conversion efficiency reduction approximately equal to 20% in the case of DPP860 used as donor polymer. Moreover, the application of eq 20 allows us to determine $V'_{oc} = V_{oc} - \Delta V_{oc}$, taking the values exhibited by P3HT-based cell as reference. Estimation of V_{oc} lies within the experimental error as observed in comparing Table 1 and Table 2.

4. CONCLUSION

We have demonstrated how electronic coupling at polymer/fullerene interfaces can have a determining influence on the kinetics of charge carrier recombination in a variety of bulk-heterojunction solar cells containing polymers of different ionization energy and absorption properties. Although transport properties have been regarded to govern carrier recombination by establishing the rate limiting mechanism, our findings situate the focus on the inner interfacial properties of the photovoltaic blends. Rather there exists a correlation between the loss in open-circuit voltage and the molecular electronic coupling of the donor/acceptor system. As derived from the Marcus approach for charge transfer, recombination in an efficient solar cell needs for reduced electronic coupling and large reorganization energy between initial and final states. Our analysis corroborates such requirements ($V_{if} < 1$ meV and $\lambda \approx 0.7$ eV) being differences in recombination coefficient connected to variations in the electronic coupling among blends. We note that a detailed knowledge about both relative molecular orientations and intermolecular distances at polymer/fullerene interfaces could be used as a fruitful guide for improvement of organic solar cell performance.

■ ASSOCIATED CONTENT

Ⓢ Supporting Information

CV analysis for the determination of the energy reference of P3HT HOMO level. This material is available free of charge via the Internet at http://pubs.acs.org.

■ AUTHOR INFORMATION

Corresponding Author

*E-mail: garciag@fca.uji.es.

Notes

The authors declare no competing financial interest.

■ ACKNOWLEDGMENTS

This work was partially supported by FP7 European Collaborative Project SUNFLOWER (FP7-ICT-2011-7, Contract No. 287594), Ministerio de Educacion y Ciencia (Spain), under Project HOPE CSD2007-00007 (Consolider-Ingenio 2010), and Generalitat Valenciana (Prometeo/2009/058 and ISIC/2012/008 Institute of Nanotechnologies for Clean Energies).

■ REFERENCES

(1) Green, M. A.; Emery, K.; Hishikawa, Y.; Warta, W.; Dunlop, E. D. *Prog. Photovoltaics: Res. Appl.* **2012**, *20*, 12−20.

(2) Maurano, A.; Hamilton, R.; Shuttle, C. G.; Ballantyne, A. M.; Nelson, J.; O'Regan, B.; Zhang, W.; McCulloch, I.; Azimi, H.; Morana, M.; Brabec, C. J.; Durrant, J. R. *Adv. Mater.* **2010**, *22*, 4987−4992.

(3) Garcia-Belmonte, G.; Bisquert, J. *Appl. Phys. Lett.* **2010**, *96*, 113301.

(4) Kaake, L. G.; Barbara, P. F.; Zhu, X.-Y. *J. Phys. Chem. Lett.* **2010**, *1*, 628−635.

(5) Jamieson, F. C.; Domingo, E. B.; McCarthy-Ward, T.; Heeney, M.; Stingelin, N.; Durrant, J. R. *Chem. Sci.* **2012**, *3*, 485−492.

(6) (a) Wienk, M. M.; Turbiez, M.; Gilot, J.; Janssen, R. A. J. *Adv. Mater.* **2008**, *20*, 2556−2560. (b) Boix, P. P.; Wienk, M. M.; Janssen, R. A. J.; Garcia-Belmonte, G. *J. Phys. Chem. C* **2011**, *115*, 15075−15080.

(7) (a) Garcia-Belmonte, G.; Boix, P. P.; Bisquert, J.; Sessolo, M.; Bolink, H. J. *Sol. Energy Mater. Sol. Cells* **2010**, *94*, 366−375. (b) Credgington, D.; Durrant, J. R. *J. Phys. Chem. Lett.* **2012**, *3*, 1465−1478.

(8) Kuik, M.; Koster, L. J. A.; G. A. H. Wetzelaer, G. A. H.; Blom, P. W. M. *Phys. Rev. Lett.* **2011**, *107*, 256805.

(9) (a) Koster, L. J. A.; Mihailetchi, V. D.; Blom, P. W. M. *Appl. Phys. Lett.* **2006**, *88*, 052104. (b) Deibel, C.; Wagenpfahl, A.; Dyakonov, V. *Phys. Rev. B* **2009**, *80*, 075203.

(10) (a) Schlenker, C. W.; Thompson, M. E. *Chem. Commun.* **2010**, *47*, 3702−3716. (b) Yamamoto, S.; Orimo, A.; Ohkita, H.; Benten, H.; Ito, S. *Adv. Energy Mater.* **2012**, *2*, 229−237.

(11) (a) Yi, Y.; Coropceanu, V.; Bredas, J.-L. *J. Am. Chem. Soc.* **2009**, *131*, 15777−15783. (b) Ko, S.; Hoke, E. T.; Pandey, L.; Hong, S.; Mondal, R.; Risko, C.; Yi, Y.; Noriega, R.; McGehee, M. D.; Brédas, J.-L.; Salleo, A.; Bao, Z. *J. Am. Chem. Soc.* **2012**, *134*, 5222−5232.

(12) (a) Blouin, N.; Michaud, A.; Leclerc, M. *Adv. Mater.* **2007**, *19*, 2295−2300. (b) Park, S. H.; Roy, A.; Beaupré, S.; Cho, S.; Coates, N.; Moon, J. S.; Moses, D.; Leclerc, M.; Lee, K.; Heeger, A. J. *Nat. Photonics* **2009**, *3*, 297−302. (c) Alem, S.; Chu, T.-Y.; Tse, S. C.; Wakima, S.; Lu, J.; Movileanu, R.; Tao, Y.; Bélanger, F.; Désilets, D.; Beaupré, S.; Leclerc, M.; Rodman, S.; Waller, D.; Gaudiana, R. *Org. Electron.* **2011**, *12*, 1788−1793.

(13) Gevaerts, V. S.; Furlan, A.; Wienk, M. M.; Turbiez, M.; Janssen, R. A. J. *Adv. Mater.* **2012**, *24*, 2130−2134.

(14) Boix, P. P.; Guerrero, A.; Marchesi, L. F.; Garcia-Belmonte, G.; Bisquert, J. *Adv. Energy Mater.* **2011**, *1*, 1073−1078.

(15) Wienk, M. M.; Turbiez, M.; Gilot, J.; Janssen, R. A. J. *Adv. Mater.* **2008**, *20*, 2556−2560.

(16) (a) Fabregat-Santiago, F.; Garcia-Belmonte, G.; Mora-Seró, I.; Bisquert, J. *Phys. Chem. Chem. Phys.* **2011**, *13*, 9083−9118. (b) Garcia-Belmonte, G.; Guerrero, A.; Bisquert, J. *J. Phys. Chem. Lett.* **2013**, *4*, 877−886.

(17) (a) Bisquert, J.; Garcia-Belmonte, G. *J. Phys. Chem. Lett.* **2011**, *2*, 1950−1964. (b) Li, J. V.; Nardes, A. M.; Liang, Z.; Shaheen, S. E.; Gregg, B. A.; Levi, D. H. *Org. Electron.* **2011**, *12*, 1879−1885.

(18) (a) Hou, J.; Chen, T. L.; Zhang, S.; Huo, L.; Sista, S.; Yang, Y. *Macromolecules* **2009**, *42*, 9217−9219. (b) Gong, X.; Tong, M.; Brunetti, F. G.; Seo, J.; Sun, Y.; Moses, D.; Wudl, D.; Heeger, A. J. *Adv. Mater.* **2011**, *23*, 2272−2277. (c) Greaney, M. J.; Das, S.; Webber, D. H.; Bradforth, S. E.; Brutchey, R. L. *ACS Nano* **2012**, *6*, 4222−4230.

(19) Bisquert, J.; Mora-Seró, I. *J. Phys. Chem. Lett.* **2010**, *1*, 450−456.

(20) Guerrero, A.; Marchesi, L. F.; Boix, P. P.; Bisquert, J.; Garcia-Belmonte, G. *J. Phys. Chem. Lett.* **2012**, *3*, 1386−1392.

(21) Shuttle, C. G.; O'Regan, B.; Ballantyne, A. M.; Nelson, J.; Bradley, D. D. C.; de Mello, J.; Durrant, J. R. *Appl. Phys. Lett.* **2008**, *92*, 093311.

(22) (a) Etzold, F.; Howard, I. A.; Mauer, R.; Meister, M.; Kim, T.-D.; Lee, K.-S.; Baek, N. S.; Laquai, F. *J. Am. Chem. Soc.* **2011**, *133*, 9469−9479. (b) Clarke, T. M.; Peet, J.; Nattestad, A.; Drolet, N.; Dennler, G.; Lungenschmied, C.; Leclerc, M.; Mozer, A. J. *Org. Electron.* **2012**, *13*, 2639−2646.

(23) (a) Sze, S. M. *Physics of Semiconductor Devices*, 2nd ed.; John Wiley & Sons: New York, 1981; (b) Enwin, P.; Thompson, M. E. *Appl. Phys. Lett.* **2011**, *98*, 223305.

(24) Yi, Y.; Coropceanu, V.; Bredas, J.-L. *J. Mater. Chem.* **2011**, *21*, 1479−1486.

Interplay between Fullerene Surface Coverage and Contact Selectivity of Cathode Interfaces in Organic Solar Cells

Antonio Guerrero,[†,*] Bernhard Dörling,[‡] Teresa Ripolles-Sanchis,[†] Mahdieh Aghamohammadi,[‡] Esther Barrena,[‡] Mariano Campoy-Quiles,[‡] and Germà Garcia-Belmonte[†,*]

[†]Photovoltaic and Optoelectronic Devices Group, Departament de Física, Universitat Jaume I, ES-12071 Castelló, Spain and [‡]Institut de Ciència de Materials de Barcelona (ICMAB-CSIC), Campus de la UAB, Bellaterra 08193, Spain

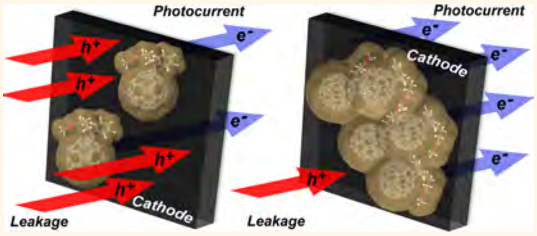

ABSTRACT Interfaces play a determining role in establishing the degree of carrier selectivity at outer contacts in organic solar cells. Considering that the bulk heterojunction consists of a blend of electron donor and acceptor materials, the specific relative surface coverage at the electrode interfaces has an impact on the carrier selectivity. This work unravels how fullerene surface coverage at cathode contacts lies behind the carrier selectivity of the electrodes. A variety of techniques such as variable-angle spectroscopic ellipsometry and capacitance−voltage measurements have been used to determine the degree of fullerene surface coverage in a set of PCPDTBT-based solar cells processed with different additives. A full screening from highly fullerene-rich to polymer-rich phases attaching the cathode interface has enabled the overall correlation between surface morphology (relative coverage) and device performance (operating parameters). The general validity of the measurements is further discussed in three additional donor/acceptor systems: PCPDTBT, P3HT, PCDTBT, and PTB7 blended with fullerene derivatives. It is demonstrated that a fullerene-rich interface at the cathode is a prerequisite to enhance contact selectivity and consequently power conversion efficiency.

KEYWORDS: organic solar cells · metal−organic interfaces · vertical segregation · surface coverage · contact selectivity

Research on materials and processing conditions in bulk heterojunction (BHJ) organic solar cells has led to impressive improvements over the past few years, with power conversion efficiencies (PCE) now reaching 10%.[1] In a BHJ cell, an interpenetrating matrix of donor and acceptor molecules harvests sun light and generates charges *via* photoinduced charge transfer that finally are collected at selective electrodes.[2] Film morphology of the donor/acceptor blends plays a crucial role in the overall device performance and has been widely studied.[3] On the other hand, the interface between the organic active layer and the outer contact (including the surface morphology) also determines the final device efficiency. Extensive work has been carried out to develop and optimize materials which allow for efficient extraction of charge carriers and enhance both power conversion efficiency (PCE) and cell stability. In order to obtain efficient selective contacts, two key requirements must be fulfilled: low contact resistance between the cathode or anode and the organic layer,[4,5] and adequate matching of energy levels to enhance electron or hole selectivity.[6] Several materials are available to enhance the electron extraction selectivity at the cathode contact, including alkali metal compounds (Ca, LiF, *etc.*), metal oxides (TiO_x, ZnO, *etc.*), and low molecular weight organic materials.[7−9] Regarding the extraction of holes at the anode, the most commonly used materials are poly(3,4-ethylenedioxythiophene):poly(styrenesulfonate) (PEDOT:PSS)[10] and MoO_3.[11,12] These additional layers have been clearly proven as useful contact selectivity enhancers. However, when considering that the bulk heterojunction consists of a blend of electron donor and acceptor materials, the specific relative surface coverage at the electrode interfaces is likely to also have an impact on the carrier selectivity. It is recognized that the nanoscale-size blend structure attaching the contact is a much less explored terrain and therefore constitutes the main aim of this work.

* Address correspondence to
aguerrer@uji.es,
garciag@fca.uji.es.

Received for review March 25, 2013
and accepted April 23, 2013.

10.1021/nn4014593

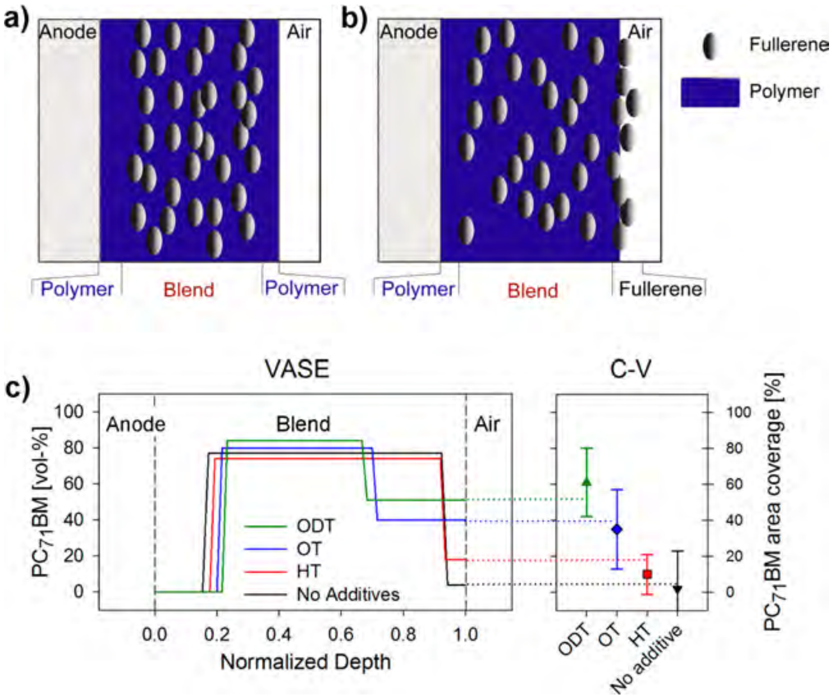

Figure 1. (a) Segregation based on three phases with the configuration polymer/blend/polymer. (b) Ideal phase segregation with the configuration polymer/blend/fullerene. (c) Comparison of phase segregation profile as inferred from VASE with fullerene surface concentration obtained by capacitance–voltage technique.

Currently, a wide range of physical techniques is available to provide information on the properties of the blends and interfaces.[6,13] Techniques such as grazing incidence X-ray diffraction (GIXRD), atomic force microscopy (AFM), or transmission electron microscopy (TEM) have been generally used to characterize the structure and length scales of the donor/acceptor domains. Additionally, information related to the depth profile concentration of organic blends has been obtained by means of grazing incidence X-ray diffraction,[14] neutron reflectivity,[15] near-edge X-ray absorption fine structure spectroscopy (NEXAFS),[16] dynamic secondary ion mass spectroscopy (SIMS),[17] variable-angle spectroscopic ellipsometry (VASE),[18] *etc.* Using this last technique, both vertical and lateral distribution of the individual components has been reported on blend films.

These techniques can be extremely useful to characterize the film morphology. They have, however, some practical limitations when a direct comparison between structure and device performance is desired to extract meaningful correlations on solar cell operation. On the one hand, some of them are destructive (cross-section SEM or SIMS), and on the other, accuracy is compromised when the metallic top contact is deposited (*e.g.*, VASE). In particular, attempts to obtain a direct relationship between vertical phase segregation and contact selectivity in operating cells have provided unexpected contradictory results. For example, using NEXAFS, a morphology comprising three different phases has been suggested for the P3HT:PC$_{61}$BM system,[19] in which a blended phase is sandwiched between two thin P3HT layers at both anode and cathode interfaces (see Figure 1a for a schematic representation). A P3HT upper layer adjacent to the cathode is expected to be detrimental to device performance due to the p-character of the polymer; however, the observed good performance has been justified by the diffusion of aluminum during deposition or the annealing step. Importantly, the specific processing conditions employed to fabricate the samples for a structural study may differ from those adapted for device fabrication, which results in different composition depth profiles, making comparisons unreliable. Therefore, a technique that could provide structural information at the contact/active layer interface on working cells would contribute to establish a direct relationship between vertical segregation (*e.g.*, donor/acceptor coverage at the interface) and device performance (*e.g.*, contact selectivity) and could potentially help to disentangle the respective contributions to the cell operation resulting from surface coverage by organic compounds and extracting/blocking interlayers.

Recently, we have used capacitance–voltage (*C*–*V*) measurements to understand the underlying mechanisms involved in the formation of dipoles at the active layer/cathode contact interface.[20] We have proposed a simple, albeit robust, model based on the role of the charge-neutrality level (CNL) located at a given position within the interfacial density of states (IDOS). CNL represents a key parameter accounting for the interface energy equilibration.[21−23] In this previous work, we noticed that $C-V$ measurements are very sensitive to all interfacial materials: donor, acceptor, metallic contact, and their relative concentration. Regarding the donor and acceptor molecules, the position of the HOMO and LUMO levels and the ratio of each of the components at the interface are determinant. It was observed that the only way to ensure efficient electric contact between the cathode metal and the active bulk layer is by the presence of chemically reduced fullerene molecules attached to the interface.[20]

The specific aim of this work is to correlate fullerene surface coverage and BHJ solar cell performance by evaluating cathode carrier selectivity. To this end, we use ellipsometry and a purely electrical technique ($C-V$) that, in combination, provide information regarding the relative donor/acceptor surface coverage at the active layer/cathode interface in operating devices. For this purpose, we have chosen the low band gap polymer poly[2,6-(4,4-bis-(2-ethylhexyl)-4*H*-cyclopenta[2,1-*b*;3,4-*b*′]dithiophene)-*alt*-4,7(2,1,3-benzothiadiazole)] (PCPDTBT) and the soluble fullerene (6,6)-phenyl C_{71} butyric acid methyl ester ($PC_{71}BM$), and fabricated films with processing additives, namely, hexanedithiol (HDT), octanethiol (OT), and octanedithiol (ODT). This allowed us to create a case study for investigating the vertical segregation. To get insight on the properties of the blend/anode system before cathode deposition, Kelvin probe and Kelvin probe force microscopy are employed. Then, we compare the $C-V$ results in completed cells and the vertical profiles deduced with a well-established technique as spectroscopic ellipsometry. The good agreement obtained between these techniques confirms the validity of $C-V$ for deducing surface coverage ratios. Moreover, we investigate the generality of the technique by testing another three donor/acceptor systems. The donors under study, poly(3-hexylthiophene) (P3HT), poly[[9-(1-octylnonyl)-9*H*-carbazole-2,7-diyl]-2,5-thiophenediyl-2,1,3-benzothiadiazole-4,7-diyl-2,5-thiophenediyl] (PCDTBT), and poly({4,8-bis[(2-ethylhexyl)-oxy]benzo[1,2-*b*:4,5-*b*′]dithiophene-2,6-diyl}{3-fluoro-2-[(2-ethylhexyl)carbonyl]thieno[3,4-*b*]thiophenediyl}) (PTB7), were used either with (6,6)-phenyl C_{61} butyric acid methyl ester ($PCB_{61}M$) or $PC_{71}BM$ to provide the following systems: P3HT:$PCB_{61}M$, PCDTBT:$PC_{71}BM$, and PTB7:$PC_{71}BM$. We finally found that solar cell parameters as leakage current, short-circuit current, and fill factor are highly determined by the degree of fullerene surface coverage at the cathode interface, which can be controlled by using proper processing additives.

RESULTS AND DISCUSSION

Vertical Segregation Measured by Variable-Angle Spectroscopic Ellipsometry. We start by characterizing the composition profile across the depth of films using ellipsometry. This highly sensitive and nondestructive spectroscopic technique has been successfully employed by us[14,18,24] and other groups[25,26] to characterize vertical segregation in bulk heterojunction blends. Here we will study thin blends (*ca.* 40 nm) of the system PCPDTBT:$PC_{71}BM$ prepared using different additives, as discussed in the Methods section. Before modeling the blends, we have determined the refractive index (n) and extinction coefficient (κ) of the specific materials that we have employed, deposited using the protocol described in the Methods section. For the substrate materials (ITO and PEDOT:PSS), the dielectric function was modeled using a Lorentz oscillator assembly coupled to a Drude tail at low frequencies. For PCPDTBT and $PC_{71}BM$, we employed the standard critical point model[27] of n and κ. These data are shown in Supporting Information (Figure SI2). Importantly, the absorption bands of the polymer do not change significantly upon blending (Figure SI1). This implies that the reference n and κ of neat materials can be used to characterize the blends by means of effective medium approximations (Bruggeman). In accordance with the previous comments, AFM images in Figure SI5 evidence the small degree of phase separation at the surface of the analyzed layers.

We have used a range of models to fit the ellipsometric experimental data for the blend films on ITO/PEDOT:PSS substrates. Reassuringly, the deduced profiles are consistent with the different models (see Figure SI3). This consists of a fullerene-rich sublayer in the middle of the film depth, sandwiched between two polymer-rich layers at the substrate and air interfaces, as schematically illustrated in Figure 1a,b. Incorporating additives in the blend solution quantitatively modifies the profile, while keeping the general trend the same. Interestingly, the deduced $PC_{71}BM$ coverage at the surface and the depth of the surface sublayer increases when going from the sample processed without additives to those with additives. The volume concentration of $PC_{71}BM$ at the surface is highest for ODT, then for OT, then HT, and finally for the samples processed without additives (Figure 1c). The full profile suggests that the fullerene molecules enriching the surface result from the depletion of $PC_{71}BM$ from the substrate side of the film, which becomes PCPDTBT richer. These results will be compared to $C-V$ measurements in the following sections.

Surface Potential of Anode/Active Layer Films. VASE strongly indicates a dependence of acceptor/donor relative surface coverage on the specific additives used in the processing of the films. We now investigate by Kelvin probe (KP) measurements the surface potential of the anode/active layer film system before the top cathode deposition. KP technique nullifies the surface potential difference between two surfaces brought in close proximity (flat-band conditions), which in the case of two metals corresponds to the difference of their respective work functions. In a complex system

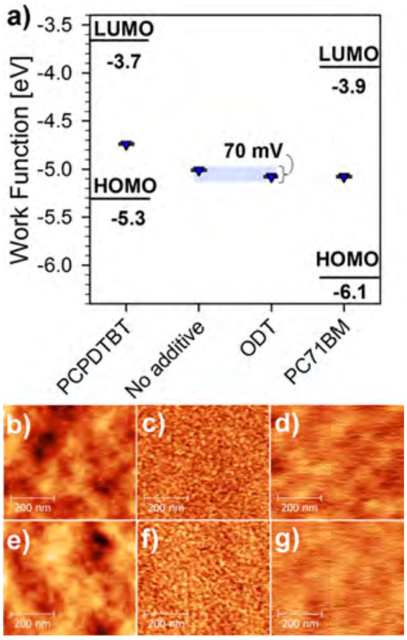

Figure 2. (a) Work function values of the ITO/PEDOT:PSS/organic films measured by KP. Topography (b,e), frequency shift (c,f), and surface potential (d,g) for the ITO/PEDOT:PSS/PCPDTBT:PCBM blends without ODT (top) and with ODT additive (bottom).

such as a polymer:fullerene film deposited on a metal electrode, the measured surface potential represents an effective, average work function. This contains information of the interfacial dipoles or band bending that may originate from the respective energy alignment of both materials and the anode. It should be noted that other factors such as trap charges at the surface of the organic[28,29] or variations in crystallinity and orientation of the polymer may be reflected in the observed surface potential, making the interpretation not always straightforward.

KP measurements were first performed with a 2 mm wide tip, which is representative for devices as it provides a relatively large area. Measurements were carried out in the dark and in nitrogen atmosphere by using a configuration ITO/PEDOT:PSS/organic layer. Work function (WF) values were calculated by calibrating the tip with a gold sample. Figure 2a shows WF values of pure films of PCPDTBT and $PC_{71}BM$ and blends processed with and without ODT additive. Low values are found for the sample containing the pure polymer (-4.7 eV) and high values for the pure fullerene (-5.1 eV). As observed in Figure 2a, WF encountered for fullerene film lies at mid-gap values. This informs on the negligible doping level of acceptor molecules as expected for chemically stable fullerenes. However, polymer films exhibit p-doping character to some extent as inferred from the WF position approaching the donor HOMO level. On the other hand, intermediate values are obtained for blends processed with and without additives, and these only differ by ~70 mV. This downward shift with respect to the polymer WF can be understood as a double effect of $PC_{71}BM$ molecules by increasing the polymer doping and averaging the blend WF. This result is a clear indication that the organic/anode interface is not largely affected by the introduction of additives and processing conditions.

Additionally, in order to understand whether we are able to observe different results at the nanoscale, Kelvin probe force microscopy (KPFM) has been employed to map the WF of the films with larger spatial resolution. Figure 2 shows topography (b and e), resonance frequency shift (c and f), and contact potential maps (d and g) for blends without (top) and with ODT (bottom). Whereas topography images are dominated by surface roughness, the frequency shift is more sensitive to the nanostructure of the organic films. Interestingly, the images show a remarkable resemblance between the morphology and the contact potential maps in the two types of samples with rms roughness values (as deduced from $10 \times 10\,\mu m^2$ areas, not shown) being 0.55 and 0.46 nm, respectively. This seeming lack of differences in the surface morphology and contact potential maps is also apparent when looking at other superficial traits, such as adhesion (see Supporting Information), and evidences a fine nanoscale intermixing of the two components constituting this system.[30] The averaged WF obtained from surface potential images is very similar regardless of the use of ODT (Supporting Information). Regarding the calculated WF values, these are very similar to those obtained by KP, and the small differences may be ascribed to the fact that films were exposed to air before the KPFM measurements.

Overall, the similarity of surface potential for both blends measured by KP and KPFM is a strong indication that the organic/anode interface is not largely affected by additive processing with regard to its electronic properties. This agrees well with the results from VASE that show a polymer-rich layer at the anode interface. Although the observed trends by VASE concerning fullerene coverage on the top active layer/air surface are qualitatively reproduced by Kelvin probe analyses, the surface voltage variation amounts to only ~70 mV for the two blends studied. As explained below, large differences are found regarding the additive effect on solar cell performance. This observation points to the fact that electronic equilibration after cathode interface formation, and the consequent dipole contribution, is a key mechanism to understand the photovoltaic performance. This issue is addressed by measuring $C-V$ characteristics.

Fullerene Surface Coverage Quantified by Capacitance–Voltage Measurements. VASE strongly indicates both a vertical segregation of components and its dependence on the processing with additives. These characterizations have been carried out on films in the absence of the metallic cathode. Although samples containing ultrathin semitransparent electrodes could be explored using VASE,[18] a more reliable comparison between surface coverage and device performance would be obtained if complete and operational devices are tested. In particular, correlation between interfacial composition and contact selectivity could be of great importance to understand the role that vertical segregation plays in device performance.

We have recently reported an extensive investigation on the cathode energy equilibration of organic bulk heterojunction solar cells using the information extracted from an exclusively electrical technique as *C*−*V* analysis.[20] Our aim here is to investigate whether *C*−*V* measurement can be confronted with the previous experiments in order to evaluate mechanisms governing the interface energy level alignment. We showed that the applied potential required to balance the mismatch between the cathode metal and the organic layer Fermi levels is divided into two contributions: a spatially extended band bending in the organic bulk, and a voltage drop at the interface dipole layer which is caused by a net charge transfer between the cathode metal and the organic blend.[20]

Figure 3a represents schematically the situation before the contact between the active layer and the metal cathode is made. The relevant energy levels of the separated parts are shown. On the active layer side, it is known that unintended oxidation of the donor polymer occurs during processing by the presence of oxygen or humidity as previously shown for P3HT:PC$_{60}$BM.[31] This confers p-doped character to the polymer, yielding as a result a background concentration of mobile holes. The position of the Fermi level is then shifted down closer to the HOMO level of the donor molecules compared to that observed for undoped blends. The polymer doping is corroborated here by the measured WF position as explained previously when KP results were shown. Once the active layer is in contact with the cathode, the energy equilibration entails the Fermi level alignment with a concomitant vacuum level offset that is divided into two contributions: (a) band bending inside the active layer which makes up a depletion zone in the vicinity of the cathode, and (b) an interface dipole layer which accommodates part of the vacuum level offset (Figure 3b).[32] The dipole layer appears as a consequence of a negative charge that is injected on the organic side reducing adjacent fullerene molecules. This negative charge is compensated by a positive charged layer at the metal contact. A simple model that integrates both voltage drops into a unified description of the contact equilibration was recently proposed.[20] An expression for the cathode equilibration can be written as follows

$$qV_{\mathrm{fb}} = E_{\mathrm{F}} - \phi_{\mathrm{c}} - \Delta \qquad (1)$$

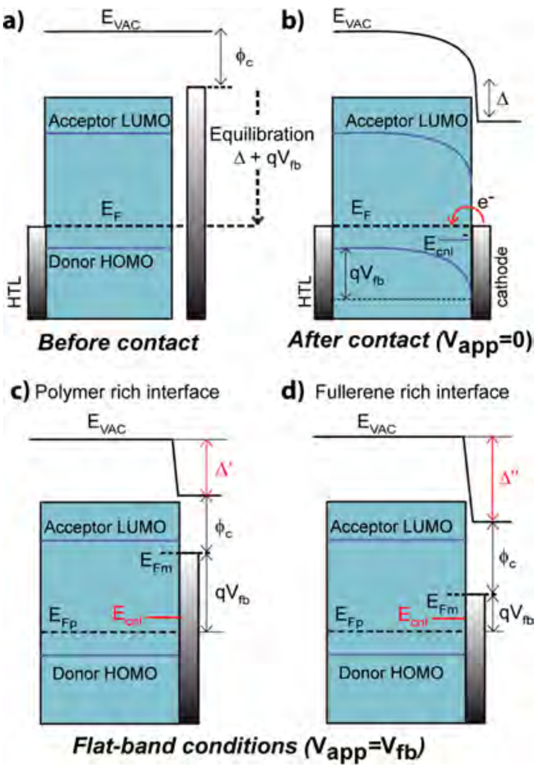

Figure 3. Energy level diagrams representing the cathode equilibration of a bulk heterojunction solar cell (a) before contact equilibration, (b) after contact deposition, (c,d) effect of CNL on dipole generation induced by donor/acceptor concentration at the active layer/cathode interface. E_{Fm} corresponds to the metal Femi level, E_{F} is the equilibrium Fermi level of the active layer, E_{cnl} is the CNL energy position. It is assumed that out of equilibrium $E_{\mathrm{Fp}} \approx E_{\mathrm{F}}$. Other energy differences correspond to that explained in eq 1.

where qV_{fb} is the voltage required to overcome the active layer band bending that leads to flat-band condition, E_{F} is the Fermi level of the active layer (interpreted in terms of the bulk work function), ϕ_{c} is the metal Fermi level, and Δ is an interfacial dipole generated between active layer and cathode contact.

A key parameter accounting for the interface equilibration is the charge-neutrality level (CNL), which is defined as the energy level that results in a surface without net charge.[21−23] When the chemical interaction between the metal and contacting conjugated molecules or polymers is not negligible, it is expected that molecules attached to the metal surface undergo both a shift and a broadening of their molecular energy levels. Energy distribution of the attached molecules should be modeled by a specific interfacial density of states (IDOS) which differs from that encountered in the bulk of the organic layer. CNL is located at a given position within the IDOS appearing because of the highly disordered energy landscape. We observed that the strength of the flat-band potential depends on the polymer-to-fullerene ratio at the surface.[20]

C−*V* response is shown in Figure 4a for devices prepared with pure polymer PCPDTBT, a fullerene-rich blend (polymer:fullerene ratio of 1:6), and two selected

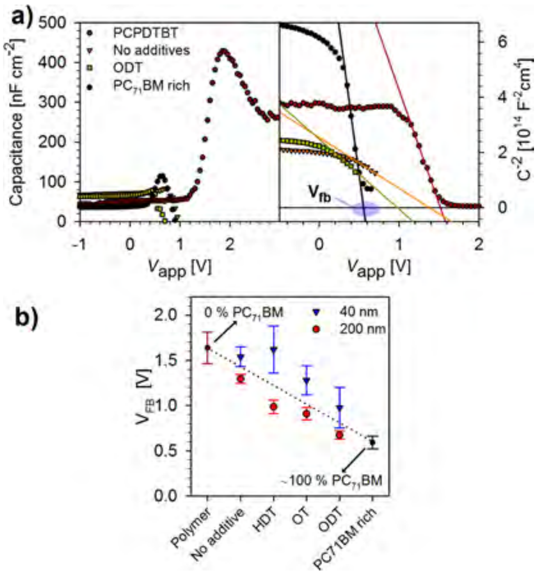

Figure 4. (a) Capacitance−voltage response (left) and Mott−Schottky analysis (right) of a selection of representative devices processed under different conditions. Data values influenced by the decrease in capacitance have been removed in the MS plot for clarity. The V_{fb} is graphically estimated from the intercept with the *x*-axis. (b) V_{fb} results extracted from *C*−*V* measurements in the dark for devices processed under different conditions. Two sets of devices with different active layer thickness are included that show that the method is valid for different active layer thicknesses.

devices fabricated from blends (1:2 ratio) without additive and with ODT. In the series of films under study, the capacitance response at intermediate frequencies (100 Hz to 1 kHz) shows the expected plateau in reverse and low forward voltage consequence of full depletion conditions. At a certain forward voltage, the capacitance starts to increase as a consequence of the depletion width reduction. For this voltage range, the Mott−Schottky (MS) analysis can be carried out (Figure 4a, right graph).[31] In the $C^{-2}(V)$ plot, V_{fb} corresponds to the intercept with the voltage axis. High V_{fb} values are obtained for the device fabricated with PCPDTBT polymer only. This is due to the fact that the dipole contribution plays a secondary role, with the work function mismatch between the polymer and metal mainly accommodated by the bulk band bending (Figure 3c). On the other hand, high concentrations of fullerenes in the blend (polymer:fullerene ratio of 1:6) lead to stronger dipoles because of the larger charge associated with fullerene reduction reaction (charge transfer from the metal). The overall net effect is the practical alignment of the metal Fermi level (E_{Fm}) and CNL position (Figure 3d). In such an interface, flat-band voltage is reached at much lower values. Implicitly, the model assumes that no band bending is taking place during equilibration at the anode due to a correct energy level alignment of the polymer HOMO level with the PEDOT:PSS. Note that values of ϕ_{org} for blends with/without ODT measured by KP only differ about 70 mV, in strong contrast with the difference above 0.7 V in V_{fb} values obtained from *C*−*V* analysis (Figure 4b). Importantly, we found differences of more than 1 V in V_{fb} among the set of analyzed devices. There is a significant variation in the dipole layer strength depending on the additive and processing conditions. We highlight here that this last observation is in agreement with results obtained by VASE.

Figure 4b shows values of V_{fb} for a whole series of devices fabricated using different additive conditions. V_{fb} of a device fabricated from a blend with no additive is slightly lower than that encountered with only polymer films. When ODT is used, the value approaches that of the fullerene-rich device. Large dispersion of results averaging over five devices is observed for thin films (40 nm) possibly due to the large impact of metal diffusion for this device thickness. It is important to note that the cathode of these devices was fabricated at slow evaporation rates (0.2−0.8 Å/s). Cells based on thicker films are considerably less sensitive to diffusion of the cathode metal, and results show a standard deviation of about 5%. Not surprisingly, V_{fb} values for the thick cells differ from those obtained for the thin cells as a result of the expected different phase segregation and band bending profile.

Because of the high sensitivity of V_{fb} on blend structure and additives used, we adopt it as a measurement of the fullerene coverage of the contact surface. We can take V_{fb} of pure PCPDTBT and fullerene-rich devices to account for the extreme cases of full active layer/cathode coverage by polymer and fullerene, respectively. If it is assumed that a linear relationship between V_{fb} values and surface coverage occurs, the V_{fb} results of devices fabricated with additives can be employed to estimate the relative surface coverage percentage. Figure 1 shows that the fullerene surface coverage percentage for the series correlates well with results obtained by VASE. This good agreement clearly indicates that *C*−*V* measurement is a useful tool to detect the degree to which fullerene or polymer is present at the active layer/cathode interface in complete devices. It is important to remark here that some discrepancies between metal-free samples and completed cells can be expected, as metal diffusion and surface morphology modification during evaporation are expected to occur. In addition, Figure 4b clearly shows that V_{fb} values obtained for the 200 nm active layer thickness devices are lower than values obtained for the thin device analogues. Then, following the same analysis, the fullerene active layer/cathode surface coverage is slightly higher for the devices with a thick active layer. Therefore, optimized devices which are typically fabricated with an active layer of 80−100 nm should show intermediate fullerene coverage to those presented in this work. In any case, the same trend is encountered regardless of the film thickness. Moreover, as we will discuss in the last section, the degree to

TABLE 1. Device Performance Parameters of Polymer:Fullerene Solar Cells Fabricated under Different Processing Conditions

donor:acceptor	J_{sc} (mA cm^{-2})	V_{oc} (V)	FF (%)	PCE (%)	fullerene cathode coverage (%)	R_{sh} (Ω cm^2)	J_{dark} (−1 V) (10^{-5} A cm^{-2})	conditions
PCPDTBT:PC$_{71}$BM	4.87	0.475	29	0.67	2	324	367.0	as-cast
	6.68	0.605	34	1.37	9	541	248.3	HT
	6.84	0.635	39	1.69	35	621	222.3	OT
	7.69	0.660	47	2.38	60	1802	57.7	ODT
P3HT: PC$_{61}$BM	2.46	0.582	33	0.48	60	89	11.4	as-cast
	8.10	0.618	66	3.31	90	8800	3.4	annealed 130 °C
PCDTBT:PC$_{71}$BM	4.72	0.861	33	1.36	28	13900	15.0	as-cast
	5.90	0.904	35	1.89	65	146200	0.1	annealed 130 °C
PTB7:PC$_{71}$BM	10.2	0.722	42	3.09	35	23000	6.3	no additive
	10.8	0.782	64	5.40	81	644000	0.3	diiodoctane

which the cathode is covered by polymer plays a significant role in the device performance parameters due to variation in contact selectivity.

In order to study whether *C*−*V* analysis can be used in general to measure the fullerene/polymer concentration at the active layer cathode interface, we carried out a similar analysis for a range of different donor:acceptor systems. In particular, we focus on the donors polythiophene P3HT:PC$_{61}$BM,[33] polycarbazole PCDTBT:PC$_{71}$BM,[34−36] and high efficiency PTB7:PC$_{71}$BM.[37] Besides resulting in higher power conversion efficiencies, these materials vary in their tendencies to self-align (from highly crystallizable to almost glassy), as well as in the protocols that have been identified in order to control their morphology (thermal annealing and additives), and thus in combination with PCPDTBT:PC$_{71}$BM provide a good span of material properties and processing schemes to generalize our findings. A complete analysis is provided as Supporting Information, indicating that that *C*−*V* technique is also sensitive to surface coverage for these systems (Figure SI6), and analogous analysis can be carried out.

Correlation between Surface Coverage and Device Performance. In order to design bulk heterojunction solar cells with optimum efficiencies, apart from a perfect control of film morphology, engineering of interfacial layers is of vital importance. This is so because strongly selective electrodes will minimize leakage current, which is an indication of undesired hole movement crossing the cathode contact. Although detailed discussion on the relation of phase segregation with the overall cell performance is complex, we will discuss in detail our results for the case study PCPDTBT:PC$_{71}$BM system, and general conclusions are partially extrapolated for other blend combinations, such as those shown in the Supporting Information.

AFM analysis previously discussed shows a lack of surface morphology differences between samples processed with additives from those not using additive. This is in contrast to the case of the P3HT:PC$_{61}$BM system, for which micrometer-scale PC$_{61}$BM aggregates appear protruding from the surface upon annealing.[18] The apparent lack of information regarding different surface coverage resulting from SPM data, readily accessible using VASE and *C*−*V*, is likely due to the nanoscale intermixing of the two components constituting this blend[30] and warns that vertical segregation in highly mixed blends cannot be accessed using surface microscopy. Additionally, it is important to note that the morphological information extracted in our measurements differs from those results previously reported by Peet *et al.*[30] In their AFM measurements, these authors were able to observe an enhanced degree of phase separation in the blend induced by the high boiling point of the ODT additive and the preferential solubility of the fullerene in the additive compared to the polymer. Therefore, it appears that under our processing conditions in which we obtain extremely thin active layers (*i.e.*, 40 nm) the scenario regarding film morphology is rather different. Here, no large differences in phase separation between samples treated with additives with those untreated are observed, and absorption suggests a similar degree of crystallinity. This observation reinforces the hypothesis that the interface is playing a determining role and explains difference in device performance.

Performance parameters of devices are shown in Table 1. The use of the additives with different boiling points in the case of PCPDTBT:PC$_{71}$BM clearly impacts the final device performance. All device performance parameters (power conversion efficiency, open-circuit voltage V_{oc}, short-circuit current J_{sc}, and FF) are found to be maximum when ODT is used, and these gradually decrease for devices fabricated without additives (see Table 1 and Figure 5a). Diode response of the same devices in the dark (Figure 5b) clearly shows a trend in the measured current at −1 V (leakage current): high currents for devices containing a low proportion of fullerene at the cathode and low leakage currents for the best performing device. The same results are found for the calculated shunt resistances, R_{sh}, that are about 1 order of magnitude higher for the device that contain a high proportion of fullerene at the contact. Injection of holes from the cathode contact at reverse bias originates with low shunt resistances. Both facts are a clear manifestation of

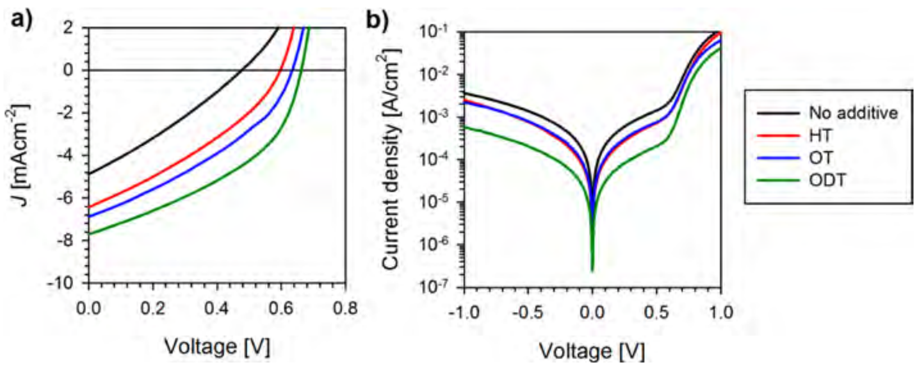

Figure 5. (a) $J-V$ response of BHJ solar cells fabricated with the system PCPDTBT:PC$_{71}$BM using different additives during processing: no additives, hexanethiol (HT), octanethiol (OT), octanedithiol (ODT). (b) Diode response of devices shown in (a) under dark conditions that shows different leakage current at negative bias.

enhanced selectivity of the contact when a high proportion of fullerene is present at the cathode.

Moreover, when the solar cell functions in the power-generating quadrant (forward voltage under illumination), the polymer-rich surface in the vicinity of the cathode offers an additional resistance to the collection of electrons. Accordingly, the total series resistance of the device increases because of the presence of the polymer layer, strongly affecting both FF and achieved photocurrent. Indeed, this is the case as both parameters, FF and J_{sc}, are nearly halved when no ODT is used. As listed in Table 1, a general correlation exists between flat-band voltage, fullerene cathode contact coverage, leakage current, and cell performance for cells comprising PCPDTBT:PC$_{71}$BM as an active layer. We highlight here that such correlation is also observed for P3HT, PCDTBT, and PTB7-based cells blended with either PC$_{61}$BM or PC$_{71}$BM (see Table 1). For P3HT and PCDTBT the annealing process increases the surface fullerene coverage (as deduced from $C-V$ analysis), in good agreement with the enhancement in J_{sc}. In the case of PTB7 the use of additive also increases the amount of fullerene at the cathode, in this case increasing more notably FF through larger shunt resistance.

CONCLUSION

We have demonstrated that a nanoscale-size fullerene-rich layer attaching the interface at cathode contacts induces higher electron selectivity, finally enhancing the device performance. It is shown how capacitance–voltage measurement is a sensitive technique to evaluate the relative donor/acceptor coverage at the blend/cathode interface. $C-V$ results are in good agreement with coverage values deduced from variable-angle spectroscopic ellipsometry. We have verified the validity of the technique with a variety of blends acting as active layers (PCPDTBT:PC$_{71}$BM, P3HT:PC$_{61}$BM, PCDTBT:PC$_{71}$BM, and PTB7:PC$_{71}$BM). System-tailored thermal annealing and the use of proper additives are able to yield favorable vertical segregation profiles so as to induce fullerene-rich interfaces at the cathode.

METHODS

Materials. PCPDTBT (1-Material), P3HT (Luminescece Tech.), PCDTBT (1-Material), PTB7 (1-Material), PC$_{61}$BM (Nano-C, 99%), PC$_{71}$BM (Nano-C, 99%), hexanethiol (Alfa Aesar, 98%), octanethiol (Alfa Aesar, 98%), octanedithiol (Alfa Aesar, 98%), diiodooctane (Alfa Aesar, 98%, copper stabilized), PEDOT:PSS (CLEVIOS P AI 4083), chlorobenzene (Aldrich, 99.9%), *o*-dichlorobenzene (Aldrich, 99.9%), Ca (Aldrich, 99.995%), and silver (Aldrich, 99.99%) were used as received without further purification. All manipulations were carried out in a glovebox under a nitrogen atmosphere unless otherwise stated. PCPDTBT:PC$_{71}$BM solutions (1:2 ratio) were prepared in *o*-dichlorobenzene (17 mg/mL) and were stirred at 60 °C overnight before spin coating. Stock solutions of additives were prepared and were stirred for 30 min before addition to the solution containing PCPDTBT:PC$_{71}$BM. The solution that did not contain additives was diluted with additional *o*-dichlorobenzene to obtain the same final concentration. Once the additive and donor:acceptor solutions were mixed, the mixtures were further stirred for 30 min at room temperature prior to device fabrication.

Preparation of a Vertically Segregated Case Study. The donor:acceptor system consisting of the low band gap donor polymer PCPDTBT and PC$_{71}$BM has previously been shown to provide differential phase segregation depending on the processing conditions.[38] In particular, the use of the additive octanedithiol in different wt % could totally modify the phase segregation as measured by VASE and GIXRD. In our study, we use the same donor:acceptor materials with a series of thiols with different alkyl chain lengths and/or number of thiol groups. Chlorobenzene solutions containing the following additives are used: hexanedithiol (HDT), octanethiol (OT), and octanedithiol (ODT). Films of small active layer thicknesses (40 nm) were fabricated in the configuration substrate/active layer with or without additives in order to measure profile concentration by VASE. The tested substrates were glass, glass/PEDOT:PSS, and glass/ITO/PEDOT:PSS, and similar trends were observed. The reported values here correspond to the latter. Reference films composed of pure PC$_{71}$BM and pure PCPDTBT were also casted and measured. Additionally, selected active layer films were used in the configuration ITO/PEDOT:PSS/active layer for analysis using Kelvin probe measurements. In the main text, the information obtained from these two techniques is compared with that obtained from a set of devices (ITO/PEDOT:PSS/active layer/Ca/Ag) of the same active layer thickness. A second series of devices with 200 nm active layer thickness was also fabricated in order to test the validity of $C-V$ measurements under a different set of conditions. Due to the high molecular weight of PCPDTBT used in this work ($\sim M_w$ = 100 kDa), films were most homogeneous when the solution was added in the prerotating spin coater. This modification in the processing conditions by itself helps to explain the observed differences with previously reported donor:acceptor profiles for this system. Almost overlapping absorption spectra of neat polymer and blends with and without additives suggest that the degrees of crystallinity of the polymer phase in the different samples do not differ greatly (see Supporting Information, Figure SI1).

Solar Cell Fabrication. Devices with different donor/acceptor systems were also fabricated to test the general validity of the measurement and correlate donor/acceptor surface coverage with performance properties (see Supporting Information for details on preparation). In addition to PCPDTBT:$PC_{71}BM$-based solar cells, fabricated devices were based on P3HT:PCBM, PCDTBT:$PC_{71}BM$, and PTB7:$PC_{71}BM$ active layers. Polymer solar cells were fabricated with a standard sandwich structure of ITO/PEDOT:PSS/donor:acceptor/Ca/Ag and 9 mm^2 active area. PEDOT:PSS was spin coated in air at 5500 rpm for 30 s onto an ITO-coated glass substrate (10 Ω/sq), resulting in a film thickness of ∼35 nm. The substrates were heated at 120 °C for 10 min to remove traces of water and were transferred to a glovebox equipped with a thermal evaporator. PCPDTBT:$PC_{70}BM$ layer was added onto the prerotating substrate at speeds of 1200 rpm for 30 s at which stage the films are visually dried. However, traces of additives are expected to be completely removed during the subsequent processing steps. Sequential evaporation of calcium (5 nm) followed by a silver layer (100 nm) was carried out at a base pressure of 3×10^{-6} mbar. Full devices, including top Ca/Ag electrodes, were then encapsulated with epoxy and a glass slide before testing. Samples were characterized outside the glovebox.

Film and Device Characterization. Variable-angle spectroscopic ellipsometry (VASE) and photometry data were acquired at five angles between 55 and 75° using a Sopra GES-5E rotating polarizer spectroscopic ellipsometer (SEMILAB). The VASE data were modeled using the WinElli II piece of software. The standard critical point model was employed accounting for the dielectric function of the pure materials. Several models were then tested in order to deduce the composition vertical profile of the blend films. These include continuous linear and parabolic profiles, as well as bilayer and trilayer effective structures. Overall, the trends observed for the different models in terms of the use of additives and surface coverage are consistent. The trilayer model, however, was found to lead to the smallest fitting standard deviations, while providing good convergence of the fitting procedure and unique solutions for the deduced profiles when varying the initial conditions/parameters.

Kelvin probe measurements were carried out with a KP010 system placed inside a glovebox from KP Technology equipped with a 2 mm wide tip. Films were fabricated in the glovebox and were measured without their exposure to air. Reference films for $PC_{71}BM$ and PCPDTBT were also fabricated for comparison. Kelvin probe force microscopy (KPFM) measurements were performed with a scanning force microscope (Nanotec) equipped with KPM capabilities. Freely available WSxM software was used for image acquisition and processing.[39] Images were acquired working in noncontact dynamic mode using the oscillation amplitude as the feedback parameter. Platinum-coated silicon tips (Budget Sensors), with nominal force constant of 3 N/m and resonance frequency of 75 kHz, were used. Frequency modulation KPFM with an AC modulation bias of 500 mV at 7 kHz was used to measure the local contact potential. All measurements were performed under a nitrogen atmosphere; however, samples exposed to air between films were casted and measured. To be sure that the measurements were not affected by the proximity of the tip, the two trace method was used. During the first trace of a scan line, the Kelvin probe measurement was performed simultaneously with the topography scan. For the second pass, the Kelvin probe measurement was performed by lifting up the tip 10−20 nm (following the topographic profile measured during the first pass). As the reference sample for absolute values of work function, we used HOPG (work function of 4.7 eV) measured between successive samples.

Current density−voltage characteristics were carried out under illumination with a 1.5 G source (1000 W m^{-2}) using an Abet Sun 2000 solar simulator. The light intensity was adjusted with a calibrated Si solar cell. Capacitance was recorded by applying a small voltage perturbation (20 mV rms) at 1000 Hz. Measurements were carried out in the dark at several bias voltages to extract the capacitance−voltage characteristics. These measurements were performed with Autolab PGSTAT-30 equipped with a frequency analyzer module.

Conflict of Interest: The authors declare no competing financial interest.

Acknowledgment. We thank financial support by Ministerio de Educacion y Ciencia (Spain) under Project HOPE CSD2007-00007 (Consolider-Ingenio 2010), MAT2009-10642, MAT2010-20020, and PLE2009-0086, and Generalitat Valenciana (Prometeo/2009/058 and ISIC/2012/008 Institute of Nanotechnologies for Clean Energies).

Supporting Information Available: Absorption, details on VASE and KPFM analyses, AFM images, surface coverage deduced from $C-V$ analysis for other polymer:fullerene blends, and details of preparation conditions. This material is available free of charge *via* the Internet at http://pubs.acs.org.

REFERENCES AND NOTES

1. Green, M. A.; Emery, K.; Hishikawa, Y.; Warta, W.; Dunlop, E. D. Solar Cell Efficiency Tables (Version 39). *Prog. Photovoltaics* **2012**, *20*, 12–20.
2. Yu, G.; Gao, J.; Hummelen, J. C.; Wudl, F.; Heeger, A. J. Polymer Photovoltaic Cells—Enhanced Efficiencies *via* a Network of Internal Donor−Acceptor Heterojunctions. *Science* **1995**, *270*, 1789–1791>.
3. Dennler, G.; Scharber, M. C.; Brabec, C. J. Polymer-Fullerene Bulk-Heterojunction Solar Cells. *Adv. Mater.* **2009**, *21*, 1323–1338.
4. Servaites, J. D.; Ratner, M. A.; Marks, T. J. Organic Solar Cells: A New Look at Traditional Models. *Energy Environ. Sci.* **2011**, *4*, 4410–4422.
5. Servaites, J. D.; Yeganeh, S.; Marks, T. J.; Ratner, M. A. Efficiency Enhancement in Organic Photovoltaic Cells: Consequences of Optimizing Series Resistance. *Adv. Funct. Mater.* **2010**, *20*, 97–104.
6. Zhou, Y.; Fuentes-Hernandez, C.; Shim, J.; Meyer, J.; Giordano, A. J.; Li, H.; Winget, P.; Papadopoulos, T.; Cheun, H.; Kim, J.; *et al.* A Universal Method To Produce Low-Work Function Electrodes for Organic Electronics. *Science* **2012**, *336*, 327–332.
7. Steim, R.; Koglera, F. R.; Brabec, C. J. Interface Materials for Organic Solar Cells. *J. Mater. Chem.* **2010**, *20*, 2499–2512.
8. Ratcliff, E. L.; Zacher, B.; Armstrong, N. R. Selective Interlayers and Contacts in Organic Photovoltaic Cells. *J. Phys. Chem. Lett.* **2011**, *2*, 1337–1350.
9. Po, R.; Carbonera, C.; Bernardia, A.; Camaioni, N. The Role of Buffer Layers in Polymer Solar Cells. *Energy Environ. Sci.* **2011**, *4*, 285–310.
10. Mishra, A.; Bäuerle, P. Small Molecule Organic Semiconductors on the Move: Promises for Future Solar Energy Technology. *Angew. Chem., Int. Ed.* **2012**, *51*, 2020–2067.
11. Sun, Y.; Takacs, C. J.; Cowan, S. R.; Seo, J. H.; Gong, X.; Roy, A.; Heeger, A. J. Efficient, Air-Stable Bulk Heterojunction Polymer Solar Cells Using MoOx as the Anode Interfacial Layer. *Adv. Mater.* **2011**, *23*, 2226–2230.
12. Tseng, Y.-C.; Mane, A. U.; Elam, J. W.; Darling, S. B. Ultrathin Molybdenum Oxide Anode Buffer Layer for Organic Photovoltaic Cells Formed Using Atomic Layer Deposition. *Sol. Energy Mater. Sol. Cells* **2011**, *99*, 235–239.
13. Chen, W.; Nikiforov, M. P.; Darling, S. B. Morphology Characterization in Organic and Hybrid Solar Cells. *Energy Environ. Sci.* **2012**, *5*, 8045–8074.
14. Agostinelli, T.; Lilliu, S.; Labram, J. G.; Campoy-Quiles, M.; Hampton, M.; Pires, E.; Rawle, J.; Bikondoa, O.; Bradley,

D. D. C.; Anthopoulos, T. D.; *et al.* Real-Time Investigation of Crystallization and Phase-Segregation Dynamics in P3HT: PCBM Solar Cells during Thermal Annealing. *Adv. Funct. Mater.* **2011**, *21*, 1701–1708.

15. Chen, D.; Nakahara, A.; Wei, D.; Nordlund, D.; Russell, T. P. P3HT/PCBM Bulk Heterojunction Organic Photovoltaics: Correlating Efficiency and Morphology. *Nano Lett.* **2011**, *11*, 561–567.
16. Zhu, S.; Liu, Y.; Rafailovich, M. H.; Sokolov, J.; Gersappe, D.; Winesett, D. A.; Ade, H. Confinement-Induced Miscibility in Polymer Blends. *Nature* **1999**, *400*, 49–51.
17. Björström, C. M.; Nilsson, S.; Bernasik, A.; Budkowski, A.; Andersson, M.; Magnusson, K. O.; Moons, E. Vertical Phase Separation in Spin-Coated Films of a Low Bandgap Polyfluorene/PCBM Blend—Effects of Specific Substrate Interaction. *Appl. Surf. Sci.* **2007**, *253*, 3906–3912.
18. Campoy-Quiles, M.; Ferenczi, T.; Agostinelli, T.; Etchegoin, P. G.; Kim, Y.; Anthopoulos, T. D.; Stavrinou, P. N.; Bradley, D. D. C.; Nelson, J. Morphology Evolution *via* Self-Organization and Lateral and Vertical Diffusion in Polymer: Fullerene Solar Cell Blends. *Nat. Mater.* **2008**, *7*, 158–164.
19. Xue, B.; Vaughan, B.; Poh, C.-H.; Burke, K. B.; Thomsen, L.; Stapleton, A.; Zhou, X.; Bryant, G. W.; Belcher, W.; Dastoor, P. C. Vertical Stratification and Interfacial Structure in P3HT:PCBM Organic Solar Cells. *J. Phys. Chem. C* **2010**, *114*, 15797–15805.
20. Guerrero, A.; Marchesi, L. F.; Boix, P. P.; Ruiz-Raga, S.; Ripolles-Sanchis, T.; Garcia-Belmonte, G.; Bisquert, J. How the Charge-Neutrality Level of Interface States Controls Energy Level Alignment in Cathode Contacts of Organic Bulk-Heterojunction Solar Cells. *ACS Nano* **2012**, *6*, 3453–3460.
21. Bardeen, J. Surface States and Rectification at a Metal Semi-conductor Contact. *Phys. Rev.* **1947**, *71*, 717–727.
22. Vázquez, H.; Flores, F.; Oszwaldowski, R.; Ortega, J.; Pérez, R.; Kahn, A. Barrier Formation at Metal–Organic Interfaces: Dipole Formation and the Charge Neutrality Level. *Appl. Surf. Sci.* **2004**, *234*, 107–112.
23. Vázquez, H.; Gao, W.; Flores, F.; Kahn, A. Energy Level Alignment at Organic Heterojunctions: Role of the Charge Neutrality Level. *Phys. Rev. B* **2005**, *71*, 041306(R).
24. Burgués-Ceballos, I.; Campoy-Quiles, M.; Francesch, L.; Lacharmoise, P. D. Fast Annealing and Patterning of Polymer Solar Cells by Means of Vapor Printing. *J. Polym. Sci., Part B: Polym. Phys.* **2012**, *50*, 1245–1252.
25. Engmann, S.; Turkovic, V.; Denner, P.; Hoppe, H.; Gobsch, G. Optical Order of the Polymer Phase within Polymer/Fullerene Blend Films. *J. Polym. Sci., Part B: Polym. Phys.* **2012**, *50*, 1363–1373.
26. Germack, D. S.; Chan, C. K.; Kline, R. J.; Fischer, D. A.; Gundlach, D. J.; Toney, M. F.; Richter, L. J.; DeLongchamp, D. M. Interfacial Segregation in Polymer/Fullerene Blend Films for Photovoltaic Devices. *Macromolecules* **2010**, *43*, 3828–3836.
27. Campoy-Quiles, M.; Nelson, J.; Bradley, D. D. C.; Etchegoin, P. G. Dimensionality of Electronic Excitations in Organic Semiconductors: A Dielectric Function Approach. *Phys. Rev. B* **2007**, *76*, 235206.
28. Kalinin, S. V.; Bonnell, D. A. Local Potential and Polarization Screening on Ferroelectric Surfaces. *Phys. Rev. B* **2001**, *63*, 125411.
29. Cunningham, S.; Larkin, I. A.; Davis, J. H. Noncontact Scanning Probe Microscope Potentiometry of Surface Charge Patches: Origin and Interpretation of Time-Dependent Signals. *Appl. Phys. Lett.* **1998**, *73*, 123–125.
30. Peet, J.; Kim, J. Y.; Coates, N. E.; Ma, W. L.; Moses, D.; Heeger, A. J.; Bazan, G. C. Efficiency Enhancement in Low-Bandgap Polymer Solar Cells by Processing with Alkane Dithiols. *Nat. Mater.* **2007**, *6*, 497–500.
31. Boix, P. P.; Garcia-Belmonte, G.; Munecas, U.; Neophytou, M.; Waldauf, C.; Pacios, R. Determination of Gap Defect States in Organic Bulk Heterojunction Solar Cells from Capacitance Measurements. *Appl. Phys. Lett.* **2009**, *95*, 233302.
32. Bisquert, J.; Garcia-Belmonte, G. On Voltage, Photovoltage, and Photocurrent in Bulk Heterojunction Organic Solar Cells. *J. Phys. Chem. Lett.* **2011**, *2*, 1950–1964.
33. Ma, W.; Yang, C.; Gong, X.; Lee, K.; Heeger, A. J. Thermally Stable, Efficient Polymer Solar Cells with Nanoscale Control of the Interpenetrating Network Morphology. *Adv. Funct. Mater.* **2005**, *15*, 1617–1622.
34. Blouin, N.; Michaud, A.; Leclerc, M. A Low-Bandgap Poly-(2,7-carbazole) Derivative for Use in High-Performance Solar Cells. *Adv. Mater.* **2007**, *19*, 2295–2300.
35. Park, S. H.; Roy, A.; Beaupré, S.; Cho, S.; Coates, N.; Moon, J. S.; Moses, D.; Leclerc, M.; Lee, K.; Heeger, A. J. Bulk Heterojunction Solar Cells with Internal Quantum Efficiency Approaching 100%. *Nat. Photonics* **2009**, *3*, 297–302.
36. Alem, S.; Chu, T.-Y.; Tse, S. C.; Wakima, S.; Lu, J.; Movileanu, R.; Tao, Y.; Bélanger, F.; Désilets, D.; Beaupré, S.; *et al.* Effect of Mixed Solvents on PCDTBT:PC70BM Based Solar Cells. *Org. Electron.* **2011**, *12*, 1788–1793.
37. Liang, Y.; Xu, Z.; Xia, J.; Tsai, S.-T.; Wu, Y.; Li, G.; Ray, C.; Yu, L. For the Bright Future—Bulk Heterojunction Polymer Solar Cells with Power Conversion Efficiency of 7.4%. *Adv. Mater.* **2010**, *22*, E135–E138.
38. Agostinelli, T.; Ferenczi, T. A. M.; Pires, E.; Foster, S.; Maurano, A.; Müller, C.; Ballantyne, A.; Hampton, M.; Lilliu, S.; Campoy-Quiles, M.; *et al.* The Role of Alkane Dithiols in Controlling Polymer Crystallization in Small Band Gap Polymer:Fullerene Solar Cells. *J. Polym. Sci., Part B: Polym. Phys.* **2011**, *49*, 717–724.
39. Horcas, I.; Fernandez, R.; Gomez-Rodriguez, J. M.; Colchero, J.; Gomez-Herrero, J.; Baro, A. M. WSXM: A Software for Scanning Probe Microscopy and a Tool for Nanotechnology. *Rev. Sci. Instrum.* **2007**, *78*, 013705-8.

Solar Energy Materials & Solar Cells 117 (2013) 564–568

Contents lists available at ScienceDirect

Solar Energy Materials & Solar Cells

journal homepage: www.elsevier.com/locate/solmat

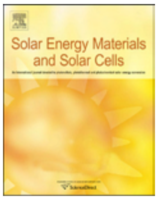

Electrodeposited NiO anode interlayers: Enhancement of the charge carrier selectivity in organic solar cells

Teresa Ripolles-Sanchis [a], Antonio Guerrero [a], Eneko Azaceta [b], Ramon Tena-Zaera [b,*], Germà Garcia-Belmonte [a,**]

[a] *Photovoltaic and Optoelectronic Devices Group, Departament de Física, Universitat Jaume I, ES-12071 Castelló, Spain*
[b] *Energy Division, IK4-CIDETEC, ES-20009 San Sebastian, Spain*

ARTICLE INFO

Article history:
Received 24 May 2013
Received in revised form
11 July 2013
Accepted 12 July 2013
Available online 17 August 2013

Keywords:
Organic photovoltaics
Nickel oxide
Hole transport layer
Charge carrier selectivity

ABSTRACT

Nickel oxide (NiO) thin films prepared by cathodic electrodeposition exhibit superior electrical performace than PEDOT:PSS when used as anode interlayers of bulk-heterojunction solar cells. Devices incorporating 30 nm-thick NiO films firstly annealed at 320 °C in air and posteriorly treated with UV-O_3 reach power conversion efficiencies comparable to that obtained for PEDOT:PSS-based cells. NiO interlayers enhance contact selectivity by simulataneously increasing shunt resistance (lower leakage current related to electron-blocking ability), and reducing hole-extraction resistance. Carrier selectivity is quantified from the resistance components associated with the impedance response of the anode contacts. The versatile electrodeposition technique of NiO interlayers permits avoiding PEDOT:PSS use as it presents disadvantages related to its acid character and hygroscopic nature.

1. Introduction

The increasing demand for renewable energy resources leads researchers to study different routes in solar energy production. Nowadays, organic bulk heterojunction (BHJ) solar cells are deeply investigated due to their potential to reduce fabrication costs. This is so because mechanical flexibility, light weight and manufacturing using solution-based processing as spray coating or inkjet printing, which are appealing for roll-to-roll production, make the technology highly attractive [1,2]. Up to now the maximum power conversion efficiency (PCE) is on the order of ~10% [3–7]. BHJ cells typically integrate blends formed by a donor polymer, such as poly (3-hexylthiophene) (P3HT) and an acceptor fullerene, such as [6,6]-phenyl-C61-butyric acid methyl ester ($PC_{60}BM$). Efficient electrodes comprise a transparent conducting oxide (TCO) anode, such as indium tin oxide (ITO), and a low work function metal cathode. A hole transport layer (HTL) is deposited between the TCO anode and bulk heterojunction layer to enhance hole extraction by reducing contact resistance, acting simultaneously as an electron-blocking layer. The most commonly employed HTL material in polymer solar cell is the copolymer poly(3,4-ethylenedioxythiophene):poly(styrenesulfonate) (PEDOT:PSS) [8], because it is insoluble in organic solvents, conductive, and highly transparent to visible light. However, PEDOT:PSS presents some disadvantages as its acid character (pH = 1.2) and hygroscopic nature cause corrosion of the ITO anode subsequently allowing indium diffusion throughout the device [9]. Other alternatives for an efficient anode interlayer material use wide band gap ($E_g \geq 3$ eV) *p*-doped materials such as several transition metal oxides (V_2O_5, MoO_3, and WO_3) [10–13] which are usually incorporated using less convenient vacuum deposition techniques. Therefore it would be necessary to investigate on HTL materials processed from solution routes. An ideal candidate can be nickel oxide (NiO). However it is known that NiO contact properties are highly sensitive to the surface chemistry, crystal orientation and thin film processing [7,14,15].

In this work, an efficient anode NiO interlayer is prepared on top of the ITO by a versatile cathodic electrochemical deposition method [16]. Surface treatments such as UV–ozone (UVO) and annealing treatment (AT) in air allows reducing contact resistance and simultaneously increasing shunt resistance, enhancing as a consequence photovoltaic parameters. In particular carrier selectivity of the anodes is quantified from the resistance components associated with the impedance response of the contacts. Compared to the PEDOT:PSS HTL, solar cells including NiO exhibit superior electrical characteristics (carrier selectivity $s > 99\%$).

2. Results and discussion

Two different HTLs were tested: namely PEDOT:PSS layers, and NiO films. PEDOT:PSS was spin coast onto ITO-coated glass substrate (10 Ω/sq) at 5500 rpm for 30 s, then 3000 rpm for 30 s in air.

---

* Corresponding author. Tel.:+ 34 943 309022.
** Corresponding author. Tel.:+ 34 964 387538.
E-mail addresses: rtena@cidetec.es (R. Tena-Zaera), garciag@uji.es (G. Garcia-Belmonte).

0927-0248/$ - see front matter © 2013 Elsevier B.V. All rights reserved.
http://dx.doi.org/10.1016/j.solmat.2013.07.020

The thickness of the PEDOT:PSS layer was about 30 nm, as determined by a VEECO DEKTACK 6M Stylus Profiler. To remove the traces of water, the substrates were heated at 130 °C for 10 min. NiO deposition on the ITO was performed from the electrochemical reduction of O_2 in an aprotic ionic liquid (i.e. 1-butyl-1-methylpyrrolidinium bis(trifluoromethanesulfonyl)imide, $PYR_{14}TFSI$)-based electrolyte containing nickel bis(trifluoromethanesulfonyl)imide (5×10^{-2} M). Further experimental details can be found elsewhere [16]. Charge densities of 13 and 25 mC/cm^2 were passed during the electrodeposition in order to obtain NiO films with thickness of 30 and 50 nm, respectively. Some of the obtained NiO samples were heated at 320 °C for 20 min (annealing treatment AT), and then UVO treatment were carried on for 10 min. Other 30 nm-thick NiO films were analyzed reversing the processing: firstly UVO treatment was performed and then submitted to AT with the same conditions as in the previous devices. Also 30 nm-thick NiO films were studied as-deposited without any post-treatments. The active layer consisting of P3HT and $PC_{60}BM$ blend was spin-cast in a glove box from orthodichlorobenzene (ODCB) solution on top of the HTL layer. The active layer was deposited at 1200 rpm for 10 s (100 nm-thick). The films were then annealed on a hot plate in the glove box at 130 °C for 10 min. Ca/Ag (5 nm/100 nm) cathodes were used as top electrodes by thermal evaporation. Devices of structure glass/ITO/HTL/P3HT:$PC_{60}BM$/Ca/Ag are analyzed by impedance spectroscopy (IS) technique under 1 sun illumination.

The morphology of NiO layers is analyzed by scanning electron microscopy. Although conformal-like ~30 nm thick coating of the ITO substrate is observed after electrodeposition experiments passing a charge density of 13 mC/cm^2 (Fig. 1b and d), a decrease of roughness – versus to the naked substrates (Fig. 1a) – can be inferred in samples obtained after applying 25 C/cm^2 (Fig. 1c). The decrease of the roughness for thicker layers was confirmed by atomic force microscopy [16]. The substrates coated with the different HTLs are characterized UV–vis spectra (Fig. 2), detecting significant changes in the transmittance of the NiO films as-deposited and after each treatment. The differences suggest changes in the NiO stoichiometry. A similar high transmittance is observed for the as-deposited and after UVO/AT treatments of 30 nm-thick NiO films and PEDOT:PSS film. Transmittance lowers when AT/UVO is performed on NiO films with different thicknesses 30 and 50 nm. This transmittance reduction is reflected in the photovoltaic characteristics as discussed later. Previous research informs that the work function of NiO is strongly dependent on the thickness, O_2-plasma, and annealing treatments [17]. For example, a O_2-plasma treatment increases the work function of NiO, by forming NiO_x layers with their electronic properties dictated by the formation of metal cation vacancies, and regions in the oxide lattice which are rich in oxygen [17]. Also deposition methods such as pulsed laser deposition, sol–gel route, or sputtering play a determining role [9,18]. We consider here that UVO treatment followed in our experiments produces similar effects as those occurring after O_2-plasma treatment [18]. Furthermore, recent research reveals that ozone exposure increased the Ni oxidation state by introducing hole states, giving rise to higher-performance aluminum-coated NiO films [19].

The electrical properties of the glass/ITO/HTL/P3HT:$PC_{60}BM$/Ca/Ag solar cells are shown as current density–voltage $j-V$ characteristics under simulated AM1.5G illumination (1000 W m^{-2}) (Fig. 3a). The photovoltaic parameters for PEDOT:PSS and all NiO interlayer-based devices are summarized in Table 1. It is clearly observed that the NiO as-deposited device has the lowest photovoltaic parameters (see Table 1) indicating that surface treatments are necessary to improve contact conditions. When NiO films are annealed before UVO treatment, the open-circuit voltage yields ~620 mV (see Table 1), a value similar to that achieved with PEDOT:PSS. However 30 nm-thick NiO-based device with firstly UVO treatment (UVO/AT) only yields 260 mV (see Table 1). Reduction in open-circuit voltage suggests that the NiO film with the

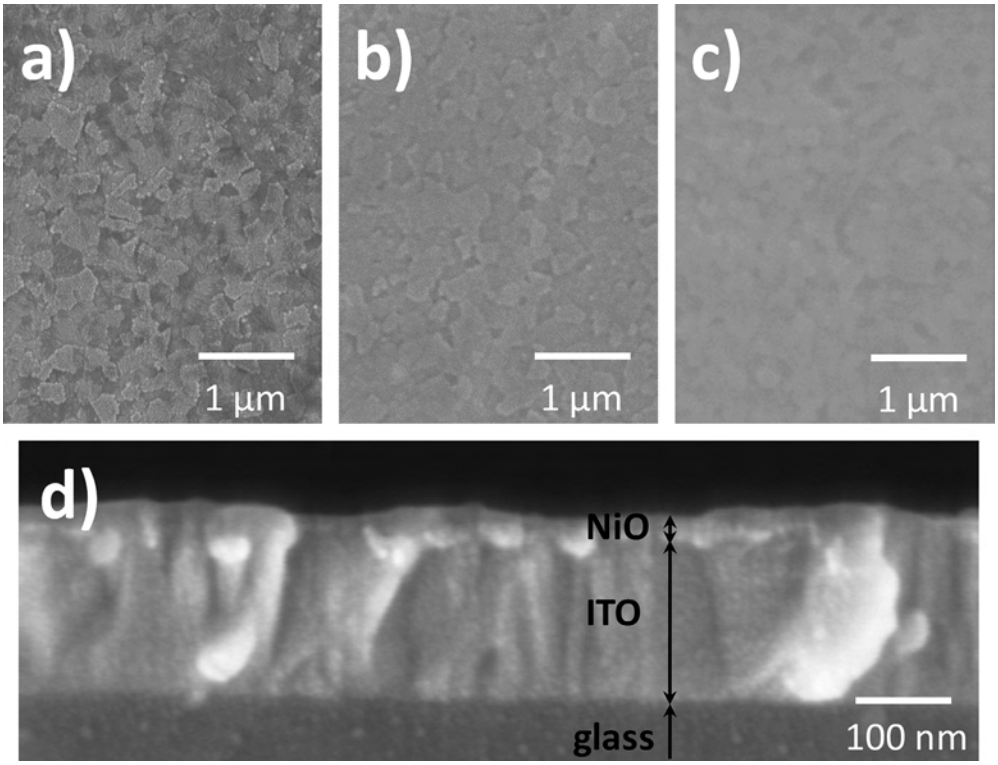

Fig. 1. Top view SEM micrographs of a naked ITO substrate (a) and NiO layers electrodeposited by passing a charge density of 13 (b) and 25 mC/cm^2 (c). The figure (d) shows a cross section SEM micrograph of the sample showed in figure (b).

previous UVO treatment exhibits blocking characteristics as next explained in describing impedance spectroscopy results. The optimum observed photovoltaic result corresponds to the 30 nm-thick NiO treated with UVO after annealing the interlayer.. This results in an power conversion efficiency of 3.44%, comparable to a common device with PEDOT:PSS. The main difference between these two cells is the short-circuit current j_{sc} and EQE response (Fig. 3b). The lower j_{sc} for the 30 nm-thick NiO (AT/UVO) solar cell is attributed to the lower transmittance spectra as observed in Fig. 1. However NiO-based cell exhibits an improved fill factor (FF) in comparison to PEDOT:PSS-based cell (see Table 1). FF is known to be connected to resistive effects, either in series or in parallel, which limits the electrical power delivered by a solar cell. Improvement in contact resistive effects derives from the capacity of the outer anode interface for simultaneous (*i*) hole extraction and (*ii*) electron blocking, a feature that states the contact selectivity [20]. We next use impedance spectroscopy to discern out the origin of such FF increment.

Impedance spectroscopy (IS) is an experimental technique able to separate different resistive and capacitance contributions to the overall solar cell electrical response [21]. NiO-based devices and a standard device with PEDOT:PSS as HTL are studied by IS under 1 sun irradiation intensity by varying bias voltage. $Z'-Z''$ plots exhibit a typical impedance response of organic solar cells displaying two arcs (see Fig. 3) [22,23]. The equivalent circuit model shown in Fig. 4 provides a high quality fit of the data for all devices. At lower frequencies, a large arc dominates in the $Z'-Z''$ plot which is represented by a *RC* subcircuit. This part is related to the recombination resistance R_{rec}, derivative of the carrier recombination flux; and the chemical capacitance C_{μ} related to carrier

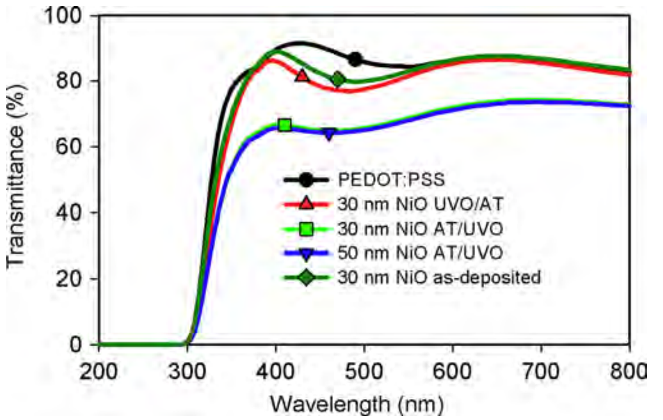

Fig. 2. Transmission spectra of HTL films on top of ITO substrates. The HTL analyzed were PEDOT:PSS film and NiO films treated by the following ways: as-deposited (30 nm), AT/UVO (30 and 50 nm) and UVO/AT (30 nm).

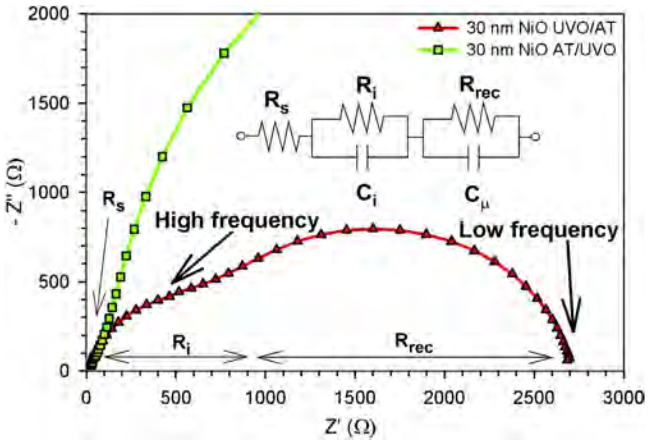

Fig. 4. $Z'-Z''$ plot of 30 nm-thick NiO UVO/AT and AT/UVO-based solar cell at 300 mV-bias voltage under 1 sun illumination. The equivalent circuit model is also indicated, which comprises a series resistance R_s, interlayer resistance R_i, interlayer capacitance C_i, recombination resistance R_{rec}, and chemical capacitance C_{μ}.

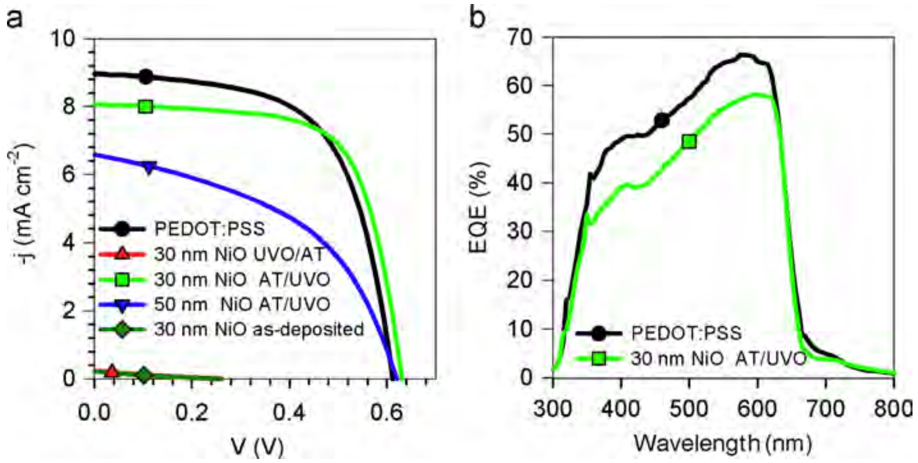

Fig. 3. (a) Current density–voltage plots under 1 sun illumination for glass/ITO/HTL/P3HT:PC$_{60}$BM/Ca/Ag BHJ solar cells fabricated with PEDOT:PSS (standard device) and NiO films (as-deposited, AT/UVO and UVO/AT for 30 nm thick and 50 nm thick for AT/UVO). (b) EQE spectra of glass/ITO/PEDOT:PSS or 30 nm NiO (AT/UVO)/P3HT:PC$_{60}$BM/Ca/Ag devices.

Table 1
Photovoltaic characteristics for P3HT:PC$_{60}$BM solar cells with PEDOT:PSS and NiO interlayers. AT=annealing treatment.

HTL	HTL thickness, nm	Process	j_{sc}, mA cm^{-2}	V_{oc}, mV	FF, %	PCE, %	Selectivity, %
PEDOT:PSS	30	standard	8.97	611	62	3.39	95.0
NiO	30	UVO/AT	0.42	260	19	0.02	–
NiO	30	AT/UVO	8.06	630	67	3.44	99.6
NiO	50	AT/UVO	6.58	620	47	1.92	85.0
NiO	30	as-deposited	0.20	258	23	0.01	–

storage [21]. At higher frequencies, an additional arc is clearly observed in the Z′–Z″ plot for the 30 nm-thick NiO (UVO/AT)-based solar cell (Fig. 4). This high-frequency arc is also visible, although to a minor extent, with the other devices (shown in Fig. 4 for 30 nm-thick NiO (AT/UVO)-based device). This extra arc at high frequencies is represented by a parallel *RC* which is directly dependent on the HTL/active layer interface. It is interpreted in terms of an interlayer resistance R_i, and capacitance C_i. The equivalent circuit model also has a series resistance R_s resulting from the electrode contacts.

IS parameters extracted from fitting of the Nyquist plots using the equivalent circuit model showed in Fig. 4 are shown in Fig. 5. NiO (UVO/AT)-based device show a voltage-independent, high R_i~70 Ω cm^2 (Fig. 5a). This is a considerable resistance that contributes to hinder hole extraction at the anode contact. We had studied a similar blocking-like behavior with a CaO layer at the cathode [23]. Performing annealing treatment before UVO seems necessary to reduce the contact resistance. This is likely due to a better matching in the energy levels at the interface. Thicker NiO interlayers (50 nm AT/UVO) exhibit intermediate R_i values (~30 Ω cm^2) in comparison to those obtained with thinner NiO (30 nm AT/UVO) and PEDOT:PSS (<10 Ω cm^2). It is interesting to note that R_i for these last cells contributes similarly to the overall series resistance. However the thinner NiO-layer cell presents lower R_i values around the maximum power point. This explains in part the increment in FF exhibited by the NiO-based cell (see Table 1). Other possible factors influencing FF are originated by recombination currents (represented by R_{rec}), and leakage current (modeled by the shunt resistance R_{sh}) determining the slope of the $j-V$ curves near short circuit.

The recombination resistance R_{rec} (Fig. 5b) follows the expected decreasing behavior at forward voltage due to the enhancement of the recombination current [21]. At low voltages R_{rec} tends to saturate because the differential resistance measured is not determined by the recombination flux but by a shunt resistance R_{sh} caused by additional leakage currents flowing in parallel [22]. In that region, R_{sh} corresponding to the 30 nm NiO (AT/UVO) solar cell is higher than that exhibited by other devices. This effect is reflected in the $j-V$ curve which has a nearly flat response at low voltages. At higher voltages, R_{rec} shows similar decreasing behavior for the working devices (PEDOT:PSS and 30 nm-thick NiO AT/UVO). This fact precludes connecting the differences in FF to recombination currents occurring within the active layer bulk. On the contrary large R_{sh} variations (from ~200 Ω cm^2 with PEDOT:PSS to ~3 kΩ cm^2 with thin NiO AT/UVO) are directly linked with the increment in FF, which finally improves performance. The interplay between hole extraction (low R_i values) and leakage current blocking (high R_{sh}) is used to define the carrier selectivity degree exhibited by the anode contact. We propose that the contact selectivity can simply be expressed as

$$s = 1 - \frac{R_i}{R_{sh}} \tag{1}$$

which results in $s=1$ for a fully selective contact. Selectivity values are summarized in Table 1. It is noted that *s* correlates with FF as expected. The definition of contact selectivity in Eq. (1) tries to capture the balance between the charge (hole) extraction ability of the anode and the detrimental leakage current flowing in parallel to the photocurrent. The ratio between R_i and R_{sh} compares the anode opposition to the hole extraction in the energy-generating quadrant of the $j-V$ curve and the resistance caused by the leakage current.

The capacitance plot C_μ (Fig. 5d) of the 30 nm-thick NiO (AT/UVO) and PEDOT:PSS-based devices exhibits at higher voltages the expected increase as fullerene states are occupied toward forward bias [21]. The 30 nm-thick NiO (UVO/AT) cell shows a voltage-independent C_μ under illumination related to the blocking behavior which approximately corresponds to the chemical capacitance found for working cells at V_{app}≈400 mV. A similar behavior was found when insulating layer were intentionally deposited at the cathode contact [23]. At lower voltages all devices exhibit the expected capacitive response originated by the modulation of the depletion zone built up at the cathode contact, which collapses to the geometrical capacitance near zero voltage [24]. Finally Fig. 5c represents C_i versus applied voltage. The 30 nm-thick NiO (AT/UVO) and PEDOT:PSS HTL-based OPV devices have the same behavior which increases toward forward bias. On the contrary the other devices exhibit almost constant, lower C_i values. The transition between low to high C_i appears to be connected to the change between dielectric to charge accumulation mechanisms at the interlayer.

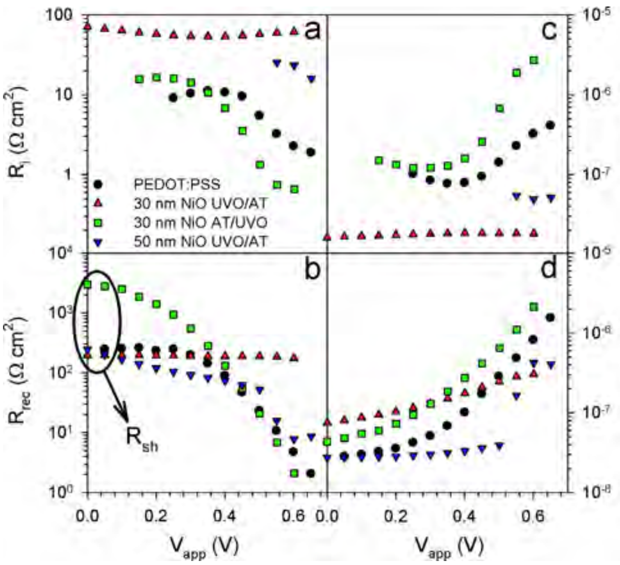

Fig. 5. (a) Interlayer resistance R_i, (b) recombination resistance R_{rec}, (c) interlayer capacitance C_i, and (d) chemical capacitance C_μ as a function of the applied voltage extracted from the fitting of the equivalent circuit model shown in Fig. 3.

3. Conclusions

We finally remark that NiO electrodeposition from aprotic ionic liquids appears to be a viable vacuum-free approach to integrate HTL in BHJ solar cells in a single-step process i.e. avoiding the post-deposition thermal treatments needed in the aqueous-based electrodeposition [15], and the consequent traces of nickel hydroxide-related phases present even after annealing treatments [25]. Surface treatments such as UVO and annealing treatment have an important effect on the electrical behavior of the NiO as anode interlayer. Different thicknesses (30 and 50 nm) and treatment order (AT/UVO or UVO/AT) have been studied in the conventional device architecture of organic solar cells. The efficiency values of the device prepared with 30 nm-thick NiO film (AT/UVO) HTL is comparable with a standard PEDOT:PSS. NiO interlayers present a superior electrical response as evidenced by the reduction in the overall series resistance, and larger shunt resistance. These two parameters allow explaining the higher FF observed for 30 nm-thick NiO AT/UVO films. The proposed analytical technique based on IS can be further used when different contact structures are compared, allowing for a quantification of the carrier selectivity.

Acknowledgments

We thank financial support from Generalitat Valenciana (Prometeo/2009/058, and ISIC/2012/008 Institute of Nanotechnologies for Clean Energies), and FP7 European Project ORION (Large CP-

IP229036-2). R.T.-Z. acknowledges the support of the Program “Ramón y Cajal” of the MICINN.

References

[1] F.C. Krebs, S.A. Gevorgyan, B. Gholamkhass, S. Holdcroft, C. Schlenker, M.E. Thompson, B.C. Thompson, D. Olson, D.S. Ginley, S.E. Shaheen, H.N. Alshareef, J.W. Murphy, W.J. Youngblood, N.C. Heston, J.R. Reynolds, S.J. Jia, D. Laird, S.M. Tuladhar, J.G.A. Dane, P. Atienzar, J. Nelson, J.M. Kroon, M.M. Wienk, R.A.J. Janssen, K. Tvingstedt, F.L. Zhang, M. Andersson, O. Inganas, M. Lira-Cantu, R. de Bettignies, S. Guillerez, T. Aernouts, D. Cheyns, L. Lutsen, B. Zimmermann, U. Wurfel, M. Niggemann, H.F. Schleiermacher, P. Liska, M. Gratzel, P. Lianos, E.A. Katz, W. Lohwasser, B. Jannon, A round robin study of flexible large-area roll-to-roll processed polymer solar cell modules, Solar Energy Materials and Solar Cells 93 (2009) 1968–1977.

[2] F.C. Krebs, Fabrication and processing of polymer solar cells: a review of printing and coating techniques, Solar Energy Materials and Solar Cells 93 (2009) 394–412.

[3] M.C. Scharber, D. Mühlbacher, M. Koppe, P. Denk, C. Waldauf, A.J. Heeger, C.J. Brabec, Design rules for donors in bulk-heterojunction solar cells—towards 10% energy-conversion efficiency, Advanced Materials 18 (2006) 789–794.

[4] Y. Sun, C.J. Takacs, S.R. Cowan, J.H. Seo, X. Gong, A. Roy, A.J. Heeger, Efficient, air-stable bulk heterojunction polymer solar cells using MoOx as the anode interfacial layer, Advanced Materials (Weinheim, Germany) 23 (2011) 2226–2230.

[5] S. Chen, C.E. Small, C.M. Amb, J. Subbiah, T.H. Lai, S.W. Tsang, J.R. Manders, J.R. Reynolds, F. So, Inverted polymer solar cells with reduced interface recombination, Advanced Energy Materials 2 (2012) 1333–1337.

[6] W. Chen, M.P. Nikiforov, S.B. Darling, Morphology characterization in organic and hybrid solar cells, Energy and Environmental Science 5 (2012) 8045–8074.

[7] L. Dou, J. You, J. Yang, C.-C. Chen, Y. He, S. Murase, T. Moriarty, K. Emery, G. Li, Y. Yang, Tandem polymer solar cells featuring a spectrally matched low-bandgap polymer, Nature Photonics 6 (2012) 180–185.

[8] G. Greczynski, T. Kugler, M. Keil, W. Osikowicz, M. Fahlman, W.R. Salaneck, Photoelectron spectroscopy of thin films of PEDOT-PSS conjugated polymer blend: a mini-review and some new results, Journal of Electron Spectroscopy and Related Phenomena 121 (2001) 1–17.

[9] K.X. Steirer, J.P. Chesin, N.E. Widjonarko, J.J. Berry, A. Miedaner, D.S. Ginley, D.C. Olson, Solution deposited NiO thin-films as hole transport layers in organic photovoltaics, Organic Electronics 11 (2010) 1414–1418.

[10] S. Schubert, M. Hermenau, J. Meiss, L. Müller-Meskamp, K. Leo, Oxide sandwiched metal thin-film electrodes for long-term stable organic solar cells, Advanced Functional Materials 22 (2012) 4993–4999.

[11] J. Meyer, S. Hamwi, M. Kroger, W. Kowalsky, T. Riedl, A. Kahn, Transition metal oxides for organic electronics: energetics, device physics and applications, Advanced Materials 24 (2012) 5408–5427.

[12] H.-Q. Wang, N. Li, N.S. Guldal, C.J. Brabec, Nanocrystal V_2O_5 thin film as hole-extraction layer in normal architecture organic solar cells, Organic Electronics 13 (2012) 3014–3021.

[13] E.L. Ratcliff, B. Zacher, N.R. Armstrong, Selective inter layers and contacts in organic photovoltaic cells, Journal of Physical Chemistry Letters 2 (2011) 1337–1350.

[14] M.D. Irwin, J.D. Servaites, D.B. Buchholz, B.J. Leever, J. Liu, J.D. Emery, M. Zhang, J.H. Song, M.F. Durstock, A.J. Freeman, M.J. Bedzyk, M.C. Hersam, R.P.H. Chang, M.A. Ratner, T.J. Marks, Structural and electrical functionality of NiO interfacial films in bulk heterojunction organic solar cells, Chemistry of Materials 23 (2011) 2218–2226.

[15] H. Yang, C. Gong, G.H. Guai, C.M. Li, Organic solar cells employing electrodeposited nickel oxide nanostructures as the anode buffer layer, Solar Energy Materials and Solar Cells 101 (2012) 256–261.

[16] E. Azaceta, S. Chavhan, P. Rossi, M. Paderi, S. Fantini, M. Ungureanu, O. Miguel, H.-J. Grande, R. Tena-Zaera, NiO cathodic electrochemical deposition from an aprotic ionic liquid: building metal oxide n–p heterojunctions, Electrochimica Acta 71 (2012) 39–43.

[17] K.X. Steirer, P.F. Ndione, N.E. Widjonarko, M.T. Lloyd, J. Meyer, E.L. Ratcliff, A. Kahn, N.R. Armstrong, C.J. Curtis, D.S. Ginley, J.J. Berry, D.C. Olson, Enhanced efficiency in plastic solar cells via energy matched solution processed NiOx interlayers, Advanced Energy Materials 1 (2011) 813–820.

[18] E.L. Ratcliff, J. Meyer, K.X. Steirer, A. Garcia, J.J. Berry, D.S. Ginley, D.C. Olson, A. Kahn, N.R. Armstrong, Evidence for near-surface NiOOH species in solution-processed NiOx selective interlayer materials: impact on energetics and the performance of polymer bulk heterojunction photovoltaics, Chemistry of Materials 23 (2011) 4988–5000.

[19] F. Lin, D. Nordlund, T.-C. Weng, R.G. Moore, D.T. Gillaspie, A.C. Dillon, R.M. Richards, C. Engtrakul, Hole doping in Al-containing nickel oxide materials to improve electrochromic performance, ACS Materials & Interfaces 5 (2013) 301–309.

[20] A. Guerrero, B. Dörling, T. Ripolles-Sanchis, M. Aghamohammadi, E. Barrena, M. Campoy-Quiles, G. Garcia-Belmonte, Interplay between fullerene surface coverage and contact selectivity of cathode interfaces in organic solar cells, ACS Nano 7 (2013) 4637–4646.

[21] G. Garcia-Belmonte, A. Guerrero, J. Bisquert, Elucidating operating modes of bulk-heterojunction solar cells from impedance spectroscopy analysis, Journal of Physical Chemistry Letters 4 (2013) 877–886.

[22] A. Guerrero, L.F. Marchesi, P.P. Boix, J. Bisquert, G. Garcia-Belmonte, Recombination in organic bulk heterojunction solar cells: small dependence of interfacial charge transfer kinetics on fullerene affinity, Journal of Physical Chemistry Letters 3 (2012) 1386–1392.

[23] T. Ripolles-Sanchis, A. Guerrero, J. Bisquert, G. Garcia-Belmonte, Diffusion–recombination determines collected current and voltage in polymer:fullerene solar cells, Journal of Physical Chemistry C 116 (2012) 16925–16933.

[24] A. Guerrero, L.F. Marchesi, P.P. Boix, S. Ruiz-Raga, T. Ripolles-Sanchis, G. Garcia-Belmonte, J. Bisquert, How the charge–neutrality level of interface states controls energy level alignment in cathode contacts of organic bulk-heterojunction solar cells, ACS Nano 6 (2012) 3453–3460.

[25] E. Azaceta, N.T. Tuyena, D.F. Pickup, C. Rogero, E. Ortega, O. Miguel, H.-J. Grande, R. Tena-Zaera, One-step wet chemical deposition of NiO from the electrochemical reduction of nitrates in ionic liquid based electrolytes, Electrochimica Acta 96 (2013) 261–267.

APPLIED PHYSICS LETTERS **103**, 243306 (2013)

Polymer defect states modulate open-circuit voltage in bulk-heterojunction solar cells

Teresa S. Ripolles, Antonio Guerrero, and Germà Garcia-Belmonte[a)]
Photovoltaic and Optoelectronic Devices Group, Departament de Física, Universitat Jaume I, ES-12071 Castelló, Spain

(Received 7 October 2013; accepted 18 November 2013; published online 13 December 2013)

Defect states influence the operation of organic solar cells altering transport, recombination, and energetic mechanisms. This work investigates how processing conditions induce morphology-related, electrically active defects in the donor polymer of bulk-heterojunction solar cells. Structural order is inferred from absorption and X-ray diffraction data, while defect density is determined from capacitance methods. A correlation is observed between the polymer nanocrystallite size, the defect concentration, and the output voltage. For the case of poly(3-hexylthiophene), processing that promote crystallinity is beneficial for the device performance as it decreases the defect density (energy disorder) that finally enlarges the maximum achievable open-circuit voltage. Defect states within the effective bandgap modulate the downshift of the hole Fermi level upon illumination that in turn establishes the achievable open-circuit voltage. © *2013 AIP Publishing LLC*. [http://dx.doi.org/10.1063/1.4841475]

Organic photovoltaic (OPV) devices have recently witnessed an impressive improvement in the power conversion efficiency (PCE) now reaching 9.2%.[1] In a bulk heterojunction device, a conjugated polymer donor is intimately blended with a fullerene acceptor molecule. In this configuration, materials form a highly connected, interpenetrating network, in which generation of excitons give rise to separated charges at the donor-acceptor interface enabling an efficient transport of carriers towards the electrodes.[2] The nanoscale morphology can be controlled by a number of ways such as the selection of appropriate solvents,[3,4] drying processes,[5] donor:acceptor ratio,[4] concentration of materials,[6] thermal treatments,[2,7] or use of additives.[8] Processing conditions of the films control the blend morphology which is then critical to ultimately improve the photovoltaic parameters and OPV performance.[4,9]

One of the strategies to enlarge the open-circuit voltage V_{oc} consists on reducing charge recombination flux.[10] Limiting recombination pathways increases the amount of free carriers within the active layer in operating conditions which in turn modifies the Fermi level position of electrons (E_{Fn}) and holes (E_{Fp}), and ultimately the output voltage as[11]

$$qV_{oc} = E_{Fn} - E_{Fp}. \tag{1}$$

Another factor influencing photovoltage has a purely energetic origin. Energy disorder of both fullerene acceptor and polymer donor induces bandgap density-of-states (DOS) (exponential or Gaussian tails and traps) that modulate the light-induced Fermi level shift.[12] This last mechanism explains how processing conditions, which modify the structural order and crystallinity of the active layer compounds, can alter the output V_{oc}. Recent studies have found that variations within the fullerene DOS related to their dissimilar aggregation ability affect the final achieved V_{oc}.[13] It was observed that large fullerene DOS limits the Fermi level upward shift yielding as a result lower V_{oc} values. However, the influence on photovoltage of the polymer energetic disorder/crystallinity has been much less explored.[14] How processing conditions induce morphology-related electronic defects in the donor polymer and the repercussion on the achieved V_{oc} will be the specific aim of this work.

One of the most commonly studied OPV system is based in the semicrystalline blend composed by the donor material poly(3-hexylthiophene) (P3HT) and the acceptor fullerene derivate [6,6]-phenyl-C61-butyric acid methyl ester ($PC_{60}BM$) with reported efficiencies around 3%-5%.[15] The efficiency of P3HT:$PC_{60}BM$ solar cells are drastically improved upon annealing as the P3HT-crystallinity is increased leading to improved optical absorption and transport of carriers.[3] The fibrillar-like P3HT crystals are embedded in a matrix mainly comprised by $PC_{60}BM$ nanocrystals and amorphous P3HT.[16] As it will be shown here, a clear correlation between the crystallinity of materials and the concentration of electrically active defects is observed. Moreover, we show how polymer structural order and defect density modulate the achievable output voltage.

The studied polymer photovoltaic devices are fabricated in the configuration glass/ITO/P3HT:$PC_{60}BM$/Ca/Ag.[17] PEDOT:PSS was deposited by spin coating over clean ITO to provide a film thickness of about 35 nm. Films were dried followed by deposition of the active layer P3HT:$PC_{60}BM$. Some samples were slowly dried, spin coating was carried out at 900 rpm for 10 s, and then substrates were introduced into a petri dish and covered for 2 h (devices 1 and 2). Other samples were completely dried during the spin coating process at 3500 rpm for 2 min. These are denoted as fast drying devices. Films were heated at the temperatures stated in Table I. The active layer thickness of the film was approximately 300 nm. Finally, the cathode electrode was deposited (5 nm Ca/100 nm Ag) by thermal evaporation for all samples at a base pressure below 3×10^{-6} mbar. The devices were then encapsulated with epoxy and a glass slide before

---

[a)]Author to whom correspondence should be addressed. Electronic mail: garciag@uji.es. Tel.: +34 964 387538. Fax: +34 964 729218

TABLE I. Photovoltaic parameters of P3HT:PC$_{60}$BM measured under 1 sun illumination using different processing conditions. Defect density n extracted from capacitance-voltage measurements under dark conditions and at 100 Hz. P3HT domain size L calculated from XRD data.

Device	Conditions	j_{sc} (mA cm^{-2})	V_{oc} (mV)	FF (%)	PCE (%)	n ($\times 10^{16}$) (cm^{-3})	L (nm)
1	Slow dry	7.31	566	54	2.2	4.0	14
2	Slow dry, 130 °C[a]	7.57	621	64	3.0	0.2	21
3	Fast dry	2.45	587	32	0.5	1.2	14
4	Fast dry, 90 °C	7.67	572	54	2.4	2.0	18
5	Fast dry, 130 °C	8.28	608	50	2.6	0.4	18

[a] Post-cathode annealing.

testing. An additional thermal treatment at 130 °C for 10 min was carried out for device 2 noted as post-cathode annealing. More experimental details can be found as supplementary material.[29]

Active layer morphology is varied by either a control of the drying time of the film (long drying times for device 1), by a thermal treatment of the deposited films (devices 3–5), or by both conditions (device 2). Absorption spectra of the films are shown in Fig. 1(a). The absorption spectrum of a neat film containing P3HT has been added as a reference. Results are similar to previously reported experiments.[3,18] Below 400 nm, the absorption of PC$_{60}$BM is dominant[19] and the P3HT band is visible between 400 and 650 nm. At about 500 nm, it is observed a characteristic peak that provides information on the degree of conjugation of the P3HT chains, and a peak at around 600 nm informs on the degree of interchain order.[5,20] Figure 1(a) shows red-shifted absorbance of the slow dried P3HT:PC$_{60}$BM films (device 1), indicating longer polymer conjugation lengths than the fast dried samples (devices 3–5) and a narrower bandgap. In fact, the band gap decreases about 85 meV, when comparing the less crystalline sample (device 3) with the more crystalline film (device 2). The height of the vibronic shoulder at 600 nm increases systematically from fast drying and un-annealed film (device 3) to fast drying, 130 °C-annealed film (device 5), being even higher for P3HT:PC$_{60}$BM slow drying films (devices 1 and 2). These results indicate a poor degree of interchain order for the un-annealed P3HT:PC$_{60}$BM film. The P3HT-polymer film absorbance spectra exhibit a slightly larger absorbance at 600 nm respect to the other blend films which evidences that the introduction of fullerene as PC$_{60}$BM into the blend film disturbs the polymer local ordering. These experiments show that absorption measurements are very sensitive to differences in crystallinity. In addition, XRD data of our films (see supplementary material) exhibit a diffraction peak that correspond to the a-axis orientation related to the packing of the alkyl chains of the P3HT crystallites. From the width and position of the diffraction peak, an estimation of the P3HT nanodomain size is calculated (see supplementary material), which results within the range of 15–20 nm (Table I). Unfortunately, XRD data do not provide any information on the b- or c-axis orientations and consequently valuable information on the packing of the thiophene rings is missing. Crystallinity issues will be discussed relying upon variations in absorption features, particularly the relative height of the vibronic shoulder at 600 nm with respect to the maximum at ~500 nm and crystallite size extracted from XRD data.

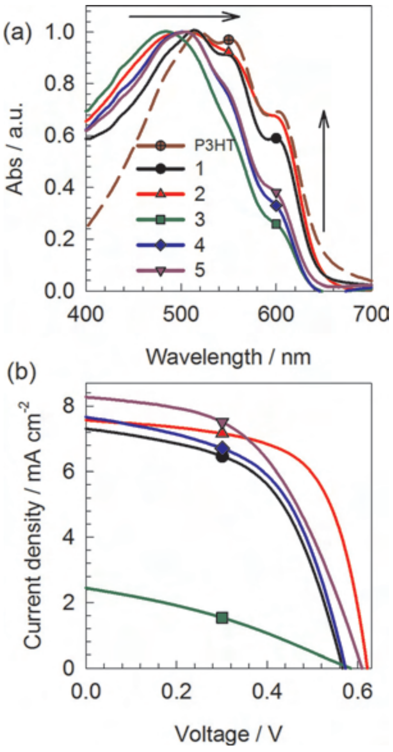

FIG. 1. (a) UV-Vis absorbance spectra of films deposited from P3HT:PC$_{60}$BM blends. The spectra have been normalized to the maximum of the P3HT peak at around 500 nm. Devices correspond to those listed in Table I. (b) Current density vs. applied voltage plot measured under simulated 1 sun illumination for the devices fabricated in this work.

The photovoltaic parameters of P3HT:PC$_{60}$BM devices are summarized in Table I and current density-voltage $j-V$ curves measured under AM1.5G illumination (1000 W m^{-2}) are shown in Fig. 1(b). Similar results are obtained for deposition conditions in which crystallinity has been enhanced either by controlling the drying process or through a thermal treatment. Only the least crystalline film dried fast with no annealing treatment (device 3) shows a remarkably lower short-circuit current (j_{sc}) and fill factor. The $j-V$ curves are in agreement with previously reported results in which film morphology is modified with similar processes.[21] Remarkably, the most crystalline film (device 2) provides higher V_{oc}.

Although absorption spectra in Fig. 1(a) and XRD data reveal variations in the polymer structural order among samples, they do not allow for a direct quantification of electrically active morphological features. For this reason, it is necessary to explore the response to purely electrical methods. It is believed that larger polymer ordering gives rise to smaller amounts of structural defects originated at less crystalline zones where the periodic spacing is broken. Polymer defect states acting as acceptor impurities might originate free holes, as evidenced by monitoring the polymer conductivity or photoluminescence quenching.[22] The density of defect states is accessible by means of capacitive methods that measure the width of the depletion zone built-up in the vicinity of the cathode contact. Here, we use capacitance-voltage measurements carried out in dark conditions from -1 to 0.5 V at constant frequency of 100 Hz following previously described methods.[23] The Mott-Schottky plots $C^{-2} - V$ are shown in Fig. 2(a), exhibiting a linear relation given by the following expression

$$C^{-2} = \frac{2}{A^2 q\varepsilon\varepsilon_0 n}(V_{\mathrm{fb}} - V). \qquad (2)$$

Here, A corresponds to the device active surface, ε is the relative dielectric constant of the blend ($\varepsilon \approx 3$), ε_0 is the permittivity of the vacuum, V_{fb} is the flat-band potential, and n is the total concentration of defects (doping level). Then, using Eq. (2), the concentration of electrically active acceptor impurities n and V_{fb} can be extracted at reverse and low forward bias from the slope and the extrapolated intersection with the voltage axis, respectively (Table I). Interestingly, the Mott-Schottky plot does not show full depletion at -1 V for most of the devices, except for the most crystalline film (device 2) in which the geometric capacitance can be derived from the saturation at reverse bias.

It is important to note that devices have not been exposed to air at any time. Then, the measured defect densities should mainly correspond to intrinsic, structural impurities/defects of the active layer rather than originated by air-related polymer oxidation.[24] Recalling now absorption measurements, it is observed that increasing the crystallinity of the polymer leads to decreased doping densities. Indeed, processing conditions that provide poorly crystalline blends such as devices 3 and 4 show relatively higher doping densities. In contrast, for a device annealed after a slow drying process (device 2), the doping density is about one order of magnitude lower than those observed for devices 3 and 4. Then, it appears that the defects are related to the actual surface area of the polymer crystallites. It is plausible to assume that polymer molecules present at the boundary between regular domains will show a different energetic landscape than those molecules found in the middle of a crystallite. Then, the doping density decreases at higher temperatures as the P3HT molecules aggregates enabling for a less disperse energetic landscape. For comparison purposes, devices based on the highly amorphous system PCDTBT:PC$_{70}$BM have been measured (see the XRD spectra and the Mott-Schottky plot in supplementary material). For this system, doping density of 1.4×10^{17} cm^3 has been observed which is two orders of magnitude higher than those observed for device 2. These results further suggest that the doping density is highly related to the polymer and its degree of structural order.

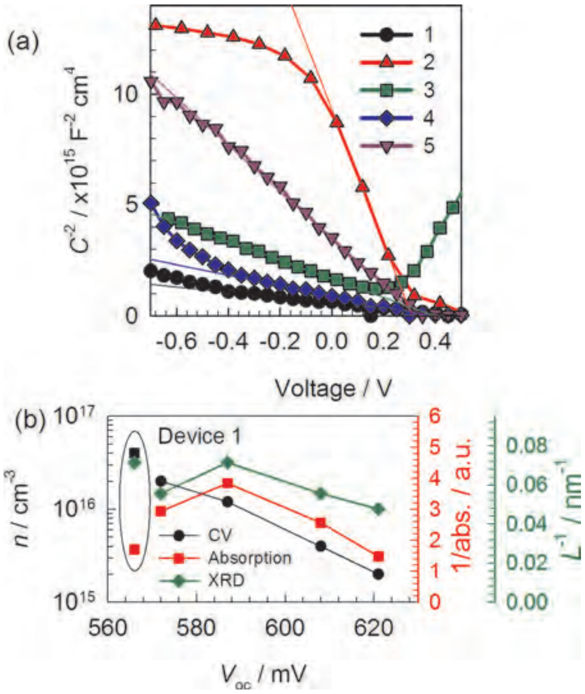

FIG. 2. (a) Mott-Schottky curves in dark conditions from -1 to 0.5 V measured at constant frequency of 100 Hz for P3HT:PC$_{60}$BM devices listed in Table I. (b) Defect density n extracted from CV analysis, inverse of the relative P3HT absorption intensity peak at 600 nm, and inverse of the crystallite nanodomain size L from XRD data vs. open-circuit voltage. Device 1 parameters do not follow the general trend.

As reported previously, V_{oc} is related to the HOMO level of the Donor and the LUMO level of the acceptor,[25] and more precisely to the difference in Fermi levels of electrons and holes of Eq. (1). It is known that thermal treatment produces an upward shift of the polymer HOMO manifold.[26] This is indeed confirmed by the red-shifted absorption spectra in Fig. 1(a). Therefore, V_{oc} for device 3 should show an increase of about 40 meV (85 meV is the difference in bandgap) in comparison with device 2 caused by differences in the polymer bandgap. However, the observed trend in our experiments is just the opposite as device 3 shows a V_{oc} about 35 mV lower than that observed for device 2. Then it is clear that apart from the effective bandgap of the materials there may be other factors affecting the achievable V_{oc}. We remark here that there exists a correlation between the polymer disorder degree (lack of crystallinity) and the defect density as observed from the doping level extracted by means of capacitive tools.

By examining Fig. 2(b), one can observe an exponential trend between the calculated doping density from capacitance analysis and V_{oc} for the P3HT:PC$_{60}$BM system, in which V_{oc} increases with a reduction of the impurities. The right axes of Fig. 2(b) correspond to a measurement of the polymer structural order, extracted either from the inverse value of the nanodomain size (XRD data) or from the inverse of the relative P3HT absorption intensity peak of the vibronic shoulder at 600 nm (data extracted from Fig. 1(a)). Inverse values are used here in order to directly compare with density measurements. It is observed that crystallinity degree and defect density correlate with the achieved V_{oc}. It is worth noting that P3HT crystallite size corresponds to a concentration of order of 10^{17} cm^{-3} in good accordance with the defect density encountered ($10^{15} - 10^{16}$cm^{-3}). The trends are observed in Fig. 2(b) for the studied devices with the exception of device 1. This is a special case (slow drying

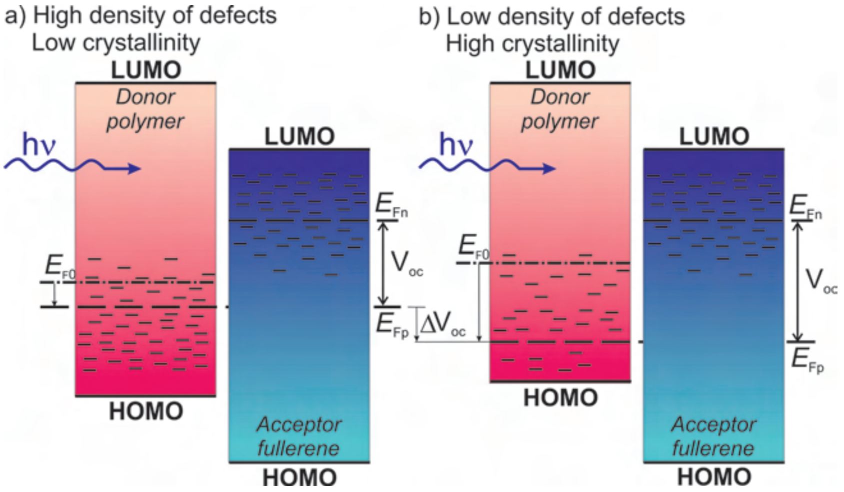

FIG. 3. Energy diagram of the polymer:fullerene blend under illumination indicating the electrically active states in the band gap of both materials. The donor HOMO level is displaced depending on the polymer crystallinity. The position of the equilibrium (dark) Fermi level is signaled as E_{F0}. The splitting of the hole Fermi Level (E_{Fp}) and the electron Fermi Level (E_{Fn}) yields the output open-circuit voltage. Two extreme cases of (a) high and (b) low defect density are shown. Lower-lying levels are occupied in the case of low defect density which produces the open-circuit voltage difference ΔV_{oc}.

without thermal treatment) in which residual solvent might be present as a source of external chemical impurities that contribute to increase the doping density. Then, in spite that slow drying promotes crystallinity, the output V_{oc} exhibited by device 1 is the lowest. This exception would imply that defect density rather than the actual structural order lies behind the achieved V_{oc}.

Only by considering differences in j_{sc} and the diode equation is not possible to explain the observed variations in V_{oc} among solar cells. The electronic effect of gap defects is linked with their ability to modulate the position of the hole Fermi level E_{Fp}, which in fact establishes the achievable V_{oc}. Under illumination conditions, E_{Fp} undergoes a downward shift with respect to the equilibrium Fermi level E_{F0} which is situated at an upper lying level for more crystalline polymers (see Fig. 3). Energy shift results larger when defect density is smaller because there are less available electronic states within the bandgap to be occupied by photogenerated charges. Then more crystalline samples that exhibit lower defect density allow for a larger E_{Fp} downshift. Therefore, the defect effect is dominant over variations in the band gap and it determines the final achievable V_{oc}. For simplicity, we consider in Fig. 3 that the number of defects created from different processing conditions and/or other annealing treatments, affects mainly the polymer. Figures 3(a) and 3(b) represent high and low density of defects of the polymer for a standard photovoltaic device under illumination, respectively. Without the decrease in the bandgap, the maximum achievable V_{oc} should be about 40 mV higher reaching values of about 660 mV. Electronic states corresponding to fullerene molecules might also vary under different device processing[27] or even more when different fullerenes derivatives are used.[28] This alters the position of the electron Fermi level and the final output V_{oc} as discussed in the previous work comparing the influence of the acceptor LUMO level bandgap tails.[13] Here, we highlight the effect of polymer structural order and how it influences (modulates) the light-induced shift of E_{Fp}. In conclusion, we have shown that device processing that enables an increased crystallinity of the film is beneficial for the device performance as it decreases the defect density (energy disorder) that finally enlarges the maximum achievable V_{oc}, despite the upward shift of the polymer HOMO manifold.

We thank financial support from Generalitat Valenciana (Prometeo/2009/058) and ISIC/2012/008 Institute of Nanotechnologies for Clean Energies. SCIC services at UJI are acknowledged.

[1] Z. He, C. Zhong, S. Su, M. Xu, H. Wu, and Y. Cao, Nature Photonics **6**, 591–595 (2012).
[2] X. N. Yang, J. Loos, S. C. Veenstra, W. J. H. Verhees, M. M. Wienk, J. M. Kroon, M. A. J. Michels, and R. A. J. Janssen, Nano Lett. **5**(4), 579 (2005).
[3] U. Zhokhavets, T. Erb, G. Gobsch, M. Al-Ibrahim, and O. Ambacher, Chem. Phys. Lett. **418**(4–6), 347 (2006).
[4] G. Dennler, M. C. Scharber, and C. J. Brabec, Adv. Mater. (Weinheim, Germany) **21**(13), 1323 (2009).
[5] B. F. Xue, B. Vaughan, C. H. Poh, K. B. Burke, L. Thomsen, A. Stapleton, X. J. Zhou, G. W. Bryant, W. Belcher, and P. C. Dastoor, J. Phys. Chem. C **114**(37), 15797 (2010).
[6] S. Wakim, S. Beaupre, N. Blouin, B.-R. Aich, S. Rodman, R. Gaudiana, Y. Tao, and M. Leclerc, J. Mater. Chem. **19**(30), 5351 (2009).
[7] F. Padinger, R. S. Rittberger, and N. S. Sariciftci, Adv. Funct. Mater. **13**(1), 85 (2003).
[8] T. Y. Chu, S. Alem, S. W. Tsang, S. C. Tse, S. Wakim, J. P. Lu, G. Dennler, D. Waller, R. Gaudiana, and Y. Tao, Appl. Phys. Lett. **98**(25), 253301 (2011).
[9] M. A. Brady, G. M. Su, and M. L. Chabinyc, Soft Matter **7**, 11065 (2011).
[10] A. Maurano, R. Hamilton, C. G. Shuttle, A. M. Ballantyne, J. Nelson, B. O'Regan, W. Zhang, I. McCulloch, H. Azimi, M. Morana, C. J. Brabec, and J. R. Durrant, Adv. Mater. **22**, 4987 (2010).
[11] G. Garcia-Belmonte and J. Bisquert, Appl. Phys. Lett. **96**, 113301 (2010); J. Widmer, M. Tietze, K. Leo, and M. Riede, "Open-circuit voltage and effective gap of organic solar cells," Adv. Funct. Mater. (published online).
[12] J. C. Blakesley and D. Neher, Phys. Rev. B **84**, 075210 (2011); J. A. Carr and S. Chaudhary, Energy Environ. Sci. **6**, 3414–3438 (2013).
[13] G. Garcia-Belmonte, P. P. Boix, J. Bisquert, M. Lenes, H. J. Bolink, A. L. Rosa, S. Filippone, and N. Martín, J. Phys. Chem. Lett. **1**, 2566 (2010); A. Sánchez-Díaz, M. Izquierdo, S. Filippone, N. Martin, and E. Palomares, Adv. Funct. Mater. **20**, 2695 (2010).
[14] Z. M. Beiley, E. T. Hoke, R. Noriega, J. Dacuña, G. F. Burkhard, J. A. Bartelt, A. Salleo, M. F. Toney, and M. D. McGehee, Adv. Energy Mater. **1**, 954 (2011).
[15] E. J. Luber and J. M. Buriak, ACS Nano **7**(6), 4708 (2013).
[16] N. D. Treat, M. A. Brady, G. Smith, M. F. Toney, E. J. Kramer, C. J. Hawker, and M. L. Chabinyc, Adv. Energy Mater. **1**(1), 82 (2011); H. W. Ro, B. Akgun, B. T. O'Connor, M. Hammond, R. J. Kline, C. R. Snyder, S. K. Satija, A. L. Ayzner, M. F. Toney, C. L. Soles, and D. M. DeLongchamp, Macromolecules **45**(16), 6587 (2012).
[17] A. Guerrero, T. Ripolles-Sanchis, P. P. Boix, and G. Garcia-Belmonte, Org. Electron. **13**(11), 2326 (2012).
[18] P. Vanlaeke, A. Swinnen, I. Haeldermans, G. Vanhoyland, T. Aernouts, D. Cheyns, C. Deibel, J. D'Haen, P. Heremans, J. Poortmans, and J. V. Manca, Sol. Energy Mater. Sol. Cells **90**(14), 2150 (2006); M. Campoy-Quiles, T. Ferenczi, T. Agostinelli, P. G. Etchegoin, Y. Kim, T. D.

Anthopoulos, P. N. Stavrinou, D. D. C. Bradley, and J. Nelson, Nature Mater. **7**(2), 158 (2008).

[19] R. B. Aich, Y. P. Zou, M. Leclerc, and Y. Tao, Org. Electron. **11**(6), 1053 (2010).

[20] P. J. Brown, D. S. Thomas, A. Kohler, J. S. Wilson, J. S. Kim, C. M. Ramsdale, H. Sirringhaus, and R. H. Friend, Phys. Rev. B **67**(6), 064203 (2003).

[21] W. Ma, C. Yang, X. Gong, K. Lee, and A. J Heeger, Adv. Funct. Mater. **15**(10), 1617 (2005); G. Li, V. Shrotriya, J. Huang, Y. Yao, T. Moriarty, K. Emery, and Y. Yang, Nature Mater. **4**(11), 864 (2005).

[22] Z. Liang and B. A. Gregg, Adv. Mater. **24**, 3258 (2012).

[23] F. Fabregat-Santiago, G. Garcia-Belmonte, I. Mora-Sero, and J. Bisquert, Phys. Chem. Chem. Phys. **13**(20), 9083 (2011).

[24] A. Guerrero, P. P. Boix, L. F. Marchesi, T. Ripolles-Sanchis, E. C. Pereira, and G. Garcia-Belmonte, Sol. Energy Mater. Sol. Cells **100**, 185 (2012); O. V. Kozlov and S. A. Zapunidi, Synth. Met. **169**, 48 (2013).

[25] M. C. Scharber, D. Mühlbacher, M. Koppe, P. Denk, C. Waldauf, A. J. Heeger, and C. J. Brabec, Adv. Mater. (Weinheim, Germany) **18**(6), 789 (2006).

[26] H. Aarnio, P. Sehati, S. Braun, M. Nyman, M. P. de Jong, M. Fahlman, and R. Österbacka, Adv. Energy Mater. **1**, 792 (2011).

[27] E. Verploegen, R. Mondal, C. J. Bettinger, S. Sok, M. F. Toney, and Z. Bao, Adv. Funct. Mater. **20**, 3519 (2010).

[28] K. Akaike, K. Kanai, Y. Ouchi, and K. Seki, Chem. Phys. **415**, 31 (2013).

[29] See supplementary material at http://dx.doi.org/10.1063/1.4841475 for experimental details, XRD data, and Mott-Schottky analysis.